[Cp*Rh] Monohydrides Supported by Diphosphine Ligands: Synthesis, Characterization, and Multifrequency Nuclear Magnetic Resonance Studies

By
© 2021
Chelsea Grindstaff Comadoll
B.S., Appalachian State University, Boone, North Carolina, 2017

Submitted to the graduate degree program in Chemistry and the Graduate Faculty of the University of Kansas in partial fulfillment of the requirements for the degree Doctor of Philosophy.

_____
Chair: Prof. James D. Blakemore

_____
Prof. Mikhail V. Barybin

_____
Prof. Helena Malinakova

_____
Prof. Aaron Teator

_____
Prof. Zarko Boskovic

Date Defended: 6 December 2021

The dissertation committee for Chelsea Grindstaff Comadoll certifies that this is the approved version of the following dissertation:

[Cp*Rh] Monohydrides Supported by Diphosphine Ligands: Synthesis, Characterization, and Multifrequency Nuclear Magnetic Resonance Studies

_____

Chair: Prof. James D. Blakemore

Date Approved: 8 December 2021

Abstract

The ability of ligands to influence the stability, spectral properties, and reactivity of transition metal complexes is a broadly well-developed area of inorganic chemistry. Likewise, the importance of developing new methodology for the transformation of small organic molecules is critical to organic chemistry. Part I of this dissertation, consisting of Chapters 1, 2, and 3, contains the core research contributions of this dissertation, performed on the [Cp*Rh] platform. The introduction in Chapter 1 of this dissertation provides a comprehensive overview of the research findings of the Blakemore Group on the [Cp*Rh] system. Chapters 2 and 3 of this dissertation describe the bookend preparative study by our group on this system, including the synthetic, spectral, and reactivity properties of [Cp*Rh] complexes supported by two different diphosphine ligands. This analysis includes multifrequency NMR characterization and digital NMR simulations to probe the rich coupling networks present in two cases. Part II consists of a collection of self-contained projects which were also completed. Chapter 4 describes a catalytic hydrogenation study for a series of heterobimetallic complexes of [Cp*Rh] previously prepared by our group. Chapter 5 describes the development of a new C–N bond-forming transformation which utilizes benzoquinones as mediators for an annulation reaction to generate N-heterocyclic compounds. Chapter 6 describes the preparation of a series of four polypyridyldicarboxylic acids for use in coordination of the uranyl dication; two of these ligands were bipyridyl-based while the other two were terpyridyl-based. Finally, Chapter 7 consists of a collection of preliminary attempts to develop conditions for photoredox asymmetric decarboxylative elimination of carboxylic acid substrates. Taken together, the works described in this dissertation contribute to the areas of organic, organometallic, and *f*-element chemistry.

Acknowledgements

Wow, what a journey this has been. Three different research groups, three unique mentors, three sets of incredible people I have had the immense pleasure of working with in the lab. I will begin with my very first mentor, Dr. Michael Clift. Mike is the reason I came to KU all the way from North Carolina; his research was the most interesting to me at the time I was applying. Meeting him during GROW Weekend and discussing the science together is a major factor that sold me on KU. During my first semester, he taught my Physical Organic 1 course. This is by far, and will forever be, the most challenging yet captivating course I have ever taken, in large part due to Mike's dynamic, exciting, difficult teaching style. His mentoring style was no different. No question was off-limits, his door was always open, and none of us questioned if he cared about us. He gave me excellent foundations in graduate school, as evidenced by the large contribution of our work together in this dissertation despite the limited amount of time we had together. We had great times, we laughed a lot, and we were a family. I still don't truly understand the way things unfolded, but God works all things together for good for His children. Mike's impact on me was lasting; he made me a better student. I would be remiss if I did not also mention former Clift lab members Dr. Xinyun Liu, Dr. Luis Mori-Quiroz, Sidnee Hedrick, and Jon Super (and one to be mentioned later). Each of you played a huge part in my story, and I will forever be grateful for the time that we all had together, though it was brief.

The circumstances that brought me into the lab of Prof. Jon Tunge in 2019 were tumultuous. Even though I did not finish my PhD as a part of his group, I cannot deny the impact that Jon had on my progress, nor will I forget the great times we had as a group. Presenting my work in Wuhan, China along with the Tunge group members is something I

will always remember. Because of his guidance through synthetic methodological processes in the face of repeated failure, I am without question a better synthetic chemist. To Dr. Alex Davies and Ebbin Joseph: Thank you for your unfailing friendship, even today. You both experienced my highs and my lows; Alex spent hour after hour with me hashing over the chemistry on multiple occasions and was always there to help me work through the issues. Ebbin always provided a fresh, new outlook on things; he is perpetually optimistic, and his smile is contagious. You are both incredible men and scientists; I am so grateful for the countless laughs you both have shared with me. My final organic thank-you goes to Shrikant Londhe. We were together from day one in the Clift lab, seemingly inseparable; we went through one of the worst experiences that graduate school can offer together when we had to say goodbye to our mentor and our entire comfort zone. We landed in a new home and persevered. Despite the way things ended up, I will always remember the good times, your support in the turbulence, and your kind heart.

After my trip around the department landing me in Group #3, I have come to the following conclusion: I don't believe there has ever been a research group like the Blakemore lab. These people welcomed me into their (already cramped) space in the middle of very uncertain times, and they did so with open arms. I'll start by thanking the newest member of the Blakemore lab: To Davis "Not Thomas" Curry, thank you for joining our group. While I only got to work alongside you this fall, your passion and drive for knowledge is incredibly inspiring. Hold onto that (and your calendar) through the tough times of graduate school. Thank you to Joe Karnes for your infallible “good morning, Chelsea” greeting every single day and for your incessant dad jokes. You are one of the nicest, most selfless people I have ever met; I am grateful to have had you around, even if you do say "I'm sorry" *way* too often.

Thank you to Riddhi Golwankar, who I had the privilege of working alongside on Radio Row for the last 8 months. Riddhi, you are incredible. I'm a bit jealous of your ongoing borane studies, not going to lie, but it has been awesome watching you grow this project, and yourself in the process. You always take my sarcasm well (and give it back to me occasionally), you're a great leader, and you're always a good sport when I spill my coffee on your desk. You've had a really positive impact on my time here, and I'm so thankful for that.

Thank you to Christian Nilles and Emily Mikeska for becoming two of my best friends over this year and a half. Christian, I will surely miss the conversations we have on a near-daily basis about baseball: How perpetually bad your Twins are and how bad my Braves *were* (until they won the World Series this year!!!). You have become one of my most favorite people. Emily, your contagious laugh when the three of us start ragging on each other is amazing. You are one of the strongest, most inspiring people I have ever met; it has been a privilege to watch you grow as a woman and a researcher. I am grateful for the small role that you both let Meemaw play in your story. Thank you to Dr. Amit Kumar who helped me with organometallic synthesis before I even joined this group; next thing you know, I'm in the group *with you* helping you conclude a catalytic study of those same complexes you helped me prepare elsewhere. You and Riddhi welcomed me into your uranium world, and you even ran my first reaction for me before I was permitted to handle the chemicals. Thank you for your continued contributions to my journey, even all the way from Penn.

A special thank you goes out to Gabe Benitez, the very first undergraduate that I mentored in the lab. I am so grateful that you came to KU for the REU program this summer.

Your inquisitive nature, intelligence, and outstanding work ethic are going to take you so far; they already led to a summer full of success in 2021 (and a publication... don't worry, I'll get it done!). Your future is bright, and you truly impacted mine; thank you for doing such awesome work to contribute to my dissertation and for your continued friendship to this day.

I offer up a tremendous thank you to Wade Henke. You are one of the most kind, patient, innovative people I have had the privilege of crossing paths with in my life. Without you, I would not have completed my rhodium project as quickly as I did upon joining the group, and I surely would not have survived teaching CHEM 661 for the first time without your help. I cannot thank you enough for all of this. I have learned so much from you and truly admire you; you are an incredible chemist with a brilliant mind, and I hope our paths cross again on the other side of graduate school.

And to my best friend from the very beginning, Julie Hopkins Leseberg: You are such a rockstar. I knew it from day one, of course, but being in this lab with you over the last year and a half has shown me what a gifted inorganic chemist you truly are. Thank you for the role you played in keeping me in the department last summer and bringing me into the Blakemore lab; you and Wade contributed equally in the success of my first project and all of my success from then on, and I am so grateful to you for your patience and guidance during that transition. On a more personal note, thank you for always supporting, encouraging, and loving me so well. We have talked, laughed, eyerolled, and prayed each other through a lot of life things since we were first years here. Thank you for being the witness in my courthouse wedding after just meeting me (ha!) and for having me be a part of your wedding, too. You and Ryley are two people that Lucas and I cherish so much – our

sweet “married friends” – and I am grateful for the time we all had here together. God truly had a hand in our friendship, and I know that He will do amazing things through you.

Additionally, I would like to thank a few more folks. To my dissertation committee, I offer my most sincere thanks for your time and dedication to me, my dissertation, and my progress in this department. Thank you to Dr. Ember Krech, whom I had the pleasure of meeting through Julie; over the time that you have been in my life, you have impacted my PhD journey and my spiritual walk so much. Thank you for always putting things into perspective for me and for always pointing me back to Christ when life gets chaotic. Thank you to Jonah Stiel, Emma Cosner, and Claire Dopp for restoring my faith in the scientific abilities of undergraduate students. You three are each a force to be reckoned with; I cannot wait to see what incredible things you will do after your time at KU is complete. Thank you to Dr. David Benson and Dr. Marina Rubin, whom I had the privilege of working closely with for 3.5 years as their GTA. You both are incredible educators who acknowledged my dedication and passion for teaching and rewarded it at the Department level; I am grateful for your support. Thank you to both Prof. Bob Dunn and Megan Belaire, who never failed to support me through some really difficult times over the last two years. You are both pivotal in my success; without the two of you, I don't know that I would've finished this degree.

I would be remiss if I did not thank some folks back home who helped get me to this point. Thank you to my in-laws, Chip and Kari Comadoll, who have supported me and Lucas endlessly. All of our home-improvement endeavors have provided me with some of my most cherished memories; I love both of you lots. (I'm still waiting for my watch, Chip.) Thank you to all of my grandparents, aunts, uncles, and cousins who prayed for me through this

process. Thank you to my church family back home, Eddy and Von Bunton in particular, who supported and prayed for me and Lucas in the good and bad times. Thank you to my former ASU professor and fellow Jayhawk, Dr. Megen Culpepper; without your recommendation to apply to KU, I wouldn't have ever considered graduate school here. Thank you to my former ASU professors Dr. BJ Yoblinski and Dr. Carol Babyak for always believing in me and playing a huge role, even today, in my story.

Thank you to my advisors from ASU, Dr. Michael Ramey and Dr. Nicholas Shaw. I didn't think I would graduate from ASU and remain in close contact with either of you, honestly, but I am so thankful that we are close friends five years later. Thank you both for bringing me back to ASU not once, but twice, to present my graduate work there. You both have guided me through some of the most extreme lows that graduate school can offer; without both of you, I wouldn't have pursued or even *finished* graduate school. All I ever wanted to do was make the two of you proud; I hope I've done that. Ramey, you've got one of the most diverse senses of humor that I have ever come across; you're genuine and irreverent, and you never forget anything at all, but you have never stopped supporting me. Shaw, you have played a huge part in my time at KU. Even though you initially did not take me into your research group back in the day (now your mistake is in print forever!), we somehow still managed to work together anyway. I may have left ASU, but you never stopped being a mentor, advisor, and friend to me; thank you for always answering when I call and for loving me and Lucas.

Thank you to my parents Tina and Barry Grindstaff, my brothers Chandler and Chad, and my sister-in-law Taylor for your love, support, and prayer. Mom and Dad, you raised one resilient daughter. Thank you for your sacrifices, your provision, your choice not to

disown me during my horrible teenage years, and your love that you have poured out on me for 27 years. Every bit of my success in this life is owed to you. Chandler and Chad, you goons are two of my best friends. Thank you for being the best brothers anyone could ever ask for. Taylor, it is such a blessing to have had you in this family for over 4 years now. I have thoroughly enjoyed walking through graduate school at the same time as you (okay, "enjoyed" may not be right word...). Either way, I can't wait to celebrate our graduations together in the spring just like we did in 2017. One of the hardest things I have ever had to do was leave North Carolina and all of you in the rearview mirror as I chased this degree, but you all have done your best to ensure that I never felt too far away. Thank God for FaceTime. I love each of you so much.

Last but certainly not least, I offer the most sincere, heartfelt thank you to my advisor, Prof. James Blakemore. It is neither understatement nor exaggeration when I say that I would have no dissertation to write and defend if not for you. I would no longer love chemistry if not for you. I would have no confidence in my knowledge or abilities in this field if not for you. When I distraughtly told you last summer that I was mastering out (or leaving outright with nothing if it came down to it), you told me the following, which I will never, ever forget: “I took this job to help students, and you need help. So, I’m going to help you.” You didn't have to do this for me, but I am so grateful that you did. God works all things together for good for His children. Two incredibly tough transitions in this department and some bad luck in the lab left me miserable, drained, lethargic, and looking for the exit door of this program, but I landed right where I was supposed to be. God used you through all of it to change my trajectory in the face of incredible difficulty, simply because you saw the opportunity to help me, and you took it. I am proud of the work I have done – the whole

body of work, not just the positives – because you reminded me every day that I am a great chemist, and that I was capable of finishing this degree as a member of your group. Thank you for believing in me, for seeing my potential, and for pouring into my life over these two years. You have been a blessing.

Dedication

I dedicate this dissertation to my husband, Lucas. He has been my rock, my person, my crying shoulder, and my very best friend through all of this. He did more than his fair share of laundry, dishes, and cooking over the last five years when I was too tired or too busy from the events of the day. He willingly loaded up his life into a U-Haul and moved across the country for me. I have said this a lot already, but truly, I would not have finished this degree without you, Lucas. It's easy to support someone in the good times; when papers are published, when the chemistry is working, and when the work atmosphere is good, it's not hard to be a great spouse. But no one sees the efforts of a spouse behind the scenes; you were consistent in the good times and the bad. You perfectly played the critical role in the absolutely miserable times of holding me together, reminding me why we came here, and telling me, "No, we can't go home yet" every time I really wanted to quit. When I was utterly unlovable along this journey, you loved me anyway. You strengthened me, prayed for me and with me, and never let a day go by without telling me how proud you are of me. Thank you for being everything that I needed, and a lot of things that I didn't even know I needed. I couldn't have done this without you. I love you so much.

Table of Contents

Part I 1

Chapter 1: Introduction to [Cp*Rh] Monohydride Complexes Supported by Imine and Phosphine Chelating Ligands 2

1.1 An Overview of Chapter Content 3

1.2 A Review of the Blakemore Group Contributions to the Area of [Cp*Rh] Complexes 6

1.3 References 78

Chapter 2: Examining the Modular Synthesis of [Cp*Rh] Monohydrides Supported by Chelating Diphosphine Ligands 83

2.1 Introduction 84

2.2 Results and Discussion 87

2.3 Conclusion 98

2.4 Experimental Details 99

2.5 Acknowledgements 105

2.6 References 107

Chapter 3: On the Advanced NMR Characterization of [Cp*Rh] Complexes of Bis(diphenylphosphino)methane 115

3.1 Introduction 116

3.2 Results and Discussion 121

3.3 Conclusion 131

3.4 Experimental Details 132

3.5 Acknowledgements 134

3.6 References 136

Part II 138

Chapter 4: On the Catalytic Activity of Heterobimetallic Group 9 Metal Complexes toward Hydrogenation of Aldehyde Compounds 139

4.1 Introduction 140

4.2 Results and Discussion 144

4.3 Conclusion 154

4.4 Experimental Details 155

4.5 Acknowledgements 157

4.6 References 158

Chapter 5: Exploiting Iminoquinones as Electrophilic at Nitrogen "N+" Synthons for C–N Bond Construction 166

5.1 Introduction 167

5.2 Results and Discussion 169

5.3 Conclusion 176

5.4 Experimental Details 177

5.5 Acknowledgements 184

5.6 References 186

Chapter 6: Coordination and Redox Chemistry of Uranyl Complexes Supported by Proton-Responsive Bipyridyl and Terpyridyl Ligands 194

6.1 Introduction 195

6.2 Results and Discussion 201

6.3 Conclusion 212

6.4 Experimental Details 213

6.5 Acknowledgements 220

6.6 References 221

Chapter 7: On the Photoredox/Cobalt Dual-Catalytic Decarboxylative Transformations of Carboxylic Acids 226

7.1 Introduction 227

7.2 Results and Discussion 231

7.3 Conclusion 242

7.4 Experimental Details 243

7.5 Acknowledgements 247

7.6 References 248

Chapter 8: Summary and Future Outlook 250

Appendix A: Supplementary Information for Chapter 2 255

Appendix B: Supplementary Information for Chapter 5 314

When I consider the multitude of associated forces which are diffused through nature – when I think of that calm balancing of their energies which enables those most powerful in themselves, most destructive to the world's creatures and economy, to dwell associated together and be made subservient to the wants of creation, I rise from the contemplation more than ever impressed with the wisdom, the beneficence, and grandeur, beyond our language to express, of the Great Disposer of us all.

The book of nature, which we have to read, is written by the finger of God.

– Michael Faraday

19th Century Chemist and Physicist

Part I

Chapter 1

Introduction to [Cp*Rh] Monohydride Complexes Supported by Imine and Phosphine Chelating Ligands

"As you navigate through the rest of your life, be open to collaboration. Other people and other people's ideas are often better than your own. Find a group of people who challenge and inspire you, spend a lot of time with them, and it will change your life." -Amy Poehler

1.1 An Overview of Chapter Content

Collaborative work in the sciences is an invaluable part of the research process. When facing a research question that needs to be answered, an organic chemist and an inorganic chemist will undoubtedly approach the question differently, finding distinct solutions to the problem at hand. The approach of one will complement that of the other; just as iron sharpens iron, so one area of expertise sharpens another in this field. Inasmuch as specializing in one given area of chemistry is important, equally important is the ability to understand and apply the concepts of multiple disciplines to a given research objective. The principles of organic chemistry complement those of inorganic chemistry such that a thorough understanding of both fields enables one to be inventive in problem solving, experimental design, data interpretation, and writing. As such, this dissertation as a unit focuses on two major disciplines of chemistry; its message rests at the crossroads of organic and inorganic chemistry, with the uniting factor between both being synthesis.

Part I of this dissertation, including both Chapters 2 and 3 and this introductory chapter, describes a study of the synthesis, characterization, and chemical properties of a series of [Cp*Rh] monohydride complexes (Cp* = pentamethylcyclopentadienyl) supported by chelating diphosphine ligands.[1] These monohydrides are an important class of compounds in organometallic chemistry, as metal hydrides are often invoked as key intermediates in catalytic cycles despite the fact that they are poorly characterized and rarely observed, particularly in the [Cp*Rh] class of compounds. The study presented in these

chapters presents a reliable reduction/protonation synthetic pathway to access the hydrides with different diphosphine ligands; a detailed characterization of these complexes including X-ray diffraction studies, multifrequency nuclear magnetic resonance (NMR) experiments, and digital NMR simulations; and an investigation into the propensity of these monohydride complexes to evolve H_2 in the presence of strong acids. Publication of this study was one of the most recent synthetic contributions of the Blakemore Group to the field of [Cp*Rh] complexes; a more in-depth view of our contributions to this area of organometallic chemistry will be presented in Section 1.2 (*vide infra*).

Building off the core set of results and the methods used to obtain them in Part I, Part II describes the findings from research extensions and self-contained projects also pursued during my doctoral studies. Chapter 4 describes the catalytic hydrogenation experiments that were conducted on a series of mono- and heterobimetallic complexes previously synthesized by our group.[2] The heterobimetallic complex involved in this study consists of the same [Cp*Rh] core described in Chapters 2 and 3 of this dissertation; as the propensity of rhodium to act as a hydrogenation catalyst is well-documented in the literature, the driving force behind the study was to probe the effects that the secondary, proximal cobalt had on the rhodium and, thereby, how the heterobimetallic complex behaved as a hydrogenation catalyst. The study was carried out utilizing NMR analysis, observing conversion of the benzaldehyde precursor to the benzyl alcohol, and quantifying the amounts using an internal standard at various timepoints. Additionally, the presence of a transient metal hydride was observed in the spectral data upon addition of hydrogen to the reaction vessel.

In Chapter 5 of this dissertation, we cross over from organometallic chemistry into traditional synthetic organic methodology. The chemistry described in this chapter from

work done in the Clift Group in 2018 involves the use of stoichiometric benzoquinone compounds as mediators for a newly developed annulation methodology, furnishing indoles and pyrroles from *ortho*-vinyl anilines and homoallylic amines, respectively.[3] The reaction is initiated through an imine condensation to give the isolable iminoquinone compounds; in the presence of catalytic acid, these iminoquinones further react, undergoing what is thought to be an aromative electrocyclization to provide the N-arylindole or N-arylpyrrole compounds. Conditions for oxidative dearylation were developed to provide the free indole or pyrrole compound and return the benzoquinone. Because C–N bond-forming reactions are critical in applications to drug discovery and natural product synthesis, the methodology could have larger, broader impacts to these industries as a result of our contributions to the field.

Chapter 6 of this dissertation focuses on the synthesis of a series of polypyridyldicarboxylic acid compounds to be used as ligands in the coordination of the uranyl dication. This class of ligands was targeted due to its broad use and success in the field of water oxidation; these ligands are widely utilized in ruthenium-based catalysts in the oxidation of water. Four different ligands were synthesized and subsequently used to prepare coordination complexes of the uranyl dication. While most of our efforts toward characterization were curtailed by low solubility of these complexes, a modest electrochemical study was conducted on the bipyridyldicarboxylato complexes. The ligand system proved to be a suitable chelator for the uranyl dication; future efforts to derivatize the ligand to encourage better solubility would be a worthy endeavor.

Finally, Chapter 7 of this dissertation describes a preliminary study on the preparation of two new cobaloxime complexes and two known diiminedioximato

cobaloxime complexes and their subsequent employment in asymmetric decarboxylative elimination methodology. This work conducted in the Tunge Group in 2020 was inspired by the dual-catalytic photoredox decarboxylative elimination developed by this group in 2020.[4] In this work, we demonstrated that cobaloxime complexes and acridinium photosensitizers can work in concert to enact the catalytic, decarboxylative elimination of feedstock carboxylic and amino acids to furnish alkenes and enamine derivatives, respectively. The attempts to make the transformation asymmetric involved ligand modifications to the cobalt metal catalyst; those newly prepared complexes were tested for their propensity in the chemistry.

1.2 A Review of the Blakemore Group Contributions to the Area of [Cp*Rh] Chemistry

The research foundations of the Blakemore Group were built on the study of [Cp*Rh] complexes. The motivation for these contributions is based in the original work by Kölle and Grätzel from 1987, in which they studied the reduction and subsequent hydrogen evolution properties of [Cp*Rh] complexes ligated by a series of bipyridyl ligands.[5] They found that the complexes were able to evolve hydrogen upon irradiation in the presence of TiO_2 and a catalytic proton source under acidic conditions. Since the discovery of this catalytic application, the [Cp*Rh] system has been utilized widely in the design of hydrogen-evolving catalysts; notably, complexes of [Cp*Rh] have been used as catalysts in the conversion of $NAD(P)^+$ to NAD(P)H, a transformation relevant to the development of bioelectrocatalytic fuel cells.[6] On the basis of this pioneering work by Kölle and Grätzel, questions about the

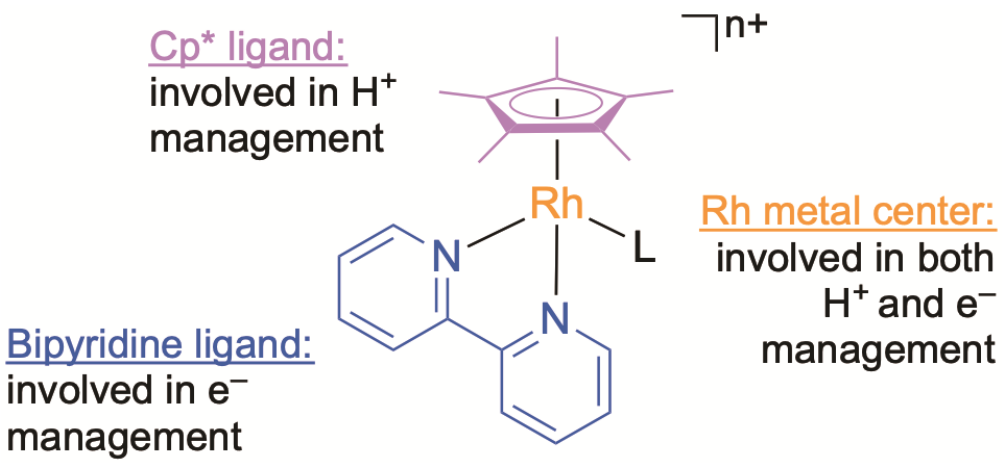

Figure 1.1. Model system of $[Cp^*Rh(bpy)(L)]^{n+}$ for structure-function studies demonstrating the role of each component in a transformation.

mechanism through which the catalytic evolution of hydrogen proceeded were asked. Many hypothesized mediation by a transient rhodium hydride complex which, upon protonolysis, would give off hydrogen; despite the fact that Kölle and Grätzel did not observe this species, this was the widely accepted hypothetical mechanism of the transformation for decades. Contributions have since been made by our group and others which have added to the understanding of this mechanistic pathway (*vide infra*). Nonetheless, our understanding of the mechanistic pathway is still limited; a better understanding of the process would allow for the development of better, more sustainable catalysts for wider applications. As a result, the Blakemore Group has endeavored over the last six years to design complexes of [Cp*Rh] which would allow for the picking-apart of the system through characterization, experimentation, and mechanistic studies.

The $18e^-$ model complex $[Cp^*Rh(bpy)(L)]^+$ (shown in Figure 1.1) consists of a rhodium metal center, the η^5-Cp* ligand, a bidentate chelating ligand of some kind (shown is **bpy**), and an auxiliary ligand (typically halide or solvent molecule). The process of

hydrogen evolution relies in part on the process of proton reduction; as such, these reactions require effective management of protons and electrons, for which it utilizes a particular ligand for a particular task. The Cp* ligand, while widely considered an inert ligand in many transition metal complexes, is actively involved in the proton reduction process. The formation of Cp*H by reaction of the reduced complex supported by **bpy** signifies the role of Cp* as being involved in proton management within the cycle (*vide infra*). Additionally, the **bpy** ligand is redox non-innocent; the extensive π-system is capable of being reduced and therefore is involved in electron management. The rhodium metal center is likewise involved in both proton and electron management, as reduction of the metal center is a key step in many catalytic mechanistic pathways. The stability of that reduced metal center influences both the reduction of the bidentate ligand and the location of the hydrogen atom upon protonation.

The early members of the Blakemore Group first hypothesized that altering the bidentate chelating ligand might tune the properties of the complex such that insight could be gained into the identity of intermediates along the pathway which leads to formation of the Cp*H intermediate; such insight would provide new strategies for catalyst design utilizing the [Cp*Rh] manifold. As such, over the last 6 years, the Blakemore Group has prepared, isolated, and characterized a library of [Cp*Rh] compounds with varied bidentate chelating ligands. The complexes shown in Chart 1.1, with exception of the first two entries, are the Rh(III) chloride precursors which were further derivatized and analyzed in each study. The ligands targeted consist of diimine, phosphine, and hybrid imine/phosphine chelators; we have shown that the identity of the ligand drastically modulates the electronics and reactivity of each complex (*vide infra*). The discussion of each complex and its

derivatives that we have prepared will be sorted by functional group; the diimine ligand complexes will be discussed, followed by the phosphine/imine hybrid ligand complexes, and finally the phosphine ligand complexes. The spectroscopic analysis, X-ray diffraction studies, electrochemical analysis, and reactivity studies of these complexes and their derivatives have provided new knowledge generously to the field, aiding in the understanding of this mechanistic pathway and the development of new catalysts for hydrogen evolution and similar processes.

Chart 1.1. The Collection of [Cp*Rh] Complexes Prepared and Characterized by the Blakemore Group.

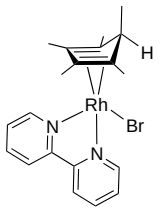

Peng et al.
2016

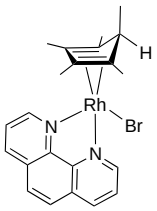

Peng et al.
2016

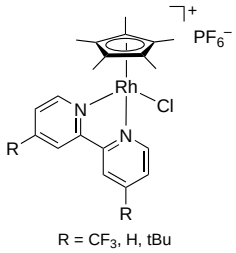

Henke et al.
2017

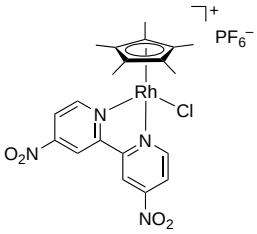

Moore et al.
2018

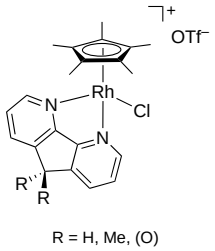

Henke et al.
2021

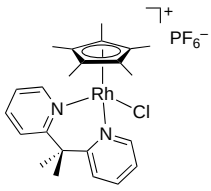

Lionetti et al.
2017

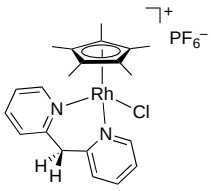

Lionetti et al.
2019

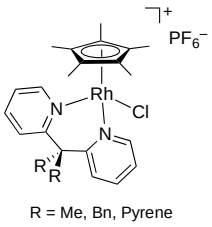

Hopkins et al.
2021

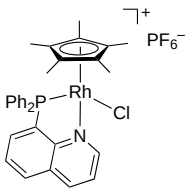

Hopkins et al.
2019

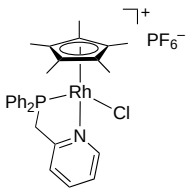

Hopkins et al.
2020

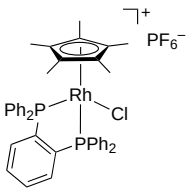

Boyd et al.
2019

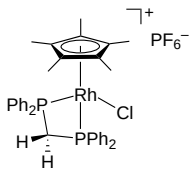

Comadoll et al.
2021

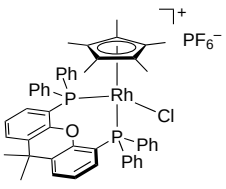

Comadoll et al.
2021

1.2.1 Preparation, Characterization, and Hydrogen Evolution Capabilities of [Cp*Rh] Phenanthroline Complexes

Our initial studies of [Cp*Rh] complexes began in 2016 when Peng et al.[7] reported the preparation of the [Cp*Rh] complex ligated by 1,10-phenanthroline (**phen**) in which the metal center is formally Rh(I) (**Cp*Rh(phen)**, see Scheme 1.1). Upon treatment of both **Cp*Rh(bpy)** and **Cp*Rh(phen)** with triethylammonium bromide, the resulting Cp*H complexes were prepared and isolated from both reactions. ^{1}H NMR spectral data of **(Cp*H)Rh(phen)(Br)** confirmed the formation of the Cp*H complex; additionally, X-ray crystallographic data showed the presence of an explicit Rh–Br bond, giving an overall neutral complex (see Figure 1.2, Right). The *endo* characterization was used to describe this complex on the basis of these X-ray diffraction studies due to the downward-facing orientation of the proton directly bound to the Cp* ring relative to the rhodium metal center.

The crystallographic data reveal some notable characteristics about the bonding in both systems, including the propensity of the diimine ligand to participate in electron management. In **Cp*Rh(phen)**, the C5–C6 distance (see Figure 1.2) is remarkably shorter than that of its cationic Rh(III)–Cl precursor (2.006(3), 2.004(2) Å in **Cp*Rh*(phen)** vs. 2.121(2), 2.100 Å in the chloride precursor). This shortening of the interpyridine bond has been observed in **bpy**-ligated systems upon reduction of the ligand,[8] such that the accessible π* orbitals of **bpy** are able to mix with those of the metal to populate those orbitals with an electron. This is the same phenomenon giving rise to the shortened C5–C6 distance in **Cp*Rh(phen)**;[9] upon reduction from Rh(III) to Rh(I), a population of electrons in π* occurs,

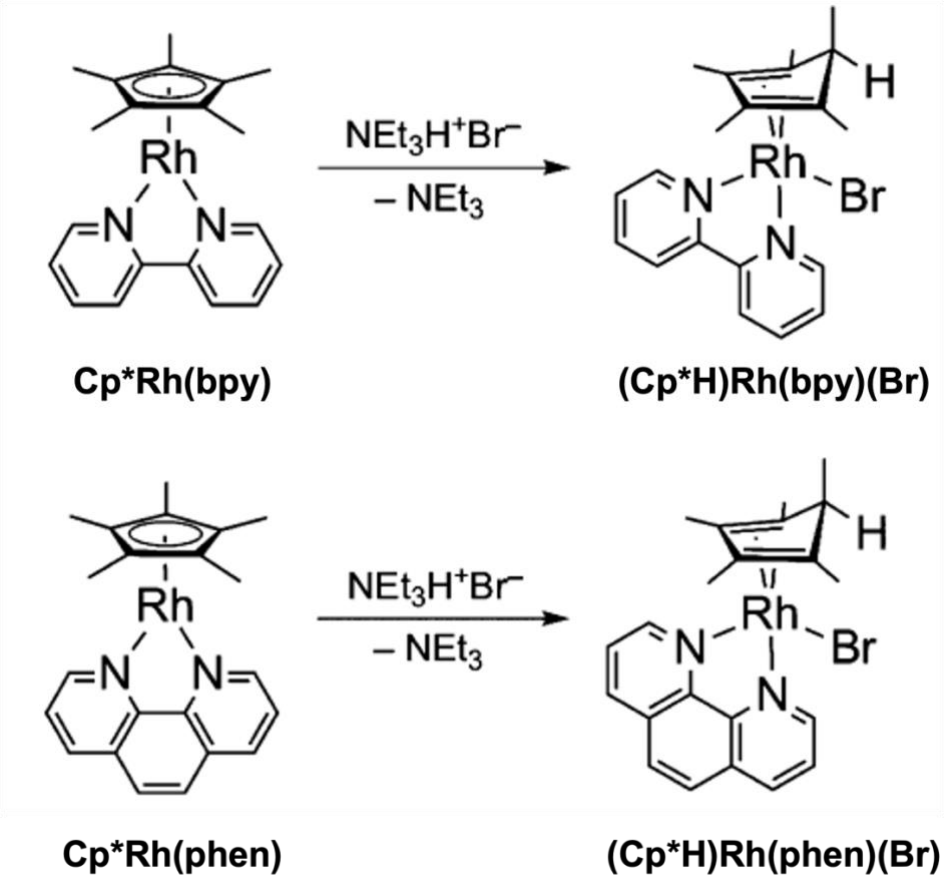

Scheme 1.1. Preparation of **(Cp*H)Rh(bpy)(Br)** and **(Cp*H)Rh(phen)(Br)** using triethylammonium bromide ($NEt_3H^+Br^-$). Adapted with permission from Peng, Y.; Ramos-Garcés, M. V.; Lionetti, D.; Blakemore, J. D., Structural and Electrochemical Consequences of [Cp*] Ligand Protonation. *Inorg. Chem.* **2017**, *56*, 10824-10831. Copyright 2017 American Chemical Society.

increasing the bond order between C5 and C6 and thereby leading to a shorter bond. When comparing **Cp*Rh(phen)** to **(Cp*H)Rh(phen)(Br)**, the characteristics of the Cp* ligand change drastically upon formation of Cp*H. The carbons of the Cp* ligand in **Cp*Rh(phen)** are all relatively identical in terms of their bond lengths; however, protonation of the ligand results in distinct single and double bond character of the C–C bonds in the ring due to

localization of the π electrons and loss of aromaticity. Additionally, the long bond distance between the rhodium metal center and C11 (2.637 Å) indicates no covalent interaction between these two nuclei and also supports pyramidalization of this carbon atom upon protonation. The surprisingly short bond distance between C13 and C14 indicates a

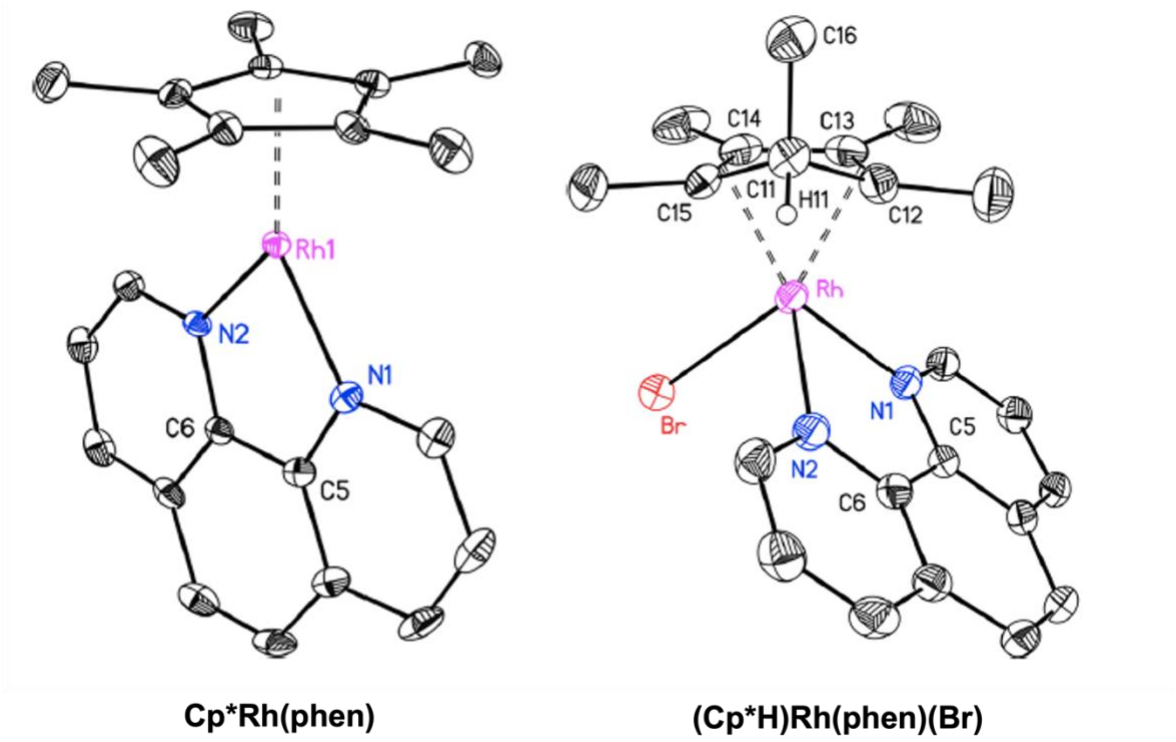

Figure 1.2. Solid-state molecular structure of **Cp*Rh(phen)** (left) and **(Cp*H)Rh(phen)(Br)** (right). Displacement ellipsoids are shown at 50 % probability. Hydrogen atoms except H11 are omitted for clarity. Adapted with permission from Peng, Y.; Ramos-Garcés, M. V.; Lionetti, D.; Blakemore, J. D., Structural and Electrochemical Consequences of [Cp*] Ligand Protonation. *Inorg. Chem.* **2017**, *56*, 10824-10831. Copyright 2017 American Chemical Society.

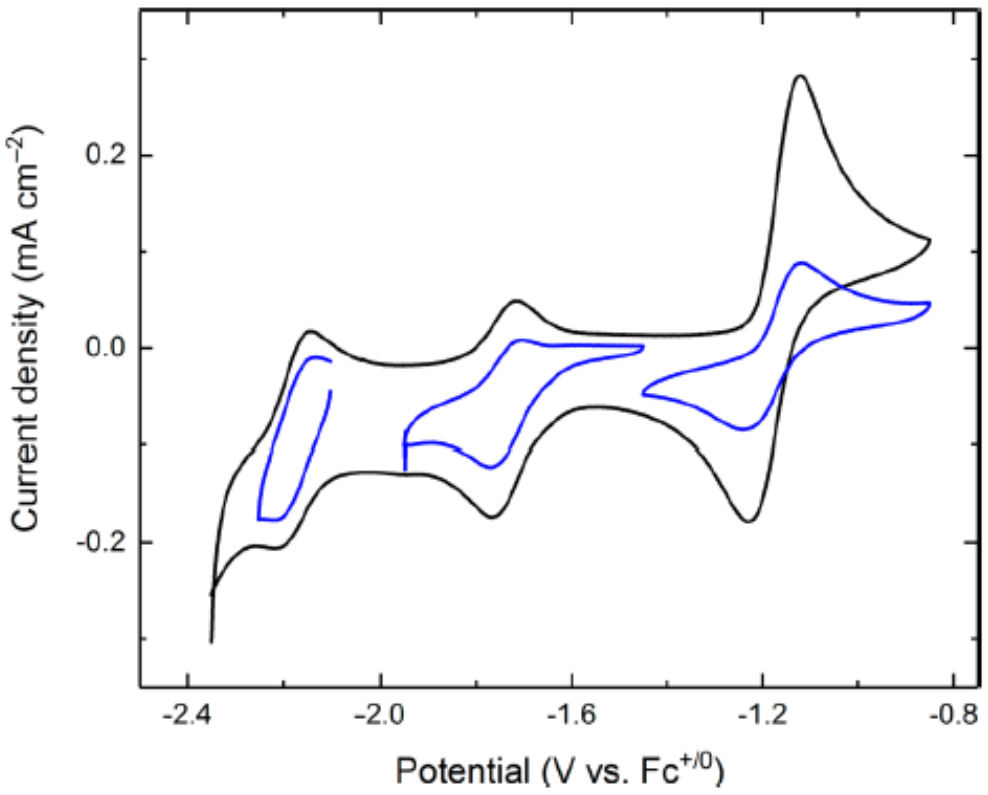

Figure 1.3. Cyclic voltammograms of **(Cp*H)Rh(phen)(Br)** ([1 mM]) in MeCN. Electrolyte = 0.1 M tetrabutylammonium hexafluorophosphate. Scan rate = 100 mV/s. The black trace represents the full scan over a wide potential range. The blue lines represent individual scans at narrow potential ranges. Reprinted with permission from Peng, Y.; Ramos-Garcés, M. V.; Lionetti, D.; Blakemore, J. D., Structural and Electrochemical Consequences of [Cp*] Ligand Protonation. *Inorg. Chem.* **2017**, *56*, 10824-10831. Copyright 2017 American Chemical Society.

population of the lowest unoccupied molecular orbital (LUMO) through π-backdonation; this population results in a shortening of the C13–C14 distance, consistent with reported butadiene ligands in reduced transition metal complexes.[10]

On the basis of electrochemical experiments, it was determined that **Cp*Rh(phen)** displays a $2e^-$ redox event at –0.96 V vs. $Fc^{+/0}$ (all potentials through the remainder of this chapter will be referenced to the ferrocene/ferrocenium couple, $Fc^{+/0}$) corresponding to the oxidation of Rh(I) to Rh(III). Interestingly, the cyclic voltammogram of **(Cp*H)Rh(phen)(Br)** reveals three quasi-reversible, single-electron features centered at –1.17, –1.73, and –2.17 V (see Figure 1.3). The diminished anodic return waves for the two most negative features indicate chemical reactivity of the reduced species; in contrast, an increased anodic return wave for the more positive feature indicates the formation of **Cp*Rh(phen)**. Because of these results, electrochemical generation of H_2 was attempted for both **Cp*Rh(bpy)** and **Cp*Rh(phen)** through bulk electrolysis experiments. Holding the potential of the cell at –1.86 V with **Cp*Rh(bpy)** for 1 hour and analyzing a sample of the headspace via gas chromatography (GC) revealed the formation of H_2 (71 % faradaic efficiency). A similar experiment with **Cp*Rh(phen)** was also shown to generate hydrogen. From this, a new viable pathway for hydrogen generation was proposed below as:

$$2\ \textbf{(Cp*H)Rh(bpy)(Br)} + 2e^- \rightarrow H_2 + 2\ \textbf{Cp*Rh(bpy)} + 2\ Br^-$$

The new reactivity described by Peng, in contrast to the established generation of H_2 by these complexes in the presence of acid, suggests a new reductive route to the generation of hydrogen by these complexes through a different cycle.

1.2.2 Investigation of the Effect of Ligand Substituents on H_2 Generation in the Cp*Rh(bpy) System

In 2017, Henke et al.[11] followed up on the study conducted by Peng by preparing two new [Cp*Rh] complexes supported by disubstituted bipyridyl rings bearing trifluoromethyl (-CF_3) and *tert*-butyl (-tBu) groups in the 4 and 4' positions (^{CF3}**bpy** and ^{tBu}**bpy**, respectively;

see Chart 1.2). These ligands were chosen to probe the effects of electron-withdrawing and -donating substituents, respectively, on the overpotential during the catalysis in comparison to the model complex supported by **bpy**. The cyclic voltammograms of **1-Cl**, **2-Cl**, and **3-Cl** revealed a $2e^-$ couple centered at –1.25 V (electrochemically reversible), –1.21 V (electrochemically irreversible), and –0.97 V (electrochemically irreversible), respectively (see Figure 1.4). The stability of the Rh(I) form of the latter two complexes gives rise to the observed electrochemical irreversibility, as both **bpy** and **^{CF3}bpy** are sufficient to stabilize the Rh(I) form, making reoxidation slower and more difficult. This finding was supported by a Hammett analysis which gave a linear trend with respect to the substituents on the **bpy** ligand; this fit points to the direct effect of the electron-withdrawing or -donating nature of the substituent on the electrochemical data.

Electrochemical experiments on the three complexes in the presence of acid revealed similar trends in the catalytic H_2-generation process for **1-Cl** and **2-Cl**, in that the onset of

Chart 1.2. Precursor Rh(III) chloride compounds prepared in this study.

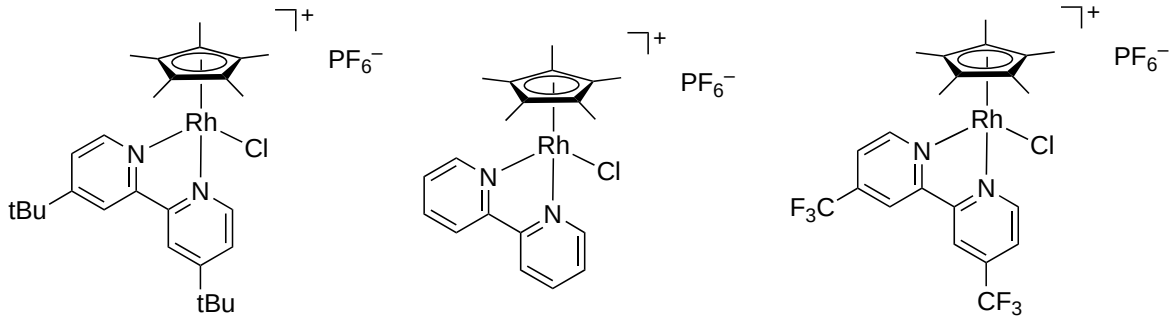

1-Cl **2-Cl** **3-Cl**

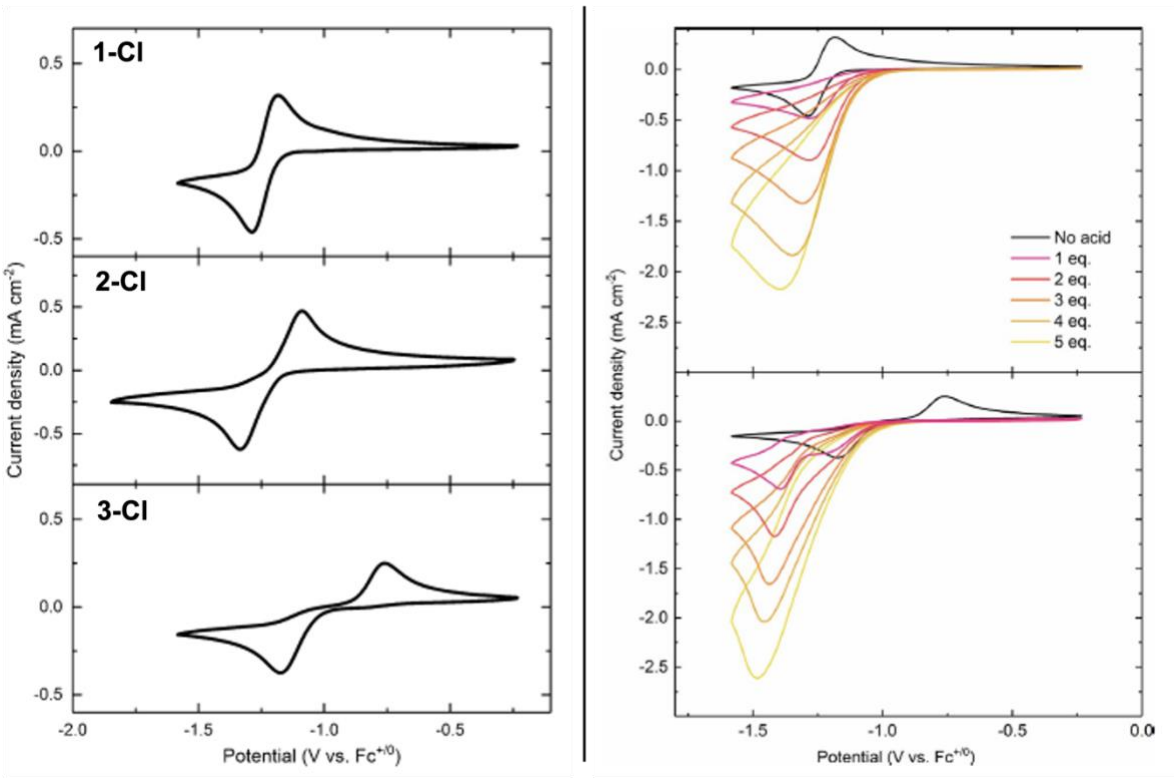

Figure 1.4. Left: Cyclic voltammograms of **1-Cl**, **2-Cl**, and **3-Cl** in MeCN. Electrolyte = 0.1 M tetrabutylammonium hexafluorophosphate. Scan rate = 100 mV/s. Right: Electrochemical response of **1-Cl** and **3-Cl** in the presence of buffered acid solution in MeCN. [Cp*Rh] = 1 mM. Electrolyte = 0.1 M tetrabutylammonium hexafluorophosphate. Scan rate = 100 mV/s. Reprinted[12] (with changed compound names) with permission from Henke, W. C.; Lionetti, D.; Moore, W. N. G.; Hopkins, J. A.; Day, V. W.; Blakemore, J. D., Ligand Substituents Govern the Efficiency and Mechanistic Path of Hydrogen Production with [Cp*Rh] Catalysts. *ChemSusChem* **2017**, *10*, 4589-4598.

an irreversible, catalytic response near the $Rh^{III/I}$ couple was observed (see Figure 1.4). For **3-Cl**, however, two observable waves were observed upon reduction in the presence of acid. This loss of the anodic wave upon addition of 1 equivalent of acid suggests an initial

reduction step to the Rh(I) complex; the second observable wave represents the reduction of a newly formed species in solution, presumably the product of the Rh(I) species reacting with acid. Reduction of this protonated species occurs at –1.45 V; this finding suggests that ^{CF3}**bpy** influences the mechanism by which the catalysis occurs for [Cp*Rh] complexes. Bulk electrolyses of each complex in the presence of 5 equivalents of anilinium triflate at a potential of –1.36 V for 1.5 hours found that all three complexes were suitable catalysts for hydrogen evolution; upon GC analysis of the headspace, **2-Cl** was deemed far superior with a turnover number (TON) of 4.39. The faradaic efficiency of **3-Cl** was far lower than the other two complexes (67 % relative to 90–93 %); this result was attributable to the formation of an off-pathway reduced compound that remains in solution. This compound was determined to be the solvento complex through chemical *in-situ* preparation. The findings of this study give credence to the ligand effects on the performance of the catalyst.

An additional study of substituent effects was conducted by Moore et al.[13] in 2018. Inspired by the intriguing results Henke observed in the ^{CF3}**bpy** system, Moore set out to interrogate even more drastic electron-withdrawing effects of the bpy ligand through use of the 4,4'-dinitrobipyridyl ligand (^{NO2}**bpy**). As a noteworthy comparison, the Hammett parameter (σ^-) values of substituents H, CF_3, and NO_2 are equal to 0, 0.65, and 1.27, respectively. In other words, the impact of substituting a hydrogen for a trifluoromethyl group is similar to the impact of substituting a trifluoromethyl group for a nitro group. Also noteworthy is the fact that this complex, [Cp*Rh(^{NO2}bpy)Cl]Cl, had been previously prepared and subjected to electrochemical analysis by Lutz and coworkers;[14] although their study was conducted in a high-throughput robotic electrochemical system, they found in

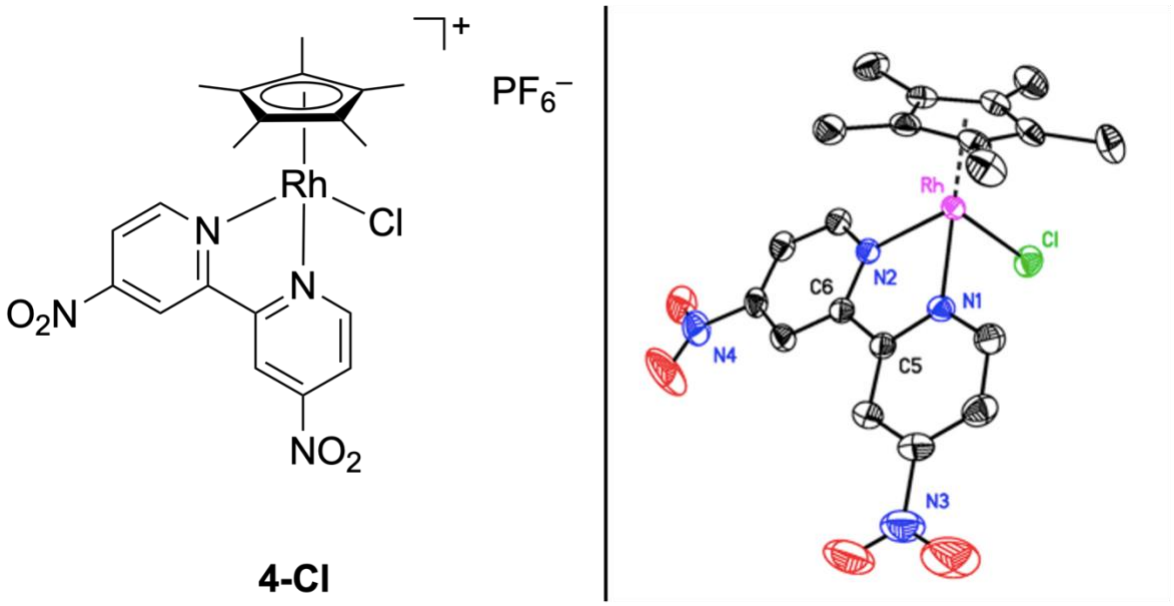

Figure 1.5. Left: Structure of **4-Cl**. Right: Solid-state structure of **4-Cl**. Displacement ellipsoids are shown at 50 % probability. Hydrogen atoms, the hexafluorophosphate counteranion, and one co-crystallized MeCN molecule are omitted for clarity. Solid-state structure reprinted with permission from Moore, W. N. G.; Henke, W. C.; Lionetti, D.; Day, V. W.; Blakemore, J. D., Single-Electron Redox Chemistry on the [Cp*Rh] Platform Enabled by a Nitrated Bipyridyl Ligand. *Molecules* **2018**, *23*, 2857.

aqueous conditions that there were no observable redox events down to –1 V vs. Ag/AgCl. Therefore, the complex [Cp*Rh(^{NO2}bpy)Cl]PF_6 (**4-Cl**, Figure 1.5) was synthesized, isolated, and fully characterized via cyclic voltammetry using organic solvents.

Upon successful preparation of **4-Cl**, X-ray diffraction studies were performed on the complex (see Figure 1.5). While the bond lengths in this complex do not differ drastically from those of **1-Cl** and **3-Cl** analyzed by Henke, this was the first recorded instance of crystallographic information for **^{NO2}bpy** on a rhodium metal center. As one might expect for an aryl nitro group, the O–N–O moiety is essentially coplanar with the pyridine ring in both

cases; this coplanarity is essential for delocalization of the ring electrons. Turning to the electrochemical analysis, the data for this complex upon electrochemical reduction in a THF solution of tetrabutylammonium hexafluorophosphate electrolyte were in stark contrast to the irreversible, $2e^-$ wave observed by Henke with **3-Cl**. Upon reduction, Moore observed four $1e^-$ events whose reversibility was dependent on the switching potential for the return anodic sweep (see Figure 1.6). The dark blue trace shows an experiment run with the switching potential set to –2.2 V; the results of this experiment show three quasi-reversible $1e^-$ reduction events with clean return anodic waves ($E_{1/2}$ = –0.94, –1.44, –1.89 V). The light blue trace, in contrast, shows a fourth reduction event ($E_{p,c}$ = –2.36 V) with an irreversible return anodic wave when the switching potential was set to –2.6 V, indicating that one or more significant chemical reactions occur upon introduction of the fourth electron. The $1e^-$ assignment of each process was confirmed through differential pulse voltammetry studies.

In order to further investigate the nature of these reduction events, the singly reduced Rh(II) complex was prepared by reacting **4-Cl** with $CoCp_2$. Indeed, the ^{1}H NMR data supported formation of the desired complex, as no diamagnetic peaks were present in the spectrum. Electron paramagnetic resonance (EPR) spectroscopy was utilized to further characterize the presumed Rh(II) complex. The results indicated a narrow, isotropic signal with a center crossing point at g = 2.006 (H = 3341 G), pointing toward the presence of an organic radical instead of the expected Rh(II) metal center. Electronic absorption spectroscopy data also point to the presence of a ^{NO2}**bpy**$^{\bullet-}$ in the complex, as the presence of absorption bands in the 800–1000 nm range have been observed for complexes containing **bpy**$^{\bullet-}$ ligands; likewise, Henke observed[11] similar bands for the reduced Rh(I) form of **3-Cl**, in which ^{CF3}**bpy** had significantly reduced character.

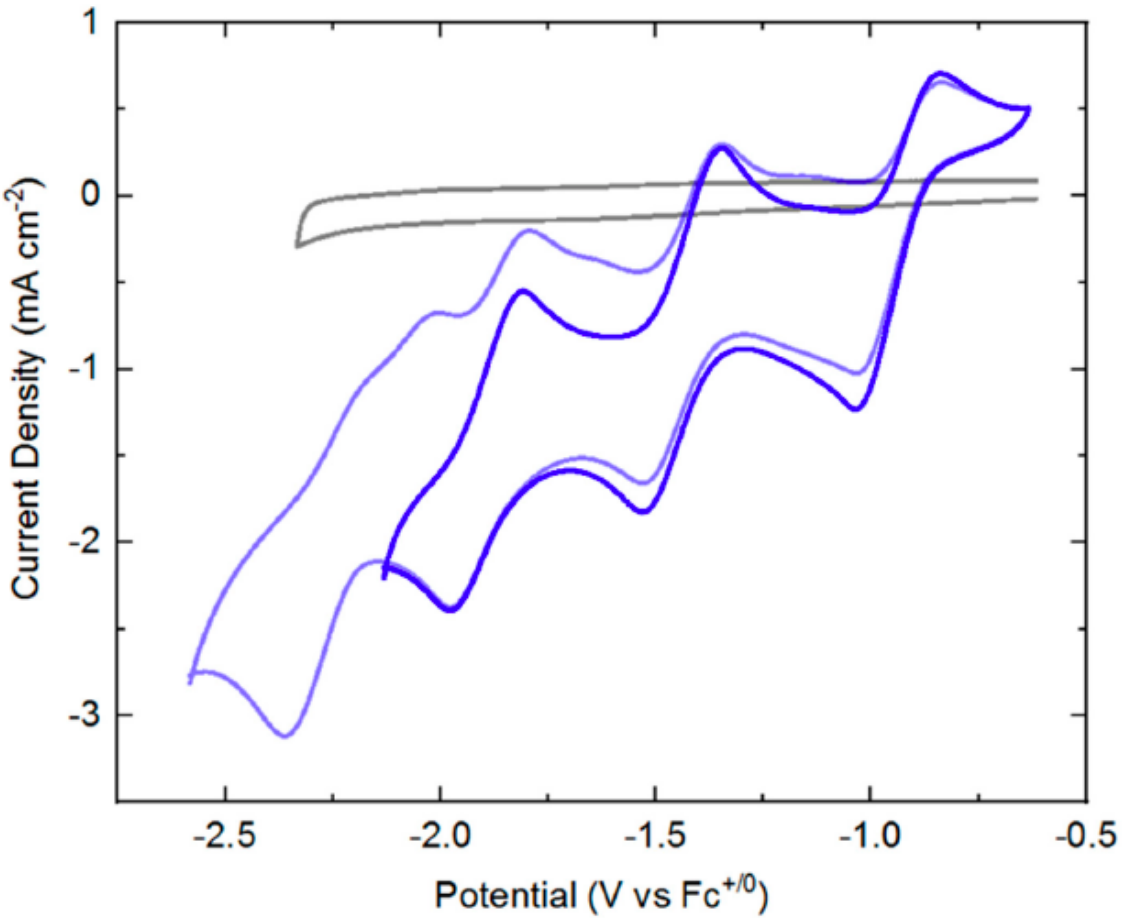

Figure 1.6. Cyclic voltammograms of **4-Cl** in THF (scan rate = 100 mV/s). [**4-Cl**] = 1 mM. Electrolyte = 0.1 M tetrabutylammonium hexafluorophosphate. The dark blue line indicates a cathodic sweep from –0.6 V to –2.2 V to –0.6 V. The light blue line indicates a cathodic sweep from –0.6 V to –2.2 V to –0.6 V. The gray line represents the blank. Reprinted with permission from Moore, W. N. G.; Henke, W. C.; Lionetti, D.; Day, V. W.; Blakemore, J. D., Single-Electron Redox Chemistry on the [Cp*Rh] Platform Enabled by a Nitrated Bipyridyl Ligand. *Molecules* **2018**, *23*, 2857.

Most [Cp*Rh] complexes follow a so-called ECE' process upon reduction: The metal center is reduced by $1e^-$, the chloride ligand is ejected (as the $17e^-$ complex formed by ligand

dissociation is more stable than the 19e$^-$ complex formed upon reduction), and the resulting complex is now favorably reduced by the second electron to give the 18e$^-$ Rh(I) complex. Because this **^{NO2}bpy** complex undergoes an initial ligand reduction event, it does not follow this exact process; therefore, Moore probed whether or not ejection of the chloride ligand still followed the initial reduction event. These cyclic voltammetry experiments were run in acetonitrile (MeCN) with the electrolyte tetrabutylammonium chloride instead of tetrabutylammonium hexafluorophosphate; in these experiments, the observation of the initial ligand reduction was unchanged. However, the second reduction gave the appearance of two cathodic waves instead of one, with only one return anodic wave. This finding led to the conclusion that in the presence of drastic excess chloride (~ 100-fold), the two complexes being formed were the solvento complex [Cp*Rh(^{NO2}bpy$^{\bullet-}$)(NCMe)]PF_6 and the neutral chloride species Cp*Rh(^{NO2}bpy$^{\bullet-}$)Cl. Therefore, in the absence of an excess of chloride (the conditions used in Figure 1.6), the second reduction event after ejection of the chloride leads exclusively to formation of the solvento complex. Subsequent UV-visible spectroelectrochemical experiments were performed and confirmed the clean conversion between all species identified in the electrochemical data through clear isosbestic behavior in the UV-visible spectral data.

Finally, the ability of the complex to generate hydrogen upon reduction in the presence of acid was examined. Cyclic voltammetry experiments of **4-Cl** in the presence of 15 equivalents of buffered Et_3NH^+/Et_3N resulted in the formation of an irreversible wave with a modest increase in current density upon reduction, which was similar to the voltammograms of the complexes studied by Peng and Henke (*vide supra*). Bulk electrolysis experiments were carried out at –1.75 V; according to GC analysis of the headspace, a

faradaic efficiency of only 5 % was observed for the production of H_2, indicating that **4-Cl** is neither an appropriate catalyst nor precatalyst for the generation of hydrogen. NMR analysis of the bulk solution concluded that decomposition of the catalyst occurs upon reduction and protonation. Even though the complex did not evolve hydrogen, the study further supported the ability to drastically tune the properties of a [Cp*Rh] complex upon alteration of the electronics of the ligand.

1.2.3 Analysis of Dipyridylmethane Ligands in the [Cp*Rh] System: Probing the Effects of Disrupting Ligand Conjugation

In 2018, Lionetti et al.[15] prepared a new ligand for the [Cp*Rh] system in which the conjugation between the pyridyl rings of bipyridyl was broken in order to directly investigate the effect of disrupted conjugation in the chelating ligand. This ligand, dimethyldipyridylmethane (**Me$_2$dpma**), brings a coordination environment to the complex similar to **bpy**, such that there is still κ^2-chelation through two pyridine rings; however, this disruption of the extensively conjugated system between the pyridine rings that is present in **bpy** was expected to have drastic effects on the reduction of the complex. It was predicted that a ligand which retains its ability to stabilize the metal center but is no longer capable of participate in strong π-backbonding could drastically alter the reducing power of a metal complex, thereby engendering diverse capabilities of the complex as a catalyst.

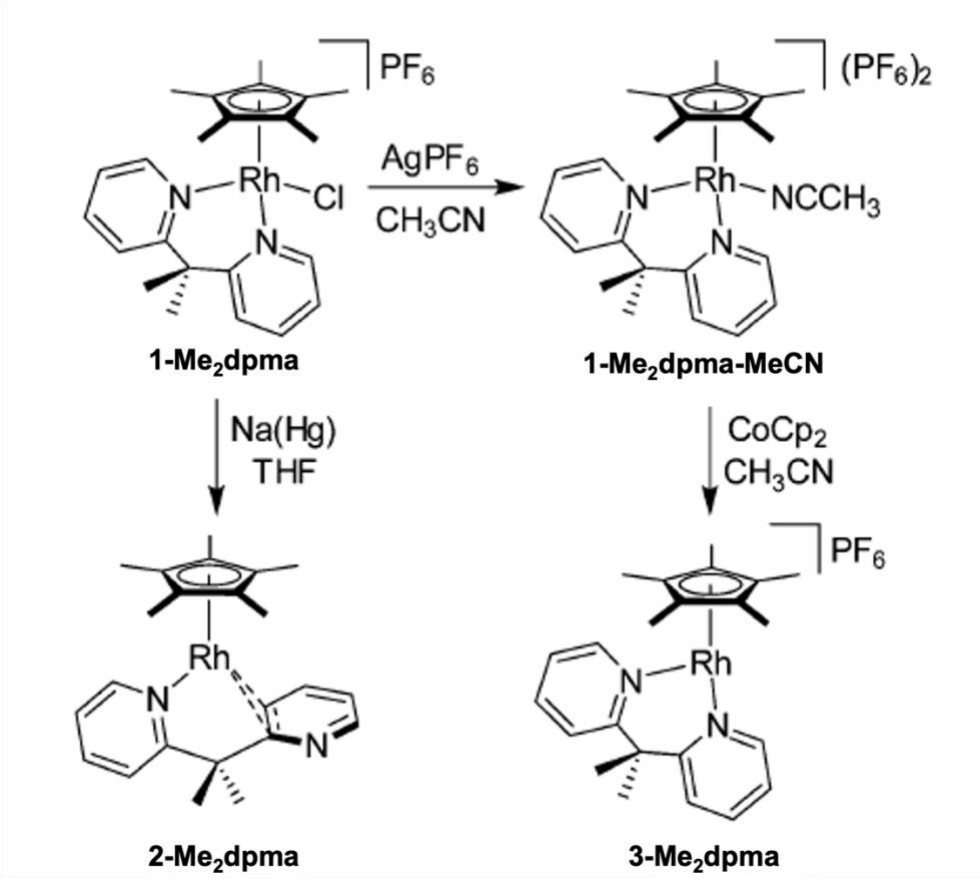

Scheme 1.2. Reactivity of precursor **1-Me$_2$dpma** upon salt metathesis and reduction. Republished with permission of Royal Society of Chemistry, from Multiple binding modes of an unconjugated bis(pyridine) ligand stabilize low-valent [Cp*Rh] complexes, Davide Lionetti, Victor W. Day, Benedikt Lassalle-Kaiser, and James D. Blakemore, volume 54, copyright 2018; permission conveyed through Copyright Clearance Center, Inc.

The complex prepared for this study, **1-Me$_2$dpma**, is shown in Scheme 1.2. To avoid complications from the presence of the chloride in cyclic voltammetry, the solvento complex **1-Me$_2$dpma-MeCN** was prepared and employed in those experiments. The cyclic voltammogram of the solvento complex showed drastically different results as compared to the aforementioned **bpy**- and **phen**-ligated complexes, as expected by the broken

conjugation; instead of a single $2e^-$ event, the data showed two unique $1e^-$ features, indicating the formation of the unusual Rh(II) complex ($Rh^{III/II}$ = –0.85 V; $Rh^{II/I}$ = –1.50 V). The negative shift in the second reduction potential for this complex as compared to that of the $2e^-$ reduction potential in the **bpy**-ligated [Cp*Rh] chloride model system (–1.50 V vs. –1.05 V, respectively) supports the disrupted π-backbonding that was expected for this complex relative to the model **bpy** system.

Inspired by these results, the chemical preparation of both the singly and doubly reduced complexes was performed through use of reductants $CoCp_2$ and sodium amalgam (Na(Hg)), respectively (Scheme 1.2). Characterization of both **2-Me$_2$dpma** and **3-Me$_2$dpma**, as well as precursor **1-Me$_2$dpma**, was achieved by X-ray diffraction studies (see Figure 1.7). While the structure of precursor **1-Me$_2$dpma** is as expected, the solid-state structures of **2-Me$_2$dpma** and **3-Me$_2$dpma** are incredibly surprising. For **2-Me$_2$dpma**, a proton on one of the methyl groups of the ligand exhibits a weak interaction with the rhodium metal center; this interaction results in noticeable distortion of the C–H bond relative to the other two geminal protons of the methyl group (1.18(7) Å vs. 0.94(10), 0.84(7) Å). The implication of this result is that the Rh(II) metal center is noticeably basic; this localized basicity is supported by the fact that the C–C and C–N bond distances of the pyridyl rings do not show drastic distortion relative to **1-Me$_2$dpma**. The solid-state structural data of **3-Me$_2$dpma** reveal a drastic rearrangement, such that one of the pyridyl moieties now interacts with the rhodium metal center facially through its π system in an η^2-fashion. This rearrangement is confirmed by the ^{1}H NMR data which show desymmetrization of the ligand. The bond lengths of the rearranged pyridyl ring (Figure 1.7, bottom) indicate a

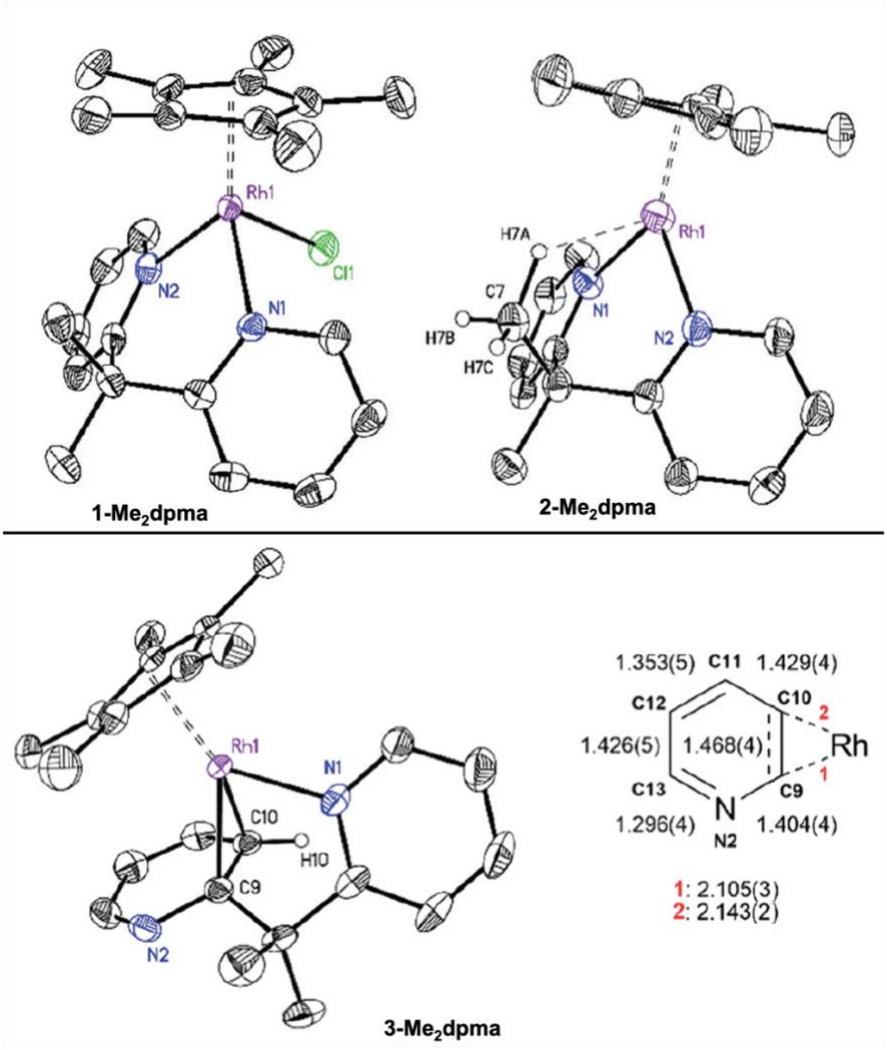

Figure 1.7. Top: Solid-state structures of **1-Me2dpma** and **2-Me2dpma**. Displacement ellipsoids are shown at 50 % probability. Hydrogen atoms except H7A–H7C and the hexafluorophosphate counteranion are omitted for clarity. Bottom: Solid-state structure of **3-Me2dpma**. Displacement ellipsoids are shown at 50 % probability. Hydrogen atoms except H10 are omitted for clarity. Bond lengths for Rh-pyridine interaction are shown. Republished with permission of Royal Society of Chemistry, from Multiple binding modes of an unconjugated bis(pyridine) ligand stabilize low-valent [Cp*Rh] complexes, Davide Lionetti, Victor W. Day, Benedikt Lassalle-Kaiser, and James D. Blakemore, volume 54, copyright 2018; permission conveyed through Copyright Clearance Center, Inc.

strong, dearomative π-backbonding interaction; the C9–C10 distance is significantly elongated, and the other atoms making up the ring display an alternating short bond/long bond pattern indicative of electron localization due to dearomatization.

This difference in behavior induced through the disruption of ligand conjugation was further interrogated in our group by two follow-up studies. In the first by Lionetti et al.,[16] the ligand **Me$_2$dmpa** was swapped out for dipyridylmethane (**dmpa**). This change was done specifically to probe the role of the ancillary methyl groups in stabilizing the Rh(II) form of the complex; by removing these stabilizing 1° methyl protons, it was expected that formation of the Rh(II) might be altered or rerouted. Additionally, interests this ligand were piqued upon finding literature reports in which use of this ligand in complexes of Pt has led to C–H bond activation and hydroarylation reactivity.[17] To this end, the complexes **1-dpma** and **1-dpma-MeCN** were prepared and characterized by ^{1}H NMR and X-ray diffraction studies. Notably, the heterotopic protons methylene protons on the backbone of the **dpma** ligand appeared as two distinct ^{1}H signals in each NMR spectrum, and an absolute assignment for each proton was made through use of Nuclear Overhauser Effect Spectroscopy (NOESY) experiments. This concept of heterotopic methylene protons and their absolute assignment in another [Cp*Rh] system will be discussed in detail in Chapter 3 of this dissertation.

A comparison of the solid-state data of **1-dpma** and **1-dpma-MeCN** relative to that of **1-Me$_2$dpma-MeCN** reveals some unique findings (see Figure 1.8). Because each complex is made up of a 6-membered rhodacycle, the N–Rh–N bite angle of each complex is far larger than that of previously discussed systems systems (**dpma**-analog bite angles range between 85–86° relative to ~76° for that of **bpy** complexes). The consequences of the steric clash of the pendant methyl groups of **1-Me$_2$dpma-MeCN** are evidenced through a

widened angle between the plane defined by the Cp* methyl groups and the plane defined by Rh and the nitrogen donors (67.4, 66.8° relative to 60.5° in **1-dpma**, see Figure 1.8). The steric effect is also observed through changes to the conformation of the rhodacycle. Each rhodacycle adopts a boat-like conformation in which Rh and C6 are pitched upward above the plane created by the four atoms that are coplanar within the rhodacycle. This boat conformation is drastically perturbed according to the substitution on the **dpma** ligand, as shown in Table 1.1. Despite the similar structure and bond connectivity, the subtle differences in the orientation of the rhodacycle are noted here and were considered in subsequent electrochemical experiments.

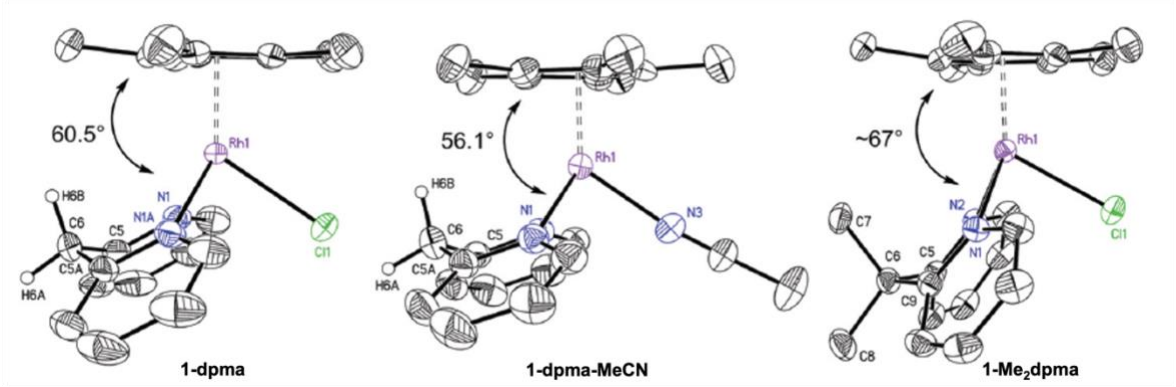

Figure 1.8. Solid-state structures of **1-dpma**, **1-dpma-MeCN**, and **1-Me$_2$dpma**, highlighting the intraplanar angle of each complex. Displacement ellipsoids are shown at 50 % probability. Hydrogen atoms except H6A–H6B and the hexafluorophosphate counteranion are omitted for clarity. Republished with permission of Royal Society of Chemistry, from Structural and chemical properties of half-sandwich rhodium complexes supported by the bis(2-pyridyl)methane ligand, Davide Lionetti, Victor W. Day, and James D. Blakemore, volume 48, copyright 2019; permission conveyed through Copyright Clearance Center, Inc.

Table 1.1. Selected bond parameters of **1-dpma**, **1-dpma-MeCN**, and **1-Me$_2$dpma**. Republished with permission of Royal Society of Chemistry, from Structural and chemical properties of half-sandwich rhodium complexes supported by the bis(2-pyridyl)methane ligand, Davide Lionetti, Victor W. Day, and James D. Blakemore, volume 48, copyright 2019; permission conveyed through Copyright Clearance Center, Inc.

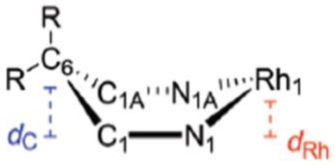

	1-dpma	1-dpma-MeCN	1-Me$_2$dpma
d_C	0.57 Å	0.54 Å	0.64 Å
d_{Rh}	0.79 Å	0.94 Å	0.45 Å

Due to the aforementioned electrochemical issues with the chloride ligand in this system, cyclic voltammetry was conducted on the solvento complex **1-dpma-MeCN**. The first redox event ($Rh^{III/II}$) occurs as a quasi-reversible wave with a reduction potential of –1.10 V which is similar in appearance to that of the wave for **1-Me$_2$dpma-MeCN** ($E_{1/2}$ = –0.85 V) (see Figure 1.9). The drastic negative shift for the unsubstituted **dpma** complex indicates that **1-dpma-MeCN** is a markedly weaker oxidant than **1-Me$_2$dpma-MeCN**; this discrepancy is likely a result of the structural changes discussed from the solid-state data, such that the smaller angle indicated in Figure 1.8 leads to better overlap of the pyridyl donor orbitals and those of the rhodium, resulting in a more electron-rich metal center. While there is no solid-state data available for **1-Me$_2$dpma-MeCN**, Lionetti postulated that such a conformational change would not be possible in the complex due to steric clash of the geminal methyl groups with the Cp* methyl groups; therefore, the conformational changes

have a drastic effect on the electronics of the metal center and, thereby, shift the first reduction event more negative upon removal of the geminal methyl groups. Upon scanning further negative, multiple cathodic and subsequent anodic events are given in the cyclic voltammogram of **1-dpma-MeCN**, a result which is in blatant contrast to that of **1-Me$_2$dpma-MeCN** which showed a subsequent 1e$^-$ quasi-reversible event after the initial reduction. This indicates that severe chemical reactivity occurs upon introduction of a second electron into the system of **1-dpma-MeCN** such that new species are formed in the cell; the fact that these processes did not occur for **1-Me$_2$dpma-MeCN** indicates the importance of the dimethyl backbone in stabilizing the reduced forms of the complex.

Attempts to chemically prepare and isolate the Rh(II) analog of **1-dpma** were unsuccessful, as the NMR revealed a complex mixture of paramagnetic peaks in conjunction with small diamagnetic peaks, which most likely point to degradation of the reduced species. EPR studies were performed on the material instead, as the major component of the complex mixture in the NMR was a paramagnetic species. Intriguingly, the EPR spectral data showed the presence of two paramagnetic complexes. In accord with literature analysis of such complexes, both radicals characterized through EPR were determined to be metal-centered. Without structural data, the exact identity of each structure cannot be determined, but it is likely that both are some Rh(II) species on the basis of the appearance of the EPR signals.

Interestingly, reaction of **1-dpma** with sodium amalgam resulted in a darkened, homogeneous solution, an observation consistent with reduction to Rh(I) species. Concentration of the solution resulted in a purple powder which, by NMR, consisted of a

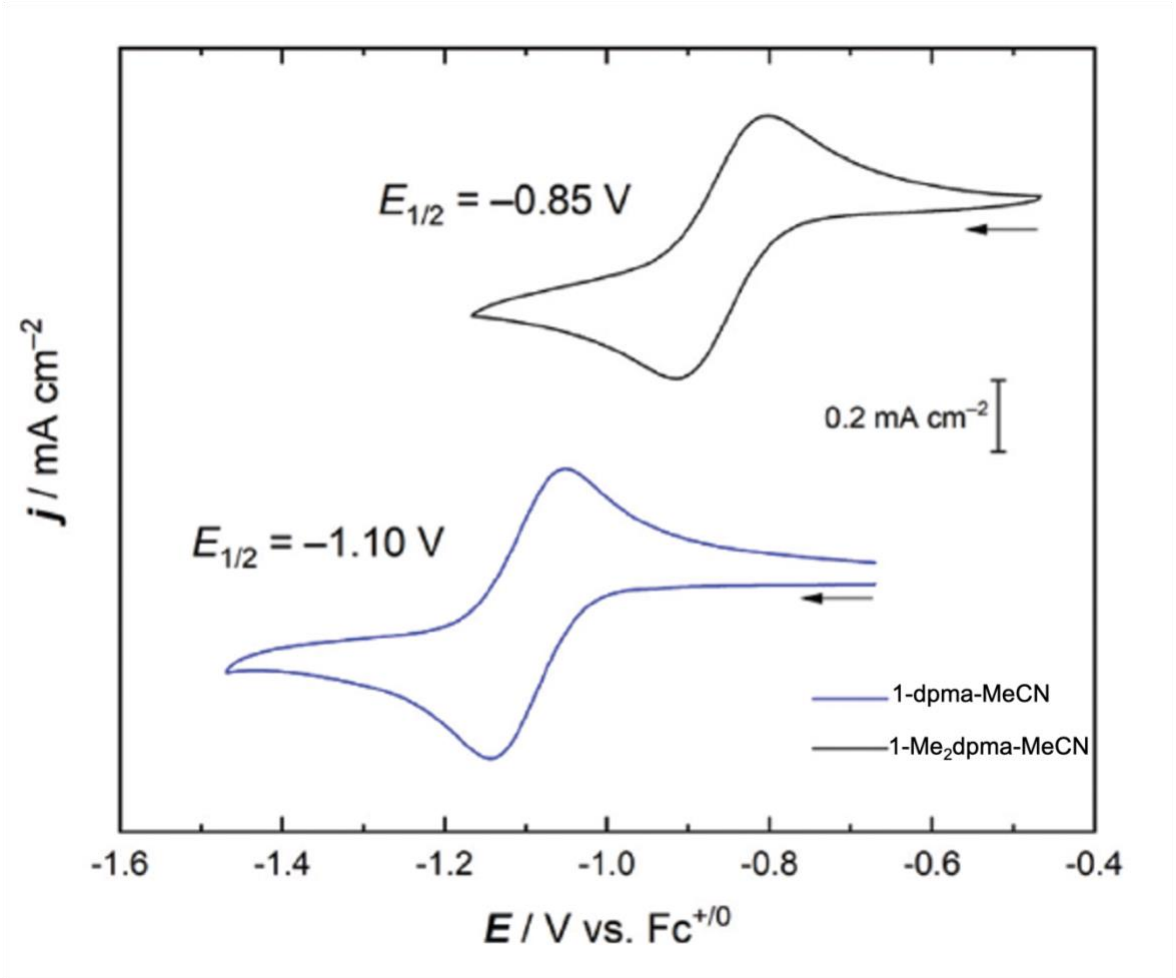

Figure 1.9. Cyclic voltammetry data of **1-dpma** and **1-dpma-MeCN** in MeCN. Electrolyte = 0.1 M tetrabutylammonium hexafluorophosphate. Republished with permission of Royal Society of Chemistry, from Structural and chemical properties of half-sandwich rhodium complexes supported by the bis(2-pyridyl)methane ligand, Davide Lionetti, Victor W. Day, and James D. Blakemore, volume 48, copyright 2019; permission conveyed through Copyright Clearance Center, Inc.

variety of different [Cp*Rh] complexes as evidenced by the presence of multiple Cp* resonances. Over time, the mixture continually decomposed, making characterization of any products therein impossible. Longer reaction times between **1-dpma** and sodium amalgam

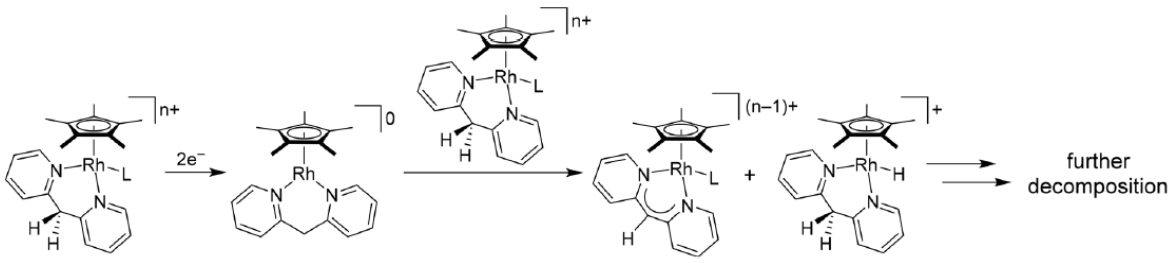

Scheme 1.3. Proposed pathway of decomposition of **dpma** complexes of [Cp*Rh] to give Rh–H complexes. Republished with permission of Royal Society of Chemistry, from Structural and chemical properties of half-sandwich rhodium complexes supported by the bis(2-pyridyl)methane ligand, Davide Lionetti, Victor W. Day, and James D. Blakemore, volume 48, copyright 2019; permission conveyed through Copyright Clearance Center, Inc.

eventually revealed a peak in the NMR spectrum at –14.6 ppm, indicative of a metal hydride. Due to the deleterious effects of chloride on various experimental methods within these complexes (*vide supra*), reduction of **1-dpma-MeCN** was attempted by the same methods. The NMR spectral data again reveal a complex mixture of products, including dissociated ligand and the presence of multiple presumed metal hydride species.

The presence of the hydride species, while they were unable to be isolated or characterized, provided insight into the mechanism occurring in this system. Reduction to a Rh(I) metal center increases the basicity of the metal; this increase was even observed upon reduction of **1-Me$_2$dpma-MeCN** to Rh(II), where the Rh(II) interacted with one of the methyl protons of the ligand backbone. The formation of Rh–H species in this system points to the possibility of Rh(I) serving as a base to deprotonate one of the methylene protons of **dpma**, as these protons are doubly benzylic and further acidified through donation of ligand electrons to the metal center. As such, Lionetti proposed a mechanistic pathway through

which the decomposition likely occurred (see Scheme 1.3). Upon reduction, the Rh(I) is sufficiently basic to extract a proton from a second complex; that complex can then react with yet another complex, leading to the formation of multiple rhodium hydrides and extensive decomposition.

Even still, a study on an additional variant of the dipyridylmethane ligands was performed by Hopkins et al.,[18] in which the ligand was further altered by the inclusion of benzyl and pyrenyl substituents. The solid-state structures of these three complexes are shown in Figure 1.10. The complexes were each prepared and characterized by ^{1}H NMR. The spectral appearance was routine for this system in each case apart from **1-Pyr$_2$dpma**, in

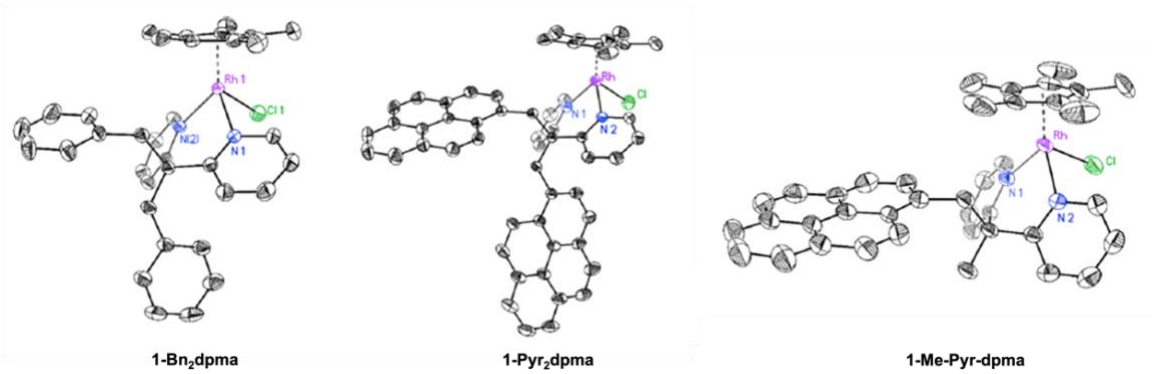

Figure 1.10. Solid-state structures of **1-Bn$_2$dpma**, **1-Pyr$_2$dpma**, and **1-Me-Pyr-dpma**. Displacement ellipsoids are shown at 50 % probability. Hydrogen atoms and the hexafluorophosphate counteranion are omitted for clarity. Adapted with permission from Hopkins Leseberg, J. A.; Lionetti, D.; Day, V. W.; Blakemore, J. D., Electrochemical Kinetic Study of [Cp*Rh] Complexes Supported by Bis(2-pyridyl)methane Ligands. *Organometallics* **2021**, *40*, 266-277. Copyright 2021 American Chemical Society.

which the methylene protons on the two pyrenyl substituents gave rise to different signals. For one pyrene arm, the two protons appeared as a 2H doublet at 4.66 ppm, as one might expect. However, the methylene protons of the other pyrene arm appear by the NMR data to be heterotopic and significantly shifted downfield, as presented by the appearance of 2 1H doublets at 6.28 and 6.59 ppm. The methylene protons marked by this heterotopicity and downfield shift likely belong to the upward-oriented pyrene arm in the solid state structure; this pyrene arm, relative to the downward-facing one, probably suffers from steric-induced hindered rotation due to its proximity to the Cp* methyl protons, resulting in an asymmetry of the methylene protons. The same heterotopicity is induced in the methylene protons of the pyrenyl substituent in **1-Me-Pyr-dpma** due to its upward orientation relative to the geminal methyl group. Analysis of the solid-state X-ray diffraction data compare well with those of **1-Me$_2$dpma**; this finding indicates that the bulkier substituents do not markedly disturb the properties or the orientation of the rhodacycle. Additionally, the bite angle is not noticeably changed by altering the identity of the geminal substituents.

As was the case in both prior studies on the **dpma** system, the solvento analog of each of these complexes was prepared for use in electrochemical studies. The cyclic voltammograms of these complexes in comparison to **1-Me$_2$dpma-MeCN** are shown in Figure 1.11. The same quasi-reversible redox event is shown for each complex centered near –0.8 V, indicating the $Rh^{III/II}$ reduction event. Additionally, the electrochemical-chemical (EC) process observed for **1-Me$_2$dpma-MeCN** upon reduction of Rh(II) to Rh(I) is observed for each complex ($E_{p,c}$ = ~ –1.4 V for each). This EC process is thought to indicate the reduction and subsequent rearrangement to the κ^2-bound pyridyl ring; indeed, chemical

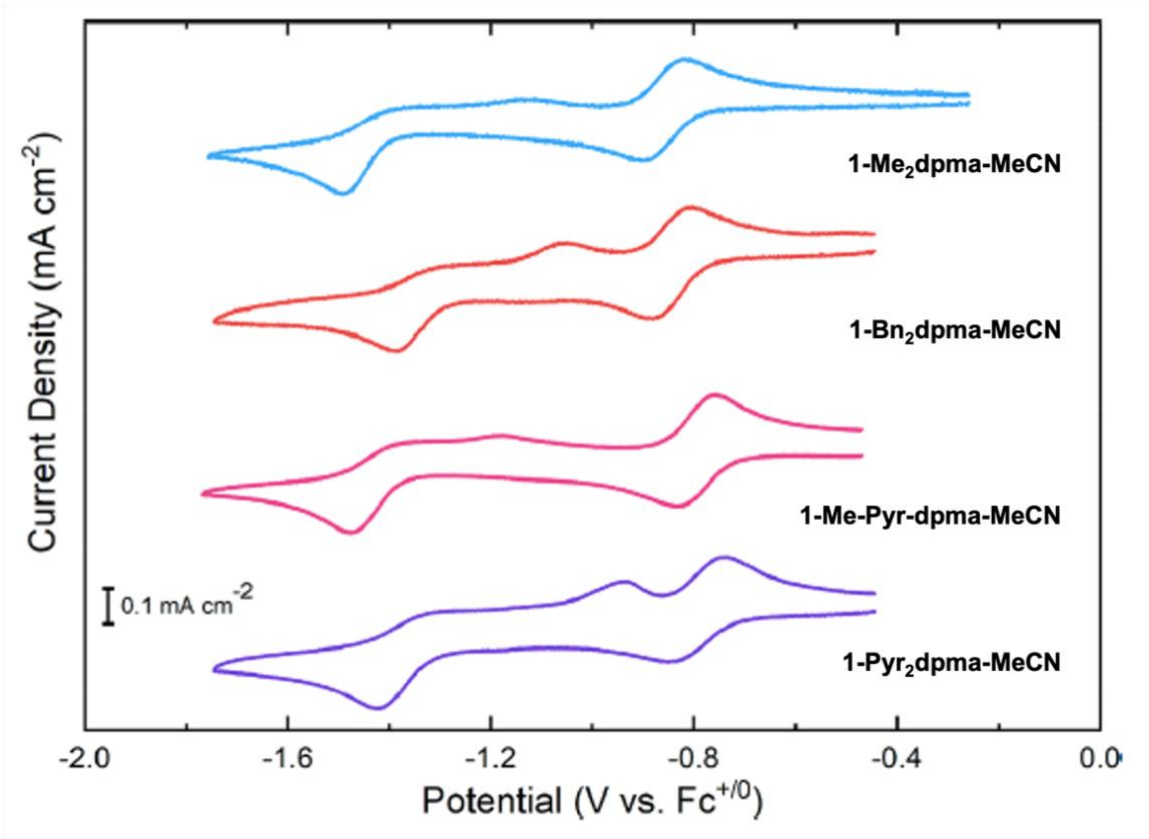

Figure 1.11. Cyclic voltammetry of the complexes compared to the dimethyl of Lionetti in MeCN. [Cp*Rh] = 1 mM. Electrolyte = 0.1 M tetrabutylammonium hexafluorophosphate. Scan rate = 50 mV/s. Adapted with permission from Hopkins Leseberg, J. A.; Lionetti, D.; Day, V. W.; Blakemore, J. D., Electrochemical Kinetic Study of [Cp*Rh] Complexes Supported by Bis(2-pyridyl)methane Ligands. *Organometallics* **2021**, *40*, 266-277. Copyright 2021 American Chemical Society.

preparation and X-ray diffraction studies of the reduced **Rh(I)-Bn$_2$dpma** complex confirm the presence of the κ^2-bound pyridyl ring. A coupled oxidation event is present on the return scan, indicating the reoxidation of this κ^2-bound form of the Rh(I) back to the Rh(II) species. While no trend exists with these irreversible cathodic and anodic features, a trend in the midpoint potential of the quasi-reversible $Rh^{III/II}$ waves reveals an electronic dependence

with respect to the identity of the geminal substituent. **1-Me$_2$dpma-MeCN** has the most negative reduction potential of this feature (–0.86 V) due to the electron-donating effects of methyl substituents, followed by **1-Bn$_2$dpma-MeCN** (–0.84 V) and the two pyrenyl substituted complexes (**1-Me-Pyr-dpma-MeCN** and **1-Pyr$_2$dpma-MeCN**, –0.80 V each). The extended aromatic π system of the pyrenyl substituents is the most electron-withdrawing of any of the substituents, making the initial reduction more facile.

Hopkins next endeavored to analyze the kinetics of the redox-induced ligand rearrangement. This was done by utilizing the zone diagrams developed by Savéant[19] which help one to elucidate the competition between the rate of diffusion, the properties of the redox-induced chemical reaction, and a dimensionless parameter λ which relates the two. The voltammograms were collected at 50, 1000, and 2500 mV/s scan rates, as Savéant gathered that the return anodic wave will eventually max out, at which point the chemical reaction will have insufficient time to affect the appearance of the data. Indeed, the appearance of the voltammogram for **1-Bn$_2$dpma-MeCN** at the varied scan rates indicated the presence of an EC reaction (see Figure 1.12); at 50 mV/s, the cathodic peak is present with no corresponding reoxidation nearby, while at 2500 mV/s, the cathodic peak now has an accompanying anodic event, pointing to an electrochemically quasi-reversible process.

This overcoming of the chemical process allowed Hopkins to measure the rate of the reduction-induced chemical rearrangement via electrochemical analysis by focusing on the anodic return wave. It was determined through a series of accompanying digital simulations that there is a direct correlation between the steric bulk of the substituent and the rate of the rearrangement. The first-order rate constant for the EC process (the ligand flip) in

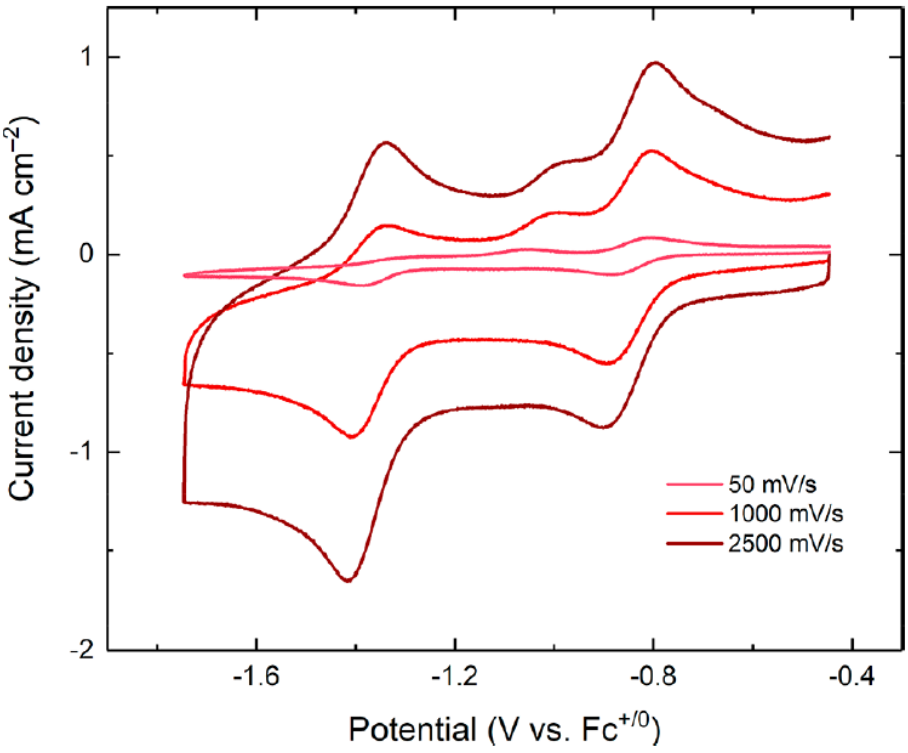

Figure 1.12. Cyclic voltammetry of **1-Bn$_2$dpma-MeCN** at increasing scan rates. [Cp*Rh] = 1 mM. Electrolyte = 0.1 M tetrabutylammonium hexafluorophosphate. Reprinted with permission from Hopkins Leseberg, J. A.; Lionetti, D.; Day, V. W.; Blakemore, J. D., Electrochemical Kinetic Study of [Cp*Rh] Complexes Supported by Bis(2-pyridyl)methane Ligands. *Organometallics* **2021**, *40*, 266-277. Copyright 2021 American Chemical Society.

1-Me$_2$dpma-MeCN, **1-Bn$_2$dpma-MeCN**, **1-Me-Pyr-dpma-MeCN**, and **1-Pyr$_2$dpma-MeCN** were 1.65 ± 0.08, 1.31 ± 0.19, 0.60 ± 0.14, and 0.16 ± 0.01, respectively; as the steric bulk of the substituent is increased, the rate of ligand rearrangement is decreased. Notably, the difference in the rate of rearrangement between the dimethyl and dipyrenyl systems differs by a full order of magnitude.

The findings of this study point to a direct correlation between the rate of stabilization of reduced rhodium complexes and steric bulk of the ligand system in [Cp*Rh] complexes.

This relationship is relevant to the design of new catalysts in this family of compounds or in others, as the rate of stabilization (and thereby the lifetime) of a given catalyst, precatalyst, or intermediate might have implications on the mechanism of the catalytic transformation being optimized. Additionally, this study presents a thorough procedure for the extraction of rate data from a complicated electrochemical study which is muddied by a complex EC process.

1.2.4 Investigation of the Effect of a Constrained Bipyridyl Ligand in [Cp*Rh] Systems

Up to this point, efforts in the Blakemore Group toward better understanding the chemical and electrochemical properties of [Cp*Rh] complexes has been carried out through use of chelating diimine-type ligands based off the bipyridyl scaffold. The utilization of **bpy**, **phen**, disubstituted analogues of **bpy**, and **dmpa** analogues in the preparation of novel [Cp*Rh] complexes has demonstrated a wide-ranging ability to control the electronics and chemical reactivity of the given system, control which will assist those in this field of work

Chart 1.3. Structures of the ligands utilized in this study by Henke. Republished from Henke, W. C.; Stiel, J. P.; Day, V. W.; and Blakemore, J. D., Evidence for Charge Delocalization in Diazafluorene Ligands Supporting Low-Valent [Cp*Rh] Complexes. **2021**, *submitted to ChemRxiv*.

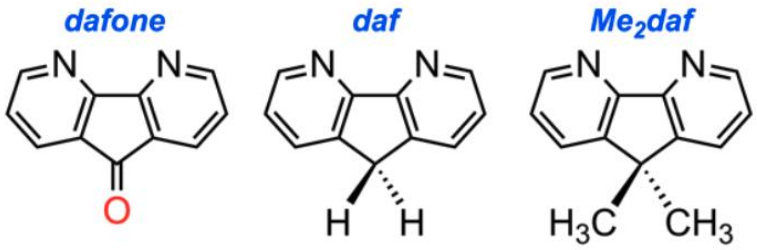

with the development of new catalysts. As a final effort to probe ligand effects of diverse diimine ligands in the [Cp*Rh] system, Henke et al.[20] turned to the diazafluorene (**daf**) ligand for use in these complexes in 2021.

Daf and its analogues are structurally and electronically similar to that of **bpy** such that coordination to a metal occurs through the two nitrogen donors and the 12e$^-$ π system is still intact (unlike the unconjugated **dpma** analogues). However, the addition of a bridging sp^3-hybridized methylene ties the two pyridyl rings together at the 3- and 3'-positions,

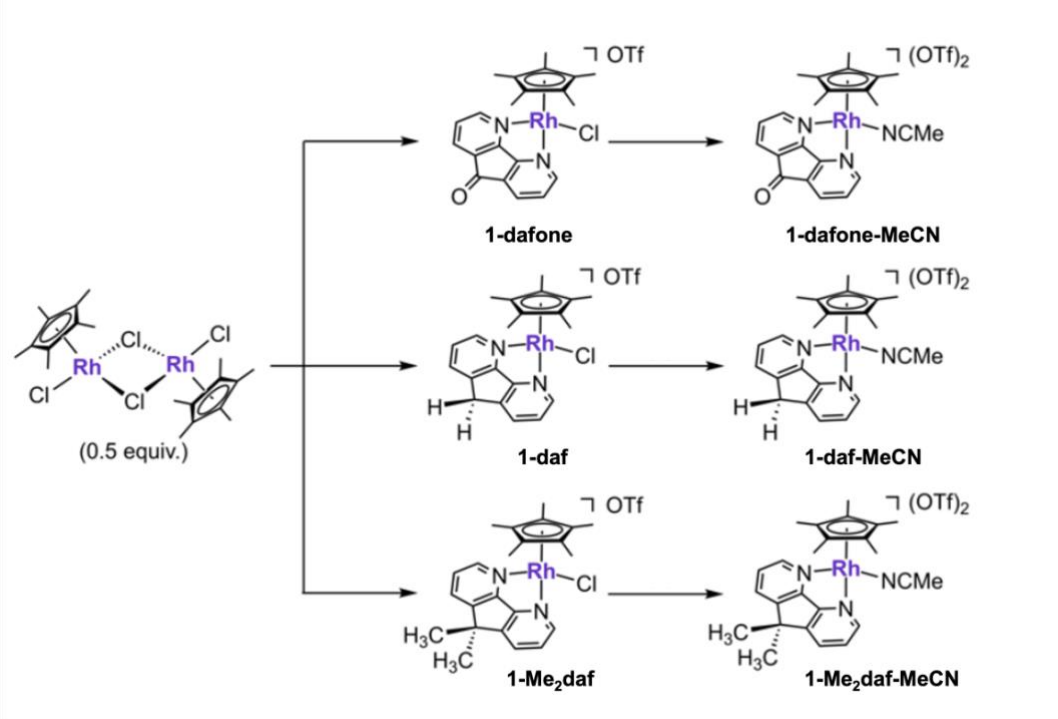

Scheme 1.4. Synthetic scheme showing the preparation of the complexes targeted in this study. Republished from Henke, W. C.; Stiel, J. P.; Day, V. W.; and Blakemore, J. D., Evidence for Charge Delocalization in Diazafluorene Ligands Supporting Low-Valent [Cp*Rh] Complexes. **2021**, *submitted to ChemRxiv*.

thereby establishing an additional five-membered ring in the compound which rigidifies the ligand core. This rigidity imparts a larger bite angle for **daf** relative to **bpy**; Henke postulated that this rigidity and subsequent change to the bite angle would change the structural and possibly the reactive properties of the [Cp*Rh] complexes supported by this ligand system. According to external literature results[21] utilizing **daf** as a ligand as well as the study discussed herein on the **dpma** system (*vide supra*), it was predicted that the backbone methylene protons of **daf**, when bound to a reduced metal species, would be sufficiently acidic to be deprotonated by the basic, reduced metal. Therefore, **daf** analogues were also targeted to complement the study herein; these analogues were **Me$_2$daf** and **dafone** (see Chart 1.3).

The complexes prepared from these three ligands are shown in Scheme 1.4. The precursor chloride complex was prepared in all cases and was treated with an additional equivalent of silver(I) triflate to generate the solvento species. This solvento species was probed in electrochemical studies for reasons discussed above with numerous other complexes (*vide supra*). As was the case in the study by Hopkins, the geminal protons and methyl groups of **1-daf-MeCN** and **1-Me$_2$daf-MeCN**, respectively, are heterotopic as a result of the asymmetry about the geminal groups. Multifrequency NMR characterization, similar to that discussed in Chapter 3 of this dissertation, was carried out on **1-daf-MeCN** to probe the observed roofing effects of the distinct 1H doublets representing each heterotopic methylene proton.

X-Ray diffraction studies were carried out for each of the 6 complexes (see Figure 1.13). Across the series, the Rh–L (L = Cl or MeCN) and Rh–Cp* distances were similar;

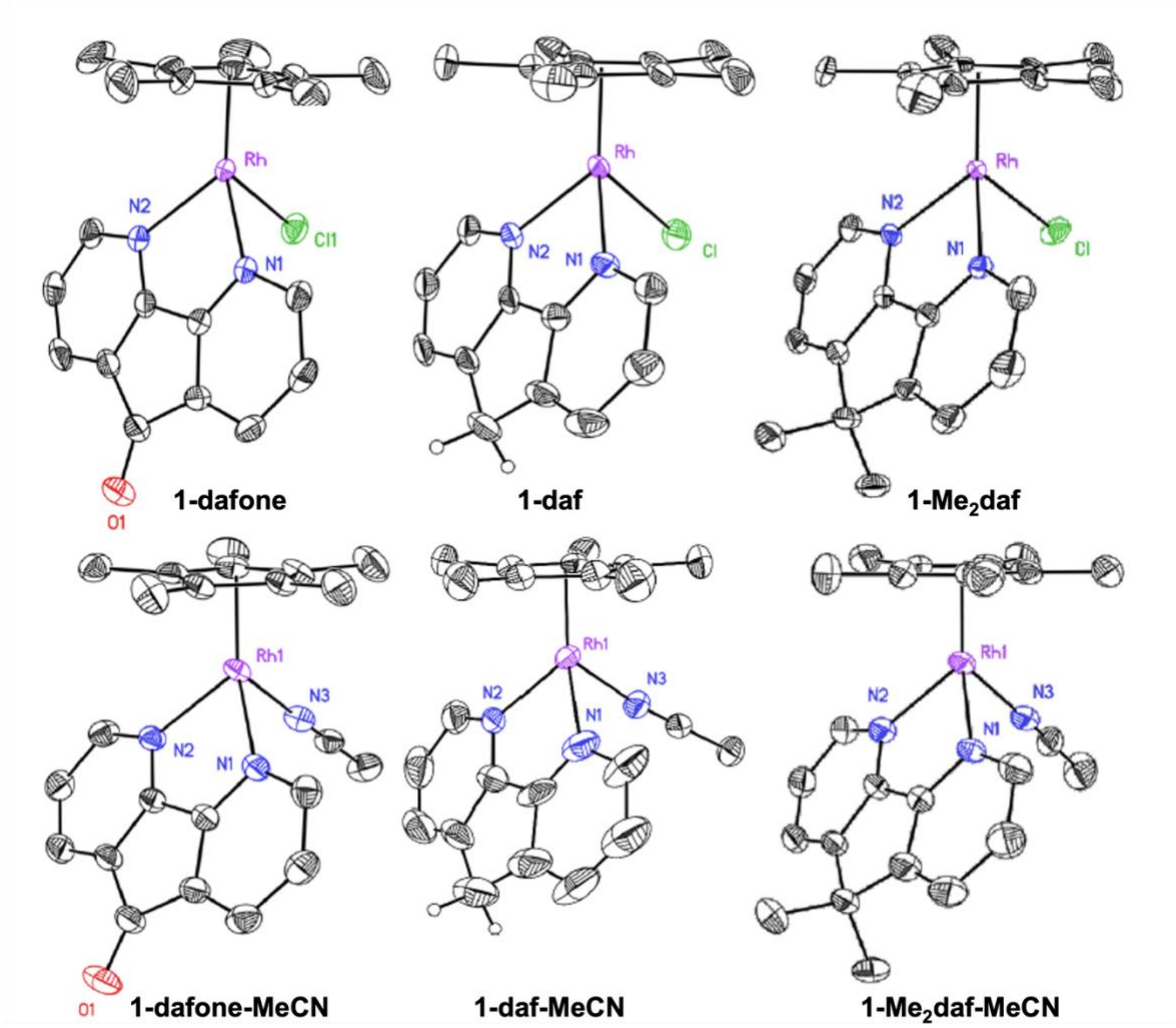

Figure 1.13. Solid-state structures of complexes prepared in this study. Displacement ellipsoids are shown at 50 % probability. Hydrogen atoms except the methylene protons of **1-daf** and **1-daf-MeCN**, the triflate counteranion, and co-crystallized solvents are omitted for clarity. Republished from Henke, W. C.; Stiel, J. P.; Day, V. W.; and Blakemore, J. D., Evidence for Charge Delocalization in Diazafluorene Ligands Supporting Low-Valent [Cp*Rh] Complexes. **2021**, *submitted to ChemRxiv*.

additionally, the angle between the Cp* centroid, the rhodium, and the centroid of the two nitrogen chelators fell within a narrow range of 147–151° for all complexes, consistent with

the structural similarity about each specific rhodacycle in the series. As a result of the strain of the **daf**-type ligand scaffold, the metallacycle is noticeably different than that of the **bpy**-ligated rhodacycles, where the N–Rh–N angle in these complexes is 4–5° larger than that of the **bpy** complexes previously discussed; also in agreement with this result is the Rh–N bond length, which is ca. 0.05–0.10 Å in the **daf** complexes compared to the **bpy** complexes. Even more, the C–C interpyridine linkage is noticeably shorter in each of these complexes relative to the **bpy** complexes. These structural properties suggest that the more rigid structure of the **daf**-based complexes results in attenuated σ-donor power through limited flexibility of the ligand relative to **bpy**-based complexes.

The subsequent electrochemical studies performed revealed initial similarities to the **dpma**-ligated complexes studies by Lionetti and Hopkins (*vide supra*). Cyclic voltammetry of **1-dafone**, **1-daf**, and **1-Me$_2$daf** revealed quasi- and irreversible features upon reduction attributable to the deleterious effect of the chloride presence. It is not surprising that this outcome was observed in both systems, as **1-dpma** and the **daf** complexes described in this study have strained metallacycles; as such, the bidentate ligands may be prone to dissociation upon formation of the labile Rh(II) in the presence of chloride. As such, all further electrochemical studies were conducted on the solvento complexes (see Figure 1.14). The voltammograms of each complex reveal two cathodic reduction waves and two return oxidation anodic waves, consistent with the $Rh^{III/II}$ and subsequent $Rh^{II/I}$ processes, which indicate that this ligand scaffold is sufficient to stabilize both reduced forms of the metal center on the electrochemical timescale, such that they can be observed within a given scan. However, the features for **1-dafone-MeCN** and **1-daf-MeCN** can be described as quasi-

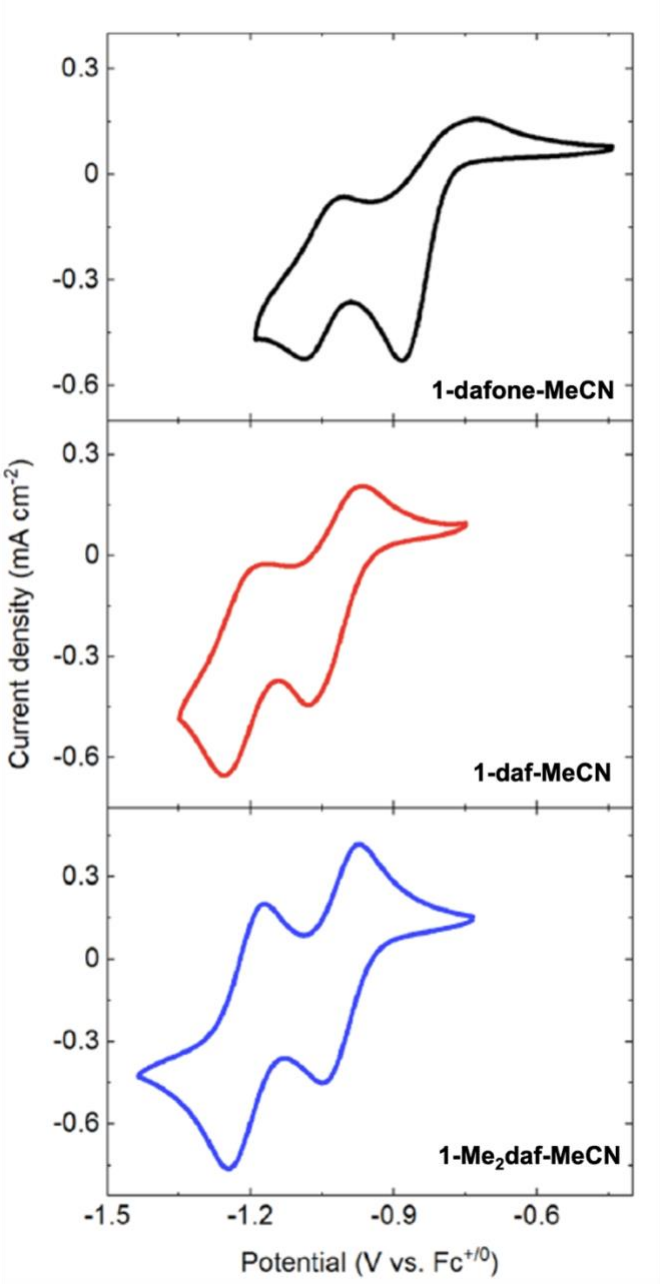

Figure 1.14. Cyclic voltammetry of the solvento complexes prepared in this study in MeCN. Electrolyte = 0.1 M tetrabutylammonium hexafluorophosphate. Scan rate = 100 mV/s. Republished from Henke, W. C.; Stiel, J. P.; Day, V. W.; and Blakemore, J. D., Evidence for Charge Delocalization in Diazafluorene Ligands Supporting Low-Valent [Cp*Rh] Complexes. **2021**, *submitted to ChemRxiv*.

reversible at the most, considering the diminished current of each return oxidation, pointing to follow-up chemical reactivity upon formation of the reduced species. This instability is to be expected for reduced metal species bearing ligands with a ketone moiety or acidic, geminal methyl protons; the **dafone** ligand can easily be reduced to form a reactive radical species similar to that of benzophenone, while the doubly benzylic methylene group can be deprotonated as discussed above. This off-cycle reactivity was supported through chemical reduction experiments. In contrast, the complex **1-Me$_2$daf-MeCN** did give a cyclic voltammogram demonstrating clean formation of the Rh(II) and Rh(I) forms, as evidenced by two chemically reversible 1e$^-$ waves ($E_{1/2}$ = –1.04 V and –1.25 V, respectively). This ligand, protected from the adverse reactivity induced by the ketone and geminal protons of the analogous ligands by inclusion of the geminal dimethyl groups, is sufficient to stabilize the complex against chemical reactivity upon generation of the reduced forms of the rhodium. It is worth noting that Henke also performed an electrochemical titration of **1-Me$_2$daf-MeCN** with chloride (tetrabutylammonium chloride) to track the generation of **1-Me$_2$daf** and thereby probe the effect of chloride in this system during electrochemistry. As chloride was introduced to the cell, the resulting voltammogram resembled a single 2e$^-$ reduction event in contrast to the two sequential 1e$^-$ events for the solvento complex, exemplifying the importance of chloride in the redox chemistry of [Cp*Rh] complexes.

On the basis of the reversible electrochemistry of **1-Me$_2$daf-MeCN**, spectrochemical experiments were performed utilizing UV-visible absorption spectroscopy. Upon addition of 1 equivalent of $CoCp_2$ to the cell, the disappearance of the band at 373 nm in concert with the growth of a new band at 716 nm marked the isosbestic transformation from Rh(III) to Rh(II). Addition of another equivalent of reductant resulted in the growth of yet another new

feature at 534 nm indicates the isosbestic formation of Rh(I). Additionally, observed vibronic bands in the UV region point to formation of the electron-rich Rh(I) complex, as similar vibronic bands have been reported for a Mn(I) complex of the same ligand.[22] These vibronic couplings have also been observed widely in **bpy** systems of reduced metals and, in those instances, have been attributed to intra-**bpy** vibrations upon excitation of electron density within the ligand π system into higher energy π* orbitals. Due to the structural and electronic similarity of the **bpy** and **daf** ligand scaffolds, these similar vibronic bands observed upon reduction of **1-Me$_2$daf-MeCN** to the Rh(I) complex are likely attributable to intra-**Me$_2$daf** vibrations. Additionally, the molar absorptivities of the two prominent bands in the Rh(I) forms of **1-Me$_2$daf-MeCN** and Cp*Rh(bpy) were compared; the findings of more modest values for **1-Me$_2$daf-MeCN** as compared to Cp*Rh(bpy) indicate a more moderate delocalization of Rh(I) electrons into the ligand system. As a result, it was concluded that **Me$_2$daf** is a weaker π-acceptor ligand than **bpy**.

Henke then attempted to chemically prepare the two reduced forms of **1-Me$_2$daf-MeCN**. The Rh(II) form was prepared *in situ* and analyzed by X-band EPR. The findings of these experiments showed the appearance of a broad rhombic signal near $g = 2$. Aided by simulations, the data were interpreted as two overlapping rhombic signals corresponding to the MeCN-bound 19e$^-$ Rh(II) complex and the MeCN-free 17e$^-$ Rh(II) complex. Next, attempts to prepare and isolate the Rh(I) complex through reaction of **1-Me$_2$daf-MeCN** with Na(Hg) were successful. The Rh(I) complex **1-Me$_2$daf-Rh(I)** exhibited the expected C_{2v} symmetry about rhodium in solution, according to the NMR data, consistent with prior characterized Rh(I) Cp* complexes. Crystals were grown and analyzed via X-ray diffraction studies (see Figure 1.15); the solid-state structural data complement the solution-state data

such that the C_{2v} symmetry about rhodium is observed. Consistent with increased electron density about rhodium, the bond lengths of Cp*–Rh is longer in **1-Me$_2$daf-Rh(I)** than that of **1-Me$_2$daf-MeCN** (1.829 Å vs. 1.768 Å); likewise, the Rh–N bond distance is shorter in **1-Me$_2$daf-Rh(I)** than in **1-Me$_2$daf-MeCN** by approximately 0.13 Å due to increased π-backbonding. Further analysis of the solid-state data, particularly the interpyridine C5–C6 bond distance, demonstrated a charge delocalization phenomenon across the series of **1-Me$_2$daf-Rh(I)**, Cp*Rh(bpy), and CpRh(bpy) (where Cp = cyclopentadienyl) (see Figure 1.15, right). The shortening of this bond in all cases indicates partially reduced ligand

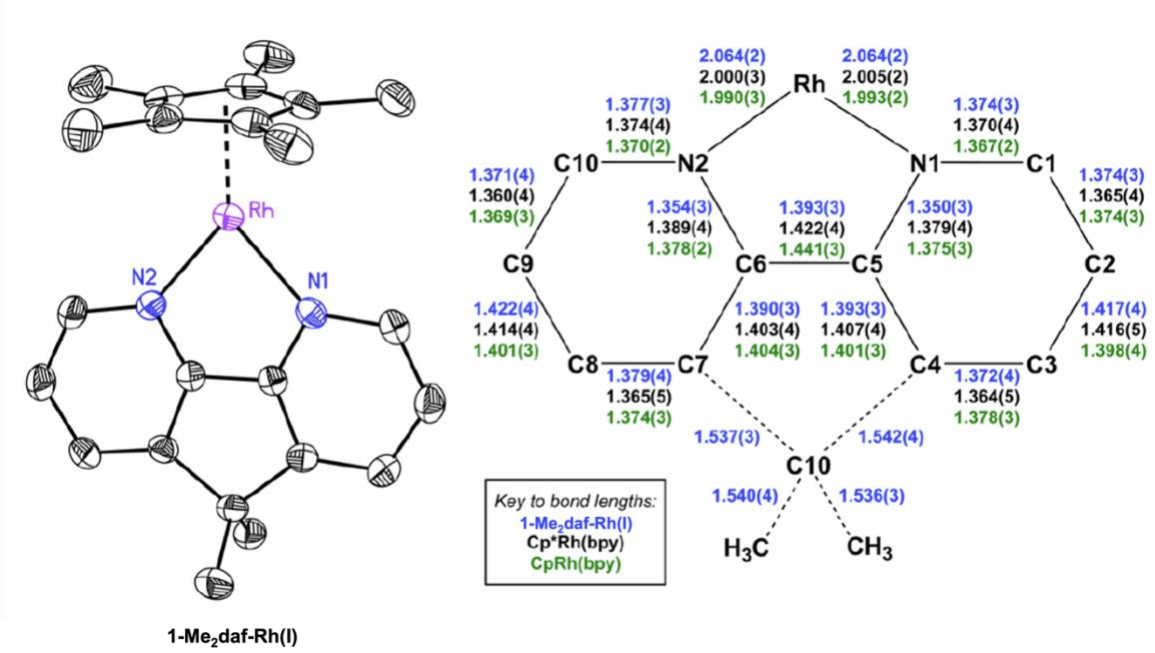

Figure 1.15. Left: Solid-state structure of **1-Me$_2$daf-Rh(I)**. Displacement ellipsoids are shown at 50 % probability. Hydrogen atoms are omitted for clarity. Right: Comparative bond distances for **1-Me$_2$daf-Rh(I)** vs. **bpy** systems. from Henke, W. C.; Stiel, J. P.; Day, V. W.; and Blakemore, J. D., Evidence for Charge Delocalization in Diazafluorene Ligands Supporting Low-Valent [Cp*Rh] Complexes. **2021**, *submitted to ChemRxiv*.

character across the series resulting from occupation of electrons in the LUMO π* orbital of the conjugated system.

Finally, attempts to prepare the Cp*H complex were pursued. **1-Me$_2$daf** was reacted with 1 equivalent of sodium formate in deuterated solvent to probe the *in-situ* formation of the Cp*H complex. Notably, the NMR spectrum showed the resonances indicating formation of the Cp*H ligand (q, 1H, 2.44 ppm; d, 3H, 0.55 ppm). The proposed mechanism of this transformation involves binding of formate to Rh(III) through displacement of the chloride ligand, subsequent β-hydride elimination to generate CO_2 and thereby form the transient Rh(III)–H, and proton/hydride tautomerization. This result is promising, inasmuch as the similar reactivity of this complex to the model catalyst Cp*Rh(bpy) system indicates that [Cp*Rh] complexes supported by **Me$_2$daf** could serve as viable catalysts.

1.2.5 Preparation, Characterization, and Electrochemical Analysis of [Cp*Rh] Complexes Supported by Hybrid Imine/Phosphine Chelators

Despite the plethora of [Cp*Rh] complexes bearing diimine ligand that our group has prepared and analyzed (*vide supra*), many questions still remain around the mechanism through which hydrogen evolution occurs in the systems which show catalytic propensity. Originally proposed explanations of the mechanism suggest that a transient Rh–H species forms which, upon protonolysis, generates H_2. As discussed in this chapter, however, a rhodium monohydride species had never been observed in our hands to this point; instead, the Cp*H complex was isolated in many instances, which was capable of generating H_2 upon either treatment with acid or subjection to electrochemical reduction (*vide supra*). Despite these advances in our understanding of the effects of ligand tuning in this process, still little is known about the mechanism of hydrogen generation in this system. Moreover, the failure

to isolate an explicit rhodium monohydride species across this library of compounds described thus far encouraged us to target systems which might allow for the explicit isolation and characterization of a monohydride species.

The efforts of our group to design a new [Cp*Rh] complex capable of stabilizing the monohydride upon formation began with the inclusion of phosphine ligands. Literature reports indicate the ability of phosphine ligands to enact formation of an explicit Rh–H formation; inspired by these results and the fact that no prior electrochemical studies had been conducted on [Cp*Rh] hydride complexes, we pursued ligands incorporating phosphine chelators for the preparation of new complexes. In 2018, our group published concurrent reports on the preparation of [Cp*Rh] monohydrides supported by phosphine chelators. The first report by Boyd et al.[23] described preparation of the complexes supported by a diphosphine ligand, while the second report by Hopkins et al.[24] was on the preparation of analogous complexes supported by hybrid imine/phosphine ligands. Because of the closer similarity of the imine/phosphine ligand functional groups to those of the diimine ligands previously discussed, the hybrid imine/phosphine ligand work from Hopkins will be discussed first in this chapter even though the work by Boyd was published three months earlier than that of Hopkins.

The work reported by Hopkins in 2018[24] involved the preparation of new [Cp*Rh] complexes supported by the hybrid ligand 8-(diphenylphosphino)quinoline (**PQN**), which presents a triarylphosphine donor and an imine donor. An attractive feature of this ligand is that the substitution pattern enables the ligand to form a 5-membered metallacycle upon

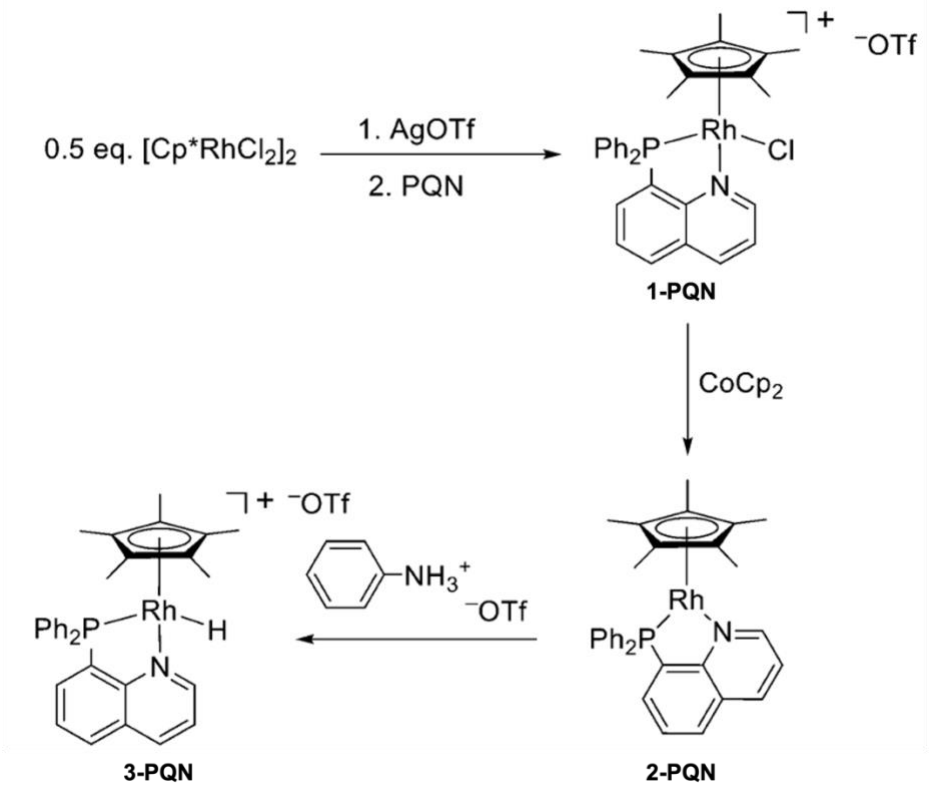

Scheme 1.5. Synthetic scheme for the preparation of the **PQN**-ligated complexes analyzed in this study. Adapted with permission from Hopkins, J. A.; Lionetti, D.; Day, V. W.; Blakemore, J. D., Chemical and Electrochemical Properties of [Cp*Rh] Complexes Supported by a Hybrid Phosphine-Imine Ligand. *Organometallics* **2019,** *38,* 1300-1310. Copyright 2019 American Chemical Society.

binding of a metal, like the 5-membered rhodacycles discussed herein with the **bpy**-derived complexes (*vide supra*). The preparation of each complex in this study is shown in Scheme 1.5, in which step one shows the preparation of Rh(III) chloride complex **1-PQN**. This complex was confirmed by ^{1}H NMR, ^{31}P{^{1}H} NMR, and X-ray diffraction studies. A comparison of the solid-state data for **1-PQN** to that of the analogous [Cp*Rh(bpy)Cl]$^{+}$ complex revealed that the angle defined by the Cp* ligand plane and the plane defined by

Rh, N, and P was 62°, similar to that of $[Cp^*Rh(bpy)Cl]^+$ (59°). No further comparisons between the solid-state data of the two systems were made.

Electrochemical studies of **1-PQN** were undertaken, in which the cyclic voltammogram revealed a quasi-reversible $2e^-$ wave at –1.19 V which corresponds to the $Rh^{III/I}$ reduction. This result is closely aligned with the ECE' processes reported for analogous **bpy** complexes; indeed, Hopkins concluded that this complex undergoes an initial $1e^-$ reduction (E), the chloride ligand subsequently dissociates (C), and the resulting complex is reduced by another electron (E') at a potential that is very similar to that of the first reduction to give the reduced Rh(I) complex. Additionally, another reductive feature appears at –2.26 V, predicted to be some sort of **PQN**-centered reduction. Interested in the role of the chloride ligand in the electrochemical studies, the solvento complex was prepared and analyzed to give a voltammogram that was distinct from that of **1-PQN**. The voltammogram of the solvento complex demonstrated two sequential $1e^-$ reductions at –0.93 V and –1.16 V, corresponding to the $Rh^{III/II}$ and $Rh^{II/I}$ couples, respectively. This result is in alignment with the electrochemical titration of chloride performed by Henke in which he saw the presence of chloride transform what was two sequential $1e^-$ reductions into one $2e^-$ reduction for **1-Me$_2$daf-MeCN**, again highlighting the role of chloride in the redox events of [Cp*Rh] complexes.

Hopkins next turned to the chemical preparation of the reduced Rh(I) complex by reacting **1-PQN** with $CoCp_2$; indeed, the reaction yielded the Rh(I) complex **2-PQN** (Scheme 1.5). Characterization of this complex by ^1H NMR and $^{31}P\{^1H\}$. Notably, a doublet was observed in the $^{31}P\{^1H\}$ spectrum for each; the resonance was a doublet due to coupling of the chelating phosphorus atom to the rhodium metal center. A comparison of the doublet

of **1-PQN** (47.90 ppm, $^{1}J_{P,Rh}$ = 143.8 Hz) to that of **2-PQN** (55.29 ppm, $^{1}J_{P,Rh}$ = 246.3 Hz) is indicative of the increased electron density about rhodium in **2-PQN**, as the doublet is shifted slightly downfield and coupling to rhodium is increased due to the resulting stronger covalent interaction between the two atoms. The solid-state data for **2-PQN** also support formation of the reduced Rh(I) complex, as both the Rh–P and Rh–N bond lengths are contracted substantially upon reduction (by 0.1216 and 0.1106 Å, respectively). Additionally, cyclic voltammetry data of **2-PQN** were collected in order to confirm that this complex is the product observed in the cyclic voltammogram of **1-PQN**. The observations were consistent with those of the voltammogram of the Rh(III) solvento complex, in that two 1e^{-} couples were observed; these results are consistent with the observable 1e^{-} processes noted in the absence of chloride in prior work. A titration of the solvento complex with tetrabutylammonium chloride, analogous to the one performed by Henke, was performed which showed the formation of **1-PQN** in the electrochemical cell as chloride concentration increased (see Figure 1.16).

With full characterization of **1-PQN** and **2-PQN** in hand, Hopkins endeavored to prepare the Rh(III)–H complex **3-PQN**. Addition of anilinium triflate to **2-PQN** resulted in the formation of the desired complex as confirmed initially by NMR (see Scheme 1.5). The ^{1}H NMR shows the diagnostic upfield peak at –9.9 ppm, indicative of metal hydride species (dd, 1H, J = 36.6, 19.9 Hz). The ^{31}P{^{1}H} NMR data reveal the expected doublet, now with less coupling to rhodium in light of the lessened electron density of the complex ($^{1}J_{P,Rh}$ = 149.2 Hz). The solid-state data of **3-PQN** confirm the presence of the hydride, as it was able

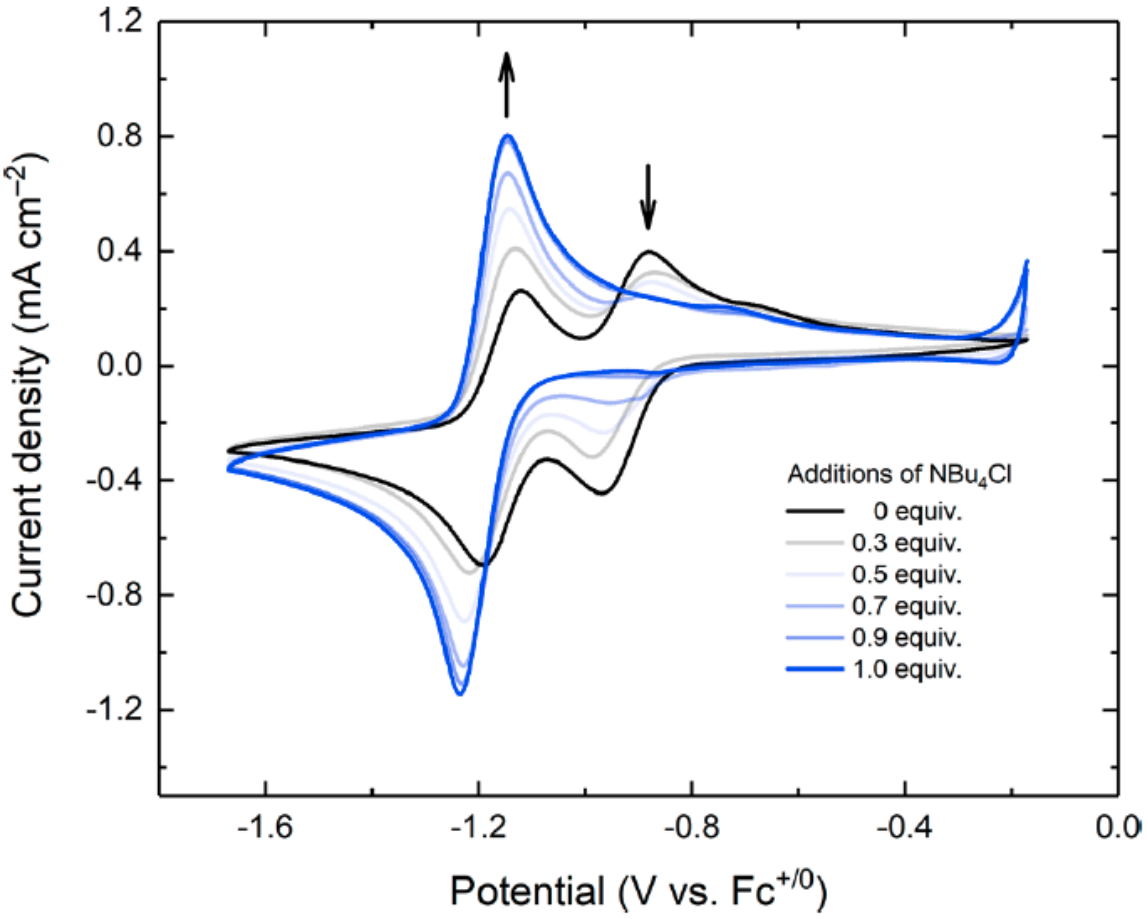

Figure 1.16. Electrochemical response of solvento complex **1-PQN** upon addition of varying amounts of tetrabutylammonium chloride in MeCN. Growth of the reduction process with $E_{1/2}$ = −1.19 V indicates coordination of chloride. Electrolyte = 0.1 M tetrabutylammonium hexafluorophosphate. Reprinted with permission from Hopkins, J. A.; Lionetti, D.; Day, V. W.; Blakemore, J. D., Chemical and Electrochemical Properties of [Cp*Rh] Complexes Supported by a Hybrid Phosphine-Imine Ligand. *Organometallics* **2019,** *38*, 1300-1310. Copyright 2019 American Chemical Society.

to be located in the Fourier difference map and freely refined to determine its location, confirming the explicit Rh–H interaction. Electrochemical analysis of **3-PQN** reveals an

irreversible wave ($E_{p,c}$ = –1.75 V) followed by two return oxidative waves, indicating a fast chemical reaction upon reduction. The complex was then subjected to acidic conditions to probe its ability to generate hydrogen. When anilinium triflate (10 equivalents, pK_a = 10.6

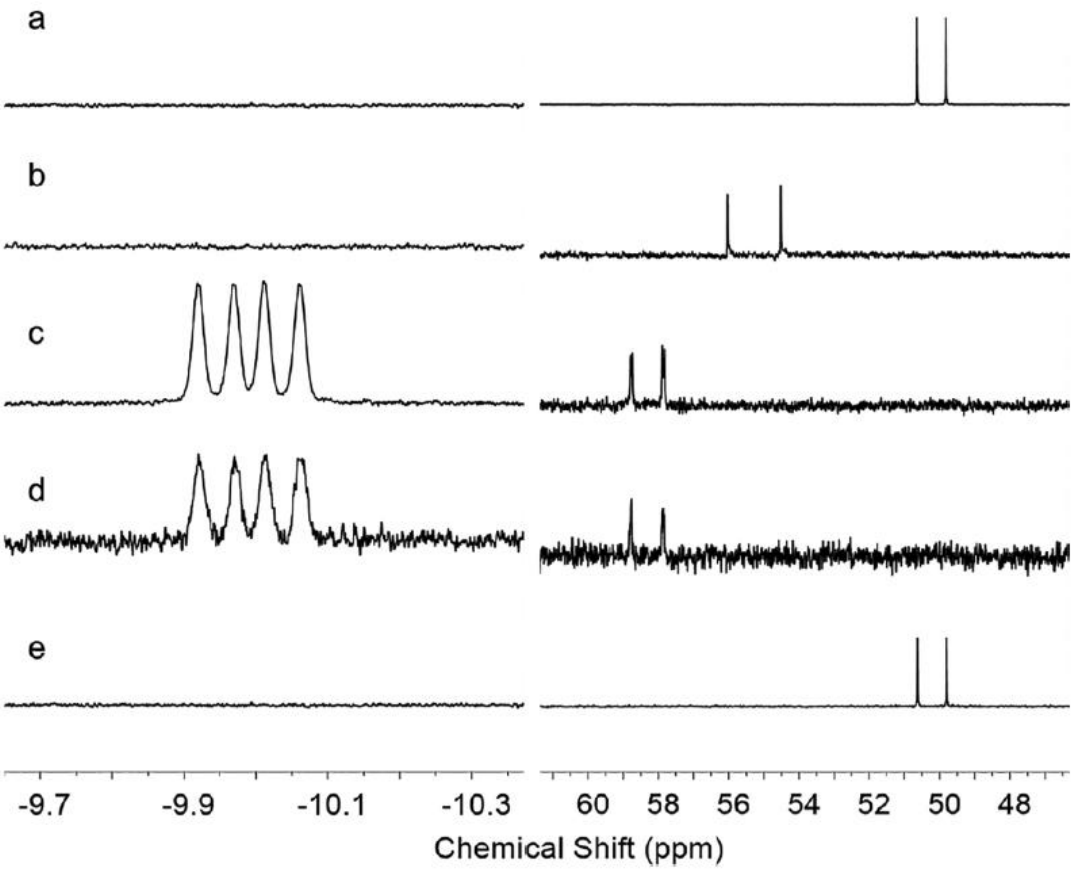

Figure 1.17. ^{1}H (left) and ^{31}P{^{1}H} (right) NMR spectra: (a) solvento-bound **1-PQN**; (b) **2-PQN**; (c) **3-PQN**; (d) addition of 10 equiv. of anilinium triflate to **3-PQN**; (e) addition of 3 equiv of $[DMFH]^{+}[OTf]^{-}$ to **3-PQN**. Reprinted with permission from Hopkins, J. A.; Lionetti, D.; Day, V. W.; Blakemore, J. D., Chemical and Electrochemical Properties of [Cp*Rh] Complexes Supported by a Hybrid Phosphine-Imine Ligand. *Organometallics* **2019,** *38*, 1300-1310. Copyright 2019 American Chemical Society.

in MeCN[25]) was used as the acid, no change to the NMR spectrum of **3-PQN** was observed over the course of days. However, when the stronger acid $[DMFH]^+[OTf]^-$ (1 equivalent, pK_a = 6.1 in MeCN[26]) was employed, **3-PQN** was completely consumed (as judged by the disappearance of the hydride resonance) and the generation of H_2 was observed over 1 hour (see Figure 1.17).

Finally, Hopkins investigated if **3-PQN** could be formed electrochemically by collecting cyclic voltammetry data on **1-PQN** in the presence of aliquots of a 1:1 mixture of $[Et_3NH]^+/Et_3N$ (see Figure 1.18). The concurrent distortion of the cathodic two-electron wave of **1-PQN** and formation of an irreversible cathodic wave at –1.75 V confirmed that **3-PQN** could be generated electrochemically in the presence of acid. Addition of further equivalents of acid resulted in current enhancement of the feature at –1.75 V; for that reason, bulk electrolysis was carried out to assess the possibility of hydrogen generation. The experiment was conducted for **1-PQN** in the presence of 10 equivalents of triethylammonium bromide for 1.5 hours at –1.75 V. The headspace was analyzed by gas chromatography to reveal a modest 34 % faradaic efficiency, giving a TON of only 1.3. The low faradaic yield indicates off-cycle side reactions. The same experiment was conducted for the Rh(III) solvento complex, and a faradaic efficiency of 36 % resulted. Therefore, these complexes were deemed unfit as catalysts for hydrogen evolution. As a last effort, chemical reduction of **3-PQN** was attempted with $CoCp^*_2$ (decamethylcobaltocene); while the contents of the solution remained homogeneous, little to no generation of hydrogen was observed by headspace analysis.

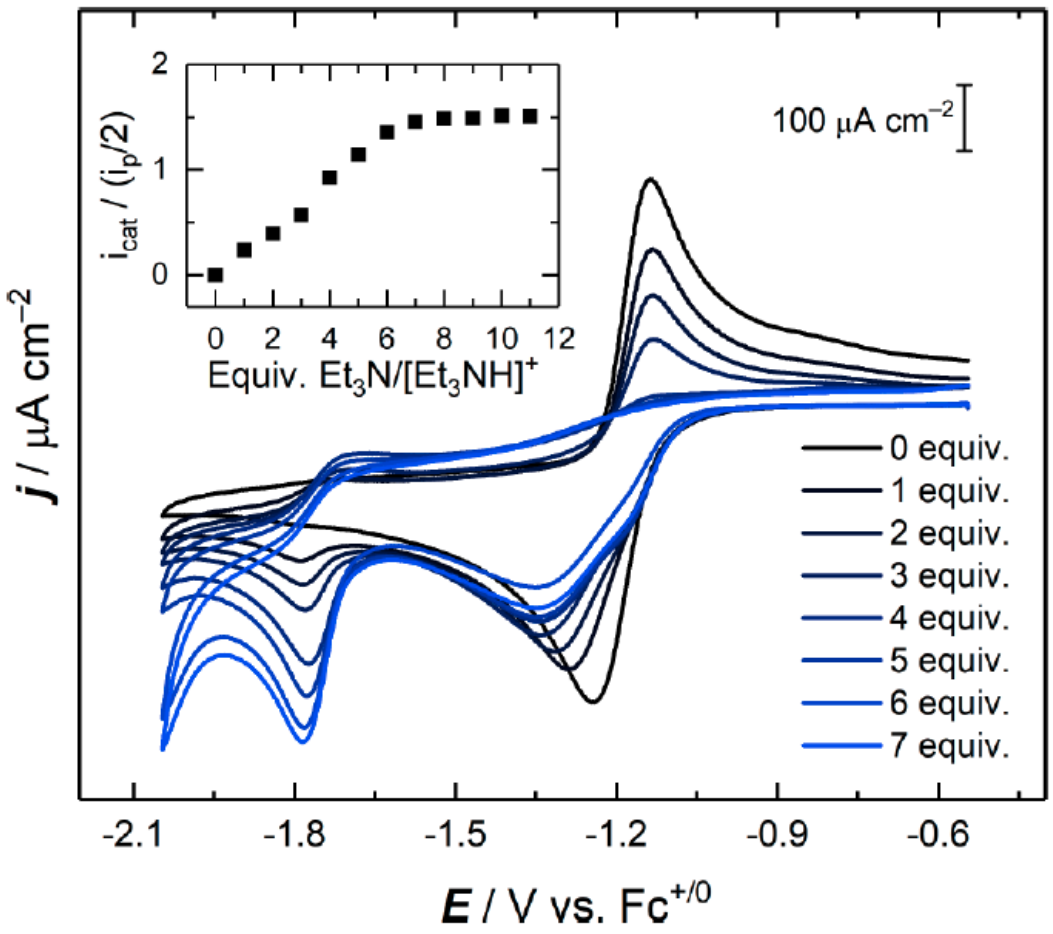

Figure 1.18. Cyclic voltammetry of **1-PQN** with 1 equiv of $[Et_3NH]^+/Et_3N$ in 50 μL additions in MeCN. Electrolyte = 0.1 M tetrabutylammonium hexafluorophosphate. Scan rate = 100 mV/s. Inset: Plot of $i_{cat}/(i_p/2)$ vs. equiv (mmol) of $[Et_3NH]^+/Et_3N$ added. Reprinted with permission from Hopkins, J. A.; Lionetti, D.; Day, V. W.; Blakemore, J. D., Chemical and Electrochemical Properties of [Cp*Rh] Complexes Supported by a Hybrid Phosphine-Imine Ligand. *Organometallics* **2019,** *38,* 1300-1310. Copyright 2019 American Chemical Society.

In a follow-up study in 2020, Hopkins et al.[27] focused on another hybrid imine/phosphine ligand bearing a methylene bridge. Lionetti and Henke showed the adverse

effects brought about by the presence of acidic methylene protons on the backbone of the **dpma** and **daf** ligands, respectively (*vide supra*); therefore, Hopkins sought to probe the reactivity effects of these methylene protons in the hybrid ligand system. The ligand chosen was 2-[(diphenylphosphino)methyl]pyridine, or **PN**; the study intended to both obtain more information on [Cp*Rh] complexes supported by this type of hybrid ligand and to examine the synthesis and properties of each analogous complex supported by this ligand as compared to those of **PQN**. Hopkins began by preparing the typical Rh(III) chloride precursor **1-PN** (see Scheme 1.6). The complex was characterized by NMR, which revealed the expected 15H Cp* methyl resonance at 1.50 ppm. As expected from the previously mentioned work of Lionetti and Henke, the methylene protons of **PN** are heterotopic as a result of chelation in the pseudo-octahedral complex; as such, two 1H resonances were evidenced at 4.43 and 4.14 ppm which display geminal coupling ($^{2}J_{H,H}$ = 17.4 Hz) and inequivalent coupling to a second nucleus (J = 14.5 and 10.7 Hz, respectively). This coupling was determined to be the result of $^{4}J_{H,P}$ coupling on the basis of $^{1}H\{^{31}P\}$ NMR experiments (see Figure 1.19). Due to the large geminal coupling relative to the small difference in chemical shift, these resonances demonstrate the second-order effect of "roofing" which is explained in depth in Chapter 3 of this dissertation for a different [Cp*Rh] system. Additionally, the $^{31}P\{^{1}H\}$ NMR data show the expected doublet corresponding to bound **PN** (51.57 ppm, $^{1}J_{P,Rh}$ = 140.3 Hz).

Complex **1-PN** was further characterized through X-ray diffraction studies. It is worth noting that solid-state structural information had previously been reported to the Cambridge Structural Database as a private communication, but no description of the structure or properties of the complex were made available with the report.[28] In our hands,

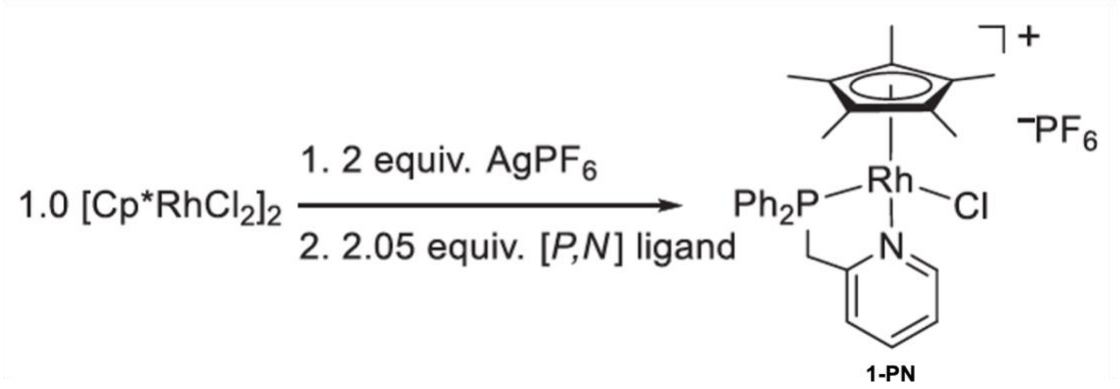

Scheme 1.6. Synthetic scheme for the preparation of **1-PN**. Reprinted from Synthesis and reactivity studies of a [Cp*Rh] complex supported by a methylene-bridged hybrid phosphine-imine ligand, volume 921, Julie A. Hopkins, Davide Lionetti, Victor W. Day, and James D. Blakemore, 121294, Copyright 2020, with permission from Elsevier.

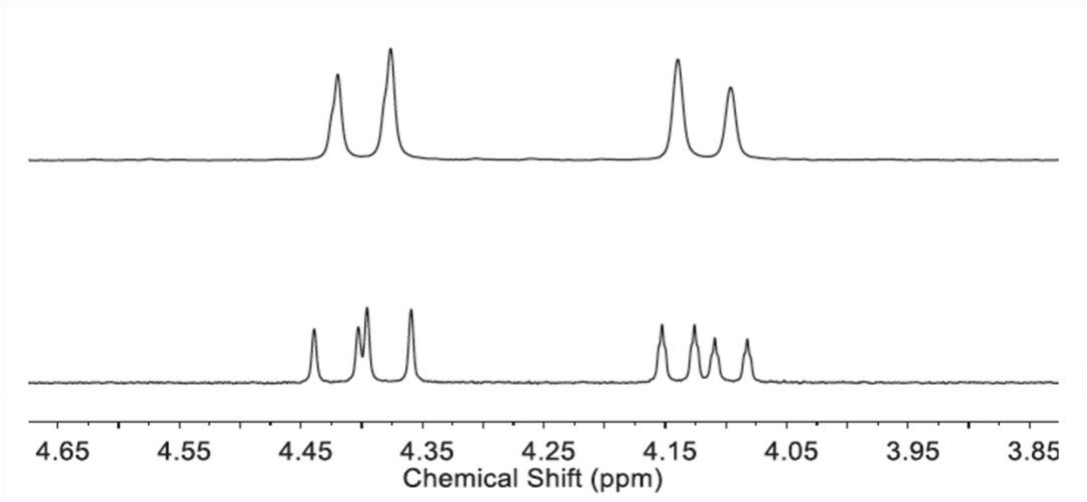

Figure 1.19. Top: $^{1}H\{^{31}P\}$ NMR of methylene protons of **1-PN**. Bottom: ^{1}H NMR of methylene protons of **1-PN**. Reprinted from Synthesis and reactivity studies of a [Cp*Rh] complex supported by a methylene-bridged hybrid phosphine-imine ligand, volume 921, Julie A. Hopkins, Davide Lionetti, Victor W. Day, and James D. Blakemore, 121294, Copyright 2020, with permission from Elsevier.

the obtained data were in agreement with the prior report. Notably, a comparison of **1-PN** to **1-PQN** reveals a similarity about the angle between the plane of the Cp* ligand and the plane of the ligand defined by Rh, N, and P (60.5° and 62.0°, respectively), indicating that the loss of rigidity of **PN** does not significantly influence the geometry about rhodium as compared to **PQN**. Additionally, there is less than 1° difference between the bite angle for both complexes despite the difference in flexibility. One marked difference, however, is found in the Rh–P bond distance; this bond is shorter in **1-PN** than in **1-PQN**. This result likely points to the stronger donor properties of the alkyl-diaryl phosphorus donor in **PN** as compared to the triaryl phosphorus donor of **PQN**, a hypothesis supported by the $^{31}P\{^{1}H\}$ NMR data of the two complexes (**1-PN** phosphorus doublet is shifted downfield ~ 4 ppm relative to that of **1-PQN**).

Hopkins next turned to cyclic voltammetry to characterize the redox properties of **1-PN**. It was observed that this complex displays similar electrochemical properties to those of **1-PQN**, such that the voltammogram shows a single $2e^-$ reduction event at –1.28 V of Rh(III) to Rh(I) (compared to –1.19 V for **1-PQN**, see Figure 1.20). This result supports both the increased electron density of **1-PN** and the occurrence of the aforementioned ECE' process, by which the first reduction occurs, chloride is ejected, and the second reduction occurs. Additionally, the second reduction event observed at –2.26 V for **1-PQN** (presumed to be ligand reduction) is not present here; this result supports the claim that the feature observed at –2.26V corresponds to reduction of **PQN**, as the quinoline π-system of **PQN** (which is not present in the pyridyl π-system of **PN**) would allow for ligand reduction not observed in **1-PN**.

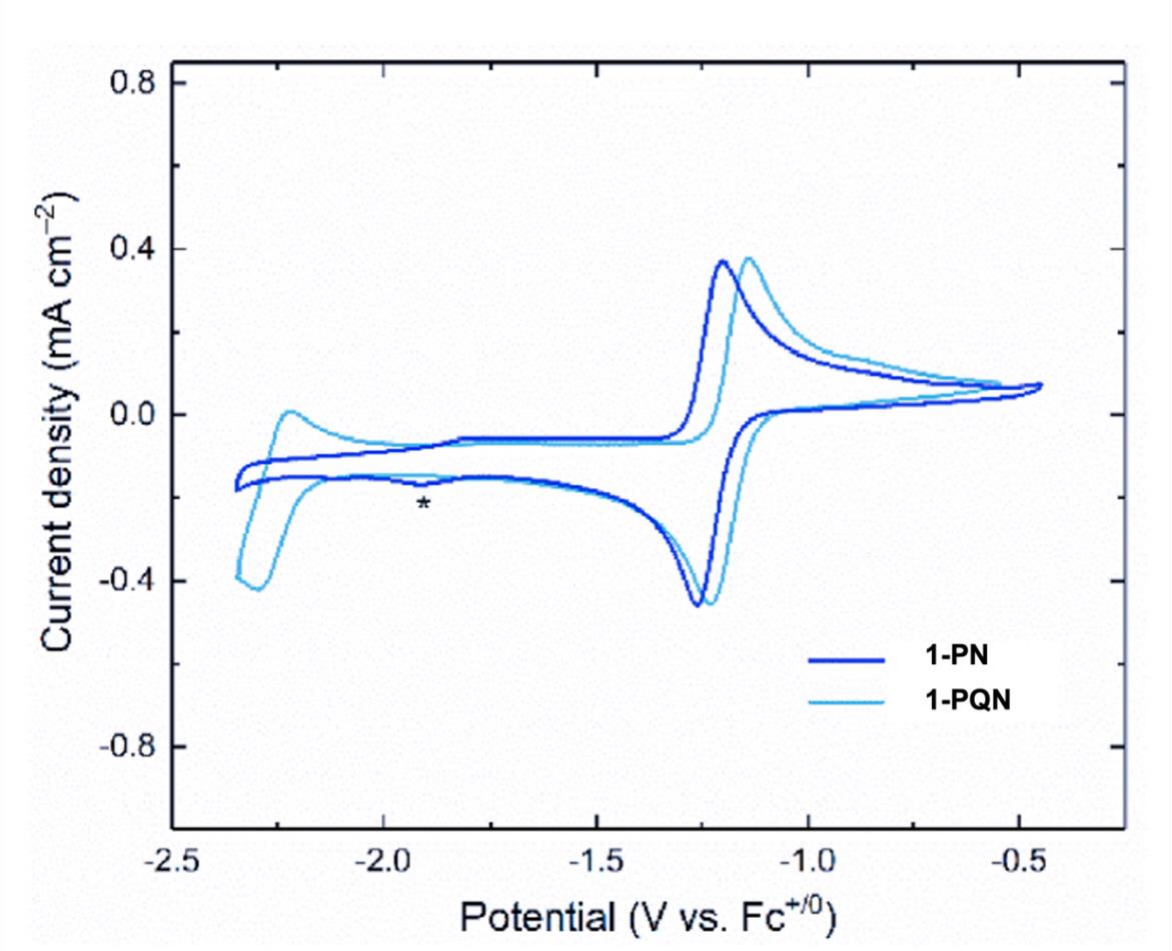

Figure 1.20. Comparison of cyclic voltammetry data for **1-PN** and **1-PQN** in MeCN. [Cp*Rh] = 1 mM. Electrolyte = 0.1 M tetrabutylammonium hexafluorophosphate. Scan rate = 100 mV/s. Reprinted from Synthesis and reactivity studies of a [Cp*Rh] complex supported by a methylene-bridged hybrid phosphine-imine ligand, volume 921, Julie A. Hopkins, Davide Lionetti, Victor W. Day, and James D. Blakemore, 121294, Copyright 2020, with permission from Elsevier.

Inspired by the remarkably clean electrochemistry of **1-PN**, Hopkins next endeavored to chemically prepare the Rh(I) form of the complex (**2-PN**) using Na(Hg). To their surprise, three rhodium species were detected in the collected spectral data of the

isolated material (see Figure 1.21, left). Upon initial investigation, it was clear to see that the three species were diamagnetic complexes in which the Cp* ligand was intact, as evidenced by three Cp* methyl peaks between 1.63–1.94 ppm. A doublet at 3.02 ppm integrates to 2H with respect to the minor Cp* compound, indicating the methylene protons of **2-PN**; because this Rh(I) complex is C_{2v}-symmetric, the methylene protons are now chemically equivalent (homotopic). This assignment was further supported by the $^{31}P\{^{1}H\}$ NMR data in which a further downfield-shifted doublet (61.1 ppm, $^{1}J_{P,Rh}$ = 244.7 Hz) showing stronger coupling to rhodium than that of **1-PN** is present. As for the other species in solution, two explicit resonances appear upfield at –12.0 and –13.3 ppm, indicating the formation of two unique Rh–H species (see Figure 1.21, right). On the basis of extensive 2D NMR characterization techniques, these two complexes were identified as the monohydride **3-PN**, analogous to monohydride **3-PQN** from the prior work, as well as a monohydride complex bearing an L,X-type ligand derived from **PN** that results from deprotonation of one methylene proton (**4-PN**).

The contrast between the clean electrochemistry and the complex chemical reactivity indicates that the formation of **3-PN** and **4-PN** must be rather slow, as their formation was not observed in the voltammogram. The electron transfer process, however, must be rapid, as evidenced by both the clean electrochemistry and the visibly fast color change upon chemical reduction observed by Hopkins. There is speculation as to which form of the complex is deprotonated to form the two hydride species; the basic Rh(I) complex upon formation can deprotonate the methylene protons of **1-PN** or the transient Rh(II) complex

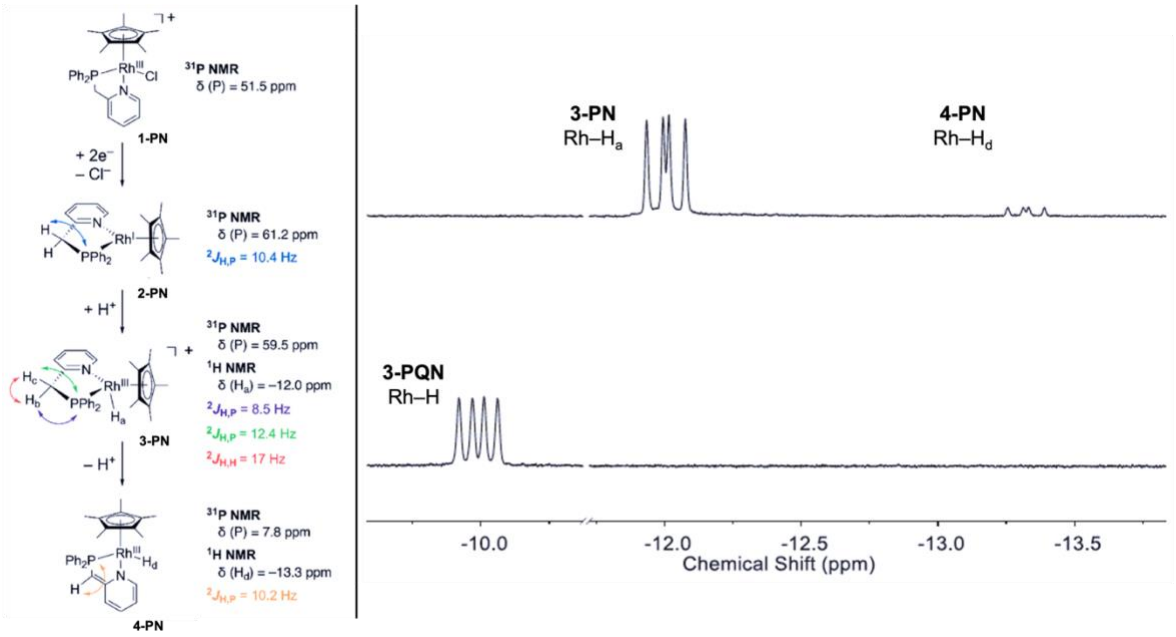

Figure 1.21. Left: Schematic reactivity of **1-PN** upon reaction with Na(Hg). Right: Upfield region of ^{1}H NMR spectra upon reaction of **1-PN** with Na(Hg) (top) and of **3-PQN** for comparison (bottom). Reprinted from Synthesis and reactivity studies of a [Cp*Rh] complex supported by a methylene-bridged hybrid phosphine-imine ligand, volume 921, Julie A. Hopkins, Davide Lionetti, Victor W. Day, and James D. Blakemore, 121294, Copyright 2020, with permission from Elsevier.

formed upon the initial reduction. Poor solubility of **1-PN** under the reaction conditions would allow for simultaneous presence of both **1-PN** and **2-PN** in the reaction vessel, supporting the likelihood that the Rh(III) chloride complex methylene protons are the ones deprotonated to form the hydrides. Similarly, deprotonation of the methylene protons of **3-PN** would result in formation of **4-PN**; this mechanistic pathway is supported through the small quantity of **4-PN** relative to **3-PN**.

On the basis of these two works towards characterization and reactivity studies of [Cp*Rh] complexes supported by hybrid imine/phosphine ligands, Hopkins has conclusively shown that the effect of including a phosphine chelator drastically modulates the reactivity of these complexes relative to the parent diimine-supported complexes. These hybrid ligands show a remarkable ability to stabilize the formation of an explicit, isolable Rh–H complex which was never achieved for the **bpy**-based systems. Despite this difference, the electrochemistry reveals the same ECE' process is in play on the electrochemical timescale as in the **bpy**-based systems, such that a quasi-reversible $2e^-$ process is observed for the clean reduction of Rh(III) to Rh(I). Additionally, both the **bpy**-based systems and **1-PQN** are able to generate hydrogen, despite the fact that the systems differ in their preference to form [Cp*H] or Rh–H upon protonation of the reduced Rh(I) species. This work complements that of the foundational **bpy**-based systems and additionally suggests the avoidance of acidic methylene protons in such systems, as their presence deters from the clean isolation of the Rh(I) reduced species which is plays a critical role in the hydrogen evolution catalysis.

1.2.6 Investigation of the Effect of Further Stabilization Imparted to [Cp*Rh] Complexes through Use of Chelating Diphosphine Ligands

In light of the efforts of the Blakemore Group to investigate the [Cp*Rh] system through use of different chelating ligands, Boyd et al.[23] ventured in 2018 to develop one additional class of these complexes which included [Cp*Rh] complexes supported by diphosphine ligands. As stated previously, this work by Boyd and the work discussed by Hopkins on the **PQN** system were conducted simultaneously; the results from both systems were obtained and discussed concurrently within our group. Therefore, it is important to

establish that this work by Boyd was not conducted *in response* to the work by Hopkins, but as a simultaneous, widespread effort within our group to develop ligand systems separate from the standard diimine-based systems.

Inspired by literature reports suggesting that phosphine ligands can stabilize [Cp*Rh] hydrides, Boyd set out to utilize the chelating diphosphine ligand bis(diphenylphosphino)benzene (**dppb**) to prepare a new series of [Cp*Rh] complexes. Despite the literature reports of [Cp*Rh] hydrides formed utilizing diphosphine chelators, no electrochemical studies on any of these complexes were reported. The processes for preparation of the precursor Rh(III) chloride, reduction of that complex to Rh(I), and formation of the Rh(III)–H (**1-dppb**, **2-dppb**, and **3-dppb**, respectively) are shown in Scheme 1.7. As was the case in the hybrid ligand **PQN** systems of Hopkins, the reduction/protonation pathway giving rise to the Rh–H complex was overall high-yielding and successful. The modularity of this pathway was tested with two other diphosphine ligands in a later study, as described in Chapter 2 of this dissertation.

X-ray diffraction studies were conducted on **1-dppb**, in which the geometry about rhodium was found to be pseudo-octahedral, as most Rh(III) chloride complexes are that we have worked with in our research. The angle between the plane defined by Cp* and the plane containing Rh and each phosphorus chelate is 66° for **1-dppb**. This value compares well to the same angle in the analogous [Cp*Rh(L)(Cl)][PF_6] structures described herein (L = **bpy**: 59°; **dpma**: 60.5°; **Me$_2$dpma**: 67.4, 66.8°; **PQN**: 60.5°; **PN**: 62°). The harmony among these angles suggests that the identity of the ligand, despite the differed electronics in each case,

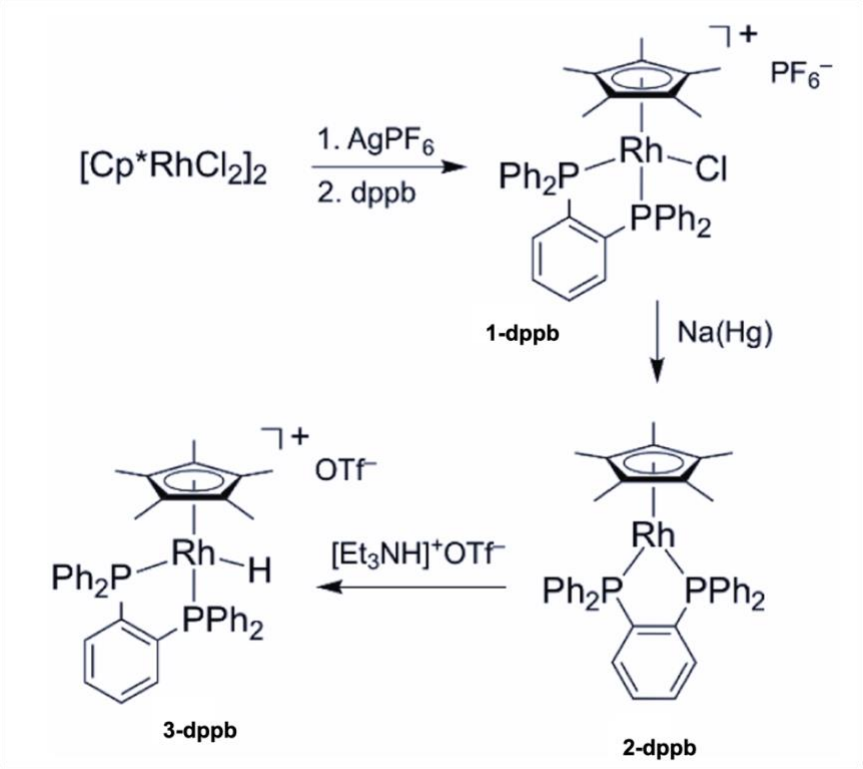

Scheme 1.7. Synthetic scheme showing the preparation of the three **dppb**-bound complexes analyzed in this study. Reprinted with permission from Boyd, E. A.; Lionetti, D.; Henke, W. C.; Day, V. W.; Blakemore, J. D., Preparation, Characterization, and Electrochemical Activation of a Model [Cp*Rh] Hydride. *Inorg. Chem*. **2019**, *58*, 3606-3615. Copyright 2019 American Chemical Society.

does little to affect the position of the bidentate chelator in the complex. A notable exception to this case is **Me$_2$dpma** which shows a slightly larger angle due to the presence of the sterically hindering methyl groups of the diimine ligand with those of the Cp* ligand.

With the solid-state data confirming the structure of **1-dppb**, Boyd endeavored to characterize the electrochemical properties of the complex. Upon reduction of **1-dppb**, an irreversible 2e$^-$ reduction was observed, centered at –0.85 V; notably, upon the second and

subsequent scans of the solution, a new reductive feature appeared at –0.82 V ($E_{p,c}$) corresponding to the formation and subsequent reduction of the Rh(III) solvento species. This 2e$^-$ reduction event of **1-dppb** is reminiscent to those quasi-reversible events arising from the ECE' process which occurs in both the diimine- and hybrid ligand-based systems (*vide supra*). While this ECE' process is more or less identical in each system, the reduction potential of –0.85 V of **1-dppb** is shifted markedly more positive than those of bpy-ligated complex **2-Cl** (Henke, –1.21 V) and **1-PQN** (–1.19 V). This shift to more positive potentials for the $Rh^{III/I}$ reduction potential of **1-dppb** is likely the result of the increased stabilization of the Rh(I) form of the complex afforded by **dppb** relative to **bpy** and **PQN**.

As shown in Scheme 1.7, **1-dppb** underwent clean reduction with Na(Hg) to give Rh(I) pentacoordinate species **2-dppb**. Characterization of the isolated material by NMR confirms the formation, as the Cp* resonance for **2-dppb** shows increased coupling to the phosphorus atoms relative to **1-dppb** (t, $^3J_{H,P}$ = 3.4 and 1.8 Hz, respectively). Additionally, the $^{31}P\{^1H\}$ NMR data reveal the expected doublet corresponding to the two equivalent phosphorus atoms of **2-dppb**, which couple to rhodium more strongly in **2-dppb** than in **1-dppb** ($^1J_{P,Rh}$ = 220 and 131 Hz, respectively); the same observation was made for the phosphorus atom in the complexes of **PQN** and **PN** characterized by Hopkins (*vide infra*). Crystals of the complex were not grown due to great solubility of the material in most organic solvents. The electrochemical analysis of **2-dppb** reveal that this species is indeed the product of electrochemical reduction of **1-dppb**.

Boyd next attempted to chemically prepare the Rh–H complex **3-dppb** (see Scheme 1.7). Anilinium triflate was employed as the acid in the reaction with **2-dppb** on the basis of

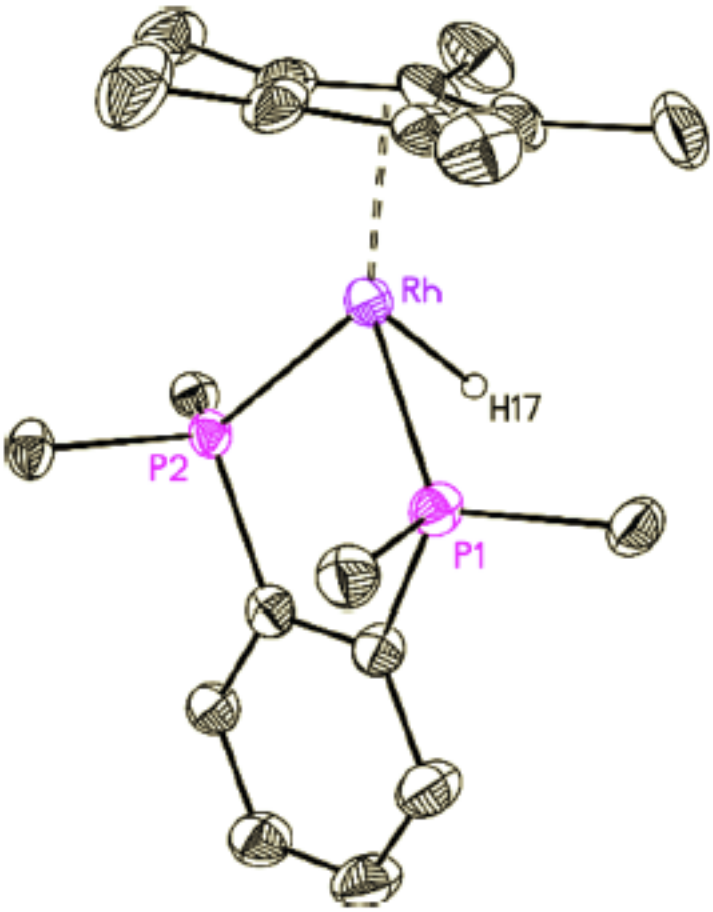

Figure 1.22. Solid-state structure of **3-dppb**. Displacement ellipsoids are shown at 50 % probability. Hydrogen atoms except H17, terminal phenyl rings, and the outersphere triflate are omitted for clarity. Reprinted with permission from Boyd, E. A.; Lionetti, D.; Henke, W. C.; Day, V. W.; Blakemore, J. D., Preparation, Characterization, and Electrochemical Activation of a Model [Cp*Rh] Hydride. *Inorg. Chem*. **2019**, *58*, 3606-3615. Copyright 2019 American Chemical Society.

its success in forming the Rh–H complex **3-PQN** (*vide supra*). Spectral data of the isolated material reveal the expected upfield signal at –11.8 ppm, indicating the formation of the desired Rh–H. The hydride was observed to couple to both rhodium and phosphorus,

resulting in an apparent quartet resonance due to coincidentally similar coupling constants for both rhodium and phosphorus; further discussion of this similarity as well as the spectral properties of this hydride resonance are discussed in Chapter 2 of this dissertation (*vide infra*). Further support for the formation of this complex was provided through evidence of Cp* retention in a single 15H resonance. Furthermore, the infrared spectrum of **3-dppb** shows the explicit Rh–H stretching frequency at 1986 cm^{-1}. Finally, solid-state analysis of the complex confirmed the retention of Cp* as well as the hydride, which was located in the Fourier difference map and was freely refined to give its location (see Figure 1.22).

To probe the hydrogen evolution capabilities of **3-dppb**, Boyd turned to *in-situ* NMR studies of the complex in the presence of acids. Based on the results of Hopkins with the **3-PQN** complex, **3-dppb** was subjected to $[DMFH]^{+}[OTf]^{-}$ and monitored via NMR. In contrast to **3-PQN**, the spectral data of this reaction with **3-dppb** resulted in no detectable reactivity over 48 hours; heating the sample to 50 °C for an additional 24 hours did not induce reactivity. This resistance to protonolysis, even in the presence of strong acids, highlights the stability of the hydride species as compared to all previously studied hydrides (Cp*H or Rh–H) imparted through use of the diphosphine chelating ligand **dppb**. This stability was further probed by Comadoll et al. through the preparation of two subsequent Rh–H complexes supported by diphosphine ligands; these complexes were also resistant to protonolysis (Chapter 2, *vide infra*).

Despite the resistance of **3-dppb** to evolve hydrogen chemically in the presence of strong acid, Boyd attempted the electrochemical evolution of hydrogen from **3-dppb**. The holding potential of the bulk electrolysis was –2.23 V based on the cyclic voltammetry experiments of this complex (see Figure 1.23); the electrolysis was run at this potential for

1 hour and the headspace was analyzed by GC. To their delight, H_2 was detected at a faradaic efficiency of 58 %. It is speculated that the process occurs through a metal-centered reduction at –2.23 V to generate a transient Rh^{II}–H complex which, upon formation, can undergo Rh–H bond homolysis or protonolysis by an auxiliary proton source. While further analysis of the mechanistic pathway for this process was not undertaken, Boyd notes that the homolysis pathway for H_2 generation within this system is reminiscent of work done by

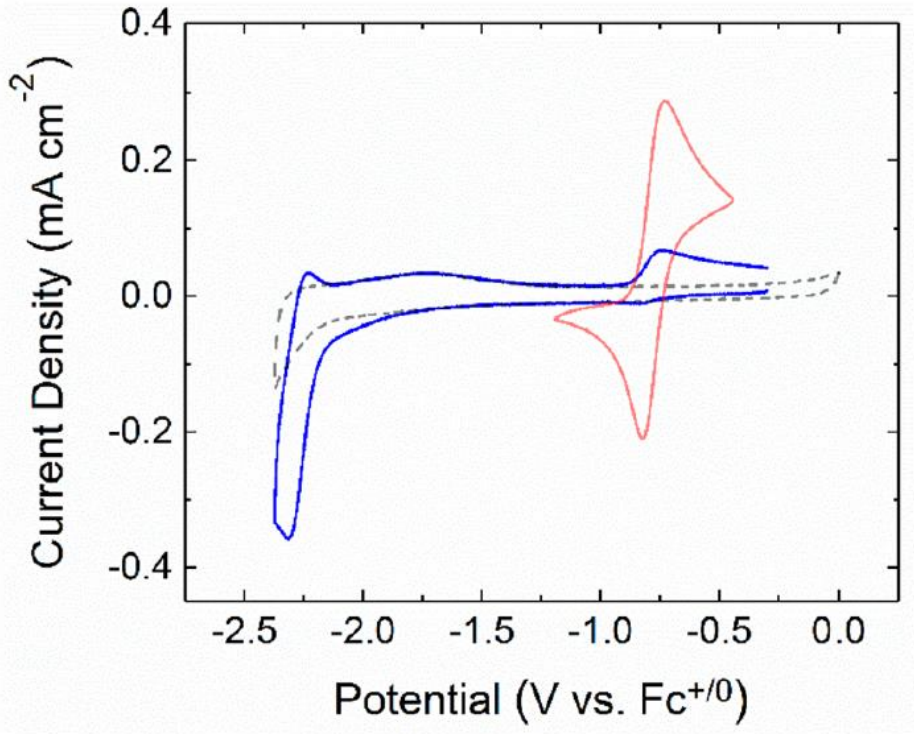

Figure 1.23. Cyclic voltammetry of **2-dppb** (red), **3-dppb** (blue), and the blank (gray) in MeCN. [Cp*Rh] = 1 mM. Electrolyte = 0.1 M tetrabutylammonium hexafluorophosphate. Scan rate = 100 mV/s. Reprinted with permission from Boyd, E. A.; Lionetti, D.; Henke, W. C.; Day, V. W.; Blakemore, J. D., Preparation, Characterization, and Electrochemical Activation of a Model [Cp*Rh] Hydride. *Inorg. Chem*. **2019**, *58*, 3606-3615. Copyright 2019 American Chemical Society.

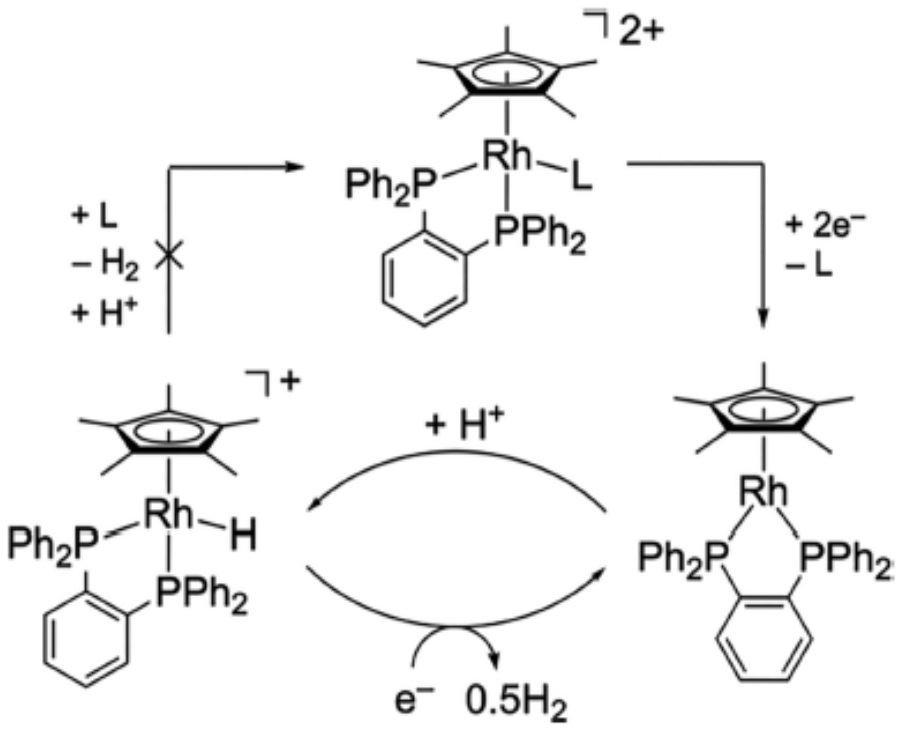

Scheme 1.8. H_2 evolution chemistry supported by the **dppb** system. Reprinted with permission from Boyd, E. A.; Lionetti, D.; Henke, W. C.; Day, V. W.; Blakemore, J. D., Preparation, Characterization, and Electrochemical Activation of a Model [Cp*Rh] Hydride. *Inorg. Chem.* **2019**, *58*, 3606-3615. Copyright 2019 American Chemical Society.

Wayland and coworkers on similar rhodium systems. A summary of results of H_2 evolution on this platform can be seen in Scheme 1.8.

As demonstrated up to this point, bulk electrolysis was utilized to analyze the propensity for H_2 generation on the complexes **(Cp*H)Rh(bpy)(Br), 1-Cl**, **2-Cl**, **3-Cl**, **4-Cl**, and **1-PQN** by Peng, Henke, Moore, and Hopkins (*vide supra*). The compiled results of all bulk electrolyses can be found below in Table 1.2. The electrolyses of protonated complexes **(Cp*H)Rh(bpy)(Br)** and **3-dppb** occurred at the most negative potentials; both

Table 1.2. Results of bulk electrolysis experiments on select complexes.

Complex	Holding Potential (V)	Time of Experiment (h)	Faradaic Efficiency	TON (#)
(Cp*H)Rh(bpy)(Br)[a]	–1.86	1	71 %	N/A[c]
1-Cl[b]	–1.36	1.5	90 %	3.36
2-Cl[b]	–1.36	1.5	93 %	4.39
3-Cl[b]	–1.36	1.5	67 %	2.72
4-Cl[b]	–1.75	1.5	5 %	N/A[c]
1-PQN[b]	–1.75	1.5	34 %	1.3
3-dppb[a]	–2.23	1.1	58 %	N/A[c]

[a] Complex tested was a hydride species, either [Cp*H] or [Rh–H]. [b] Complex tested was a Rh(III) chloride species. Therefore, excess quantities of acid or a buffered acid solution was used. [c] The authors did not report a TON.

experiments resulted in the production of hydrogen in moderate faradaic efficiencies. Contrasting with this result is the poor production of hydrogen by Moore's dinitro complex **4-Cl** and Hopkins' hybrid PQN complex **1-PQN**. Finally, Henke's **bpy** complexes **1-Cl** and **2-Cl** proved to be superior, with the ^{CF3}**bpy**-bound **3-Cl** suffering slightly in comparison.

As a follow-up study to the work done by Boyd, Comadoll et al.[1] prepared two series of analogous complexes to those prepared by Boyd which were ligated by bis(diphenylphosphino)methane (**dppm**) and 4,5-bis(diphenylphosphino)-9,9-dimethylxanthene (**Xantphos**). The preparation, characterization, and chemical properties of these complexes are discussed at length in Chapters 2 and 3 of this dissertation (*vide*

infra). In short, the synthesis for each of these complexes was shown to be modular across the series of diphosphine ligands; each complex was prepared in good yield, despite the changing rhodacycle size. The heterotopicity of the methylene protons of **dppm** when ligated to a Rh(III) metal center were investigated thoroughly through multifrequency NMR analysis as well as digital NMR simulations. The chemical reactivity of the prepared Rh–H complexes in the presence of strong acid was equivalent to that of **3-dppb**, such that the generation of hydrogen was not observed. No electrochemical studies were done on the complexes as a result.

1.2.7 Discussion

When the Blakemore Group first endeavored to study the [Cp*Rh] system in 2016, much consideration was given to the ability of the system to manage the protons and electrons required for hydrogen evolution. As previously mentioned, the hypothesis was that the **bpy** ligand of the parent complex discovered by Kölle and Grätzel was responsible for electron management, the Cp* was responsible for proton management, and the rhodium metal center played a role in both (see Figure 1.1). Our efforts described in this chapter demonstrate the explicit role that the ligand plays in controlling the electronics of the complexes, thereby controlling in some way whether a reduced species reacts with a proton to form Rh–H or a Cp*H interaction. The role of ligands such as **bpy** to manage electrons has been well-discussed to this point; the observation that reduction of the metal center results in drastically reduced character within **bpy** and its derivatives supports this notion. The lesser elucidated part of this process revolves around the behavior of Cp*. Despite the work we have done on this system, the reason why **bpy** systems prefer to store the first

proton equivalent on the Cp* ring is still not clear to us; likewise, we do not know why that process is disfavored with diphosphine ligands, which prefer to form a Rh–H bond.

In attempts to shed light on this discrepancy, Boyd notes in her study of the **dppb** system that the analogous Rh(I) complexes supported by disubstituted **bpy** ligands studied by Henke were reacted with anilinium triflate and analyzed *in situ* by NMR. It is worth noting that this is the same acid Henke used in his bulk electrolysis studies of these complexes which led to hydrogen evolution with high faradaic efficiencies.[11] The spectra for reaction of anilinium triflate with the complexes of **bpy** and **^{tBu}bpy**, both ligands which supported catalytic hydrogen evolution on the [Cp*Rh] scaffold, showed the formation of the respective Cp*H complex as well as trace Rh–H formation, evidenced by resonances at ~ –10 ppm. The result was interesting, inasmuch as no hydride was observed in the NMR when triethylammonium acid salts were used to prepare the Cp*H complexes by Peng.[7] Even more strange is the result of the reaction of anilinium triflate with the Rh(I) complex supported by **^{CF3}bpy**, a ligand which performed poorly as a catalyst for hydrogen evolution; this spectrum showed only the generation of the Cp*H complex and no evidence of Rh–H generation. Indeed, Henke postulated[11] upon observation of the electrochemical data in the presence of acid that **^{CF3}bpy** as the ligand altered the mechanism through which the catalysis occurred; this difference in mechanism that he referred to in 2017 could have been the absence of Rh–H formation. These results suggest that utilization of an acid whose conjugate base is protic (anilinium/aniline, as opposed to triethylammonium/triethylamine) might enact some form of proton transfer mediation, allowing for a lower kinetic barrier for interconversion between the Rh–H and Cp*H tautomers. Efforts are ongoing in our research group to probe the kinetics of tautomerization in these systems.

The preferential formation of one tautomer over the other (Cp*H vs. Rh–H) in a given system has a marked effect on the catalytic hydrogen evolution capabilities of the complexes, as evidenced by the respective protonated complexes of **bpy** and **dppb**. Even more importantly, in light of this NMR study performed by Boyd, there appears to be a direct correlation between the number of species formed upon protonation with anilinium triflate and the performance of catalytic hydrogen evolution. Complexes of ^{tBu}**bpy** and **bpy** formed both tautomers in the NMR data and both perform well as catalysts, while complexes of ^{CF3}**bpy** and **dppb** form *only one* species upon protonation (Cp*H and Rh–H, respectively) and show either attenuated or no catalytic propensity. Indeed, computational studies on the mechanism of proton transfer in these systems involve intermediates which rely on the first acid equivalent acting as a "bridge" between Cp* and rhodium. In other words, catalytic activity appears to depend on the ability of a protonated complex to adopt this bridging conformation, or at least the ability to tautomerize between the two forms in some fashion; on the other hand, overstabilization of either Cp*H or Rh–H introduces a barrier to tautomerization and, therefore, stifles catalytic activity.

Within this idea that tautomerization and relative stability influence the catalysis lies the ability to tune the relative basicity of Cp* and rhodium through the bidentate ligand used. Rhodium is less electron-dense when **bpy** ligands are employed, as the extended π system is reduced noticeably upon reduction of the metal center. In these instances, the basicity of the Cp* ligand appears to be stronger than that of rhodium, thereby giving preference to formation of Cp*H. Conversely, hybrid imine/phosphine and diphosphine ligands are not as stabilizing to the metal center, as evidenced by the virtually unaffected C–C bond lengths in **2-PQN** upon reduction relative to the drastically shortened interpyridine C–C bond length.

As such, the rhodium is more electron dense and therefore more basic, resulting in the formation of Rh–H in these systems. Taken together, the results of our work suggest the ability to find the "sweet spot" for tuning these catalysts through the employment of altered bidentate chelating ligand systems, such that neither form of the protonated tautomer is overly stabilized. According to our studies, this is best achieved through use of **bpy** ligands which, if substituted, are electron-donating, as electron-withdrawing substituents overly stabilize the Cp*H form of the complexes. Even still, there are many ligand systems which have yet to be employed in this sort of study which could furnish even better performing catalysts for hydrogen generation.

1.2.8 Conclusion

The research contributions provided by Blakemore and coworkers on the [Cp*Rh] system are thorough, compelling, and exciting. Through careful choosing of the desired ligand scaffold modifications for each study, we have performed a comprehensive ligand structure-reactivity analysis for the [Cp*Rh] scaffold. In the diimine ligand scaffold, the **bpy**-derived complexes reported by Peng, Henke, and Moore show a modular preparation of Rh(III) chloride, Rh(I), and the corresponding [Cp*H] complexes despite the presence of extended π systems (**phen**) or disubstitution of the **bpy** ligand with electron-withdrawing (-NO_2, -CF_3) and electron-donating (-tBu) groups. The structural information obtained through solid-state studies both supports and strengthens existing literature reports, specifically regarding the observable bond metric changes which occur upon reduction of the ligand π system. Additionally, each of these ligands allowed the generation of hydrogen in bulk electrolysis experiments in varied faradaic efficiencies, with the electron-withdrawing groups visibly hampering the catalytic properties of the given complexes.

Additionally, Henke's efforts to diversify the **bpy** ligand scaffold through use of the various **daf**-derived ligands in the preparation of new [Cp*Rh] complexes provided insight into the effects of employing a strained bipyridyl ligand in these efforts. Likewise, the electrochemistry of complexes supported by **daf**-like ligands bearing reactive functional groups such as a ketone or a doubly benzylic methylene group proved incapable of stabilizing the reduced metal center due to undesired reactivity upon the increase of electron density in the system. Taken together, the comprehensive work on the **bpy**-derived ligands has added to and strengthened our understanding of the reactivity of these complexes.

Lionetti and Hopkins took the ligand derivatization studies one step further in their work on the **dpma**-derived ligands. This work was initiated by Lionetti in his investigation of **Me$_2$dpma** as a ligand in this system. Notably, the "ligand flip" phenomenon was observed upon reduction of the complex to the Rh(I) oxidation state, where a pyridyl ring associated the rhodium in a κ^2-fashion; solid-state structural analysis led to the determination that this interaction was dearomative with respect to the pyridyl ring. From there, the modifications they made to this class of ligand allowed for the probing of a multitude of effects across the series; they investigated the structural and chemical properties as a result of broken conjugation between the pyridyl rings on the stability of [Cp*Rh] complexes, reactivity of acidic methylene protons, addition of substituents bearing extended π systems, and steric effects of large geminal substituents on these ligands. Additionally, Hopkins spearheaded a complex electrochemical study in which the rate constant for the ligand flip EC process was determined across the entire series using Savéant's developed zone diagrams. These studies comprehensively elucidate the importance of extended conjugation across the π system of

the chelating ligand in stabilizing the more reduced, catalytically important forms of these [Cp*Rh] complexes.

Hopkins then shifted away from the **bpy** ligand system all together in pursuit of the preparation of [Cp*Rh] complexes bearing hybrid imine/phosphine ligands. As a result of the proven stabilizing properties of phosphines in metal complexes, the preliminary idea behind this work was that the inclusion of a phosphine atom might finally allow for the isolation of an explicit Rh–H species. Indeed, the **PQN**-ligated system afforded clean reduction to the Rh(I) complex and subsequent protonation to furnish the Rh–H complex with the Cp* ligand retained. The complex, despite the stabilization afforded through the phosphorus chelator, was able to generate hydrogen chemically under acidic conditions. Modifications to this ligand scaffold included substitution of the quinoline core with a methylpyridine moiety in the **PN** system; using this ligand proved deleterious as compared to **PQN** due to the acidic methylene protons on the backbone of **PN**. The system was incredibly reactive upon reduction to the Rh(I); isolation of this complex, in contrast to that of **PQN**, was precluded by the formation of two Rh–H byproducts resulting from basic Rh(I) deprotonating the methylene protons of **PN**. Taken together, the results shown by Hopkins using this hybrid ligand system support the stability imparted by the inclusion of phosphine and represent the first instance in our group of the clean generation and isolation of a [Cp*Rh–H].

Finally, Boyd led the efforts in furthering the stability observed by Hopkins' **PQN** ligand by employing diphosphine ligand **dppb** in the [Cp*Rh] scaffold. In line with the increased stability upon inclusion of two phosphine chelators, the isolated Rh–H complex was unable to evolve hydrogen under any attempted chemical methods. However, the

complex was able to evolve hydrogen under reductive electrochemical conditions, albeit with less faradaic efficiency than those of the **bpy** system. In spite of the success herein, two additional [Cp*Rh] complexes supported by diphosphine ligands **dppm** and **Xantphos** were prepared. Both the synthetic efforts across the series and the chemical reactivity of the Rh–H complexes prepared from these ligands were in line with the results of Boyd, such that the synthetic reduction/protonation route to access each complex was shown to be modular across the series, despite the varied rhodacycle size, and the hydrides were stable in the presence of strong acid. These complexes add much to the literature, as reports of characterization and chemical reactivity studies of [Cp*Rh] hydrides supported by phosphine ligands are few.

Taken together, the results of our study have provided new insight into the electronics and reactivity of the [Cp*Rh] system when ligated with a variety of different bidentate chelating ligands. We have shown the effects of ligand substitution, modification through breaking conjugation of the ligand, changing the chelating atom, including reactive functionalities in the ligand backbone, and changing the size of the rhodacycle; as a result, our efforts to date provide insight to the properties which govern the catalytic processes of these complexes, thereby offering new considerations for catalyst design on this platform through tuning of catalyst properties with different ligands.

1.2.9 Acknowledgements

Those who contributed to this body of work from the Blakemore group from 2016-2021 collectively thank Dr. Justin Douglas and Sarah Neuenswander for assistance with NMR spectroscopy, as well as Dr. Victor Day, Dr. Michael Takase, and Dr. Allen Oliver for assistance with crystallography. All work in this chapter was supported by one or more of

the following funding sources: the State of Kansas through an award from the University of Kansas New Faculty General Research Fund, the National Science Foundation through the NSF CCI Solar Fuels Program (CHE-1305124), US National Science Foundation through award OIA-1833087, the US NIH Graduate Training Program in the Dynamic Aspects of Chemical Biology (T32 GM008545-25), the Kansas Academy of Science, the Beckman Scholars Program at the University of Kansas, the KU Center for Undergraduate Research, the NSF REU Program in Chemistry at the University of Kansas (CHE-1560279). The contributors also acknowledge the following sources which provided instrumentation: the U.S. National Institutes of Health Shared Instrumentation Grants (NMR: S10OD016360, S10RR024664, and CHE-0320648; X-ray diffractometers: CHE-0079282 and CHE-0923449; EPR: CHE-0946883), NSF MRI funding (CHE-1625923), SOLEIL for provision of synchrotron radiation facilities (proposal 20161346), and the Caltech EPR facility.

1.3 References

[1] Comadoll, C. G.; Henke, W. C.; Hopkins Leseberg, J. A.; Douglas, J. T.; Oliver, A. G.; Day, V. W.; Blakemore, J. D., Examining the Modular Synthesis of [Cp*Rh] Monohydrides Supported by Chelating Diphosphine Ligands. *Organometallics* **2021**, *40*, 3808-3818.

[2] Kumar, A.; Comadoll, C. G.; King, D. S.; Oliver, A. G.; Day, V. W.; Blakemore, J. D., Incorporation of [Cp*Rh] and [Cp*Ir] Species into Heterobimetallic Complexes via Protonolysis Reactivity and Dioximato Chelation. *Inorg. Chem.* **2021**, *60*, 14047-14059.

[3] Mori-Quiroz, L. M.; Comadoll, C. G.; Super, J. E.; Clift, M. D., Exploiting Iminoquinones as Electrophilic at Nitrogen "N+" Synthons for C–N Bond Construction. *Org. Lett.* **2021**, *23*, 7008-7013.

[4] Cartwright, K. C.; Joseph, E.; Comadoll, C. G.; Tunge, J. A., Photoredox/Cobalt Dual-Catalyzed Decarboxylative Elimination of Carboxylic Acids: Development and Mechanistic Insight. *Chem. Eur. J.* **2020**, *26*, 12454-12471.

[5] (a) Kölle, U.; Grätzel, M., Rhodium(III) complexes as homogeneous catalysts for the photoreduction of protons to hydrogen. *Angew. Chem.* **1987**, *99*, 572-574. (b) Kölle, U.; Grätzel, M., Organometallic Rhodium(III) Complexes as Catalysts for the Photoreduction of Protons to Hydrogen on Colloidal TiO_2. *Angew. Chem. Int. Ed. Engl.* **1987**, *26*, 567-570.

[6] Ruppert, R.; Herrmann, S.; Steckhan, E., Very efficient reduction of $NAD(P)^+$ with formate catalysed by cationic rhodium complexes. *J. Chem. Soc., Chem. Commun.* **1988**, 1150-1151.

[7] Peng, Y.; Ramos-Garcés, M. V.; Lionetti, D.; Blakemore, J. D., Structural and Electrochemical Consequences of [Cp*] Ligand Protonation. *Inorg. Chem.* **2017**, *56*, 10824-10831.

[8] Gore-Randall, E.; Irwin, M.; Denning, M. S.; Goicoechea, J. M., Synthesis and Characterization of Alkali-Metal Salts of 2,2′- and 2,4′-Bipyridyl Radicals and Dianions. *Inorg. Chem*. **2009**, *48*, 8304-8316.

[9] Kaim, W.; Reinhardt, R.; Waldhoer, E.; Fiedler, J., Electron transfer and chloride ligand dissociation in complexes $[(C_5Me_5)\text{-}ClM(bpy)]^+/[(C_5Me_5)M(bpy)]^n$ (M = Co, Rh, Ir; n = 2+, + , 0, –): A combined electrochemical and spectroscopic investigation. *J. Organomet. Chem*. **1996**, *524*, 195-202.

[10] (a) Crabtree, R. H., *The Organometallic Chemistry of the Transition Metals*, 4th ed.; Wiley-Interscience: Hoboken, NJ, 2005. (b) Chatt, J.; Venanzi, L. M., 955. Olefin co-ordination compounds. Part VI. Diene complexes of rhodium(I). *J. Chem. Soc.* **1957**, 4735-4741. (c) Ibers, J. A.; Snyder, R. G., Structure of (rhodium(I) chloride-1,5-cyclooctadiene)$_2$. *J. Am. Chem. Soc.* **1962**, *84*, 495-496.

[11] Henke, W. C.; Lionetti, D.; Moore, W. N. G.; Hopkins, J. A.; Day, V. W.; Blakemore, J. D., Ligand Substituents Govern the Efficiency and Mechanistic Path of Hydrogen Production with [Cp*Rh] Catalysts. *ChemSusChem* **2017,** *10*, 4589-4598.

[12] The licensing agreement can be found at the following link: https://s100.copyright.com/CustomerAdmin/PLF.jsp?ref=0e897690-4e17-4886-9052-94144fada4da

[13] Moore, W. N. G.; Henke, W. C.; Lionetti, D.; Day, V. W.; Blakemore, J. D., Single-Electron Redox Chemistry on the [Cp*Rh] Platform Enabled by a Nitrated Bipyridyl Ligand. *Molecules* **2018**, *23*, 2857.

[14] Hildebrand, F.; Kohlmann, C.; Franz, A.; Lütz, S., Synthesis, Characterization and Application of New Rhodium Complexes for Indirect Electrochemical Cofactor Regeneration. *Adv. Synth. Catal.* **2008**, *350*, 909-918.

[15] Lionetti, D.; Day, V. W.; Lassalle-Kaiser, B.; Blakemore, J. D., Multiple binding modes of an unconjugated bis(pyridine) ligand stabilize low-valent [Cp*Rh] complexes. *Chem. Comm.* **2018**, *54*, 1694-1697.

[16] Lionetti, D.; Day, V. W.; Blakemore, J. D., Structural and chemical properties of half-sandwich rhodium complexes supported by the bis(2-pyridyl)methane ligand. *Dalton Trans.* **2019**, *48*, 12396-12406.

[17] (a) Zhang, F.; Kirby, C. W.; Hairsine, D. W.; Jennings, M. C.; Puddephatt, R. J., Activation of C−H Bonds of Arenes: Selectivity and Reactivity in Bis(pyridyl) Platinum(II) Complexes. *J. Am. Chem. Soc.* **2005**, *127*, 14196-14197. (b) Abo-Amer, A.; McCready, M. S.; Zhang, F.; Puddephatt, R. J., The role of solvent in organometallic chemistry — Oxidative addition with dichloromethane or chloroform. *Can. J. Chem.* **2012**, *90*, 46-54. (c) McKeown, B. A.; Gonzalez, H. E.; Michaelos, T.; Gunnoe, T. B.; Cundari, T. R.; Crabtree, R. H.; Sabat, M., Control of Olefin Hydroarylation Catalysis

via a Sterically and Electronically Flexible Platinum(II) Catalyst Scaffold. *Organometallics* **2013**, *32*, 3903-3913. (d) McKeown, B. A.; Gonzalez, H. E.; Gunnoe, T. B.; Cundari, T. R.; Sabat, M., Pt^{II}-Catalyzed Ethylene Hydrophenylation: Influence of Dipyridyl Chelate Ring Size on Catalyst Activity and Longevity. *ACS Catal.* **2013**, *3*, 1165-1171.

[18] Hopkins Leseberg, J. A.; Lionetti, D.; Day, V. W.; Blakemore, J. D., Electrochemical Kinetic Study of [Cp*Rh] Complexes Supported by Bis(2-pyridyl)methane Ligands. *Organometallics* **2021**, *40*, 266-277.

[19] Savéant, J.. *Elements of Molecular and Biomolecular Electrochemistry*, 1st ed.; Wiley: 2006.

[20] Henke, W. C., Stiel, J. P., Day, V. W., and Blakemore, J. D., Evidence for Charge Delocalization in Diazafluorene Ligands Supporting Low-Valent [Cp*Rh] Complexes. **2021**, *submitted to ChemRxiv*, doi: 10.33774/chemrxiv-2021-d2scz

[21] (a) Bordwell, F. G., Equilibrium Acidities in Dimethyl Sulfoxide Solution. *Acc. Chem. Res.* **1988**, *21*, 456-463. (b) Jiang, H.; Stepowska, E.; Song, D., Aerobic oxidation of $C(sp^3)$–H bonds of 4,5-diazafluorene promoted by coordination *Dalton Trans.* **2008**, 5879-5881. (c) Tan, R.; Chiu, F. S. N.; Hadzovic, A.; Song, D., Construction of Rhodium(I) and Gold(I) Macrocycles by Transferring a Phosphine-Functionalized 4,5-Diazafluorenide Ligand from Its Copper(I) N-Heterocyclic Carbene Complex. *Organometallics* **2012**, *31*, 2184-2192. (d) Annibale, V. T.; Batcup, R.; Bai, T.; Hughes, S. J.; Song, D., RuCp* Complexes of Ambidentate 4,5-Diazafluorene Derivatives:

From Linkage Isomers to Coordination-Driven Self-Assembly. *Organometallics* **2013**, *32*, 6511-6521.

[22] Henke, W. C.; Hopkins, J. A.; Anderson, M. L.; Stiel, J. P.; Day, V. W.; Blakemore, J.D., 4,5-Diazafluorene and 9,9´-Dimethyl-4,5-Diazafluorene as Ligands Supporting Redox-Active Mn and Ru Complexes, *Molecules* **2020**, *25*, 3189.

[23] Boyd, E. A.; Lionetti, D.; Henke, W. C.; Day, V. W.; Blakemore, J. D., Preparation, Characterization, and Electrochemical Activation of a Model [Cp*Rh] Hydride. *Inorg. Chem.* **2019**, *58*, 3606-3615.

[24] Hopkins, J. A.; Lionetti, D.; Day, V. W.; Blakemore, J. D., Chemical and Electrochemical Properties of [Cp*Rh] Complexes Supported by a Hybrid Phosphine-Imine Ligand. *Organometallics* **2019**, *38*, 1300-1310.

[25] Muckerman, J. T.; Skone, J. H.; Ning, M.; Wasada-Tsutsui, Y. Toward the accurate calculation of pKa values in water and acetonitrile. *Biochim. Biophys. Acta, Bioenerg.* **2013**, *1827*, 882-891.

[26] Appel, A. M.; Helm, M. L. Determining the Overpotential for a Molecular Electrocatalyst. *ACS Catal.* **2014**, *4*, 630-633.

[27] Hopkins, J. A.; Lionetti, D.; Day, V. W.; Blakemore, J. D., Synthesis and reactivity studies of a [Cp∗Rh] complex supported by a methylene-bridged hybrid phosphine-imine ligand. *J. Organomet. Chem.* **2020,** *921*, 121294.

[28] Brunner, H.; Kollnberger, A.; Mehmood, A.; Tsuno, T.; Zabel, M., CSD Communication. **2009**, 233218.

Chapter 2

Examining the Modular Synthesis of [Cp*Rh] Monohydrides Supported by Chelating Diphosphine Ligands

This chapter is adapted from a published manuscript:

Comadoll, C. G.; Henke, W. C.; Hopkins Leseberg, J. A.; Douglas, J. T.; Oliver, A. G.; Day, V. W.; Blakemore, J. D., Examining the Modular Synthesis of [Cp*Rh] Monohydrides Supported by Chelating Diphosphine Ligands. *Organometallics* **2021**, *40*, 3808-3818.

2.1 Introduction

Metal hydrides are an important class of compounds in organometallic chemistry, serving as key intermediates in a variety of catalytic processes.[1] Attention is often paid to these species for their high relevance to electrocatalysis as well, in that metal-mediated production of H_2 from H_2O and reduction of CO_2 often involve metal hydride intermediates generated under reductive conditions.[2]

One such catalytic system that has attracted significant attention is the generation of H_2 by [Cp*Rh] complexes (where Cp* is η^5-pentamethylcyclopentadienyl) supported by the workhorse 2,2′-bipyridyl ligand (bpy) and its analogues.[3] This system is readily prepared from common ligands and the useful precursor $[Cp^*RhCl_2]_2$,[4] and can operate both chemically and electrochemically.[5] Mechanistically, the catalyst supported by bpy undergoes a two-electron reduction followed by protonation;[6] such a reaction sequence has conventionally been discussed to yield a [Cp*Rh] monohydride that could undergo protonolysis to generate H_2 and close the catalytic cycle. The same hydride intermediate has also been proposed to be involved in generation of NADH from NAD^+ in related bioelectrochemical work, magnifying its importance on this platform.[7]

The [Cp*Rh] hydride supported by bpy has a central role in the chemistry of this system, but so far, this species has eluded isolation or full characterization. In part, this is due to formation of favored η^4-pentamethylcyclopentadiene (Cp*H) complexes under some conditions; on the other hand, the precise relationship of the Cp*H complexes to the catalytic mechanism is not yet fully mapped.[8] Notably, signals attributable to a hydride species have been observed upon treatment of a [Cp*Rh] complex supported by 6,6′-dimethyl-2,2′-bipyridyl with excess sodium formate under stringent reaction conditions.[9] Similarly,

Chart 2.1. [Cp*Rh] hydride species supported by bidentate chelating ligands. Rhodium is in the formally +III oxidation state in all cases.

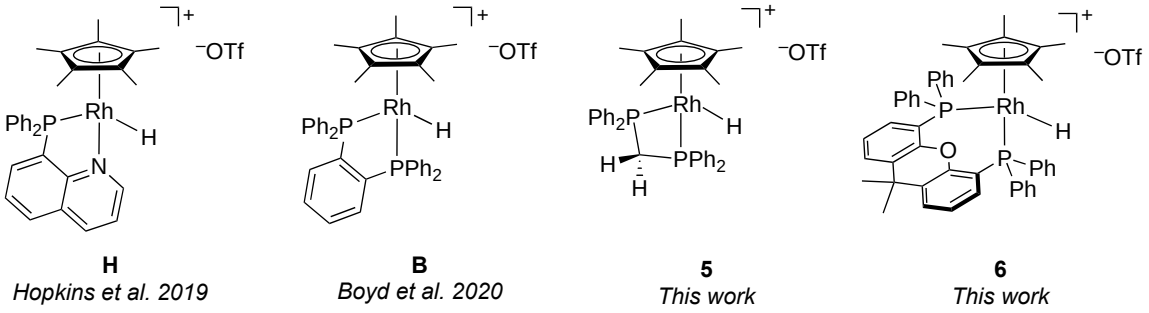

H *Hopkins et al. 2019* | **B** *Boyd et al. 2020* | **5** *This work* | **6** *This work*

hydride signals have been observed in low temperature nuclear magnetic resonance (NMR) spectroscopy experiments with the bpy system in the presence of strong acid (HCl, pK_a < 10 in MeCN).[10] And, the analogous [Cp*Ir] hydride is well known and has been crystallographically characterized,[11] lending credence to proposals for involvement of [Cp*Rh] monohydrides in these systems.

In light of the probable involvement of transient hydride complexes in the chemistry of [Cp*Rh] catalysts, we have recently been developing synthetic routes to access model [Cp*Rh] monohydrides in order to study their chemical properties. In prior work, we have prepared and isolated two monomeric [Cp*Rh] hydride complexes bearing the ligands (diphenylphosphino)quinoline (pqn)[12] and bis(diphenylphosphino)benzene (dppb)[13] (**H** and **B**, respectively, see Chart 2.1). These hydrides are remarkably resistant to further reactivity upon preparation, with cleavage of the Rh–H bond via protonolysis being disfavored in the presence of excess anilinium triflate (pK_a = 10.6 in MeCN[14]). Although **H** does evolve hydrogen in the presence of stronger acids, **B** does not; this finding is consistent with prior literature reports which have shown that metal hydride complexes are stabilized by phosphine ligands.[15,16,17,18,19,20]

Isolation of hydride species **H** and **B** enabled thorough characterization of the compounds in both cases and provided new insights into the chemistry of the parent catalytic system. However, these two cases represent disparate examples of hydride generation on the [Cp*Rh] platform via a common sequential reduction/protonation pathway. This reaction sequence is directly relevant to chemical and electrochemical use of these complexes and thus is deserving of further scrutiny; most applications of these compounds rely on the air-stable Rh(III) complexes as starting materials, and thus reduction and protonation can be identified as critical steps in the chemistry of these compounds.[21] In this context, significant prior work across many platforms has shown that the tuning of phosphine ligands can induce significant structural and electronic changes to the corresponding metal complexes. We anticipated here that examination of the modularity of the reduction/protonation reaction sequence on the [Cp*Rh] platform across varying κ^2-diphosphine ligands could provide new details on factors that enable clean generation of [Cp*Rh] monohydride species, as well as reveal the impact of changing rhodacycle size on the structure and reactivity of [Cp*Rh] hydrides.

Here, we report the synthesis and full characterization of two new [Cp*Rh] monohydride complexes supported by the chelating diphosphine ligands bis(diphenylphosphino)methane (dppm) and 4,5-bis(diphenylphosphino)-9,9-dimethylxanthene (Xantphos). The synthetic chemistry is modular for both systems and affords good yields for all three steps involved (preparation of the Rh(III) precursor, reduction, and protonation, respectively; each step $\geq$ 80 %). All six of the complexes involved here were characterized by NMR techniques as well as single-crystal X-ray crystallographic analysis, highlighting the distinctive four- and eight-membered rhodacycles

present in the dppm and Xantphos systems, respectively. The dppm complexes display uncommonly rich NMR spectral properties, which were elucidated through both multifrequency experiments (spanning 400 to 800 MHz) and related digital simulations; these results are discussed at length in Chapter 2. Taken together with prior work, our findings show that [Cp*Rh] complexes ligated by a variety of diphosphine ligands display remarkably clean and modular reactivity toward the generation of Rh–H species.

2.2 Results and Discussion

2.2.1 Synthesis and Characterization of the Bis(phosphino) Complexes

We have previously found that the dimeric complex $[Cp^*RhCl_2]_2$, developed by Maitlis and co-workers,[4] is a reliable synthetic precursor to a variety of [Cp*Rh] complexes. Using this material, we developed a synthetic route for the preparation and isolation of a monomeric [Cp*Rh] hydride complex **B** which relies on a sequential redox chemistry approach.[13,15] In this procedure, initial preparation of a rhodium(III) complex is followed by reduction to a formally rhodium(I) intermediate. We found that this rhodium(I) form could undergo clean protonation to a rhodium(III) hydride, contrasting with recent findings for diimine-type ligands in which exposure of the reduced form to acid results in protonation of the η^5-Cp* ligand.[5] In order to investigate the modularity of the synthetic route developed for **B**, we explored similar methods here for the synthesis of [Cp*Rh] complexes bearing the related diphosphine ligands dppm and Xantphos (Scheme 1.1), which differ from dppb in that they commonly form four- and eight-membered rhodacycles, respectively, in contrast with the five-membered rhodacycle of **B**.

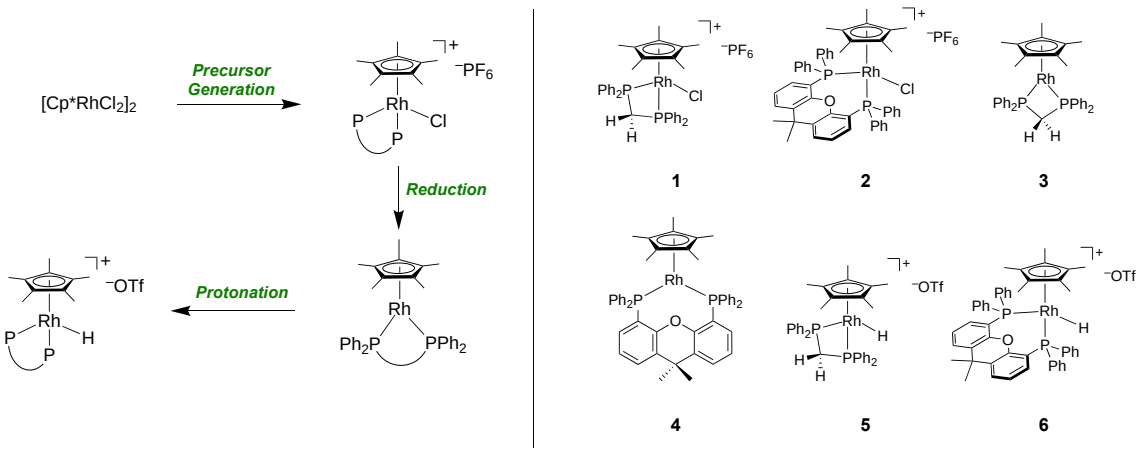

Scheme 2.1. Preparation of Cp*Rh complexes. Left: Synthetic strategy using sequential reduction/protonation. Right: Structures of the compounds described in this work.

To begin, we reacted 0.5 equivalents of $[Cp^*RhCl_2]_2$ with 1.0 equivalent of $AgPF_6$, followed by the addition of 1.05 equivalents of dppm or Xantphos, giving good yields of 1 and 2 (see Scheme 2.1) as yellow and orange air-stable solids, respectively. Notably, preparation of **1** has been reported previously by two groups; the Tatsumi group isolated **1** as a byproduct (in 26 % yield) in the context of a synthetic route targeting alkenylated [Cp*Rh] species,[22a] whereas the Nakajima group reported preparation of **1** (in 80 % yield) so that it could be used as a reference compound.[22b] However, neither group reported full characterization, crystallographic analysis, or reactivity studies for **1**, as the chemistry of the compound was incidental to their work in both cases. Here, full spectroscopic confirmation of the formulations of **1** and **2** came from ^{1}H NMR. All NMR spectral data for **1** and **2** can be found in Appendix A. For both **1** and **2**, a triplet integrating to 15 protons is present at 1.74 and 0.97 ppm, respectively, representing the equivalent Cp* methyl protons. The peak is a triplet in both cases due to coupling to the chelating phosphorus atoms ($^4J_{H,P}$ = 4.1 Hz for both **1** and **2**). Additionally, the $^{31}P\{^1H\}$ NMR spectra of both complexes reveal a septet

representing the PF_6^- counterion, along with a doublet corresponding to the respective diphosphine ligand which couples to rhodium ($^1J_{P,Rh}$ = 115.1 Hz, 143.4 Hz for **1** and **2**, respectively).

Interestingly, the ^{1}H spectrum of **1** shows two distinct and unique sets of resonances centered at 4.91 ppm (dtd) and 4.51 ppm (dt) belonging to the heterotopic[23] methylene protons on the backbone of the dppm ligand (δ = 4.91 ppm, dtd, $^2J_{H,H}$ = 15.6 Hz, $^2J_{H,P}$ = 10.1 Hz, $^3J_{H,Rh}$ = 1.7 Hz; δ = 4.51 ppm, dt, $^2J_{H,H}$ = 15.6 Hz, $^2J_{H,P}$ = 13.0 Hz). The difference in the splitting pattern between these two protons arises as a result of their distinct chemical and magnetic environments, as well as the overall rich nuclear spin system of the complex. While both methylene protons couple to the two phosphorus atoms, the more upfield of the two couples more strongly to phosphorus. Seemingly in contradiction with this observation, only the other, more downfield methylene proton couples to rhodium. This difference between these observed couplings is likely attributable to geometric differences between the two protons in solution, because their positions with respect to the phosphorus atoms and rhodium center in the solid state are similar (*vide infra*). Likewise, the ^{1}H NMR spectrum of **2** displays two singlets at 2.00 and 1.68 ppm, representing the heterotopic geminal methyl groups on the Xantphos ligand. However, as expected, these singlets contrast with the intricate splitting observed for the heterotopic methylene protons of the dppm framework.

Vapor diffusion of diethyl ether into a concentrated acetonitrile solution of **1** or an acetone solution of **2** afforded orange and red crystals, respectively, that were suitable for X-ray diffraction (XRD) studies. Details on the crystallographic work can be found in Appendix A. The solid-state structures reveal the geometries around the formally Rh(III)

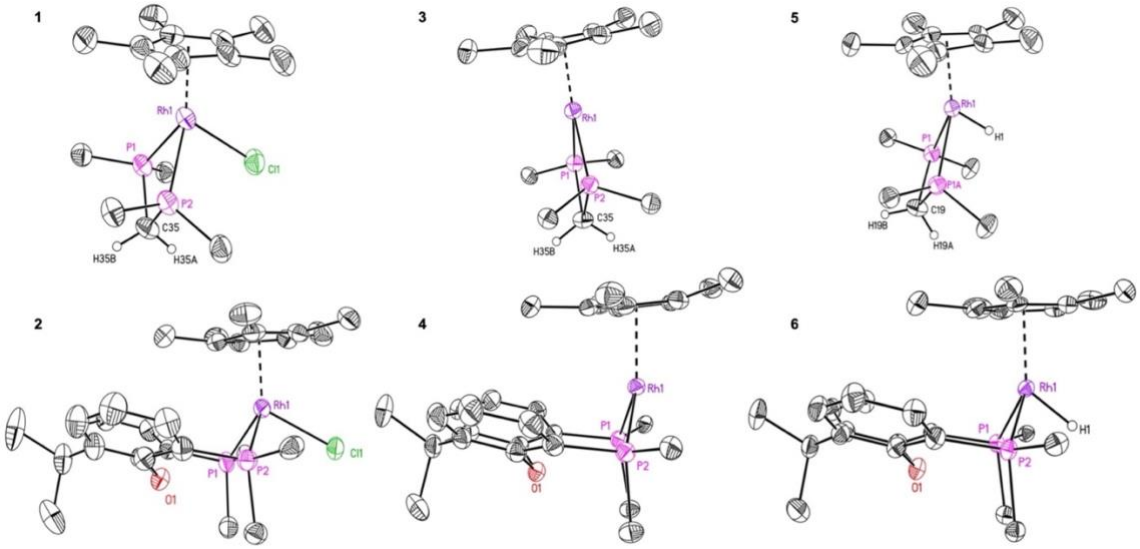

Figure 2.1. Solid-state structures of the [Cp*Rh] complexes reported in this work. Left column: chloride complexes with formal Rh(III) oxidation state; **1** (upper), **2** (lower). Middle column: reduced complexes with formal Rh(I) oxidation state; **3** (upper), **4** (lower). Right column: monohydride complexes with formal Rh(III) oxidation state; **5** (upper), **6** (lower). Displacement ellipsoids are shown at the 50% probability level. Phenyl rings, hydrogen atoms (except H35A, H35B, H19A, H19B, and H1), outer sphere counteranions, and co-crystallized solvent molecules are omitted for clarity.

centers to be *pseudo*-octahedral in both cases (see Figure 2.1). Each rhodium center has a first coordination sphere containing the [η^5-Cp*] ligand, the expected κ^2-diphosphine ligand, and a single chloride ligand. The bond metrics for **1** and **2** show, as could be anticipated, that the Rh–P bond lengths are longer in **2** than they are in **1**; this is attributed to the larger, more distorted eight-membered rhodacycle present in **2** (see Table 2.1). The P1–Rh–P2 angles of

Table 2.1. Bond Lengths (Å) and Angles (°) of Compounds **1**–**6**.

Complex	Rh–P Length	Rh–Cp^*_{cent} Length	∠ P–Rh–P	θ (∠ Cp^*_{cent}–Rh–$P1/P2_{cent}$)
1	2.325(1), 2.311(1)	1.846	72.20(5)	153.9
2	2.383(1), 2.378(1); 2.376(1), 2.369(4)	1.888; 1.882	95.38(3); 95.69(3)	149.2; 148.5
3	2.192(1), 2.211(1)	1.925	73.04(2)	179.3
4	2.231(1), 2.237(1)	1.983	96.96(3)	164.7
5	2.258(1)	1.878	73.20(3)	158.2
6	2.297(1), 2.305(1); 2.296(1), 2.305(1)	1.925; 1.928	97.56(3); 98.35(3)	154.1; 152.9

the diphosphine ligands also reflect this situation, as use of dppm results in a much tighter bite angle for **1** of 72.20(5)° relative to 95.38(3)°/95.69(3)° for Xantphos in **2**. On the other hand, we also found the angles defined by the Cp* centroids (Cp^*_{cent}), Rh centers, and centroids calculated between the phosphorus atoms to be compressed in **2** (149.2°/148.5°) relative to **1** (153.9°), no doubt an influence of the constrained geometry of ligand binding. The Rh–Cl distances of 2.383(2) Å for **1** and 2.395(1) Å/2.398(1) Å for **2** are similar, consistent with the common formal +III oxidation state of rhodium for both complexes.

To our delight, both **1** and **2** could be reduced to the corresponding formally Rh(I) complexes **3** and **4**, respectively, upon treatment with sodium amalgam in THF (see Scheme 1). Consistent with prior results using the dppb ligand, the solution darkens over the course of the reaction. Extraction of the crude material with hexane afforded **3** and **4** in pure form

as light brown and dark brown solids, respectively. Characterization of the desired, pure forms of **3** and **4** by ^{1}H NMR reveals similar Cp* triplets in each case, now shifted downfield to 2.12 and 1.36 ppm, respectively, attributable to the increased electron density about the rhodium metal center upon reduction (all NMR data for **3** and **4** can be found in Appendix A. The coupling constants between the equivalent Cp* methyl protons and the phosphorus atoms decrease for the Rh(I) complexes in comparison with the Rh(III) forms ($^{4}J_{H,P}$ = 2.4 Hz for **3**; $^{4}J_{H,P}$ = 1.7 Hz for **4**), a feature attributable again to the increased electron density about rhodium. The ^{31}P{^{1}H} NMR spectra for **3** and **4** give only the expected doublets corresponding to the bound diphosphine ligands (δ = –12.28 ppm, $^{1}J_{P,Rh}$ = 190.2 Hz for **3**; δ = 51.46 ppm, $^{1}J_{P,Rh}$ = 227.2 Hz for **4**). As observed previously in our dppb complexes, the value of $^{1}J_{P,Rh}$ increases significantly upon reduction, consistent with increased back donation from the electron-rich metal center.

Due to the change of geometry about the rhodium metal center upon reduction (*vide infra*), the formerly heterotopic methylene protons in **1** become homotopic in **3**, as demonstrated by the single resonance integrating to 2H at 3.80 ppm (td, $^{2}J_{H,P}$ = 10.5 Hz, $^{3}J_{H,Rh}$ = 1.4 Hz). Notably, the geminal methyl groups of **4** are also equivalent, corresponding to a lone singlet integrating to 6H at 1.65 ppm. This result contrasts with the crystallographic data (see Figure 2.1), implying that the complex behaves more symmetrically (C_{2v}) in solution that differs from the solid-state structure (*pseudo*-C_s). Fluxionality in the Xantphos backbone may contribute to these observations, such that the form of the complex in solution relaxes the θ values closer to 180°, resembling the solid-state form of **3** (see Table 2.1). The T-shaped geometry imparted by such a relaxation would render the two methyl groups on

the Xantphos backbone equivalent and, thereby, homotopic, as they appear in the ^{1}H NMR spectral data.

Single crystals of **3** and **4** suitable for XRD analysis were obtained by slow cooling of concentrated solutions of **3** in hexane and of **4** in hexane containing 2 drops of toluene. The solid-state structures (see Figure 2.1) show the geometries about the formally Rh(I) centers to be distorted T-shapes in both cases. Each rhodium center has a first coordination sphere containing the [η^5-Cp*] ligand and the expected κ^2-diphosphine ligand (see Table 2.1). In **3**, the T-shape is quite tight, with a value for θ of 179.3°, near the ideal value of 180° and similar to the value of 177.3° found for Cp*Rh(bpy).[24] On the other hand, the θ value of 164.7° for **4** reveals greater distortion, again attributable to the non-planar nature of the eight-membered rhodacycle induced by the rather rigid structure of the Xantphos backbone. As expected, the P–Rh–P angles do not change significantly (< 1°) in either system upon reduction, confirming the limited flexibilities of dppm and Xantphos in this regard. And, as observed with our dppb system, reduction results in significant elongation of the Rh–Cp*$_{cent}$ distances, consistent with the π-donating nature of Cp*, the electron-rich character of rhodium(I), and the anticipated greater ionic radius for Rh(I) vs. Rh(III).[25] Taken together, these findings support the versatility and modularity of [Cp*Rh] diphosphine chemistry across multiple oxidation states.

Upon successful isolation of both Rh(I) complexes, we were able to prepare the corresponding rhodium hydride species. Reacting 1 equivalent of **3** or **4** with 0.95 equivalents of anilinium triflate (pK_a = 10.6 in MeCN[14]) in 1:1 MeCN/THF furnished the desired monomeric rhodium hydrides **5** and **6**, respectively. The slightly substoichiometric amount of acid was utilized for the purpose of simplifying purification of the products;

having even slight quantities of unreacted acid present during workup resulted in compromised purity during fractionation due to its similar solubility with the hydride. Characterization of both **5** and **6** by ^{1}H NMR showed characteristic resonances corresponding to the hydride ligand bound to rhodium at –9.74 ppm (q, $^{1}J_{H,Rh}$ = 27.4 Hz, $^{2}J_{H,P}$ = 27.4 Hz) and –11.04 ppm (td, $^{2}J_{H,P}$ = 33.7 Hz, $^{1}J_{H,Rh}$ = 17.7 Hz), respectively (all NMR data for **5** and **6** can be found in Appendix A). Additionally, the Cp* signal appears in both spectra as a triplet of doublets (δ = 1.81 ppm, $^{4}J_{H,P}$ = 3.5 Hz, $^{4}J_{H,H}$ = 1.2 Hz for **5**; δ = 1.11 ppm, $^{4}J_{H,P}$ = 3.4 Hz, $^{4}J_{H,H}$ = 1.2 Hz for **6**), indicating that the hydride couples to the 15 equivalent methyl protons of the Cp* ligand.

The methylene protons of **5** are heterotopic, as they were in **1**. These protons appear as two separate but complex groupings of resonances (each centered near 4.86 and 3.98 ppm), integrating to 1H each for the expected total of two methylene protons. The more downfield signal, which appeared as a dtd in **1**, is additionally split by the hydride ligand in **5** to give rise to a dtdd (δ = 4.86 ppm; $^{2}J_{H,H}$ = 16.2 Hz, $^{2}J_{H,P}$ = 9.7 Hz, $^{3}J_{H,Rh}$ = 4.5 Hz, $^{4}J_{H,H}$ = 3.2 Hz),[26] while the further upfield methylene proton remains a dt that is shifted upfield relative to **1** (δ = 3.98 ppm; $^{2}J_{H,H}$ = 16.2 Hz, $^{2}J_{H,P}$ = 12.1 Hz). These complex splitting patterns were assigned with the aid of multifrequency NMR studies and can be successfully and faithfully reproduced with digital simulations incorporating both first- and second-order field effects, each of which is described in detail in Chapter 3. The heterotopic geminal methyl groups of **6** also appear as two distinct singlets, as was the case in **2**.

The ^{31}P{^{1}H} NMR spectrum for **5** includes the expected doublet for the dppm ligand (δ = 1.34 ppm, $^{1}J_{P,Rh}$ = 119.2 Hz). However, the spectrum for **6** shows a dd (δ = 41.32 ppm, $^{1}J_{P,Rh}$ = 148.2 Hz, $^{2}J_{P,H}$ = 6.3 Hz), indicating a small but observable coupling between the

phosphorus atoms of Xantphos and the hydride ligand, despite the proton decoupling for this spectrum. This finding is attributable to the finite bandwidth of the 2.8 kHz WALTZ-16 ^{1}H-decoupling[27] in the standard ^{31}P{^{1}H} experiment acquired on our 400 MHz NMR spectrometer. ^{1}H decoupling[28] does not follow a strict turn-on/turn-off behavior, but rather a non-linear, sine-like chemical shift dependence with incomplete decoupling (sometimes referred to as "spin tickling") of ^{1}H resonances outside of the nominal range of –3 to 11 ppm, as determined by our experimental parameters.[29] The observation of complete decoupling for **5** and only partial decoupling for **6** is attributable to the influence of decoupling sidebands at the respective resonance frequencies for these compounds.[30]

Vapor diffusion of diethyl ether into concentrated THF solutions of **5** and **6** afforded crystals suitable for XRD analysis in both cases. The solid-state structures (see Figure 2.1) confirm the geometries about the formally Rh(III) centers to be *pseudo*-octahedral, as they were in **1** and **2**. The geometry of each rhodium center has changed significantly from the cases of **3** and **4**, as judged by the θ values (158.2° and 154.1°/152.9° for **5** and **6**, respectively), confirming distortion away from the T-shaped geometries found for the Rh(I) compounds (see Table 2.1). Gratifyingly, the hydride ligands (labeled as H1 for **5** and **6** in Figure 2.1) were both located in Fourier difference maps, and their positions were freely refined in the final XRD data modeling. Infrared spectroscopic data confirm the Rh–H stretching frequencies for these new compounds in the expected region, with values of 1982 and 1936 cm^{-1}, respectively, for **5** and **6** (see Appendix A). These values compare well with the corresponding value measured for **B** of 1986 cm^{-1}.[13] In light of all these data, the sequential reduction/protonation route can be concluded to be effectively modular for

preparation of [Cp*Rh] monohydride complexes supported by diphosphine ligands, complementing existing examples from the literature.

2.2.2 Chemical Properties of the Rh–H Species

With full characterization in hand, we next examined the chemical and spectral properties of the two new [Cp*Rh] hydride species. A comparison of the hydride resonances in the ^{1}H NMR spectra of **B**, **5**, and **6** provides insight into the effect of rhodacycle size on the splitting of the hydride resonance. The rhodacycles in **5**, **B**, and **6** are 4-, 5-, and 8-membered, respectively; as seen in Figure 2.2, these different sizes give rise to different splitting patterns and chemical shifts for each hydride resonance. Most notably, as seen in Figure 2.2 (b), the splitting pattern of each broadened hydride resonance can be seen trending from a quartet to a triplet of doublets as the rhodacycle size increases, due to both increased coupling between the hydride and the pendant phosphorus atoms ($^{2}J_{H,P}$ = 27.4 Hz, 29.1 Hz, and 33.7 Hz for **5**, **B**, and **6**, respectively) and decreased coupling between the hydride and rhodium ($^{1}J_{H,Rh}$ = 27.4 Hz, 25.4 Hz, and 17.7 Hz for **5**, **B**, and **6**, respectively) as the rhodacycle size increases.

We next sought to investigate the hydrogen evolution capabilities of **5** and **6**. Prior work has demonstrated that [Cp*Rh] hydride species have unique hydrogen evolution properties depending on the bidentate ligand chosen for the given scaffold. Work with bpy-ligated [Cp*Rh] complexes has shown that treatment of the formally Rh(I) species with anilinium triflate (pK_a = 10.6 in MeCN[14]) gives rise to the Cp*H form of the complex, which is sufficiently basic to produce hydrogen upon addition of another equivalent of the same acid.[5b] Work with the mixed-ligand PQN system showed that the Rh–H, formed upon

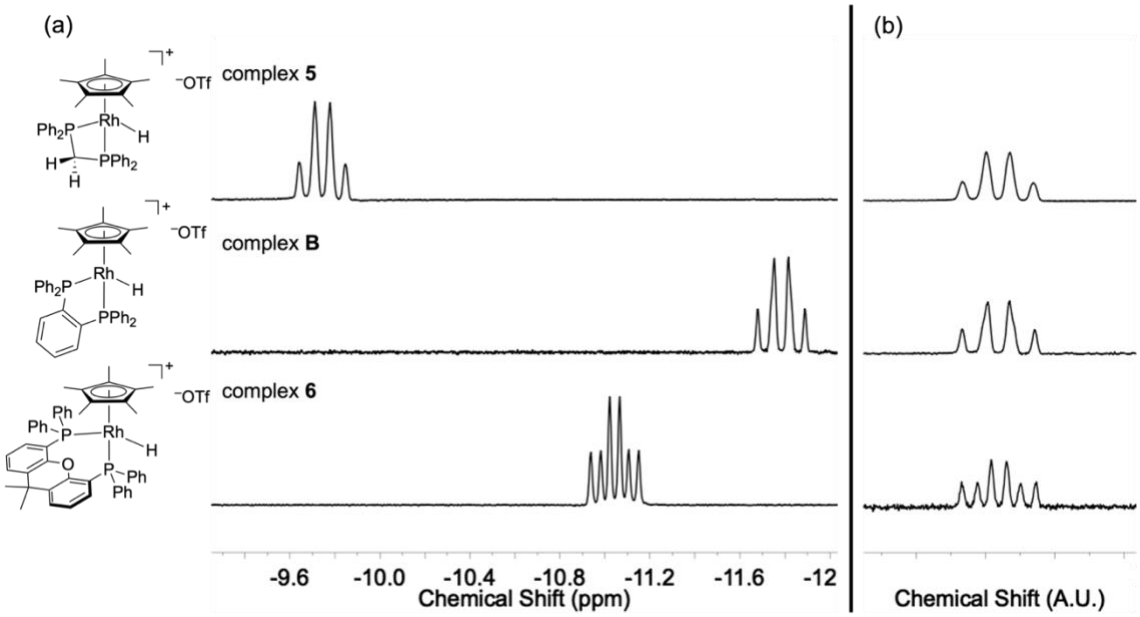

Figure 2.2. (a): Stacked, partial ^{1}H NMR spectra depicting the hydride ligand resonance of the formally Rh(III) hydride complexes **5**, **B**, and **6**, with their chemical structures included. (b): Stacked ^{1}H NMR spectra depicting the hydride resonances of **5**, **B**, and **6** aligned vertically (with arbitrary units on the x-axis).

protonation of the Rh(I) species by anilinium triflate (**H**, Chart 2.1), was isolable and characterizable; however, the only acid with which this hydride was able to evolve hydrogen was $[DMFH]^{+}[OTf]^{-}$ (pK_a = 6.1 in MeCN[31]).[12] Finally, the dppb-ligated Rh–H species (**B**) was not sufficiently basic to evolve hydrogen in the presence of either of these acids, even after heating to 50 °C in the presence of $[DMFH]^{+}[OTf]^{-}$.[13]

In order to probe the reactivity of these new hydride species, we subjected **5** and **6** to $[DMFH]^{+}[OTf]^{-}$ in CD_3CN (see Scheme 2.2). The details of this set of experiments are found in Section 2.4.3. Both hydride complexes were stable at room temperature in the presence of this acid for up to 6 days. Heating each of these samples to 65 °C for an additional 48 hours showed the formation of small triplets near the td of the Cp* methyl protons in the ^{1}H

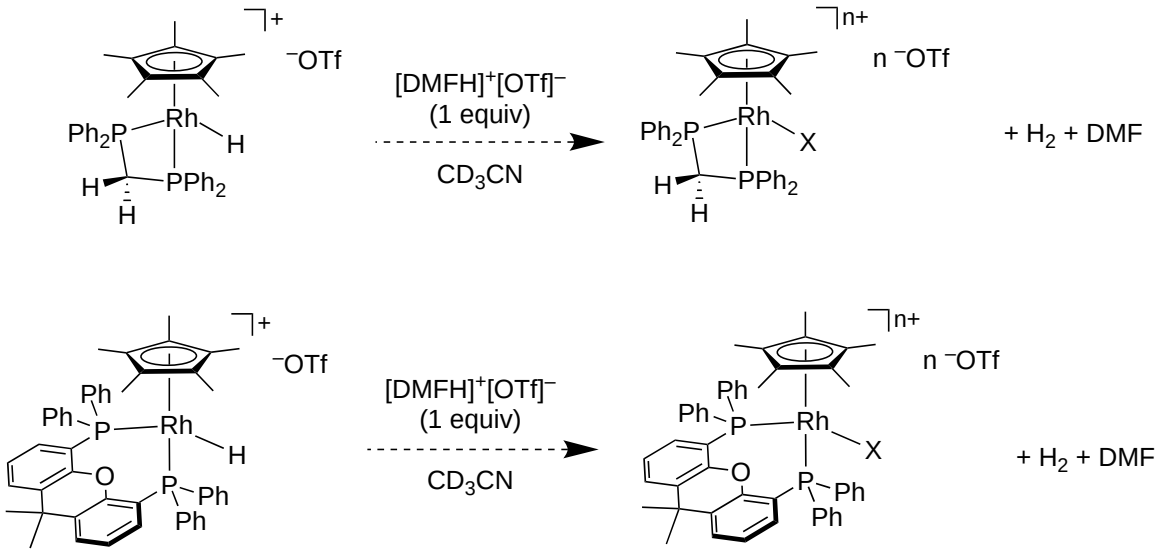

Scheme 2.2. Hydrogen evolution reaction of **5** and **6** with $[DMFH]^+[OTf]^-$ in CD_3CN. X can either be a bound triflate ligand (n = 1) or a bound acetonitrile (n = 2).

NMR spectrum of each compound, attributable to a new [Cp^*Rh^{III}] species formed upon evolution of hydrogen in each case (see Appendix A). Dihydrogen was not observed in the NMR spectra, however, which is consistent with a very low yield and/or loss from the J. Young tubes; additionally, the new Cp* species correspond to conversion of less than 3 % of the starting hydride material in both instances. While these complexes appear thermally resistant to hydrogen evolution, future work could explore photo-induced hydride transfer; light excitation can drive hydrogen evolution with related [Cp*Ir] hydride systems.[32] These findings underscore the high stability of Rh–H complexes supported by diphosphine ligands relative to previously studied diimine ligand systems, even in the presence of a strong acid.

2.3 Conclusion

This work demonstrates the synthetic modularity of our sequential reduction/protonation route in the context of preparation, isolation, and characterization of two new [Cp*Rh] monohydride complexes bearing the diphosphine ligands dppm and

Xantphos. The synthesis of these compounds is straightforward, considering the relative scarcity of such compounds in the literature, and enables preparation of both Rh(III) and Rh(I) complexes through redox transformations. All structures were characterized by NMR methods as well as single-crystal X-ray diffraction analysis, and the hydrides were additionally characterized by IR spectroscopy. The effect of changing the rhodacycle size on the hydride resonance of each of the three diphosphine complexes was elucidated through ^{1}H NMR data, demonstrating a difference in chemical shifts and, more interestingly, the splitting patterns. Additionally, the remarkable stability of each monohydride complex, afforded by each chelating diphosphine ligand, was demonstrated by the resistance of each complex to evolve hydrogen in the presence of a sufficiently strong acid. Taken together, these results demonstrate the power of the reduction/protonation synthetic sequence in [Cp*Rh] monohydride chemistry, and stability of these complexes towards further potential catalytic reactivity with acids.

2.4 Experimental Details

2.4.1 General Considerations

All manipulations were carried out in dry N_2-filled gloveboxes (Vacuum Atmospheres Co., Hawthorne, CA, USA) or under an N_2 atmosphere using standard Schlenk techniques, unless otherwise noted. All solvents were of commercial grade and dried over activated alumina using a PPT Glass Contour (Nashua, NH, USA) solvent purification system prior to use, and were stored over molecular sieves. All chemicals were obtained from major commercial suppliers and used as received after extensive drying. $[Cp^*RhCl_2]_2$ was prepared according to literature methods with minor modifications.[4] Deuterated solvents for NMR studies were purchased from Cambridge Isotope Laboratories (Tewksbury, MA,

USA); CD_3CN was dried with CaH_2 and stored over molecular sieves, and C_6D_6 was dried over sodium/benzophenone. ^1H, ^{13}C, ^{19}F, and ^{31}P NMR spectra were collected with 400, 500, 600, or 800 MHz Bruker spectrometers and were referenced to the residual protio-solvent signal in the cases of ^1H and ^{13}C unless otherwise noted.[33] Heteronuclear NMR spectra were referenced to the appropriate external standard following the recommended scale based on ratios of absolute frequencies (Ξ). ^{19}F NMR spectra are reported relative to CCl_3F, and ^{31}P NMR spectra are reported relative to H_3PO_4.[34,35] Chemical shifts (δ) and coupling constants (*J*) are reported in ppm and Hz, respectively. IR spectra were collected in the solid-state using a Shimadzu IRSpirit Fourier Transform Infrared Spectrometer in transmission mode using a high-throughput diamond QATR-S single reflection attenuated total reflectance attachment at an incident angle of 45°. Elemental analyses were performed by Midwest Microlab, Inc. (Indianapolis, IN). Elemental analysis could not be obtained for **3**, **4**, **5**, or **6** due to their acute air sensitivity, but was obtained for **2**. Analysis for **1** has been reported previously.[22]

2.4.2 Synthetic Procedures

Synthesis of [Cp*Rh(dppm)Cl]PF_6 (1)

To a 20-mL scintillation vial equipped with a Teflon stir bar, $[Cp^*RhCl_2]_2$ (0.062 g, 0.100 mmol) was dissolved in MeCN (ca. 2 mL) to give a red suspension. To this suspension, $AgPF_6$ (0.051 g, 0.20 mmol) in MeCN (ca. 2 mL) was added, and the solution immediately changed from red to orange upon formation of AgCl as a white precipitate. The solution was allowed to stir for 5 min, then the resulting AgCl precipitate was filtered off over Celite into a 25-mL Schlenk flask. To this solution were added a Teflon stir bar and dppm (0.119 g, 0.20 mmol) dissolved in THF (ca. 2 mL). The Schlenk flask was closed and capped with a

greased glass stopper, removed from the glovebox, connected to the Schlenk line, and stirred overnight at 65 °C under N_2. The next day, the flask was opened to air and the orange solution was concentrated. The resulting material was transferred to a 500-mL Erlenmeyer flask with minimal MeCN and a large excess of diethyl ether (ca. 300 mL) was added, causing precipitation of the desired product in the freezer overnight. The yellow solid was then filtered and washed thoroughly with diethyl ether to afford the title compound. Yield: 0.143 g (89 %). ^{1}H NMR (400 MHz, CD_3CN): δ = 7.65 – 7.51 (m, 12H), 7.48 (td, 4H, *J* = 7.6, 7.1, 3.8 Hz), 7.30 – 7.22 (m, 4H), 4.91 (dtd, 1H, *J* = 15.6, 10.1, 1.7 Hz), 4.51 (dt, 1H, *J* = 15.6, 13.0 Hz), 1.74 (t, 15H, *J* = 4.1 Hz) ppm. ^{13}C{^{1}H} NMR (126 MHz, CD_3CN): δ = 133.61 (td, *J* = 5.7, 4.0 Hz), 133.33 (d, *J* = 1.8 Hz), 132.80 (d, *J* = 1.5 Hz), 130.39 – 130.21 (m), 130.05 – 129.82 (m), 104.77 (dt, *J* = 6.1, 3.2 Hz), 40.32 (d, *J* = 28.5 Hz), 10.21 ppm. ^{19}F NMR (376 MHz, CD_3CN): δ = –73.81 (d, *J* = 706.2 Hz) ppm. ^{31}P{^{1}H} NMR (162 MHz, CD_3CN): δ = –6.26 (d, $^1J_{P,Rh}$ = 115.1 Hz), –145.48 (septet) ppm.

Synthesis of [Cp*Rh(Xantphos)Cl]PF_6 (2)

To a 20-mL scintillation vial equipped with a Teflon stir bar, $[Cp^*RhCl_2]_2$ (0.062 g, 0.100 mmol) was dissolved in MeCN (ca. 2 mL) to give a red suspension. To this suspension, $AgPF_6$ (0.051 g, 0.20 mmol) in MeCN (ca. 2 mL) was added, and the solution immediately changed from red to orange upon formation of AgCl as a white precipitate. The solution was allowed to stir for 5 min, then the resulting AgCl precipitate was filtered off over Celite into a 25-mL Schlenk flask. To this solution were added a stirbar and Xantphos (0.119 g, 0.21 mmol) dissolved in THF (ca. 2 mL). The Schlenk flask was closed and capped with a greased glass stopper, removed from the glovebox, connected to the Schlenk line, and stirred overnight at room temperature. The next day, the flask was opened to air and the resulting

bright red solution was concentrated. The resulting material was transferred to a 500-mL Erlenmeyer flask with minimal MeCN and a large excess of diethyl ether (ca. 300 mL) was added, causing precipitation of the desired product in the freezer overnight. The orange solid was then filtered and washed thoroughly with diethyl ether to afford the title compound. Yield: 0.168 g (84 %). ^{1}H NMR (400 MHz, CD_3CN): δ = 7.87 (dd, 2H, *J* = 7.6, 1.6 Hz), 7.77 – 7.68 (m, 4H), 7.63 – 7.39 (m, 10H), 7.05 (s, 4H), 6.90 (tt, 2H, *J* = 7.4, 1.1 Hz), 6.70 (t, 4H, *J* = 7.7 Hz), 2.00 (s, 3H), 1.68 (s, 3H), 0.97 (t, 15H, *J* = 4.1 Hz) ppm. ^{13}C{^{1}H} NMR (126 MHz, CD_3CN): δ = 155.38 (t, *J* = 3.0 Hz), 137.31 (t, *J* = 5.7 Hz), 136.50 – 136.29 (m), 132.70, 131.95, 130.84 (t, *J* = 1.9 Hz), 130.06, 129.59 – 129.34 (m), 129.31 – 128.97 (m), 125.94 (t, *J* = 3.9 Hz), 106.27 (ddd, *J* = 8.7, 5.9, 2.2 Hz), 37.72, 31.29, 22.73, 9.48 ppm. ^{19}F NMR (376 MHz, CD_3CN): δ = –73.80 (d, *J* = 706.3 Hz) ppm. ^{31}P{^{1}H} NMR (162 MHz, CD_3CN): δ = 18.29 (d, $^{1}J_{P,Rh}$ = 143.4 Hz), –144.63 (septet) ppm. Anal. Calcd. for $C_{49}H_{47}ClF_6OP_3Rh$: C, 59.02; H, 4.75. Found: C, 59.06; H, 4.82.

Synthesis of Cp*Rh(dppm) (**3**)

A suspension of 1 (0.033 g, 0.04 mmol) in THF (ca. 2 mL) was added to a 20-mL scintillation vial containing 1% Na(Hg) (0.020 g, 0.89 mmol Na, ca. 20 equiv.). The yellow suspension darkened immediately to a dark orange color and continued to darken while stirring overnight. The next day, the reaction solution was filtered through Celite to remove Hg and $NaPF_6$ precipitate. THF was then removed in vacuo and the resulting solid was extracted with hexanes to obtain the title compound as a light brown solid. Yield: 0.024 g (92 %). ^{1}H NMR (400 MHz, C_6D_6): δ = 7.69 (dddd, 8H, *J* = 8.1, 6.9, 5.7, 1.4 Hz), 7.12 (tt, 8H, *J* = 7.0, 0.9 Hz), 7.08 – 7.01 (m, 4H), 3.80 (td, 2H, *J* = 10.5, 1.4 Hz), 2.12 (t, 15H, *J* = 2.4 Hz) ppm. ^{13}C{^{1}H} NMR (126 MHz, C_6D_6): δ = 140.18 – 139.50 (m), 132.60 – 132.06 (m), 128.81,

94.24 (q, J = 3.6 Hz), 52.07 – 51.00 (m), 11.99 ppm. $^{31}P\{^{1}H\}$ NMR (162 MHz, C_6D_6): δ = –12.28 (d, $^{1}J_{P,Rh}$ = 190.2 Hz) ppm.

Synthesis of Cp*Rh(Xantphos) (**4**)

A suspension of **2** (0.051 g, 0.05 mmol) in THF (ca. 2 mL) was added to a 20 mL scintillation vial containing freshly prepared 1% Na(Hg) (0.023 g, 1.0 mmol Na, ca. 20 equiv.). The orange suspension darkened immediately to a deep brown color and continued to darken while stirring overnight. The next day, the reaction solution was filtered through Celite to remove Hg and $NaPF_6$ precipitate. THF was then removed in vacuo and the resulting solid was extracted with hexanes to obtain the title compound as a dark brown solid. Yield: 0.037 g (88 %). ^{1}H NMR (400 MHz, C_6D_6): δ = 7.63 (s, 8H), 7.39 – 7.32 (m, 2H), 7.19 (dd, 2H, J = 7.7, 1.2 Hz), 6.88 (t, 2H, J = 7.6 Hz), 6.81 (s, 12H), 1.65 (s, 6H), 1.36 (t, 15H, J = 1.7 Hz) ppm. $^{13}C\{^{1}H\}$ NMR (126 MHz, C_6D_6): δ = 156.11 (t, J = 4.0 Hz), 139.05, 135.92, 99.10 – 96.73 (m), 36.91, 29.88, 10.77 ppm. $^{31}P\{^{1}H\}$ NMR (162 MHz, C_6D_6): δ = 51.46 (d, $^{1}J_{P,Rh}$ = 227.2 Hz) ppm.

Synthesis of [Cp*Rh(dppm)H]OTf (**5**)

To a red suspension of **3** (0.021 g, 0.033 mmol) in the minimum amount of 1:1 THF/MeCN (ca. 2 mL) was added a solution of anilinium triflate (0.008 g, 0.031 mmol) in MeCN (ca. 1 mL). The solution immediately became yellow in color. The vial was capped, and the solution was allowed to stir for 1 hr. The solvent was then removed in vacuo and the solid was fractionated with hexane, diethyl ether, toluene, and THF to obtain the title compound from THF as a light yellow solid. Yield: 0.023 g (89 %). ^{1}H NMR (400 MHz, CD_3CN): δ = 7.64 – 7.48 (m, 16H), 7.36 (dtd, 4H, J = 8.5, 6.6, 1.3 Hz), 4.86 (dtdd, 1H, J = 16.2, 9.7, 4.5, 3.2 Hz), 3.98 (dt, 1H, J = 16.2, 12.1 Hz), 1.81 (td, 15H, J = 3.5, 1.2 Hz), –9.74 (q, 1H, J =

27.4 Hz) ppm. $^{13}C\{^{1}H\}$ NMR (126 MHz, CD_3CN): δ = 133.59 (t, *J* = 6.8 Hz), 132.89, 132.84 – 132.68 (m), 132.50, 130.03 (dt, *J* = 16.5, 5.9 Hz), 102.22 (q, *J* = 3.1 Hz), 47.32 – 46.65 (m), 21.38, 10.52 ppm. ^{19}F NMR (376 MHz, CD_3CN): δ = –80.16 ppm. $^{31}P\{^{1}H\}$ NMR (162 MHz, CD_3CN): δ = 1.34 (d, $^{1}J_{P,Rh}$ = 119.2 Hz) ppm. IR Spectroscopy: ν (cm^{-1}) = 1982 (Rh–H).

Synthesis of [Cp*Rh(Xantphos)H]OTf (6)

To a brown suspension of **4** (0.033 g, 0.040 mmol) in the minimum amount of 1:1 THF/MeCN (ca. 2 mL) was added a solution of anilinium triflate (0.009 g, 0.037 mmol) in MeCN (ca. 1 mL). The solution immediately became dark yellow in color. The vial was capped and the solution was allowed to stir for 1 hr. The solvent was then removed in vacuo and the solid was fractionated with hexane, diethyl ether, toluene, and THF to obtain the title compound from THF as a yellow solid. Yield: 0.029 g (80 %). ^{1}H NMR (400 MHz, CD_3CN): δ = 7.84 (dd, 2H, *J* = 7.8, 1.3 Hz), 7.76 (tdd, 4H, *J* = 8.0, 3.8, 1.9 Hz), 7.60 (ddd, 2H, *J* = 7.6, 5.3, 2.1 Hz), 7.51 (tdd, 6H, *J* = 7.4, 4.5, 1.9 Hz), 7.46 – 7.40 (m, 2H), 6.87 – 6.62 (m, 10H), 2.01 (s, 3H), 1.70 (s, 3H), 1.11 (td, 15H, *J* = 3.4, 1.2 Hz), –11.04 (td, 1H, *J* = 33.7, 17.7 Hz) ppm. $^{13}C\{^{1}H\}$ NMR (126 MHz, CD_3CN): δ = 155.87 (d, *J* = 3.4 Hz), 137.05, 136.73 – 136.04 (m), 132.28, 130.37 (d, *J* = 13.9 Hz), 129.50 (t, *J* = 5.7 Hz), 129.30, 125.43 – 124.97 (m), 104.59 (d, *J* = 5.3 Hz), 37.89, 30.99, 22.78, 10.11 ppm. ^{19}F NMR (376 MHz, CD_3CN): δ = –80.19 ppm. $^{31}P\{^{1}H\}$ NMR (162 MHz, CD_3CN): δ = 41.32 (dd, $^{1}J_{P,Rh}$ = 148.2, $^{2}J_{P,H}$ = 6.3 Hz) ppm. IR Spectroscopy: ν (cm^{-1}) = 1936 (Rh–H).

2.4.3 Hydrogen Evolution Experiments with 5 and 6

To a J. Young tube was added **5** or **6** (12 μmol) and 1.5 mL CD_3CN. A stock solution of $[DMFH]^+[OTf]^-$ in CD_3CN (0.023 M) was made, from which an aliquot (0.5 mL, 12 μmol)

was added to each of the tubes. Each tube was capped quickly, brought out of the glovebox, and left to react at room temperature. ^{1}H NMR spectra were collected at various timepoints. After 6 days, no reactivity was observed by NMR. At this point, each tube was placed in an oil bath heated to 65 °C for an additional 48 hours.

2.4.4 X-Ray Crystallography

Single crystals of **1** were obtained by vapor diffusion of diethyl ether into a concentrated acetonitrile solution of the complex. Single crystals of **2** were obtained by vapor diffusion of diethyl ether into a concentrated acetone solution of the complex. Single crystals of **3** were obtained by slow cooling a concentrated solution of the complex in hexanes. Single crystals of **4** were obtained by adding two drops of toluene to a concentrated hexane solution of the complex and slow cooling for three weeks. Single crystals of **5** and **6** were obtained by vapor diffusion of diethyl ether into a concentrated THF solution of the appropriate complex. Single-crystal X-ray diffraction data were collected with a Bruker Proteum diffractometer equipped with two CCD detectors (Apex2 and Platinum 135) sharing a common MicroStar microfocus Cu rotating anode generator running at 45 mA and 60 kV (Cu Kα = 1.54178 Å).

2.5 Acknowledgements

The authors thank Sarah Neuenswander for assistance with NMR spectroscopy. This work was supported by the US National Science Foundation through award OIA-1833087. The authors also acknowledge the U.S. National Institutes of Health for support of the NMR instrumentation used in this study (Grants S10OD016360 and S10RR024664).

The synthesis and characterization procedures (NMR spectroscopy, elemental analysis, and IR spectroscopy) described in this chapter were performed by CGC. Crystals

of **1** and **3** suitable for X-ray diffraction studies were grown by JHL. Crystals of **2** suitable for X-ray diffraction studies were grown by WCH. Crystals of **4**, **5**, and **6** suitable for X-ray diffraction studies were grown by CGC. Efforts in the interpretation and analysis of all solid-state data were largely performed by WCH and JHL, with assistance from CGC.

2.6 References

[1] Kaesz, H. D.; Saillant, R. B., Hydride complexes of the transition metals. *Chem. Rev.* **1972,** *72*, 231-281.

[2] Rakowski Dubois, M.; Dubois, D. L., Development of Molecular Electrocatalysts for CO2 Reduction and H2 Production/Oxidation. *Accounts of Chemical Research* **2009,** *42*, 1974-1982.

[3] (a) Kölle, U.; Grätzel, M., Rhodium(III) complexes as homogeneous catalysts for the photoreduction of protons to hydrogen. *Angew. Chem.* **1987,** *99*, 572-574. (b) Kölle, U.; Grätzel, M., Organometallic Rhodium(III) Complexes as Catalysts for the Photoreduction of Protons to Hydrogen on Colloidal TiO_2. *Angew. Chem. Int. Ed. Engl.* **1987,** *26*, 567-570.

[4] (a) White, C.; Yates, A.; Maitlis, P. M., (η^5-Pentamethylcyclopentadienyl)Rhodium and -Iridium Compounds. *Inorg. Synth.* **1992,** *29*, 228-234. (b) Mantell, M. A.; Kampf, J. W.; Sanford, M., Improved Synthesis of $[Cp^RRhCl_2]_2$ Complexes. *Organometallics* **2018,** *37*, 3240-3242.

[5] (a) Peng, Y.; Ramos-Garcés, M. V.; Lionetti, D.; Blakemore, J. D., Structural and Electrochemical Consequences of [Cp*] Ligand Protonation. *Inorg. Chem.* **2017,** *56*, 10824-10831. (b) Henke, W. C.; Lionetti, D.; Moore, W. N. G.; Hopkins, J. A.; Day, V. W.; Blakemore, J. D., Ligand Substituents Govern the Efficiency and Mechanistic Path of Hydrogen Production with [Cp*Rh] Catalysts. *ChemSusChem* **2017,** *10*, 4589-4598.

[6] Kölle, U.; Kang, B. S.; Infelta, P.; Comte, P.; Grätzel, M., Electrochemical and pulse-radiolytic reduction of (pentamethylcyclopentadienyl)(polypyridyl)rhodium complexes. *Chem. Ber.* **1989,** *122*, 1869-1880.

[7] Ruppert, R.; Herrmann, S.; Steckhan, E., Very efficient reduction of $NAD(P)^+$ with formate catalysed by cationic rhodium complexes. *J. Chem. Soc., Chem. Commun.* **1988**, 1150-1151.

[8] Quintana, L. M. A.; Johnson, S. I.; Corona, S. L.; Villatoro, W.; Goddard, W. A.; Takase, M. K.; VanderVelde, D. G.; Winkler, J. R.; Gray, H. B.; Blakemore, J. D., Proton-hydride tautomerism in hydrogen evolution catalysis. *Proc. Nat. Acad. Sci. U.S.A.* **2016,** *113*, 6409-6414.

[9] (a) Steckhan, E.; Herrmann, S.; Ruppert, R.; Dietz, E.; Frede, M.; Spika, E., Analytical study of a series of substituted (2,2'-bipyridyl)(pentamethylcyclopentadienyl)rhodium and -iridium complexes with regard to their effectiveness as redox catalysts for the indirect electrochemical and chemical reduction of $NAD(P)^+$. *Organometallics* **1991,** *10*, 1568-1577. (b) Nam, D. H.; Park, C. B., Visible light-driven NADH regeneration sensitized by proflavine for biocatalysis. *Chembiochem* **2012,** *13*, 1278-1282.

[10] Pitman, C. L.; Finster, O. N. L.; Miller, A. J. M., Cyclopentadiene-mediated hydride transfer from rhodium complexes. *Chem. Commun.* **2016,** *52*, 9105-9108.

[11] Abura, T.; Ogo, S.; Watanabe, Y.; Fukuzumi, S., Isolation and Crystal Structure of a Water-Soluble Iridium Hydride: A Robust and Highly Active Catalyst for Acid-Catalyzed Transfer Hydrogenations of Carbonyl Compounds in Acidic Media. *J. Am. Chem. Soc.* **2003,** *125*, 4149-4154.

[12] Hopkins, J. A.; Lionetti, D.; Day, V. W.; Blakemore, J. D., Chemical and Electrochemical Properties of [Cp*Rh] Complexes Supported by a Hybrid Phosphine-Imine Ligand. *Organometallics* **2019,** *38*, 1300-1310.

[13] Boyd, E. A.; Lionetti, D.; Henke, W. C.; Day, V. W.; Blakemore, J. D., Preparation, Characterization, and Electrochemical Activation of a Model [Cp*Rh] Hydride. *Inorg. Chem.* **2019,** *58*, 3606-3615.

[14] Muckerman, J. T.; Skone, J. H.; Ning, M.; Wasada-Tsutsui, Y., Toward the accurate calculation of pKa values in water and acetonitrile. *Biochim. Biophys. Acta Bioenerg.* **2013,** *1827*, 882-891.

[15] (a) Klingert, B.; Werner, H., Basische Metalle, XLII. Die Metall-Basizität der Komplexe $C_5Me_5Rh(PMe_3)_2$, $C_5Me_5Rh(C_2H_4PMe_3$ und $C_5Me_5Rh(C_2H_4)P_2Me_4$: Neue Pentamethyl-cyclopentadienylrhodium(I)- und -rhodium(III)-Verbindungen. *Chem. Ber.* **1983,** *116*, 1450-1462. (b) Klingert, B.; Werner, H., Synthese und reaktivität von $[C_5Me_5Rh(\mu\text{-}PMe_2)]_2$: Additions- und insertionsreaktionen von sauerstoff und seinen homologen an die Rh_2P_2-einheit. *J. Organomet. Chem.* **1983**, *252*, C47-C52. (c) Klingert, B.; Werner, H., Metallkomplexe mit verbrückenden Dimethylphosphido-Liganden: VIII. Protonierung zweifach verbrückter Pentamethylcyclopentadienylrhodium(II)-Komplexe und Folgereaktionen des μ-Hydridodirhodium-Kations $[(C_5Me_5R)_2(\mu\text{-}PMe_2)_2(\mu\text{-}H)]^+$. *J. Organomet. Chem.* **1987,** *333*, 119-128.

[16] (a) Faraone, F.; Bruno, G.; Schiavo, S. L.; Tresoldi, G.; Bombieri, G., η^5-Cyclopentadienylrhodium(I) complexes containing diphosphines and their reactions

with the electrophiles H^+ and Me^+. Crystal and molecular structure of [Rh(η-C_5H_5)(CO)($Ph_2PCH_2PPh_2$)], a complex with a unidentate bis(diphenylphosphino)methane ligand. *J. Chem. Soc., Dalton Trans.* **1983**, 433-438. (b) Carmona, D.; Cativiela, C.; Garcia-Correas, R.; Lahoz, F. J.; Lamata, M. P.; Lopez, J. A.; De Viu, M. P. L.-R.; Oro, L. A.; Jose, E. S.; Viguri, F., Chiral rhodium complexes as catalysts in Diels-Alder reactions. *Chem. Commun.* **1996**, 1247-1248. (c) Faller, J. W.; D'Alliessi, D. G., Tunable Stereoselective Hydrosilylation of PhC⁝CH Catalyzed by Cp*Rh Complexes. *Organometallics* **2002,** *21*, 1743-1746. (d) Bajo, S.; Alférez, M. G.; Alcaide, M. M.; López-Serrano, J.; Campos, J., Metal-only Lewis Pairs of Rhodium with s, p and d-Block Metals. *Chem. – Eur. J.* **2020,** *26*, 16833-16845.

[17] References given in endnotes 15 and 16 represent prior reports of half-sandwich rhodium complexes supported by phosphine ligands. Citation 16b is one notable example, wherein a [Cp*Rh] hydride supported by a chelating diphosphine ligand was reported as a minor product appearing under catalytic conditions. The reported details for the resonances associated with this hydride (δ = –12.2 ppm, dt, $^1J_{Rh,H}$ = 36 Hz, $^2J_{P,H}$ = 24 Hz) are in general agreement with findings from our work reported here. Findings in citation 16d are similar, wherein [Cp*Rh(PMe_3)$_2$H]$^+$ is reported (δ = –13.4 ppm, dt, $^1J_{Rh,H}$ = 35 Hz, $^2J_{P,H}$ = 23 Hz) as a minor product of reaction of Klingert's complex Cp*Rh(PMe_3)$_2$ with adventitious water present in solvents used for NMR experiments.

[18] Johnson, S. I.; Gray, H. B.; Blakemore, J. D.; Goddard, W. A., Role of Ligand Protonation in Dihydrogen Evolution from a Pentamethylcyclopentadienyl Rhodium Catalyst. *Inorg. Chem.* **2017**, *56*, 11375-11386.

[19] (a) Zhang, F.; Jia, J.; Dong, S.; Wang, W.; Tung, C.-H., Hydride Transfer from Iron(II) Hydride Compounds to $NAD(P)^+$ Analogues. *Organometallics* **2016,** *35*, 1151-1159. (b) Castillo, C. E.; Stoll, T.; Sandroni, M.; Gueret, R.; Fortage, J.; Kayanuma, M.; Daniel, C.; Odobel, F.; Deronzier, A.; Collomb, M.-N., Electrochemical Generation and Spectroscopic Characterization of the Key Rhodium(III) Hydride Intermediates of Rhodium Poly(bipyridyl) H_2-Evolving Catalysts. *Inorg. Chem.* **2018,** *57*, 11225-11239. (c) Roy, S.; Sharma, B.; Pécaut, J.; Simon, P.; Fontecave, M.; Tran, P. D.; Derat, E.; Artero, V., Molecular Cobalt Complexes with Pendant Amines for Selective Electrocatalytic Reduction of Carbon Dioxide to Formic Acid. *J. Am. Chem. Soc.* **2017,** *139*, 3685-3696. (d) Elgrishi, N.; Kurtz, D. A.; Dempsey, J. L., Reaction Parameters Influencing Cobalt Hydride Formation Kinetics: Implications for Benchmarking H_2-Evolution Catalysts. *J. Am. Chem. Soc.* **2017,** *139*, 239-244. (e) Takahashi, K.; Yamashita, M.; Nozaki, K., Tandem Hydroformylation/Hydrogenation of Alkenes to Normal Alcohols Using Rh/Ru Dual Catalyst or Ru Single Component Catalyst. *J. Am. Chem. Soc.* **2012,** *134*, 18746-18757.

[20] Heinekey and co-workers have reported the synthesis of half-sandwich iridium dihydrides, as well, which provide a counterpoint to the monohydrides investigated here. See: Gelabert, R.; Moreno, M.; Lluch, J. M.; Lledós, A.; Pons, V.; Heinekey, D. M., Synthesis and Properties of Compressed Dihydride Complexes of Iridium: Theoretical and Spectroscopic Investigations. *J. Am. Chem. Soc.* **2004,** *126*, 8813-8822.

[21] (a) Pal, S.; Kusumoto, S.; Nozaki, K., Dehydrogenation of Dimethylamine–Borane Catalyzed by Half-Sandwich Ir and Rh Complexes: Mechanism and the Role of Cp*

Noninnocence. *Organometallics* **2018,** *37*, 906-914. (b) Banerjee, S.; Soldevila-Barreda, J. J.; Wolny, J. A.; Wootton, C. A.; Habtemariam, A.; Romero-Canelón, I.; Chen, F.; Clarkson, G. J.; Prokes, I.; Song, L.; O'Connor, P. B.; Schünemann, V.; Sadler, P. J., New activation mechanism for half-sandwich organometallic anticancer complexes. *Chem. Sci.* **2018,** *9*, 3177-3185.

[22] (a) Ogata, K.; Seta, J.; Yamamoto, Y.; Kuge, K.; Tatsumi, K., One-pot syntheses of alkenyl-phosphonio complexes of ruthenium(II), rhodium(III) and iridium(III) bearing *p*-cymene or pentamethylcyclopentadienyl groups. *Inorganica Chim. Acta* **2007,** *360*, 3296-3303. (b) Tanase, T.; Yoshii, A.; Otaki, R.; Nakamae, K.; Mikita, Y.; Kure, B.; Nakajima, T., Synthesis and structures of dinuclear Rh^{III} and Ir^{III} complexes supported by a tetraphosphine, *meso*- or *rac*-bis{[(diphenylphosphinomethyl)phenyl]phosphino]}methane. *J. Organomet. Chem.* **2015,** *797*, 37-45.

[23] IUPAC. *Compendium of Chemical Terminology*, 2nd ed. (the "Gold Book"). Compiled by A. D. McNaught and A. Wilkinson. Blackwell Scientific Publications, Oxford (1997). Online version (2019-) created by S. J. Chalk. https://doi.org/10.1351/goldbook.

[24] (a) Blakemore, J. D.; Hernandez, E. S.; Sattler, W.; Hunter, B. M.; Henling, L. M.; Brunschwig, B. S.; Gray, H. B., Pentamethylcyclopentadienyl rhodium complexes. *Polyhedron* **2014,** *84*, 14-18. (b) Nakai, H.; Jeong, K.; Matsumoto, T.; Ogo, S., Catalytic C–F Bond Hydrogenolysis of Fluoroaromatics by [(η^5-C_5Me_5)RhI(2,2′-bipyridine)]. *Organometallics* **2014,** *33*, 4349-4352.

[25] Shannon, R. D., Revised effective ionic radii and systematic studies of interatomic distances in halides and chalcogenides. *Acta Cryst. A* **1976,** *32*, 751-767.

[26] Regarding the assignment of $^{3}J_{H,Rh}$ = 4.5 Hz and $^{4}J_{H,H}$ = 3.2 Hz for the downfield methylene proton: These coupling constants cannot be assigned concretely with inference from the appearance of the hydride resonances alone, due to broadness and the I = 1/2 nature of both H and Rh. The assignment of $^{3}J_{H,Rh}$ vs. $^{4}J_{H,H}$ is tentative, and based on the general assumption that a three-bond coupling should have a higher magnitude than a four-bond coupling. ^{103}Rh NMR could solidify this assignment, but such work is challenging due to the low gyromagnetic ratio of Rh.

[27] Shaka, A. J.; Keeler, J.; Freeman, R., Evaluation of a new broadband decoupling sequence: WALTZ-16. *J. Magn. Reson.* **1983,** *53*, 313-40.

[28] Shaka, A. J.; Keeler, J., Broadband spin decoupling in isotropic liquids. *Prog. Nucl. Magn. Reson. Spectrosc.* **1987,** *19*, 47-129.

[29] (a) Hoffman, R. A.; Forsén, S., High Resolution Nuclear Magnetic Double and Multiple Resonance. *Prog. NMR Spec.* **1966,** *1*, 15-204. (b) Cotton, F. A.; Marks, T. J., Interpretation of a Spin-Tickling Experiment on (Monohaptocyclopentadienyl)-(methyl)(dichloro)silane. *Inorg. Chem.* **1970,** *9*, 2802-2804.

[30] (a) Kupce, E.; Freeman, R.; Wider, G.; Wuethrich, K., Suppression of cycling sidebands using bi-level adiabatic decoupling. *J. Magn. Reson., Ser. A* **1996,** *122*, 81-84. (b) Weigelt, J.; Hammarstroem, A.; Bermel, W.; Otting, G., Removal of zero-quantum coherence in protein NMR spectra using SESAM decoupling and suppression of decoupling sidebands. *J. Magn. Reson., Ser. B* **1996,** *110*, 219-224. (c) Tenailleau, E.;

Akoka, S., Adiabatic ^{1}H decoupling scheme for very accurate intensity measurements in ^{13}C NMR. *J. Magn. Reson.* **2007,** *185*, 50-58.

[31] Appel, A. M.; Helm, M. L., Determining the Overpotential for a Molecular Electrocatalyst. *ACS Catal.* **2014,** *4*, 630-633.

[32] Pitman, C. L.; Miller, A. J. M., Molecular Photoelectrocatalysts for Visible Light-Driven Hydrogen Evolution from Neutral Water. *ACS Catal.* **2014,** *4*, 2727-2733.

[33] Fulmer, G. R.; Miller, A. J. M.; Sherden, N. H.; Gottlieb, H. E.; Nudelman, A.; Stoltz, B. M.; Bercaw, J. E.; Goldberg, K. I., NMR Chemical Shifts of Trace Impurities: Common Laboratory Solvents, Organics, and Gases in Deuterated Solvents Relevant to the Organometallic Chemist. *Organometallics* **2010,** *29*, 2176-2179.

[34] Harris, R. K.; Becker, E. D.; Cabral De Menezes, S. M.; Goodfellow, R.; Granger, P., NMR nomenclature: Nuclear spin properties and conventions for chemical shifts (IUPAC recommendations 2001). *Concepts Magn. Reson.* **2002,** *14*, 326-346.

[35] Harris, R. K.; Becker, E. D.; De Menezes, S. M. C.; Granger, P.; Hoffman, R. E.; Zilm, K. W., Further Conventions for NMR Shielding and Chemical Shifts. *IUPAC Standards Online* **2016**, *80*, 59-84.

Chapter 3

On the Advanced NMR Characterization of [Cp*Rh] Complexes of Bis(diphenylphosphino)methane

This chapter is adapted from a published manuscript:

Comadoll, C. G.; Henke, W. C.; Hopkins Leseberg, J. A.; Douglas, J. T.; Oliver, A. G.; Day, V. W.; Blakemore, J. D., Examining the Modular Synthesis of [Cp*Rh] Monohydrides Supported by Chelating Diphosphine Ligands. *Organometallics* **2021**, *40*, 3808-3818.

3.1 Introduction

One of the great hurdles to a comprehensive understanding of nuclear magnetic resonance (NMR) spectra is the interpretation of complex splitting patterns. The interpretation of any splitting pattern, complex or simple, is reliant on an understanding of spectral ordering; the appearance of splitting patterns is governed through either first-order or second-order rules.[1] Spectral data containing resonances that are first-order in nature mimic the expected splitting patterns for a given resonance, such that the observed splitting obeys the $n + 1$ rule derived from Pascal's triangle.[2] In such instances, the resonance is centrosymmetric with respect to the peak intensity of the splitting pattern, resembling splitting and intensities one would predict based on the chemical environment of a particular nucleus. A first-order spectrum would show a doublet with observed 1:1 peak intensity, a triplet with observed 1:2:1 peak intensity, and so on. The nature of such spectra is driven by equivalence: Nuclei that are chemically and magnetically equivalent will obey first-order rules in their appearance.

The situations become more complicated when splitting patterns display second-order effects; these effects are brought about through a similarity between the coupling constant (J, Hz) and chemical shift difference ($\Delta\delta$, Hz) for two nuclei, most often driven by an intrinsic chemical inequivalence of the nuclei.[3] The visual manifestation of such effects is most commonly evidenced by irregular peak intensities, or *distortion* from the expected centrosymmetric peak intensity, and often by irregular line positions. In other words, the spectral data contain information which cannot be determined by methods of prediction as simple as Pascal's triangle. One common second-order field effect is a phenomenon that is

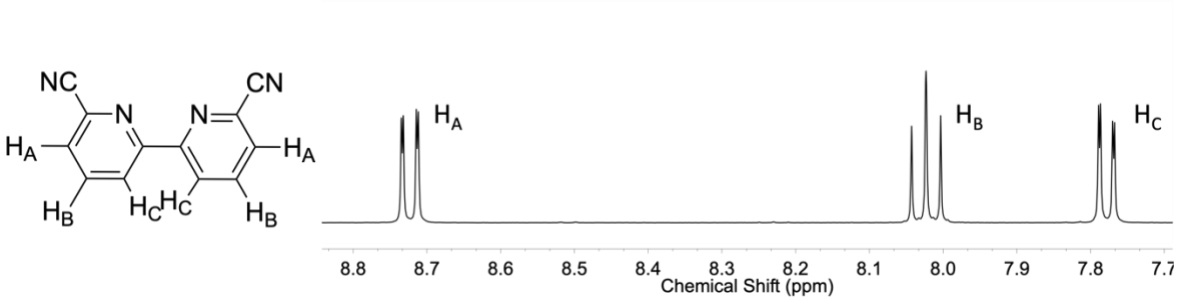

Figure 3.1. Aromatic resonances in the ^{1}H NMR spectrum of 6,6'-dicyano-2,2'-bipyridine. Each doublet of doublet resonance at 8.75 ppm and 7.75 ppm displays roofing toward the triplet at 8.05 ppm.

commonly referred to in the field as "roofing." Roofing is the term used to describe a distortion in peak intensities such that two resonances appear to *lean* towards one another. A triplet which displays roofing might have a 0.75:2:1.25 peak intensity, for example, instead of the expected 1:2:1 peak intensity. Roofing is often seen in aromatic systems strongly between *ortho* protons,[4] which are inequivalent but couple to one another in a $^3J_{H,H}$ fashion. Figure 3.1 shows the aromatic protons of 6,6'-dicyano-2,2'-bipyridine, in which the doublet of doublets representing protons H_A and H_C display roofing with the triplet through *ortho* $^3J_{H,H}$ coupling. The effect is subtle but noticeably larger for the doublet of doublets for H_C due to its proximity to the triplet, with respect to the doublet of doublets for H_A.

An often, even more pronounced manifestation of roofing is common in compounds possessing homonuclear, geminal, inequivalent nuclei. In the case of inequivalent geminal nuclei, this inequivalence of chemical environment often arises due to asymmetry, as is the case in the methylene protons of compounds **1** and **5** (see Chart 3.1, spectral data *vide infra*). If two geminal nuclei are not related through a symmetry element (most often a mirror plane), then they lie in different environments, are therefore inequivalent or *heterotopic*, and

will couple to one another. Despite their inequivalence, they are still geminal homonuclei; their chemical shifts will most often be *similar* as a result, such that the coupling constant (J, Hz) and chemical shift difference ($\Delta\delta$, Hz) will be on the same order of magnitude, giving rise to a second-order roofing effect. The degree to which roofing distortion is observable between two resonances is dependent on the magnitude of both $\Delta\delta$ and J.

When considering the second-order field effects between two nuclei, the distortion which is present in a system can be quantified when we consider the ratio of $\Delta\delta$ and J (i.e., $\Delta\delta/J$). When these two values are of a similar order of magnitude, the ratio will be closer to 1; the closer to 1 this ratio is, the more distortion will be present. As $\Delta\delta$ increases or J decreases, the ratio becomes greater than 1, thereby lessening the distortion. Because J is an intrinsic chemical property between two nuclei, it is impossible to manipulate this value; however, it *is* possible to manipulate $\Delta\delta$, as it is a quantitative measure of chemical inequivalence influenced by the B_0 field (i.e., ^{1}H resonant frequency). Because δ is directly proportional to the B_0 field [δ (Hz) = δ (ppm) * B_0 (Hz) * 10^{-6}], increasing the B_0 field frequency increases $\Delta\delta$, diminishing the distortion caused by such effects by moving toward a situation where $J << \Delta\delta$; thus, increasing the B_0 field can often simplify spectral interpretation.[5] In general, at a high-field limit (which may or may not be accessible for a given system based on the exact values of J and $\Delta\delta$), a spectrum displaying second-order effects may be made to appear first-order.[6] Multifrequency NMR experiments, where the B_0 field frequency is increased across experiments, provide the opportunity to resolve the observed second-order field effects that give rise to the roofing phenomenon in a given system.

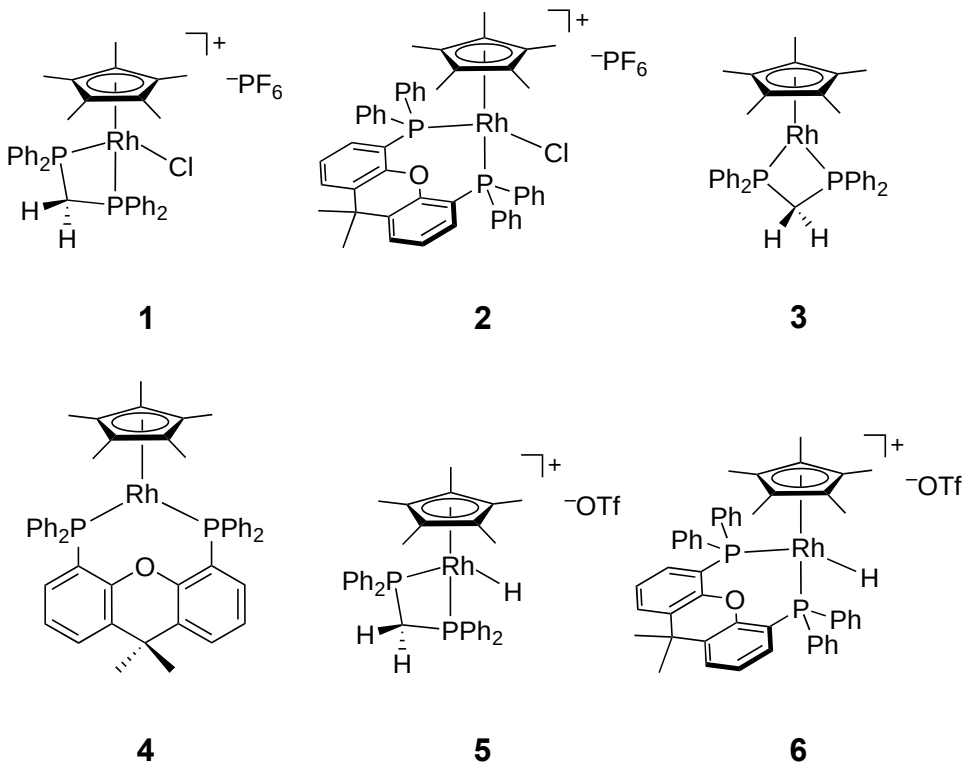

Chart 3.1. Preparation of Cp*Rh complexes. Left: Synthetic strategy using sequential reduction/protonation. Right: Structures of the compounds described in this work.

As discussed in Chapter 2, a series of [Cp*Rh] complexes consisting of the chelating diphosphine ligands dppm and Xantphos were prepared and characterized (see Chart 3.1). These complexes display rich NMR spectroscopic properties due to the presence of multiple spin-active nuclei in each system, including H, C, P, and Rh. Particularly for **1** and **5**, the ^{1}H NMR spectra of these compounds are among the most complex that we have encountered in our work with organometallic rhodium systems. This complexity is owed to both the presence of the geminal, heterotopic methylene protons in the backbone of the dppm ligand, diagnostic of the *pseudo*-octahedral geometry of the rhodium centers in **1** and **5**, and

to the multiple NMR-active nuclei in the complexes; the combination of these two factors gives rise to incredibly complex spectral data from these particular systems.

Based on the appearance of the resonances corresponding to the methylene protons of dppm within **1** and **5** (corresponding to H35A/H35B and H19A/H19B, respectively, that were identified in the crystallography; see Figure 3.2), we anticipated that the observable second-order effects could be minimized if multifrequency NMR experiments were performed on both systems. Additionally, we performed digital simulations of the collected multifrequency data for each complex to elucidate coupling interactions giving rise to the

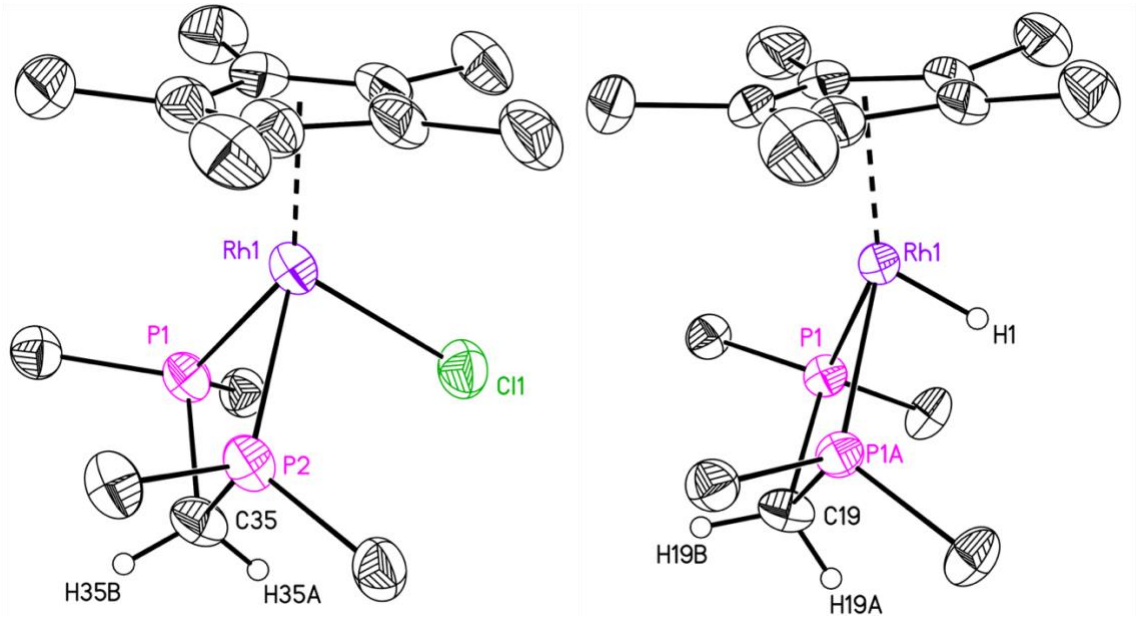

Figure 3.2. Solid-state structure of the dppm-supported chloride (**1**) and monohydride (**5**). Displacement ellipsoids are shown at 50% probability level. Hydrogen atoms (except H19A, H19B, and H1), terminal phenyl rings, hexafluorophosphate counteranion, and triflate counteranion are omitted for clarity.

intricate splitting patterns within the data. Finally, we utilized 2D NMR experiments to make an absolute assignment of the geminal methylene protons of **5** with respect to the solid-state orientation of the two protons, shown in Figure 3.2.

3.2 Results and Discussion

3.2.1 Multifrequency NMR Characterization of 1 and 5

In our efforts toward multifrequency NMR experiments on **1** and **5**, we performed the desired experiments on both complexes using spectrometers with B_0 field frequency at 400, 500, 600, and 800 MHz. As previously mentioned, we anticipate that the roofing distortion brought about by second-order field effects in both systems will be lessened, if not diminished in full, as B_0 increases. Indeed, the ^{1}H NMR spectra of **1** collected at 400, 500, 600, and 800 MHz show decreased roofing between the methylene protons as the frequency of the instrument increases (see Figure 3.3). The roofing is still visible at 800 MHz, which can be explained if we consider the ratio of the difference between the chemical shifts ($\Delta\delta$ in Hz) and the relevant coupling constant ($^2J_{H,H}$ in Hz); the further this ratio is from 1, the less observable the second-order field effects will be in a given spectrum (for H35A/H35B: at 400 MHz, 163.3 Hz/15.6 Hz = 10.5; at 800 MHz, 320.7 Hz/15.7 Hz = 20.4). A larger $\Delta\delta$ (in Hz, at a given field frequency) gives a larger ratio when divided by the coupling constant, confirming that the second-order field effects are minimized when $\Delta\delta$ is larger.

Relative to **1**, the effects of increasing the field strength on the methylene protons were far more noticeable for **5** due to the greater difference in chemical shift ($\Delta\delta$ value) for H19A/H19B in **5** vs. the corresponding protons in **1**. For H35A/H35B in **1**, the $\Delta\delta$ is much smaller than that of H19A/H19B in **5** ($\Delta\delta$ = 0.40 ppm for **1**, 0.88 ppm for **5**). This increase

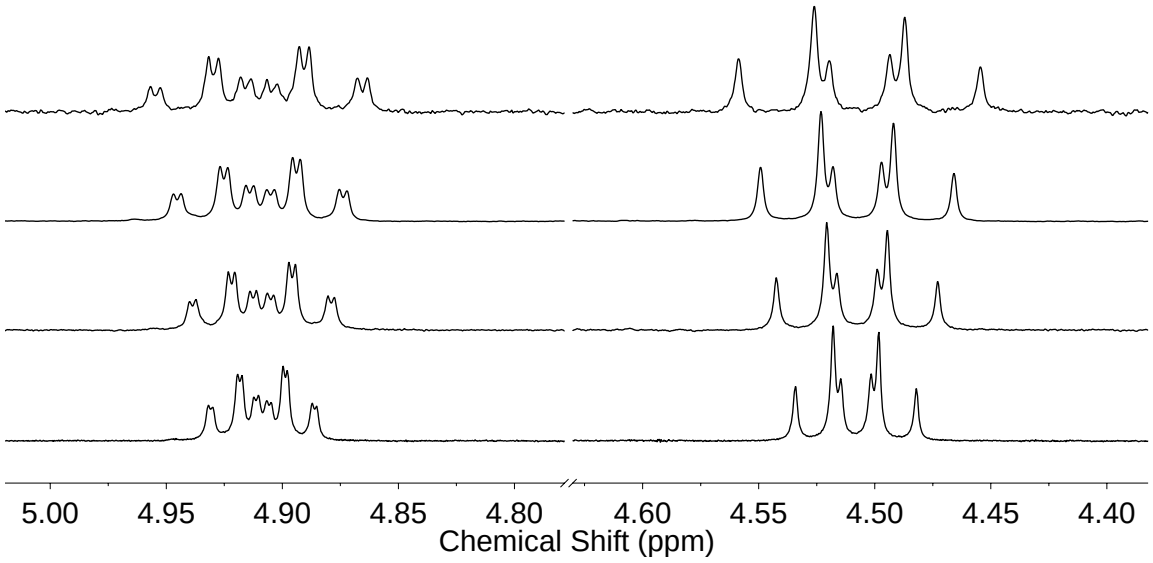

Figure 3.3. Partial ^{1}H NMR stack of **1** methylene proton resonances. From upper row to lower row: 400, 500, 600, and 800 MHz spectrometer field strength.

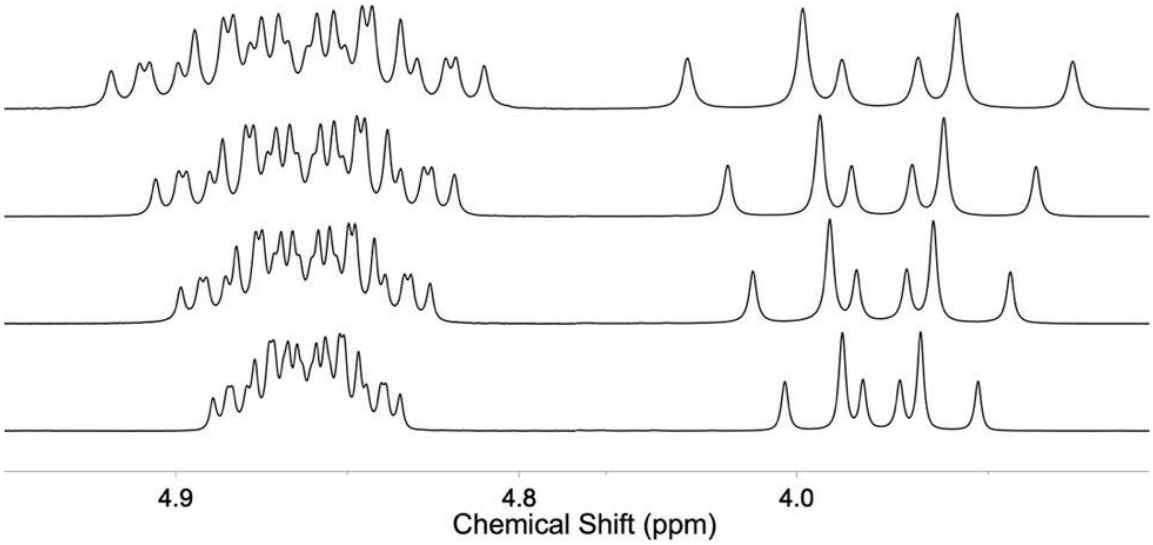

Figure 3.4. Partial ^{1}H NMR stack of **5** methylene proton resonances. From upper row to lower row: 400, 500, 600, and 800 MHz spectrometer field strength. Resonances are not shown to scale.

of Δδ in **5** relative to **1** reflects diminished roofing, which is evidenced by the ratio of Δδ to *J* in this system as well (for H19A/H19B: at 400 MHz, 355.2 Hz/16.2 Hz = 21.9; at 800 MHz, 708.1 Hz/16.4 Hz = 43.2). Indeed, the roofing observed for H19A/H19B in **5** at 400 MHz is essentially eliminated in the spectrum obtained at 800 MHz (see Figure 3.4), an occurrence not reached for H35A/H35B in **1**, as the roofing was still clearly observable for those methylene protons even at 800 MHz. Taken together, these parameters quantify the effect of the inequivalence of the methylene protons on the spectral data in both systems and set the stage for a full assignment of the coupling networks underlying their appearance in the data.

3.2.2 Digital Simulations of 1 and 5

In order to assign the coupling networks involving the methylene protons in complexes **1** and **5**, as well as confirm the field-dependence of the observed experimental data, spectral simulations of the NMR data for **1** and **5** were performed using the Spin Simulation function of the MestReNova software package.[7] Full details for all simulations are found in Section 3.4.2. Simulations serve as a powerful tool to aid in understanding the coupling interactions between NMR-active nuclei because individual couplings in a given network can be activated or deactivated on-demand during spectral visualization, affording insights from pattern recognition that would not be available otherwise. An example simulation is shown in Figure 3.5 for **5** at 400 MHz. In each simulation, the experimental *J* values and chemical shifts (Figure 3.5b) are determined and entered in to the Spin Simulation dialog box within MestReNova (Figure 3.5c). To build the spin system, the chemical shift is input for each nucleus (corresponding to the labels in Figure 3.5a), along

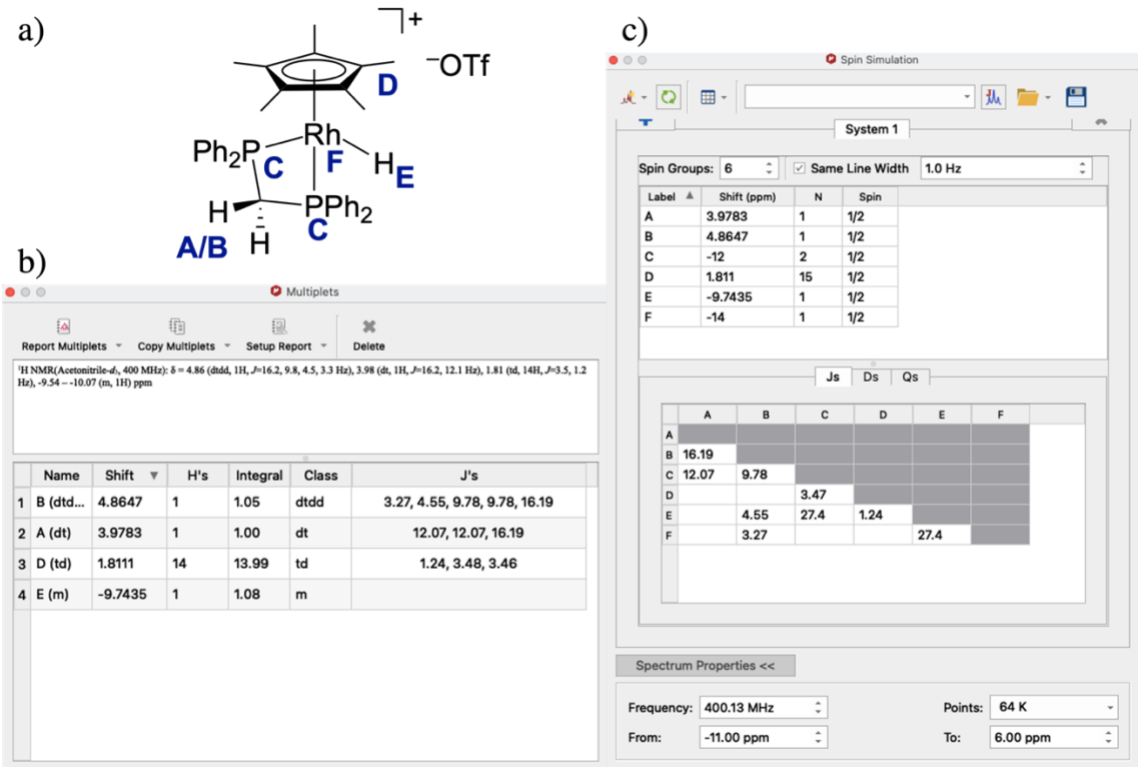

Figure 3.5. a) Complex **5** with NMR-active nuclei labeled for use in Spin Simulation. b) Experimental data for **5**, collected at 400 MHz in CD_3CN. c) Spin Simulation dialog box within MestReNova software. The top half of this dialog box contains entries for the label (corresponding to those in Figure 3.4a), experimental chemical shift, number of atoms per nucleus (N), and the spin of the given nucleus. The bottom half of the box contains entries for the experimental *J* values assigned to specific nuclei.

with the number of atoms for the given nucleus and the spin of the nucleus. The coupling constants are then assigned in the lower half of the dialog box between the appropriate nuclei. Once all assignments have been made, the data are simulated.

For **1**, the spin system can be described as $ABM_{15}Y_2Z$ in Pople notation,[8] where A and B are methylene protons H35A/H35B, M_{15} refers to the Cp* methyl protons, Y_2

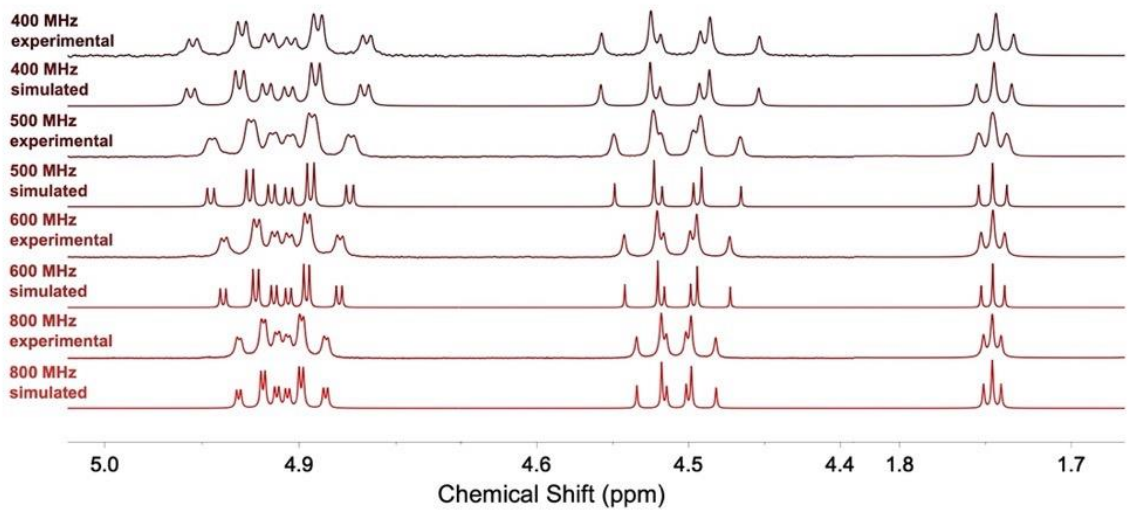

Figure 3.6. Stacked, partial multifrequency ^{1}H NMR spectra for **1**, depicting alternating experimental and simulated spectra for both methylene protons and the Cp* methyl protons (from left to right). Resonances are not shown to scale.

represents the two phosphorus atoms of dppm, and Z represents the rhodium metal center.[9] In accord with this spin system assignment, the expected dtd and dt resonances for each methylene proton were reproduced to a very high degree across all frequencies by the simulations (see Figure 3.6). Additionally, the expected triplet of the Cp* methyl protons was also reproduced with accuracy. With this understanding of the spin system of **1** in hand, we turned our attention to the more complex system present in **5**. For these simulations, we expanded the simulation spectral window to model both resonances arising due to the hydride ligand as well as the Cp* methyl resonances (for reasons discussed below). This system can be described as $ABM_{15}XY_2Z$, similar to that of **1**, but with substitution of the protons corresponding to H19A/H19B as A and B and inclusion of the hydride ligand as X.[9] Appealingly, the simulated spectrum closely models the experimental spectrum of **5** at 400 MHz (see Figure 3.7, uppermost two spectra).

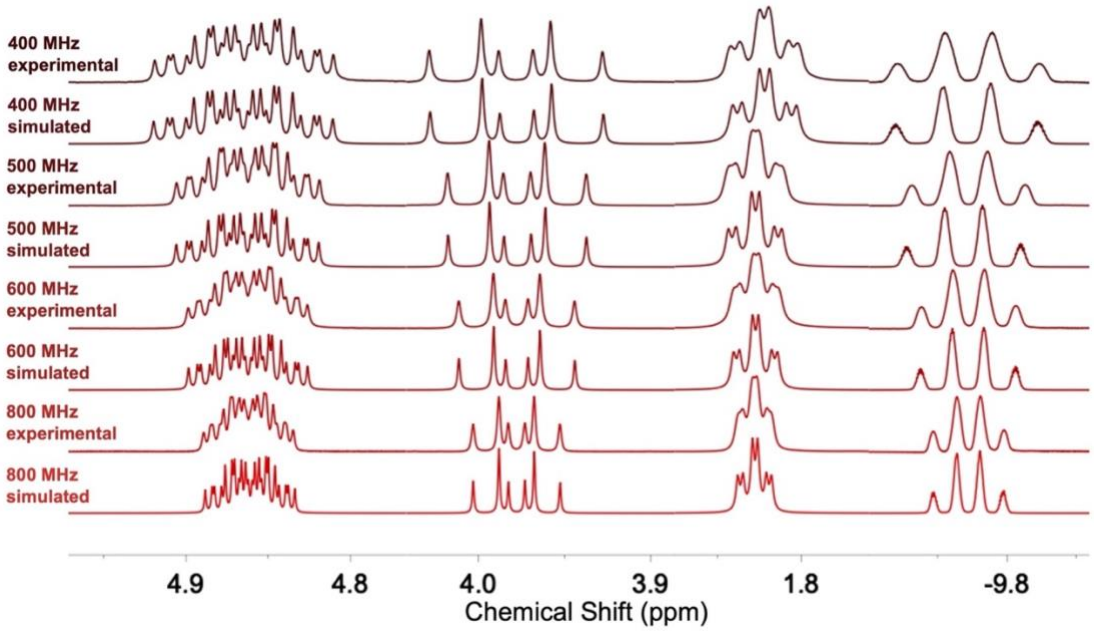

Figure 3.7. Stacked, partial multifrequency ^{1}H NMR spectra of **5**, depicting alternating experimental and simulated spectra for both methylene protons, the Cp* methyl protons, and the hydride ligand (from left to right). Intensities of the resonances are not shown to scale.

The observable broadening of the quartet resonance for the hydride ligand (Figure 3.7, rightmost side of the spectra) is the direct result of coupling to the 15 Cp* methyl protons at 1.2 Hz; such coupling of the hydride to the many equivalent Cp* methyl protons at a low magnitude gives rise to the broadened shape. To confirm this situation, the individual couplings involving the hydride were investigated with sequential simulations of increasing complexity to probe the consequences in the final appearance of the hydride resonances (see Figure 3.8). The simulations support this hypothesis regarding the origin of the broadening of the hydride resonances, in that the quartet for the hydride of **5** could be simulated when only coupling of the hydride to rhodium and phosphorus is considered (Figure 3.8, spectrum

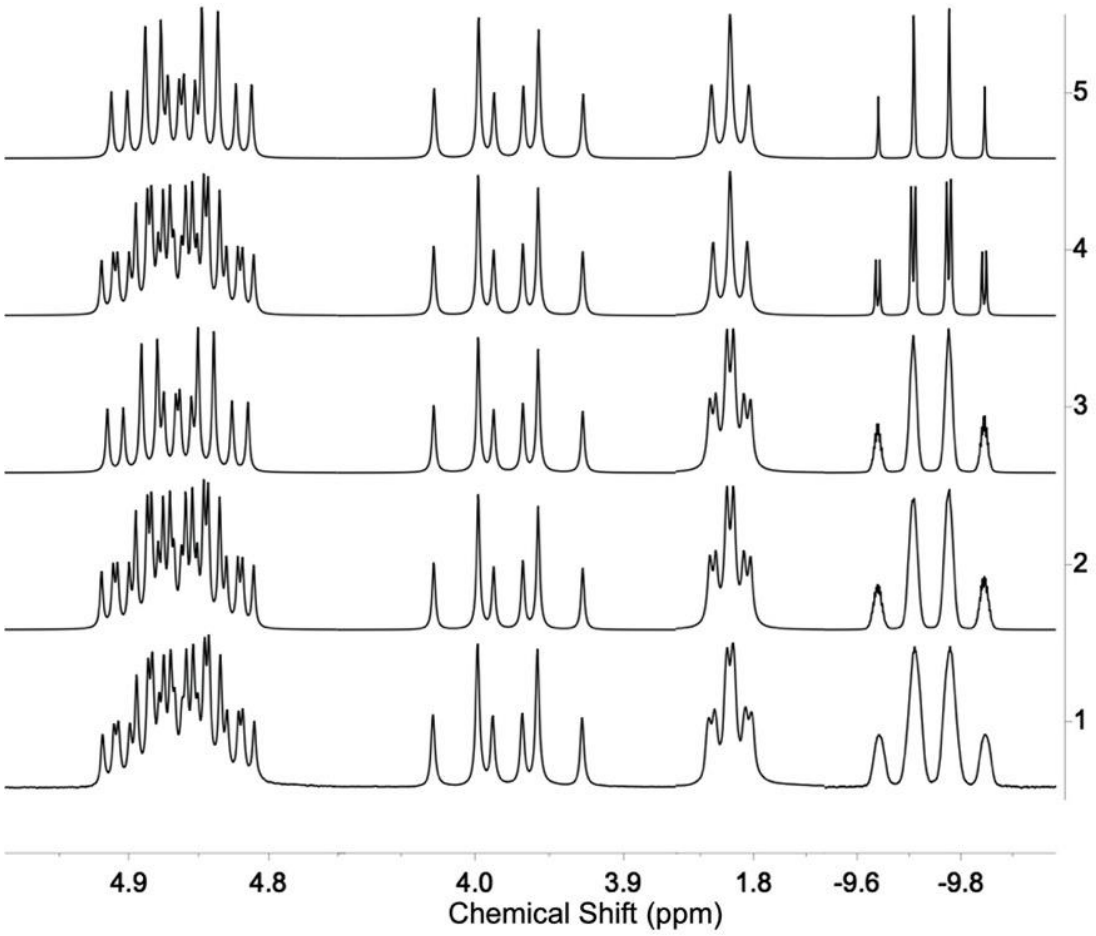

Figure 3.8. Stacked partial ^{1}H NMR spectra of **5** at 400 MHz showing the experimental spectrum (lowest row, 1) and the simulated spectra (upper rows, 2-5) that resulted when changing coupling constant pairing assignments. Peaks are not to scale. **Spectrum 1**: Experimental data. **Spectrum 2**: Simulation of hydride coupling with Cp* methyl protons, one methylene proton, phosphorus, and rhodium. **Spectrum 3**: Simulation of hydride coupling with Cp* methyl protons, phosphorus, and rhodium. **Spectrum 4**: Simulation of hydride coupling with one methylene proton, phosphorus, and rhodium. **Spectrum 5**: Simulation of hydride coupling with phosphorus and rhodium.

5). Additionally, the quartet of doublets expected from coupling of the hydride in **5** to only rhodium, phosphorus, and one methylene proton is also confirmed through the simulation (Figure 3.8, spectrum 4). The splitting of the dtdd methylene proton and the td Cp* methyl proton resonances correspondingly deviate from the appearance of the experimental data when coupling to the hydride is omitted, further supporting their role in the broadness of the quartet of the hydride (see Figure 3.8, spectra 1-3 for the remaining simulations).

Taken together, the multifrequency experimental studies and paired comprehensive simulations of **1** and **5** help disentangle the chemical and magnetic complexity of these systems and resolve the nature of the inequivalence of several of the nuclei in these systems. The second-order field effects giving rise to the appearance of roofing about the methylene protons can be understood and are nearly resolved by moving to spectrometers that operate at higher frequencies; at 800 MHz, the second-order effects remain visible, however, due to the intrinsic value of $\Delta\delta$ for the methylene protons. Nonetheless, the simulations of **1** and **5** faithfully reproduce the needed resonances and splitting patterns in all cases, providing a concrete inventory of the nuclear coupling interactions that govern the spectral properties of both **1** and **5**.

3.2.3 Absolute Assignment of Methylene Protons

The chemical inequivalence of the methylene protons present in the dppm backbone of **5** encouraged us to pursue an absolute assignment of the spectral signatures associated with these individual H-atoms. These are labelled as H19A and H19B in the related solid-state structure obtained from single-crystal XRD analysis (see Figure 3.9). To accomplish the spectral assignment, 2D-NMR experiments were conducted (see Figure 3.10). NOESY

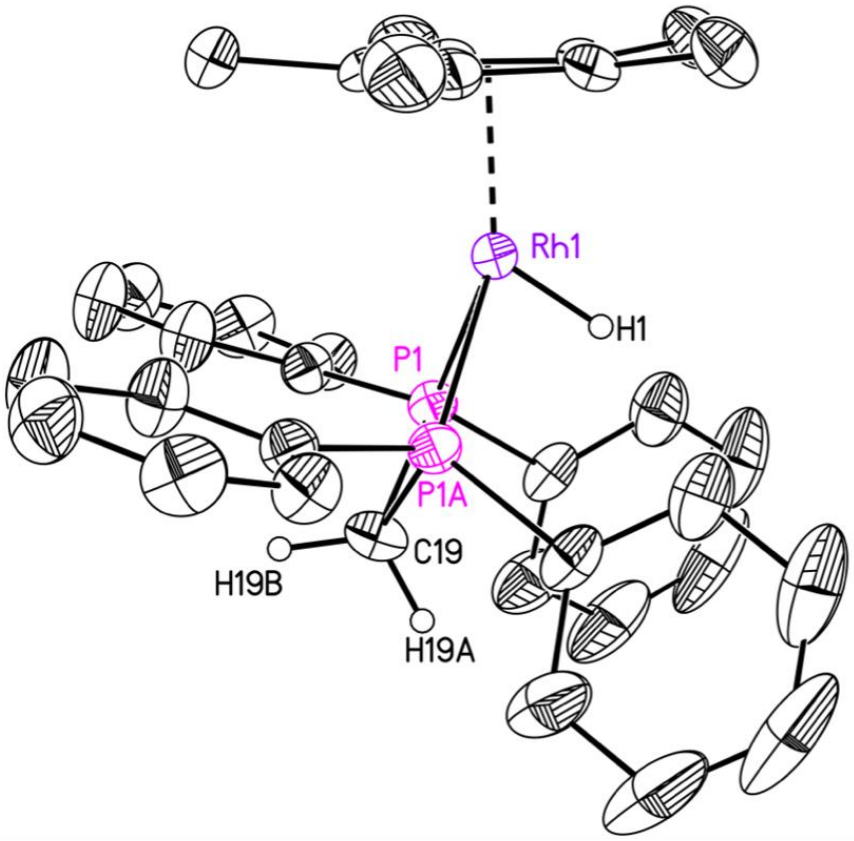

Figure 3.9. Solid-state structure of the dppm-supported monohydride **5** showing terminal phenyl rings. Displacement ellipsoids are shown at 50% probability level. Hydrogen atoms (except H19A, H19B, and H1) and triflate counteranion are omitted for clarity.

NMR data indicate that the more downfield methylene resonance (δ = 4.89 ppm, dtdd) is spatially close to the aromatic protons observed at 7.36 ppm in a way that the dt at 3.98 ppm is not; these aromatic protons appear as a dtd and correspond to four of the protons on the phenyl rings of the dppm ligand. In turn, these four aromatic protons are spatially close to the Cp* methyl protons according to NOESY, a finding which points to their proximity to the Cp* ring. Of the four phenyl rings of the dppm ligand (Figure 3.9) the two rings shown as oriented up and to the left in the solid-state structure are in closer proximity to the Cp*

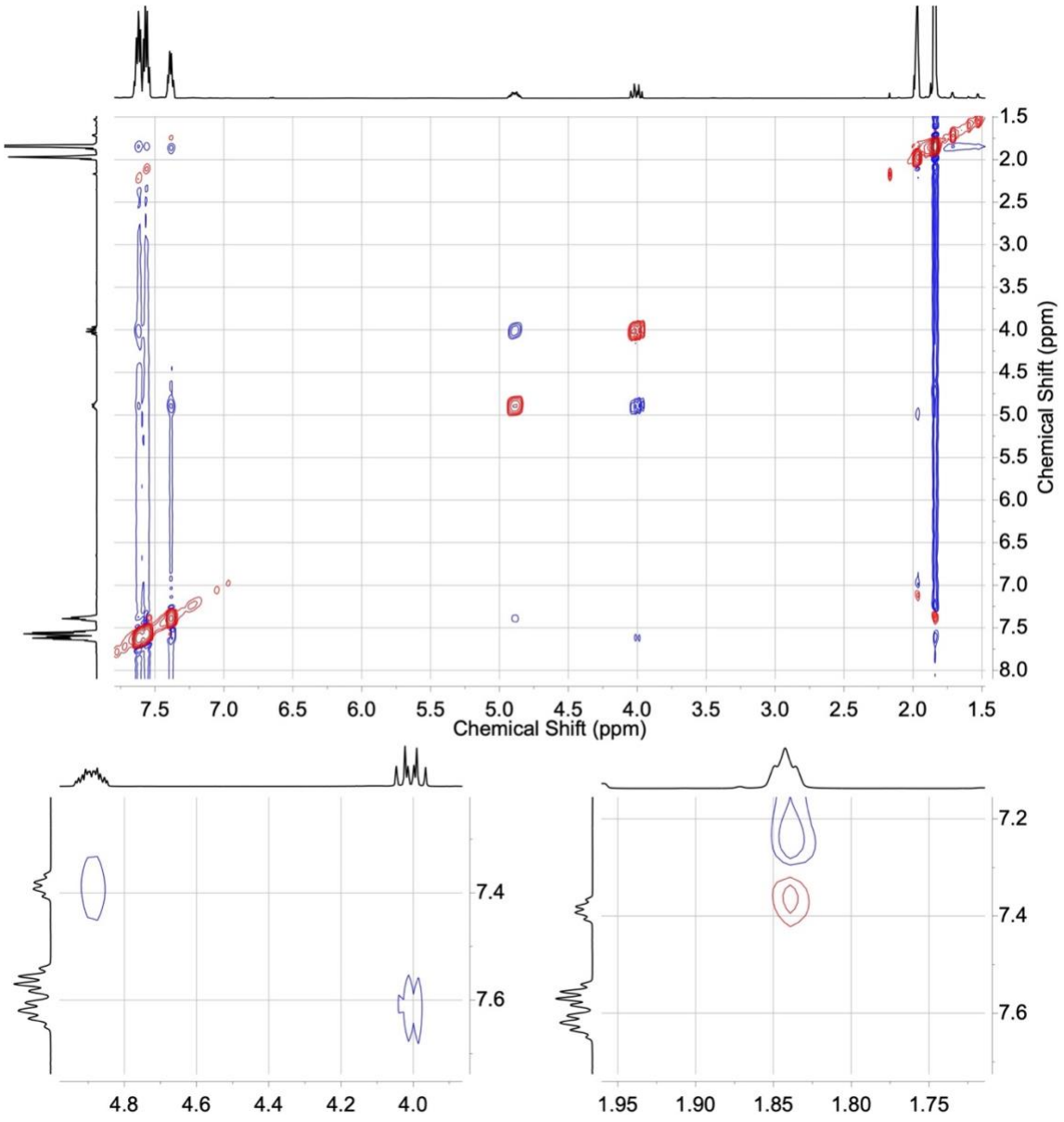

Figure 3.10. NOESY-NMR spectrum (CD_3CN) of **5** (upper large panel) and inset of methylene protons, aromatic region, and Cp* methyl protons (lower two panels).

ring; as a result, the 4H dtd at 7.36 ppm most likely belongs to the four *ortho* protons of those two phenyl rings. On the basis of this coupling map, we assign the dtdd at 4.89 ppm as corresponding to the heterotopic methylene proton which is oriented upward toward the Cp* ring in **5**. This corresponds to H19B in Figure 3.9. By elimination, the downward-facing

proton (labeled as H19A in Figure 3.9) can thus be assigned as the dt at 3.98 ppm. This assignment is supported by the XRD data, in that strong NOESY cross-peaks occur when the distance between two atoms is near 2.5 Å, with medium and weak cross-peaks occurring at distances near 3.5 Å and 5.0 Å, respectively.[10] The closer proximity of H19B to the nearest *ortho* proton in the solid-state structure (2.58 Å) relative to H19A (3.97 Å) is in harmony with the stronger cross-peak present in the NOESY spectral data for the dtdd. Therefore, we can confidently identify H19A as the dt at 3.98 ppm and H19B as the dtdd at 4.89 ppm in the ^{1}H NMR data for **5**.

3.3 Conclusion

This work demonstrates and provides a comprehensive explanation for the intricate spectral properties of [Cp*Rh] complexes bearing the chelating dppm ligand. These intricacies arise from the geminal, heterotopic methylene protons on the dppm backbone, influenced by the lack of symmetry and multiple NMR-active nuclei at play in the systems of **1** and **5**. The complexities of the nuclear spin systems featured in these compounds were elucidated using both multifrequency experimental studies and full-spectrum digital simulations. The findings explain the inequivalence of the heterotopic methylene protons and enable faithful replication of the diagnostic experimental data through reliable coupling constant assignments obtained with digital NMR simulations. The simulations clarified the spin systems which give rise to the complex splitting patterns displayed by **5,** in particular, demonstrating that the hydride ligand couples to rhodium, both phosphorus atoms, the Cp* methyl protons, and one of the methylene protons. These assignments would have been tentative at best if not for the use of simulations, as the coupling of the hydride to both the Cp* methyl protons and one methylene proton could not be measured directly from the

broadened quartet corresponding to the hydride. The absolute assignment of both methylene protons, aided by 2D NMR experiments, allowed us to relate the geometry observed in the crystal structure to the spectroscopic data. Taken together, these results demonstrate the utility of multifrequency NMR experiments and digital simulations to aid the understanding of complicated, second-order spectral data.

3.4 Experimental Details

3.4.1 General Considerations

All manipulations were carried out in dry N_2-filled gloveboxes (Vacuum Atmospheres Co., Hawthorne, CA, USA) or under an N_2 atmosphere using standard Schlenk techniques, unless otherwise noted. All solvents were of commercial grade and dried over activated alumina using a PPT Glass Contour (Nashua, NH, USA) solvent purification system prior to use, and were stored over molecular sieves. All chemicals were obtained from major commercial suppliers and used as received after extensive drying.

Deuterated solvents for NMR studies were purchased from Cambridge Isotope Laboratories (Tewksbury, MA, USA); CD_3CN was dried with CaH_2 and stored over molecular sieves, and C_6D_6 was dried over sodium/benzophenone. ^{1}H, ^{13}C, ^{19}F, and ^{31}P NMR spectra were collected with 400, 500, 600, or 800 MHz Bruker spectrometers and were referenced to the residual protio-solvent signal in the cases of ^{1}H and ^{13}C unless otherwise noted.[11] Heteronuclear NMR spectra were referenced to the appropriate external standard following the recommended scale based on ratios of absolute frequencies (Ξ). ^{19}F NMR spectra are reported relative to CCl_3F, and ^{31}P NMR spectra are reported relative to H_3PO_4.[12,13] Chemical shifts (δ) and coupling constants (*J*) are reported in ppm and Hz,

respectively. Simulations of NMR spectra were carried out using the Advanced Spin Simulation program in MestReNova (Mestrelab Research, chemistry software solutions).

3.4.2 Details of Digital Simulations within MestReNova Spin Simulation

General considerations for simulations.

All ^{1}H NMR digital simulations were performed within MestReNova software using the Spin Simulation function. In all cases, for all non-proton nuclei included within the spin system, a chemical shift outside of the range of the simulation was assigned. This was done so that the coupling interactions between these nuclei and the proton nuclei of interest could be simulated without also simulating a peak for a non-proton nucleus. Please refer to Figure 3.4 when the Spin Simulation Dialog Box is discussed.

Digital simulations of 1

To conduct a simulation of **1**, the number of spin groups was entered as 4. The two methylene protons were assigned arbitrarily as A and B, the two phosphorus nuclei were assigned as C, and the rhodium metal center was assigned as D. In the first table, the experimental chemical shift of A and B were entered, as well as the number of each nucleus present (N) and the spin of each nucleus (Spin); C and D were assigned outside-of-window chemical shifts, and the value for N and Spin were also included. Next, the experimental *J* values were entered in the second table. Assigning *J* values to the correct corresponding nuclei is critical for obtaining a simulated spectrum which resembles the experimental spectrum. Lastly, the Spectrum Properties dropdown allowed for insertion of the field frequency and the window of simulation. This frequency was adjusted for each multifrequency experimental spectrum obtained. For 1, the spectral data was simulated between 3.0-6.0 ppm, as only the methylene protons were of interest.

Digital simulations of 5

To conduct a simulation of **5**, the number of spin groups was entered as 6 (as now, the Cp* methyl protons and the hydride ligand were also included). The two methylene protons were assigned arbitrarily as A and B, the two phosphorus nuclei were assigned as C, the Cp* methyl protons were assigned as D, the hydride ligand was assigned as E, and the rhodium metal center was assigned as F. As in **1**, the chemical shift and values of N and Spin were entered for each nucleus. Experimental *J* values were entered; in this spin system, it was insightful to simulate a variety of different spectral data to understand the effects of coupling particularly between the Cp* methyl protons and the hydride ligand. For **5**, the spectral data was simulated between –11.0-6.0 ppm, as the methylene protons, Cp* methyl protons, and hydride ligand were of interest.

The hydride resonance is an apparent quartet (q_{app}) in the experimental data, which is noticeably broadened as compared to a normal quartet. This broadness led to the software commonly labeling this resonance as a multiplet, thus preventing us from consistently determining precise coupling constants for this peak. The coupling constant of 27.4 Hz assigned to this resonance in the simulation above was obtained from a separate set of experimental data and applied here. Likewise, the broadness indicates the likelihood that some unobserved coupling interactions are present between the hydride and other nuclei, but are undeterminable from this specific, broadened q_{app} resonance. The following simulations probed these interactions.

3.5 Acknowledgements

The authors thank Sarah Neuenswander for assistance with NMR spectroscopy. This work was supported by the US National Science Foundation through award OIA-1833087.

The authors also acknowledge the U.S. National Institutes of Health for support of the NMR instrumentation used in this study (Grants S10OD016360 and S10RR024664).

All experiments and characterization described in this chapter were performed by CGC. Digital simulations were performed by CGC with guidance from JTD.

3.6 References

[1] Mann, B. E., The Analysis of First-Order Coupling Patterns in NMR Spectra. *J. Chem. Ed.* **1995,** *72*, 614.

[2] Harris, R. K., *Nuclear Magnetic Resonance Spectroscopy: A Physicochemical View*, Pearson Education, 1987, pp. 26-27.

[3] Jacobsen, N. E., *NMR Data Interpretation Explained: Understanding 1D and 2D NMR Spectra of Organic Compounds and Natural Products*, John Wiley & Sons, 2017, p. 123.

[4] Jacobsen, N. E., *NMR Data Interpretation Explained: Understanding 1D and 2D NMR Spectra of Organic Compounds and Natural Products*, John Wiley & Sons, 2017, pp. 106-110.

[5] (a) Akitt, J. W.; Mann, B. E., *NMR and Chemistry: An Introduction to Modern NMR Spectroscopy*, CRC Press, 2000, 4th edn., p. 69. (b) Harris, R. K., *Nuclear Magnetic Resonance Spectroscopy: A Physicochemical View*, Pearson Education, 1986. p. 26.

[6] Stevenson, P. J., Second-order NMR spectra at high field of common organic functional groups. *Org. Biomol. Chem.* **2011,** *9*, 2078-2084.

[7] Willcott, M. R., MestRe Nova. *J. Am. Chem. Soc.* **2009,** *131*, 13180-13180.

[8] Bernstein, H. J.; Pople, J. A.; Schneider, W. G., Analysis of Nuclear Magnetic Resonance Spectra. I. Systems of Two and Three Nuclei. *Can. J. Chem.* **1957,** *35*, 65-81.

[9] Regarding the reasoning behind indicated Pople notation: Because of the complexity of the spin system in complexes **1** and **5**, the authors simply aim to use Pople notation as a guide to explain the nuclei involved. The A and B notations were chosen for the methylene protons because they are geminal, inequivalent nuclei. The Cp* methyl

protons were denoted as M to indicate distance between the methylene protons and the methyl protons in the spectrum, moving upfield. Y and Z denote phosphorus and rhodium, respectively, because these two nuclei are not present in the ^{1}H NMR spectrum. For **5**, the hydride ligand was denoted as X to indicate even further separation upfield from the Cp* methyl protons, inserted in front of phosphorus and rhodium symbols because it does appear in the spectrum.

[10] Redfield, C., "Proteins Studied by NMR" in *Encyclopedia of Spectroscopy and Spectrometry*, Lindon, J. C.; Tranter, G. E.; Koppenaal, D. W., Eds. Academic Press: Oxford, 2017; 3rd edn., pp 759-765.

[11] Fulmer, G. R.; Miller, A. J. M.; Sherden, N. H.; Gottlieb, H. E.; Nudelman, A.; Stoltz, B. M.; Bercaw, J. E.; Goldberg, K. I., NMR Chemical Shifts of Trace Impurities: Common Laboratory Solvents, Organics, and Gases in Deuterated Solvents Relevant to the Organometallic Chemist. *Organometallics* **2010,** *29*, 2176-2179.

[12] Harris, R. K.; Becker, E. D.; Cabral De Menezes, S. M.; Goodfellow, R.; Granger, P., NMR nomenclature: Nuclear spin properties and conventions for chemical shifts (IUPAC recommendations 2001). *Concepts Magn. Reson.* **2002,** *14*, 326-346.

[13] Harris, R. K.; Becker, E. D.; De fMenezes, S. M. C.; Granger, P.; Hoffman, R. E.; Zilm, K. W., Further Conventions for NMR Shielding and Chemical Shifts. *IUPAC Standards Online* **2016**, *80*, 59-84.

Part II

Chapter 4

On the Catalytic Activity of Heterobimetallic Group 9 Metal Complexes toward Hydrogenation of Aldehyde Compounds

This chapter is adapted from a published manuscript:

Kumar, A.; Comadoll, C. G.; King, D. S.; Oliver, A. G.; Day, V. W.; Blakemore, J. D., Incorporation of [Cp*Rh] and [Cp*Ir] Species into Heterobimetallic Complexes via Protonolysis Reactivity and Dioximato Chelation. *Inorg. Chem.* **2021**, *60*, 14047-14059.

4.1 Introduction

Bringing two different metal centers into close proximity attracts considerable interest across a number of research areas. This is in part due to the unique properties and cooperativity that can be engendered in such compounds in comparison to their monometallic analogues.[1,2] Bimetallic complexes incorporating redox-active centers are especially notable for their redox flexibility and, often, improved substrate-binding capabilities. Indeed, nature takes advantage of multimetallic systems in many metalloenzymes capable of small-molecule activation. The oxygen-evolving complex (OEC) of Photosystem II utilizes four Mn centers and a conserved redox-inactive Ca^{2+} ion to catalyze the oxidation of water to oxygen.[3] Other multimetallic active sites perform reduction reactions such as conversion of O_2 by [Cu,Fe] cytochrome *c* oxidase,[4] fixation of N_2 by Fe- and Mo-containing nitrogenase,[5] and reduction of protons to dihydrogen by [Ni,Fe] hydrogenase.[6] Inspired by these systems, many researchers have endeavored to design artificial metal complexes that engender synergistic involvement of multiple metals.[7] One especially vigorous area of investigation centers on use of secondary redox-inactive metals to tune the chemical properties of primary redox-active metal centers,[8,9,10] an approach of particular interest to us considering its versatility.[11,12,13] However, a unifying theme of all this work is the bringing together of two metals selectively, enabling studies of their individual roles in observed reactivity.

Tetraazamacrocyclic complexes containing the earth-abundant metals nickel and cobalt are perhaps best known as catalysts for electrochemical hydrogen generation.[14,15] A subset of these complexes can be derivatized by placement of a cationic [BF_2] bridging moiety in place of a bridging proton (H^+).[16,17,18] Such reactivity is conceptually related to the

early work of Busch and co-workers regarding glyoxime-type ligands and their macrocyclic metal complexes.[19] However, metal complexes supported by proton-bridged macrocyclic diimine-monooxime-monooximato-type ligand frameworks have also been attractive as synthons for construction of bimetallic complexes. Chaudhuri, Wieghardt, and co-workers were perhaps the first to realize potential in this space, and showed that a variety of first-row transition metals (Cr, Mn, Fe, Co, Ni, Cu) could be installed divergently in the dioximato site (see Chart 4.1).[20] Peters & co-workers leveraged the binucleating nature of these ligands to install Mg and Zn in close proximity to Co and Ni metal centers.[21] And, more recently, Cossairt and co-workers extended this approach further to incorporation of 4*d* metals, isolating [Co,Ru] and [Co,Cd] complexes.[22] A general feature uniting all this work is the net removal of a proton from the dioximato site and installation of a cationic metal fragment in its place.

Half-sandwich Group 9 metal complexes supported by Cp* ligands (where Cp* is η^5-pentamethylcyclopentadienyl) represent a useful and synthetically versatile class of organometallic species.[23] Structures containing [Cp*M] fragments tend to be quite stable, due to the steric bulk and strong donor properties of Cp*,[24] but can also serve as catalysts for a variety of transformations.[25] In our own work in the Blakemore Group, we have relied on the synthetic versatility of [Cp*Rh] complexes for preparation of new metal complexes useful for studies of proton management during catalysis; in Chapters 2 and 3 of this dissertation, work on this topic was described wherein the useful [Cp*Rh] framework was used to support two different hydride complexes. The general robustness of the Cp*Rh core enabled synthesis of these hydrides with different diphosphine ligands.[26] Others have also

Chart 4.1. Heterobimetallic complexes based upon diimine-dioximato ligands.

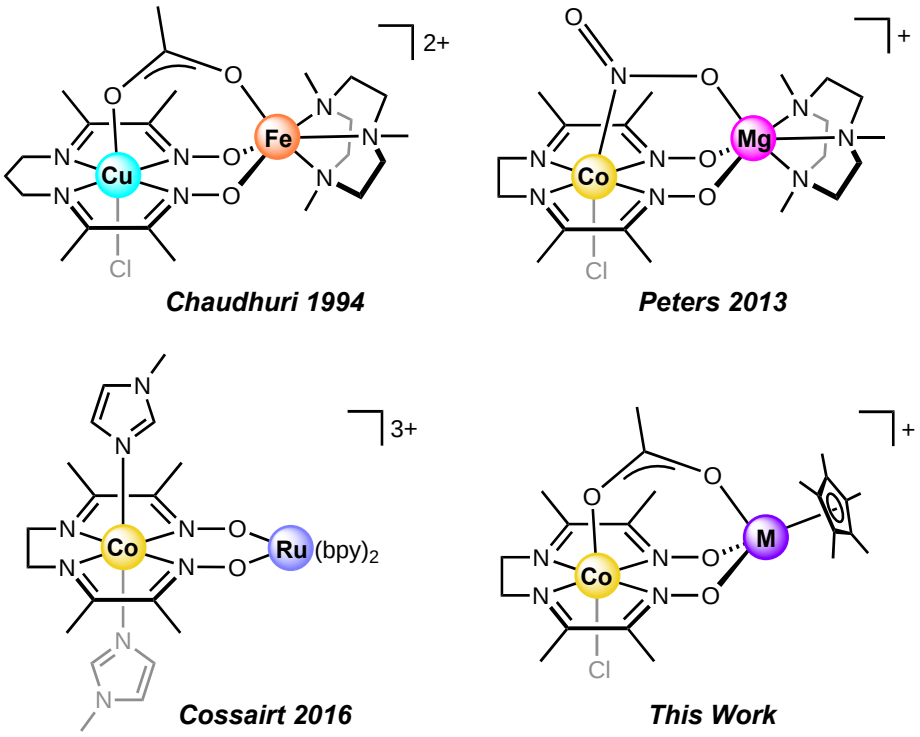

leveraged this versatility to prepare attractive new types of heterobimetallic complexes and catalysts.[27,28,29] We examined the literature and were surprised to find no prior synthetic work aimed at incorporating organometallic fragments like the [Cp*Rh] or [Cp*Ir] cores into metal complexes bearing dioximato sites, nor were there any studies of the catalytic properties of such species. In preliminary work, new heterobimetallic compounds containing organometallic [Cp*M] sites had been prepared, but no catalytic data were available regarding their properties. General procedures had been developed for synthesis of heterobimetallic complexes based upon diimine-dioximato ligands that incorporate half-sandwich [Cp*M] fragments (where M is Rh or Ir) (see Scheme 4.1), but the properties of the resulting species were unknown.

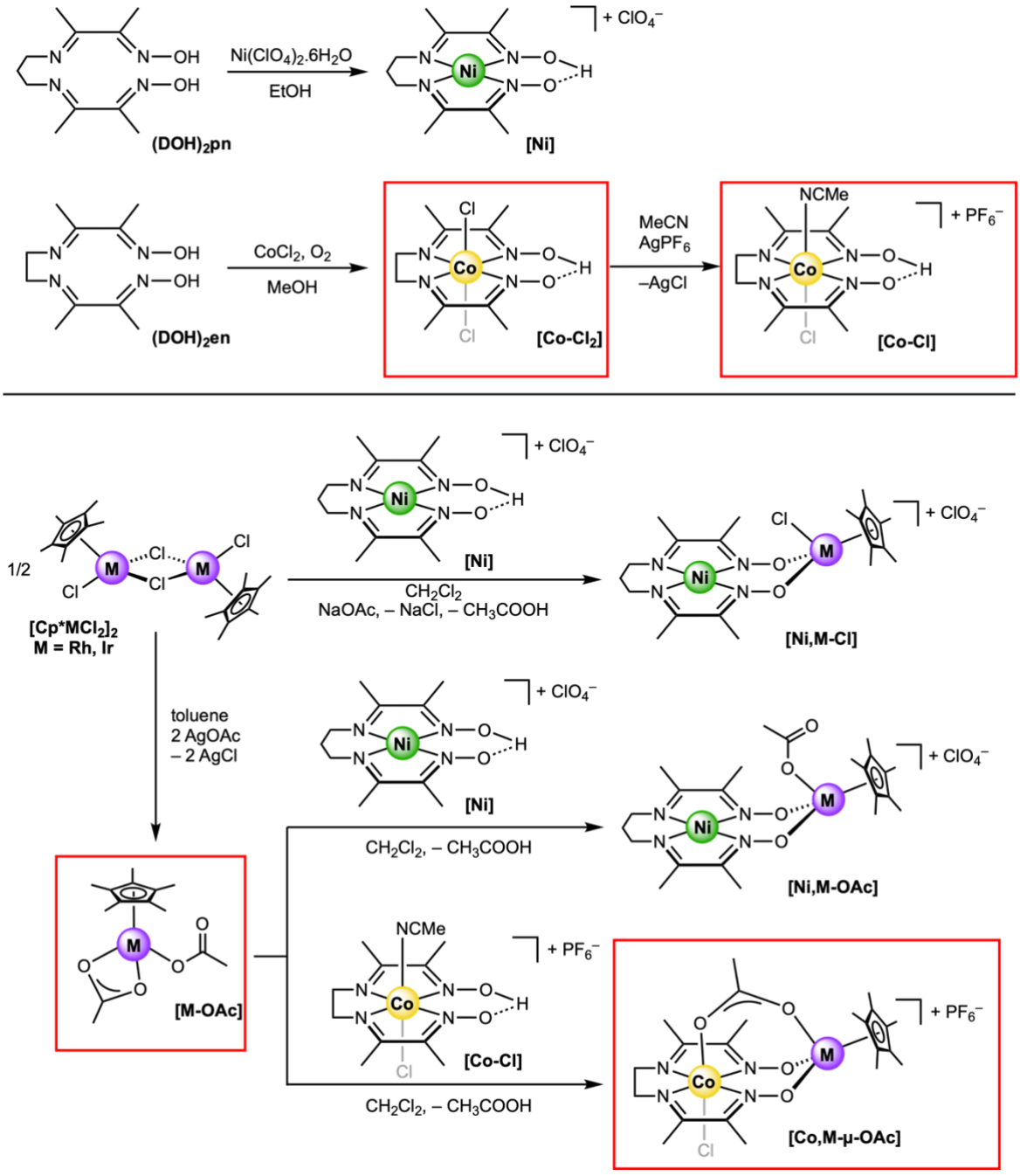

Scheme 4.1. Scheme of the reactivity study designed to focus on key compounds representing the major classes of metal complexes in the overall effort to develop the new heterobimetallic complexes. The complexes tested in catalysis are boxed.

For that reason, we endeavored to prepare heterobimetallic complexes uniting first row 3*d* metals with the [Cp*Rh] and [Cp*Ir] moieties. Using these protonolysis-driven procedures, we prepared and fully characterized six new heterobimetallic complexes containing [Cp*Rh] or [Cp*Ir] fragments contained within diimine-dioximato chelating frameworks. In these systems, the tetraazamacrocyclic core functions as a heteroditopic ligand, hosting either Ni(II) or Co(III) in its central tetradentate site and either Rh(III) or Ir(III) in its peripheral bidentate site. Our report[30] of these complexes contained the first examples of structurally characterized oximato-bridged heterobimetallics containing [Cp*Rh] and [Cp*Ir] moieties paired with 3*d* metals.[31]

Inspired by the potential catalytic applications of these heterobimetallic complexes, we endeavored to test some of the novel complexes in a catalytic hydrogenation experiment of 4-(trifluoromethyl)benzaldehyde. These experiments were carried out on NMR-scale and the results were monitored by ^{1}H and ^{19}F NMR spectroscopy; the CHD_2CN solvent residual was used as an internal standard, allowing for direct quantification of both the starting benzaldehyde derivative and the corresponding benzyl alcohol product.

4.2 Results and Discussion

4.2.1 Probing the Catalytic Activity of Metal Complexes in Hydrogenation

Many laboratories today are focused on the development of heterobimetallic complexes for use in transformations of small molecules; these transformations can be achieved either stoichiometrically or catalytically. In our attempts to probe the catalytic hydrogenation properties of these complexes, the structures of which can be seen in Chart 4.2, we sought a model substrate which could be modeled reliably through multiple methods

Chart 4.2. Complexes tested in the catalytic hydrogenation experiments.

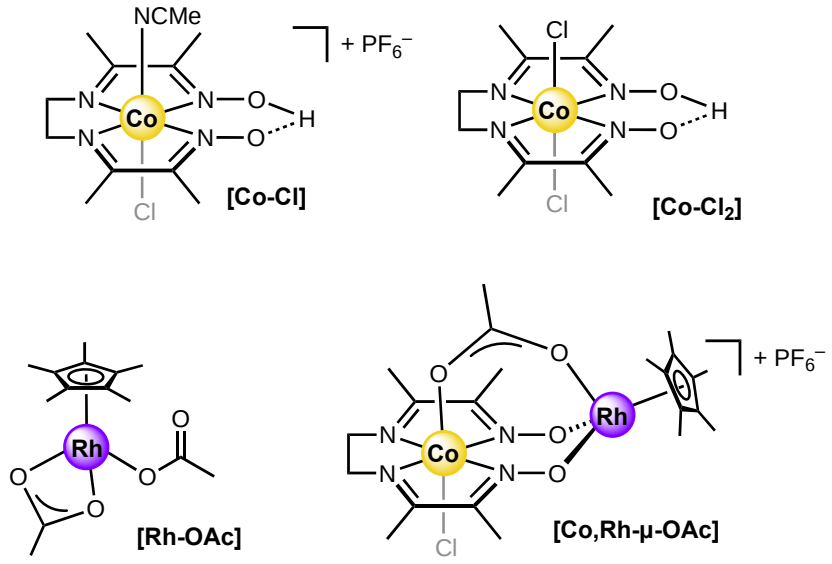

of NMR analysis. We chose the substrate 4-(trifluoromethyl)benzaldehyde (**A**, Scheme 4.2) for these studies, as this substrate and its hydrogenated product (**B**, 4-(trifluoromethyl)benzyl alcohol; Scheme 4.2) would be observable through both ^{1}H and ^{19}F NMR. The heterobimetallic complex we chose to investigate primarily was the Co,Rh complex **Co,Rh-μ-OAc**, due to the propensity of complexes of Rh to act as catalysts in both hydrogenation and hydrogen evolution reactions;[32] based on the observed cooperativity between metals in heterobimetallic complexes in catalysis, we anticipated the possibility that a cobalt proximal to rhodium might improve its catalytic activity. We also investigated the hydrogenation using a 1:1 mixture of **Co-Cl** and **Rh-OAc**; a comparison of the results of the heterobimetallic complex and the two monometallic complexes provided insight into the

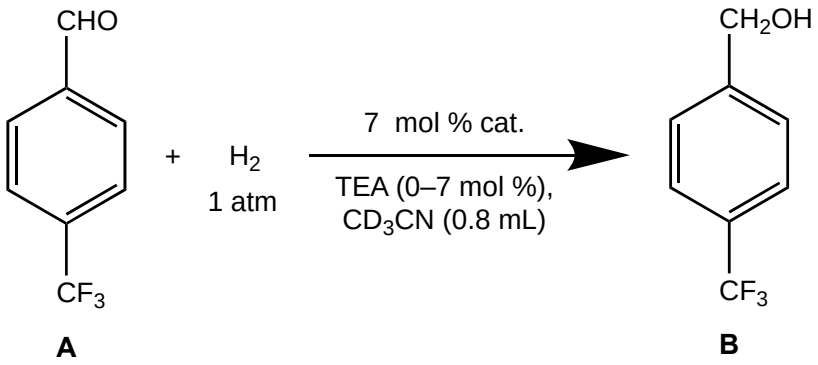

Scheme 4.2. Conditions of catalytic hydrogenation experiments using 4-(trifluoromethyl)benzaldehyde.

effect of cooperativity between the Co and Rh metal centers of **Co,Rh-μ-OAc** versus the effectiveness of the free metals in monometallic complexes in the hydrogenation. As a control, we also tested the monometallic complexes **Co-Cl**, **Co-Cl$_2$**, and **Rh-OAc** individually in the hydrogenation chemistry. Additionally, triethylamine (TEA) was tested as a catalytic additive in some instances. Each reaction was analyzed via NMR periodically until the conversion of **A** to **B** leveled off, at which point the reaction was halted. Figure 4.1 shows an example of the ^{1}H NMR data used to determine relative integrations of **A** and **B**. Upon first analyzing the data, we realized that the conversion could be determined from the ^{1}H NMR data alone through use of the CHD_2CN solvent residual as an internal standard (*vide infra*); therefore, the ^{19}F data were not used in the quantitative analysis of the experimental results.

The tabulated results of catalyst performance in the hydrogenation reactions are show in Table 4.1. Notably, a control reaction was run in which no metal complex was included;

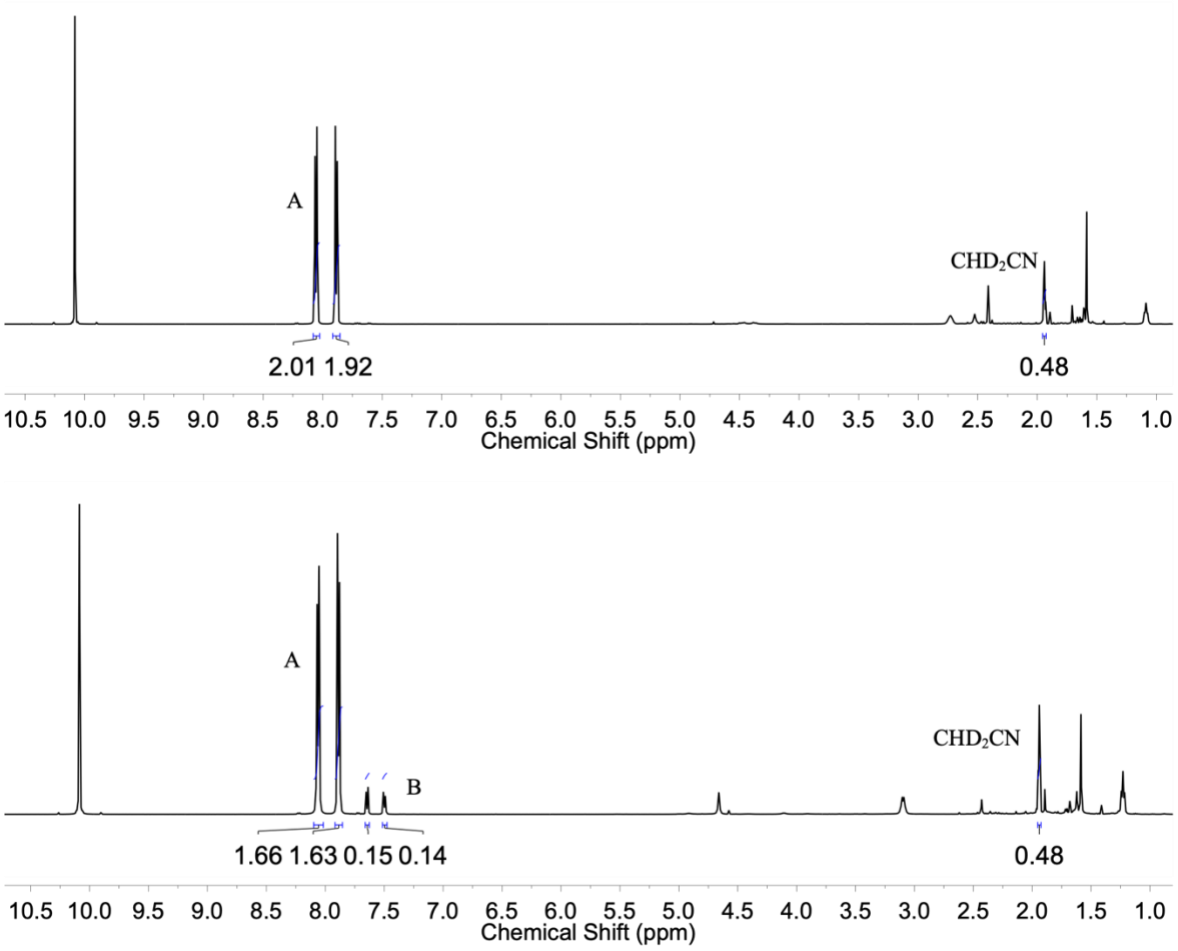

Figure 4.1. Stacked ^{1}H NMR spectra (500 MHz, CD_3CN) showing one example of using the solvent residual as an internal standard. Top: Integration of solvent residual determined from amount of **A** precursor added to the tube. Bottom: Upon hydrogenation, the solvent residual was integrated and set to the predetermined integration to determine the amount of **A** and **B** present at each time point.

no conversion of **A** to **B** was observed in this reaction. In entries 1–4, the results of hydrogenation with **Co,Rh-μ-OAc** are presented with varying temperature and loading of TEA. The conversion to **B** in each entry is modest, at best, indicating a low propensity of

Table 4.1. Summary of catalyst performance in hydrogenation.

Entry	Catalyst	TEA Loading	Temperature	Time (h)	Conversion (mmol B, %)	TON (#)
1	**Co,Rh-μ-OAc**	0 mol %	RT	29	0.0122 (6.5 %)	< 1 (0.93)
2	**Co,Rh-μ-OAc**	0 mol %	50 °C	29	0.0187 (9.9 %)	1.42
3	**Co,Rh-μ-OAc**	7 mol %	RT	26	0.0149 (7.9 %)	1.14
4	**Co,Rh-μ-OAc**	7 mol %	50 °C	26	0.0183 (9.7 %)	1.39
5	**Co-Cl_2**	7 mol %	50 °C	6.5	0.0124 (6.6 %)	< 1 (0.95)
6	**Rh-OAc**	7 mol %	50 °C	6.5	0.0276 (14.7 %)	2.10
7	**Rh-OAc + Co-Cl**	7 mol %	50 °C	6.5	0.0096 (5.1 %)	< 1 (0.73)
8	**Co-Cl**	7 mol %	50 °C	20	0 (0 %)	0

Co,Rh-μ-OAc to behave as a catalyst in the given transformation. However, there are noticeable trends that can be extracted from the data. A comparison of entries 1 and 2 demonstrate the effect of temperature, such that the conversion of **A** to **B** is increased from 6.5 % to 9.9 % when the temperature is increased. Comparing entries 1 and 3 shows the effect of the TEA additive; inclusion of 7 mol % of TEA in the reaction at room temperature increases the conversion of **B** from 6.5 % to 7.9 %. Notably, the effect of TEA at 50 °C was negligible (entries 2 and 4). The turnover number (TON) of each of these experiments, regardless of the reaction conditions, lies between 1–1.42, indicating stoichiometric propensity for hydrogenation, but little to no propensity to act as a catalyst in hydrogenation of the given aldehyde substrate.

In comparison, the results of the monometallic complexes in the hydrogenation show modest conversion of **A** to **B** as well (entries 5–8). Complex **Co-Cl_2** at 50 °C performed

similarly to **Co,Rh-μ-OAc** in entry 1, with a TON less than 1 (entry 5). Surprisingly, the monometallic rhodium complex **Rh-OAc** gave a 14.7 % conversion of **B** for a TON of 2.10 (entry 6). While we were disappointed to see that the monometallic complex outperformed **Co,Rh-μ-OAc** in the hydrogenation, the result is understandable, as rhodium complexes are well-known catalysts in hydrogenation reactions. Notably, a comparison of entries 4 and 7 indicates that the heterobimetallic complex **Co,Rh-μ-OAc** outperformed the two individual monometallic complexes **Rh-OAc** and **Co-Cl** reacted together; while the reactivity in both instances is modest at best, the cooperativity of both metals in the heterobimetallic complex **Co,Rh-μ-OAc** is evidenced when compared to entry 7. Finally, entry 8 shows that **Co-Cl** alone does not perform in the hydrogenation, as **B** was not detected via NMR after 20 hours.

4.2.2 Quantitative, Time-Dependent Reactivity Profiles for Hydrogenation

In each reaction, the ^{1}H NMR data were analyzed using the CHD_2CN solvent residual as an internal standard for the quantification of **A** and **B**. The integrations of both **A** and **B** were plotted versus time for each reaction; at the point when the conversion of both **A** and **B** began to level off, the reaction was stopped. The data were fit exponentially considering the first-order nature of the reaction with respect to the substrate in the rate-determining step (RDS) and monitored over time. These reactivity profiles can be seen below in Figures 4.2–4.8.

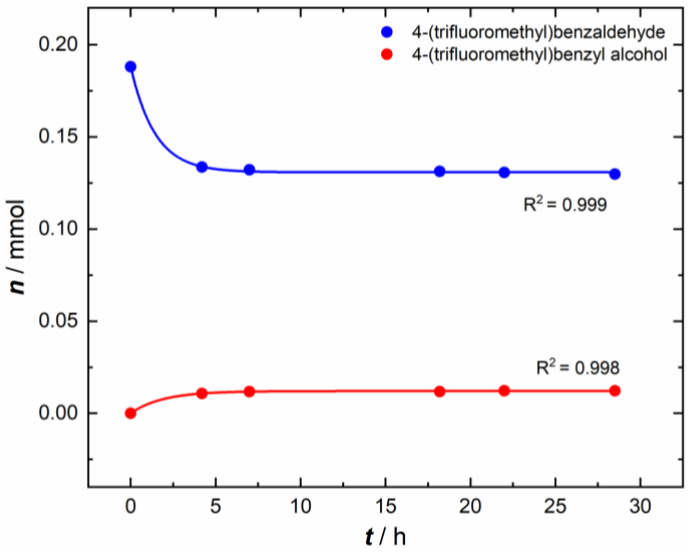

Figure 4.2. Results from Table 4.1, entry 1 plotted as amount (mmol) of **A** and **B** (blue and red, respectively) vs. time (h). Catalyst = **Co,Rh-μ-OAc**, TEA loading = 0 mol %, T = room temperature.

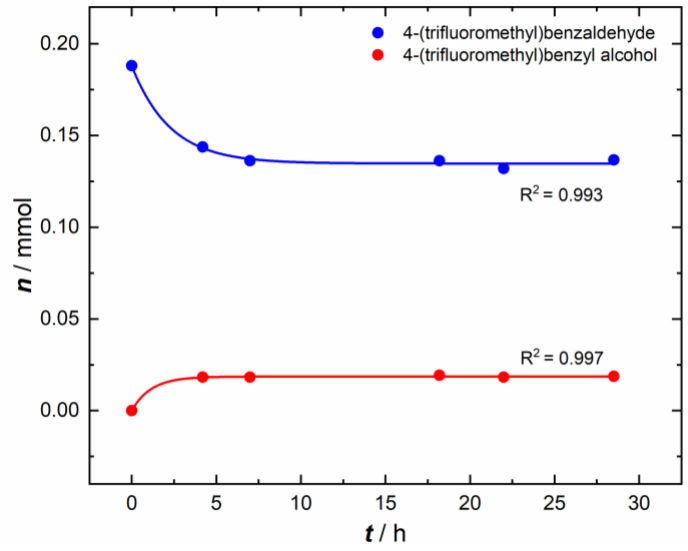

Figure 4.3. Results from Table 4.1, entry 2 plotted as amount (mmol) of **A** and **B** (blue and red, respectively) vs. time (h). Catalyst = **Co,Rh-μ-OAc**, TEA loading = 0 mol %, T = 50 °C.

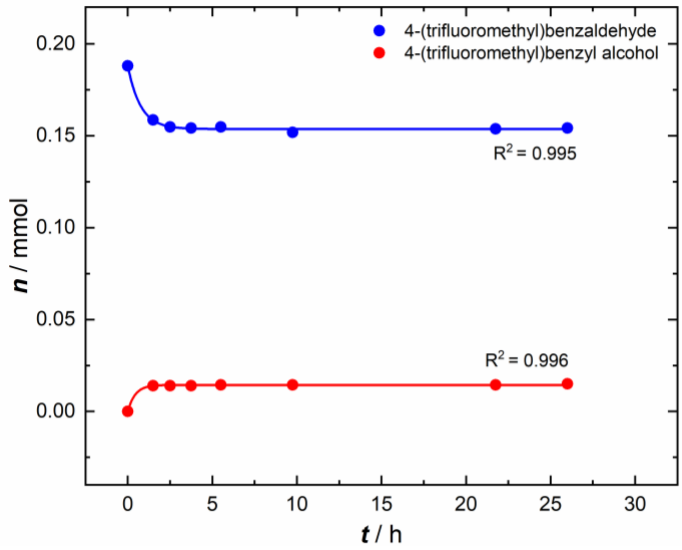

Figure 4.4. Results from Table 4.1, entry 3 plotted as amount (mmol) of **A** and **B** (blue and red, respectively) vs. time (h). Catalyst = **Co,Rh-μ-OAc**, TEA loading = 7 mol %, T = room temperature.

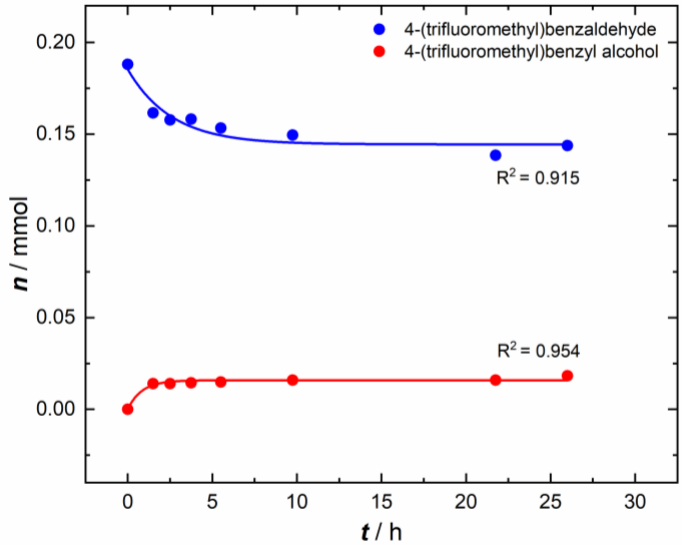

Figure 4.5. Results from Table 4.1, entry 4 plotted as amount (mmol) of **A** and **B** (blue and red, respectively) vs. time (h). Catalyst = **Co,Rh-μ-OAc**, TEA loading = 7 mol %, T = 50 °C.

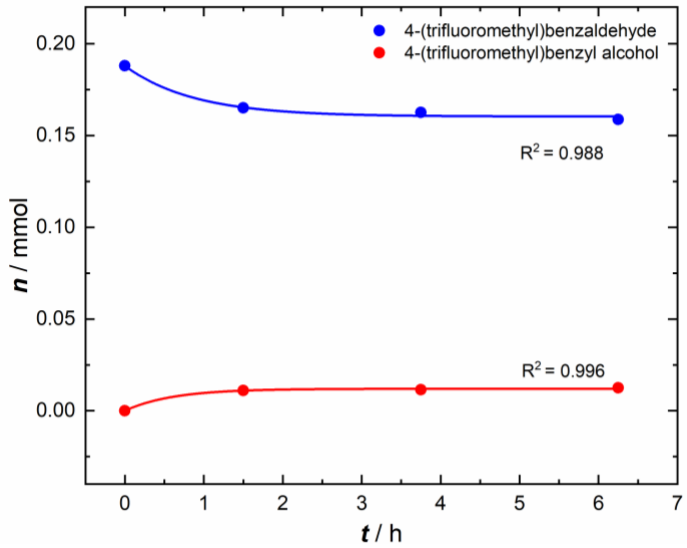

Figure 4.6. Results from Table 4.1, entry 5 plotted as amount (mmol) of **A** and **B** (blue and red, respectively) vs. time (h). Catalyst = **$CoCl_2$**, TEA loading = 7 mol %, T = 50 °C.

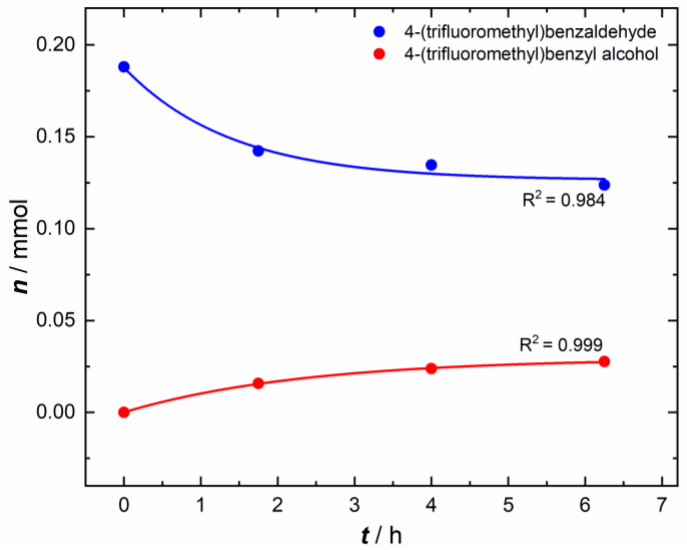

Figure 4.7. Results from Table 4.1, entry 6 plotted as amount (mmol) of **A** and **B** (blue and red, respectively) vs. time (h). Catalyst = **RhOAc**, TEA loading = 7 mol %, T = 50 °C.

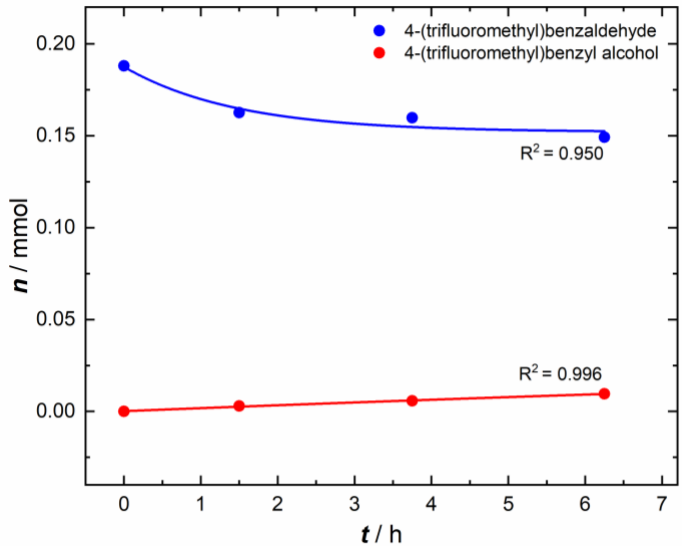

Figure 4.8. Results from Table 4.1, entry 7 plotted as amount (mmol) of **A** and **B** (blue and red, respectively) vs. time (h). Catalyst = 7 mol % **RhOAc** + 7 mol % **CoCl**, TEA loading = 7 mol %, T = 50 °C.

This first-order RDS is likely to involve a metal hydride form of the catalyst, which could transfer a hydride to the carbonyl. Indeed, stability tests of **Co,Rh-μ-OAc** performed in the presence of both H_2 and H_2/NEt_3 *in situ* were monitored by ^1H NMR. In each case, both spectra contain multiple signals in the upfield region, indicating the formation of various metal hydrides upon addition of H_2 (see Figure 4.9). The formation of these species indicates that a metal hydride species is likely involved as an active catalyst in the mechanism of hydrogenation studied here; however, the formation of *multiple* of these species may explain the limited success upon employment as a catalyst, as the formation of multiple hydrides (Co–H, Rh–H, or both) could pull the catalyst off-cycle in a deleterious fashion.

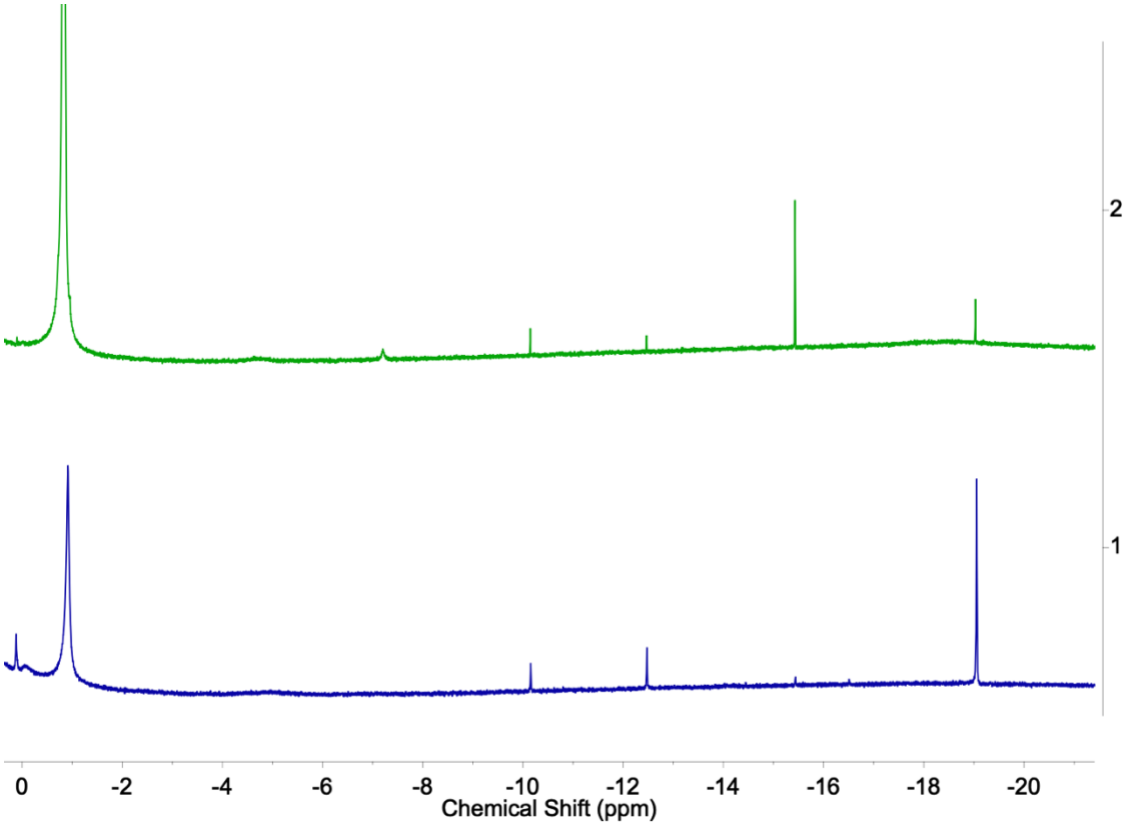

Figure 4.9. Zoomed-in stacked ^{1}H NMR spectra (500 MHz, CD_3CN) for testing the thermal stability of **Co,Rh-μ-OAc** at 60 °C in the presence of NEt_3 and/or H_2. The zoomed in spectra of the metal complex including H_2 (top) and H_2 + NEt_3 (bottom) show the presence of multiple metal hydride species which are not present in the original, isolated **Co,Rh-μ-OAc**. These spectra confirm reaction of **Co,Rh-μ-OAc** with H_2 with or without exogeneous base.

4.3 Conclusion

In prior work, several series of heterobimetallic complexes of cobalt, nickel, rhodium, and iridium were prepared through two newly developed methods. Because of the successful application of heterobimetallic complexes in catalytic transformations of small organic molecules in literature systems, the Co,Rh complex **Co,Rh-μ-OAc** was tested as a catalyst in the hydrogenation of 4-(trifluoromethyl)benzaldehyde and monitored over time

via ^{1}H NMR. Additionally, a selection of monometallic cobalt and rhodium complexes were also tested. Across the full series of complexes investigated in this study, the catalytic activity was modest at best, giving TONs between 0.73–2.10 for the complexes which demonstrated any catalytic activity at all. Notably, the complexes could potentially be employed as stoichiometric hydrogenating agents in the given transformation; however, the complexes should not be considered as hydrogenation catalysts.

4.4 Experimental Details

4.4.1 General Considerations

All manipulations were carried out in dry N_2-filled gloveboxes (Vacuum Atmospheres Co., Hawthorne, CA, USA) or under an N_2 atmosphere using standard Schlenk techniques, unless otherwise noted. All solvents were of commercial grade and dried over activated alumina using a PPT Glass Contour (Nashua, NH, USA) solvent purification system prior to use, and were stored over molecular sieves. All chemicals were obtained from major commercial suppliers and used as received after extensive drying.

Ligands $(DOH)_2$en and $(DOH)_2$pn were prepared according to literature procedures.[33] $[Cp^*RhCl_2]_2$ was synthesized according to the modified procedure reported by Sanford & co-workers, but the original procedure by Maitlis & co-workers was used in the synthesis of $[Cp^*IrCl_2]_2$.[34] **M-OAc** complexes were synthesized using methods described by Merola.[35] **Ni** complex was prepared using a literature procedure described by Uhlig and Friedrich.[33a] Deuterated NMR solvents were purchased from Cambridge Isotope Laboratories (Tewksbury, MA, USA). ^{1}H and ^{19}F NMR spectra were collected on a 500 MHz Bruker spectrometer (Bruker, Billerica, MA, USA) and referenced to the residual protio-solvent signal[36] in the case of ^{1}H. ^{19}F NMR spectra were referenced and reported

relative to CCl_3F as an external standard following the recommended scale based on ratios of absolute frequencies (Ξ).[37,38] All experiments were conducted at room temperature (298 K).

4.4.2 Catalytic Hydrogenation Procedure

In a typical catalytic run, in an inert atmosphere glovebox a J. Young NMR Tube was charged with 4-(trifluoromethyl)benzaldehyde, **A** (0.188 mmol, 26 μL), the metal complex being studied as a hydrogenation catalyst (7 mol %), and 0.8 mL CD_3CN. In select cases, TEA (7 mol %, 1.8 μL) was subsequently added to the tube as a base. We tested TEA as an additive in case it might act as a catalytic base to assist in catalysis. The sealed tube was then transferred to a Schlenk line and degassed using three freeze-pump-thaw cycles. After degassing, the tube was sparged with 1 atmosphere of H_2 gas for a few seconds, and the resultant mixture was kept at either room temperature or 50 °C and monitored periodically for up to 29 h for the formation of hydrogenated product, **B**, by ^1H and $^{19}F\{^1H\}$ NMR.

Note: The CHD_2CN solvent residual in the ^1H NMR spectrum was used as an internal standard in each experiment. Because the amount of CD_3CN added to each tube was constant and the amount added to each tube was unchanged through the course of each reaction, the integration of this residual was monitored relative to the known amount of **A** at the start of the experiment before hydrogenation began. In this way, the integration of the solvent residual at each time point to the initially determined integration allowed for the determination of the amount (mmol) of **A** (known) and **B** (unknown) in each sample (see Figures for raw data on the following pages). From the total library of collected data, the percent conversion and turnover number (TON) were determined for each metal complex (or complexes) under each set of conditions for comprehensive comparison.

4.5 Acknowledgements

The authors thank Dr. Justin Douglas and Sarah Neuenswander for assistance with NMR spectroscopy and Prof. Davide Lionetti for assistance with the preliminary refinement of solid-state XRD data. This work was supported by the US National Science Foundation through award OIA-1833087. Preliminary synthetic work was supported by the US National Science Foundation through the NSF REU Program in Chemistry at the University of Kansas (CHE-1560279). The authors also acknowledge the US National Institutes of Health for support of the NMR instrumentation used in this study (S10OD016360 and S10RR024664).

The studies of hydrogenation catalysis described in this chapter were conducted by CGC, and the data resulting from those studies was analyzed by CGC with assistance from AK. The metal complexes tested as catalysts were synthesized by AK and DSK in the context of the broader study.

4.6 References

[1] Cooper, B. G.; Napoline, J. W.; Thomas, C. M., Catalytic Applications of Early/Late Heterobimetallic Complexes. *Catal. Rev.* **2012,** *54*, 1-40.

[2] Buchwalter, P.; Rosé, J.; Braunstein, P., Multimetallic catalysis based on heterometallic complexes and clusters. *Chem. Rev.* **2015**, *115*, 28-126.

[3] (a) McEvoy, J. P.; G. W. Brudvig, G. W., Water-splitting chemistry of photosystem II. *Chem. Rev.* **2006**, *106*, 4455–4483. (b) Yano, J.; Yachandra, V. Mn_4Ca Cluster in Photosynthesis: Where and How Water is Oxidized to Dioxygen. *Chem. Rev.* **2014**, *114*, 4175-4205.

[4] Tsukihara, T.; Shimokata, K.; Katayama, Y.; Shimada, H.; Muramoto, K.; Aoyoma, H.; Mochizuki, M.; Shinzawa-Itoh, K.; Yamashita, E.; Yao, M.; Ishimura, Y.; Yoshikawa, S., The low-spin heme of cytochrome *c* oxidase as the driving element of the proton-pumping process. *Proc. Natl. Acad. Sci. USA* **2003**, *100*, 15304-15309.

[5] Spatzal, T.; Aksoyoglu, M.; Zhang, L. M.; Andrade, S. L. A.; Schleicher, E.; Weber, S.; Rees, D. C.; Einsle, O., Evidence for interstitial carbon in nitrogenase FeMo cofactor. *Science* **2011**, *334*, 940.

[6] (a) Volbeda, A.; Martin, L.; Cavazza, C.; Matho, M.; Faber, B. W.; Roseboom, W.; Albracht, S. P. J.; Garcin, E.; Rousset, M.; Fontecilla-Camps, J. C., Structural differences between the ready and unready oxidized states of [NiFe] hydrogenases. *J. Biol. Inorg. Chem.* **2005**, *10*, 239-249. (b) Bachmeier, A.; Armstrong, F. Solar-driven proton and carbon dioxide reduction to fuels - lessons from metalloenzymes. *Curr. Op. Chem. Biol.* **2015,** *25*, 141-151.

[7] Appel, A. M.; Bercaw, J. E.; Bocarsly, A. B.; Dobbek, H.; DuBois, D. L.; Dupuis, M.; Ferry, J. G.; Fujita, E.; Hille, R.; Kenis, P. J. A.; Kerfeld, C. A.; Morris, R. H.; Peden, C. H. F.; Portis, A. R.; Ragsdale, S. W.; Rauchfuss, T. B.; Reek, J. N. H.; Seefeldt, L. C.; Thauer, R. K.; Waldrop, G. L., Frontiers, opportunities, and challenges in biochemical and chemical catalysis of CO_2 fixation. *Chem. Rev.* 2013, *113*, 6621-6658.

[8] Tsui, E. Y.; Tran, R.; Yano, J.; Agapie, T., Redox-inactive metals modulate the reduction potential in heterometallic manganese-oxido clusters. *Nat. Chem.* **2013**, *5*, 293-299.

[9] Lee, Y.-M.; Bang, S.; Kim, Y. M.; Cho, J.; Hong, S.; Nomura, T.; Ogura, T.; Troeppner, O.; Ivanović-Burmazović, I.; Sarangi, R.; Fukuzumi, S.; Nam, W., A mononuclear nonheme iron(III)–peroxo complex binding redox-inactive metal ions. *Chem. Sci.* **2013**, *4*, 3917-3923.

[10] Li, F.; Van Heuvelen, K. M.; Meier, K. K.; Münck, E.; Que, L., Sc^{3+}-Triggered Oxoiron(IV) Formation from O_2 and its Non-Heme Iron(II) Precursor via a Sc^{3+}–Peroxo–Fe^{3+} Intermediate. *J. Am. Chem. Soc.* **2013**, *135*, 10198-10201.

[11] Kumar, A.; Lionetti, D.; Day, V. W.; Blakemore, J. D., Trivalent Lewis Acidic Cations Govern the Electronic Properties and Stability of Heterobimetallic Complexes of Nickel. *Chem. Eur. J.* **2018,** *24*, 141-149.

[12] Kumar, A.; Lionetti, D.; Day, V. W.; Blakemore, J. D., Redox-Inactive Metal Cations Modulate the Reduction Potential of the Uranyl Ion in Macrocyclic Complexes. *J. Am. Chem. Soc.* **2020,** *142*, 3032-3041.

[13] Kelsey, S.; Kumar, A.; Oliver, A. G.; Day, V. W.; Blakemore, J. D., Promotion and Tuning of the Electrochemical Reduction of Hetero- and Homobimetallic Zinc Complexes. *ChemElectroChem* **2021**, *8*, 2792-2802.

[14] Jacques, P.-A.; Artero, V.; Pécaut, J.; Fontecave, M., Cobalt and nickel diimine-dioxime complexes as molecular electrocatalysts for hydrogen evolution with low overvoltages. *Proc. Natl. Acad. Sci. U.S.A* **2009,** *106*, 20627-20632.

[15] McCrory, C. C.; Uyeda, C.; Peters, J. C., Electrocatalytic hydrogen evolution in acidic water with molecular cobalt tetraazamacrocycles. *J. Am. Chem. Soc.* **2012,** *134*, 3164-3170.

[16] (a) Schrauzer, G. N., Organocobalt chemistry of vitamin B12 model compounds (cobaloximes). *Acc. Chem. Res.* **1968,** *1*, 97-103 (b) Connolly, P.; Espenson, J. H., Cobalt-catalyzed evolution of molecular hydrogen. *Inorg. Chem.* **1986,** *25*, 2684-2688 (c) Dempsey, J. L.; Winkler, J. R.; Gray, H. B., Mechanism of H_2 Evolution from a Photogenerated Hydridocobaloxime. *J. Am. Chem. Soc.* **2010,** *132*, 16774-16776.

[17] Laga, S. M.; Blakemore, J. D.; Henling, L. M.; Brunschwig, B. S.; Gray, H. B., Catalysis of Proton Reduction by a [BO_4]-Bridged Dicobalt Glyoxime. *Inorg. Chem.* **2014,** *53*, 12668-12670.

[18] Cartwright, K. C.; Joseph, E.; Comadoll, C. G.; Tunge, J. A., Photoredox/Cobalt Dual-Catalyzed Decarboxylative Elimination of Carboxylic Acids: Development and Mechanistic Insight. *Chem. Eur. J.* **2020,** 26, 12454-12471.

[19] Lance, K. A.; Goldsby, K. A.; Busch, D. H., Effective new cobalt(II) dioxygen carriers derived from dimethylglyoxime by the replacement of the linking protons with difluoroboron(1+). *Inorg. Chem.* **1990,** *29*, 4537-4544.

[20] Birkelbach, F.; Winter, M.; Floerke, U.; Haupt, H.-J.; Butzlaff, C.; Lengen, M.; Bill, E.; Trautwein, A. X.; Wieghardt, K.; Chaudhuri, P., Exchange Coupling in Homo-and Heterodinuclear Complexes CuIIM [M= Cr (III), Mn (III), Mn (II), Fe (III), Co (III), Co (II), Ni (II), Cu (II), Zn (II)]. Synthesis, Structures, and Spectroscopic Properties. *Inorganic Chemistry* **1994,** *33*, 3990-4001.

[21] (a) Uyeda, C.; Peters, J. C., Access to formally Ni (I) states in a heterobimetallic NiZn system. *Chem. Sci.* **2013,** *4*, 157-163. (b) Uyeda, C.; Peters, J. C., Selective nitrite reduction at heterobimetallic CoMg complexes. *J. Am. Chem. Soc.* **2013,** *135*, 12023-12031.

[22] Henckel, D. A.; Lin, Y. F.; McCormick, T. M.; Kaminsky, W.; Cossairt, B. M., A doubly deprotonated diimine dioximate metalloligand as a synthon for multimetallic complex assembly. *Dalton Trans.* **2016,** *45*, 10068-10075.

[23] Maitlis, P. M., (Pentamethylcyclopentadienyl)rhodium and -iridium complexes: approaches to new types of homogeneous catalysts. *Acc. Chem. Res.* **1978,** *11*, 301-307.

[24] (a) Brintzinger, H.; Bercaw, J. E., Bis(pentamethylcyclopentadienyl)titanium(II). Isolation and reactions with hydrogen, nitrogen, and carbon monoxide. *J. Am. Chem. Soc.* **1971,** *93*, 2045-2046. (b) Manriquez, J. M.; Bercaw, J. E., Preparation of a dinitrogen complex of bis(pentamethylcyclopentadienyl)zirconium(II). Isolation and protonation leading to

stoichiometric reduction of dinitrogen to hydrazine. *J. Am. Chem. Soc.* **1974**, *96*, 6229-6230.

[25] (a) Kölle, U.; Grätzel, M., Organometallic Rhodium(III) Complexes as Catalysts for the Photoreduction of Protons to Hydrogen on Colloidal TiO_2. *Angew. Chem. Int. Ed. Engl.* **1987,** *26*, 567-570. (b) Blakemore, J. D.; Schley, N. D.; Balcells, D.; Hull, J. F.; Olack, G. W.; Incarvito, C. D.; Eisenstein, O.; Brudvig, G. W.; Crabtree, R. H., Half-Sandwich Iridium Complexes for Homogeneous Water-Oxidation Catalysis. *J. Am. Chem. Soc.* **2010,** *132*, 16017-16029.

[26] (a) Boyd, E. A.; Lionetti, D.; Henke, W. C.; Day, V. W.; Blakemore, J. D., Preparation, Characterization, and Electrochemical Activation of a Model [Cp*Rh] Hydride. *Inorg. Chem.* **2019**, *58*, 3606-3615. (b) Hopkins, J. A.; Lionetti, D.; Day, V. W.; Blakemore, J. D., Chemical and Electrochemical Properties of [Cp*Rh] Complexes Supported by a Hybrid Phosphine-Imine Ligand. *Organometallics* **2019,** *38*, 1300-1310. (c) Hopkins, J. A.; Lionetti, D.; Day, V. W.; Blakemore, J. D., Synthesis and reactivity studies of a [Cp*Rh] complex supported by a methylene-bridged hybrid phosphine-imine ligand. *J. Organomet. Chem.* **2020**, *921*, 121294. (d) Comadoll, C. G.; Henke, W. C.; Hopkins Leseberg, J. A.; Douglas, J. T.; Oliver, A. G.; Day, V. W.; Blakemore, J. D., Examining the Modular Synthesis of [Cp*Rh] Monohydrides Supported by Chelating Diphosphine Ligands. *Organometallics*, **2021**, *40*, 3808-3818.

[27] Brewster, T. P.; Nguyen, T. H.; Li, Z.; Eckenhoff, W. T.; Schley, N. D.; DeYonker, N. J., Synthesis and Characterization of Heterobimetallic Iridium–Aluminum and Rhodium–Aluminum Complexes. *Inorg. Chem.* **2018,** *57*, 1148-1157.

[28] (a) Oishi, M.; Kino, M.; Saso, M.; Oshima, M.; Suzuki, H., Early–Late Heterobimetallic Complexes with a Ta–Ir Multiple Bond: Bimetallic Oxidative Additions of C–H, N–H, and O–H Bonds. *Organometallics* **2012,** *31*, 4658-4661. (b) Lassalle, S.; Jabbour, R.; Schiltz, P.; Berruyer, P.; Todorova, T. K.; Veyre, L.; Gajan, D.; Lesage, A.; Thieuleux, C.; Camp, C., Metal–Metal Synergy in Well-Defined Surface Tantalum–Iridium Heterobimetallic Catalysts for H/D Exchange Reactions. *J. Am. Chem. Soc.* **2019,** *141*, 19321-19335.

[29] Hostetler, M. J.; Bergman, R. G., Synthesis and reactivity of $Cp_2Ta(CH_2)_2Ir(CO)_2$: an early-late heterobimetallic complex that catalytically hydrogenates, isomerizes and hydrosilates alkenes. *J. Am. Chem. Soc.* **1990,** *112*, 8621-8623.

[30] Kumar, A.; Comadoll, C. G.; King, D. S.; Oliver, A. G.; Day, V. W.; Blakemore, J. D., Incorporation of [Cp*Rh] and [Cp*Ir] Species into Heterobimetallic Complexes via Protonolysis Reactivity and Dioximato Chelation. *Inorg. Chem.* **2021,** *60*, 14047-14059.

[31] Groom, C. R.; Bruno, I. J.; Lightfoot, M. P.; Ward, S. C., The Cambridge Structural Database. *Acta Cryst. B.* **2016,** *72*, 171-179.

[32] (a) Burk, M. J.; Harper, T. G. P.; Lee, J. R.; Kalberg, C., Efficient rhodium-catalyzed hydrogenation of aldehydes and ketones. *Tet. Lett.* **1994,** *35*, 4963-4966. (b) Matharu, D. S.; Morris, D. J.; Kawamoto, A. M.; Clarkson, G. J.; Wills, M., A Stereochemically Well-Defined Rhodium(III) Catalyst for Asymmetric Transfer Hydrogenation of Ketones. *Org. Lett.* **2005,** *7*, 5489-5491. (c) Aboo, A. H.; Bennett, E. L.; Deeprose, M.; Robertson, C. M.; Iggo, J. A.; Xiao, J., Methanol as hydrogen source: transfer

hydrogenation of aromatic aldehydes with a rhodacycle. *Chem. Comm.* **2018,** *54*, 11805-11808.

[33] (a) Uhlig, E.; Friedrich, M. Untersuchungen an Oximkomplexen. III. Nickelchelate des Bis-(diacetylmonoxim-imino)-propans-1,3 und des Bis-(diacetylmonoxim-imino)-äthans-1,2. *Z. Anorg. Allg. Chem.* **1966**, *343*, 299-307. (b) Roy, A. S.; Weyhermüller, T.; Ghosh, P. A new cobalodioxime and its three levels of H-bondings to 1D helical strand, 2D helices and 3D framework. *Inorg. Chem. Commun.* **2008**, *11*, 167-170.

[34] (a) White, C.; Yates, A.; Maitlis, P. M.; Heinekey, D. M., (η^5-Pentamethylcyclopentadienyl)Rhodium and -Iridium Compounds. *Inorg. Synth.* **1992**, *29*, 228-234. (b) Mantell, M. A.; Kampf, J. W.; Sanford, M. Improved Synthesis of $[Cp^RRhCl_2]_2$ Complexes. *Organometallics* **2018**, *37*, 3240-3242.

[35] Boyer, P. M.; Roy, C. P.; Bielski, J. M.; Merola, J. S. Pentamethylcyclopentadienylrhodium bis-carboxylates: monohapto carboxylate coordination, dihapto carboxylate coordination, and water coordination to Cp∗Rh. *Inorg. Chim. Acta* **1996**, *245*, 7-15.

[36] Fulmer, G. R.; Miller, A. J. M.; Sherden, N. H.; Gottlieb, H. E.; Nudelman, A.; Stoltz, B. M.; Bercaw, J. E.; Goldberg, K. I., NMR Chemical Shifts of Trace Impurities: Common Laboratory Solvents, Organics, and Gases in Deuterated Solvents Relevant to the Organometallic Chemist. *Organometallics* **2010**, *29*, 2176-2179.

[37] Harris, R. K.; Becker, E. D.; Cabral de Menezes, S. M.; Goodfellow, R.; Granger, P., NMR nomenclature. Nuclear spin properties and conventions for chemical shifts (IUPAC Recommendations 2001)**.** *Pure Appl. Chem.* **2001**, *73*, 1795-1818.

[38] Harris, R. K.; Becker, E. D.; Cabral de Menezes, S. M.; Granger, P.; Hoffman, R. E.; Zilm, K. W., Further conventions for NMR shielding and chemical shifts (IUPAC Recommendations 2008)**.** *Pure Appl. Chem.* **2008**, *80*, 59-84.

Chapter 5

Exploiting Iminoquinones as Electrophilic at Nitrogen "N+" Synthons for C–N Bond Construction

This chapter is adapted from a published manuscript:

Mori-Quiroz, L. M.; Comadoll, C. G.; Super, J. E.; Clift, M. D. Exploiting Iminoquinones as Electrophilic at Nitrogen "N+" Synthons for C–N Bond Construction. *Org. Lett.* **2021**, *23*, 7008-7013.

5.1 Introduction

In general, C–N bond-forming processes exploit the intrinsic nucleophilicity of nitrogen, thereby enabling a wide range of reactions with electrophilic coupling partners.[1] While these conventional transformations have been extensively developed and broadly applied, C–N bond-forming reactions that unite electrophilic nitrogen sources[2] with carbon nucleophiles represent a complementary and under-explored platform for the synthesis of amines and their derivatives.

Broadly speaking, electrophilic nitrogen sources are characterized by the presence of a good leaving group[3] and/or a substituent that acts as an electron sink[4] on the nitrogen atom, thereby inverting its classical reactivity. More reactive, electron-deficient species (i.e. aminyl radicals,[5] nitrenes[6]) are competent in amination reactions with milder nucleophiles, often assisted by transition metal catalysts. Common to the spectrum of available electrophilic nitrogen sources is the need for pre-functionalization and/or preparative steps to access the desired "N+" synthon. Although this requirement is trivial for reagents that allow general, selective, and predictable C–N bond formation, the generation or preparation of electrophilic nitrogen sources from more complex alkyl- or arylamines is typically limited to certain classes of N-containing functional groups, requires multi-step synthesis, or suffers from instability issues that arise from the highly reactive nature of the required intermediates. Therefore, methods that minimize or completely avoid the need for preparation/isolation of advanced electrophilic nitrogen sources are of significant value.

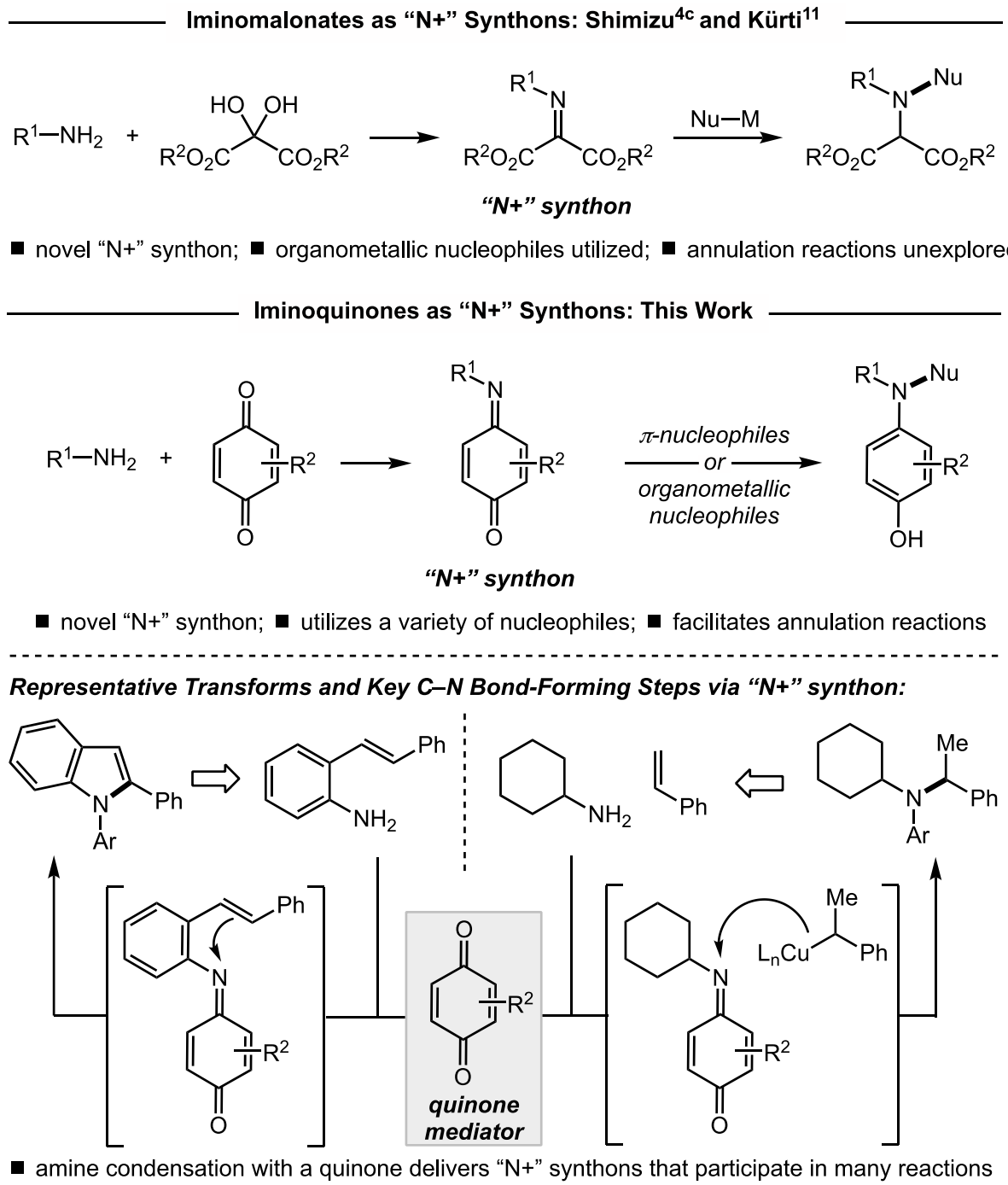

Scheme 5.1. Iminomalonates[4c,11] and iminoquinones[12,13,14] as electrophilic nitrogen sources.

Recent progress in the development of C–N bond-forming reactions using electrophilic nitrogen sources include hydroxylamine-based aminating reagents,[7,8]

photocatalytic amination reactions,[9] and other transition metal-catalyzed processes that exploit electrophilic nitrogen species generated *in situ* (e.g. aminyl or nitrene intermediates).[10] Among these, the work by the Kürti group stands out because it enables the generation of electrophilic nitrogen sources (iminomalonates) from both aliphatic and aromatic amines by simple condensation with a ketomalonate which subsequently engages in C–N bond-forming reactions with both alkyl- and arylmetal nucleophiles (Scheme 5.1).[11]

Iminoquinones represent a class of "N+" synthons that has been only sparsely evaluated[12,13,14] and no general approach for the exploitation of these intermediates has been developed.[15] In this work, we show that iminoquinones (Scheme 5.1), readily accessed by condensation of alkyl or arylamines with 1,4-benzoquinones, display electrophilic character at nitrogen. In these reactions, iminoquinone intermediates are generated *in situ* and undergo spontaneous C–N bond formation in the presence of an acid catalyst, providing indoles[16] and pyrroles[17]. We further show that iminoquinones derived from primary alkylamines react with organometallic reagents to afford tertiary amines.

5.2 Results and Discussion

5.2.1 Optimization of Quinone-Promoted Indole Synthesis

Our research group has developed several quinone-catalyzed[18] or quinone-mediated[19] transformations for the synthesis of amine derivatives. During the development of a stepwise umpolung approach for the α-allylation of benzylic amines with allylpalladium species[20] we observed that iminoquinones derived from 3-butenyl amines underwent cyclization by intramolecular C–N bond formation leading to pyrrole products in low yields

Table 5.1. Optimization of quinone-promoted indole synthesis. Reactions were run under Ar at 0.3 M. Yields refer to isolated products.

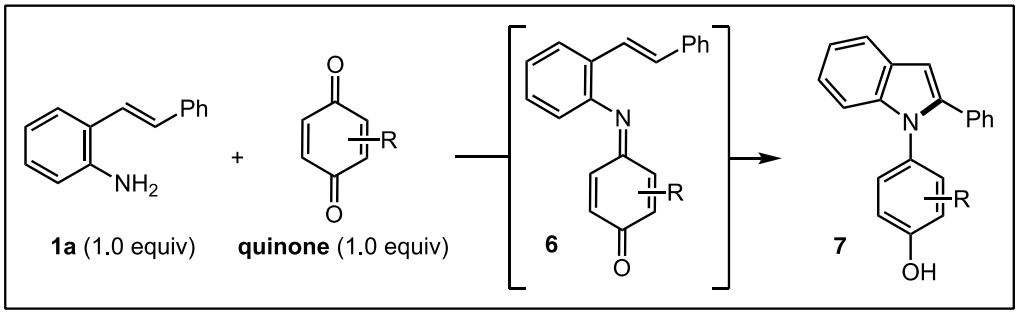

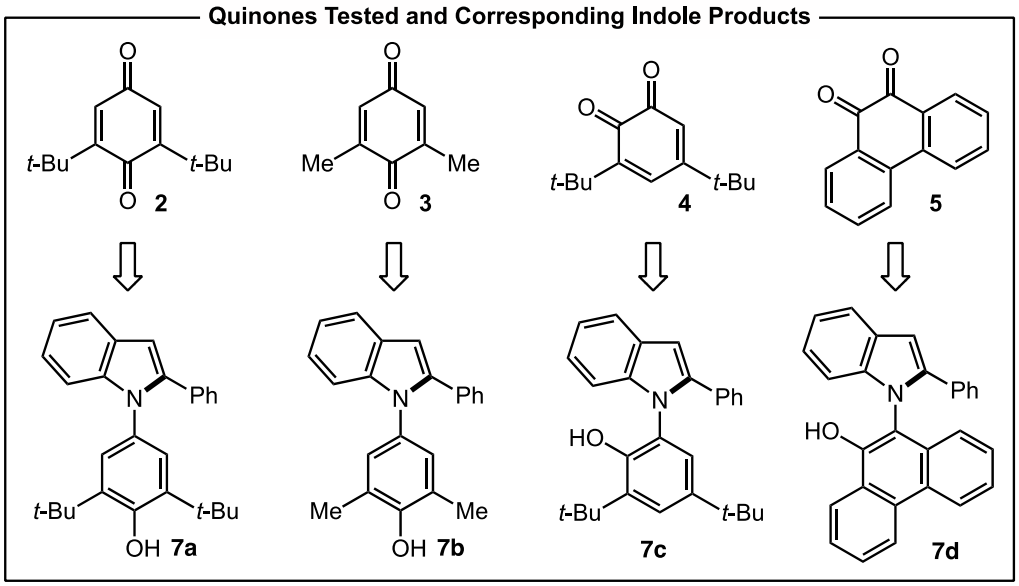

Entry	Quinone	Acid	Solvent	Temp. (°C)	Yield of 7
1	**2**	BF_3•OEt_2	THF	70	49 %
2	**2**	$La(OTf)_3$	THF	70	52 %
3	**2**	*p*-TSA	THF	70	78 %
4	**2**	TFA	THF	70	90 %
5	**2**	TFA	dioxane	100	97 %
6	**3**	TFA	dioxane	100	90 %
7	**4**	TFA	dioxane	100	84 %
8	**5**	TFA	dioxane	100	92 %

(see Appendix B). Importantly, control experiments ruled out the intervention of Pd as a catalyst. We speculated that the nitrogen atom of iminoquinones was behaving as a source of electrophilic nitrogen, in line with a few reports demonstrating that iminoquinones are capable of reacting with π-nucleophiles to form C–N bonds.[14] Despite the existence of these pioneering examples, no methods exploiting iminoquinones as general sources of electrophilic nitrogen have emerged.

Consequently, we hypothesized that iminoquinones derived from *ortho*-vinyl anilines would engage in a similar C–N bond-forming process to generate indoles (Table 5.1). Encouragingly, our attempts to prepare N-aryliminoquinone **6a** from amine **1** and quinone **2** using previously reported conditions[21] afforded not only the desired iminoquinone (37 % yield), but also indole **7a** in in 49 % yield (entry 1). $La(OTf)_3$ provided indole **7a** in similar yield (52 %, entry 2), whereas protic acids such as *p*-TSA (tosic acid) and TFA (trifluoroacetic acid) provided higher yields under similar conditions (78 % and 90 %, respectively). Optimal conditions (5 mol % TFA, dioxane, 100 ºC) afforded indole **7a** in 97 % isolated yield. Evaluation of the quinone scope demonstrated that the reaction is not limited to **2**. The less hindered quinone, **3**, provided the corresponding indole **7b** in 90 % yield, whereas 1,2-quinones **4** and **5** gave the corresponding indoles **7c** and **7d** in 84 % and 92 %, respectively. The full scope of quinone evaluation can be found in Appendix B.

Next, we evaluated the scope of this transformation with respect to *ortho*-vinyl anilines (Table 5.2). Diverse substitution at the vicinal aryl groups (R_1) was tolerated. Chloro- (**7e** and **7f**), fluoro- (**7g**), electron-withdrawing (**7h**), alkyl (**7i**), and electron-donating (**7j** and **7k**) substituents afforded 2-arylindole products consistently in good yields.

Table 5.2. Indole synthesis via quinone-promoted C–N bond construction.

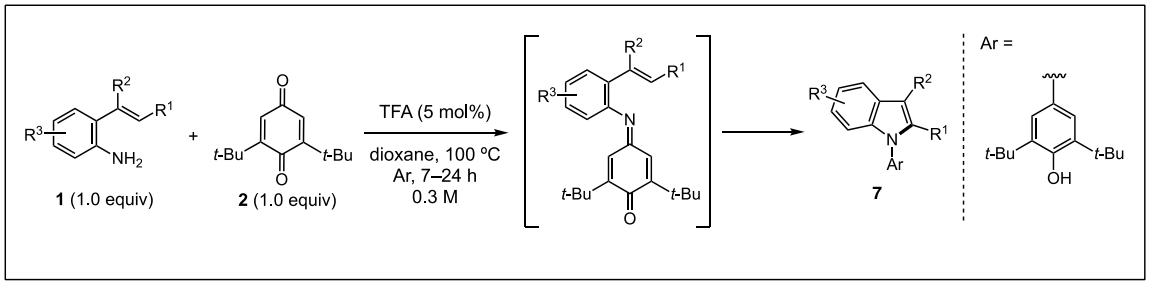

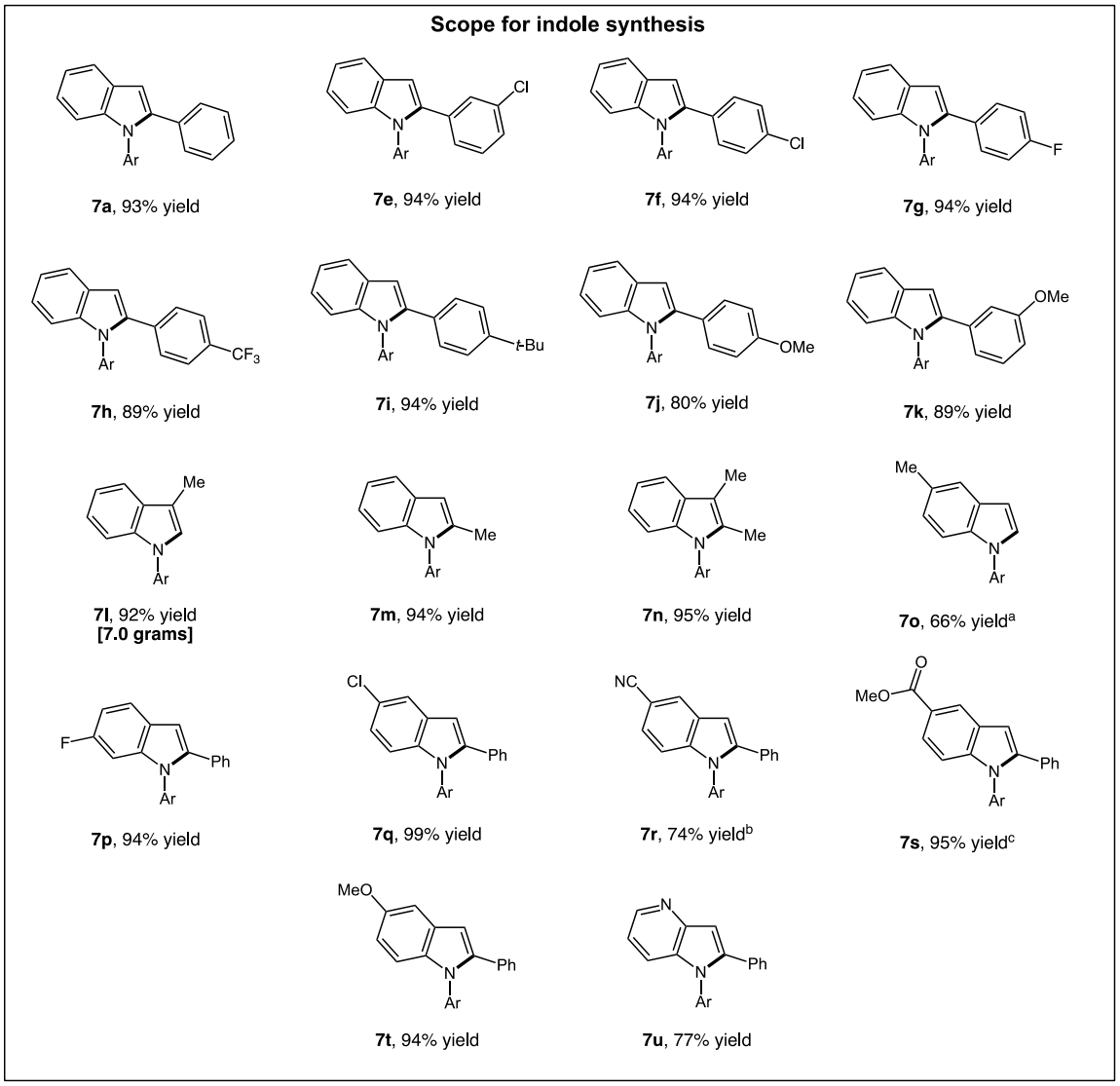

[a] Reaction was run at 0.04 M with 10 mol % of TFA. [b] Reaction was run in toluene with 10 mol% TFA at 120 ºC for 4 h in a sealed tube. [c] A second loading of TFA (5 mol %) was added after 21 h; reaction was stopped after an additional 7 h.

Alkyl substituents at the internal (**7l**), terminal (**7m**), or both positions (**7n**) of the olefin were tolerated. The reaction is robust and could be scaled up without rigorous exclusion of air and moisture to give **7l** in excellent yield (92 %, 7.0 grams of product isolated) after recrystallization. The efficient access to 2,3-disubstituted indole **7n** is particularly advantageous relative to the classic Fischer indole synthesis,[22] since the latter would lead to a mixture of isomeric products. Reaction of a monosubstituted *ortho*-vinyl aniline provided indole **7o** in low yield (15 %) together with an unidentified dimerization product (not shown), as suggested by mass spectrometry analysis. We conjectured that this unproductive reaction might arise from reaction of the electron-deficient iminoquinone intermediate with the electron-rich indole **7o** and rationalized it could be minimized at higher dilution. Indeed, lower reaction concentration (0.04 M) provided the desired product **7o** in 66 % yield. We also evaluated the effect of substitution at the aniline fragment. Halogen (**7p** and **7q**) substituents, as well as more (**7p** and **7q**) substituents, as well as more electronegative groups such as cyano- (**7r**) or methylcarboxy- (**7s**) substituents participated in the reaction, although the latter two required either higher temperature or a slightly higher catalyst loading for efficient conversion. Electron-donating groups were also tolerated (**7t**) and the reaction allowed efficient access to other heterocycles such as 4-azaindole **7u**. It is important to point out that the N-aryl substituent in these products can be conveniently removed under oxidative conditions to provide N–H indoles.

Evidence that supports the intermediacy of a carbocation was uncovered during these studies (Scheme 5.2). Specifically, exposure of aniline **1v** to the optimized reaction conditions provided indole **7v** in 88 % yield. This observation supports a mechanism wherein iminoquinone **6v** undergoes C–N bond formation to deliver carbocation **8**. A subsequent 1,2-

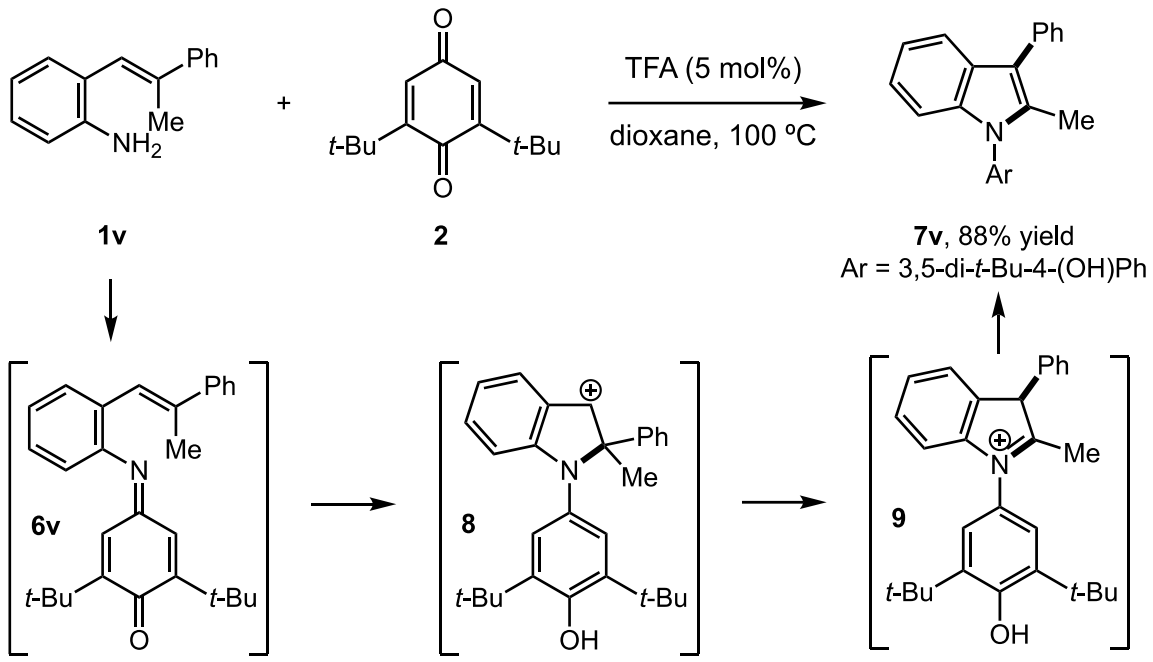

Scheme 5.2. Evidence for a carbocationic intermediate.

aryl migration to generate iminium ion **9** likely involves a phenonium ion intermediate.[23] The key bond-forming event may proceed by way of 1) simple nucleophilic addition of the alkene to the N-atom of the iminoquinone,[14a,b] 2) an aza-Nazarov cyclization,[24,25] or 3) a single electron transfer followed by radical recombination.

5.2.2 Expanding the Scope to Pyrroles and Alkylamines

After successful implementation of the iminoquinone-mediated indole synthesis, we re-evaluated our initial discovery with the aim to develop a new method to access pyrrole products (Table 5.3). These transformations would implement alkylamine substrates (**10**), rather than anilines. By modifying our initial conditions, we found that 5 mol % of TFA and excess quinone **2** (2 equiv) enabled *in-situ* formation of the iminoquinone intermediate and secured complete oxidation to the pyrrole product. Reaction of 1-(phenyl)but-3-en-1-ylamine with **2** afforded pyrrole 1**1b** in 49 % yield. 4-fluoro (**11a**) and 3-methoxy (**11c**) analogues were obtained in similar yields. *Ortho*-substitution (**11d**) and electron-rich

heterocyclic motifs (**11e**) were tolerated. The reaction allows access to 2,5-disubstituted pyrroles such as **11f** (59 %). Oxidation or C-3 arylation of the desired pyrrole products may explain the relatively modest yields observed for these reactions; however, the corresponding decomposition products were never isolated from the reaction mixtures.

Encouraged by the success of these annulation reactions, we wondered whether it might be possible to utilize iminoquinones as more general "N+" synthons. Towards that end, the intermolecular amination of organometallic nucleophiles using iminoquinones was studied. Addition of ethylmagnesium chloride to iminoquinone **12** afforded the corresponding tertiary amine **13** in 83 % (Scheme 5.3, eq. 1). We have further demonstrated that iminoquinones are competent "N+" synthons in hydroamination reactions (Scheme

Table 5.3. Pyrrole synthesis via quinone-promoted C–N bond construction.

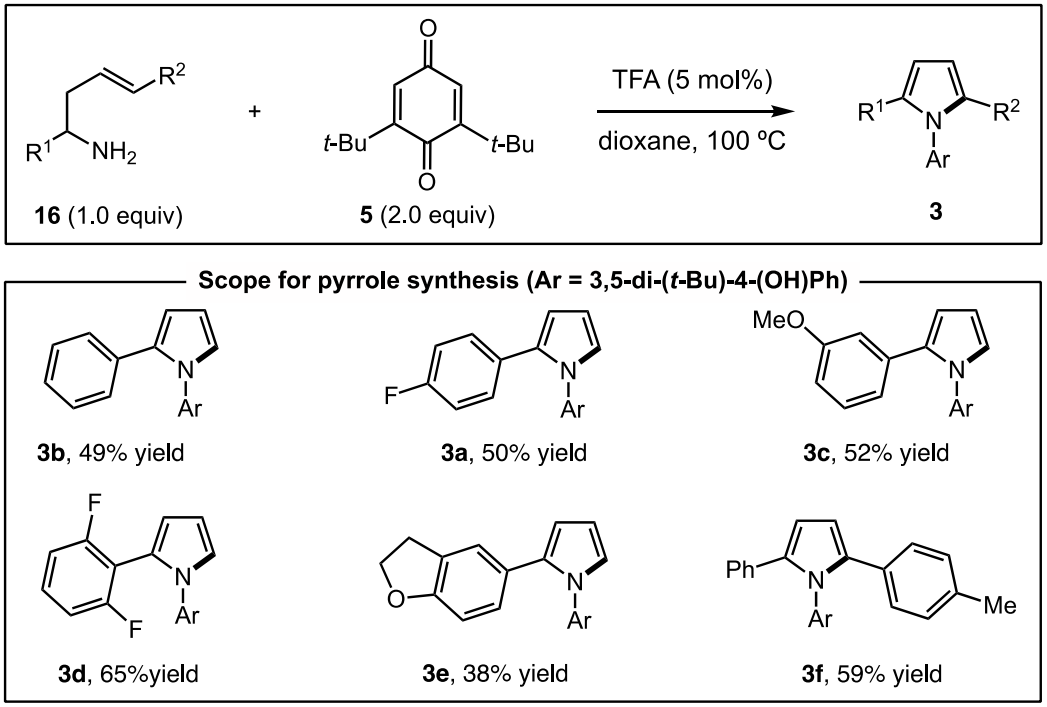

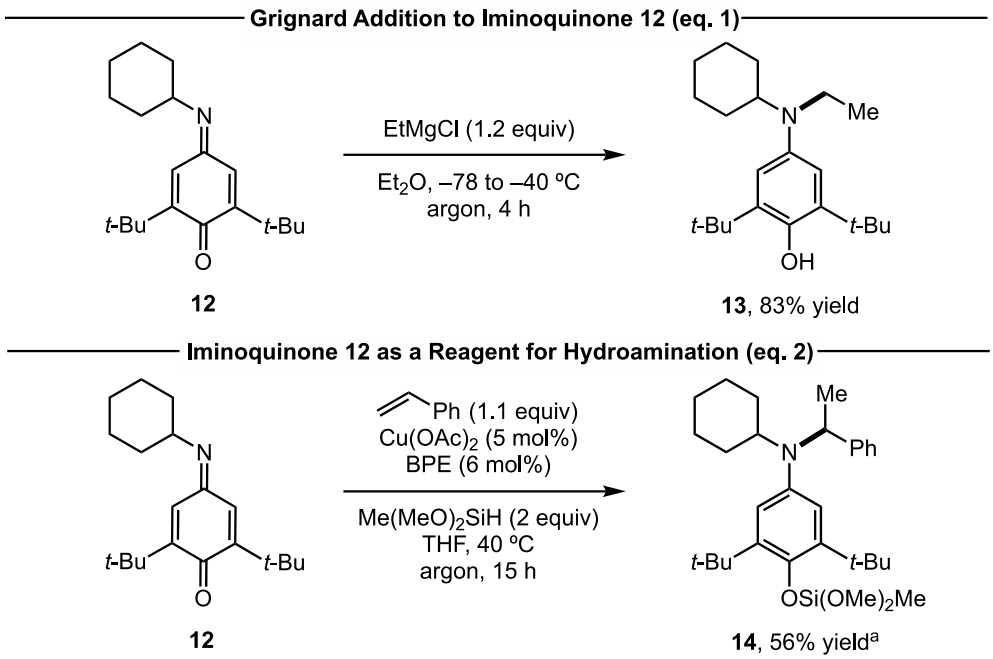

Scheme 5.3. Iminoquinones as versatile "N+" synthons. [a] NMR yield determined using 1,3,5-trimethoxybenzene as internal standard.

5.3, eq. 2).[26,27] Using reaction conditions that are nearly identical to those reported by Buchwald,[27] except without an N–O reaction partner, iminoquinone **12** participates in a copper-catalyzed hydroamination with styrene to deliver amine **14** in 56 % yield.

5.3 Conclusion

In conclusion, we have introduced a new manifold for inverting the reactivity of classical nitrogen nucleophiles. This chemistry harnesses the surprising N-electrophilicity of iminoquinones to enable a variety of C–N bond forming reactions. We expect that these new reactions will find applications as fundamental tools for C–N bond construction and inspire the future development of related processes.

5.4 Experimental Details

5.4.1 General Considerations

Reactions were run in oven-dried or flame-dried glassware under argon atmosphere and stirred magnetically. Acetonitrile, THF, triethylamine, and toluene were purified by passing the solvent through activated alumina using a solvent purification system. Anhydrous dioxane and DMF were purchased from Sigma-Aldrich and used as received. Diisopropylamine was distilled from calcium hydride under nitrogen prior to use. Homoallylic amine precursors were made as previously described by our group.[20] Unless otherwise noted, purification of products was carried out by flash chromatography using silica gel (230-400 Mesh, Grade 60). Reactions were monitored by Thin Layer Chromatography (TLC, silica gel 60 F254), or by ^{1}H NMR using 1,3,5-trimethoxybenzene as an internal standard. TLCs were visualized using UV or $KMnO_4$, phosphomolybdic acid (PMA), and ceric ammonium molybdate (CAM) stain solutions. ^{1}H NMR and ^{13}C NMR were recorded at room temperature in a Bruker 400, Bruker 500, or Bruker 600 instrument. Chemical shifts are reported in ppm and referenced with respect to residual protic solvents: chloroform at 7.26 ppm (^{1}H NMR); and the carbon resonances of the solvent: chloroform at 77.16 ppm (^{13}C NMR). Infrared spectra were recorded using a Shimadzu FTIR-8400S spectrometer. Mass spectra were obtained on a Micromass LCT Premier quadrupole and time-of-flight tandem mass analyzer. All crystallographic information can be found in Appendix B.

5.4.2 Synthesis of Aniline Precursors

Synthesis of 2-alkenylanilines

General Procedure A[28]

To a round bottom flask were added a magnetic stir bar, 2-bromoaniline derivative (1 equiv), tri(o-tolyl)phosphine (0.08 equiv) and $Pd(OAc)_2$ (1 mol %). A reflux condenser was attached, and the system was evacuated/backfilled with Ar (3 cycles). Triethylamine (reaction concentration with respect to aniline = 1 M) and styrene derivative (1.2 equiv) were added by syringe and the reaction was heated in an oil bath at the indicated temperature. After 3–10 h, the reaction was cooled down to room temperature, diluted with dichloromethane (~50 mL), and extracted with water (2 x 5 mL). The organic phase was dried over sodium sulfate, filtered, and concentrated. The aniline derivative **1** was purified by flash column chromatography.

Amines **1a**, **1e**, **1f**, **1g**, **1h**, **1i**, **1j**, **1k**, **1p**, **1q**, **1v**, and **1w** were prepared by Heck reaction of 2-bromo- or 2-iodoaniline precursors with the corresponding styrene derivatives using **General Procedure A**. The characterization data for new amines are provided below.

Preparation of 1e

Following General Procedure A, amine **1e** was obtained in 78% yield as a light yellow solid. ^{1}H NMR (500 MHz, $CDCl_3$) δ 7.51 (s, 1H), 7.40 (dd, *J* = 7.8, 1.5 Hz, 1H), 7.37 (d, *J* = 7.6 Hz, 1H), 7.29 (t, *J* = 7.8 Hz, 1H), 7.27 – 7.22 (m, 1H), 7.18 (d, *J* = 16.1 Hz, 1H), 7.13 (td, *J* = 7.5, 1.5 Hz, 1H), 6.93 (d, *J* = 16.1 Hz, 1H), 6.82 (t, *J* = 7.5 Hz, 1H), 6.73 (d, *J* = 7.9 Hz, 1H), 3.82 (s, 2H). ^{13}C NMR (126 MHz, $CDCl_3$) δ 144.3, 139.7, 134.8, 130.3, 129.2, 128.8, 127.6, 127.4, 126.3, 125.8, 124.8, 123.4, 119.4, 116.5. FTIR 3450, 3372, 3022, 2921, 1616, 1590, 1490, 1456, 1261, 959, 778 cm^{-1}.

Preparation of 1i

Following General Procedure A, amine **1i** was obtained in 70% yield as a light yellow oil. ^{1}H NMR (500 MHz, $CDCl_3$) δ 7.47 (d, *J* = 8.1 Hz, 2H), 7.44 – 7.36 (m, 3H), 7.18 – 7.07 (m, 2H), 6.99 (d, *J* = 16.0 Hz, 1H), 6.83 (t, *J* = 7.5 Hz, 1H), 6.74 (dd, *J* = 7.9, 1.4 Hz, 1H), 3.94 (s, 2H), 1.35 (s, 18H). ^{13}C NMR (126 MHz, $CDCl_3$) δ 150.9, 143.8, 135.0, 130.4, 128.6, 127.4, 126.3, 125.8, 124.36, 123.6, 119.4, 116.5, 34.8, 31.4.

Preparation of 1k

Following General Procedure A, amine **1k** was obtained in 72% yield as a light yellow oil. ^{1}H NMR (500 MHz, $CDCl_3$) δ 7.40 (d, *J* = 7.7 Hz, 1H), 7.28 (t, *J* = 7.8 Hz, 1H), 7.16 (d, *J* = 16.1 Hz, 1H), 7.15 – 7.08 (m, 2H), 7.05 (d, *J* = 2.7 Hz, 1H), 6.97 (d, *J* = 16.1 Hz, 1H), 6.86 – 6.78 (m, 2H), 6.72 (d, *J* = 8.0 Hz, 1H), 3.85 (s, 3H), 3.81 (s, 2H). ^{13}C NMR (126 MHz, $CDCl_3$) δ 160.1, 144.1, 139.2, 130.4, 129.8, 128.9, 127.4, 124.7, 123.9, 119.3 (2 overlapped C), 116.4, 113.4, 111.9, 55.4. FTIR 3443, 3368, 3023, 2936, 2833, 1596, 1574, 1491, 1455, 1268, 1154, 1045 cm^{-1}.

General Procedure B[29]

To a round bottom flask were added a magnetic stir bar, 2-bromoaniline derivative (1 equiv), trans-2-phenylboronic acid (1.2 equiv), potassium carbonate (4 equiv), and $Pd(PPh_3)_4$ (5 mol %). The flask was evacuated/backfilled with Ar (3 cycles) and toluene, water, and ethanol (5:2:1 ratio, reaction concentration with respect to aniline = 0.15 M) were added by syringe. The reaction was heated in an oil bath to 100 ºC for 14–17 h. The reaction was then cooled to room temperature, opened to air, diluted with water (5 mL), and extracted with dichloromethane (3 x 30 mL). The combined organic extracts were washed with water (10

mL) and brine (10 mL), dried over sodium sulfate, and concentrated. The aniline derivative **1** was purified by flash column chromatography.

Amines **1m**, **1n**, **1r**, **1s**, **1t**, and **1u** were prepared by Suzuki coupling reaction of 2-bromoaniline precursors with *trans*-2-phenylvinylboronic acid using General Procedure B. The spectral data of each amine prepared by this procedure matched literature data.

5.4.3 Synthesis of N-Aryl Indoles from 2-Alkenylanilines

General Procedure C

To a 10 mL round bottom flask were added a magnetic stir bar, quinone (1 equiv), and the corresponding aryl amine **1** (1 equiv). The flask was sealed with a septum and evacuated/backfilled with Ar (3 cycles). Dioxane (reaction concentration = 0.25 M) and TFA (0.05 equiv) were added by syringe. The reaction was heated in an oil bath to 100 ºC and monitored by TLC. The reaction was cooled to room temperature, opened to air, and 1–2 drops of triethylamine were added. The reaction mixture was concentrated *in vacuo,* and the product was purified by flash column chromatography.

Note: In a typical experiment, the initial yellow/orange solution turns dark red within minutes, indicating the formation of the iminoquinone intermediate. The red color gradually dissipates until a light orange solution is obtained, consistent with the consumption of the iminoquinone and formation of the colorless indole product.

All characterization data for N-arylindoles **7a**–**7u** are found in Appendix B.

5.4.4 Synthesis of N-Aryl Pyrroles from 3-Butenylamines

General Procedure D

To a 10 mL round bottom flask were added a magnetic stir bar, 2,6-di-*tert*-butyl-1,4-benzoquinone **2** (2 equiv), and the corresponding amine (1 equiv). The flask was sealed with

a septum and evacuated/backfilled with Ar (3 cycles). Dioxane (reaction concentration = 0.25 M with respect to the amine) and TFA (0.05 equiv) were added by syringe. The reaction was heated in an oil bath to 100 ºC for 18–24 h. The reaction was cooled to room temperature, opened to air, and 1–2 drops of triethylamine were added. The reaction mixture was concentrated *in vacuo*, and the product was purified by flash column chromatography. Note: a stock solution of TFA in dioxane (0.0125 M) was used in small-scale reactions that required minute amounts of TFA.

All characterization data for N-arylpyrroles **11a–11f** are found in Appendix B.

5.4.5 Oxidative Dearylation of N-Aryl Indole 7a

To a round bottom flask were added a magnetic stir bar, indole **7a** (213.0 mg, 0.54 mmol, 1 equiv), and dichloromethane (54 mL). The flask was sealed with a septum and cooled to –78 ºC in an acetone/dry ice bath. Then, a solution of ammonium cerium(IV) nitrate (592.1 mg, 1.08 mmol, 2 equiv) in MeOH (5.4 mL) was added dropwise by syringe. The reaction was monitored by TLC until the indole **7a** was consumed. After completion, the flask was removed from the ice bath and immediately quenched with a solution of 10 % sodium thiosulfate$_{(aq)}$ which caused the solution to freeze. The solution was allowed to warm to room temperature with stirring. Once melted, the solution was diluted with dichloromethane and organic layer was separated from the aqueous sodium thiosulfate and then washed with water and brine, dried with Na_2SO_4, filtered, and concentrated *in vacuo*. This left a crude mixture of desired indole, quinone methide **QM**, and an aminal (see Appendix B for structural information and further discussion of the intermediates). To this crude material was added a magnetic stir bar, $HCl_{(aq)}$ (1.1 mL, 0.108 mmol, 0.2 equiv), and THF (11 mL). The reaction was capped and stirred at room temperature and monitored by TLC until all **QM** and aminal

were hydrolyzed. The reaction was diluted with EtOAc and washed with H_2O and brine. The organic layer was dried with Na_2SO_4, filtered, and concentrated *in vacuo*. Flash column chromatography (5 % ethyl acetate in hexanes) afforded 2-phenyl-1H-indole.

Preparation of 2-phenyl-1H-indole

2-phenyl-1H-indole was obtained (79.2 mg, 76 %) as a white solid. ^{1}H NMR (500 MHz, $CDCl_3$) δ 8.33 (s, 1H), 7.68 (d, J = 8.1 Hz, 2H), 7.64 (d, J = 7.9 Hz, 1H), 7.49 – 7.43 (m, 2H), 7.41 (d, J = 8.1 Hz, 1H), 7.34 (td, J = 7.5, 1.4 Hz, 1H), 7.21 (t, J = 7.5 Hz, 1H), 7.13 (t, J = 7.5 Hz, 1H), 6.84 (d, J = 2.2 Hz, 1H). ^{13}C NMR (126 MHz, $CDCl_3$) δ 138.0, 137.0, 132.5, 129.4, 129.2, 127.9, 125.3, 122.5, 120.8, 120.4, 111.0, 100.2. Spectral data is in accord with published values.[30]

5.4.6 Amination of Alkyl Grignard Reagents with Iminoquinones

Preparation of Iminoquinone 12

To a 50-mL round bottom flask were added a magnetic stir bar, cyclohexylamine (1.14 mL, 10 mmol, 1 equiv), 2,6-di-*tert*-butyl-1,4-benzoquinone (2.20 g, 10 mmol, 1 equiv), and ethanol (12 mL). The flask was capped with a septum and flushed with Ar. The reaction was heated in an oil bath to 80 ºC with stirring and monitored by TLC until the quinone was consumed. The reaction was cooled to room temperature, opened to air, and concentrated *in vacuo*. The crude product was recrystallized from warm hexanes to give 2.52 g (84 %) of **12** as a yellow solid. m.p.: 113–114 °C. ^{1}H NMR (500 MHz, $CDCl_3$) δ 7.06 (s, 1H), 6.84 (s, 1H), 3.79 (td, J = 10.8, 5.3 Hz, 1H), 1.86 (dt, J = 13.2, 3.3 Hz, 2H), 1.80 – 1.66 (m, 3H), 1.60 (dt, J = 13.2, 10.1 Hz, 2H), 1.48 – 1.37 (m, 2H), 1.30 (s, 9H), 1.29 (m, overlapped, 1H), 1.28 (s, 9H). ^{13}C NMR (126 MHz, $CDCl_3$) δ 188.0, 157.4, 153.0, 151.3, 136.4, 118.3, 60.7,

35.9, 35.2, 34.6, 29.7, 29.6, 25.6, 24.86. FTIR 3047, 2961, 2927, 1638, 1629, 1450, 1361, 1223, 1157, 1088 cm^{-1}. HRMS (ESI) *m/z* calcd for $[C_{32}H_{40}NO]^+$ 454.3110, found 454.3089.

General Procedure E

To a 50 mL round bottom flask were added a magnetic stir bar, the corresponding iminoquinone (1 equiv), and dry Et_2O (reaction concentration = 0.1 M). The flask was sealed with a septum and evacuated/backfilled with Ar (3 cycles). The solution was cooled to –78 ºC with stirring in an acetone/dry ice bath. Ethylmagnesium chloride (1.2 equiv, 2 M in THF) was then added dropwise. The reaction was warmed to –40 ºC in an MeOH/H_2O/dry ice bath (55:45 MeOH/H_2O) and monitored by TLC until the iminoquinone was consumed. After completion, the reaction was warmed to room temperature, opened to air, and quenched with H_2O and NH_4Cl. The organic layer was washed with water and brine, dried with Na_2SO_4, filtered, and concentrated *in vacuo*. The product was purified by flash column chromatography.

Preparation of 13

Following General Procedure E, **12** (500 mg, 1.66 mmol, 1 equiv) afforded, after column chromatography (2.5 % ethyl acetate in hexanes), 455.7 mg (83 %) of **13** as an orange solid. m.p.: 81–83 °C. ^{1}H NMR (500 MHz, $CDCl_3$) δ 6.67 (s, 2H), 4.58 (s, 1H), 3.28 (ddt, J = 10.8, 6.6, 3.3 Hz, 1H), 3.19 (q, J = 7.0 Hz, 2H), 1.93 – 1.76 (m, 4H), 1.69 – 1.61 (m, 1H), 1.44 (s, 18H), 1.37 – 1.27 (m, 4H), 1.28 – 1.20 (m, 1H), 1.12 (t, J = 7.0 Hz, 3H). ^{13}C NMR (126 MHz, $CDCl_3$) δ 145.9, 141.7, 136.7, 113.0, 59.2, 41.0, 34.8, 30.9, 30.5, 29.8, 26.43, 26.25, 15.5. FTIR 3630, 3122, 3004, 2961, 2931, 1605, 1441, 1263, 1200, 1147 cm^{-1}. HRMS (ESI) *m/z* calcd for $[C_{22}H_{38}NO]^+$ 332.2953, found 332.2953.

5.4.7 Inter- and Intramolecular Alkene Hydroamination with Iminoquinones

On the bench, a dry 7-mL vial was charged with a magnetic stir bar, iminoquinone **12** (30.1 mg, 0.1 mmol, 1 equiv), $Cu(OAc)_2$ (0.9 mg, 0.05 mmol, 5 mol %), and (R,R)-BPE (3.0 mg, 0.06 mmol, 6 mol %) and was capped, evacuated/backfilled with Ar (3 cycles), and THF (0.2 mL), styrene (13 μL, 0.11 mmol, 1.1 equiv), and $Me(MeO)_2SiH$ (25 μL, 0.485 mmol, 2 equiv) were added sequentially by syringe. The septum of the cap was sealed with grease and the reaction was heated in a preheated aluminum block at 40 ºC. After 15 h, the reaction was cooled to room temperature, opened to air, and 1,3,5-trimethoxybenzene (40.8 mg, 0.2426 mmol, 1 equiv) was added, followed by DCM (~ 1 mL). The reaction was concentrated *in vacuo* and analyzed by ^1H NMR (**14**, 56 % NMR yield). See Appendix B for discussion of desilylative procedure.

5.5 Acknowledgements

Dr. Victor Day (The University of Kansas) is acknowledged for crystallographic analysis. The authors acknowledge financial support from The University of Kansas and the NIH Chemical Biology of Infectious Disease CoBRE Grant (P20 GM113117) at The University of Kansas. Support for NMR instrumentation was provided by NIH Shared Instrumentation Grants (S10RR024664 and S10OD16360) and NSF Major Instrumentation Grants (9977422 and 1625923). Support for X-ray instrumentation was provided by NSF-MRI Grant (CHE0923449).

The reactions described herein which contributed to initial reaction optimization and the scope studies were conducted through a joint effort by LMQ, CGC, and JES. The development of the oxidative dearylation conditions, the growth of crystals of **QM** suitable for X-ray diffraction studies, and the full quinone scope study (Appendix B) were performed

by CGC as the sole graduate student on the project. LMQ led most other efforts described herein and in Appendix B as the postdoctoral researcher on the project. JES contributed to the scope expansion of N-arylindoles and N-arylpyrroles.

5.6 References

[1] (a) Lawrence, S. A., Amines: Synthesis, Properties and Applications; Cambridge University Press, 2004. (b) Nugent, T. C., Chiral Amine Synthesis: Methods, Developments and Applications; Wiley-VCH, 2010. (c) Ricci, A.; Bernardi, L., Methodologies in Amine Synthesis. Challenges and Applications; Wiley-VCH, Weinheim, 2021.

[2] (a) Erdik, E.; Ay, M., Electrophilic Amination of Carbanions. *Chem. Rev.* **1989**. *89*, 1947-1980. (b) Ciganek, E., Electrophilic Aminations of Carbanions, Enolates, and their Surrogates *Org. React.* **2008**, *72*, Ch. 1. (c) Corpet, M.; Gosmini, C., Recent Advances in Electrophilic Amination Reactions. *Synthesis*, **2014**, 2258-2271. (d) Dong, X. Liu, Q.; Dong, Y.; Liu, H., Transition-Metal-Catalyzed Electrophilic Amination: Application of *O*-Benzoylhydroxylamines in the Construction of the C–N Bond. *Chem. Eur. J.* **2017**, *23*, 2481-2511. (e) Korch, K. M.; Watson, D. A., Cross-Coupling of Heteroatomic Electrophiles. *Chem. Rev.* **2019**, *119*, 8192-8228.

[3] (a) Beak, P.; Kokko, B. J., A Modification of the Sheverdina-Kocheshkov Amination: The Use of Methoxyamine–Methyllithium as a Convenient Synthetic Equivalent of NH_2^+. *J. Org. Chem.* **1982**, *47*, 2822-2823. (b) Andreae, S.; Schmitz, E., Electrophilic Aminations with Oxaziridines. *Synthesis*, **1991**, 327-341. (c) Smulik, J. A.; Vedejs, E., Improved Reagent for Electrophilic Amination of Stabilized Carbanions. *Org. Lett.* **2003**, *5*, 4187-4190.

[4] (a) Hagopian, R A.; Therien, M. J.; Murdoch, J. R., Synthesis of Amines through Nucleophilic Addition on Nitrogen. *J. Am. Chem. Soc.* **1984**, *106*, 5753-5754. (b) Tsuitsui, H.; Ichikawa, T.; Narasaka, K., Preparation of Primary Amines by the

Alkylation of *O*-Sulfonyloximes of Benzophenone Derivatives with Grignard Reagents. *Bull. Chem. Soc. Jp.* **1999**, *72*, 1869-1878. (c) Niwa, Y.; Takayama, K.; Shimizu, M., Electrophilic Amination with Iminomalonate. *Tetrahedron Lett.* **2001**, *42*, 5473-5476. (d) List, B., Direct Catalytic Asymmetric α-Amination of Aldehydes. *J. Am. Chem. Soc.* **2002**, *124*, 5656-5657. (e) Kitamura, M.; Suga, T.; Chiba, S.; Narasaka, K., Synthesis of Primary Amines by the Electrophilic Amination of Grignard Reagents with 1,3-Dioxolan-2-one-*O*-Sulfonyloxime. *Org. Lett.* **2004**, *6*, 4619-4621.

[5] (a) Zard. S. Z., Recent Progress in the Generation and Use of Nitrogen-Centred Radicals. *Chem. Soc. Rev.* **2008**, *37*, 1603-1618. (b) Xiong, T.; Zhang, Q., New Amination Strategies Based on Nitrogen-Centered Radical Chemistry. *Chem. Soc. Rev.* **2016**, *45*, 3069-3087.

[6] (a) Müller, P.; Fruit, C., Enantioselective Catalytic Aziridinizations and Asymmetric Nitrene Insertions into C–H Bonds. *Chem. Rev.* **2003**, *103*, 2905-2920. (b) Dequirez, G.; Pons, V.; Dauban, P., Nitrene Chemistry in Organic Synthesis: Still in Its Infancy? *Angew. Chem. Int. Ed.* **2012**, *51*, 7384-7395. (c) Park, Y.; Kim, Y.; Chang, S., Transition Metal-Catalyzed C–H Amination: Scope, Mechanism, and Applications. *Chem. Rev.* **2017**, *117*, 9247-9301.

[7] (a) Lardy, S. W.; Schmidt, V. A., Intermolecular Radical Mediated Anti-Markovnikov Alkene Hydroamination Using *N*-Hydroxyphthalimide. *J. Am. Chem. Soc.* **2018**, *140*, 12318-12322. (b) Farndon, J. J.; Young, T. A.; Bower, J. F., Stereospecific Alkene Aziridinization Using a Bifunctional Amino-Reagent: An Aza-Prilezhaev Reaction. *J. Am. Chem. Soc.* **2018**, *140*, 17846-17850. (c) Farndon, J. J.; Ma, X.; Bower, J. F., Transition Metal Free C–N Bond Forming Dearomatizations and Aryl C–H Aminations

by in Situ Release of a Hydroxylamine-Based Aminating Reagent. *J. Am. Chem. Soc.* **2017**, *139*, 14005-14008. (d) Zhou, Z.; Cheng, Q.-Q.; Kürti, L., Aza-Rubottom Oxidation: Synthetic Access to Primary α-Aminoketones. *J. Am. Chem. Soc.* **2019**, *141*, 2242-2246.

[8] (a) Paudyal, M. P.; Adebesin, A. M.; Burt, S. R.; Ess, D. H.; Ma, Z.; Kürti, L.; Falck, J. R., Dirhodium-Catalyzed C–H Arene Amination Using Hydroxylamines. *Science* **2016**, *353*, 1144-1147. (b) Angelini, L.; Davies, J.; Simonetti, M.; Sanz, L. M.; Sheikh, N. S.; Leonori, D., Reaction of Nitrogen Radicals with Organometallics under Nickel Catalysis: N-Arylations and Amino-Functionalization Cascades. *Angew. Chem. Int. Ed.* **2019**, *58*, 5003-5007.

[9] (a) Musacchio, A. J.; Lainhart, B. C.; Zhang, X.; Naguib, S. G.; Sherwood, T. C.; Knowles, R. R., Catalytic Intermolecular Hydroaminations of Unactivated Olefins with Secondary Alkyl Amines. *Science* **2017**, *355*, 727-730. (b) Wappes, E. A.; Nakafuku, K. M.; Nagib, D. A., Directed β C–H Amination of Alcohols via Radical Relay Chaperones. *J. Am. Chem. Soc.* **2017**, *139*, 10204-10207.

[10] (a) Liang, C.; Collet, F.; Robert-Peillard, F.; Müller, P.; Dodd, R. H.; Dauban, P., Toward a Synthetically Useful Stereoselective C–H Amination of Hydrocarbons. *J. Am. Chem. Soc.* **2008**, *130*, 343-350. (b) Badiei, Y. M.; Dinescu, A.; Dai, X.; Palomino, R. M.; Heinemann, F. W.; Cundari, T. R.; Warren, T. H., Copper-Nitrene Complexes in Catalytic C–H Amination. *Angew. Chem. Int. Ed.* **2008**, *47*, 9961-9964. (c) Hennessy, E. T.; Betley, T. A., Complex N-Heterocycle Synthesis via Iron-Catalyzed, Direct C–H Bond Amination. *Science* **2013**, *340*, 591-595.

[11] Kattamuri, P. V.; Yin, J.; Siriwongsup, S.; Kwon, D.-H.; Ess, D. H.; Li, Q.; Li, G.; Yousufuddin, M.; Richardson, P. F.; Sutton, S. C.; Kürti, L., Practical Singly and Doubly Electrophilic Aminating Agents: A New, More Sustainable Platform for Carbon–Nitrogen Bond Formation. *J. Am. Chem. Soc.* **2017**, *139*, 11184-11196.

[12] Honzl, J.; Metalová, M., Polyaniline Compounds III. Reaction of Phenyl- and Methyllithium with N,N'-Diphenyl-*p*-quinone Diimine. *Tetrahedron*, **1969**, *25*, 3641-3652.

[13] Brachi, J.; Rieker, A., Umsetzung von 3,5-Di-*t*-butyl-4-imino-2,5-cyclohexadienon mit Organometall-Verbidungen. Synthese Sterich Gehinderter Aniline. *Synthesis* **1977**, 706-708.

[14] (a) Ukhin, L. Y.; Suponitskii, K. Y.; Belousova, L. V.; Gribanova, T. N., Synthesis and Crystal Structure of 5-(3,5-di-*tert*-butyl-4-hydroxyphenyl)-1,2,3,5-tetrahydrophenazine. *Russ. Chem. Bull. Int. Ed.* **2009**, *58*, 940-943. (b) Guo, J.; Chaithanya Kiran, I. N.; Reddy, S.; Gao, J.; Tang, M.; Liu, Y.; He, Y., Synthesis of Carbazolequinones by Formal [3+2] Cycloaddition of Arynes and 2-Aminoquinones. *Org. Lett.* **2016**, *18*, 2499-2502.

[15] (a) Raju, S.; Annamalai, P.; Chen, P.-L.; Liu, Y.-H.; Chuang, S.-C., Palladium-Catalyzed C–H Bond Activation by Using iminoquinone as a Directing Group and an Internal Oxidant or a Co-Oxidant: Production of Dihydrophenanthridines, Phenanthridines, and Carbazoles. *Org. Lett.* **2017**, *19*, 4134-4137. (b) Liu, L.; Chen, K.; Wu, W.-Z.; Wang, P.-F.; Song, H.-Y.; Sun, H.; Wen, X.; Xu, Q.-L., Organocatalytic *para*-Selective Amination of Phenols with Iminoquinone Monoacetals. *Org. Lett.* **2017**, *19*, 3823-3826. (c) Jillella, R.; Raju, S.; Hsiao, H.-C.; Hsu, D.-S.; Chuang, S.-C., Pd-Catalyzed Redox-

Neutral C–N Coupling Reaction of Iminoquinones with Electron-Deficient Alkenes without Esternal Oxidants: Access of Tertiary (*E)*-Enamines and Application to the Synthesis of Indoles and Quinolin-4-ones. *Org. Lett.* **2020**, *22*, 6252-6256.

[16] (a) Humphrey, G. R.; Kuethe, J. T., Practical Methodologies for the Synthesis of Indoles. *Chem. Rev.* **2006**, *106*, 2875-2911. (b) Stokes, B. J.; Dong, H.; Leslie, B. E.; Pumphrey, A. L. Driver, T. G., Intramolecular C–H Amination Reactions: Exploitation of the Rh_2(II)-Catalyzed Decomposition of Azidoacrylates. *J. Am. Chem. Soc.* **2007**, *129*, 7500-7501. (c) Fra, L.; Millán, A.; Souto, J. A.; Muñiz, K., Indole Synthesis Based on a Modified Koser Reagent. *Angew. Chem. Int. Ed.* **2014**, *53*, 7349-7353. (d) Andries-Ulmer, A.; Brunner, C.; Rehbein, J.; Gulder, T., Fluorine as a Traceless Directing Group for the Regiodivergent Synthesis of Indoles and Tryptophans. *J. Am. Chem. Soc.* **2018**, *140*, 13034-13041. (e) Nykaza, T. V.; Ramirez, A.; Harrison, T. S.; Luzung, M. R.; Radosevich, A. T., Biphilic Organophosphorus-Catalyzed Intramolecular C_{sp2}–H Amination: Evidence for a Nitrenoid in Catalytic Cadogan Cyclizations. *J. Am. Chem. Soc.* **2018**, *140*, 3103-3113.

[17] (a) Gulevich, A. V.; Dudnik, A. S.; Chernyak, N.; Gevorgyan, V., Transition Metal-Mediated Synthesis of Monocyclic Aromatic Heterocyclic. *Chem. Rev.* **2013**, *113*, 3084-3213. (b) Estévez, V.; Villacampa, M.; Menéndez, J. C., Recent Advances in the Synthesis of Pyrroles by Multicomponent Reactions. *Chem. Soc. Rev.* **2014**, *43*, 4633-4657.

[18] (a) Leon, M. A.; Liu, X.; Phan, J. H.; Clift, M. D., Amine Functionalization through Sequential Quinone-Catalyzed Amine Oxidation/Nucleophilic Addition. *Eur. J. Org. Chem.* **2016**, *26*, 4508-4515. (b) Haugeberg, B. J.; Phan, J. H.; Liu, X.; O'Connor, T.

J.; Clift, M. D., Homologation of α-Amino Acids through Quinone-Catalyzed Oxidative Decarboxylation/Mukaiyama-Mannich Addition. *Chem. Commun.* **2017**, *53*, 3062-3065. (c) Liu, X.; Phan, J. H.; Haugeberg, B. J.; Londhe, S. S.; Clift, M. D., Quinone-Catalyzed Oxidative Deformylation: Synthesis of Imines from Amino Alcohols. *Beilstein J. Org. Chem.* **2017**, *13*, 2895-2901.

[19] Mori-Quiroz, L. M.; Clift, M. D., Exploiting Alkylquinone Tautomerization: Amine Benzylation. *Org. Lett.* **2016**, *18*, 3446-3449.

[20] Mori-Quiroz, L. M.; Londhe, S. S.; Clift, M. D., Formal α-Allylation of Primary Amines by a Dearomative, Palladium-Catalyzed Umpolung Allylation of *N*-(Aryloxy)imines *J. Org. Chem.* **2020**, *85*, 14827-14846.

[21] McDonagh, A. M.; Cifuentes, M. P.; Lucas, N. T.; Humphrey, M. G.; Houbrechts, S.; Persoons, A., Organometallic Complexes for Nonlinear Optics Part 19. Synthesis and Molecular Quadratic Hyperpolarizabilities of Indoanilino-Alkynyl-Ruthenium Complexes. *J. Organomet. Chem.* **2000**, *205*, 184-192.

[22] Palmer, M. H.; McIntyre, P. S., Fischer Indole Synthesis on Unsymmetrical Ketones. The Effect of the Acid Catalyst. *J. Chem. Soc. B* **1969**, 446-449.

[23] (a) Sundberg, R. J.; Kotchmar, G. S., An Investigation of Stereochemistry and Migratory Aptitude in the Reductive Cyclization of β,β-Disubstituted *o*-Nitrostyrenes to 2,3-Disubstituted Indoles. *J. Org. Chem.* **1969**, *34*, 2285-2288. (b) Jana, N.; Driver, T. G., Assembly of Functionalized Carbocycles or N-Heterocycles through a Domino Electrocyclization-[1,2] Migration Reaction Sequence. *Org. Biomol. Chem.* **2015**, *13*, 9720-9741.

[24] (a) Dieker, J.; Fröhlich, R.; Würthwein, E.-U., Substituted 3-Hydroxypyrroles from 1-Azapenta-1,4-dien-3-ones: The Aza-Nazarov Reaction – Synthesis and Quantum Chemical Calculations. *Eur. J. Org. Chem.* **2006**, 5339-5356. (b) Narayan, R.; Daniliuc, C.-G.; Würthwein, E.-U., Preparation of N*H*-Pyrroles under Superelectrophilic Conditions by an Aza-Nazarov Reaction Cascade with Indole as Neutral Leaving Group: Experiment and Theory. *Eur. J. Org. Chem.* **2012**, 6021-6032. (c) Klumpp, D. A.; Zhang, Y.; O'Connor, M. J.; Esteves, P. M.; de Almeida, L. S., Aza-Nazarov Reaction and the Role of the Superelectrophiles. *Org. Lett.* **2007**, *9*, 3085-3088. (d) Sai, K. K. S.; O'Connor, M. J.; Klumpp, D. A., Aza-Nazarov Cyclization Cascades. *Tetrahedron Lett.* **2011**, *52*, 2195-2198. (e) Donmez, S. E.; Soydas, E.; Aydin, G.; Sahin, O.; Bozkaya, U.; Türkmen, Y. E., Aza-Nazarov Cyclization Reactions via Anion Exchange Catalysis. *Org. Lett.* **2019**, *21*, 554-558.

[25] (a) Shu, C.; Wang, Y.-H.; Shen, C.-Y.; Ruan, P.-P.; Lu, X.; Ye, L.-W., Gold-Catalyzed Intermolecular Ynamide Amination-Initiated Aza-Nazarov Cyclization: Access to Functionalized 2-Aminopyrroles. *Org. Lett.* **2016**, *18*, 3254-3257. (b) Das, S. K.; Roy, S.; Khatua, H.; Chattopadhyay, B., Ir-Catalyzed Intramolecular Transannulation/C(sp^2)–H Amination of 1,2,3,4-Tetrazoles by Electrocyclization. *J. Am. Chem. Soc.* **2018**, *140*, 8429-8433.

[26] Sakae, R.; Hirano, K.; Miura, M., Ligand-Controlled Regiodivergent Cu-Catalyzed Aminoboration of Unactivated Terminal Alkenes. *J. Am. Chem. Soc.* **2015**, *137*, 6460-6463.

[27] Thomas, A. A.; Speck, K.; Kevlishvili, I.; Lu, Z.; Liu, P.; Buchwald, S. L., Mechanistically Guided Design of Ligands that Significantly Improve the Efficiency of CuH-Catalyzed Hydroamination Reactions. *J. Am. Chem. Soc.* **2018**, *140*, 13976-13984.

[28] Youn, S. W.; Ko, T. Y.; Jang, M. J.; Jang, S. S., Silver(I)-Mediated C–H Amination of 2-Alkenylanilines: Unique Solvent-Dependent Migratory Aptitude. *Adv. Synth. Catal.* **2015**, *357*, 227-234.

[29] Shen, M.; Leslie, B. E.; Driver, T. G., Dirhodium(II)-Catalyzed Intramolecular C–H Amination of Aryl Azides. *Angew. Chem. Int. Ed.* **2008**, *47*, 5056-5059.

[30] Guan, X.; Zhu, H.; Zhao, Y.; Driver, T. G., Pd-Catalyzed Reductive Cyclization of Nitroarenes with CO_2 as the CO Source. *Eur. J. Org. Chem.* **2020**, 57-60.

Chapter 6

Coordination and Redox Chemistry of Uranyl Complexes Supported by Proton-Responsive Bipyridyl and Terpyridyl Ligands

6.1 Introduction

Nuclear fission of uranium is an attractive, green source of energy, as the methods for generating nuclear power do not directly produce carbon dioxide.[1] As of December 31, 2020, nuclear power plants have generated approximately 20 % of U.S. electricity since 1990;[2] our ability to improve the nuclear fuel cycle processes is critical to improving the sustainability of this method for energy generation. The nuclear fuel cycle involves the mining, milling, conversion, and enrichment of mined uranium ore to uranium hexafluoride (UF_6). Once enriched to U–235 UF_6, the solid is converted into nuclear fuel by heating to the gaseous form, followed by conversion to uranium dioxide (UO_2) powder. The powder is then pressed into small pellets of fuel which are loaded into 12-foot metal tubes to form fuel rods. Fuel assemblies are made by bundling the fuel rods together; the assemblies are then loaded into the reactor.[3] The addition of water begins the nuclear fission process, at which point the water is heated through the exothermicity of the fission and the resultant steam is used to turn wind turbines, thereby generating energy.

Despite these advantages, nuclear fission is currently classified as a nonrenewable energy source because there is no method for reprocessing the spent nuclear fuel inside of the fuel rods. According to the U.S. Energy Information Administration, from 1968 to 2017 in the United States alone, the number of fuel assemblies that have been discharged and stored at nuclear reactor sites across the country is 276,879.[3] Additionally, the fuel assemblies are far more radioactive after the nuclear fission process than they were at the point of assembly; for that reason, the spent nuclear fuel assemblies are stored in pools of

cooled water at reactor sites for years to prevent the release of radiation into the environment until a permanent storage facility is developed in the U.S.

The Fukushima Daiichi nuclear accident of 2011, brought about by improper cooling of spent nuclear fuel assemblies, resulted in spent fuel leaking from the fuel rods into the seawater in which they were cooling.[4] Burns and Navrotsky have since shown[5] through in-lab experimentation that the peroxides, formed from radiative water-splitting, can enhance the rate of corrosion of spent fuel rods by oxidizing uranium dioxide, the major component of the fuel rods, to the water-soluble uranyl dication $[U^{VI}O_2]^{2+}$. Additionally, they found that peroxide can complex the uranyl dication aided by the presence of sodium ions in the seawater, further enhancing its solubility in alkaline solutions. These uranyl-peroxide complexes were able to cluster through bridging interactions of the peroxide ligands, forming nanoscale cage clusters stabilized by sodium ions containing upwards of 60 uranyl ions. The ultimate conclusion from their work was that these species are thermodynamically stable, are kinetically persistent upon formation even in the absence of peroxide, and have the potential to transport uranium over long distances. For these reasons, it is critical that procedures for repurposing spent nuclear fuel are enacted through the recycling of the reacted uranium dioxide; additionally important is the fact that we must understand the chemistry of the uranyl dication and develop procedures for its capture from aqueous and non-aqueous media and its subsequent recycling.

The uranyl dication is a water-soluble cation that is made up of strong U–O bonds ($\Delta H_{U=O,gas}$ = 148 kcal mol^{-1}).[6] The reversion of uranyl back to uranium (i.e., to uranium hexafluoride in the fuel cycle) requires the cleavage of these U–O bonds; because of the robustness of these bonds, the uranyl dication demonstrates incredibly persistent resistance

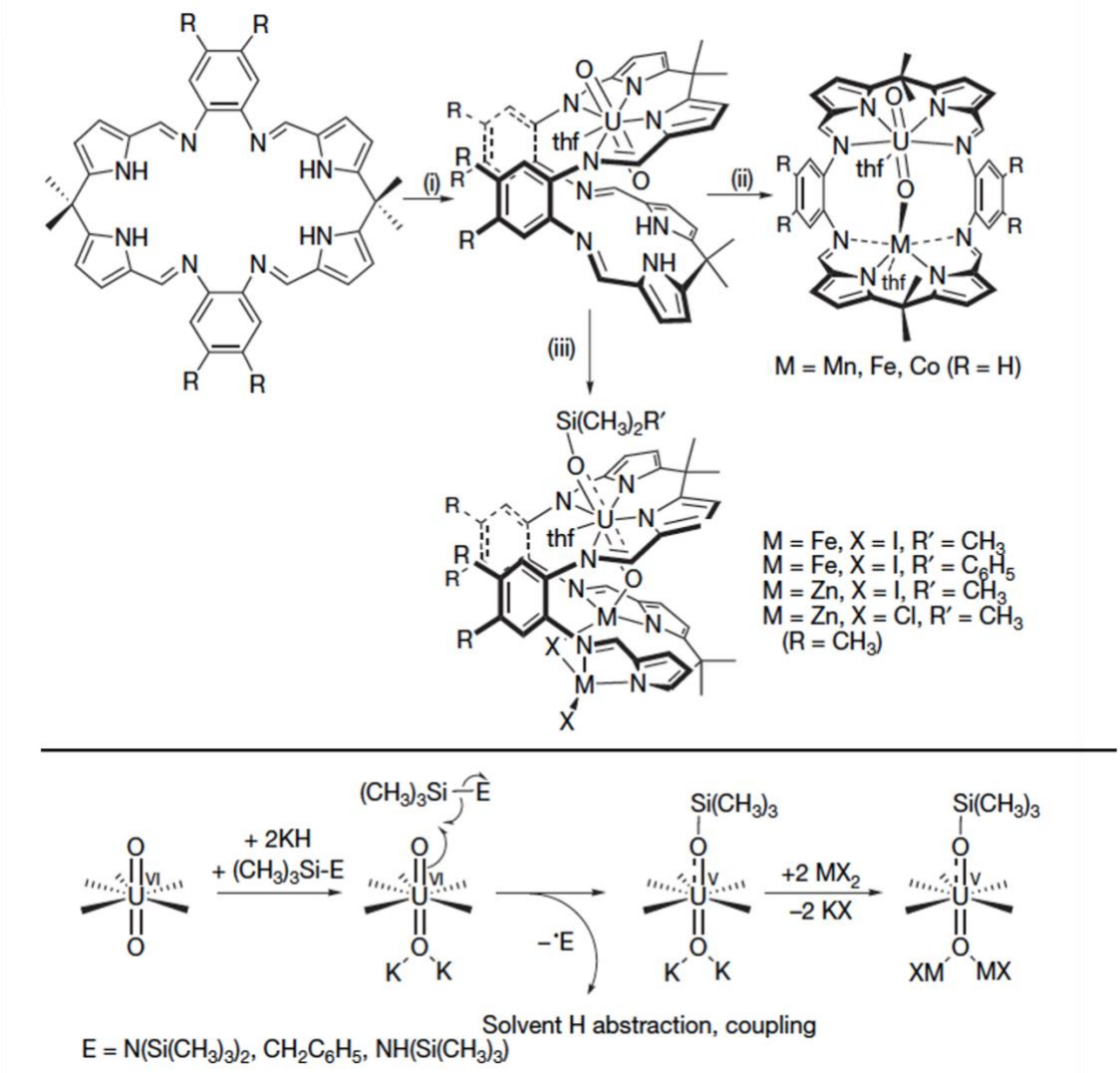

Scheme 6.1. Macrocyclic ligand and complexing of uranyl dication by Love and coworkers.[8] Adapted and reprinted by permission from Springer Nature Customer Service Centre GmbH: Springer Nature, Nature. Reduction and selective oxo group silylation of the uranyl cation, Polly L. Arnold et al., Copyright 2008.

to the cleavage of these bonds. The complexation of the uranyl dication in an organic ligand framework and subsequent functionalization of the U–O bond is a promising method toward

functionalizing the bond, thereby leading to the possibility of its eventual cleavage. Many of these attempts to functionalize the U–O bond of the uranyl dication have relied on reductive conditions since the U^{VI}/U^{V} redox couple is readily accessible.[7] The addition of electron density to the metal center should weaken the U–O bond, making the oxo ligand more Lewis basic and more prone to functionalization. If improperly stabilized, however, the $[U^{V}O_2]^{+}$ cation can readily disproportionate to give the more stable $[U^{VI}O_2]^{2+}$ and the water-insoluble uranium(IV) dioxide $[U^{IV}O_2]$.

A field dedicated to the preparation of molecular complexes of uranyl has emerged with the intention to design ligand systems which can sufficiently stabilize the reduced U^{V} form upon formation. In 2008, the groups of Arnold and Love reported one of the first instances of simultaneous single-electron reduction and selective covalent bond formation at one of the oxo groups (see Scheme 6.1).[8] This was achieved through use of an octadentate, macrocyclic iminopyrrolidine ligand scaffold which, upon complexation of uranyl, was able to bend into a conformation bearing two asymmetric binding pockets. This orientation afforded a geometry where the inner, *endo* oxo ligand was activated by addition of two potassium cations, thereby activating the other, *exo* oxo ligand toward reductive silylation in the presence of a hexamethyldisilazide (HMDS) reagent. Subsequent installation of a secondary metal, either from the HMDS reagent or added as a halide salt, into the bottom, empty pocket of the macrocycle added stabilization to the U^{V} form of the metal center. Arnold and Love have since successfully functionalized the oxo ligands of the uranyl dication through use of triarylboranes, aluminum salts, lithium metal bases, and other Lewis acidic additives.[9] Other significant work in the field is being done to probe the electrochemical reduction of the uranyl dication in organometallic complexes.[10]

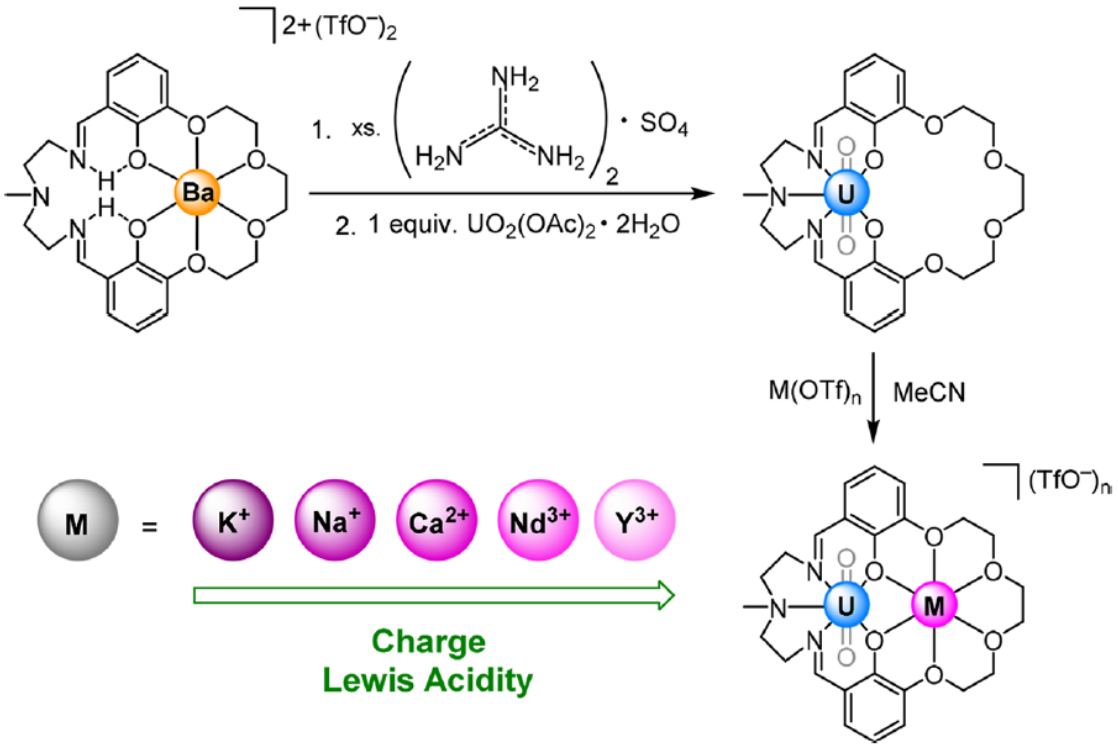

Scheme 6.2. Ligand design and uranyl complexation by Kumar et al. Reprinted with permission from Kumar, A.; Lionetti, D.; Day, V. W.; Blakemore, J. D., Redox-Inactive Metal Cations Modulate the Reduction Potential of the Uranyl Ion in Macrocyclic Complexes. *J. Am. Chem. Soc.* **2020**, *142*, 3032-3041. Copyright 2020, American Chemical Society.

Similarly, ongoing efforts in our group have revolved around the stabilization of the $[U^{V}O_2]^{+}$ cation through use of both metal and metalloid Lewis acids. In 2020, Kumar and coworkers[11] utilized a Schiff-base macrocyclic ligand designed by Reinhoudt and coworkers[12] to bind both the uranyl dication and a secondary redox-inactive Lewis acidic metal (see Scheme 6.2). They were able to synthesize a variety of different heterobimetallic complexes and investigate the modulation by the secondary Lewis acidic metal of parameters like reduction potential, λ_{max}, and k^0 as compared to the monometallic uranyl

complex as a function of pK_a. Kumar found that the adjacent Lewis acid not only stabilized the U^V form of the complex, but it shifted the reduction potential in the system to more positive potentials by 61 (±9) mV/pK_a, with trivalent redox-inactive cations imparting the strongest perturbations in all spectral and electrochemical data.

After the success of Kumar, we envisioned the implementation of a polypyridyl non-macrocyclic ligand which could also allow for complexation of the uranyl dication. In the field of water oxidation, ligands of bipyridyl- and terpyridyldicarboxylic acids (**bdcH$_2$** and **tdcH$_2$**, respectively) have been utilized to prepare complexes of ruthenium that are suitable for the catalytic oxidation of water.[13] We envisioned that these ligands would be ideal for the capture of uranyl, as **bdcH$_2$** and **tdcH$_2$** are polydentate with two ionizable carboxylic acid protons and could form neutral complexes of uranyl in a proton-responsive fashion. Additionally, we anticipated that the known resistance of these ligands to oxidation would make them suitable for interaction with the high-valent uranium center present in the uranyl dication.

In this chapter, the preparation and partial characterization of four complexes of the uranyl dication are reported, two of which bear the tetradentate bipyridyldicarboxylate (**bdc**) ligand scaffold and two of which bear the pentadentate terpyridyldicarboxylate (**tdc**) ligand scaffold. The preparation required addition of auxiliary base to the reaction conditions due to limited solubility of the diprotic ligand in each case, but the reactions to form the coordination complexes were efficient and high yielding in most cases. Solubility issues prohibited most of the usual characterization methods, but the redox properties of two of the bipyridyldicarboxylato complexes were investigated through cyclic voltammetry in dimethylformamide-based electrolyte.

6.2 Results and Discussion

6.2.1 Synthesis and Characterization of Polypyridyl Carboxylic Acid Ligands

When considering the design of a ligand scaffold for the uranyl cation, it is important to consider the high valency of the uranium metal center. Because we intended to target ligands that were non-macrocyclic for this study, it was crucial that the ligands we chose could provide enough chelators to keep uranyl in the binding pocket. Drawing from the literature, an established understanding is that uranyl prefers a pentadentate ligand system, particularly when the ligand system engenders formation of five-membered metallacycles. As a result of the success of **bdcH$_2$** and **tdcH$_2$** as ligands for ruthenium catalysts in water oxidation,[13] we chose to prepare these two ligands and their derivatives. Chart 6.1 shows the ligands that we targeted. Our efforts to search for the commercial availability of any substituted derivatives of **bpy** and **tpy** were largely unsuccessful; however, because the 4,4'-ti-*tert*-butyl-substituted bipyridyl derivative was available, we also decided to prepare 2,2'-bipyridyl-4,4'-di-*tert*-butyl-6,6'-dicarboxylic acid (**^{tbu}bdcH$_2$**). Due to the relative paucity of known substituted terpyridyl compounds, we looked to the literature for inspiration toward

Chart 6.1. Structures of each polypyridyl ligand prepared.

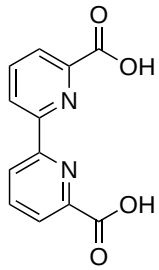

bdcH$_2$

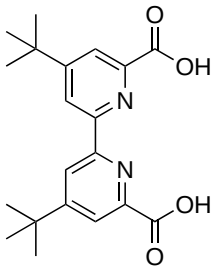

^{tbu}bdcH$_2$

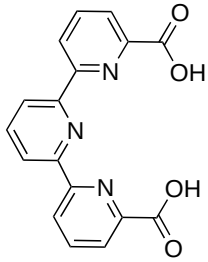

tdcH$_2$

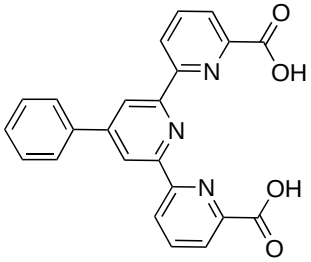

^{Ph}tdcH$_2$

the preparation of substituted terpyridyl compounds. Fortunately, we came upon a reliable, large-scale procedure for the preparation of 4'-phenyl-2,2':6',2''-terpyridyl (**^{Ph}tpy**).[14] Therefore, we were able to prepare from that precursor the 4'-phenyl-terpyridyldicarboxylic acid (**^{Ph}tdcH$_2$**) for use in the study as well.

As a result of the widespread use of this ligand scaffold, synthetic routes to access the dicarboxylic acid-substituted polypyridyl ligands were previously developed by other research groups. The most reliable route that we found in the literature involved three steps to convert terpyridyl (**tpy**) to **tdcH$_2$** (see Scheme 6.3); we applied this methodology across the bipyridyl (**bpy**) system to access **bdcH$_2$** and its derivatives, as well. The first step of the synthetic process involves conversion of **tpy** to the terpyridyl-1,1''-di-N-oxide (**tpyNO**) using *meta*-chloroperoxybenzoic acid (*m*CPBA).[15] This reaction relies on the transfer of an oxygen atom from the *peroxy* unit of *m*CPBA to each nitrogen atom on the outer rings of the **tpy** system, resulting in the formation of benzoic acid as the only byproduct. Basic workup allows for removal of benzoic acid, leaving behind the desired N-oxide in excellent yields (89–97 % across the full series) as a pure solid. The N-oxide is then subjected to trimethylsilyl cyanide (TMS–CN),[16] a cyanating reagent, to form a dicationic pyridinium O–TMS intermediate. This pyridinium ring is now appropriately activated to participate in nucleophilic aromatic substitution with the resulting cyanide ion, forming the desired C–CN bond. In the presence of benzoyl chloride, the N–O bond is cleaved, furnishing the desired terpyridyl-6,6''-dicarbonitrile (**tpyCN**). The success of this reaction varied depending on the substitution of the starting N-oxide; the electron-donating *tert*-butyl groups on the ^{tbu}bpy

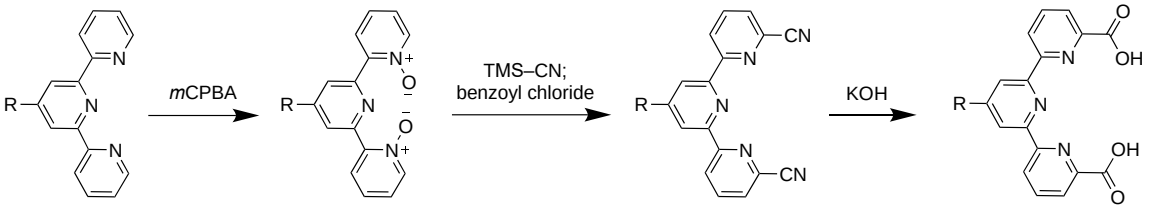

Scheme 6.3. Generic synthetic route toward the preparation of the **tdcH$_2$** scaffold.

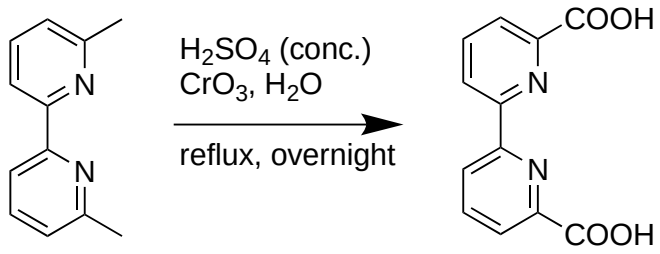

Scheme 6.4. Synthetic route to prepare **bdcH$_2$** using the Jones oxidation methodology.

ligand scaffold likely discourage the nucleophilic aromatic substitution step of the process in which the desired C–CN bond is formed (**^{tbu}bpyCN**: 46 % yield), while all other dinitrile derivatives were formed in great yields (70–91 % across the series).

The bipyridyldinitrile compounds were then subjected to base-promoted hydrolysis of the nitrile functionality using potassium hydroxide to furnish the desired dicarboxylic acid derivatives.[17] In this reaction, the dinitrile was taken up as a suspension in an ethanol/water mixture and refluxed in the presence of potassium hydroxide overnight. The resulting dicarboxylate was dissolved in water, at which point acidification caused precipitation of the desired dicarboxylic acid ligands **bdcH$_2$** and **^{tbu}bdcH$_2$**. For these ligands in particular, this reaction was very successful, giving yields > 90 % in both instances. The success of the hydrolysis in the tpy-derived ligands by this procedure was far more modest, likely attributable to the dramatic insolubility of the diamide intermediate that forms in the process.

This insolubility imparted the requirement to isolate the diamide first, and then subject it to more harsh hydrolysis conditions using a refluxing mixture of sulfuric acid and glacial acetic acid.[18] While inconvenient and lower-yielding as compared to the procedure for the analogous bpy-derived compounds, the stronger hydrolysis conditions did convert the diamide fully to the dicarboxylic acid **tdcH$_2$** and **^{Ph}tdcH$_2$** in both cases.

We also prepared **bdcH$_2$** by an alternative method. We were able to convert 6,6'-dimethyl-2,2'-bipyridyl directly to **bdcH$_2$** in one step using Jones reagent (chromium(VI) trioxide), a strong oxidant (see Scheme 6.4).[19] This pathway was attractive particularly because it could achieve the desired result in one single step; however, it was also disadvantageous due to the acute toxicity of the chromium reagents in use and the prerequisite of having to start with the dimethyl compound. Because of the lack of sources for purchasing of substituted **tpy** compounds, including the needed dimethyl derivative mentioned above, this methodology was only applied to the preparation of **bdcH$_2$**. While the preparation did furnish the desired dicarboxylic acid ligand, it did so in modest yields (55 %). Nevertheless, we obtained the pure, desired ligand from this method.

6.2.2 Synthesis and Characterization of Uranyl Polypyridyldicarboxylate Complexes

With the desired polypyridyldicarboxylic acid ligands in hand, we set out to prepare the uranyl dicarboxylate complexes. The targeted complexes can be seen in Chart 6.2. When considering the structural differences of the bpy-derived ligands as compared to the tpy-derived ligands, we anticipated that the **tdcH$_2$** ligands would coordinatively saturate uranyl, as those ligands are pentacoordinate. Because the **bdcH$_2$** ligands are only tetracoordinate, we expected the need for a fifth, auxiliary ligand to bind to the uranium metal center. This

Chart 6.2. Structure of each uranyl dicarboxylate complex prepared in this study.

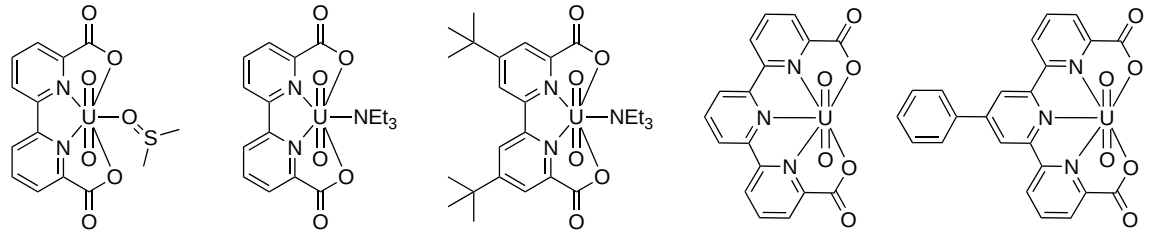

expectation was supported by a literature report from the Rao group in 2019,[20] in which they reported a crystal structure of **bdcUO$_2^{DMSO}$**. Their structure displays the uranyl cation coordinated to both nitrogen atoms, both carboxylate oxygen atoms, and one dimethylsulfoxide (DMSO) molecule, ligated through a lone pair on the oxygen atom. While this article provides crystallographic information, the authors provided neither a procedure for the preparation of this complex nor any additional characterization data. Therefore, we pursued the preparation of this complex first. The ligand **bdcH$_2$** was dissolved in DMSO, and then the uranyl acetate dihydrate precursor was added to the solution. The clear solution became vibrant yellow; after stirring overnight, the product was precipitated from solution using diethyl ether and isolated as a pale-yellow solid in quantitative yield. As hoped, the ^{1}H NMR data in d_6-DMSO show the three expected aromatic resonances in a 2:2:2 ratio, a broad 6H singlet at 2.54 ppm corresponding to bound DMSO, and the absence of the carboxylic acid protons. Unfortunately, attempts to grow crystals of **bdcUO$_2^{DMSO}$** for X-ray diffraction studies were unsuccessful.

With NMR indication of complexation, we moved on to novel complexes of uranyl which were not present in the literature. Previous work in our group toward the preparation

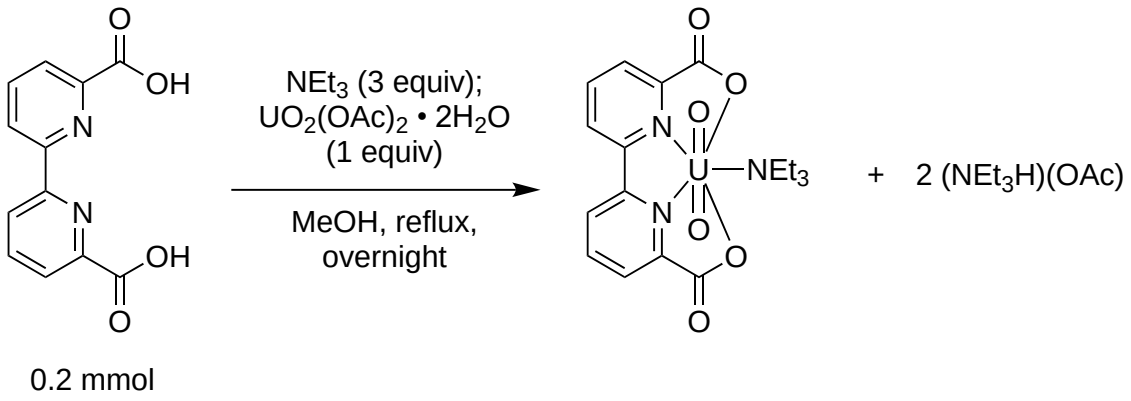

Scheme 6.5. Reaction of **bdcH$_2$** with uranyl acetate dihydrate and TEA to form **bdcUO$_2^{TEA}$**.

of molecular uranyl complexes has shown that, most often, the complexes precipitate from the reaction mixture upon formation when the reaction is performed in nonpolar organic solvents. This method, unfortunately, was not an option with the ligands discussed herein, as each of the dicarboxylic acid ligands was insoluble in all solvents except for DMSO and dimethylformamide (DMF). Therefore, performing the reactions in any nonpolar solvent was unfeasible. Initial attempts to solubilize the ligands involved heating in methanol; even at refluxing temperatures, the ligands were insoluble. It was discovered, however, that the carboxylic acid ligands became soluble in methanol upon deprotonation with triethylamine (TEA). Because of this, methanol was used as the solvent for all preparations of novel complexes. During the optimization of this reaction, it was found that using a 1:2 mixture of **bdcH$_2$** to TEA provided inconsistent results via ^{1}H NMR analysis; however, when 3 equivalents of TEA were used, the TEA-bound complex **bdcUO$_2^{TEA}$** was formed cleanly in quantitative yields as a yellow solid (see Scheme 6.5). The ^{1}H NMR data in deuterated methanol (MeOD) show the three expected aromatic resonances in a 2:2:2 ratio; a quartet and triplet at 3.24 ppm and 1.32 ppm, respectively, corresponding to the bound TEA; and the absence of the carboxylic acid protons. While attempts to grow crystals were successful

in some solvent systems, the resulting crystals were not found to be suitable for X-ray diffraction. Therefore, structural information is not yet available for this complex.

This same procedure was utilized with the ligand ^{tbu}**bdcH$_2$**; however, an off-white precipitate was present at the end of the reaction. This precipitate was collected, but characterization of the material was prevented due to insolubility of the material in DMSO. The filtrate was concentrated to provide pure ^{tbu}**bdcUO$_2^{TEA}$** as a yellow solid in a modest 50 % yield. Formation of the product was supported by ^{1}H NMR data in MeOD, which showed the two expected aromatic resonances in a 2:2 ratio; a quartet and triplet at 3.23 ppm and 1.32 ppm, respectively, corresponding to bound TEA; and the absence of the carboxylic acid protons. Similar to **bdcUO$_2^{TEA}$**, crystals of this complex that were grown were not suitable for XRD analysis.

Recent work by Mazzanti and coworkers[21] toward the preparation of uranyl bis(dipicolinate) complexes similar to those described herein discloses the formation of an insoluble dimer of the complex which could be broken up and thereby solubilized by addition of 2.2.2.cryptand. It is possible that the insoluble material that was filtered off of the reaction mixture in the preparation of ^{tbu}**bdcUO$_2^{TEA}$** was a dimerized form of the complex, where the fifth ligand bound to each uranium metal center is either the oxo-ligand or the chelating carboxylate oxygen of another complex (see Figure 6.1). Either of these complexes could be a stable, predictable side product to form if, under the reaction conditions, TEA did not bind to the uranium center; the solubility of either complex might also be expected to be diminished with respect to the TEA-bound adduct, as these tightly bound dimers would likely prevent the interaction of solvent molecules with the complex at large.

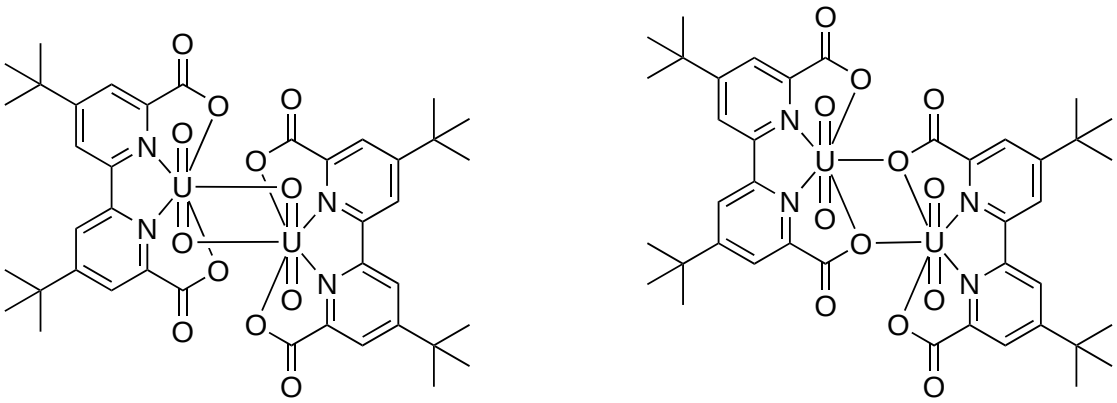

Figure 6.1. Possible dimeric structures of insoluble side product in the reaction to form ^{tbu}**bdcUO$_2$**^{TEA}.

The preparation of complexes **tdcUO$_2$** and ^{Ph}**tdcUO$_2$** were performed in a similar manner (see Scheme 6.6), such that the ligand was suspended in methanol and solubilized by the addition of TEA. The main two differences in these preparations are that they were run at room temperature and only 2 equivalents of TEA were required, since an additional auxiliary base ligand was not expected to be necessary for these ligand systems. As soon as a drop of the uranyl precursor solution was added to the stirring solution of dicarboxylate, a precipitate immediately formed. This precipitation increased as the uranyl solution was added; at the end of the addition, so much precipitate had formed that the reaction stopped stirring. In one instance, more methanol was added to the flask and the solution was heated to reflux in an attempt to solubilize the precipitate, unsuccessfully. The contents were transferred to a Büchner funnel, and the precipitate was washed with methanol to give off-white and yellow solids for **tdcUO$_2$** and ^{Ph}**tdcUO$_2$**, respectively. These solids, much like the

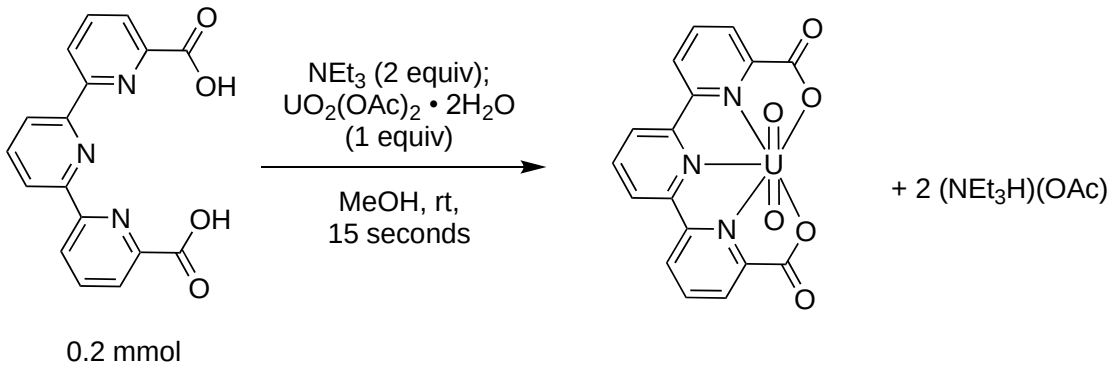

Scheme 6.6. Reaction of **tdcH$_2$** with uranyl acetate dihydrate and TEA to form **tdcUO$_2$**.

precipitated byproduct filtered off of the reaction to form **^{tbu}bdcUO$_2^{TEA}$**, are insoluble in all possible solvents, including water, DMSO, and DMF. For this reason, characterization was not pursued further.

6.2.3 Electrochemistry

In order to probe the redox properties of uranyl in these ligand systems, cyclic voltammetry was performed on **bdcUO$_2^{TEA}$** and **bdcUO$_2^{DMSO}$**. Our electrochemical study was limited to these two substrates on the basis of solubility; these experiments were run in a DMF-based electrolyte solution of tetrabutylammonium hexafluorophosphate. The voltammogram of each complex can be seen in Figure 6.2. Both voltammograms display chemically irreversible cathodic reductions near –1.3 V and –1.6 V vs. $Fc^{+/0}$ and two corresponding reoxidations near –1.3 V and –0.7 V vs. $Fc^{+/0}$. The observation of two reductive waves implies either the presence of multiple species in the electrochemical cell or the transfer of multiple electrons to the uranium metal center in the complexes. The reduction potentials are consistent with uranium-centered reductions,[11] but due to poor solubility and the reactive nature of the system, further electrochemical characterization was

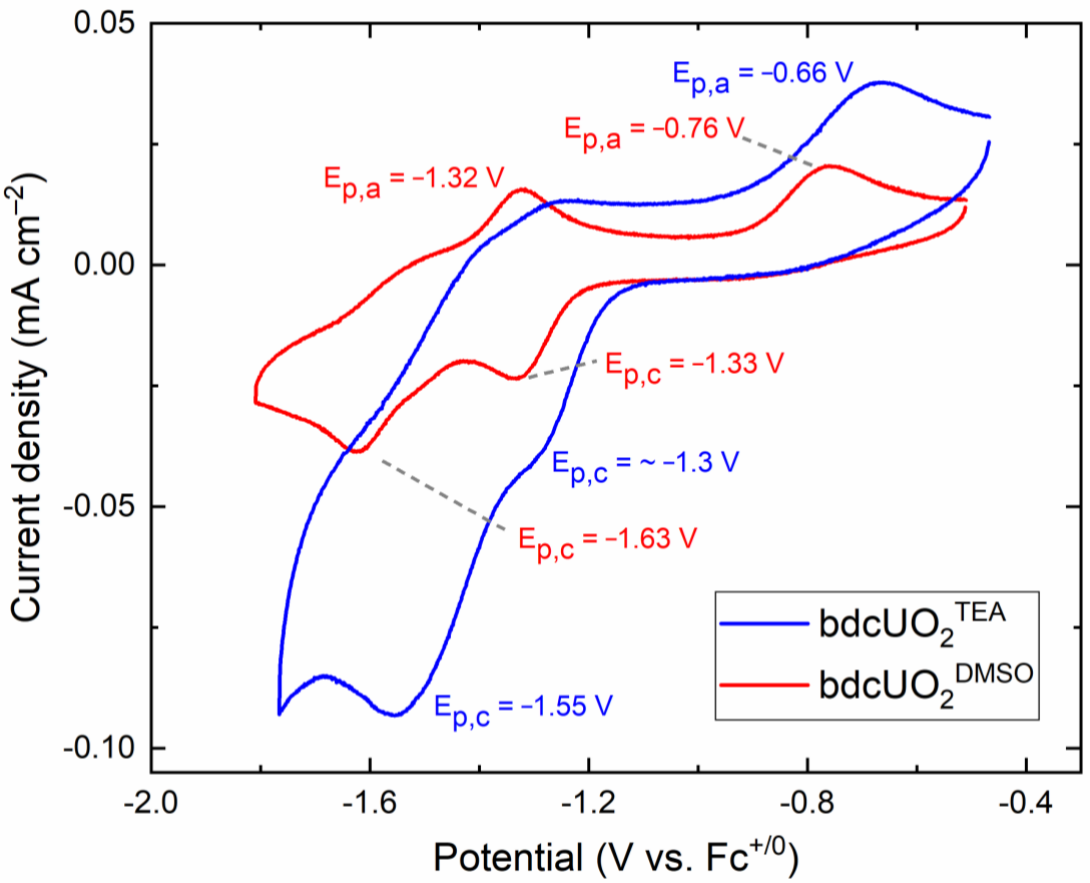

Figure 6.2. Cyclic voltammetry of **bdcUO$_2^{TEA}$** and **bdcUO$_2^{DMSO}$** in DMF. Electrolyte = 0.1 M tetrabutylammonium hexafluorophosphate. Scan rate = 100 mV/s.

not pursued. However, the observation of well-defined molecular redox chemistry suggests that bipyridyl- and terpyridyldicarboxylate platforms could be useful in the study of uranyl electrochemistry if current solubility issues could be solved through ligand derivatization.

The reductive electrochemical properties of **bdc** as a ligand were not known before this study. Many electrochemical studies have been conducted on complexes of this ligand system, but all of these studies involved only oxidative conditions. Therefore, taking the solutions shown for both complexes in Figure 6.2 and scanning further negative revealed a

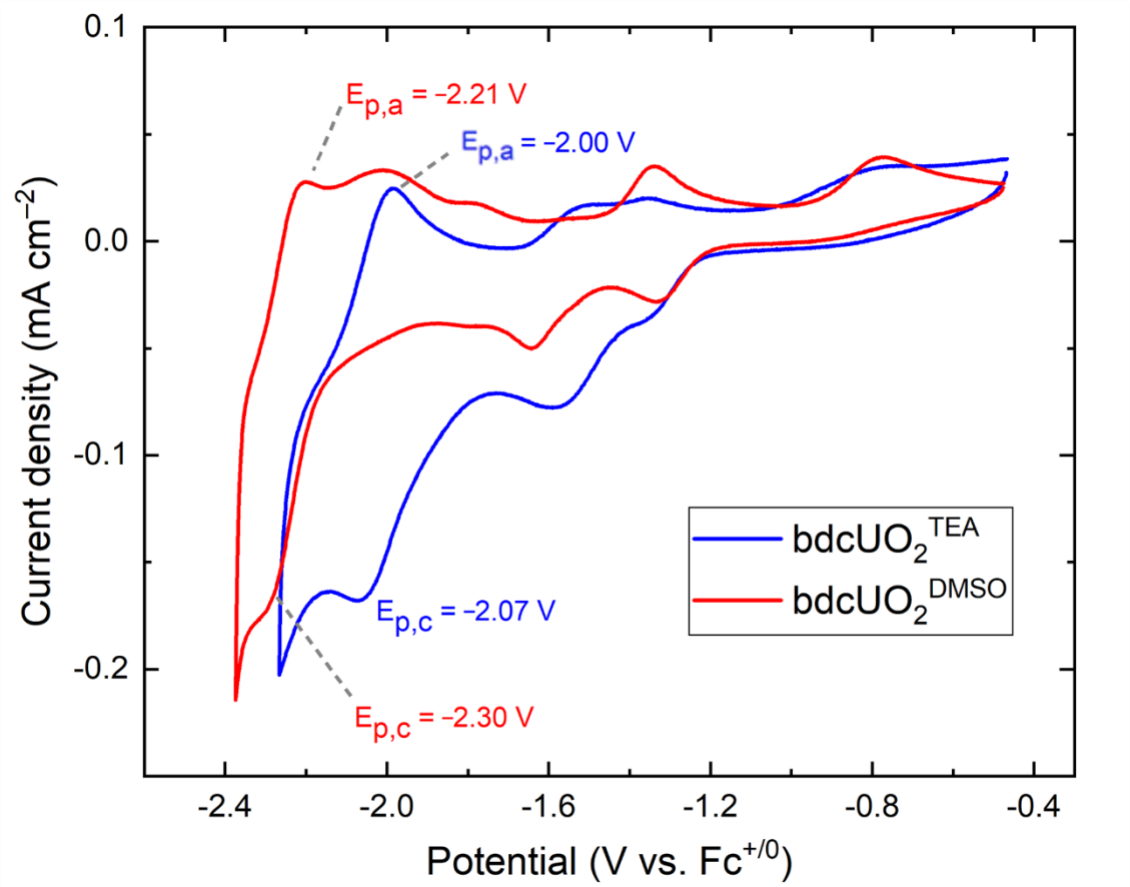

Figure 6.3. Cyclic voltammetry of **bdcUO$_2^{TEA}$** and **bdcUO$_2^{DMSO}$** in DMF at a more negative potential scan. Electrolyte = 0.1 M tetrabutylammonium hexafluorophosphate. Scan rate = 100 mV/s.

chemically reversible reduction that was assigned to the 1e$^-$ reduction of the conjugated bipyridyl framework ($E_{p,c}$ = –2.07 V or –2.30 V, see Figure 6.3). Further support of the assignment of this feature to ligand reduction comes from preliminary electrochemical studies performed in our group by summer undergraduate student Gabriel Benitez (not shown) in which the water oxidation ruthenium complexes of **bdc** and **tdc** were prepared and investigated electrochemically under reductive conditions. These voltammograms showed one chemically reversible feature near those shown in Figure 6.3. To ensure that the

event did not correspond to a $Ru^{II/I}$ event, analogous zinc complexes of **bdc** and **tdc** were also prepared and analyzed, finding the same potential for complexes of both Ru and Zn. Additionally, the similarity between the reduction potentials of the ligand in each complex of Figure 6.3 suggests that the orbitals housing the electron upon reduction are similar here. Notably, the potential of **bpy** as a ligand is more positive when bound to metals than that of the bipyridyldicarboxylato ligand (as described in Chapter 1, *vide supra*). This observation is attributable to the presence of two electron-donating anionic carboxylate groups which push the reduction potential to more negative values.

6.3 Conclusion

Capture and activation of the uranyl dication from organic solution is an exciting area in the field of coordination chemistry, as it could contribute to improvement of the sustainability of the nuclear fuel cycle. Our efforts toward the preparation of polypyridyl dicarboxylic acid ligands were largely successful, as we made two compounds from the literature (**bdcH$_2$** and **tdcH$_2$**) as well as two new compounds for ligation of uranyl (**^{tBu}bdcH$_2$** and **^{Ph}tdcH$_2$**). The two bipyridyl-derived ligands successfully bound uranyl and were soluble in polar solvents methanol, DMSO, and DMF; while attempts to grow crystals suitable for crystallographic analysis were unsuccessful, the complexes could be characterized by ^{1}H NMR and cyclic voltammetry. Although solubility issues precluded with full characterization of the complexes bearing terpyridyl-derived ligands, the material could potentially be characterized by mass spectrometry in future work. Further efforts in characterization may be pursued in future work on these complexes and other new derivatives based on these frameworks.

6.4 Experimental Details

6.4.1 General Considerations

All manipulations were carried out or under an N_2 atmosphere using standard Schlenk techniques, unless otherwise noted. All solvents were of commercial grade and dried over activated alumina using a PPT Glass Contour (Nashua, NH, USA) solvent purification system prior to use, and were stored over molecular sieves. All chemicals were obtained from major commercial suppliers and used as received after extensive drying. The compound 2,2'-bipyridyl-1,1''-di-N-oxide (**bpyNO**) was previously made in our lab.[22]

Deuterated solvents for NMR studies were purchased from Cambridge Isotope Laboratories (Tewksbury, MA, USA); CD_3CN was dried with CaH_2 and stored over molecular sieves, and C_6D_6 was dried over sodium/benzophenone. ^1H, ^{13}C, ^{19}F, and ^{31}P NMR spectra were collected with 400 or 500 MHz Bruker spectrometers and were referenced to the residual protio-solvent signal in the cases of ^1H and ^{13}C unless otherwise noted.[23] Chemical shifts (δ) and coupling constants (J) are reported in ppm and Hz, respectively.

Electrochemical experiments were carried out in a N_2-filled glovebox in dry, degassed DMF. 0.10 M tetra(n-butylammonium) hexafluorophosphate [($[nBu_4N]^+[PF_6]^-$); Sigma-Aldrich, electrochemical grade] served as the supporting electrolyte. Measurements were made with a Gamry Reference 600+ Potentiostat/Galvanostat using a standard three-electrode configuration. The working electrode was the basal plane of highly oriented pyrolytic graphite (HOPG) (GraphiteStore.com, Buffalo Grove, Ill.; surface area: 0.09 cm^2), and the counter electrode and reference electrode were a platinum wire (Kurt J. Lesker, Jefferson Hills, PA; 99.99%, 0.5 mm diameter). Ferrocene (Sigma Aldrich; twice-sublimed) was added to electrolyte solution prior to the beginning of each experiment; the midpoint

potential of the ferrocenium/ferrocene couple (denoted as $Fc^{+/0}$) served as an external standard for comparison of the recorded potentials. Concentrations of analyte for CV were ca. 1 mM unless otherwise noted.

Regarding special safety precautions needed for this work, depleted uranium is a weak alpha-particle emitter; all manipulations of U-containing materials should be carried out in a laboratory equipped with appropriate radiation safety protocols.

6.4.2 Synthesis and Characterization of Ligands and Uranyl Complexes

Synthesis of 4'-phenyl-2,2':6',2"-terpyridyl (^{Ph}tpy)

The compound 4'-phenyl-2,2':6',2"-terpyridyl was prepared according to an existing literature procedure with minor adjustments.[14] To a solution of benzaldehyde (1 equiv.) in 190-proof ethanol (0.2 M) was added acetylpyridine (2 equiv.). Solid KOH pellets (2.5 equiv.) were added to the solution and stirred until dissolved, at which point $NH_4OH_{(aq)}$ (5 mol %) was added. The solution was left to stir at room temperature for 4 hours. The precipitate was then collected via vacuum filtration and washed with water and ethanol. The product was crystallized by taking up in hot methanol, adding chloroform dropwise until dissolved, cooling at –20 °C, and collecting the precipitate.

^{Ph}tpy. Yield: 68 %. ^{1}H NMR (400 MHz, $CDCl_3$) δ (ppm): 8.75 (s, 2H), 8.74 (ddd, 2H, $^3J_{H,H}$ = 4.8 Hz, $^4J_{H,H}$ = 1.8, $^4J_{H,H}$ = 0.9), 8.68 (dt, 2H, $^3J_{H,H}$ = 8.0 Hz, $^4J_{H,H}$ = 1.1 Hz), 7.95–7.86 (m, 4H), 7.52 (ddt, 2H, $^3J_{H,H}$ = 8.1 Hz, $^3J_{H,H}$ = 6.6, $^4J_{H,H}$ = 1.1), 7.48–7.43 (m, 1H), 7.36 (ddd, 2H, $^3J_{H,H}$ = 7.5 Hz, $^3J_{H,H}$ = 4.8, $^4J_{H,H}$ = 1.2).

Synthesis of Polypyridyl N-Oxide Intermediate

The polypyridyl N-oxide ligands were prepared according to an existing literature procedure with minor adjustments.[15] To a solution of the corresponding polypyridyl compound (1

equiv.) in DCM (0.1 M) was added a solution of *m*-chloroperbenzoic acid (3.75 equiv.) in DCM (0.1 M). The solution was refluxed overnight. The next day, the solution was cooled, the organic layer was washed with 5 % sodium carbonate, and the water layer was then extracted with ethyl acetate. The organic layers were combined, dried with $MgSO_4$, and concentrated *in vacuo* to give the desired, N-oxide product. In some instances, the colorless solid required further purification by washing with acetone.

^{tbu}bpyNO. Yield: 93 %. ^{1}H NMR (400 MHz, $CDCl_3$) δ (ppm): 8.30 (d, 2H, $^3J_{H,H}$ = 6.9 Hz), 7.71 (d, 2H, $^4J_{H,H}$ = 2.8 Hz), 7.36 (dd, 2H, $^3J_{H,H}$ = 7.0 Hz, $^4J_{H,H}$ = 2.8 Hz), 1.35 (s, 18H).

tpyNO. Yield: 97 %. ^{1}H NMR (400 MHz, $CDCl_3$) δ (ppm): 8.94 (d, 2H, $^3J_{H,H}$ = 7.9 Hz), 8.37 (dd, 2H, $^3J_{H,H}$ = 6.5 Hz, $^4J_{H,H}$ = 1.3 Hz), 8.21 (dd, 2H, $^3J_{H,H}$ = 8.0 Hz, $^4J_{H,H}$ = 2.2 Hz), 8.00 (t, 1H, $^3J_{H,H}$ = 8.0 Hz), 7.41 (td, 2H, $^3J_{H,H}$ = 7.8 Hz, $^4J_{H,H}$ = 1.3 Hz), 7.32 (ddd, 2H, $^3J_{H,H}$ = 7.5 Hz, $^3J_{H,H}$ = 6.5 Hz, $^4J_{H,H}$ = 2.2 Hz).

^{Ph}tpyNO.Yield: 89 %. ^{1}H NMR (400 MHz, $CDCl_3$) δ (ppm): 9.21 (s, 2H), 8.40 (dd, 2H, $^3J_{H,H}$ = 6.5 Hz, $^4J_{H,H}$ = 1.3 Hz), 8.23 (dd, 2H, $^3J_{H,H}$ = 8.1 Hz, $^4J_{H,H}$ = 2.2 Hz), 7.88–7.80 (m, 2H), 7.54–7.40 (m, 5H), 7.34 (ddd, 2H, $^3J_{H,H}$ = 7.6 Hz, $^3J_{H,H}$ = 6.4 Hz, $^4J_{H,H}$ = 2.2 Hz).

Synthesis of Polypyridyl Dinitrile Intermediate

The polypyridyl dinitrile ligands were prepared according to an existing literature procedure with minor adjustments.[16] To a suspension of the corresponding polypyridyl N-oxide (1 equiv.) in DCM (0.1 M) was added trimethylsilyl cyanide (10 equiv.). The homogeneous solution was allowed to stir at refluxing temperatures for 5 minutes, at which point benzoyl chloride (4 equiv.) was added. The solution was refluxed overnight. The next day, the mixture was neutralized with a 10 % potassium carbonate solution and the aqueous layer was extracted with chloroform. The organic layers were combined and dried with $MgSO_4$

and concentrated *in vacuo*. The resulting residue was washed with acetonitrile and dried to give the pure dinitrile product as a colorless solid.

bpyCN. Yield: 72 %. ^{1}H NMR (400 MHz, $CDCl_3$) δ (ppm): 8.72 (dd, 2H, $^{3}J_{H,H}$ = 8.2 Hz, $^{4}J_{H,H}$ = 1.3 Hz), 8.02 (t, 2H, $^{3}J_{H,H}$ = 7.9 Hz), 7.78 (dd, 2H, $^{3}J_{H,H}$ = 7.6 Hz, $^{4}J_{H,H}$ = 1.2 Hz). $^{13}C\{^{1}H\}$ NMR (126 MHz, $CDCl_3$) δ (ppm): 155.69, 138.55, 133.56, 129.23, 124.81, 117.18.

^{tbu}bpyCN. Yield: 46 %. ^{1}H NMR (400 MHz, $CDCl_3$) δ (ppm): 8.67 (d, 2H, $^{4}J_{H,H}$ = 1.8 Hz), 7.74 (d, 2H, $^{4}J_{H,H}$ = 1.8 Hz), 1.42 (s, 18H).

tpyCN. Yield: 70 %. ^{1}H NMR (400 MHz, $CDCl_3$) δ (ppm): 8.82 (dd, 2H, $^{3}J_{H,H}$ = 8.2 Hz, $^{4}J_{H,H}$ = 1.1 Hz), 8.57 (d, 2H, $^{3}J_{H,H}$ = 7.8 Hz), 8.08-7.97 (m, 3H), 8.00 (t, 1H, $^{3}J_{H,H}$ = 8.0 Hz), 7.75 (dd, 2H, $^{3}J_{H,H}$ = 7.6 Hz, $^{4}J_{H,H}$ = 1.1 Hz).

^{Ph}tpyCN. Yield: 91 %. ^{1}H NMR (400 MHz, $CDCl_3$) δ (ppm): 8.87 (dd, 2H, $^{3}J_{H,H}$ = 8.1 Hz, $^{4}J_{H,H}$ = 1.1 Hz), 8.83 (s, 2H), 8.03 (t, 2H, $^{3}J_{H,H}$ = 7.9 Hz), 7.96–7.87 (m, 2H), 7.77 (dd, 2H, $^{3}J_{H,H}$ = 7.6 Hz, $^{4}J_{H,H}$ = 1.0 Hz), 7.63–7.44 (m, 5H).

Synthesis of Bipyridyldicarboxylic Acid Ligands $bdcH_2$ and $^{tbu}bdcH_2$

The bipyridyldicarboxylic acid ligands were prepared using one of two different methods. These preparations were utilized from existing literature procedures with minor adjustments.

Method A: Base-Promoted Nitrile Hydrolysis[17]

To a solution of the corresponding bipyridyldinitrile (1 equiv.) in 180 proof ethanol (0.05 M) was added a solution of potassium hydroxide (10 equiv.) in water (3.7 M). The reaction mixture was refluxed overnight. The next day, the solvent was evaporated *in vacuo* and the resulting residue was dissolved in the minimal amount of water and the pH was adjusted to ca. 4 with 1 M HCl. The white precipitate was removed by filtration and washed with cold water and acetonitrile to give the pure product as a colorless solid.

Note: The ^{1}H NMR spectrum of **bdcH$_2$** shows contamination of the intermediate diamide product. For **^{tbu}bdcH$_2$**, the diamide was also present in the spectral data. Subsequent subjection of the crude material to these hydrolysis conditions for another 24 hours resulted in complete conversion to the desired product.

Method B: Jones Oxidation of 6,6'-Dimethyl-2,2'-Bipyridyl[19]

To a solution of concentrated sulfuric acid cooled by an ice bath was added 6,6'-dimethyl-2,2'-bipyridyl (1 equiv., 0.27 M). Chromium(VI) trioxide (6 equiv.) was added slowly to the stirring solution, and the mixture was allowed to stir at room temperature for 24 hours. The next day, ice was added to the solution until a precipitate formed. The solid was collected via vacuum filtration and washed sequentially with water, methanol, and acetone.

bdcH$_2$. Yield (Method A): 97 %. Yield (Method B): 55 %. ^{1}H NMR (400 MHz, d_6-DMSO) δ (ppm): 13.31 (bs, 2H), 8.75 (d, 2H, $^{3}J_{H,H}$ = 7.7 Hz), 8.22–8.10 (m, 4H).

^{tbu}bdcH$_2$. Yield (Method A): 91 %. ^{1}H NMR (400 MHz, d_6-DMSO) δ (ppm): 13.29 (bs, 2H), 8.75 (d, 2H, $^{4}J_{H,H}$ = 1.6 Hz), 8.12 (d, 2H, $^{4}J_{H,H}$ = 1.9 Hz), 1.39 (s, 18H). ^{13}C{^{1}H} NMR (126 MHz, d_6-DMSO) δ (ppm): 166.14, 162.34, 154.82, 148.15, 121.86, 121.07, 35.03, 30.17.

Synthesis of Terpyridyldicarboxylic Acid Ligands tdcH$_2$ and ^{Ph}tdcH$_2$

The terpyridyldicarboxylic acid ligands were prepared according to an existing literature procedure with minor adjustments.[18] To a solution of the corresponding terpyridyldinitrile (1 equiv.) in 180 proof ethanol (0.05 M) was added a solution of potassium hydroxide (10 equiv.) in water (3.7 M). The reaction mixture was refluxed overnight. The next day, a white precipitate was present. The solvent was evaporated *in vacuo* and the resulting residue was dissolved in the minimal amount of water and the pH was adjusted to ca. 1 with 1 M HCl. The resulting white precipitate was removed by filtration and analyzed via ^{1}H NMR. In all

instances, a mixture of diamide and dicarboxylic acid was obtained. This crude mixture was taken up in 1:1 H_2SO_4/CH_3COOH (0.1 M with respect to starting amount of dinitrile) and refluxed at 140 °C. The resulting black mixture was poured over ice and a white precipitate formed, which was filtered off and washed with water and acetonitrile to give the pure product as an off-white solid.

tdcH$_2$. Yield: 74 %. ^{1}H NMR (400 MHz, d_6-DMSO) δ (ppm): 13.31 (bs, 2H), 8.87 (dd, 2H, $^3J_{H,H}$ = 7.8 Hz, $^4J_{H,H}$ = 1.3 Hz), 8.65 (d, 2H, $^3J_{H,H}$ = 7.8 Hz), 8.21 (t, 3H, $^3J_{H,H}$ = 7.8 Hz), 8.15 (dd, 2H, $^3J_{H,H}$ = 7.7 Hz, $^4J_{H,H}$ = 1.3 Hz).

^{Ph}tdcH$_2$. Yield: 39 %. ^{1}H NMR (400 MHz, d$_6$-DMSO) δ (ppm): 8.96–8.91 (m, 4H), 8.25 (t, 2H, $^3J_{H,H}$ = 7.7 Hz), 8.21–8.18 (m, 2H), 7.98 (d, 2H, $^3J_{H,H}$ = 7.4 Hz), 7.66 (t, 2H, $^3J_{H,H}$ = 7.4 Hz), 7.59 (dd, 1H, $^3J_{H,H}$ = 8.4 Hz, $^3J_{H,H}$ = 6.0 Hz).

Synthesis of bdcUO$_2^{TEA}$ Complexes

To a refluxing slurry of ligand (0.2 mmol) in methanol (ca. 10 mL) was added triethylamine (3 equiv.), at which point the slurry became mostly homogeneous. A solution of uranyl acetate dihydrate (1 equiv.) in the minimum amount of methanol was added to the stirring solution, turning the solution vibrant yellow in color. The solution was allowed to reflux overnight. The next day, the still-homogeneous solution was pipet-filtered to remove any insolubles. The filtrate was concentrated to yield the pure product as a yellow solid.

bdcUO$_2^{TEA}$. Yield: Quantitative. ^{1}H NMR (500 MHz, MeOD) δ (ppm): 9.04 (d, 2H, $^3J_{H,H}$ = 7.9 Hz), 8.70 (d, 2H, $^3J_{H,H}$ = 7.6 Hz), 8.62 (t, 2H, $^3J_{H,H}$ = 7.8 Hz), 3.24 (q, 9H, $^3J_{H,H}$ = 7.3 Hz), 1.32 (t, 13H, $^3J_{H,H}$ = 7.2 Hz). ^{13}C{^{1}H} NMR (126 MHz, MeOD) δ (ppm): 174.37, 158.45, 158.35, 143.81, 128.45, 126.88, 47.87, 9.21.

^{tbu}bdcUO$_2^{TEA}$. Yield: 50 %. ^{1}H NMR (500 MHz, MeOD) δ (ppm): 9.11 (s, 2H), 8.76 (s, 2H), 3.23 (q, 6H, $^3J_{H,H}$ = 7.2 Hz), 1.64 (s, 18H), 1.32 (t, 9H, $^3J_{H,H}$ = 7.2 Hz).

Synthesis of bdcUO$_2^{DMSO}$ Complex

To a solution of bdcH$_2$ (0.2 mmol) in the minimum amount of dimethylsulfoxide in a 20-mL scintillation vial was added uranyl acetate dihydrate (1 equiv.) as a solid, turning the solution vibrant yellow in color. The solution was allowed to stir overnight. The next day, the still-homogeneous solution was transferred to an Erlenmeyer flask and flooded with ca. 400 mL diethyl ether. Parafilm was added to the flask and it was placed in the 6 °C freezer. The pale yellow precipitate was collected via filtration and washed with diethyl ether. The pure product was collected from the filter paper as a pale yellow solid.

bdcUO$_2^{DMSO}$. Yield: Quantitative. ^{1}H NMR (500 MHz, d_6-DMSO) δ (ppm): 9.27 (d, 2H, $^3J_{H,H}$ = 7.9 Hz), 8.76 (t, 2H, $^3J_{H,H}$ = 7.8 Hz), 8.68 (d, 2H, $^3J_{H,H}$ = 7.7 Hz), 2.54 (s, 6H, $^3J_{H,H}$ = 7.3 Hz).

Synthesis of tdcUO$_2$ Complexes

To a round-bottom flask was added the ligand (0.2 mmol) and methanol (ca. 10 mL). If the ligand was insoluble, triethylamine (2 equiv.) was added to solubilize the ligand. The solution was stirred at room temperature and a solution of uranyl acetate dihydrate in the minimum amount of methanol was made. Upon dropwise addition of this solution to the ligand, a precipitate formed. This precipitation continued until all uranyl acetate dihydrate solution was added, over the course of approximately 15 seconds. The reaction was brought to reflux in attempt to dissolve the solid, which was unsuccessful. The reaction was cooled, and the precipitate was collected and washed with methanol. Unfortunately, all tdcUO$_2$

complexes were insoluble in every available solvent, including water. For that reason, any characterization was impossible.

tdcUO$_2$. Yield (based on mass of isolated off-white precipitate): 73 %.

^{Ph}tdcUO$_2$. Yield (based on mass of isolated yellow precipitate): Quantitative.

6.5 Acknowledgements

The authors thank Sarah Neuenswander for assistance with NMR spectroscopy, as well as Julie Leseberg, Riddhi Golwankar, and Christian Nilles for assistance with cyclic voltammetry. The authors also acknowledge the U.S. National Institutes of Health for support of the NMR instrumentation used in this study (Grants S10OD016360 and S10RR024664). This work was supported by the US Department of Energy, Office of Science, Office of Basic Energy Sciences through the Early Career Research Program (DE-SC0019169). Preliminary synthesis and characterization of the organic ligands discussed in this chapter was assisted by Gabriel Benitez and was supported financially by the US National Science Foundation through the NSF REU Program in Chemistry at the University of Kansas (CHE-1950293).

6.6 References

[1] *Nuclear explained: Nuclear power and the environment*; U.S. Energy Information Administration: Washington, DC, 2020. https://www.eia.gov/energyexplained/nuclear/nuclear-power-and-the-environment.php (accessed 2021-11-02).

[2] *Nuclear explained: Nuclear power plants*; U.S. Energy Information Administration: Washington, DC, 2021. https://www.eia.gov/energyexplained/nuclear/nuclear-power-plants.php

[3] *Nuclear explained: The nuclear fuel cycle*; U.S. Energy Information Administration: Washington, DC, 2021. https://www.eia.gov/energyexplained/nuclear/the-nuclear-fuel-cycle.php

[4] Augustyn, A. *Fukushima accident*; Britannica, April 20, 2011. https://www.britannica.com/event/Fukushima-accident

[5] Armstrong, C. R.; Nyman, M.; Shvareva, T.; Sigmon, G. E.; Burns, P. C.; Navrotsky, A., Uranyl peroxide enhanced nuclear fuel corrosion in seawater. *Proc. Natl. Acad. Sci. U.S.A.* **2012,** *109*, 1874-1877.

[6] Meinrath, G., Coordination of uranyl(VI) carbonate species in aqueous solutions. *J. Radioanal. Nucl. Chem.* **1996**, *211*, 349-362.

[7] Cowie, B. E.; Purkis, J. M.; Austin, J.; Love, J. B.; Arnold, P. L., Thermal and Photochemical Reduction and Functionalization Chemistry of the Uranyl Dication, $[U^{VI}O_2]^{2+}$. *Chem. Rev.* **2019,** *119*, 10595-10637.

[8] Arnold, P. L.; Patel, D.; Wilson, C.; Love, J. B., Reduction and selective oxo group silylation of the uranyl dication. *Nature* **2008,** *451*, 315-317.

[9] (a) Bell, N. L.; Shaw, B.; Arnold, P. L.; Love, J. B., Uranyl to Uranium(IV) Conversion through Manipulation of Axial and Equatorial Ligands. *J. Am. Chem. Soc.* **2018,** *140*, 3378-3384. (b) Zegke, M.; Nichol, G. S.; Arnold, P. L.; Love, J. B., Catalytic one-electron reduction of uranyl(VI) to Group 1 uranyl(V) complexes *via* Al(III) coordination. *Chem. Comm.* **2015,** *51*, 5876-5879. (c) Arnold, P. L.; Pécharman, A.-F.; Hollis, E.; Yahia, A.; Maron, L.; Parsons, S.; Love, J. B., Uranyl oxo activation and functionalization by metal cation coordination. *Nat. Chem.* **2010,** *2*, 1056-1061.

[10] (a) Niklas, J. E.; Hardy, E. E.; Gorden, A. E. V., Solid-state structural elucidation and electrochemical analysis of uranyl naphthylsalophen. *Chem. Comm.* **2018,** *54*, 11693-11696. (b) Coughlin, E. J.; Qiao, Y.; Lapsheva, E.; Zeller, M.; Schelter, E. J.; Bart, S. C., Uranyl Functionalization Mediated by Redox-Active Ligands: Generation of O–C Bonds via Acylation. *J. Am. Chem. Soc.* **2019,** *141*, 1016-1026. (c) Lewis, A. J.; Yin, H.; Carroll, P. J.; Schelter, E. J., Uranyl-oxo coordination directed by non-covalent interactions. *Dalton Trans.* **2014,** *43*, 10844-10851.

[11] Kumar, A.; Lionetti, D.; Day, V. W.; Blakemore, J. D., Redox-Inactive Metal Cations Modulate the Reduction Potential of the Uranyl Ion in Macrocyclic Complexes. *J. Am. Chem. Soc.* **2020,** *142*, 3032-3041.

[12] (a) Van Staveren, C. J.; Fenton, D. E.; Reinhoudt, D. N.; Van Eerden, J.; Harkema, S., Co-complexation of urea and UO_2^{2+} in a Schiff base macrocycle: a mimic of an enzyme binding site. *J. Am. Chem. Soc.* **1987,** *109*, 3456-3458. (b) Van Staveren, C. J.; Van

Eerden, J.; Van Veggel, F. C. J. M.; Harkema, S.; Reinhoudt, D. N., Cocomplexation of neutral guests and electrophilic metal cations in synthetic macrocyclic hosts. *J. Am. Chem. Soc.* **1988,** *110*, 4994-5008.

[13] (a) Duan, L.; Wang, L.; Inge, A. K.; Fischer, A.; Zou, X.; Sun, L., Insights into Ru-Based Molecular Water Oxidation Catalysts: Electronic and Noncovalent Interaction Effects on Their Catalytic Activities. *Inorg. Chem.* **2013**, *52*, 7844-7852. (b) Duan, L.; Bozoglian, F.; Mandal, S.; Stewart, B.; Privalov, T.; Llobet, A.; Sun, L., A molecular ruthenium catalyst with water oxidation activity comparable to that of photosystem II. *Nat. Chem.* **2012**, *4*, 418-423. (c) Richmond, C. J.; Matheu, R.; Poater, A.; Falivene, L.; Benet-Buchholz, J.; Sala, X.; Cavallo, L.; Llobet, A., Supramolecular water oxidation with Ru−bda-based catalysts. *Chem. Eur. J.* **2014**, *20*, 17282-17286. (d) Matheu, R.; Ertem, M. Z.; Benet-Buchholz, J.; Coronado, E.; Batista, V. S.; Sala, X.; Llobet, A., Intramolecular proton transfer boosts water oxidation catalyzed by a Ru complex. *J. Am. Chem. Soc*. **2015**, *137*, 10786-10795. (e) Matheu, R.; Neudeck, S.; Meyer, F.; Sala, X.; Llobet, A., Foot of the wave analysis for mechanistic elucidation and benchmarking applications in molecular water oxidation catalysis. *ChemSusChem* **2016**, *9*, 3361-3369.

[14] This experiment was adapted from “Inorganic Experiments, Third Edition”. Housecroft, C. E.; Constable, E. C.; Dunphy, E. L. Wiley-VCH Verlag GmbH & Co. KGaA, Weinheim, 2010.

[15] Thummel, R. P.; Jahng, Y., N-Oxides of 2,2':6',2''-terpyridine. *J. Org. Chem.* **1985**, *50*, 3636-3638.

[16] Mukkala, V.-M.; Sund, C.; Kwiatkowski, M.; Pasanen, P.; Högberg, M.; Kankare, J.; Takalo, H., New Heteroaromatic Complexing Agents and Luminescence of Their Europium(III) and Terbium(III) Chelates. *Helv. Chim. Acta* **1992**, *75*, 1621-1632.

[17] Jalba, A.; Levitre, G.; Keipour, H.; Lauzon, S.; Ollevier, T., New chiral bis(oxazolinyl)bipyridine ligands and application in the iron catalyzed asymmetric hydrosilylation of ketones. *Fr.-Ukr. J. Chem.* **2015**, *3*, 44-53.

[18] 1. Galaup, C.; Couchet, J.-M.; Bedel, S.; Tisnès, P.; Picard, C., Direct Access to Terpyridine-Containing Polyazamacrocycles as Photosensitizing Ligands for Eu(III) Luminescence in Aqueous Media. *J. Org. Chem.* **2005**, *70*, 2274–2284

[19] Yazdani, S.; Silva, B. E.; Cao, T. C.; Rheingold, A. L.; Grotjahn, D. B., X-ray crystallography and electrochemistry reveal electronic and steric effects of phosphine and phosphite ligands in complexes RuII(κ^4-bda)(PR_3)$_2$ and RuII(κ^3-bda)(PR_3)$_3$ (bda = 2,2′-bipyridine-6,6′-dicarboxylato). *Polyhedron* **2019,** *161*, 63-70.

[20] Yang, Y.; Zhang, Z.; Yang, L.; Liu, J.; Xu, C.; Luo, S.; Rao, L., Complexation of U(VI) with BiPDA, DmBiPDA, and PhenDA: Comparison on Structures and Binding Strengths in Aqueous and DMSO/20%(v)H_2O Solutions. *Inorg. Chem.* **2019**, *58*, 6064-6074.

[21] Faizova, R.; Farzaneh, F.-T.; Chauvin, A.-S.; Mazzanti, M., Synthesis and Characterization of Water Stable Uranyl(V) Complexes. *Angew. Chem. Int. Ed.* **2021**, *60*, 8227-8235.

[22] Moore, W. N. G.; Henke, W. C.; Lionetti, D.; Day, V. W.; Blakemore, J. D., Single-Electron Redox Chemistry on the [Cp*Rh] Platform Enabled by a Nitrated Bipyridyl Ligand. *Molecules* **2018,** *23,* 2857.

[23] Fulmer, G. R.; Miller, A. J. M.; Sherden, N. H.; Gottlieb, H. E.; Nudelman, A.; Stoltz, B. M.; Bercaw, J. E.; Goldberg, K. I., NMR Chemical Shifts of Trace Impurities: Common Laboratory Solvents, Organics, and Gases in Deuterated Solvents Relevant to the Organometallic Chemist. *Organometallics* **2010,** *29,* 2176-2179.

Chapter 7

On the Photoredox/Cobalt Dual-Catalytic Decarboxylative Transformations of Carboxylic Acids

7.1 Introduction

Transition metals have been used to promote chemical transformations for centuries; during the 1820s, Edmund Davy and Johann Wolfgang Döbereiner concurrently reported the efficiency of platinum metal to influence the oxidation of alcohols and the combustion of hydrogen and oxygen, respectively.[1] The impact of these early discoveries opened the floodgates for transition metals to be studied more widely in a variety of organic transformations, revolutionizing the methods by which we as chemists can manipulate chemical bonds. One of the greatest advancements in the realm of transition metal-mediated transformations is the utilization of transition metals as catalysts. Transition metal catalysis (TMC) is advantageous, as it allows for otherwise difficult or impossible transformations to occur, mediated by a metal whose redox properties allow for said difficult transformations to take place. The first-row transition metals are the most investigated when it comes to the d-block elements; the ability to utilize these metals catalytically in reactions is particularly attractive when considering the cost, abundance, and toxicity of said metals. Despite the advancements made towards our understanding of TMC and its applications to organic transformations, there are still many areas of interest which have yet to be explored.

Notwithstanding the success brought by the rise of TMC, even transition metals have their limitations. One of the strategies employed to overcome these limitations in especially difficult redox processes is the pairing of TMC to photoredox catalysis in a dual-catalytic fashion. This process involves the cooperation between two catalysts in a given system to accomplish a photoinduced transformation, which neither catalyst is able to achieve on its own. Dual-catalytic photoredox methodology has been utilized extensively in decarboxylative transformations, which rely on the loss of carbon dioxide to serve as the

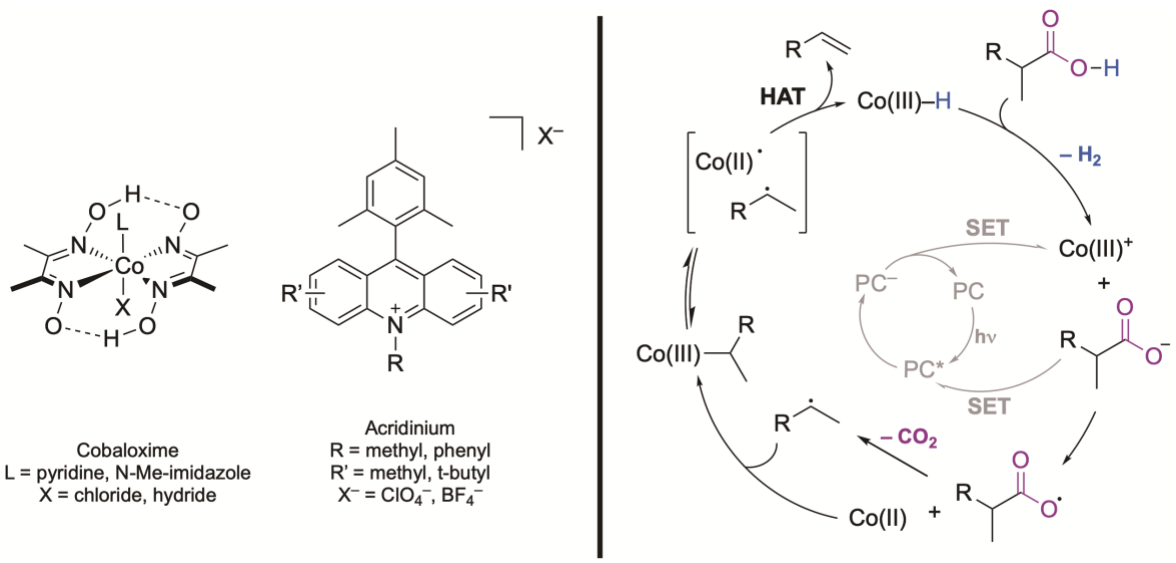

Scheme 7.1. Left: Structures of cobaloxime and acridinium catalysts investigated over the course of reaction optimization. Right: Proposed catalytic cycle for photoinduced decarboxylative elimination of carboxylic acid.

driving force; such transformations are environmentally friendly, atom-economical, and often incredibly selective. The development of new decarboxylative methodology has been a focal point of the group of Tunge and coworkers for nearly two decades;[2] recently, this group developed a system which utilizes feedstock carboxylic acids and amino acids to furnish enamine derivatives via a photoredox/cobalt dual-catalytic decarboxylative elimination process.[3] This decarboxylative elimination methodology is attractive for the preparation of enamine derivatives (enamides and enecarbamates within our scope) for a few reasons. Photoinduced decarboxylative transformations, which involve oxidation of a carboxylate anion to the carboxyl radical as an intermediary step, are most often regioselective transformations due to the formation of an explicit carbon-centered radical

upon decarboxylation. These reactions are also more environmentally friendly than their TMC-mediated alternatives; in our system, the only stoichiometric byproducts are carbon dioxide and hydrogen gas. The developed decarboxylative elimination pathway relies on two catalysts: A cobaloxime and an acridinium photosensitizer (see Scheme 7.1**,** Left). These catalysts work harmoniously together upon exposure to a blue light emitting diode (LED) light to convert a given carboxylic acid or amino acid precursor into the desired, sometimes-isomeric elimination product(s). The process relies on a series of single electron transfer (SET) steps between the cobaloxime, the acridinium, and the substrate. Because these various redox processes involve multiple reactive intermediates, precise tuning of the reduction potentials of each species in a given transformation must be considered, such that the electron transfers occurring are those which we desire, as opposed to off-cycle processes.

The proposed catalytic cycle (Scheme 7.1, right) of the decarboxylative elimination transformation is initiated by deprotonation of the carboxylic acid, either by the axial base ligand of cobaloxime or a catalytic borohydride additive, to give the carboxylate. The cobalt(III) cation in solution is formed by initial dissociation of the chloride ligand. The ground state acridinium photocatalyst in the presence of blue LEDs is converted to its excited state by promotion of an electron to a higher energy level; this excited state acridinium favorably oxidizes the carboxylic acid, providing the reduced acridine radical[4] and the carboxyl radical, which spontaneously gives off carbon dioxide to furnish an alkyl radical. The acridine radical, upon formation, is a suitable reductant to reduce the cobalt(III) cation to a cobalt(II) radical, returning the acridinium to its cationic ground state. Cobalt(II) is able to trap the alkyl radical; through hydrogen atom transfer (HAT), the elimination product is

Chart 7.1. Complexes employed in this study.

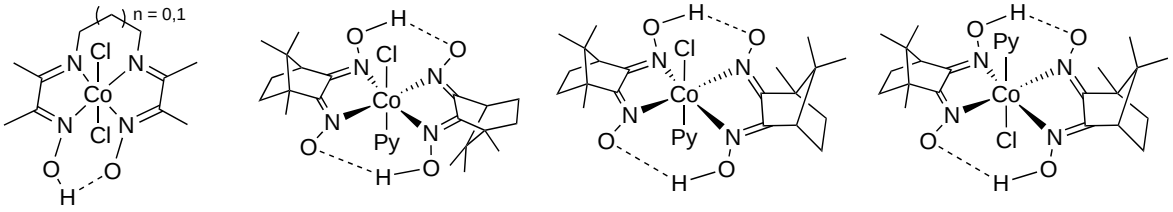

Co-en (n = 0)
Co-pn (n = 1)

Co-CQD–1

Co-CQD–2a

Co-CQD–2b

formed. The resulting cobalt species, a cobalt(III)–hydride, is sufficiently basic to deprotonate the next molecule of acid, thereby generating H_2 and turning over the catalytic cycle.

The success and broad scope of this methodology encouraged us pursue two new decarboxylative transformations. The ability to perform the decarboxylative elimination asymmetrically was an attractive direction of study, as the ability to select for a given enantiomer of product would further improve the scope and provide potential insight into the mechanism at play. Additionally, the development of new asymmetric methods is of paramount importance to drug development within the pharmaceutical industry. To this end, we targeted two literature cobalt(III) complexes bearing diimine dioxime ligands and one novel cobalt(III) complex bearing camphorquinone dioxime ligands (**CQD**) and employed them in the elimination chemistry (Chart 7.1). The complexes of **CQD** that we prepared were chiral; two different isomers of the complex were isolated and employed in the elimination chemistry. While the efforts did not lead to any significant asymmetric innovations, the results of the preliminary study shed light on the importance of the model catalyst in the elimination, as derivations of the catalyst simply were not functional in the elimination.

7.2 Results and Discussion

7.2.1 Cobaloxime Catalysts Suitable for Elimination Conditions

In our attempts to enact asymmetric decarboxylative elimination of carboxylic acids, we focused on feedstock carboxylic acid precursors which would allow for enantioselectivity of the resulting alkene products. As shown in Scheme 7.2, the given carboxylic acid precursor is achiral, as is the radical intermediate upon decarboxylation. However, the hydrogens on each α-carbon are prochiral upon decarboxylation, as HAT occurring from one of those carbons over the other would provide a specific enantiomer of product. In our initial efforts, we first focused on structural modifications of the cobalt catalyst. It was determined in our prior work[3] that the ideal cobalt catalyst for the desired

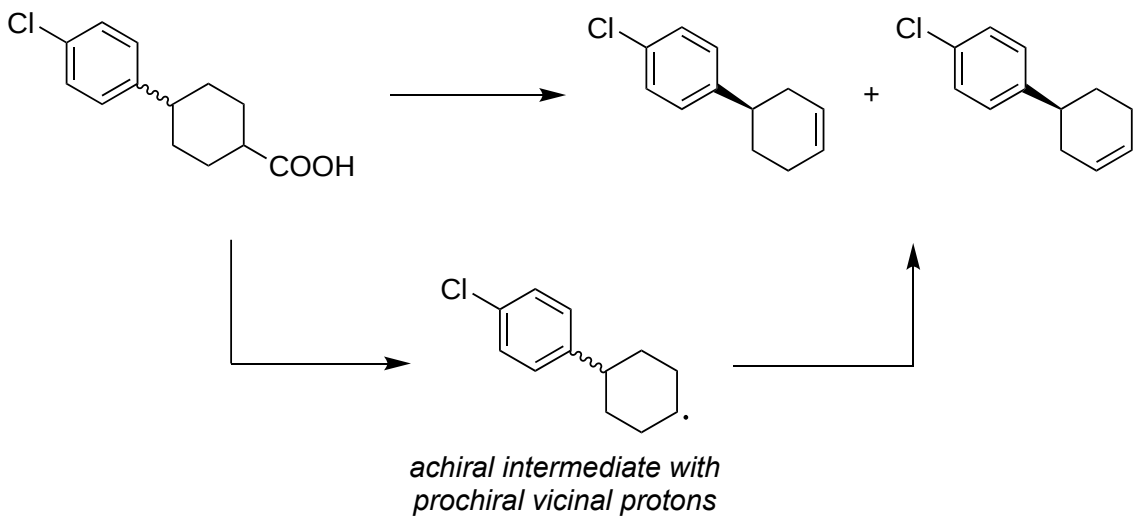

Scheme 7.2. Proposed process of asymmetric elimination from a feedstock carboxylic acid precursor depicting prochiral radical intermediate.

Chart 7.2. Left: Optimal cobaloxime catalysts in decarboxylative elimination reaction. Right: Equatorial ligands used in the preparation of other cobalt catalysts during optimization.

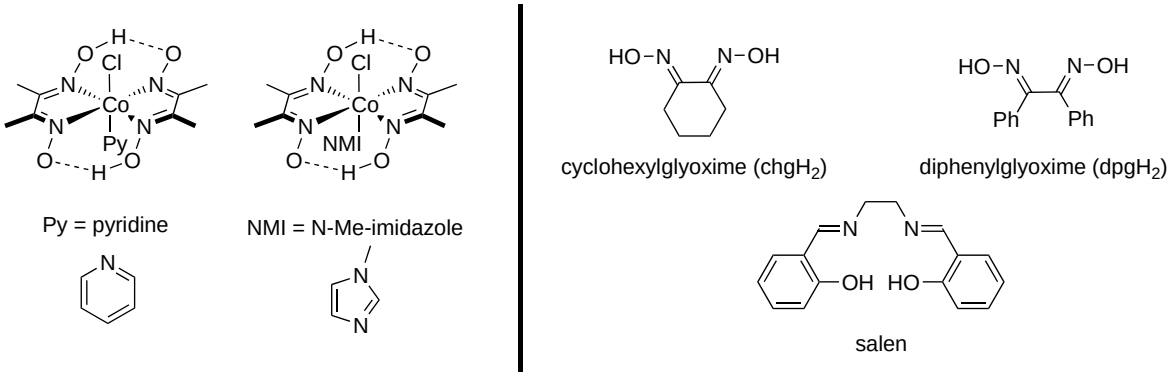

eliminations consisted of two equatorial dimethylglyoximato (dmgH) ligands, an axial chloride ligand, and an axial nitrogenous base ligand (see Chart 7.2, Left). We observed that changing the nitrogenous base had significant effects on the outcome of the reaction; a screening of cobaloximes with varying nitrogenous axial bases in the elimination reaction showed that pyridine and N-methyl-imidazole (NMI) provided the highest yields of the given enamine derivative and alkene products, respectively. Additionally, varying the equatorial ligand system had noticeable effects on the efficiency of elimination. Cobaloxime complexes with an equatorial ligand system consisting of two cyclohexylglyoximato (chgH) or diphenylglyoximato (dpgH) ligands were also synthesized and tested in the elimination (see Chart 7.2, Right); however, in nearly all cases these catalysts were subpar relative to the analogous dmgH-ligated cobaloxime. Additionally, Co(salen) was tested, but a noticeably diminished yield (< 30 %) was observed during optimization using this catalyst. This result supports the notion that the four imine donors of the glyoxime are critical to the success of the elimination.

7.2.2 Preparation of Ligands

With all of this in mind, we set out to synthesize cobaloxime complexes which could impart stereoselectivity in the elimination process. This required initial preparation of the ligands, the first of which was a camphor derivative (Chart 7.3, Left). The chirality and steric bulk of this ligand was attractive for employment in asymmetric studies; the low cost of the chiral camphor starting material and the fact that there was literature precedence for the synthesis of this ligand made this a sensible starting place. The two-step synthetic procedure (see Scheme 7.3) begins by reacting the chiral camphor precursor with potassium *tert*-butoxide and isopentyl nitrite at sub-zero temperatures.[5] The camphor and base react to form an enolate; on addition of isopentyl nitrite, the nitrogen atom is attacked by the enolate, installing the nitroso group and displacing the leaving group isopentoxide. The methyne α-proton is again deprotonated, forming the imine N-oxide from the nitroso group. Subsequent washing, acidification, and extraction provided the desired camphorquinone oxime in an 86:14 *anti*/*syn* ratio, with respect to the oxime. This mixture was refluxed in water for 24 hours, resulting in a pure solid present in a 95:5 E/Z ratio, with respect to the oxime.

Chart 7.3. Structures of ligands targeted and synthesized in this study.

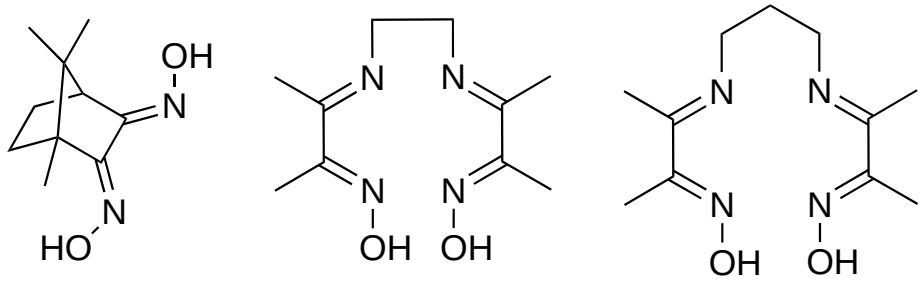

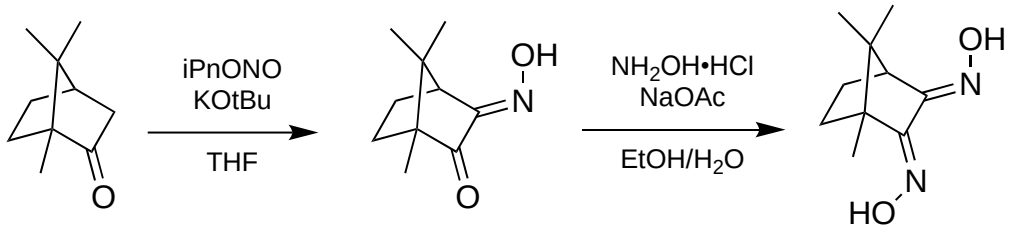

Scheme 7.3. Synthetic sequence for formation of camphorquinone dioxime.

Subsequent refluxing of the isolated quinone oxime with hydroxylamine hydrochloride and sodium acetate in a mixture of water and ethanol gave a white solid which precipitated from the reaction mixture.[6] Upon isolation via vacuum filtration, a precipitate also formed in the filtrate and was isolated. Because both oxime groups of **CQD** are stereogenic centers, there are four possible stereoisomers with respect to the oxime functionalities (see Figure 7.1). Indeed, all four were observed in the spectra of the initially isolated precipitate, while the major component was the desired 1*E*,2*E*-isomer; this isomer was not present in the collected filtrate from the vacuum filtration. Because the 1*E*,2*E*-isomer collected was slightly contaminated with the other three isomers, it was boiled in acetone and hot filtered thrice; this isomerization resulted in pure, desired 1*E*,2*E*-isomer. Attempts to isomerize the material consisting of the undesired isomers by the same procedure were unsuccessful.

Another class of ligands we pursued is diimine dioxime ligands. These ligands have been used in the synthesis of a variety of metal complexes; recently, we reported use of this ligand scaffold in the preparation of heterobimetallic complexes of cobalt, nickel, rhodium, and iridium as described in part in Chapter 4 of this dissertation.[7] Because this scaffold

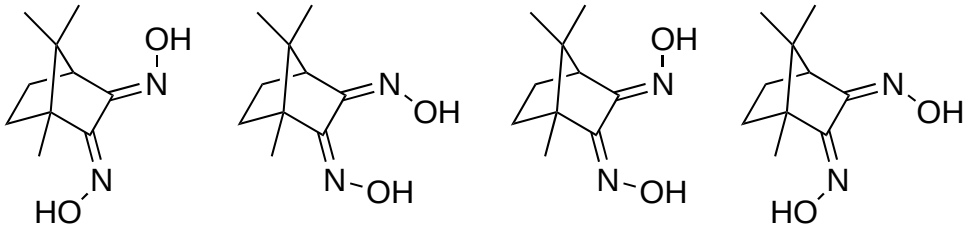

1E,2E *60 %* 1Z,2Z *33 %* 1Z,2E *4 %* 1E,2Z *3 %*

Figure 7.1. Four stereoisomers of **CQD** composing the isolated precipitate. The percentages represent the amount present in the mixture, as determined by the relative integrations of the bridgehead methyne proton.

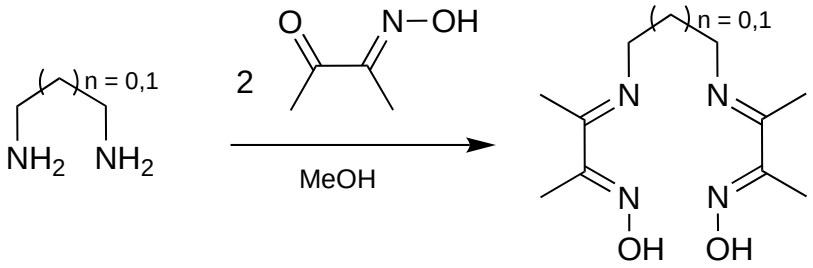

Scheme 7.4. Preparation of **en** and **pn** by imine condensation with 2,3-butanedione monooxime.

contains four chelating nitrogen donor atoms, similar to the dmgH-ligated cobaloxime complexes, we sought to make the corresponding cobalt complexes and test them in the elimination chemistry. This ligand system differs from that of dmgH by the fact that two of the nitrogen atoms exist as imines instead of oximes and are bound together by an alkyl chain, usually either an ethylene or propylene bridge (Scheme 7.4). This creates a tetradentate ligand upon complexation to capture a given metal, as opposed to the two bidentate dmgH ligands used in our previous system. The complexes formed from these

ligands are similar to those formed from dmgH; the cyclic nature of the equatorial plane about a metal when two dmgH ligands are bound to a metal is still present within the diimine dioxime ligand scaffold. The only difference with respect to the macrocycle is that one of the O–H–O proton bridges in the dmgH complexes is replaced by an alkyl chain in the present complexes. Both the ethylene- and propylene-bridged ligands (**en** and **pn**, respectively) were synthesized from the corresponding diamine and 2,3-butanedione monooxime in a 1:2 ratio (see Scheme 7.4).[8] Each product precipitated from the reaction mixture upon formation and was collected, and subsequently was reacted to generate the corresponding cobalt complex. Their spectral data were in agreement with those in the literature.

7.2.3 Preparation of Cobalt Complexes

With the desired ligands in hand, we set out to synthesize the corresponding cobalt complexes. Ligand **CQD** was reacted with cobalt(II) chloride tetrahydrate in acetone to give a hot pink solution. The acetone was blown off with air and methanol was added, giving a pale pink color. Upon addition of pyridine, the solution became deep brown, and a brown solid precipitated upon addition of water; these observations are consistent with the preparation of the aforementioned dmgH complexes (Scheme 7.1, Left). According to ^{1}H

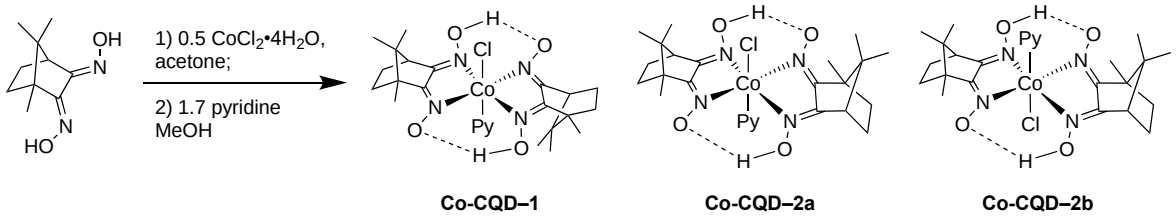

Scheme 7.5. Preparation of isomeric cobaloxime complexes derived from camphorquinone dioxime ligand.

NMR, this brown solid consisted of a mixture of stereoisomers **Co-CQD–1** and **Co-CQD–2a/Co-CQD–2b** in a 27:73 ratio, respectively (seen in Scheme 7.5). It is worth noting that the complexes **Co-CQD–2a/Co-CQD–2b** cannot be distinguished by NMR; the isolated material could have consisted of one or both of the complexes. These isomers were separated by column chromatography to afford **Co-CQD–1** and **Co-CQD–2a/2b**, each as a brown solid. Figure 7.2 shows the ^{1}H NMR spectra for each complex. The diagnostic information utilized in the structural determination of each complex is the number of methyl resonances in each spectrum. Because **Co-CQD–2a/2b** is *C*$_2$-symmetric, the methyl groups which are

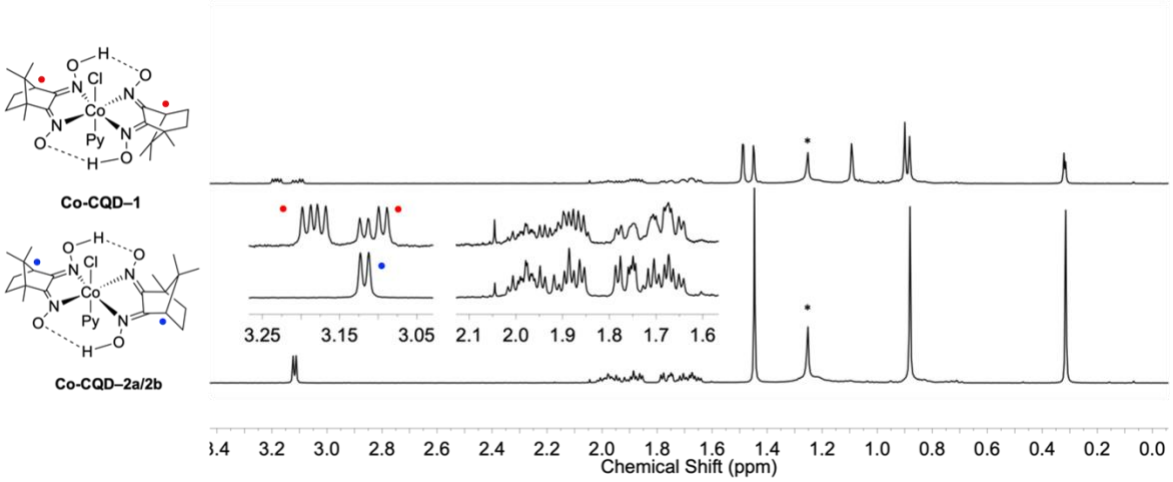

Figure 7.2. ^{1}H NMR (400 MHz, $CDCl_3$) spectra of isolated complexes **Co-CQD–1** and **Co-CQD–2a/Co-CQD–2b**. The lower symmetry complex (top) shows two 1H doublet of doublets for the bridgehead methyne protons (indicated by red dot •), while the higher symmetry complex (bottom) shows one 2H doublet for those bridgehead methyne protons (indicated by blue dot •). The peaks designated by an asterisk near ~ 1.2 ppm correspond to H grease.

related through symmetry appear in the spectral data as three sets of 6H singlets; in **Co-CQD–1**, however, the complex is C_i such that all methyl groups are unique and integrate to 3H each, as seen in the spectral data. Additionally, each methyne bridgehead proton is depicted as a 2H doublet for the symmetric **Co-CQD–2a/2b** while there are two unique doublet of doublets for each methyne bridgehead proton in **Co-CQD–1**.

Similarly, both **en** and **pn** were metalated with cobalt(II) chloride tetrahydrate by stirring in ethanol to afford the desired dichlorocobalt species **Co-en** and **Co-pn**, respectively. The green solution was stirred for 5 hours until a precipitate formed, which was then collected and washed with ether. The resulting dichlorocobalt(III) diiminedioximato complexes **Co-en** and **Co-pn** were formed in moderate yields as bright green and dark green solids, respectively (see Scheme 7.6). The spectral data of the complexes matched those reported in the literature, and they were used in the elimination chemistry without further purification. Efforts to substitute an axial chloride ligand for pyridine via salt metathesis with potassium hexafluorophosphate were unsuccessful.

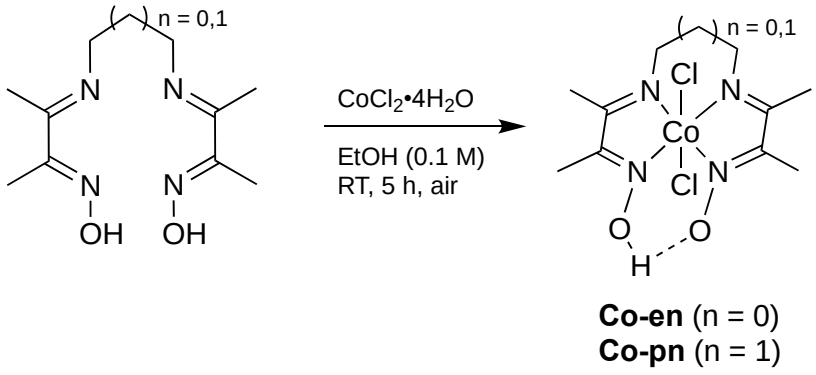

Scheme 7.6. Preparation of dichlorocobalt diimine dioximato complexes.

7.2.4 Employing Cobalt Complexes in Decarboxylative Elimination Chemistry

With the desired cobalt complexes in hand, we turned to the photocatalytic decarboxylative elimination utilizing these complexes under the same conditions previously developed by Cartwright et al.[3] Asymmetric transformations were not considered unless the complexes proved efficient in the elimination. The complexes **Co-CQD–1a** and **Co-CQD–2a/2b** were screened in the elimination chemistry with two carboxylic acid derivatives which were previously shown to be successful in the elimination under the optimized conditions; the conditions and the three possible products of the reaction are shown in Scheme 7.7. In each case, the ratio of Zaitsev alkene (**Zait**) to Hofmann alkene (**Hof**) was determined; additionally, Cartwright observed in the elimination chemistry with cobaloximes that, at times, trace amounts of protonated product (**Protonated**) were observed, resulting from decarboxylation and subsequent trapping of the alkyl radical with a hydrogen atom. A selection of the preliminary results of the attempted asymmetric elimination with both **Co-CQD–1** and **Co-CQD–2a/2b** is shown in Table 7.1.

In Table 7.1, entries 1 and 4 serve as control reactions in which the previously determined optimized conditions were employed. Entries 2 and 3 detail both **Co-CQD–1** and **Co-CQD–2a/2b**, respectively, being screened using the benzyl carbamate carboxylic acid starting material. Both catalysts returned recovered starting material and **Protonated**, while **Co-CQD–1** did show trace **Hof** in the ^{1}H NMR. For this reason, **Co-CQD–1** was also screened using the methyl ester-substituted derivative of the starting acid (see entry 5), with no better luck relative to entry 2. Each reaction which was run with these cobalt catalysts

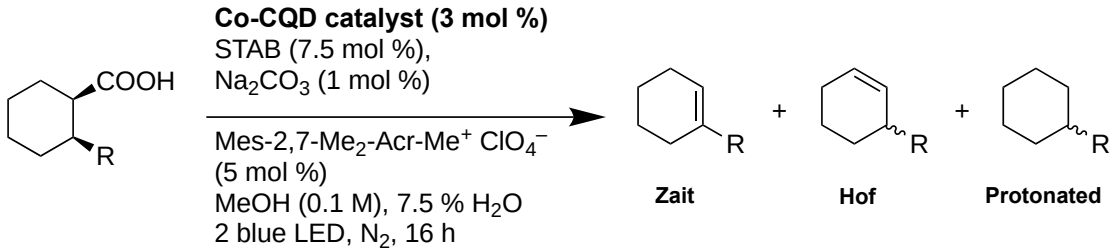

Scheme 7.7. Camphorquinone dioxime catalyst screening. R = NHCbz or CO_2Me.

Table 7.1. Select results of elimination chemistry with **CQD–1** and **CQD–2a/2b**.

Entry	Co catalyst	R	% Yield[a]	Zait:Hof:Protonated[b]
1	**Co(dmgH)$_2$Cl(NMI)**	NHCbz	76 %	0.4 : 99.6 : 0
2	**CQD–1**	NHCbz	0 %[c,d]	0 : 0 : 100
3	**CQD–2a/b**	NHCbz	0 %[d]	0 : 0 : 100
4	**Co(dmgH)$_2$Cl(NMI)**	CO_2Me	61 %	27 : 73 : 0
5	**CQD–1**	CO_2Me	0 %[d]	0 : 0 : 100

[a] Yield determined from isolated material. [b] Ratio based on coeluted, isolated material after column chromatography, determined by ^{1}H NMR. [c] Trace **Hof** present in ^{1}H NMR. [d] Flushing the column with ethyl acetate provided recovered, unreacted carboxylic acid.

resulted in poor conversion and recovered starting acid upon flushing the column with ethyl acetate. As a result, it can be concluded that the poor results are due to incompatibility of the complex to turn over the photocatalyst. If the photocatalyst and the metal catalyst are not compatible with respect to their redox potentials, or if the cobalt complex degrades or dissociates upon introduction to the reaction, then the cobalt catalyst is unable to oxidize the reduced form of the photocatalyst back to its ground state; therefore, the catalytic cycle is

never able to be turned over. Because these complexes were prepared for the first time in this study, no information on their redox properties is known.

With this result, we turned our attention to complexes **Co-en** and **Co-pn**. These complexes were tested as catalysts in the elimination using one carboxylic acid precursor and one amino acid precursor (see Scheme 7.8). In the optimized elimination conditions, we found that amino acid substrates performed better using the pyridyl-bound cobaloxime, while carboxylic acid substrates were more compatible in the elimination when the NMI-bound cobaloxime was employed[3] (see Scheme 7.1 for structural information on these complexes). Therefore, we tested these complexes with both substrates to see if there was a difference in the outcome with these complexes. Select results from these experiments are summarized in Table 7.2. While these complexes performed far better in the elimination as compared to the camphorquinone-derived cobalt complexes, with the **Co-pn** complex giving 22 % yield of the eliminated product the yields are still very low. It is possible that re-optimization of the reaction conditions with these given complexes, including the inclusion of catalytic base, might result in increased yields.

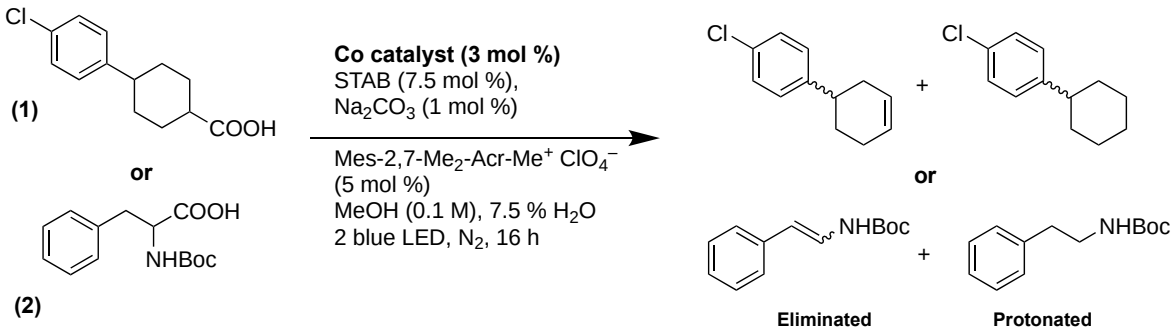

Scheme 7.8. Camphorquinone dioxime catalyst screening.

Table 7.2. Select results of elimination chemistry with **Co-en** and **Co-pn**.

Entry	Co catalyst	Precursor	% Yield[a]	Eliminated:Protonated[b]
1	**$Co(dmgH)_2Cl(NMI)$**	**(1)**	57 %	100:0
2	**Co-en**	**(1)**	11 %[c]	81:19
3	**Co-pn**	**(1)**	6 %[c]	66:34
4	**$Co(dmgH)_2Cl(py)$**	**(2)**	75 %	100:0
5	**Co-en**	**(2)**	< 5 %[d]	3:97
6	**Co-pn**	**(2)**	21 %[d]	100:0
7	**Co-pn**	**(2)**	22 %[d,e]	100:0

[a] Yield determined from isolated material. [b] Ratio based on coeluted, isolated material after column chromatography, determined by ^{1}H NMR. [c] Flushing the column with ethyl acetate provided recovered, unreacted carboxylic acid. [d] Side product aminal, formed by trapping of a-amino radical with methanol in solution, present in larger quantity than that of elimination product. [e] Yield determined from ^{1}H NMR using pyridine as internal standard.

7.3 Conclusion

The decarboxylative photoredox dual-catalytic elimination of carboxylic and amino acids is an important development in the field of green chemistry to furnish a variety of alkenes and enamine derivatives. Attempts to make this elimination asymmetric are a worthy effort, as the implications of such development could positively impact the medicinal and drug discovery industry. Our attempts at such development, while unsuccessful preliminarily, were insightful nonetheless. A new cobaloxime catalyst consisting of camphorquinone dioxime ligands was prepared and characterized by ^{1}H NMR; it is possible

that the complex could be made compatible in the chemistry if a photocatalyst with a suitably synced redox potential were selected. Electrochemical analysis of the reduction potentials of the cobaloxime catalysts would allow for the selection of an appropriate photocatalyst. Additionally, based on the preliminary observations, optimization of the reaction with diimine dioxime catalyst **Co-pn** might prove a worthy endeavor, as the propylene bridge allows for installation of asymmetry in the catalyst. The preliminary results described herein warrant further exploration into the asymmetric elimination under these conditions.

7.4 Experimental Details

7.4.1 General Considerations

All manipulations were carried out under N_2 atmosphere using standard Schlenk techniques, unless otherwise noted. All solvents were of commercial grade and were stored over molecular sieves. All chemicals were from major commercial suppliers and used as received or after extensive drying. Deuterated NMR solvents were purchased from Cambridge Isotope Laboratories (Tewksbury, MA, USA). ^{1}H spectra were collected on a 400 MHz Bruker spectrometer (Bruker, Billerica, MA, USA) and referenced to the residual protio-solvent signal in the case of ^{1}H.

7.4.2 Ligand Synthetic Procedures

Synthesis of Camphorquinone Monoxime

The title compound was prepared according to an existing literature procedure with minor adjustments.[5] To a flame-dried Schlenk flask was added potassium *tert*-butoxide (1.2 equiv.) and dry THF (4 M with respect to the base). The solution was flushed with N_2 and cooled to –30 °C in a xylene/dry ice bath. To a separate Schlenk flask was added camphor (1 equiv.) and dry THF (5 M with respect to camphor); this solution was sparged with N_2 for 5 minutes

and subsequently added slowly to the cooled solution of base with stirring. This solution was then stirred for 10 minutes, at which point isopentylnitrite (1.5 equiv.) was added. The now red solution was warmed to room temperature and stirred. After two hours, an orange precipitate had formed. THF was added to the slurry and was then concentrated *in vacuo*. Water and diethyl ether were added to the crude orange solid; the water layer was removed, the ether layer was acidified with glacial acetic acid, and the water was extracted with ether. The organic layers were dried and concentrated *in vacuo* to afford a pale yellow solid, which was subsequently crystallized by dissolving solid in the minimum amount of ethanol and flooding with hexane. The solid was isolated by vacuum filtration and washed with hexane to afford a white solid (86:14 E/Z by ^{1}H NMR). The solid was taken up in water and heated to reflux for 24 hours. The water was cooled to room temperature and the product was extracted with ether to afford the desired compound as a white solid (94:6 E/Z by ^{1}H NMR). Yield: 24 %. ^{1}H NMR (400 MHz, $CDCl_3$) δ (ppm): 8.55 (bs, 1H), 3.25 (d, 1H, $^{3}J_{H,H}$ = 4.5 Hz), 2.10–1.99 (m, 1H), 1.86–1.72 (m, 1H), 1.63–1.51 (m, 2H), 1.03 (s, 3H), 1.00 (s, 3H), 0.88 (s, 3H).

Synthesis of CQD

The title compound was prepared according to an existing literature procedure with minor adjustments.[6] To a round bottom flask was added camphorquinone monoxime (1 equiv.) in 200 proof ethanol (1.1 M). A solution of hydroxylamine hydrochloride (2.1 equiv.) and sodium acetate (3.6 equiv.) in water (2 M with respect to hydroxylamine) was made and added to the solution of camphorquinone monoxime with stirring. The solution was stirred for 30 minutes and then refluxed overnight. The next day, the white precipitate was collected via vacuum filtration and washed with water. This precipitate consisted of a mixture of

isomers (60:33:4:3 1*E*,2*E*/1*Z*,2*Z*/1*Z*,2*E*/1*E*,2*Z*). In order to isomerize to the desired 1*E*,2*E* isomer, the solid was added to a solution of acetone and boiled. The solution was hot filtered three times. The solid isolated from the hot filtrations was combined and washed with boiling acetone three times to provide **CQD** as a white solid pure by ^{1}H NMR.

Yield (1*E*,2*E*): 17 %. ^{1}H NMR (400 MHz, d_6-DMSO) δ (ppm): 10.70 (bs, 2H), 2.97 (d, 1H, $^{3}J_{H,H}$ = 4.5 Hz), 1.91–1.79 (m, 1H), 1.72–1.50 (m, 2H), 1.32 (s, 3H), 1.25 (ddd, 1H, $^{2}J_{H,H}$ = 13.1 Hz, $^{3}J_{H,H}$ = 9.1 Hz, $^{3}J_{H,H}$ = 4.4 Hz), 0.82 (s, 3H), 0.81 (s, 3H).

Synthesis of Diimine Dioxime Ligands

The diimine dioxime ligands were prepared according to an existing literature procedure with minor adjustments.[8] To a solution of 2,3-butanedione monoxime (2 equiv.) in methanol (4 M) was added the corresponding diamine compound (1 equiv.) and the solution was stirred at room temperature until a white precipitate formed. The precipitate was isolated by vacuum filtration and washed with methanol. The filtrate was then concentrated *in vacuo* to give more white solid. The solids were combined to give the diimine dioxime ligand as a pure white solid.

en. Yield: 90 %. The NMR data matched literature reports.[8a]

pn. Yield: 73 %. The NMR data matched literature reports.[8b]

7.4.3 Cobalt Complex Synthetic Procedures

Synthesis of Co-CQD–1a and Co-CQD–2a/2b

To a blue solution of cobalt(II) dichloride tetrahydrate (1 equiv.) in acetone was added **CQD** (3.2 equiv.). The now-pink solution was stirred for 1 hour with air blowing on the solution; the acetone was replenished over the course of the hour. After an hour, acetone was fully evaporated and methanol was added, giving a pale peachy colored solution. To this solution

was added pyridine (1.7 equiv.), at which point the solution became murky brown. After 30 minutes, water was added, and a brown precipitate formed. The solid was isolated and washed with water and ether to provide a mixture of the title complexes, which were subsequently isolated by flash column chromatography on silica gel (1:1 to 1:2 hexane/ethyl acetate gradient). The two complexes, isolated cleanly, were pure by ^{1}H NMR as brown solids (49 % total yield, 42:58 **Co-CQD–1a**/**Co-CQD–2a/2b**).

Co-CQD–1a. ^{1}H NMR (400 MHz, $CDCl_3$) δ (ppm): 8.46–8.25 (m, 2H), 7.81–7.68 (m, 1H), 7.27–7.24 (m, 2H), 3.18 (dd, 1H, $^3J_{H,H}$ = 7.8 Hz, $^3J_{H,H}$ = 4.3 Hz), 3.11 (dd, 1H, $^3J_{H,H}$ = 9.7 Hz, $^3J_{H,H}$ = 4.3 Hz), 2.03–1.61 (m, 8H), 1.49 (d, 3H, $^4J_{H,H}$ = 1.7 Hz), 1.45 (s, 3H), 1.09 (s, 3H), 0.90 (s, 3H), 0.88 (s, 3H), 0.32 (d, 3H, $^4J_{H,H}$ = 2.5 Hz).

Co-CQD–2a/2b. ^{1}H NMR (400 MHz, $CDCl_3$) δ (ppm): 8.47–8.31 (m, 2H), 7.74 (tt, 1H, $^3J_{H,H}$ = 7.6 Hz, $^4J_{H,H}$ = 1.5 Hz), 7.27–7.23 (m, 2H), 3.12 (d, 2H, $^3J_{H,H}$ = 4.3 Hz), 2.03–1.62 (m, 8H), 1.45 (s, 6H), 0.88 (s, 6H), 0.31 (s, 6H).

Synthesis of Co-en and Co-pn

The diimine dioxime ligands were prepared according to an existing literature procedure with minor adjustments.[9] To a solution of cobalt(II) dichloride tetrahydrate (1 equiv.) in 200 proof ethanol (0.1 M) was added the corresponding diimine dioxime ligand (1 equiv.). The solution was stirred for 5 hours, during which time a green precipitate formed. The solid was filtered via vacuum filtration and washed with ether to give the corresponding complex as a light or dark green solid which was pure by ^{1}H NMR.

Co-en. Yield: 60 %. ^{1}H NMR (400 MHz, CD_3CN) δ (ppm): 4.66 (s, 4H), 2.55 (s, 6H), 2.43 (s, 6H0.

Co-pn. Yield: 47 %. ^{1}H NMR (400 MHz, $CDCl_3$) δ (ppm): 4.09–3.98 (m, 4H), 2.58 (s, 6H), 2.51 (s, 6H), 2.49–2.43 (m, 2H).

7.5 Acknowledgement

The authors thank Sarah Neuenswander for her assistance with NMR spectroscopy. This work was supported by the National Science Foundation (CHE-1800147) and the Kansas Bioscience Authority Rising Star program. Support for the NMR instrumentation was provided by NSF Academic Research Infrastructure Grant No. 9512331, NIH Shared Instrumentation Grant No. S10RR024664, and NSF Major Research Instrumentation Grant No. 0320648.

7.6 References

[1] Lindström, B.; Pettersson, L. J., A Brief History of Catalysis. *CATTECH* **2003,** *7*, 130-138.

[2] Select Tunge decarboxylative chemistry publications: (a) Burger, E. C.; Tunge, J. A., Synthesis of Homoallylic Amines via the Palladium-Catalyzed Decarboxylative Coupling of Amino Acid Derivatives. *J. Am. Chem. Soc.* **2006**, *128*, 10002-10003. (b) Waetzig, S. R.; Tunge, J. A., Palladium-Catalyzed Decarboxylative sp^3–sp^3 Coupling of Nitrobenzene Acetic Esters. *J. Am. Chem. Soc.* **2007**, *129*, 14860-14861. (c) Lang, S. B.; O'Nele, K. M.; Tunge, J. A., Decarboxylative Allylation of Amino Alkanoic Acids and Esters via Dual Catalysis. *J. Am. Chem. Soc.* **2014**, *136*, 13606-13609. (d) Lang, S. B.; O'Nele, K. M.; Douglas, J. T.; Tunge, J. A., Dual Catalytic Decarboxylative Allylations of α-Amino Acids and Their Divergent Mechanisms. *Chem. Eur. J.* **2015**, *21*, 18589-18593. (e) Li, T.-R.; Maliszewski, M. L.; Xiao, W.-J.; Tunge, J. A., Stereospecific Decarboxylative Benzylation of Enolates: Development and Mechanistic Insight. *Org. Lett.* **2018**, *20*, 1730-1734. (f) Senaweera, S.; Cartwright, K. C.; Tunge, J. A., Decarboxylative Acetoxylation of Aliphatic Carboxylic Acids. *J. Org. Chem.* **2019**, *84*, 12553-12561.

[3] Cartwright, K. C.; Joseph, E.; Comadoll, C. G.; Tunge, J. A., Photoredox/Cobalt Dual-Catalyzed Decarboxylative Elimination of Carboxylic Acids: Development and Mechanistic Insight. *Chem. Eur. J.* **2020**, *26*, 12454-12471.

[4] MacKenzie, I. A.; Wang, L.; Onuska, N. P. R.; Williams, O. F.; Begam, K.; Moran, A. M.; Dunietz, B. D.; Nicewicz, D. A., Discovery and characterization of an acridine radical photoreductant. *Nature* **2020**, *580*, 76-80.

[5] Roy, S.; Chakraborti, A. K., An efficient synthesis of anti-(1R)-(+)-camphorquinone 3-oxime. *Tet. Lett.* **1998**, *39*, 6355-6356.

[6] Nakamura, A.; Konishi, A.; Tatsuno, Y.; Otsuka, S., A highly enantioselective synthesis of cyclopropane derivatives through chiral cobalt(II) complex catalyzed carbenoid reaction. General scope and factors determining the enantioselectivity. *J. Am. Chem. Soc.* **1978**, *100*, 3443-3448.

[7] Kumar, A.; Comadoll, C. G.; King, D. S.; Oliver, A. G.; Day, V. W.; Blakemore, J. D., Incorporation of [Cp*Rh] and [Cp*Ir] Species into Heterobimetallic Complexes via Protonolysis Reactivity and Dioximato Chelation. *Inorg. Chem.* **2021**, *60*, 14047-14059.

[8] (a) Uhlig, E.; Friedrich, M. Untersuchungen an Oximkomplexen. III. Nickelchelate des Bis-(diacetylmonoxim-imino)-propans-1,3 und des Bis-(diacetylmonoxim-imino)-äthans-1,2. *Z. Anorg. Allg. Chem.* **1966**, *343*, 299-307. (b) Roy, A. S.; Weyhermüller, T.; Ghosh, P. A new cobalodioxime and its three levels of H-bondings to 1D helical strand, 2D helices and 3D framework. *Inorg. Chem. Commun.* **2008**, *11*, 167-170.

[9] (a) Mohapatra, M.; Dash, K. C., Cobalt (III) chelates of tetradentate dioxime schiff bases. *Indian J. Chem. B.* **1990**, *29A*, 342-345. (b) Costa, G.; Mestroni, G.; de Savorgnani, E., Vitamin b_{12} model compounds - cobalt chelates of bis(diacetylmonoxime - imino)propane 1–3. *Inorg. Chim. Acta* **1969**, *3*, 323-328.

Chapter 8

Summary and Future Outlook

In Chapters 2 through 7, work was presented from a variety of different research areas. The work described in these chapters, while seemingly unrelated, has been knit together such that the uniting theme of synthesis is demonstrated in each individual body of work. The areas of traditional organic methodology, organometallic synthesis, and inorganic chemistry really aren't that different from one another; indeed, the principles applied throughout each chapter are the same, despite the changing nature of the of synthetic targets.

Part I consisted of contributions to furthering the field of [Cp*Rh] systems. The inspiration for the work described in Chapters 2 and 3 was covered extensively through the review of Blakemore Group chemistry of [Cp*Rh] complexes in Chapter 1; as the work presented in these chapters is likely the final synthetic endeavor for our group in [Cp*Rh] chemistry for the time being, it is important that the foundations for the work are fully understood. In Chapters 2 and 3, the work on [Cp*Rh] complexes supported by chelating diphosphine ligands dppm and Xantphos was discussed, in which the complexes were synthesized, characterized, and investigated for their propensity to evolve hydrogen. The complexes demonstrated no catalytic activity, similarly to the analogous dppb-ligated complexes, giving credence to the stabilizing effects granted by diphosphine ligands to Rh–H in this system. The in-depth NMR analysis of the dppm-bound complexes utilizing multifrequency NMR and digital simulations provided valuable insight into the intricate coupling interactions present in the system.

Despite all that our group has contributed to the field of [Cp*Rh] chemistry, there is still much to be discovered regarding the mechanistic pathway for hydrogen evolution. While our group has endeavored to investigate some of the kinetic properties of the catalysis (efforts underway currently), the use of even more diverse ligand frameworks might enable

the isolation of a stable Rh–H bearing a diimine ligand or observation of Cp*H with a phosphine ligand, two outcomes that we never achieved. Additionally, use of a dppm-analogue in the complexes in which one or both methylene protons are exchanged for other NMR-active nuclei might provide the opportunity for another in-depth full NMR endeavor. Finally, studying the prepared complexes, particularly those bearing dppm ligands, by ^{103}Rh NMR would be an enlightening endeavor which would complement the study described in Chapter 3 well.

The works described in Part II (Chapters 4-7) entailed the smaller, one-off projects completed over the course of degree pursuits. For the hydrogenation catalysis of heterobimetallic complexes demonstrated in Chapter 4, the modest TON and production of hydrogenation products in the preliminary catalytic screening imply that modification to the complexes could indeed increase the catalytic efficiency of these complexes; this notion is supported further by the multiple hydride signals observed on introduction to hydrogen. The ability to select for a given M–H species from the range possible (as well as ligand-protonated species) through modifications to the supporting ligand system might allow for more optimal catalysis.

In Chapter 5, the development of a new C–N bond-forming reaction was discussed, in which benzoquinone compounds were able to mediate the formation of pyrroles and indoles upon reaction with homoallylic amines and *ortho*-vinyl anilines, respectively. The work complemented well the field of iminoquinone-mediated transformations involving amines; the good yields of the N-aryl indoles described in our work describe the modularity of the transformation. Additionally, the oxidative dearylation conditions developed to provide the free indole compounds could have implications to other transformations, such

as removal of protecting groups in synthetic procedures. As for future endeavors for this work, the opportunity exists within this work to optimize the formation of other N-heterocycles, such as carbazoles. Few attempts by our group were made to furnish carbazoles, but were never successful; indeed, dedication to optimizing the conditions to allow for the formation of carbazoles would be a major step forward, also it would shed light on the mechanism of the transformation.

In Chapter 6, the preparation of four polypyridyldicarboxylic acid ligands, two of which were novel, was discussed for use in capture of the uranyl dication in solution. This work demonstrated a preliminary investigation of the capability of this ligand system to house the uranyl dication; indeed, in all instances complexation of the uranyl dication was confirmed. However, ever-present solubility issues prevented much of our characterization and analytical efforts to probe the system towards U=O bond activation. Nonetheless, a quick electrochemical analysis was done on two complexes bearing one of the ligand scaffolds, in which the data show complex cyclic voltammograms. A useful piece of information can be extracted, however, which is the potential for reduction of the bipyridyldicarboxylate ligand, which was previously unknown.

The applications of this work on capturing uranyl from solution are widespread, as nuclear fuel processing and optimization are currently of interest to many in the industry. The more information we gain on the reactivity, properties, and functionalization of uranyl, the more likely we are to bridge the gap between sustainability and nuclear fuel processes. As such, this ligand system studied herein provides an opportunity for such analysis of the dication, considering the system was able to capture uranyl and form molecular complexes. Efforts toward derivatizing these ligands through use of aliphatic groups to increase the

solubility of the ligands in common organic solvents would allow for more facile crystallization and electrochemical studies; additionally, the development and/or employment of other pentadentate, proton-responsive, non-macrocyclic ligands into this type of chemistry (which may be more soluble) could be a valuable investment for the field.

Finally, the asymmetric elimination attempts described in Chapter 7, while unsuccessful, showed that the potential to develop chiral cobalt complexes for employment in the reaction is a worthwhile endeavor. The applications of asymmetric transformations are widespread through organic and organometallic methodology, with great impact on the pharmaceutical and drug discovery industries. Optimization of the conditions described in this chapter or utilization of a new catalyst might be a worthy endeavor.

Appendix A

Supplementary Information for Chapter 2

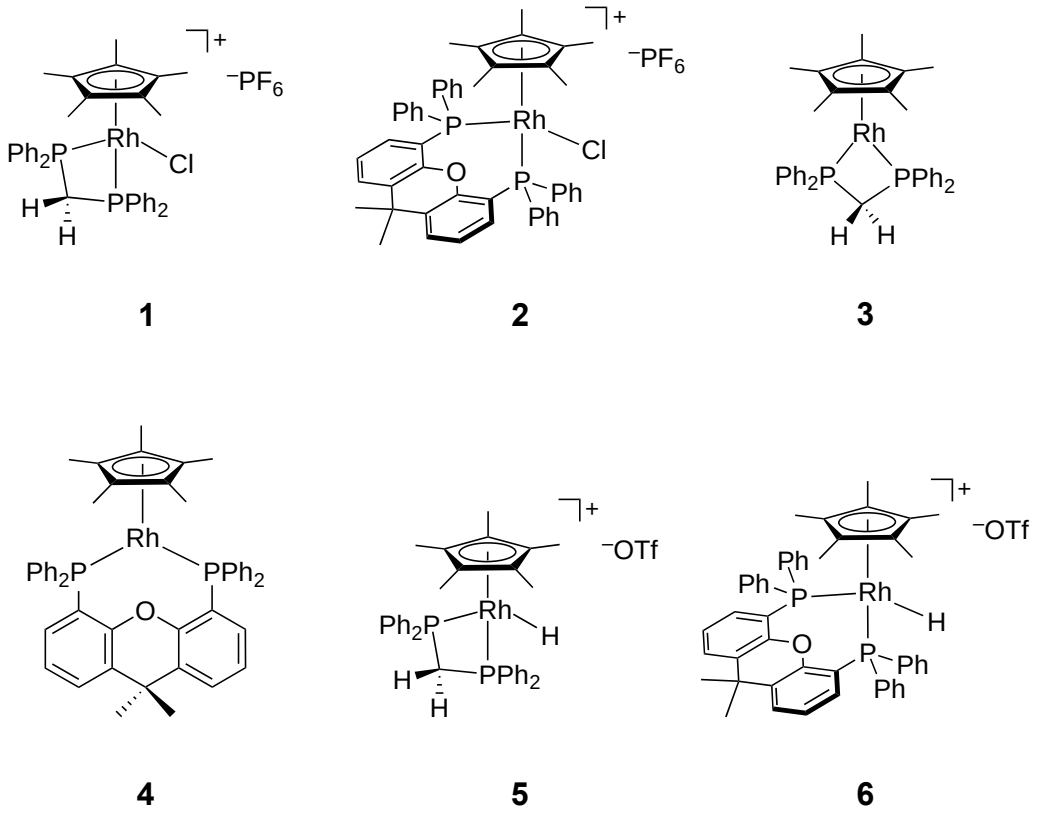

Chart A1: Complexes described in the supporting information.

NMR Spectra

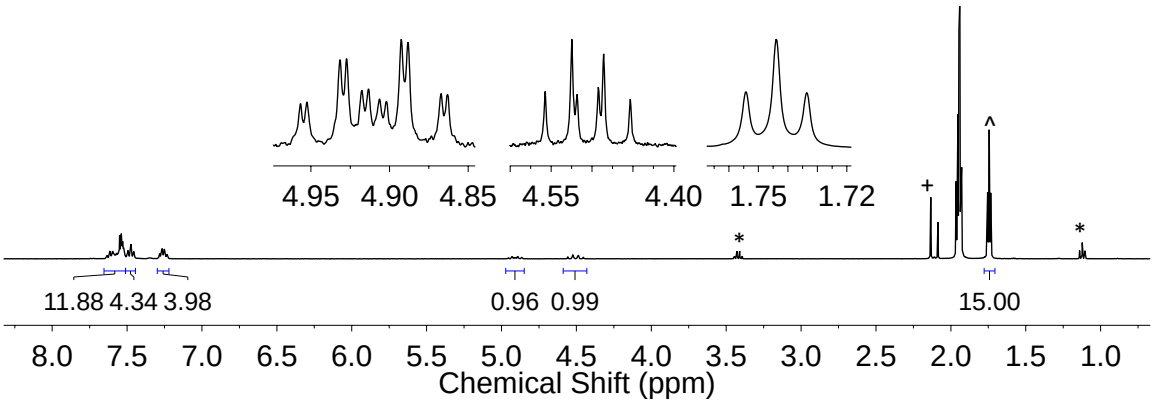

Figure A1: ^{1}H NMR spectrum (400 MHz, CD_3CN) of **1**. The signals indicated by * are diethyl ether. The signal indicated by + is water. The signal indicated by ^ is toluene.

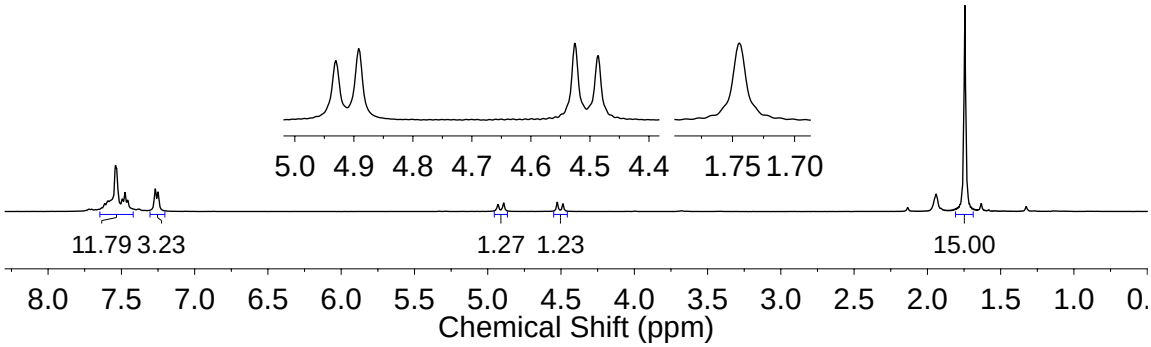

Figure A2: $^{1}H\{^{31}P\}$ NMR spectrum (400 MHz, CD_3CN) of **1**. Because deuterated solvent signal is diminished in this spectrum, the signal for Cp* methyl protons was used as internal reference and set to value of 1.7444 ppm based on nondecoupled data shown in Figure A1.

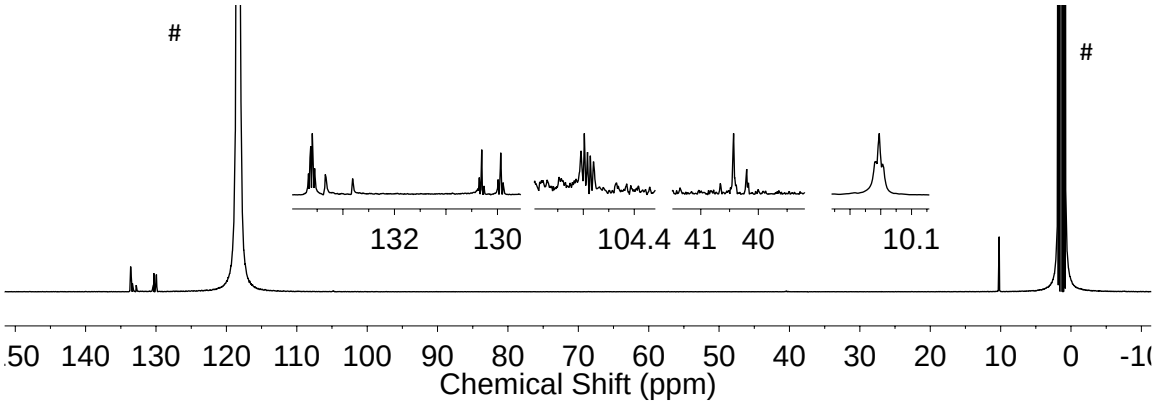

Figure A3: $^{13}C\{^{1}H\}$ NMR spectrum (126 MHz, CD_3CN) of **1**. The signals indicated by # are associated with acetonitrile.

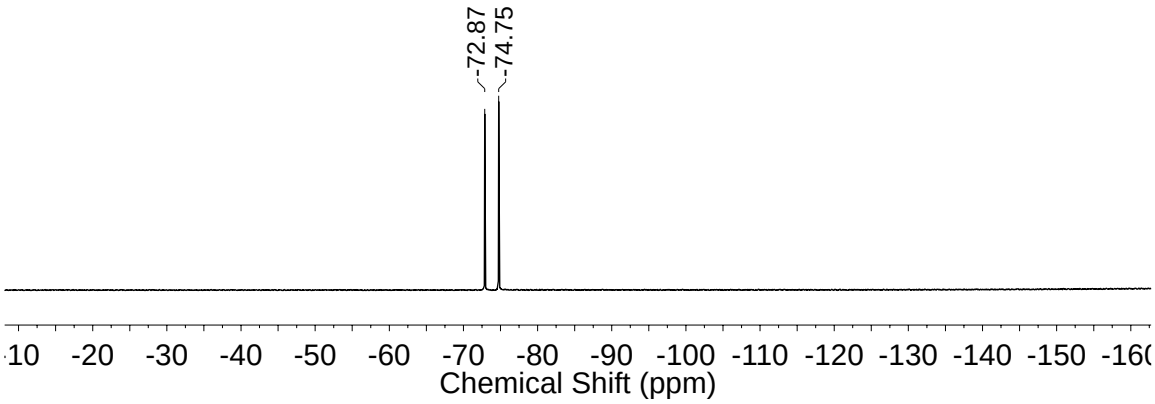

Figure A4: ^{19}F NMR spectrum (376 MHz, CD_3CN) of **1**.

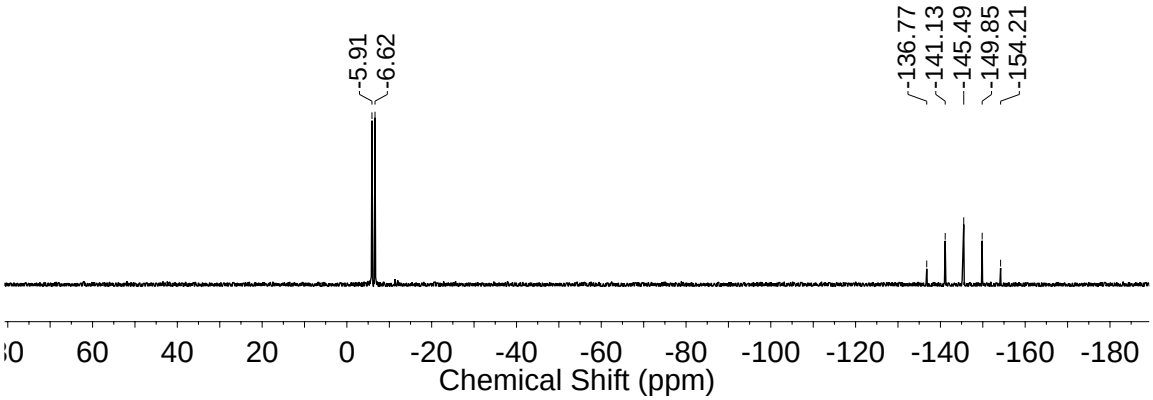

Figure A5: $^{31}P\{^{1}H\}$ NMR spectrum (162 MHz, CD_3CN) of **1**.

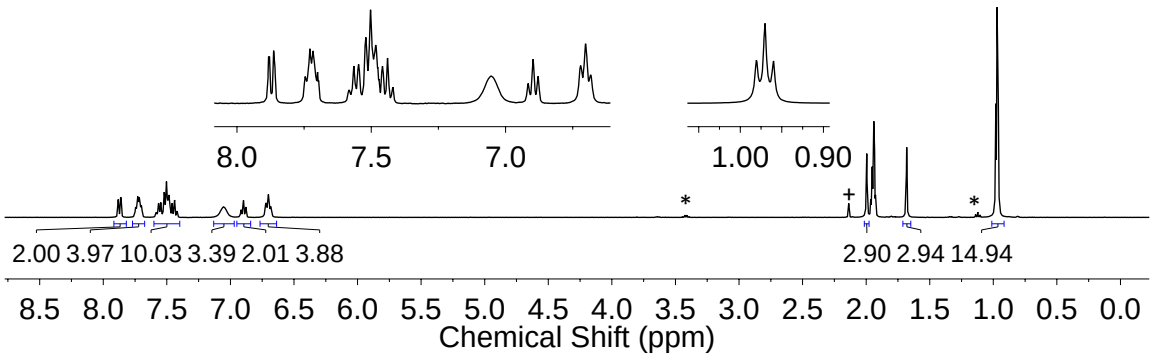

Figure A6: ^{1}H NMR spectrum (400 MHz, CD_3CN) of **2**. The signals indicated by * are diethyl ether. The signal indicated by + is water.

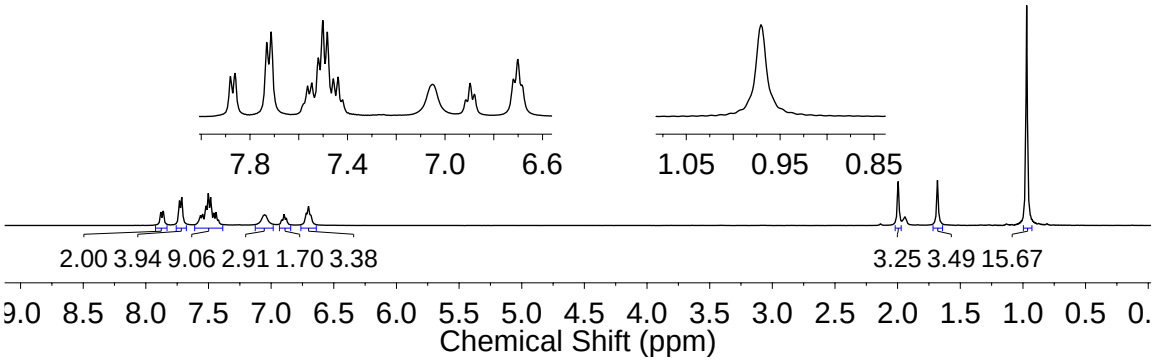

Figure A7: $^{1}H\{^{31}P\}$ NMR spectrum (400 MHz, CD_3CN) of **2**. Because deuterated solvent signal is diminished in this spectrum, the signal for Cp* methyl protons was used as internal reference and set to value of 0.9703 ppm based on nondecoupled data shown in Figure A6.

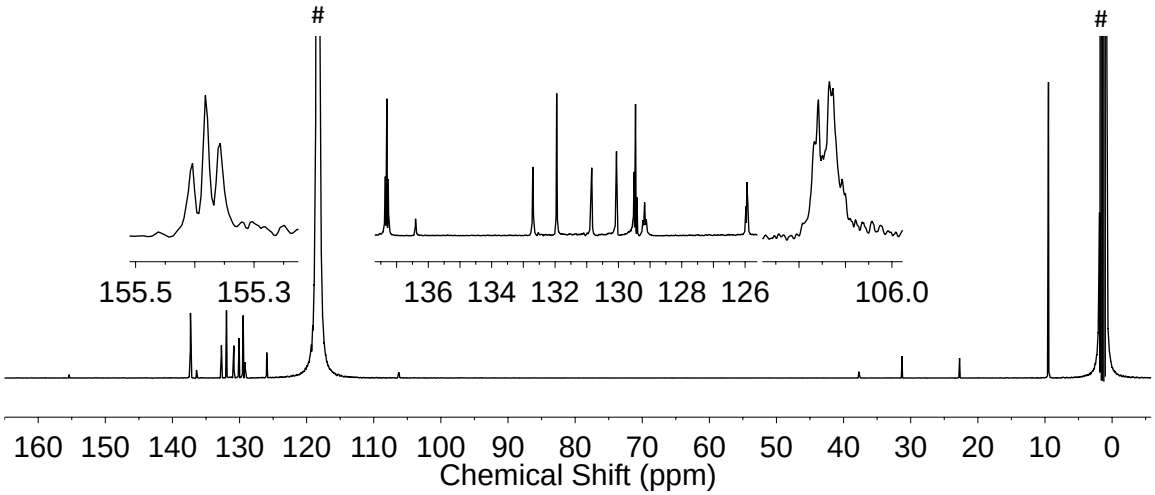

Figure A8: $^{13}C\{^{1}H\}$ NMR spectrum (126 MHz, CD_3CN) of **2**. The signals indicated by # are associated with acetonitrile.

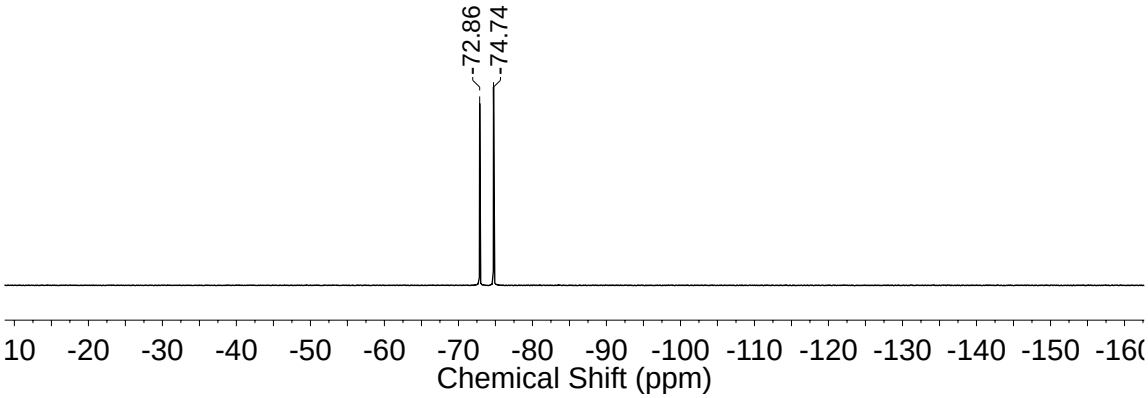

Figure A9: ^{19}F NMR spectrum (376 MHz, CD_3CN) of **2**.

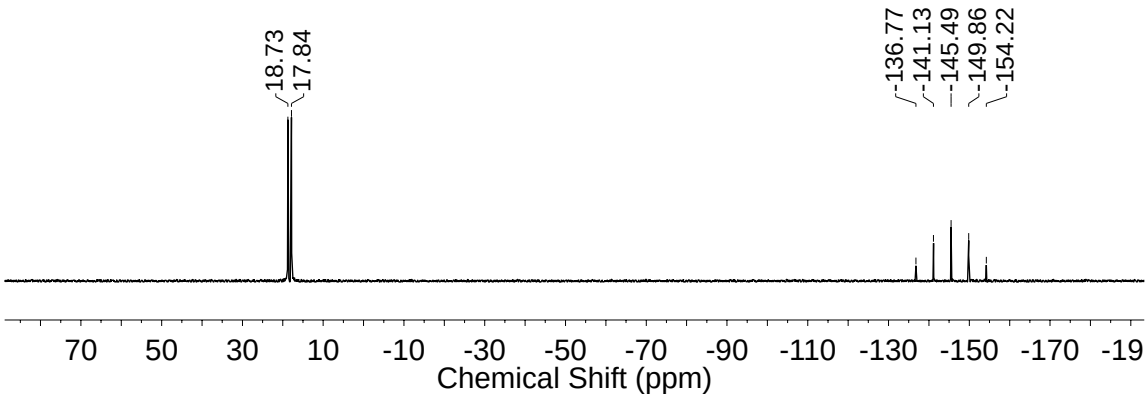

Figure A10: $^{31}P\{^1H\}$ NMR spectrum (162 MHz, CD_3CN) of **2**.

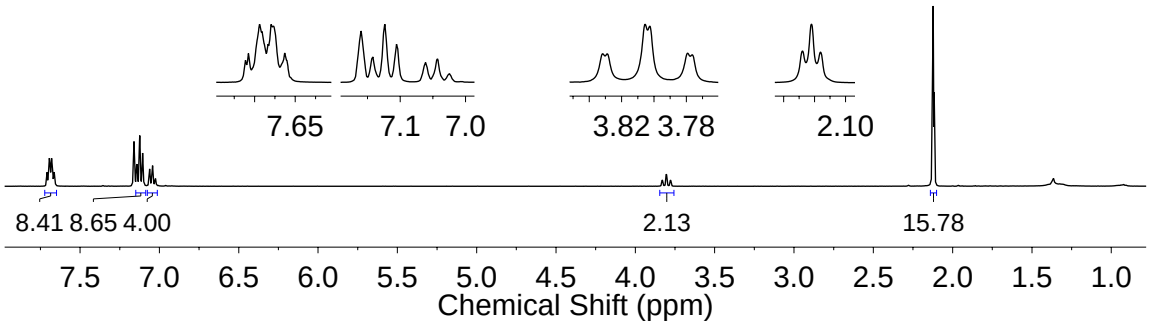

Figure A11: ^{1}H NMR spectrum (400 MHz, C_6D_6) of **3**.

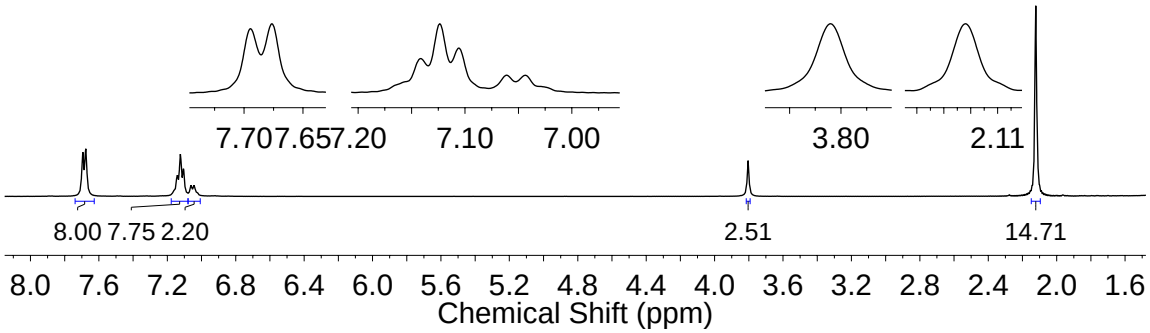

Figure A12: $^{1}H\{^{31}P\}$ NMR spectrum (400 MHz, C_6D_6) of **3**. Because deuterated solvent signal is diminished in this spectrum, the signal for Cp* methyl protons was used as internal reference and set to value of 2.1220 ppm based on nondecoupled data shown in Figure A11.

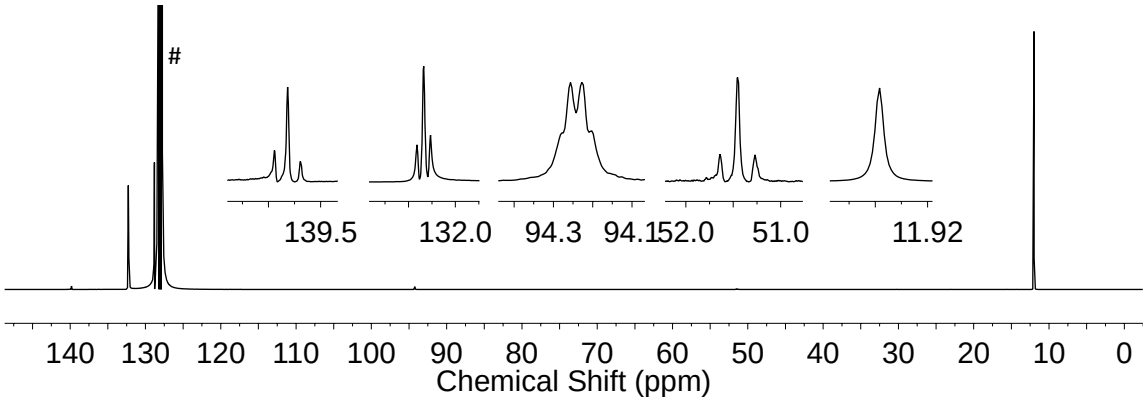

Figure A13: $^{13}C\{^{1}H\}$ NMR spectrum (126 MHz, C_6D_6) of **3**. The signal indicated by # is associated with benzene.

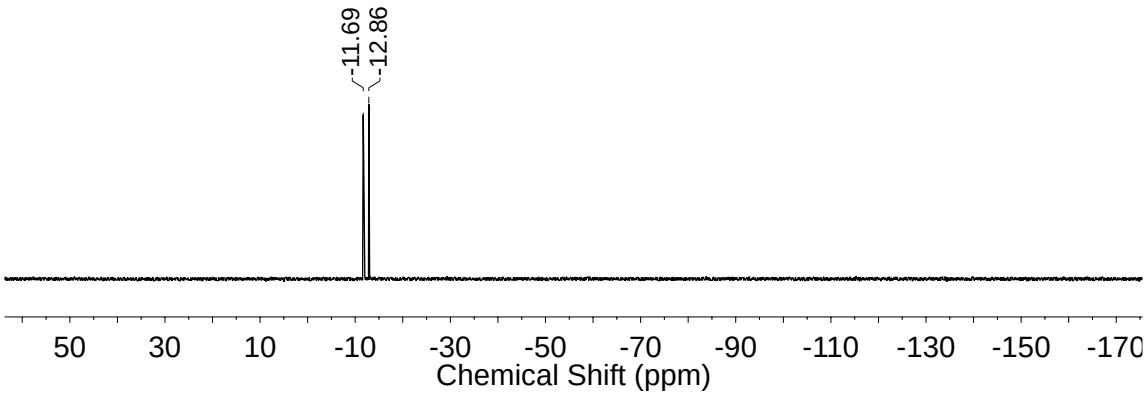

Figure A14: $^{31}P\{^{1}H\}$ NMR spectrum (162 MHz, C_6D_6) of **3**.

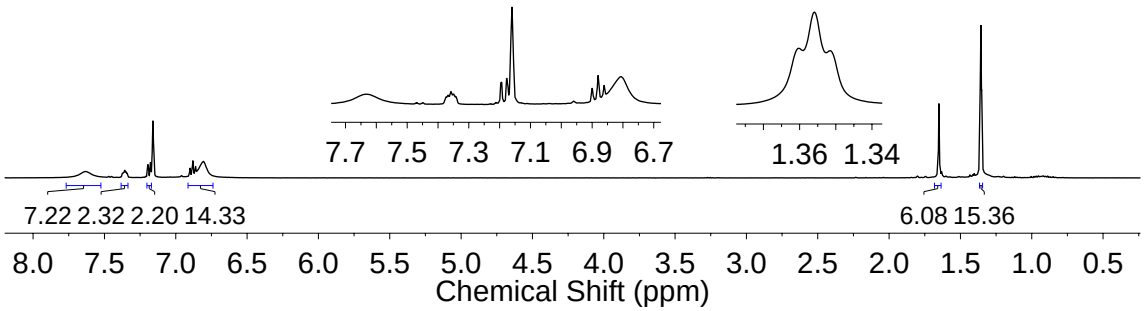

Figure A15: ^{1}H NMR spectrum (400 MHz, C_6D_6) of **4**.

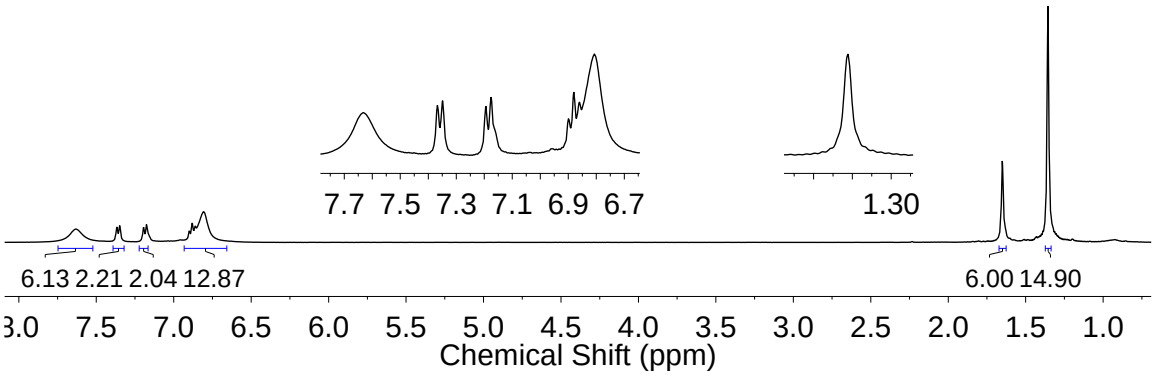

Figure A16: ^{1}H{^{31}P} NMR spectrum (400 MHz, C_6D_6) of **4**. Because deuterated solvent signal is diminished in this spectrum, the signal for Cp* methyl protons was used as internal reference and set to value of 1.3559 ppm based on nondecoupled data shown in Figure A15.

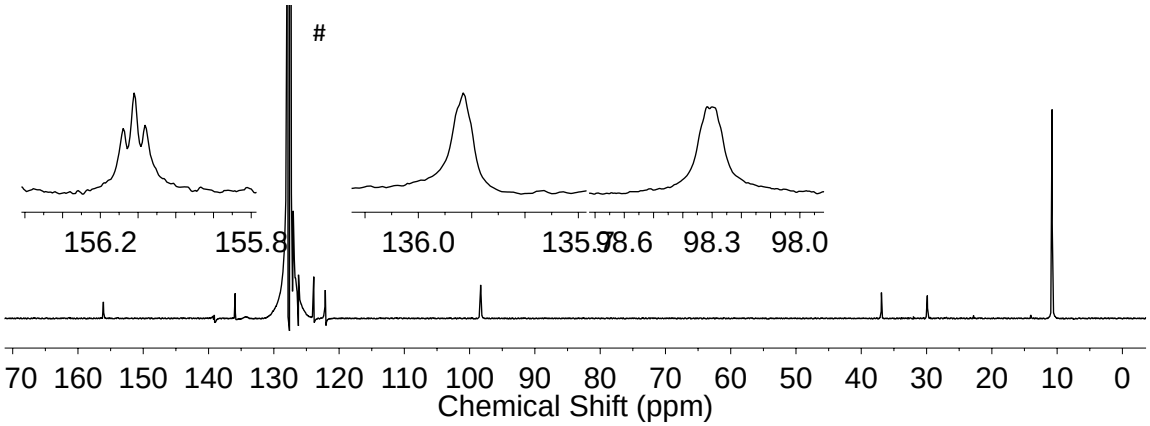

Figure A17: $^{13}C\{^{1}H\}$ NMR spectrum (126 MHz, C_6D_6) of **4**. The signal indicated by # is associated with benzene.

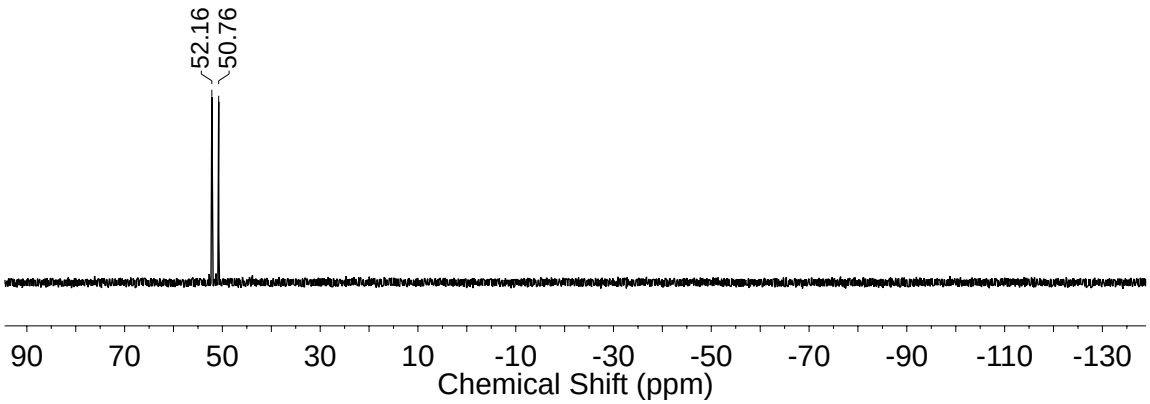

Figure A18: $^{31}P\{^{1}H\}$ NMR spectrum (162 MHz, C_6D_6) of **4**.

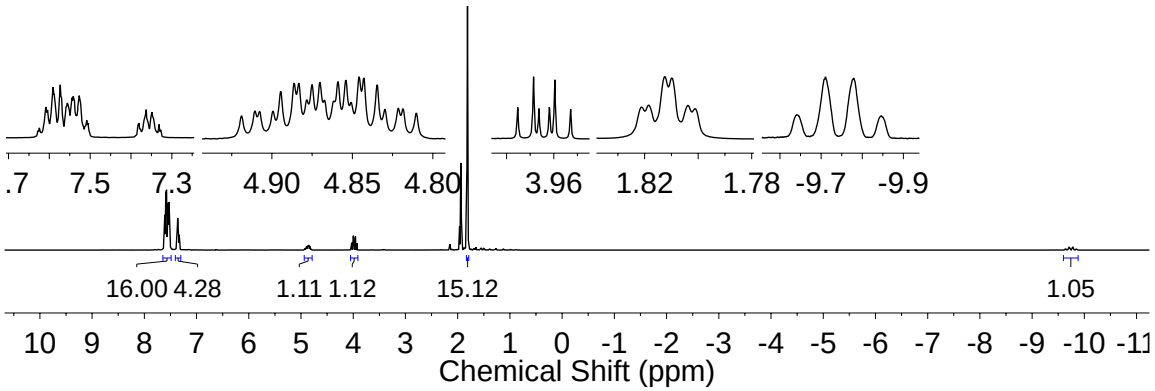

Figure A19: ^{1}H NMR spectrum (400 MHz, CD_3CN) of **5**.

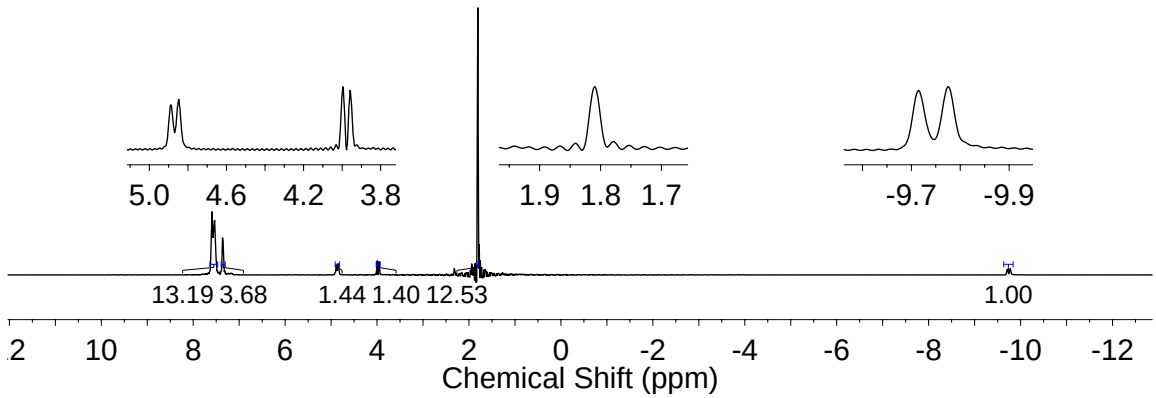

Figure A20: $^{1}H\{^{31}P\}$ NMR spectrum (400 MHz, CD_3CN) of **5**. Because deuterated solvent signal is diminished in this spectrum, the signal for Cp* methyl protons was used as internal reference and set to value of 1.8096 ppm based on nondecoupled data shown in Figure A19.

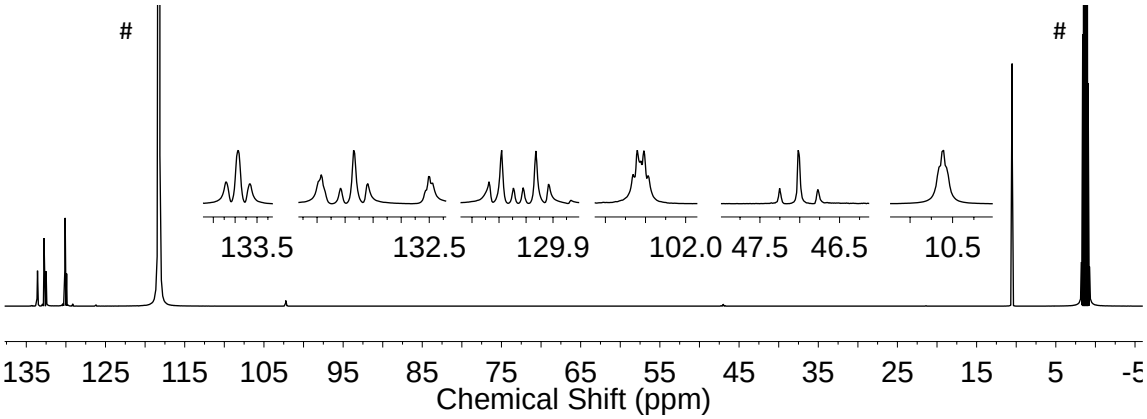

Figure A21: $^{13}C\{^{1}H\}$ NMR spectrum (126 MHz, CD_3CN) of **5**. The signals indicated by # are associated with acetonitrile.

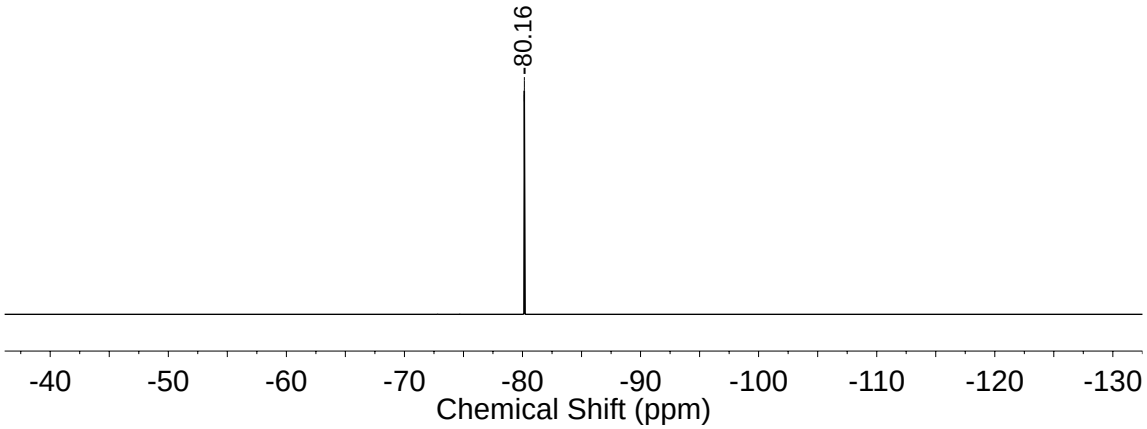

Figure A22: ^{19}F NMR spectrum (376 MHz, CD_3CN) of **5**.

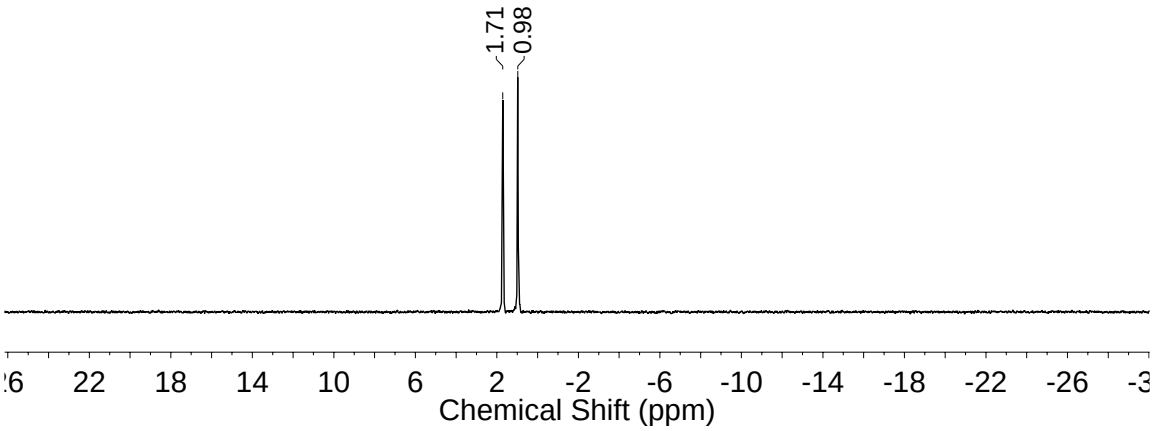

Figure A23: $^{31}P\{^{1}H\}$ NMR spectrum (162 MHz, CD_3CN) of **5**.

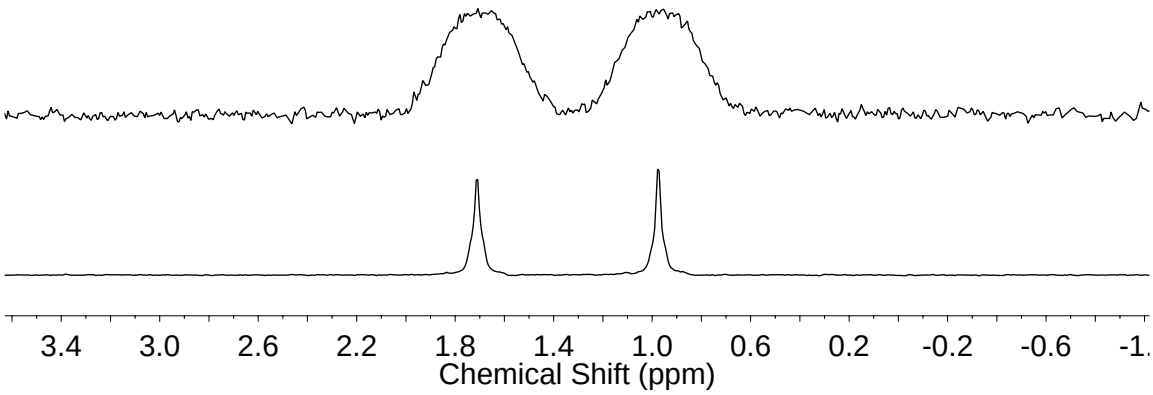

Figure A24: ^{31}P NMR spectrum (upper) and $^{31}P\{^{1}H\}$ NMR spectrum (lower) of **5** (162 MHz, CD_3CN).

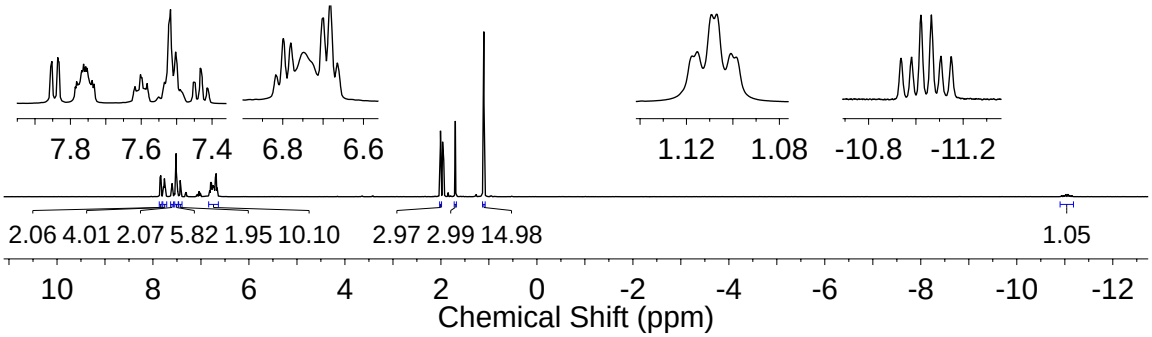

Figure A25: ^{1}H NMR spectrum (400 MHz, CD_3CN) of **6**.

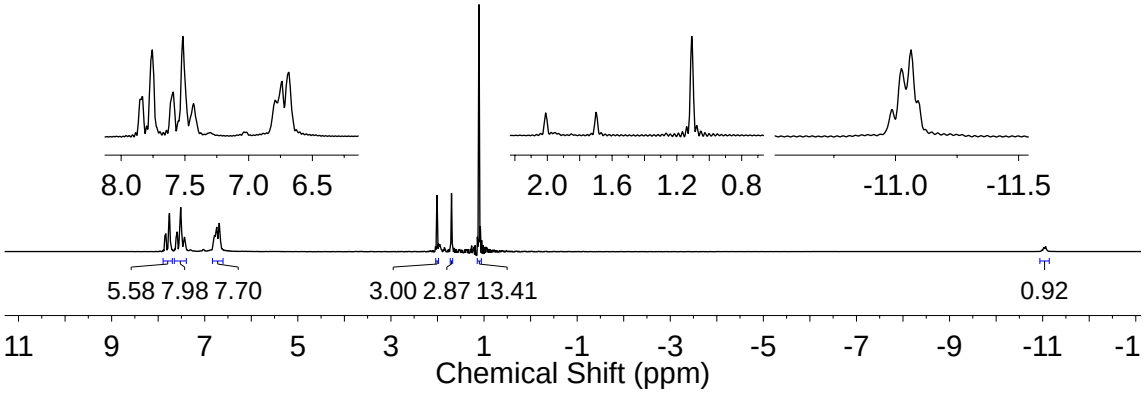

Figure A26: $^{1}H\{^{31}P\}$ NMR spectrum (400 MHz, CD_3CN) of **6**. Because deuterated solvent signal is diminished in this spectrum, the signal for Cp* methyl protons was used as internal reference and set to value of 1.1081 ppm based on nondecoupled data shown in Figure A24.

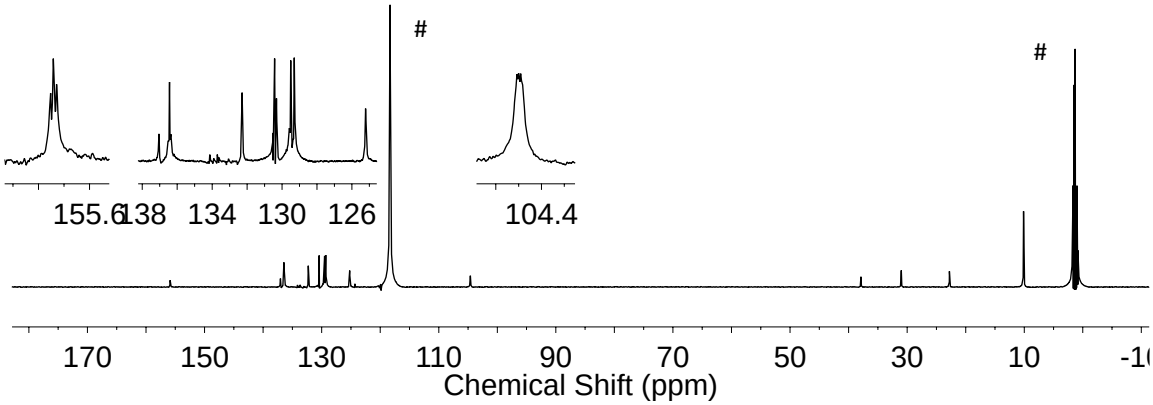

Figure A27: $^{13}C\{^{1}H\}$ NMR spectrum (126 MHz, CD_3CN) of **6**. The signals indicated by # are associated with acetonitrile.

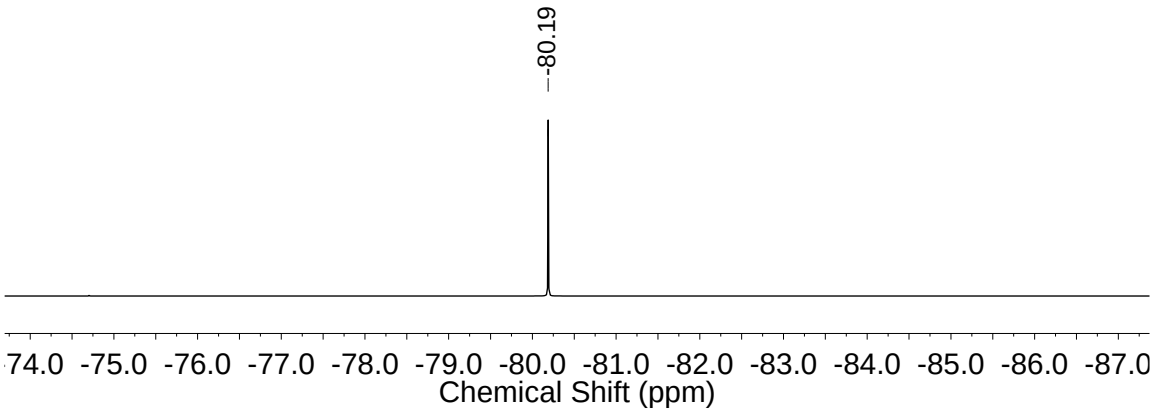

Figure A28: ^{19}F NMR spectrum (376 MHz, CD_3CN) of **6**.

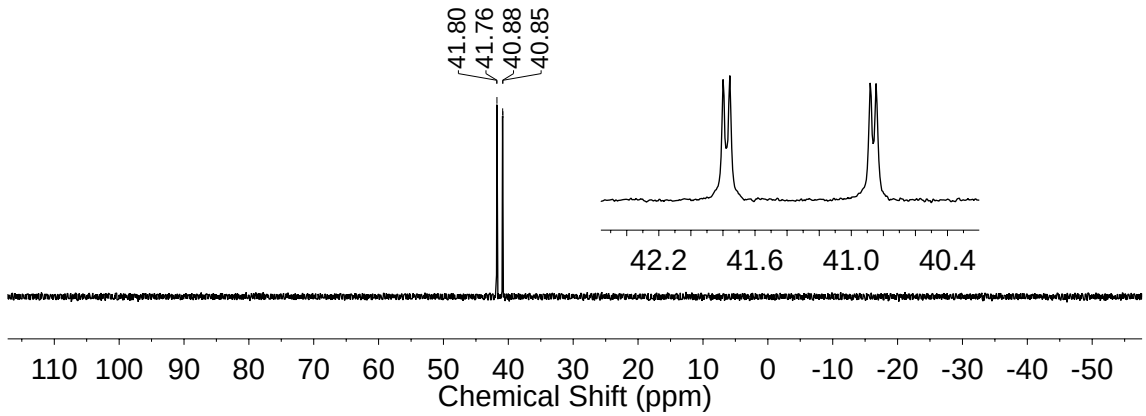

Figure A29: $^{31}P\{^{1}H\}$ NMR spectrum (162 MHz, CD_3CN) of **6**.

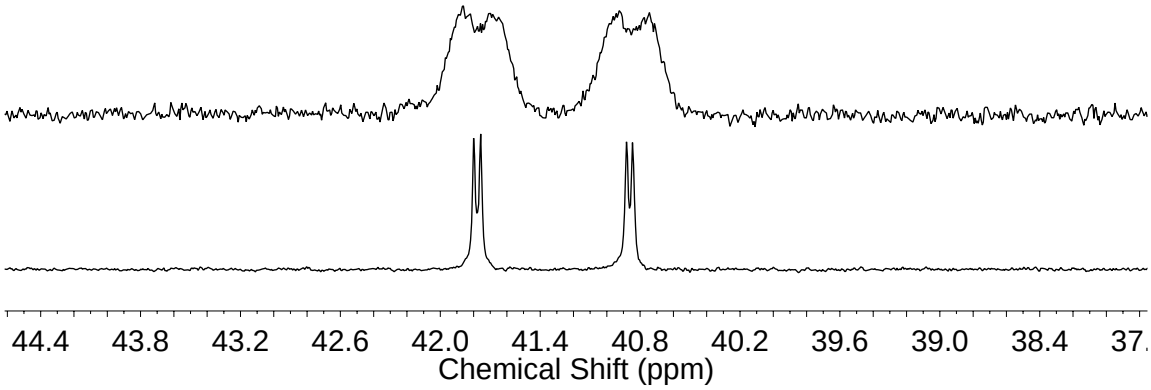

Figure A30: ^{31}P NMR spectrum (upper) and $^{31}P\{^{1}H\}$ NMR spectrum (lower) of **6** (162 MHz, CD_3CN).

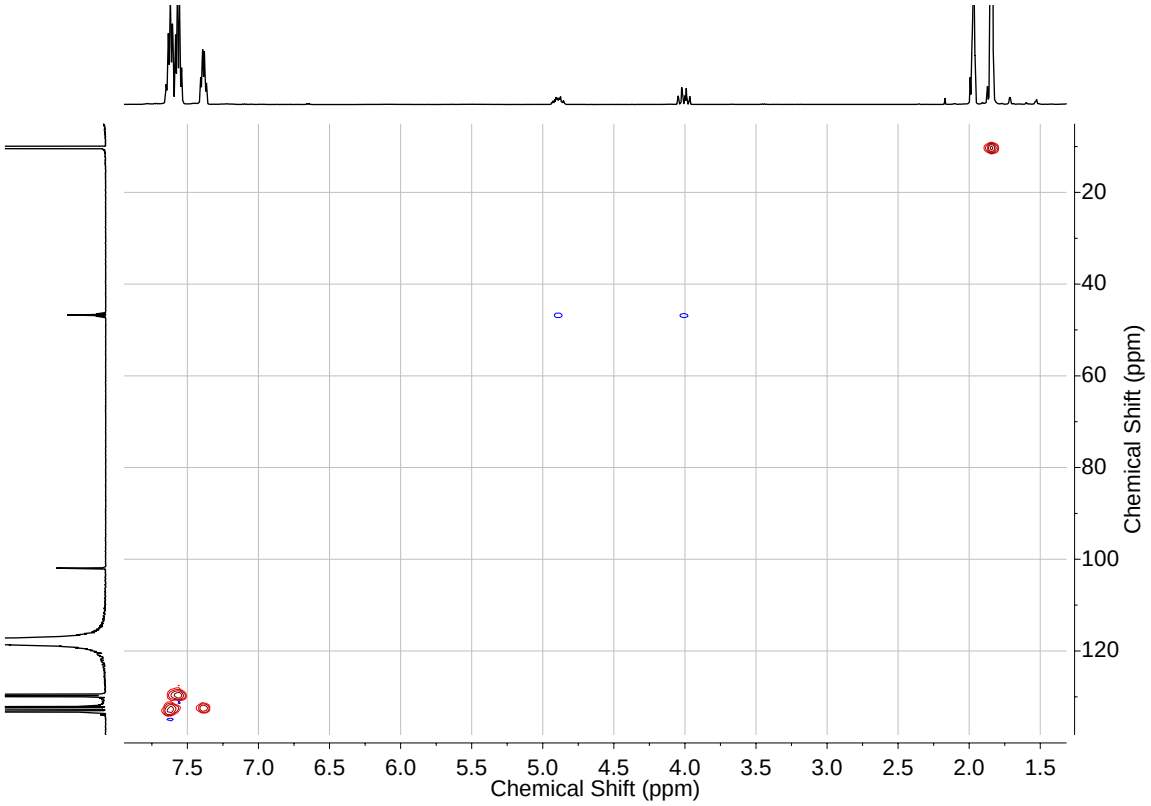

Figure A31: Full HSQC-NMR spectrum (CD_3CN) of **5** (above) and inset of aromatic region (right).

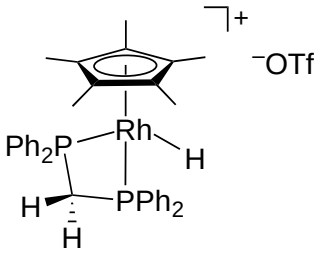

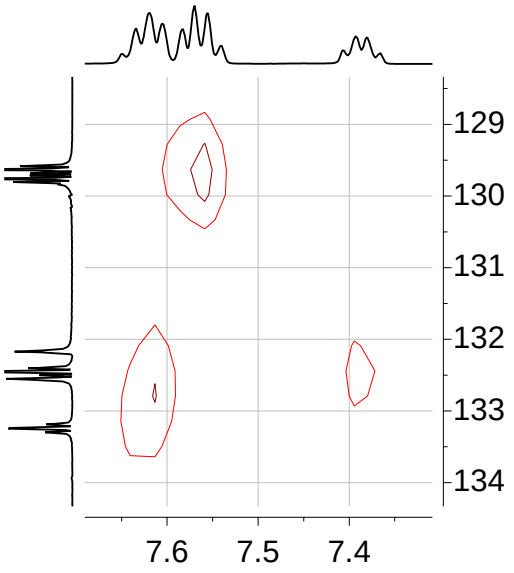

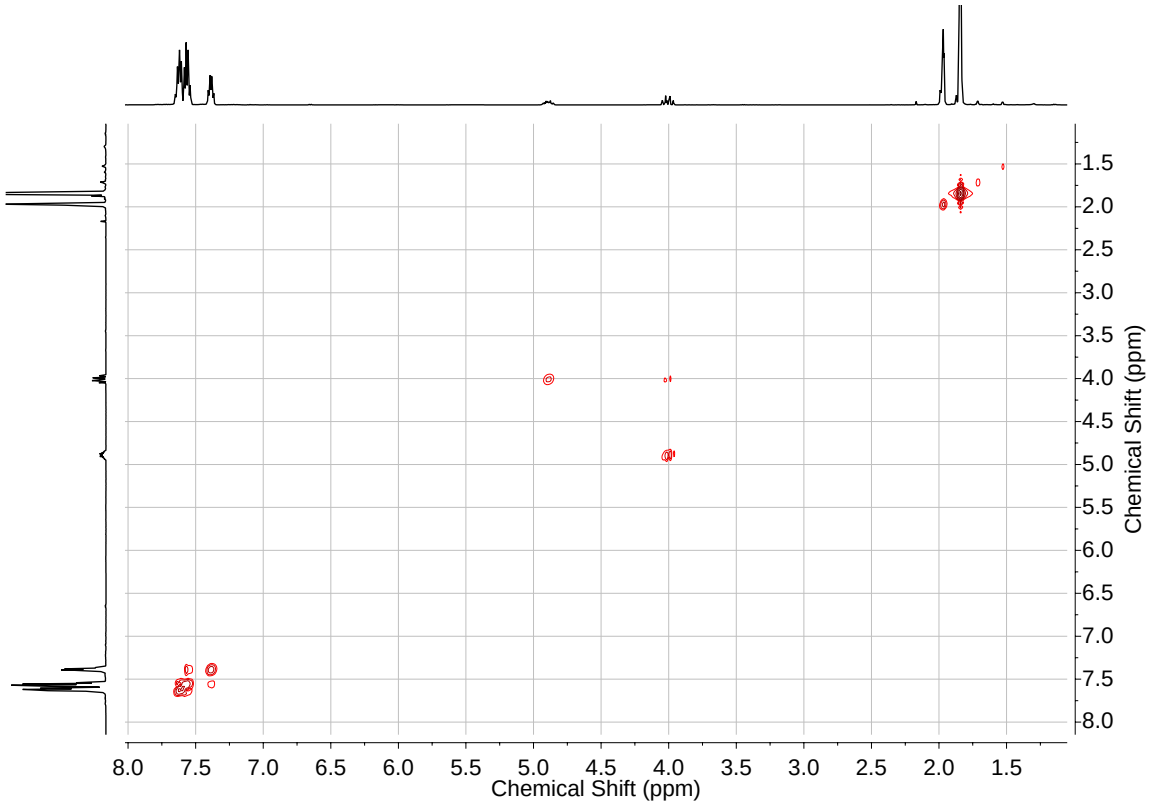

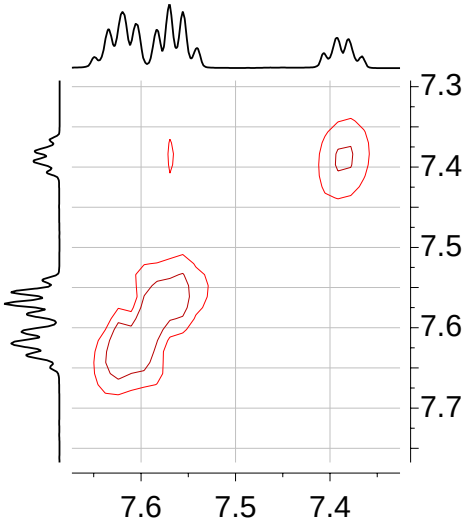

Figure A32: COSY-NMR spectrum (CD_3CN) of **5** (above) and inset of aromatic region (right).

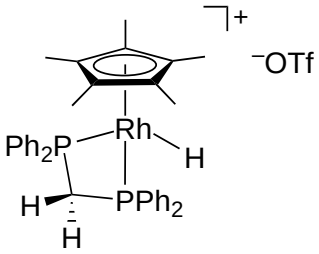

Infrared Spectroscopy

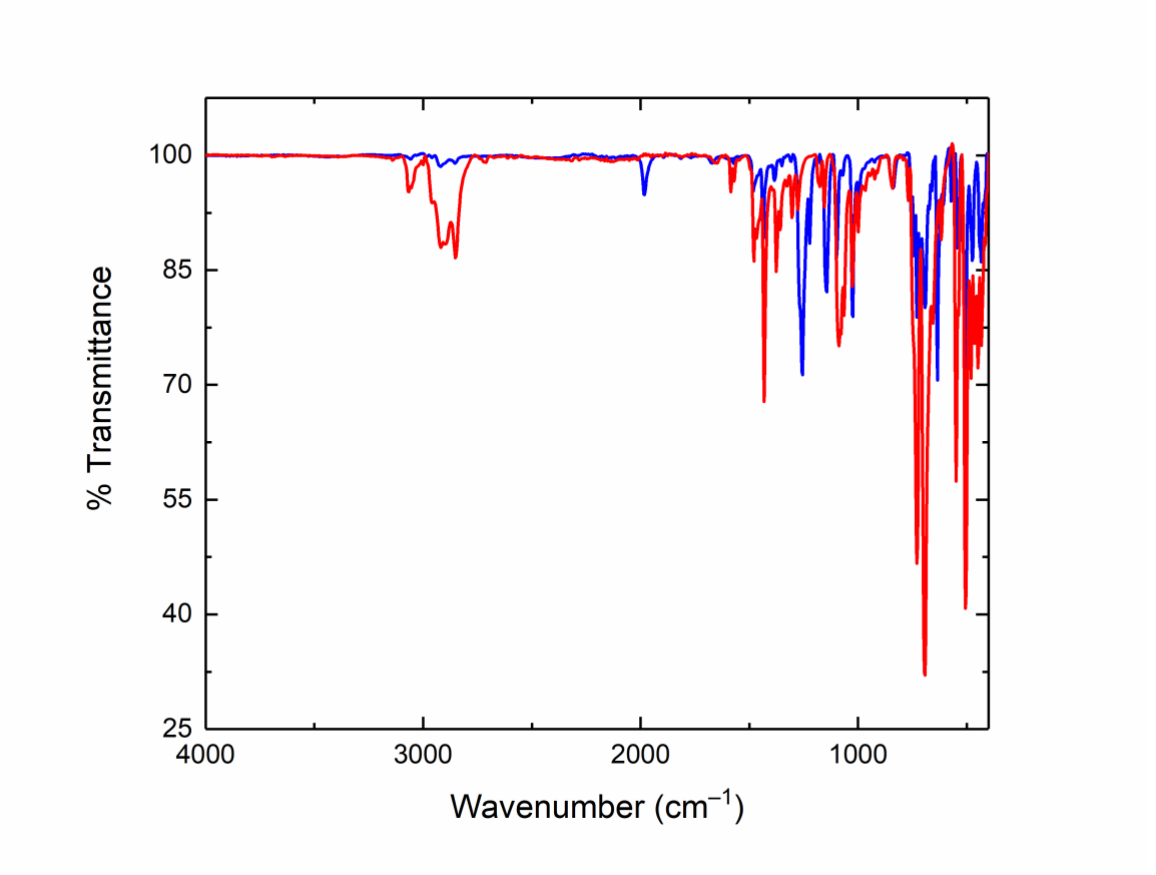

Figure A33: Infrared Spectrum of **3** (red) overlaid with **5** (blue). The peak present at 1982 cm^{-1} represents the Rh–H frequency.

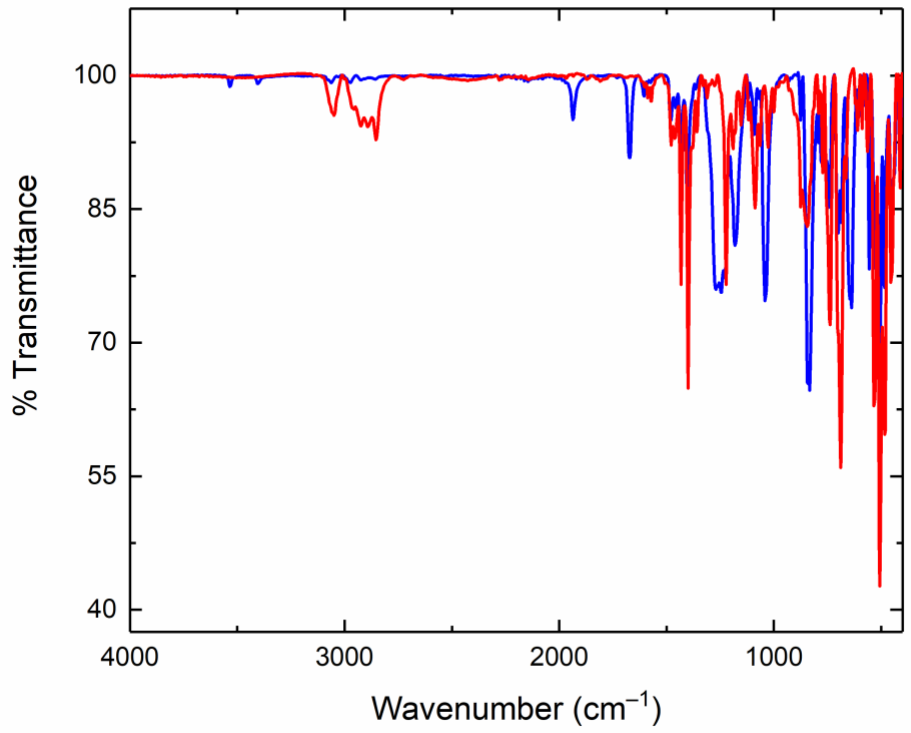

Figure A34: Infrared Spectrum of **4** (red) overlaid with **6** (blue). The peak present at 1936 cm^{-1} represents the Rh–H frequency.

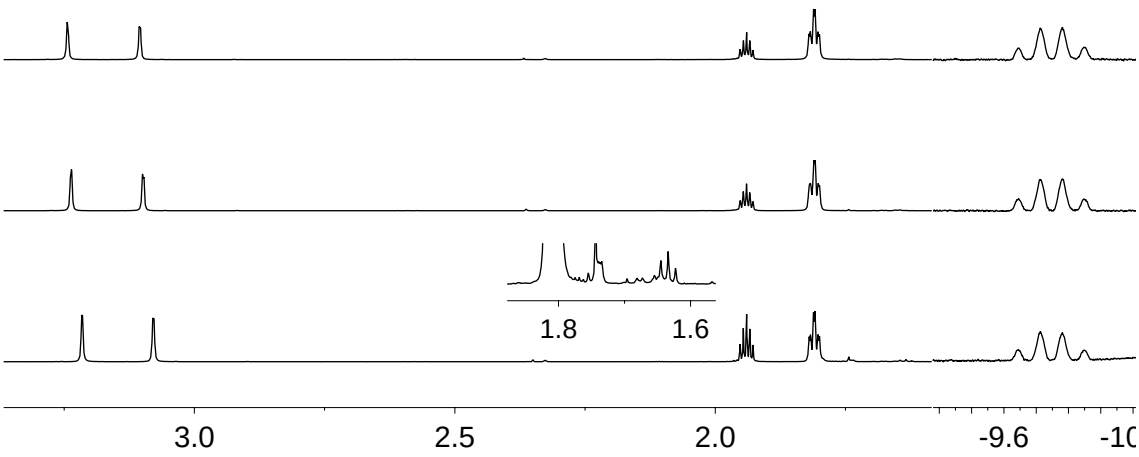

Figure A35: Partial ^{1}H NMR spectra (400 MHz, CD_3CN) of 1:1 mixture of **5** and $[DMFH]^+[OTf]^-$ in CD_3CN after 30 min, 6 days, and then heating for an additional 48 hours (from upper row to lower). The inset of the spectrum on the lowest row shows the new triplet. Hydride peak is not shown to scale.

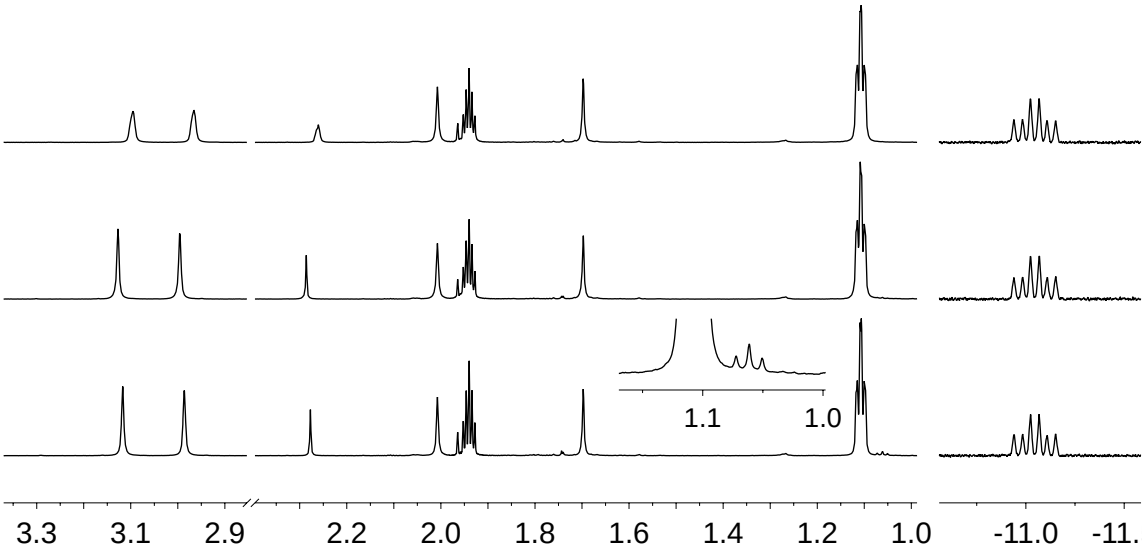

Figure A36: Partial ^{1}H NMR spectra (400 MHz, CD_3CN) of 1:1 mixture of **6** and $[DMFH]^+[OTf]^-$ in CD_3CN after 30 min, 6 days, and then heating for an additional 48 hours (from upper row to lower row). The inset of the spectrum on the lowest row shows the new triplet. Hydride peak is not shown to scale.

Crystallographic Information

Refinement Details

X-ray Crystallographic Studies for 1 (v50e), 2 (v53e), 3 (v87e), 4 (q03l_ago), 5 (q88k), and 6 (q96k).

Crystals of **1** (v50e), **2** (v53e), **3** (v87e), **4** (q03l_ago), **5** (q88k), and **6** (q96k) were mounted with Paratone N oil in MiTeGen nylon loops under a cold stream and placed on a Bruker Proteum diffractometer equipped with two CCD detectors (Apex2 and Platinum 135) sharing a common Microstar microfocus Cu rotating anode generator running at 45 mA and 60 kV (Cu Kα = 1.54178 Å). Complete sets of low temperature (200 K) X-ray diffraction data were obtained for all six compounds using monochromated Cu radiation with the Apex2 detector (**4**, **5**, and **6**) positioned at 50.0 mm and equipped with Helios multilayer mirror optics or the Platinum 135 detector (**1**, **2**, and **3**) positioned at 80.0 mm and equipped with Helios high-brilliance multilayer mirror optics. Totals of 2220 (**1**), 3324 (**2**), 2216 (**3**), 2292 (**4**), 1635 (**5**), and 1963 (**6**) 1.0°-wide ω- or ϕ-scan frames were collected with counting times of 4-6 seconds (**1**–**6**).

Preliminary lattice constants were obtained with SMART in the Bruker Apex2 Software Suite.[1] Integrated reflection intensities for all six compounds were produced using SAINT in the Bruker Apex2 Software Suite.[1] Data sets for **1** (v50e), **2** (v53e), **3** (v87e), **4** (q03l_ago) and **5** (q88k) were corrected empirically for variable absorption effects with SADABS[2] using equivalent reflections; the data set for **6** (q96k) was corrected for variable absorption effects using a numerical face-indexed absorption correction. The Bruker software package SHELXTL was used to generate the initial .INS instruction file, and

OLEX2 was then used to solve each structure using intrinsic phasing. Final stages of weighted full-matrix least-squares refinement were conducted using F_o^2 data with SHELXTL[3] or the OLEX2 software package equipped with XL.[4] The relevant crystallographic and structure refinement data for all six structures are given in Table S1.

The final structural model for each structure incorporated anisotropic thermal parameters for all full-occupancy, non-hydrogen atoms. All non-hydride hydrogen atoms were included in the model at geometrically calculated positions and refined using a riding model. Non-methyl hydrogen atoms were fixed at idealized riding model sp^2- or sp^3-hybridized positions with C–H bond lengths of 0.95 – 0.99 Å. Hydrogen atoms for the Cp* methyl groups in **3** were located from a difference Fourier and their fractional atomic coordinates were allowed to vary in least squares refinement cycles. Methyl groups for the remaining Cp* ligands, Xantphos ligands, and acetonitrile molecules of crystallization were incorporated into the structural model as idealized sp^3-hybridized rigid rotors with C-H bond lengths of 0.98 Å that were allowed to rotate freely about their C–C bonds in least-squares refinement cycles. The toluene methyl groups for **4** were fixed at idealized staggered positions. Hydride hydrogen atoms in **5** and **6** were located from difference Fouriers and included in the structural model as independent isotropic atoms whose parameters were allowed to vary in least-squares refinement cycles.

Table A1: Crystal Refinement Data

	1 (v50e)	**2** (v53e)	**3** (v87e)
CCDC accession code	**2044718**	**2044719**	**2067364**
Empirical formula	$C_{37}H_{40}ClF_6NP_3Rh$	$C_{50}H_{49}Cl_3F_6OP_3Rh$	$C_{35}H_{37}P_2Rh$
Formula weight	843.97	1082.06	622.49
Temperature	200 K	200 K	200 K
Wavelength	1.54178 Å	1.54178 Å	1.54178 Å
Crystal system	monoclinic	triclinic	monoclinic
Space group	*C2* (No. 5)	*P-1* (No. 2)	$P2_1/n$ (No. 14)
a	22.5645(10) Å	10.8320(4) Å	9.0090(4) Å
b	8.6211(4) Å	20.8901(8) Å	8.9292(4) Å
c	22.3120(10) Å	21.2052(8) Å	36.9176(17) Å
a	90°	97.7441(10)°	90°
β	119.2692(10) °	93.2743(11) °	91.606(2)°
γ	90°	91.0432(10) °	90°
Volume	3786.2(3) $Å^3$	4745.2(3) $Å^3$	2968.6(2) $Å^3$
Z	4	4	4
Density (calculated)	1.481 g/cm^3	1.515 g/cm^3	1.393 g/cm^3
Absorption coefficient	5.989 mm^{-1}	5.941 mm^{-1}	5.825 mm^{-1}
F(000)	1720	2208	1288
Crystal size	0.21 × 0.08 × 0.045 mm^3	0.12 × 0.10 × 0.09 mm^3	0.185 × 0.075 × 0.075 mm^3
Number of data frames/time	2220/4-6 seconds	3324/4-6 seconds	2216/4-6 seconds
Theta range	5.60 to 68.35°	2.11 to 68.39°	4.79 to 68.33°
Index ranges	$-26 \le h \le 26$, $-7 \le k \le 10$, $-25 \le l \le 26$	$-12 \le h \le 13$, $-25 \le k \le 20$, $-25 \le l \le 24$	$-10 \le h \le 10$, $-7 \le k \le 10$, $-44 \le l \le 43$
Reflections collected	12133	43756	19379
Independent reflections	4847 [R_{int} = 0.032, Rsigma = 0.048]	16483 [R_{int} = 0.029, Rsigma = 0.033]	5311 [R_{int} = 0.029, Rsigma = 0.029]
Completeness/θ_{max}	98.5%/66.00°	97.5%/66.00°	98.6%/67.68°
Absorption correction	Multi-scan	Multi-scan	Multi-scan
Max. and min. transmission	1.000 and 0.638	1.000 and 0.873	1.000 and 0.876
Refinement method	Full-matrix least-squares on F^2	Full-matrix least-squares on F^2	Full-matrix least-squares on F^2
Data / restraints / parameters	4847 / 1 / 452	16483 / 6 / 1167	5311 / 0 / 389
Goodness-of-fit on F^2	1.025	1.024	1.046
Final R indices [I>2σ(I)]	R_1 = 0.033, wR_2 = 0.085	R_1 = 0.042, wR_2 = 0.108	R_1 = 0.025, wR_2 = 0.060
R indices (all data)	R1 = 0.035, wR_2 = 0.085	R_1 = 0.046, wR_2 = 0.111	R_1 = 0.027, wR_2 = 0.061
Largest diff. peak and hole	0.41 and -0.85 $e^-/Å^3$	1.29 and -1.42 $e^-/Å^3$	0.30 and -0.39 $e^-/Å^3$

	4 (q03l_ago)	**5** (q88k)	**6** (q96k)
CCDC accession code	**2067366**	**2067363**	**2067365**
Empirical formula	$C_{54.25}H_{53}OP_2Rh$	$C_{36}H_{38}F_3O_3P_2RhS$	$C_{50}H_{48}F_3O_4P_2RhS$
Formula weight	885.81	772.57	966.79
Temperature	200 K	200 K	200 K
Wavelength	1.54178 Å	1.54178 Å	1.54178 Å
Crystal system	monoclinic	orthorhombic	orthorhombic
Space group	*C2/c* (No. 15)	*Pnma* (No. 62)	*Pca2₁* (No. 29)
a	29.5173(4) Å	18.8596(3) Å	22.4478(6) Å
b	18.4213(3) Å	18.9169(3) Å	11.2787(3) Å
c	22.0747(3) Å	9.7134(2) Å	34.9472(10) Å
a	90°	90°	90°
β	127.4030(10)	90°	90°
γ	90°	90°	90°
Volume	9535.0(3) $Å^3$	3465.40(11) $Å^3$	8848.0(4) $Å^3$
Z	8	4	8
Density (calculated)	1.234 g/cm^3	1.481 g/cm^3	1.452 g/cm^3
Absorption coefficient	3.799 mm^{-1}	5.852 mm^{-1}	4.726 mm^{-1}
F(000)	3692	1584	3984
Crystal size	0.085 × 0.03 × 0.02 mm^3	0.065 × 0.055 × 0.05 mm^3	0.216 × 0.071 × 0.04 mm^3
Number of data frames/time	2292/4-6 seconds	1635/4-6 seconds	1963/4-6 seconds
Theta range	3.05 to 70.18°	4.69 to 70.06°	2.53 to 70.18°
Index ranges	$-35 \le h \le 35$, $-19 \le k \le 21$, $-26 \le l \le 26$	$-22 \le h \le 19$, $-22 \le k \le 19$, $-11 \le l \le 11$	$-26 \le h \le 24$, $-13 \le k \le 11$, $-41 \le l \le 40$
Reflections collected	33394	12431	41479
Independent reflections	8645 [R_{int} = 0.034, R_{sigma} = 0.028]	3260 [R_{int} = 0.033, R_{sigma} = 0.027]	13475 [R_{int} = 0.031, R_{sigma} = 0.046]
Completeness/θ_{max}	97.9%/67.68°	98.9%/66.00°	99.6%/66.00°
Absorption correction	Multi-scan	Multi-scan	Numerical face-indexed
Max. and min. transmission	1.000 and 0.784	1.000 and 0.764	1.000 and 0.354
Refinement method	Full-matrix least-squares on F^2	Full-matrix least-squares on F^2	Full-matrix least-squares on F^2
Data / restraints / parameters	8645 / 13 / 517	3260 / 0 / 226	13475 / 1 / 1122
Goodness-of-fit on F^2	1.049	1.076	1.023
Final R indices [I>2σ(I)]	R_1 = 0.037, wR_2 = 0.113	R_1 = 0.032, wR_2 = 0.081	R_1 = 0.024, wR_2 = 0.058
R indices (all data)	R_1 = 0.043, wR_2 = 0.120	R_1 = 0.033, wR_2 = 0.082	R_1 = 0.025, wR_2 = 0.062
Largest diff. peak and hole	1.13 and -0.47 $e^-/Å^3$	0.53 and -0.48 $e^-/Å^3$	0.60 and -0.38 $e^-/Å^3$

Special Refinement Details for 1

Complex **1** crystallizes in the monoclinic space group *C2*. The crystal was refined as a two-component inversion twin with the first component comprising 96.7% and the second component comprising 3.3%. The secondary methylene group was refined using riding coordinates. There are two crystallographically-independent outer-sphere hexafluorophosphate counterianions. Both utilize a crystallographic C_2 axis and are therefore included in the structural model with occupancy factors of 0.50. Each one accounts for a formal negative charge of –1/2 in the asymmetric unit.

Solid-State Structure of Molecular Cation of Compound 1

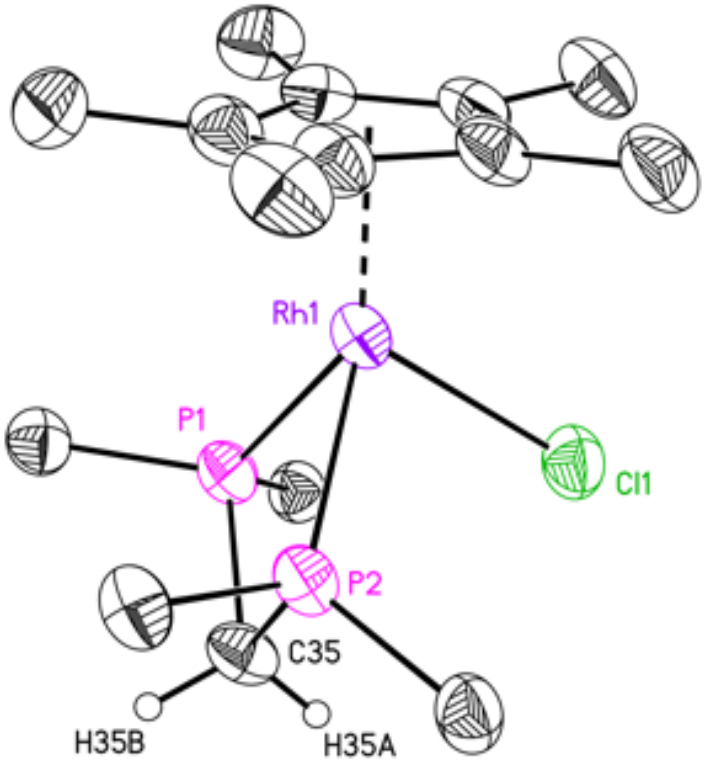

Figure A37: Solid-state structure for the core of the molecular cation in the asymmetric unit of **1**. The hexafluorophosphate counteranions (each having an occupancy of 0.5, *vide supra*), a co-crystallized acetonitrile molecule, all hydrogen atoms except for H35A and H35B, and the additional atoms associated with the phosphine phenyl rings are omitted for clarity. Displacement ellipsoids are shown at the 50% probability level.

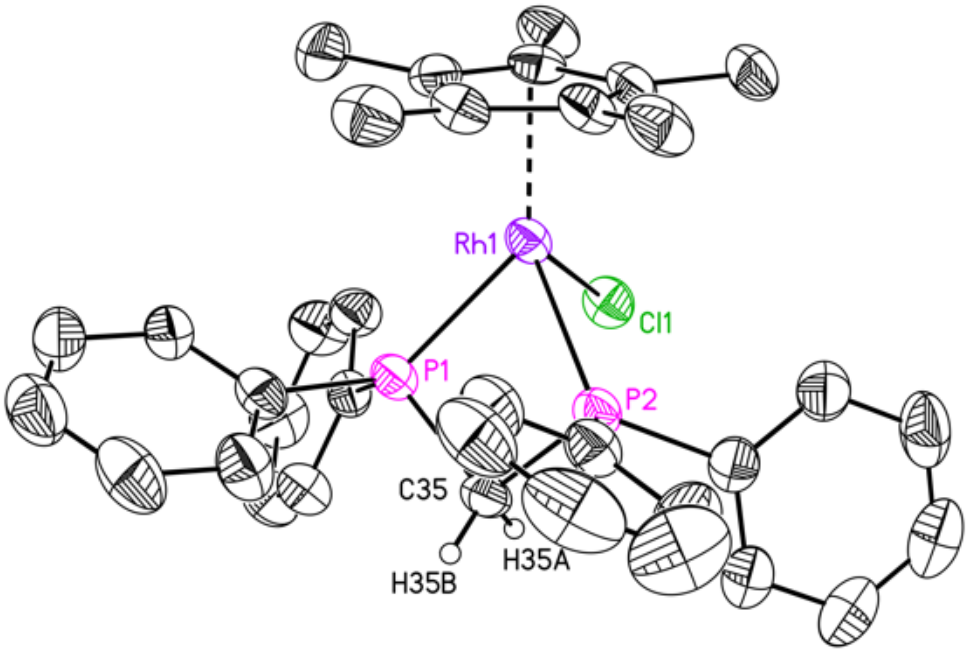

Figure A38: Solid-state structure of the molecular cation in the asymmetric unit of **1**. The hexafluorophosphate counteranions and a co-crystallized acetonitrile molecule are omitted for clarity, as are all hydrogen atoms except for H35A and H35B. Displacement ellipsoids are shown at the 50% probability level.

Full Asymmetric Unit of 1

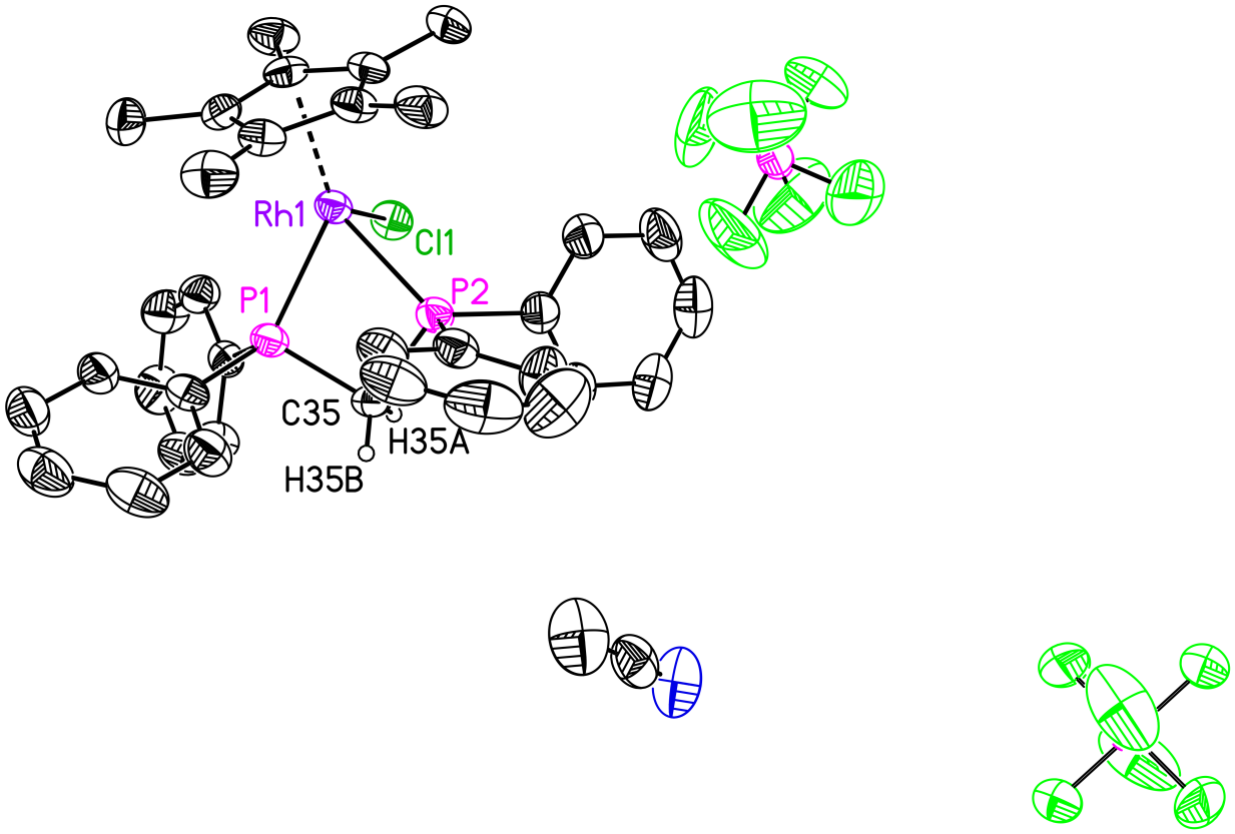

Figure A39: Solid-state structure for the asymmetric unit of **1**. All hydrogen atoms, except H35A and H35B, are omitted for clarity. There are two crystallographically-independent outer-sphere hexafluorophosphate counterianions. Both utilize a crystallographic C_2 axis and are therefore included in the structural model with occupancy factors of 0.50. Each one accounts for a formal negative charge of –1/2 in the asymmetric unit. Displacement ellipsoids are shown at the 50% probability level.

Special Refinement Details for 2

Complex **2** crystallizes in the triclinic space group *P-1*. Mild ISOR restraints (in OLEX2) were applied to the anisotropic displacement ellipsoid of C27.

Solid-State Structure of First Molecular Cation in 2

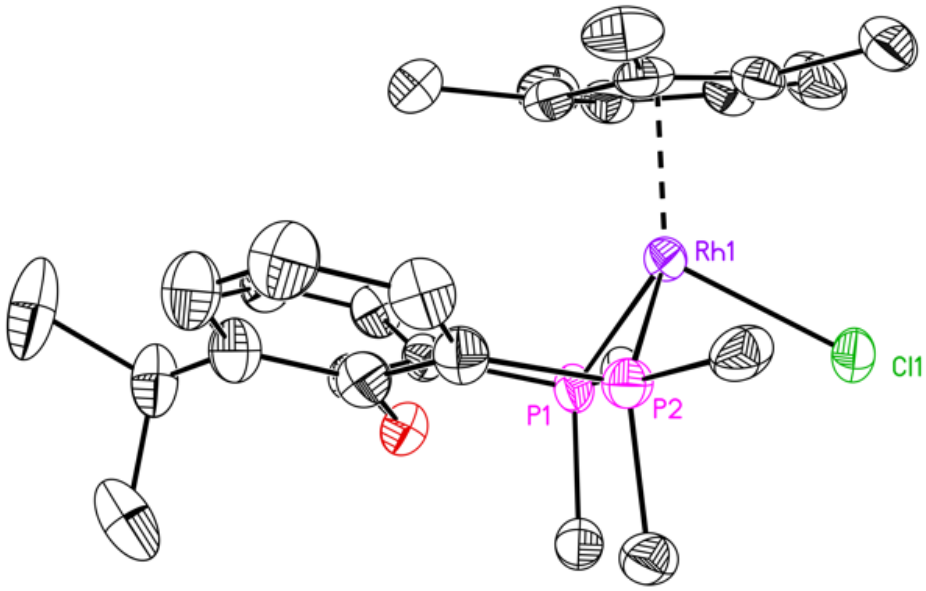

Figure A40: Solid-state structure for the non-hydrogen core for the first of two crystallographically-independent and virtually identical molecular cations in the asymmetric unit of **2**. A second molecular cation of **2**, two co-crystallized hexafluorophosphate counteranions, and two co-crystallized dichloromethane molecules are omitted for clarity, as are all hydrogen atoms and additional atoms for the phosphine phenyl rings. Displacement ellipsoids are shown at the 50% probability level.

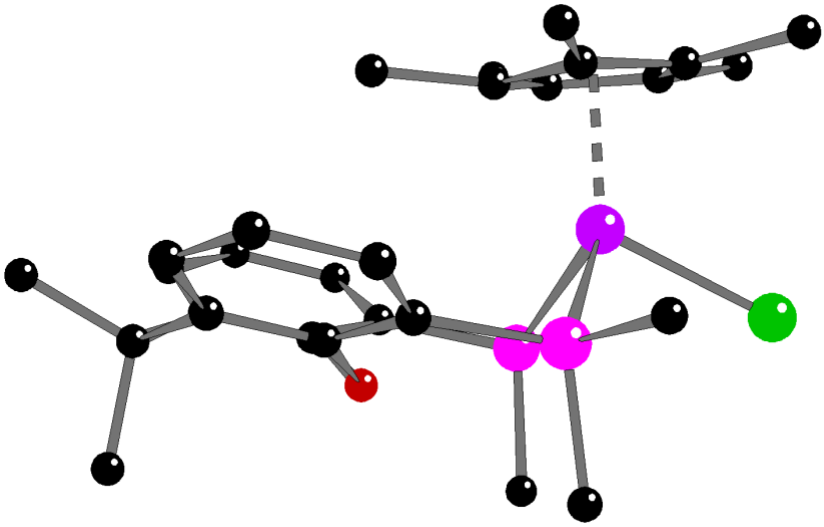

Figure A41: Ball-and-stick representation for the non-hydrogen core for the first of two crystallographically-independent and virtually identical molecular cations in the asymmetric unit of **2**. A second molecular cation of **2**, two co-crystallized hexafluorophosphate counteranions and two co-crystallized dichloromethane molecules are omitted for clarity as are all hydrogen atoms and additional atoms for the phosphine phenyl rings.

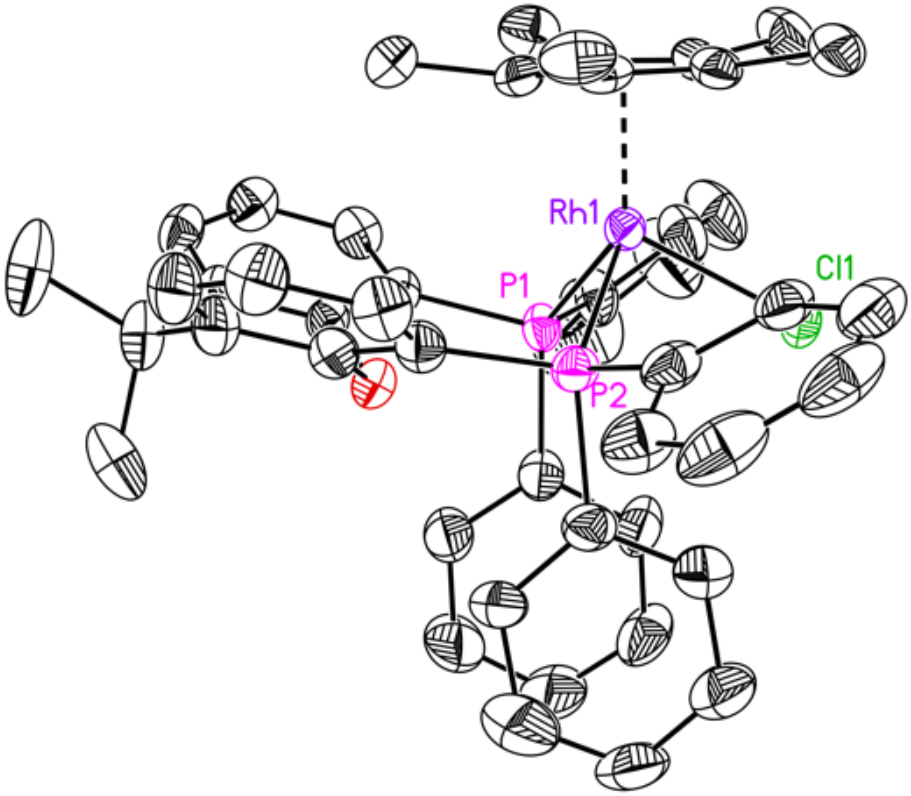

Figure A42: Solid-state structure for the non-hydrogen atoms for the first of two crystallographically-independent and virtually identical molecular cations in the asymmetric unit of **2**. A second molecular cation of **2**, two co-crystallized hexafluorophosphate counteranions and two co-crystallized dichloromethane molecules are omitted for clarity. All hydrogen atoms are also omitted for clarity. Displacement ellipsoids are shown at the 50% probability level.

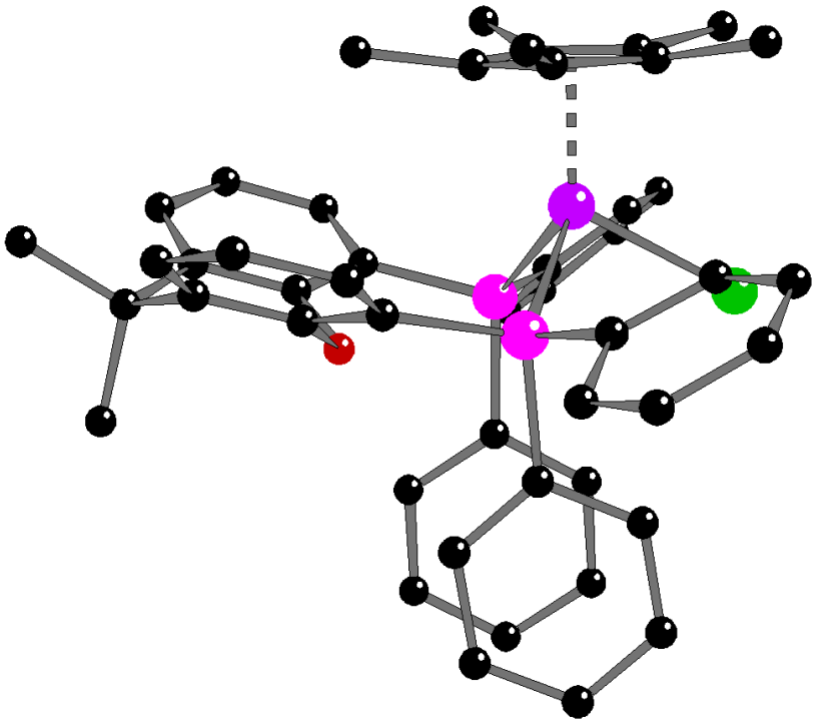

Figure A43: Ball-and-stick representation for the non-hydrogen atoms for the first of two crystallographically-independent and virtually identical molecular cations in the asymmetric unit of **2**. A second molecular cation of **2**, two co-crystallized hexafluorophosphate counteranions and two co-crystallized dichloromethane molecules are omitted for clarity, as are all hydrogen atoms.

Full Solid-State Asymmetric Unit for 2

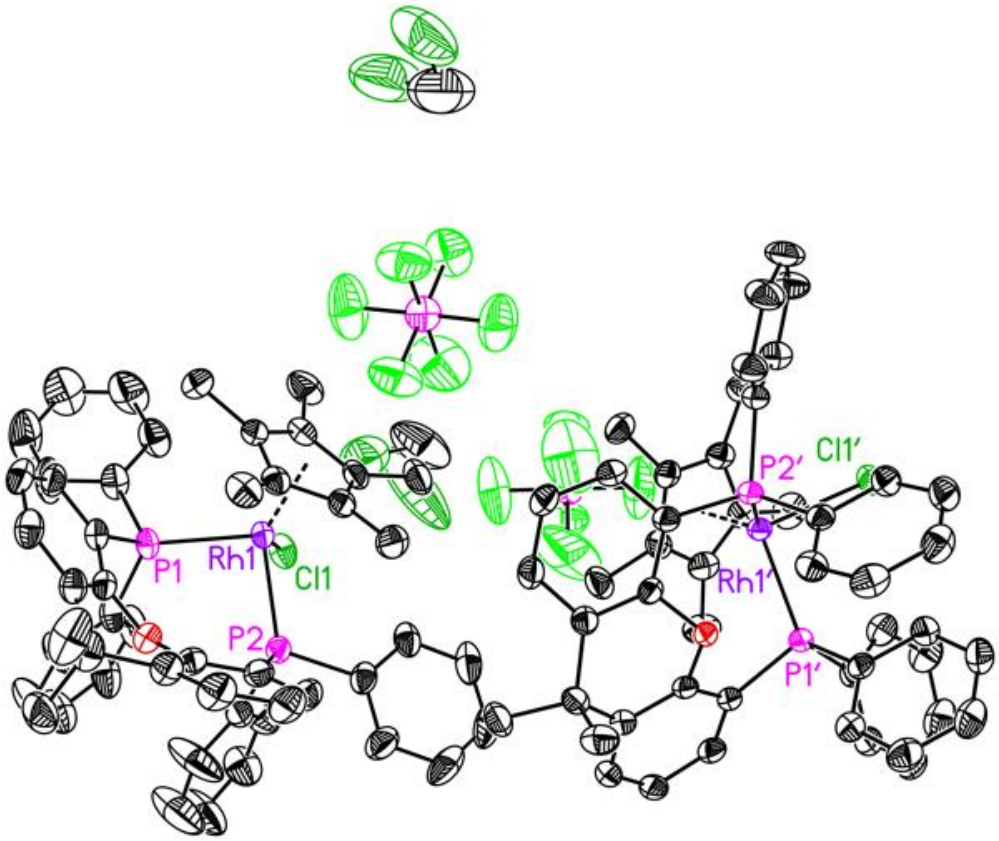

Figure A44: Full solid-state asymmetric unit for **2**. Atoms of the second crystallographically-independent cation are labeled with a prime (′). Hydrogen atoms are omitted for clarity. Displacement ellipsoids are shown at the 50% probability level.

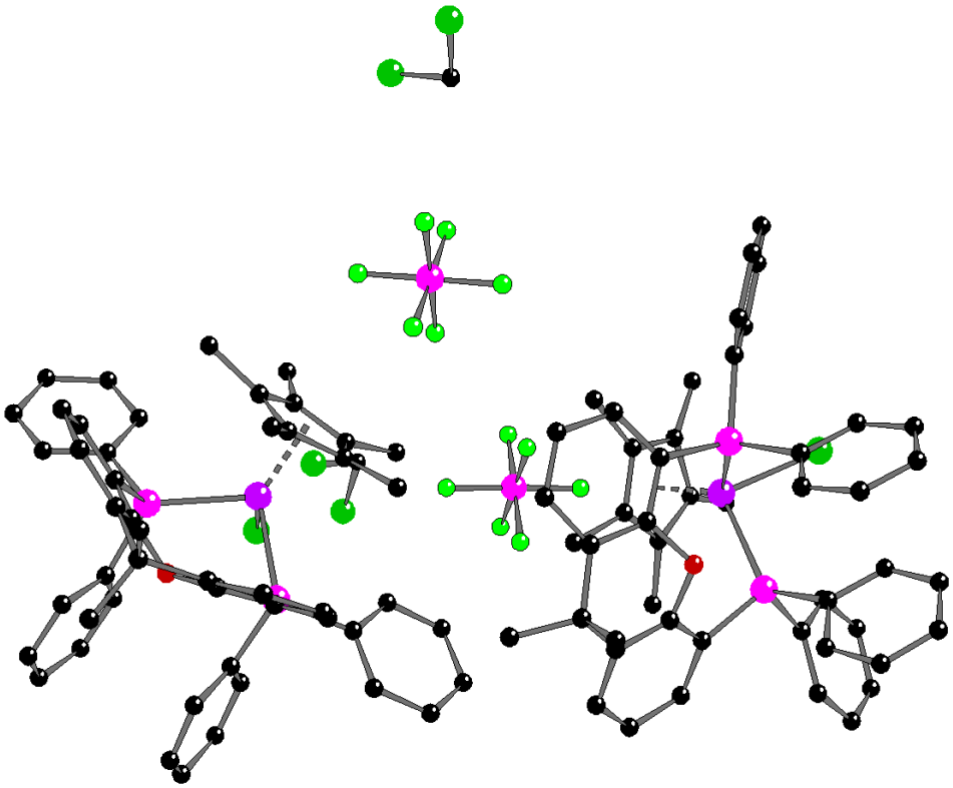

Figure A45: Ball-and-stick representation for the solid-state asymmetric unit of **2**. Hydrogen atoms are omitted for clarity.

Special Refinement Details for 3

No special refinement was required.

Solid-State Structure of 3

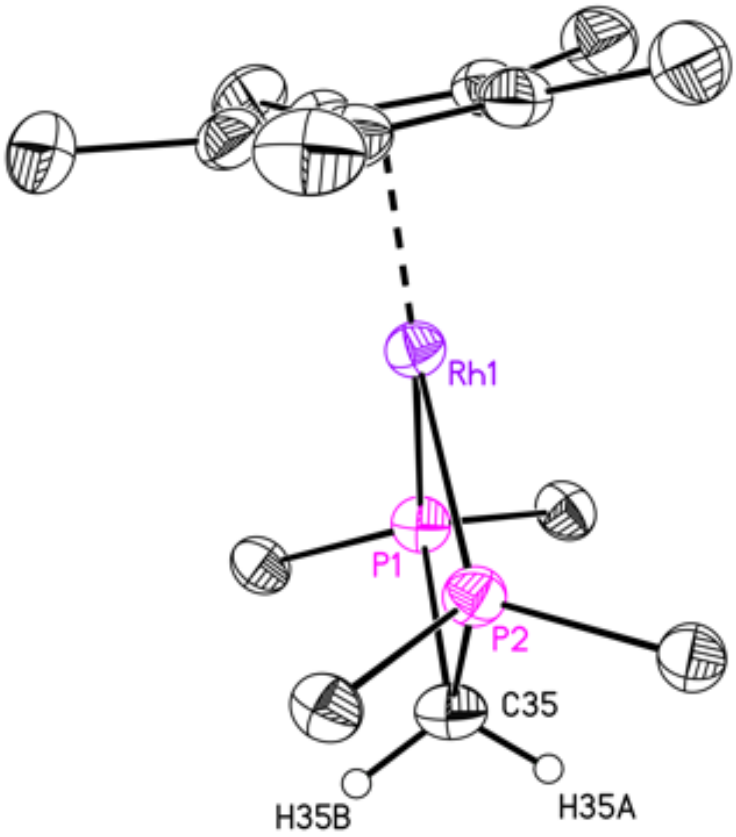

Figure A46: Structure of the molecular core for the asymmetric unit in crystals of **3**. All hydrogen atoms except for H35A and H35B and additional atoms for the phosphine phenyl rings are deleted for clarity. Displacement ellipsoids are shown at the 50% probability level.

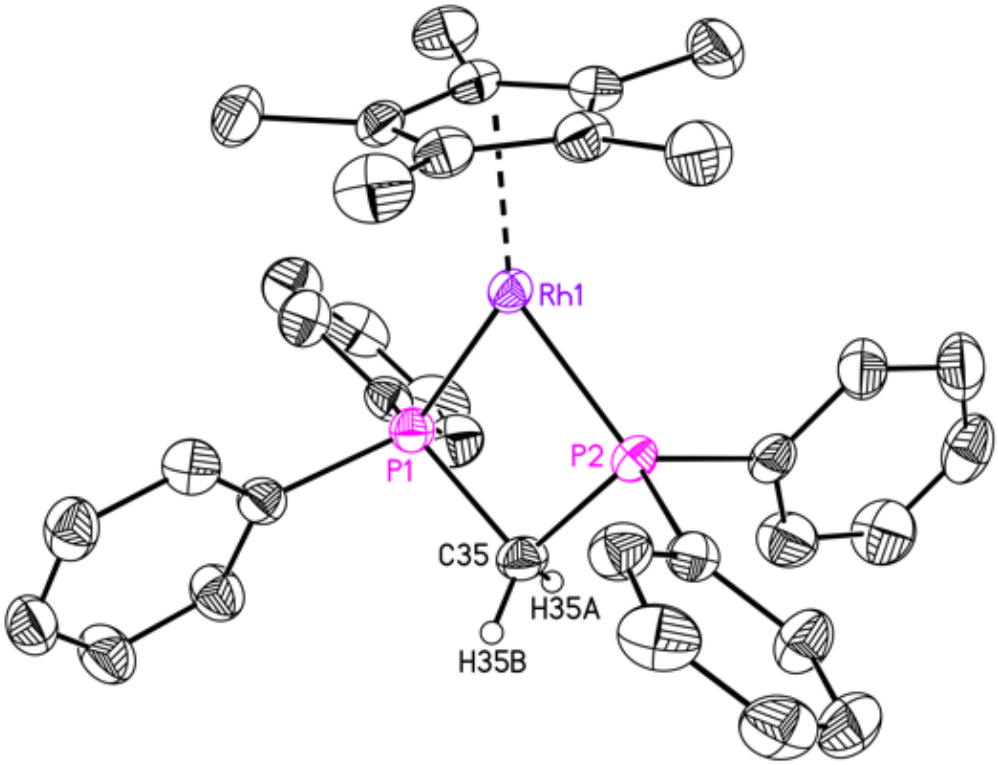

Figure A47: Structure for the asymmetric unit in crystals of **3**. Hydrogen atoms, except for H35A and H35B, are omitted for clarity. Displacement ellipsoids are shown at the 50% probability level.

Special Refinement Details for 4

Complex **4** crystallizes in the monoclinic space group *C2/c*. Two co-crystallized toluene molecules are present within the asymmetric unit. One is located in a general position, while the other is disordered across an inversion center. In the final model, both of the aromatic portions of the toluene molecules were fit to ideal hexagons and were allowed to freely rotate. The methyl group was restrained to have reasonable 1,2- and 1,3-C•••C distances and to retain a reasonable geometry. The occupancy of the atoms comprising the toluene molecule in the general position was modified by inspection of the displacement parameters yielding a 25% occupancy. The toluene that is disordered across the inversion center was modeled at 50% occupancy. However, mild similarity restraints were applied to the displacement parameters. In the final model, the toluene carbon atoms were modeled with isotropic displacement parameters.

Solid-State Structure of 4

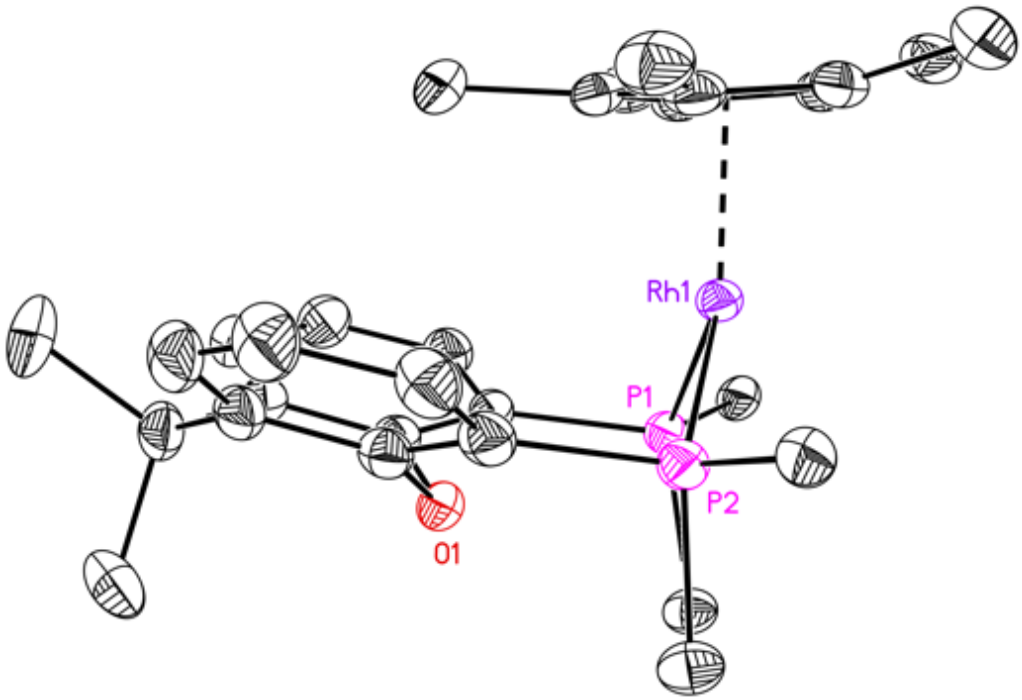

Figure A48: Solid-state structure for the molecular core of the Rh(I) complex in the asymmetric unit of **4**. All hydrogen atoms, additional atoms for the phosphine phenyl rings and the co-crystallized toluene molecules are omitted for clarity. Displacement ellipsoids are shown at the 50% probability level.

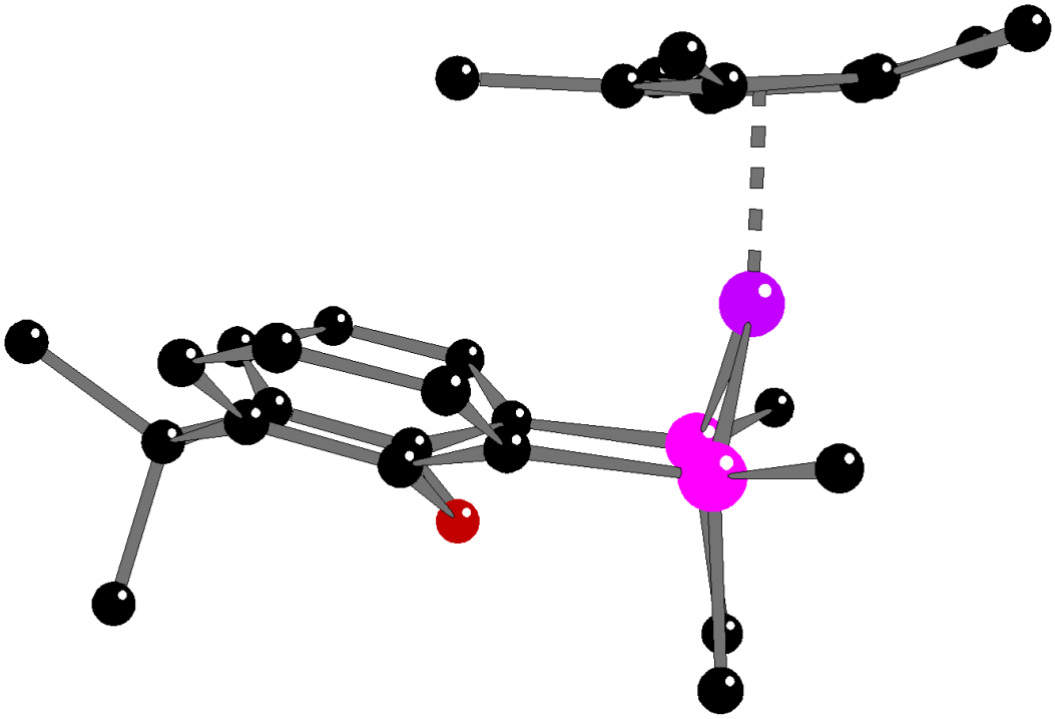

Figure A49: Ball-and-stick representation for the molecular core of the Rh(I) complex in the asymmetric unit for **4**. All hydrogen atoms, additional atoms for the phosphine phenyl rings and the co-crystallized toluene molecules are omitted for clarity.

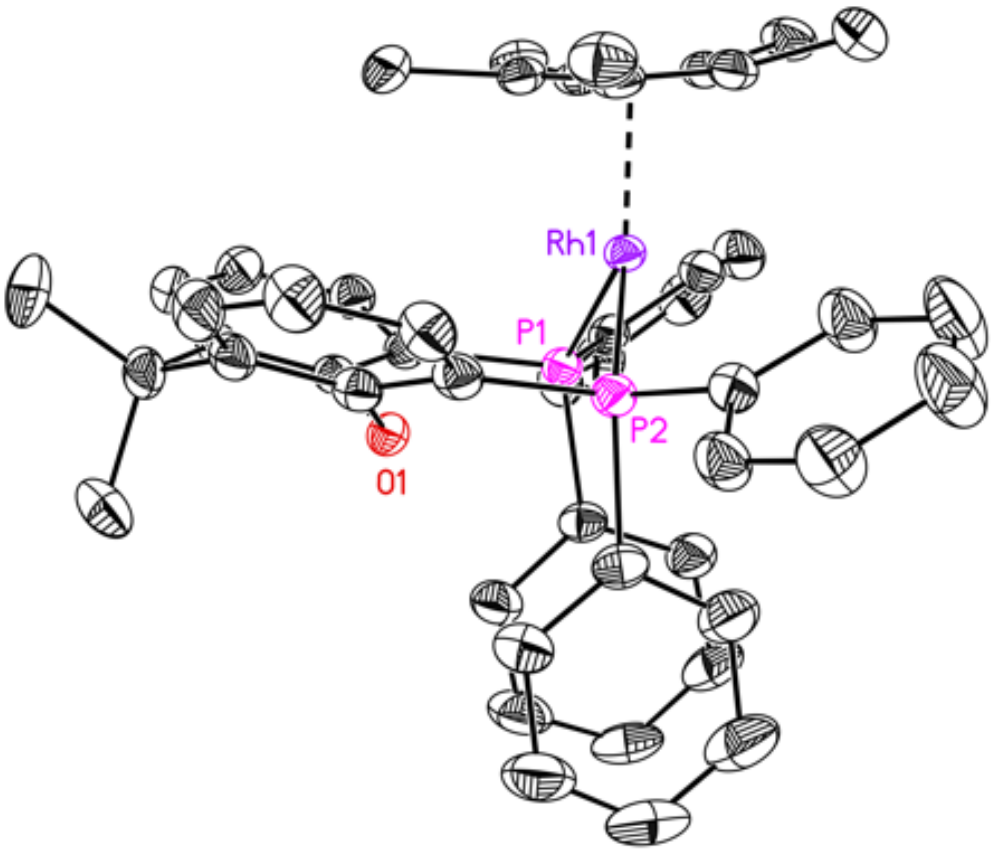

Figure A50: Solid-state structure for the Rh(I) complex in the asymmetric unit of **4**. All hydrogen atoms and the co-crystallized toluene molecules are omitted for clarity. Displacement ellipsoids are shown at the 50% probability level.

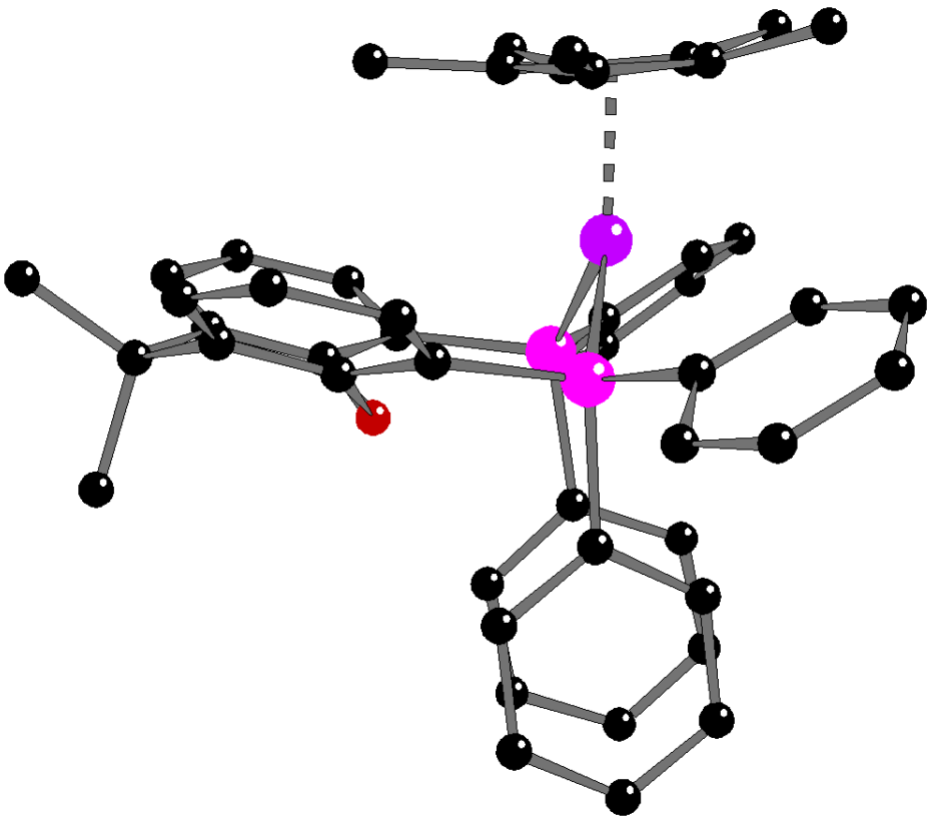

Figure A51: Ball-and-stick representation for the Rh(I) complex in the asymmetric unit of **4**. All hydrogen atoms and the co-crystallized toluene molecules are omitted for clarity.

Full Asymmetric Unit of 4

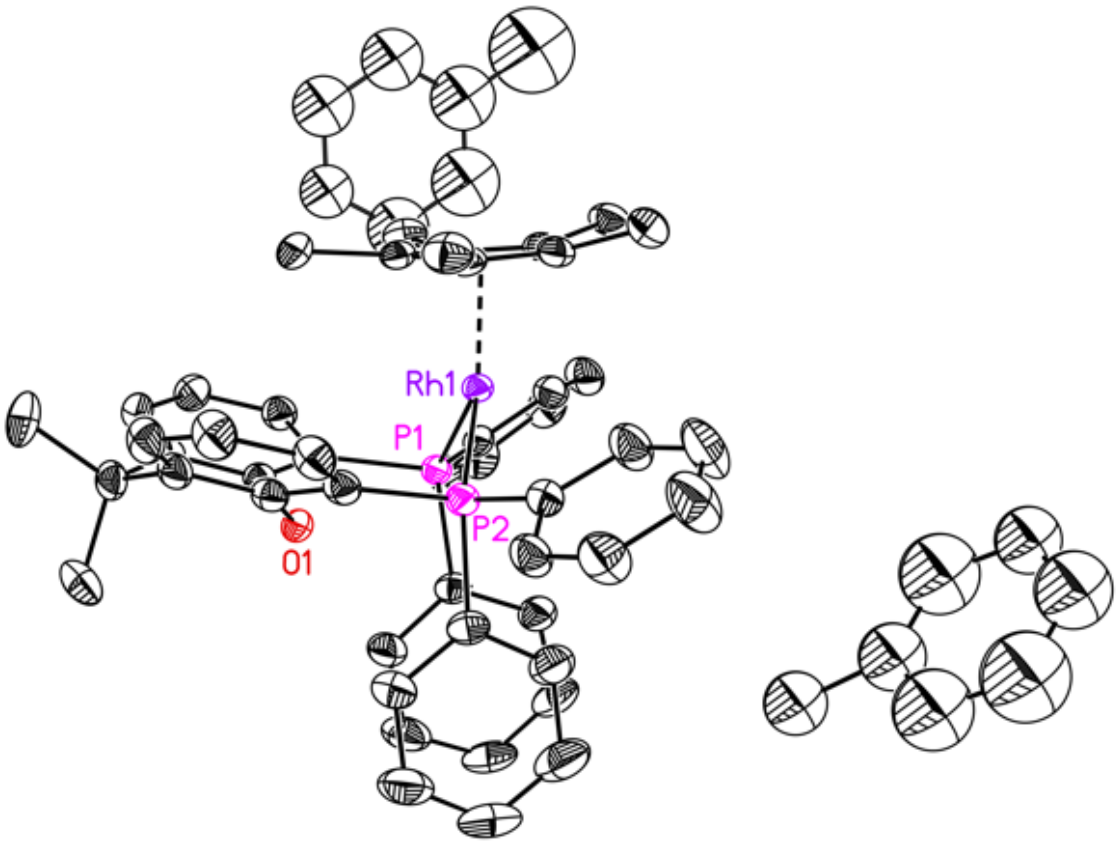

Figure A52: Solid-state structure for the asymmetric unit of **4**. Hydrogen atoms are omitted for clarity. Displacement ellipsoids are shown at the 50% probability level.

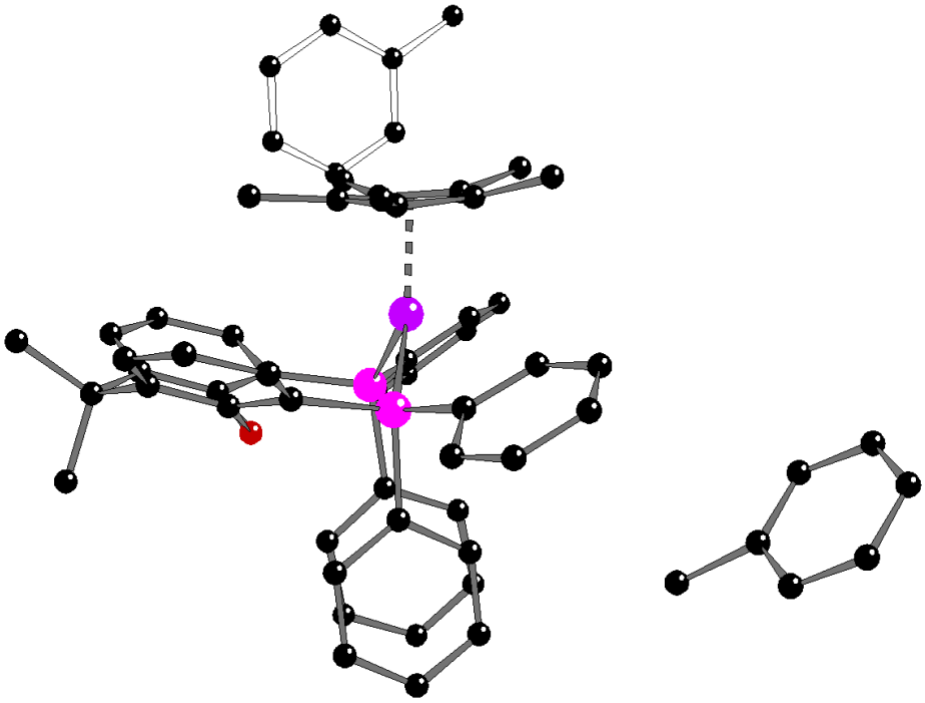

Figure A53: Ball-and-stick representation for the solid-state asymmetric unit of **4**. Hydrogen atoms are omitted for clarity.

Special Refinement Details for 5

Hydride hydrogen atom H1 was located from a difference Fourier and included in the structural model as an independent isotropic atom whose parameters were allowed to vary in least-squares refinement cycles.

Solid-State Structure of the Molecular Cation in 5

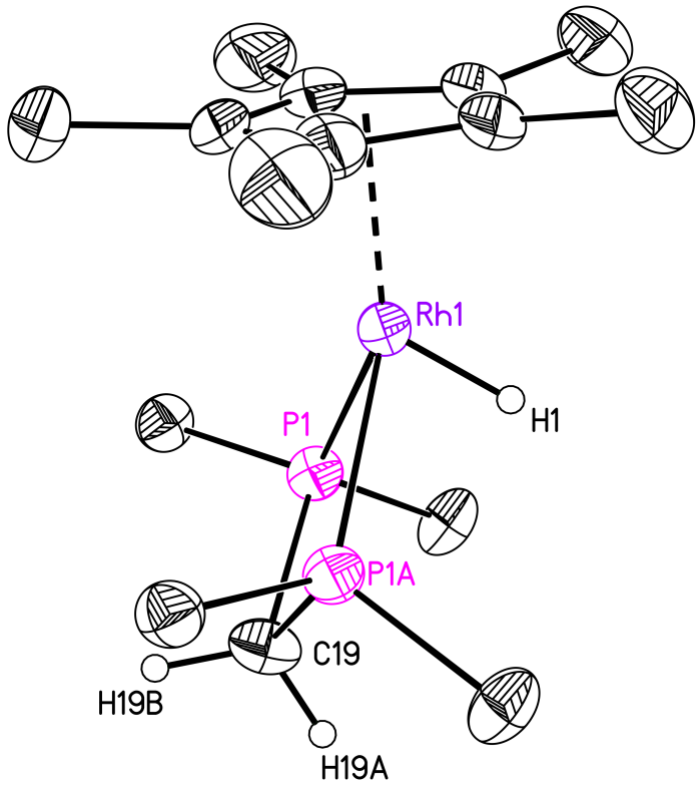

Figure A54: Solid-state structure of the core for the molecular cation in **5**. The triflate counteranion is omitted for clarity. The cation possesses rigorous C_s molecular symmetry with Rh1, H1, C19, H19A, H19B and two Cp* carbon atoms lying in a crystallographic mirror plane at y = 0.25. The triflate counteranion, all hydrogen atoms except for H1, H19A and H19B and additional atoms for the phosphine phenyl rings are omitted for clarity. Displacement ellipsoids are shown at the 50% probability level.

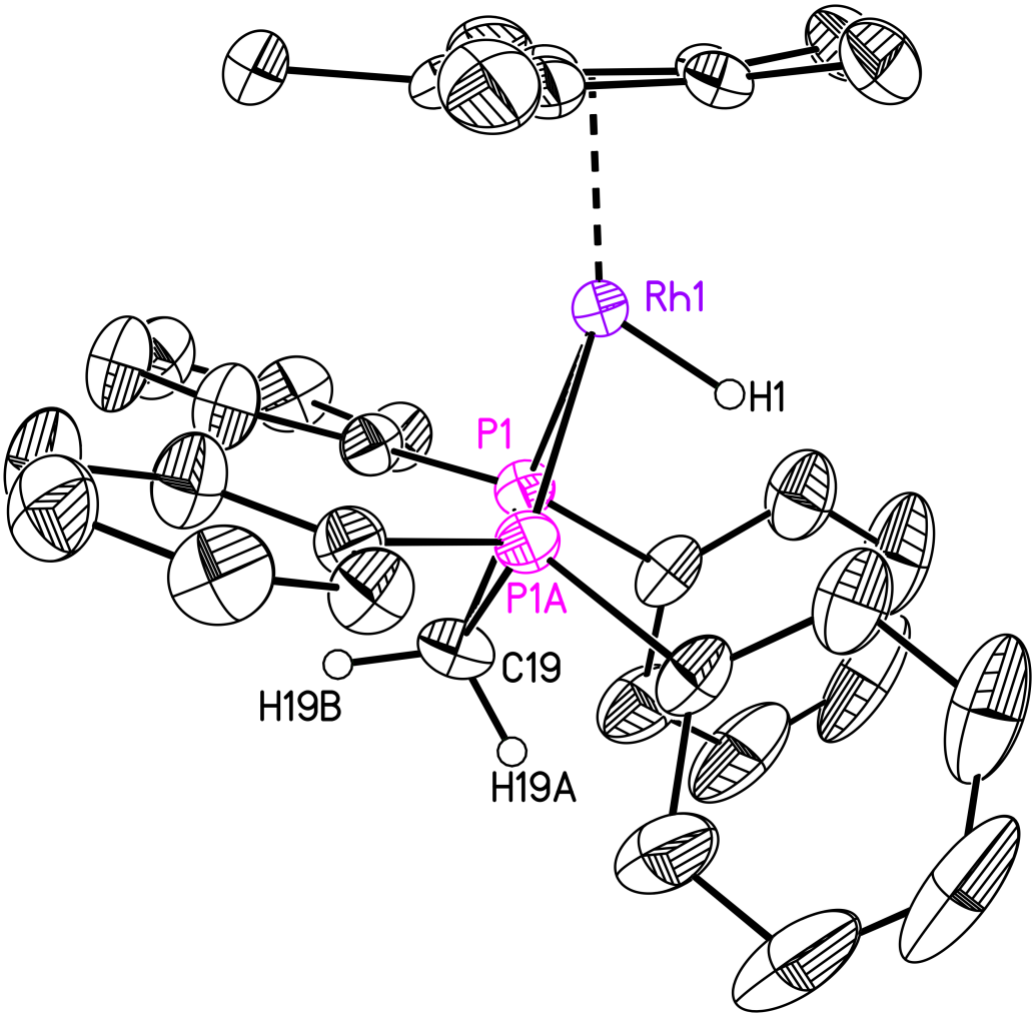

Figure A55: Solid-state structure for the molecular cation in **5**. The triflate counteranion and all hydrogen atoms except for H1, H19A and H19B are omitted for clarity. The cation possesses rigorous C_s molecular symmetry with Rh1, H1, C19, H19A, H19B and two Cp* carbon atoms lying in a crystallographic mirror plane at y = 0.25. Displacement ellipsoids are shown at the 50% probability level.

Solid-State Structure for a Complete Cation/Anion Pair in 5

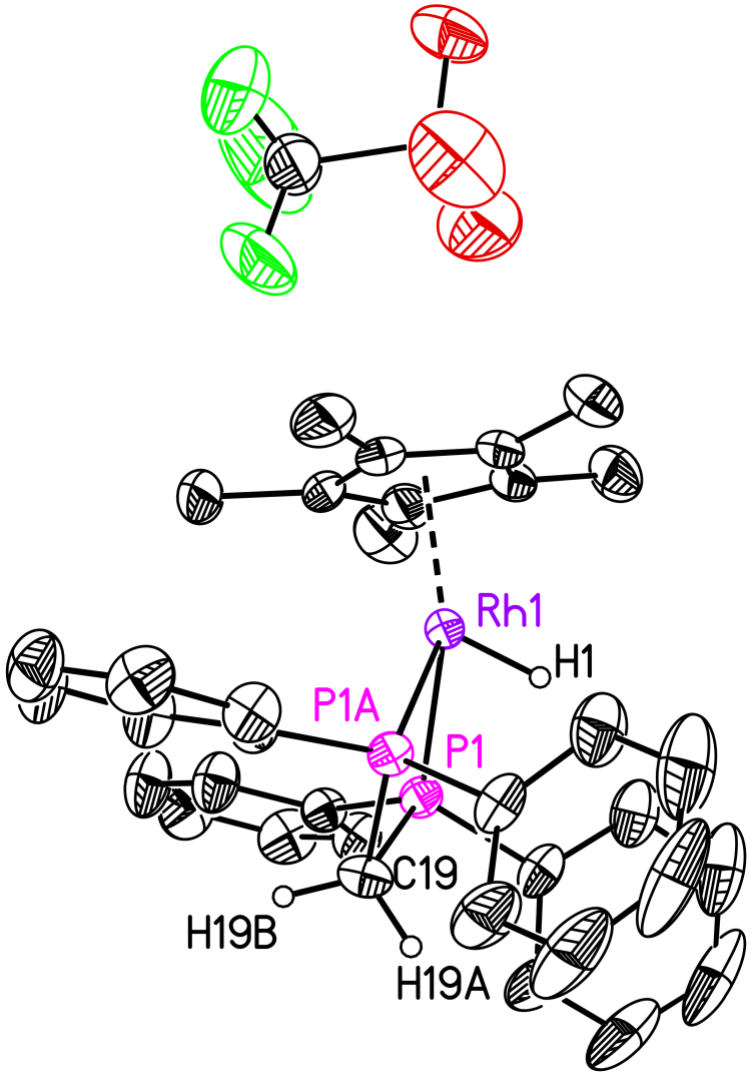

Figure A56: Solid-state structure for two asymmetric units of **5**. Hydrogen atoms, except for H1, H19A, and H19B, are omitted for clarity. The cation possesses rigorous C_s molecular symmetry with Rh1, H1, C19, H19A, H19B and two Cp* carbon atoms lying in a crystallographic mirror plane at y = 0.25. The triflate anion also lies on a crystallographic mirror plane and possesses rigorous C_s molecular symmetry. Displacement ellipsoids are shown at the 50% probability level.

Special Refinement Details for 6.

Hydride hydrogen atoms H1 and H1′ in **6** were located from a difference Fourier and included in the structural model as independent isotropic atoms whose parameters were allowed to vary in least-squares refinement cycles.

Solid-State Structure of 6

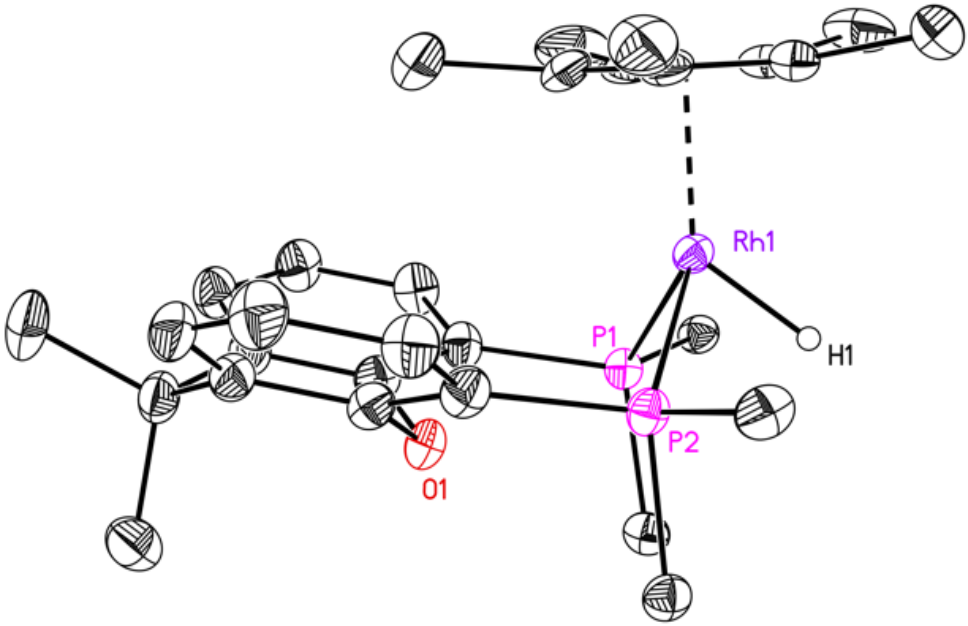

Figure A57: Solid-state structure of the non-hydrogen core for the first of two crystallographically-independent and virtually identical molecular cations in the asymmetric unit of **6**. A second molecular cation of **6**, two co-crystallized triflate counteranions, all hydrogen atoms except H1 and additional atoms for the phosphine phenyl rings are all omitted for clarity. Displacement ellipsoids are shown at the 50% probability level.

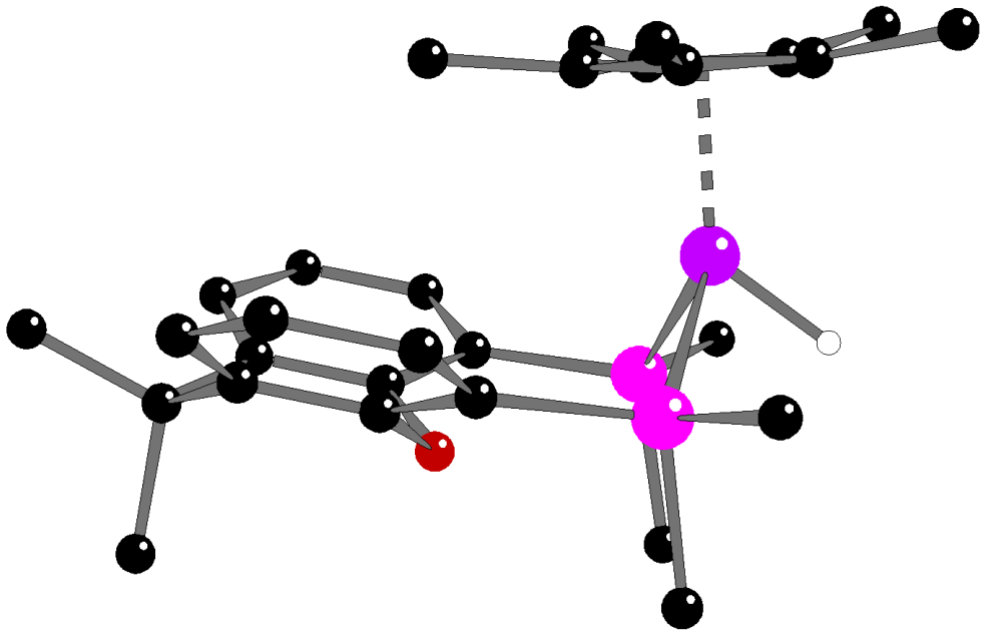

Figure A58: Ball and stick representation of the solid-state structure for the non-hydrogen core for the first of two crystallographically-independent and virtually identical molecular cations in the asymmetric unit of **6**. A second molecular cation of **6**, two co-crystallized triflate counteranions, all hydrogen atoms except for the hydride (H1) and additional atoms for the phosphine phenyl rings are all omitted for clarity.

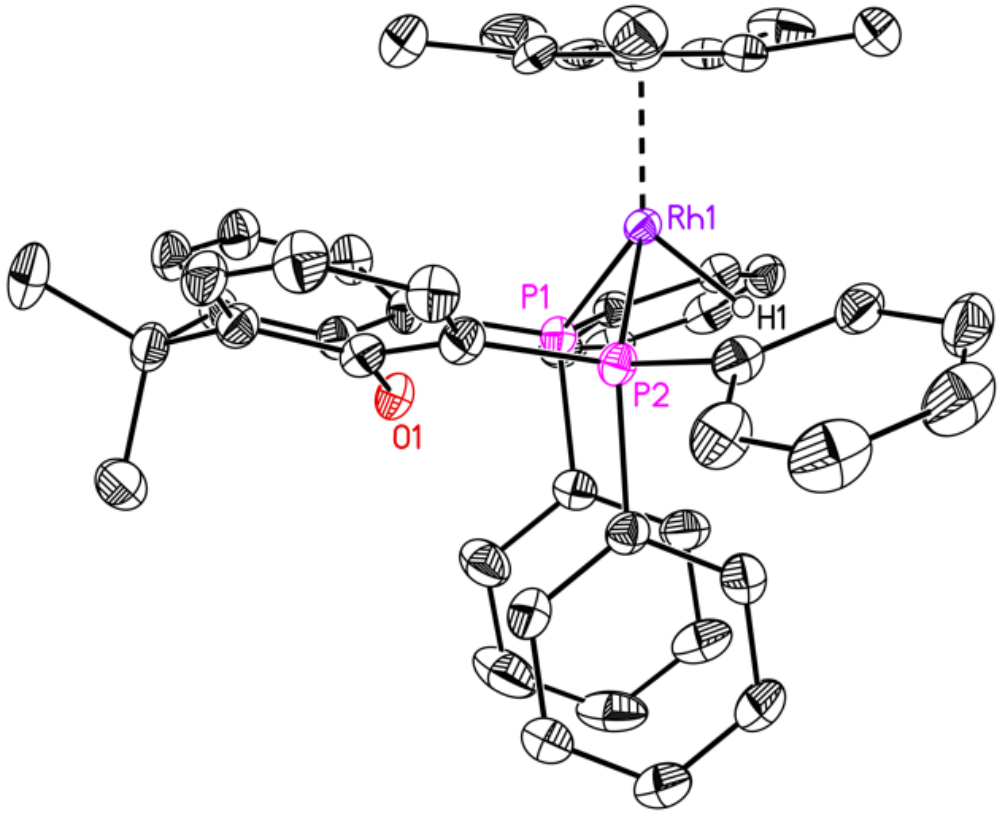

Figure A59: Solid-state structure for the first of two crystallographically-independent and virtually identical molecular cations in the asymmetric unit of **6**. A second molecular cation of **6**, two co-crystallized triflate counteranions and all hydrogen atoms except H1 are omitted for clarity. Displacement ellipsoids are shown at the 50% probability level.

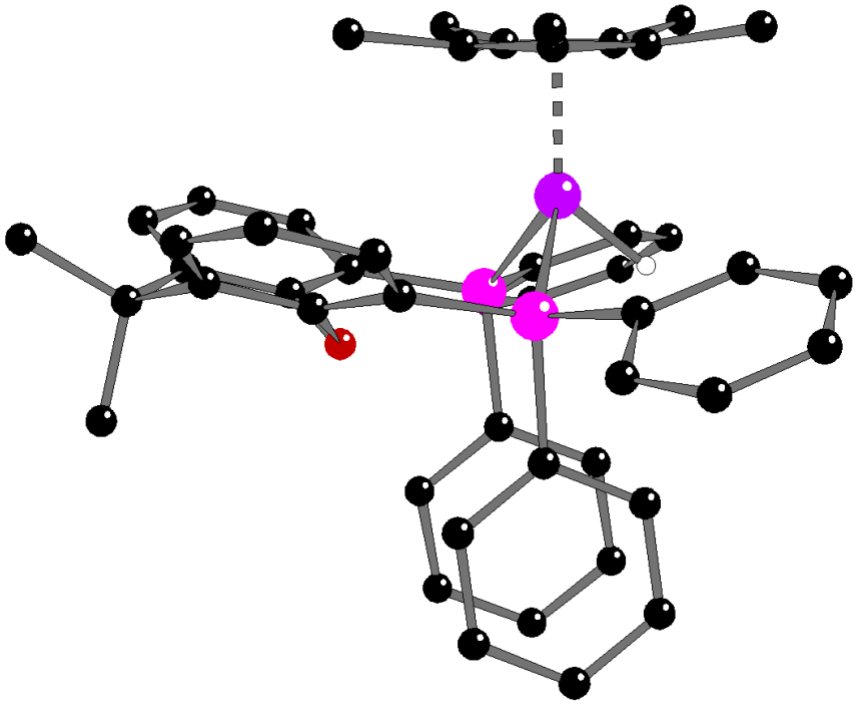

Figure A60: Ball-and-stick representation for the first of two crystallographically-independent and virtually identical molecular cations in the asymmetric unit of **6**. A second molecular cation of **6**, two co-crystallized triflate counteranions and all hydrogen atoms except the hydride are all omitted for clarity.

Asymmetric Unit of 6

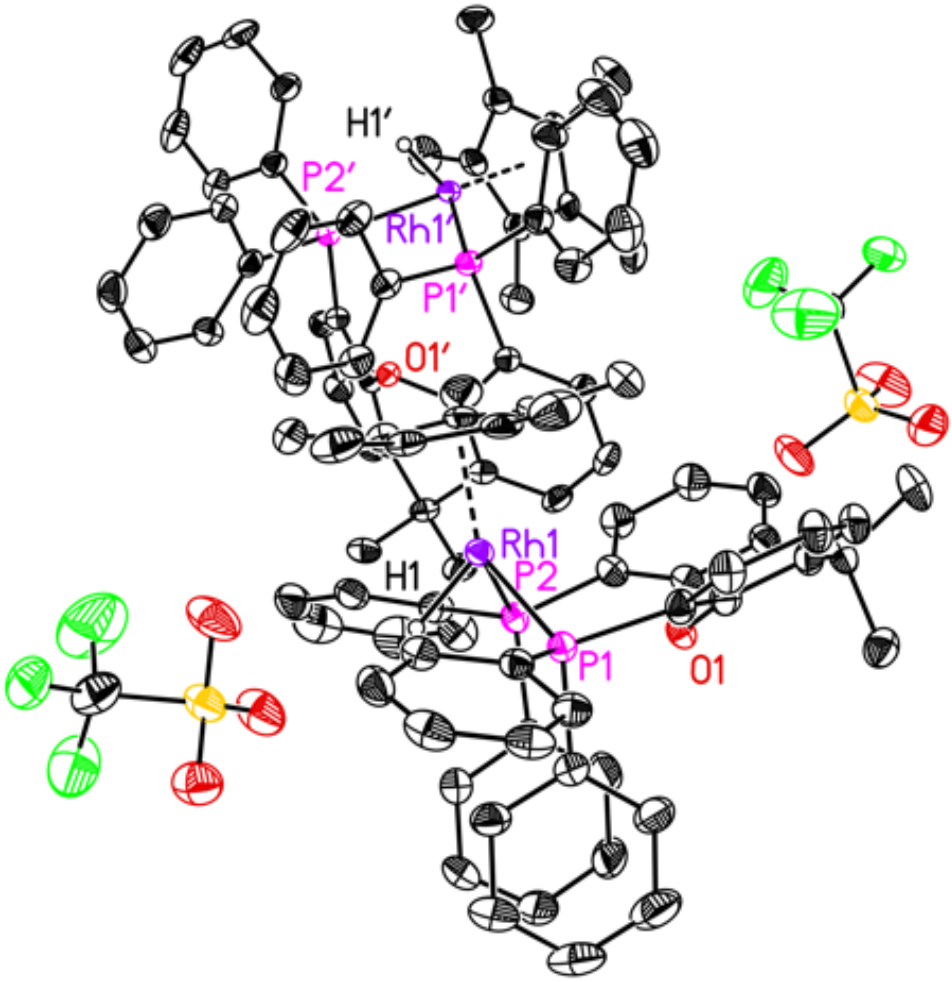

Figure A61: Solid-state structure of the asymmetric unit for **6**. Hydrogen atoms except the hydrides are all omitted for clarity. Displacement ellipsoids are shown at the 50% probability level. Atoms of the second crystallographically-independent cation are labeled with a prime (′).

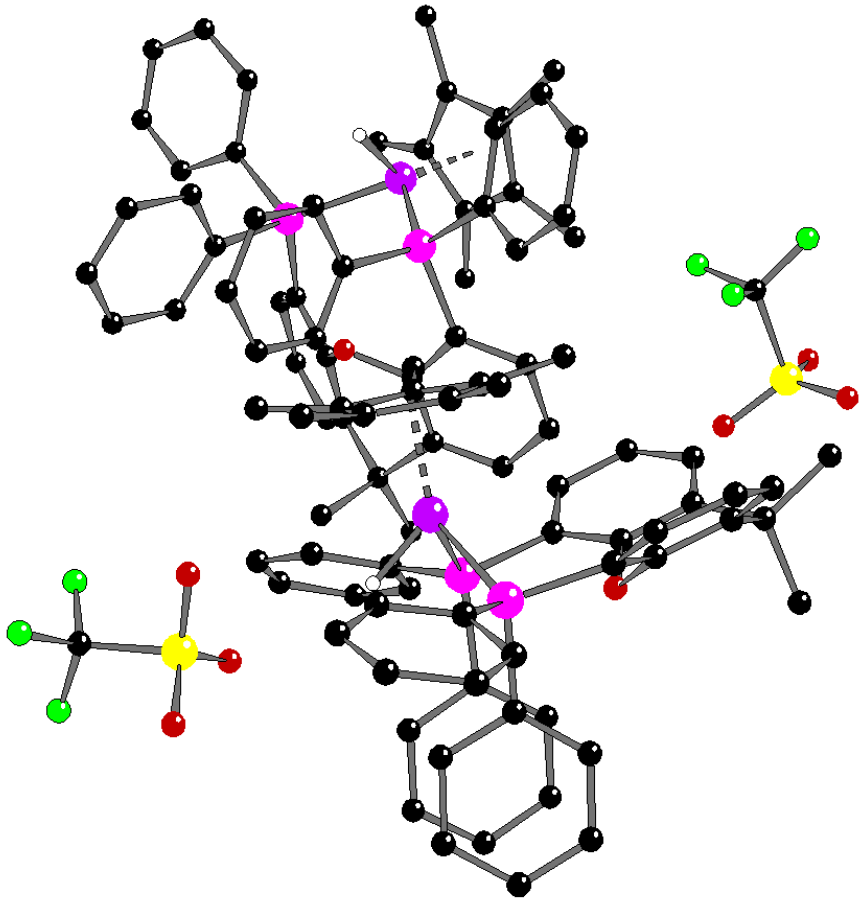

Figure A62: Ball and stick representation of the solid-state asymmetric unit for **6**. Hydrogen atoms except the hydrides are all omitted for clarity.

References

[1] APEX2, Version 2 User Manual, M86-E01078; Bruker Analytical X-ray Systems: Madison, WI, June 2006.

[2] G. M.Sheldrick, SADABS (version 2008/1): Program for Absorption Correction for Data from Area Detector Frames, University of Göttingen, 2008.

[3] G. Sheldrick, Crystal structure refinement with SHELXL. *Acta Crystallogr., Sect. A: Found. Crystallogr.* **2015**, *71*, 3-8.

[4] O. V. Dolomanov, L. J. Bourhis, R. J. Gildea, J. A. K. Howard, H. J. Puschmann, *Appl. Crystallogr.* **2009**, *42*, 339-341.

Appendix B

Supplementary Information for Chapter 5

Starting Materials Synthesized in this Study

For a description of all General Procedures, please consult the Experimental section of Chapter 5.

2-Alkenyl Anilines

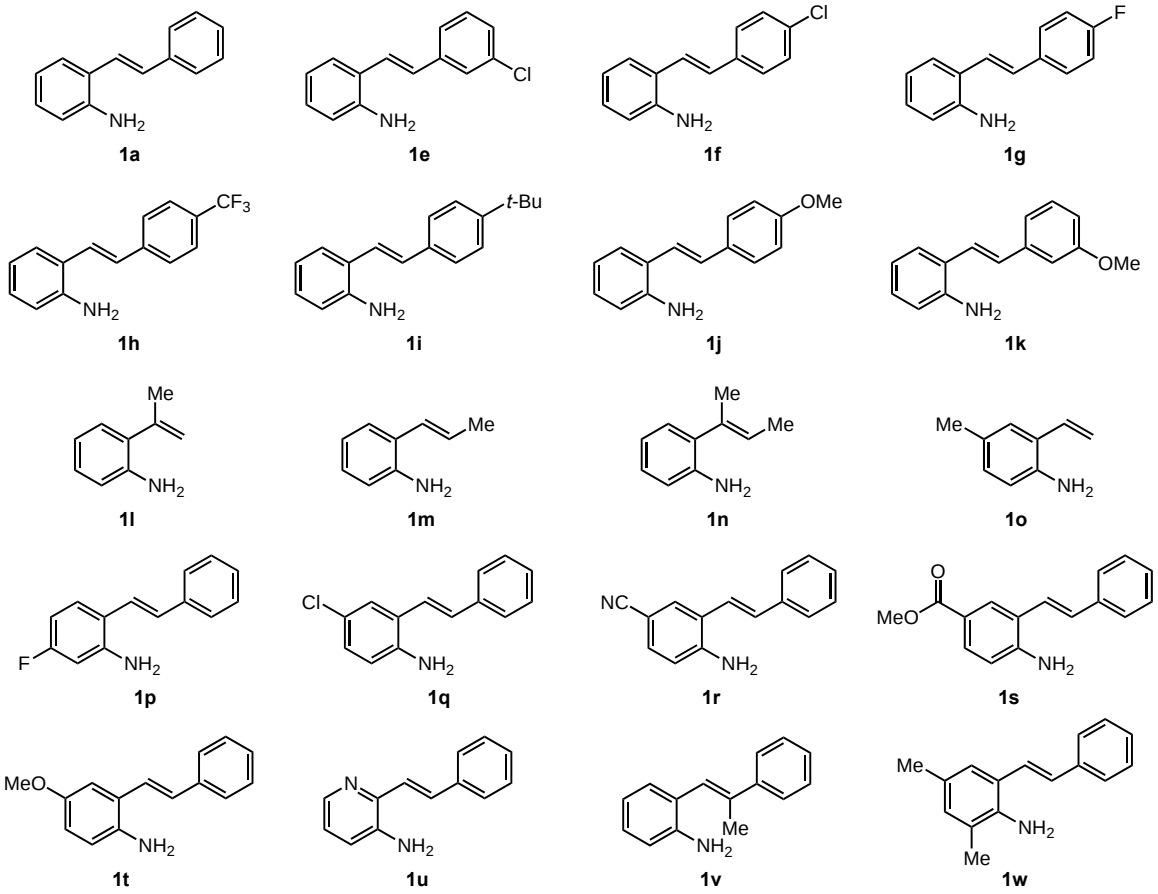

Chart B1. Aniline derivatives synthesized for this study.

Amines **1a**,[1] **1e**, **1f**,[1] **1g**,[2] **1h**,[2] **1i**, **1j**,[3] **1k**, **1p**,[4] **1q**,[3] **1v**,[5] and **1w**[6] were prepared by Heck reaction of 2-bromo- or 2-iodoaniline precursors with the corresponding styrene derivatives using **General Procedure A**.[7] Amine **1o**[8] was prepared in 2 steps by palladium-catalyzed

vinylation of 2-iodo-5-methylnitrobenzene with 1,3,5,7-tetramethyl-1,3,5,7-tetravinylcyclotetrasiloxane[9] followed by iron-mediated nitro reduction. Amines **1m**,[10] **1n**,[11] **1r**,[3] **1s**,[3] **1t**,[2] and **1u**[3,12] were prepared by Suzuki coupling reaction of 2-bromoaniline precursors with *trans*-2-phenylvinylboronic acid using **General Procedure B**.[2] Amine **1l** was purchased.

Homoallylic Amines

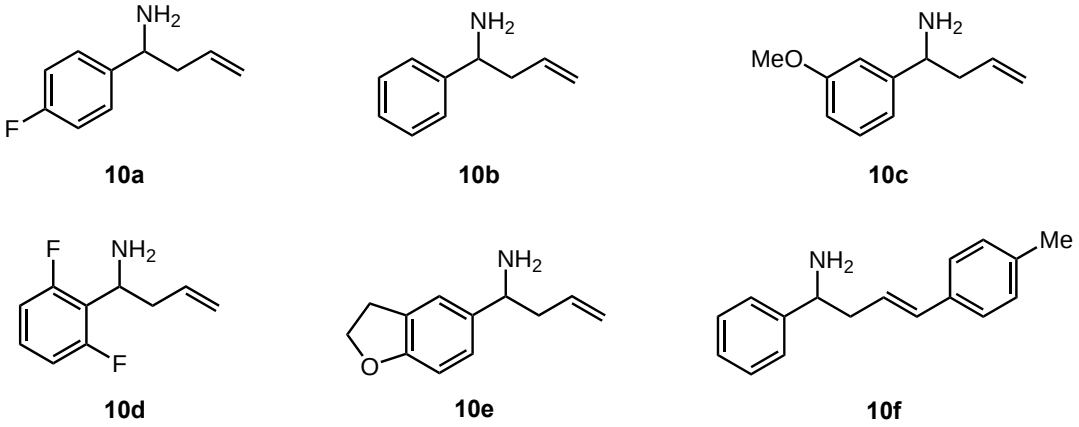

Chart B2. Homoallylic amines synthesized for this study.

Amines **10a-f** were prepared as previously described.[13]

Reaction Discovery and Optimization

Preparation of Iminoquinone B

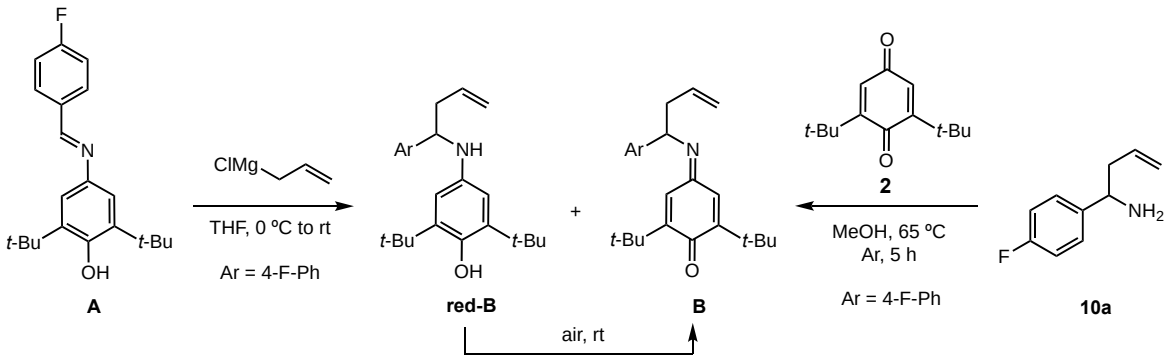

A 7-mL vial was charged with amine **10a**[13] (80 mg, 0.484 mmol, 1 equiv), 2,6-di-*tert*-butyl-1,4-benzoquinone **2** (106 mg, 0.484 mmol, 1 equiv), and methanol (1 mL). The vial was capped, flushed with Ar, and warmed in an oil bath at 65 ºC. The reaction was monitored by ^{1}H NMR. After 5 h, the reaction was cooled down, concentrated *in vacuo*, and the crude iminoquinone **B** was dried under high vacuum.

Alternatively, iminoquinone **B** can also be prepared by addition of allylmagnesium bromide to imine **A**[13] whose primary product **red-B** slowly oxidizes on exposure to air to **B**, or by palladium-catalyzed *umpolung* allylation of imine **A** with allylcarbonate, as described in reference 13 (not shown).

Uncatalyzed Pyrrole Formation from Iminoquinone 2

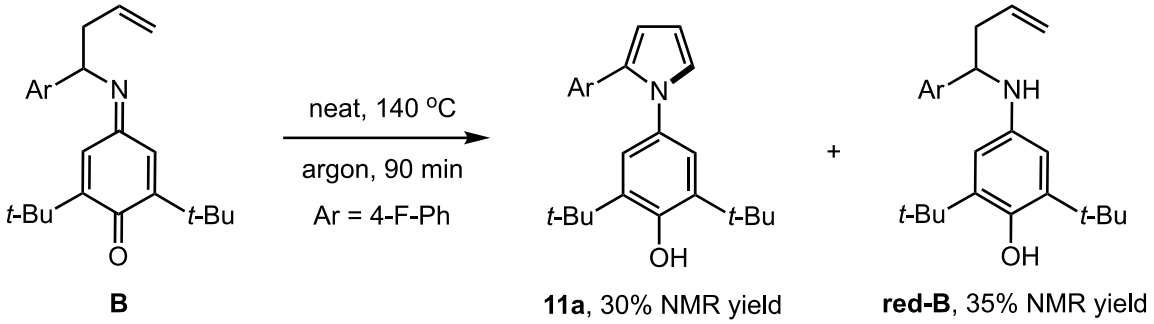

B **11a**, 30% NMR yield **red-B**, 35% NMR yield

A dry 7-mL vial was charged with crude iminoquinone **B**[13] (48 mg, 0.131 mmol, 1 equiv) and a magnetic stir bar. The vial was capped with an open-top cap bearing a Teflon-lined septum and evacuated/backfilled with Ar (3 cycles). The septum was sealed with grease and the vial was heated to 140 ºC in a preheated aluminum block. After 1.5 h, the vial was removed from the heating block and cooled to room temperature. The vial was then opened to air and 1,3,5-trimethoxybenzene (22 mg, 0.131 mmol, 1 equiv) was added. Ethyl acetate (~2 mL) was added to dissolve and homogenize the mixture. An aliquot (~1 mL) was taken, concentrated *in vacuo*, and analyzed by ^{1}H and ^{19}F NMR (Figures B1 and B2).

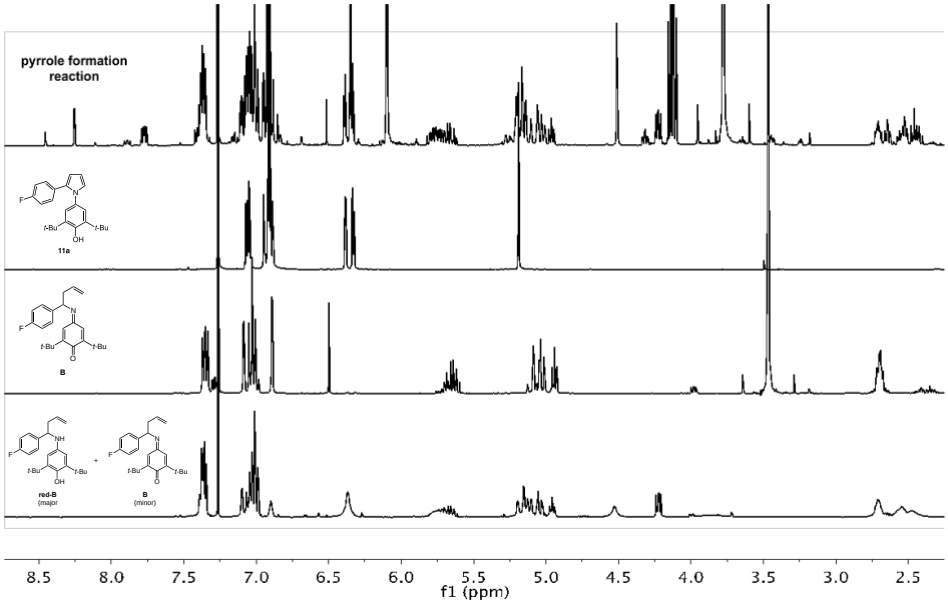

Figure B1. ^{1}H NMR stacked spectra of crude reaction mixture (Top) vs. isolated pyrrole **11a**, iminoquinone **B**, and a mixture of **B** and its reduced form, aminophenol **red-B**.

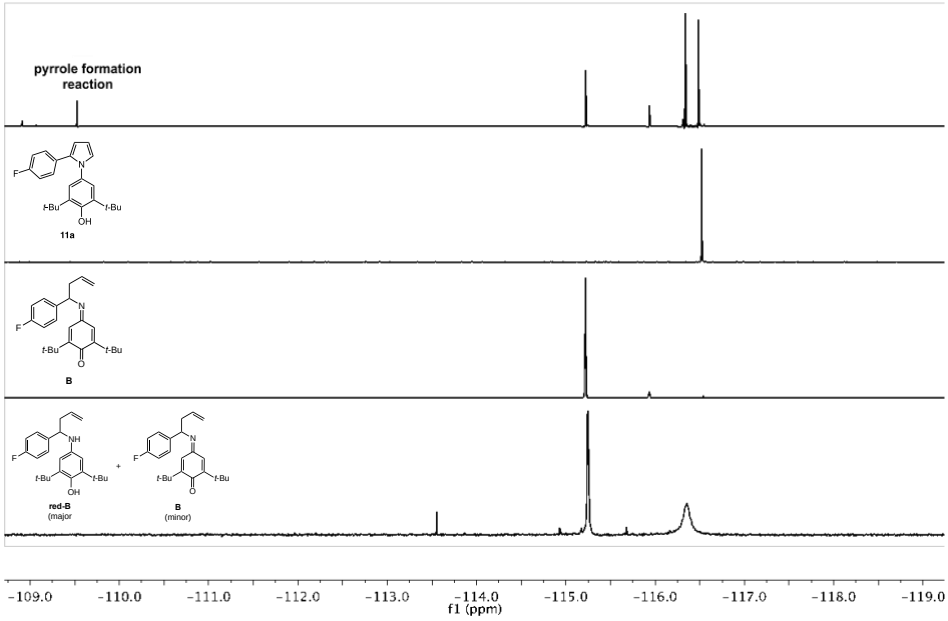

Figure B2. ^{19}F NMR stacked spectra of crude reaction mixture (Top) vs. isolated pyrrole **11a**, iminoquinone **B**, and a mixture of **B** and its reduced form, aminophenol **red-B**.

Acid-catalyzed indole formation from alkenylaniline 1a

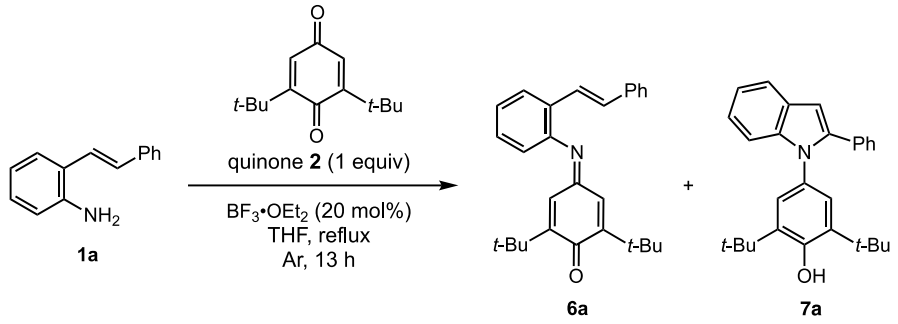

A dry 50-mL round bottom flask was charged with a magnetic stir bar, alkenylaniline **1a** (747 mg, 3.825 mmol. 1 equiv), 2,6-di-*tert*-butyl-1,4-benzoquinone **2** (843 mg, 3.825 mmol, 1 equiv), and dry THF (18 mL). The flask was flushed with Ar and BF_3•OEt_2 (94 μL, 0.765 mmol, 0.2 equiv) was added by syringe. A reflux condenser was attached to the flask and the system was again flushed with Ar and heated to reflux in an oil bath. After 13 h, the reaction was cooled to room temperature, opened to air, and concentrated *in vacuo*. Column chromatography (40 % dichloromethane in hexanes) afforded iminoquinone **6a** (486 mg, 32 %) as a red solid and indole **7a** (743 mg, 49 %) as a white foam.

Characterization of iminoquinone **6a**: m.p.: 110 –112 ºC. ^{1}H NMR (500 MHz, $CDCl_3$) δ 7.73 (dd, *J* = 7.6, 1.6 Hz, 1H), 7.48 (m, 2H), 7.34 (m, 2H), 7.29 – 7.21 (s, 3H), 7.19 (d, *J* = 16.4 Hz, 1H), 7.13 (d, *J* = 2.6 Hz, 1H), 7.07 (d, *J* = 16.3 Hz, 1H), 6.73 (d, *J* = 2.6 Hz, 1H), 6.66 (dd, *J* = 7.5, 1.5 Hz, 1H), 1.36 (s, 9H), 1.16 (s, 9H). ^{13}C NMR (126 MHz, $CDCl_3$) δ 187.8, 159.1, 153.9, 153.3, 147.9 137.7, 134.6, 130.2, 129.6, 128.8, 127.9, 127.8, 126.8, 126.2, 126.0, 125.0, 122.2, 120.7, 35.9, 35.6, 29.6, 29.5. FTIR 3035, 2958, 1650, 1631, 1456, 1362 cm^{-1}. HRMS (ESI) *m/z* calcd for $[C_{28}H_{32}NO]^+$ 398.2484, found 398.2478. See main text for characterization of indole **7a**.

Profile of Indole Formation Reaction

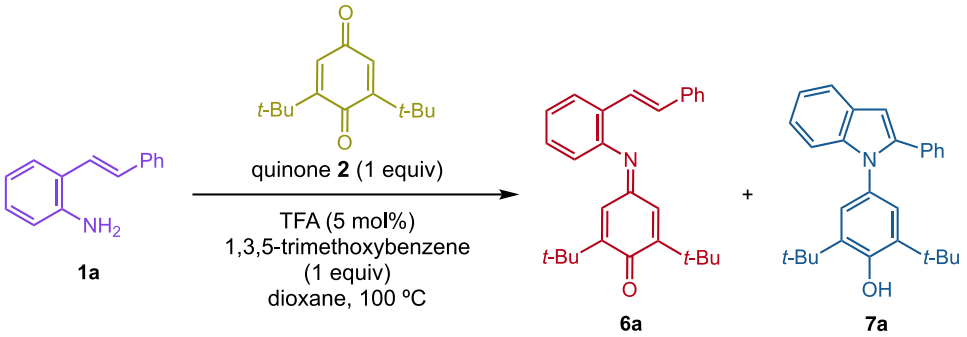

To a 7-mL vial were added a magnetic stir bar, 2,6-di-*tert*-butyl-1,4-benzoquinone **2** (220.3 mg, 1 mmol, equiv), amine **1a** (193. 4 mg, 1 mmol, 1 equiv), and 1,3,5-trimethoxybenzene (168.2 mg, 1 mmol. 1 equiv). The vial was sealed and evacuated/backfilled with Ar (3 cycles). Dioxane (4 mL) and TFA (4 µL, 0.05 mmol, 0.05 equiv) were added by syringe. The reaction was heated in an oil bath to 100 °C and monitored by removing aliquots, concentrating them *in vacuo*, and analyzing them by ^{1}H NMR.

Figure B3 (*vide infra*) shows the qualitative reaction profile. Stacked NMR spectra are shown in Figure B4 (7.80 – 6.40 ppm region) and Figure B5 (1.39 – 1.13 ppm region). Rapid consumption of amine **1a** and 2,6-di-*tert*-butyl-1,4-benzoquinone takes place (> 50% conversion in < 30 min) with concomitant formation of iminoquinone **6a** (ca. 43%) and **7a** (ca. 25 %). Gradual disappearance of **6a** leads to an increase in the yield of indole **7a**.

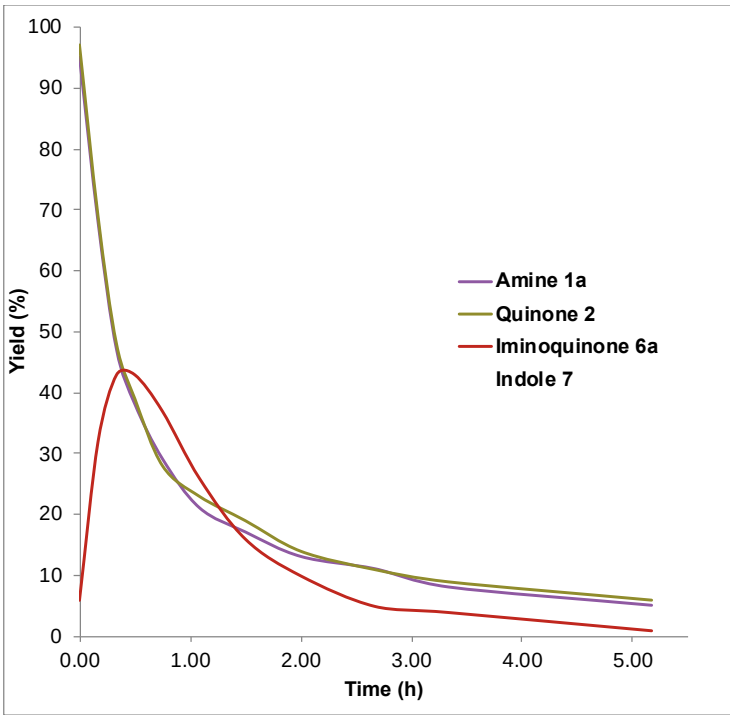

Figure B3. Plot of yield vs. time for the reaction of **1a** with 2,6-di-*tert*-butyl-1,4-benzoquinone **2**.

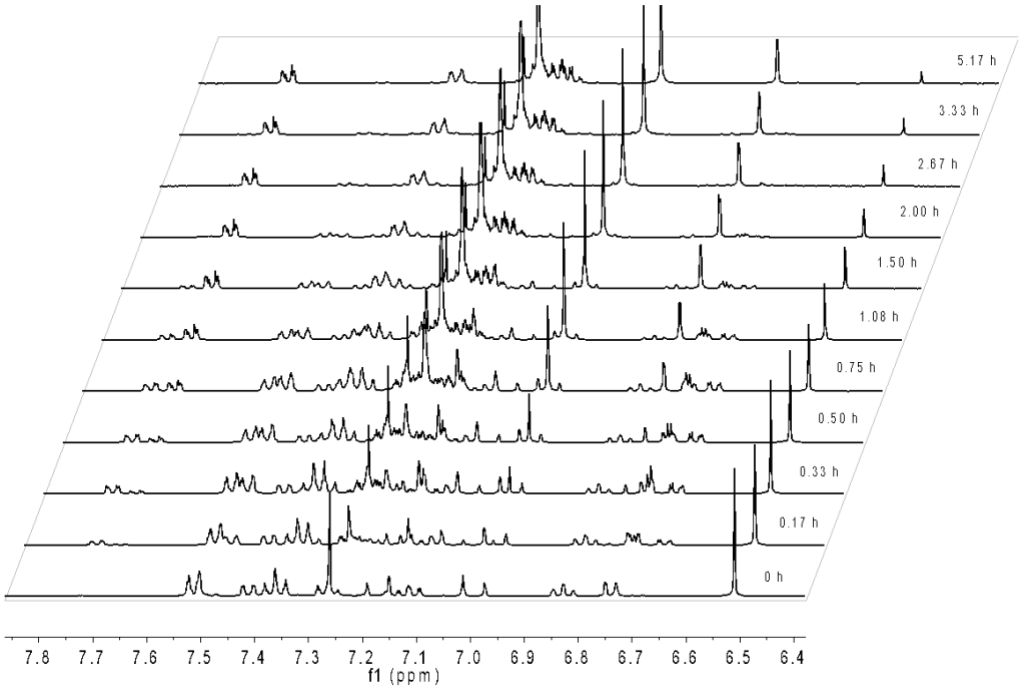

Figure B4. Reaction profile determined by ^{1}H NMR (C(sp^2)–H protons, 7.80 – 6.40 ppm).

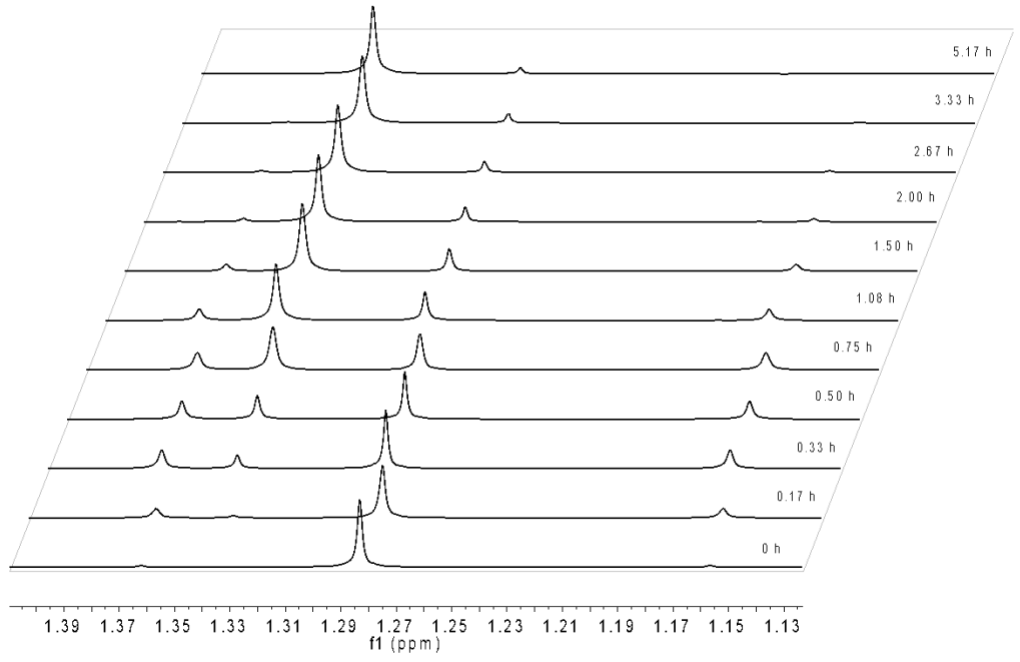

Figure B5. Reaction profile determined by ^{1}H NMR (*tert*-butyl protons, 1.39 – 1.13 ppm).

Evaluation of Other Quinones

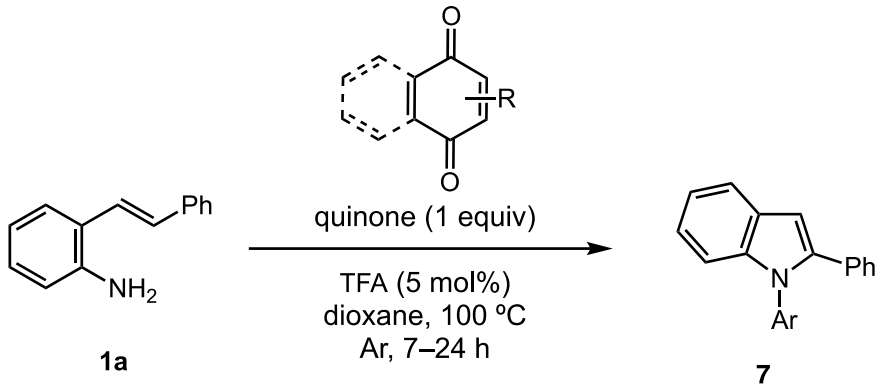

A 7-mL vial was charged with a magnetic stir bar, quinone (1 equiv), and alkenylamine **1a** (1 equiv). The flask was sealed with a septum and evacuated/backfilled with Ar (3 cycles). Dioxane (reaction concentration = 0.25 M) and TFA (0.05 equiv) were added by syringe. The reaction was heated in an aluminum block at 100 ºC for 6–24 h and monitored by TLC. The reaction was then cooled at room temperature and analyzed by ^{1}H NMR.

In general, most quinones (see Chart B3) shown above either led to complex mixtures of products or were unreactive under the standard reaction conditions (5 mol % TFA in dioxane, 100 ºC). The reactive quinones presumably undergo various reactions with the amine other than imine formation (i.e. unselective 1,4-additions, substitution, electron transfer). Two exceptions were notable: 2,5-dimethyl-1,4-benzoquinone afforded the corresponding indole in ~75 % yield but this compound could not be purified and characterized, and 2-hydroxy-1,4-naphthoquinone led to clean iminoquinone formation, but no indole formation was detected.

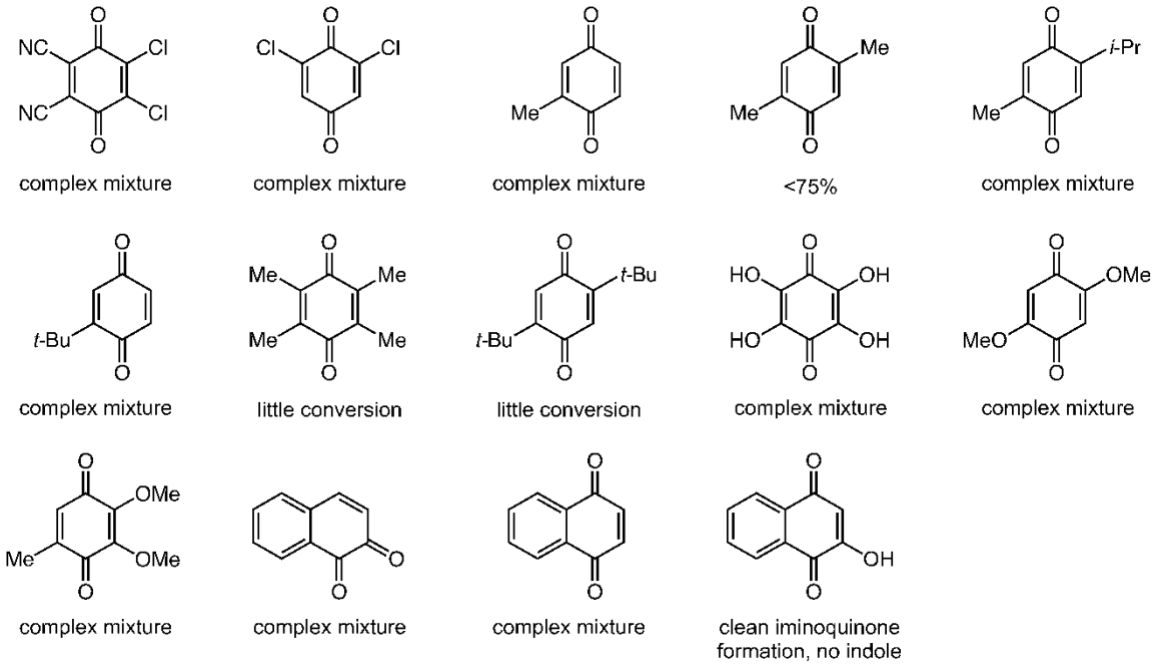

Chart B3. Quinones used in the screening and the results of each reaction.

Characterization of N-Aryl Indoles (7)

Preparation of 2,6-di-*tert*-butyl-4-(2-phenyl-1*H*-indol-1-yl)phenol (7a)

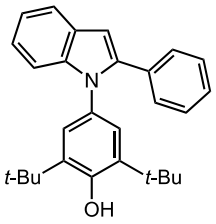

7a

Following General Procedure C, amine **1a** (195.3 mg, 1.0 mmol, 1 equiv), 2,6-di-tert-butyl-1,4-benzoquinone (220.3 mg, 1.0 mmol, 1 equiv), TFA (4 μL, 0.05 mmol, 0.05 equiv), and dioxane (4 mL) at 100 ºC for 7 h afforded, after column chromatography (20 % dichloromethane in hexanes), 386.1 mg (97 %) of indole **7a** as a white solid. m.p.: 120–121 °C. ^{1}H NMR (500 MHz, $CDCl_3$) δ 7.69 (m, 1H), 7.37 (d, *J* = 7.8 Hz, 1H), 7.25 – 7.14 (m, *7*H), 6.99 (s, 2H), 6.78 (s, 1H), 5.23 (s, 1H), 1.34 (s, 18H). ^{13}C NMR (126 MHz, $CDCl_3$) δ 152.6, 141.1, 138.7, 136.7, 133.1, 129.9, 129.3, 128.2, 128.0, 127.2, 124.6, 122.2, 120.6, 120.5, 110.9, 102.7, 34.5, 30.3. FTIR 3626, 3060, 2954, 1601, 1457, 1437, 1204, 1150, 789, 761, 747, 697 cm^{-1}. HRMS (ESI) *m/z* calcd for $[C_{28}H_{32}NO]^+$ 398.2484, found 398.2467.

Preparation of 2,6-dimethyl-4-(2-phenyl-1*H*-indol-1-yl)phenol (7b)

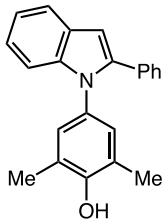

7b

Following General Procedure C, amine **1a** (102.5 mg, 0.525 mmol, 1 equiv), 2,6-dimethyl -1,4-benzoquinone (71.5 mg, 0.525 mmol, 1 equiv), TFA (3 μL, 0.03 mmol, 0.05 equiv), and dioxane (2 mL) at 100 ºC for 6 h afforded, after column chromatography (50–60 % dichloromethane in hexanes), 148.3 mg (90%) of indole **7b** as a white solid. m.p.: 177–178 ºC. ^{1}H NMR (400 MHz, $CDCl_3$) δ 7.72 (m, 1H), 7.37 (m, 2H), 7.33 – 7.25 (m, 4H), 7.21 (m, 2H), 6.94 (s, 2H), 6.83 (s, 1H), 4.74 (s, 1H), 2.27 (s, 6H). ^{13}C NMR (101 MHz, $CDCl_3$) δ 151.4, 141.0, 139.7, 132.9, 130.8, 128.9, 128.3, 128.2, 128.2, 127.3, 124.0, 122.2, 120.5, 120.5, 110.9, 103.0, 16.1. FTIR 3563, 3056, 2922, 1489, 1456, 1192 cm^{-1}. HRMS (ESI) *m/z* calcd for $[C_{22}H_{20}NO]^+$ 314.1545, found 314.1536.

Preparation of 2,4-di-*tert*-butyl-6-(2-phenyl-1*H*-indol-1-yl)phenol (7c)

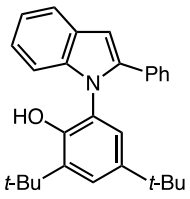

7c

Following General Procedure C, amine **1a** (100 mg, 0.512 mmol, 1 equiv), 3,5-di-tert-butyl-1,2-benzoquinone (112.8 mg, 0.512 mmol, 1 equiv), TFA (2 μL, 0.026 mmol, 0.05 equiv), and dioxane (2 mL) at 100 ºC for 5 h afforded, after column chromatography (3–7 % ethyl acetate in hexanes), 171 mg (84 %) of indole **7c** as an off-white solid. m.p.: 143–144 ºC. ^{1}H NMR (500 MHz, $CDCl_3$) δ 7.75 (d, *J* = 9.0 Hz, 1H), 7.35 (d, *J* = 2.2 Hz, 1H), 7.30 – 7.22 (m, 7H), 7.14 (m, 1H), 6.94 (s, 1H), 6.83 (m, 1H), 5.23 (s, 1H), 1.46 (s, 9H), 1.18 (s, 9H). ^{13}C NMR (126 MHz, $CDCl_3$) δ 148.6, 142.8, 141.6, 138.9, 136.7, 132.0, 128.9, 128.4, 128.3, 127.7, 124.8, 124.0, 123.7, 122.9, 121.3, 120.9, 111.1, 104.0, 35.3, 34.4, 31.5, 29.6. FTIR 3630, 3056, 2959, 1601, 1460, 1436, 1209 cm^{-1}. HRMS (ESI) *m/z* calcd for $[C_{28}H_{32}NO]^+$ 398.2484, found 398.2476.

Preparation of 10-(2-phenyl-1*H*-indol-1-yl)phenanthren-9-ol (7d)

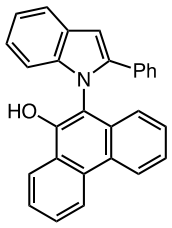

7d

Following General Procedure C, amine **1a** (50 mg, 0.256 mmol, 1 equiv), 9,10-phenanthrenequinone (53.3 mg, 0.256 mmol, 1 equiv), TFA (1 μL, 0.013 mmol, 0.05 equiv), and dioxane (1 mL) at 100 ºC for 8 h afforded, after column chromatography (5 % ethyl acetate in hexanes), 90.8 mg (92 %) of indole **7d** as a light-yellow solid. m.p.: 154–156 ºC. ^{1}H NMR (500 MHz, $CDCl_3$) δ 8.72 (d, *J* = 8.3 Hz, 1H), 8.62 (d, *J* = 8.3 Hz, 1H), 8.42 (dd, *J* = 8.2, 1.3 Hz, 1H), 7.78 (m, 2H), 7.70 (t, *J* = 7.5 Hz, 1H), 7.46 (t, *J* = 7.6 Hz, 1H), 7.37 (m, 2H), 7.32 (t, *J* = 7.6 Hz, 1H), 7.24 (t, *J* = 7.6 Hz, 1H), 7.15 – 7.08 (m, 4H), 7.06 (s, 1H), 6.88 (d, *J* = 8.2 Hz, 1H), 6.84 (d, *J* = 8.2 Hz, 1H), 5.85 (s, 1H). ^{13}C NMR (126 MHz, $CDCl_3$) δ 148.0, 142.5, 139.5, 131.9, 131.6, 130.9, 129.1, 128.6, 128.3, 128.0, 127.9, 127.7, 127.0, 126.8, 124.9, 124.8, 123.8,

123.2, 122.9 (2C), 122.4, 121.7, 120.9, 114.1, 111.2, 104.6. FTIR 3480, 3059, 1629, 1602, 1451, 1208, 748 cm^{-1}. HRMS (ESI) *m/z* calcd for $[C_{28}H_{20}NO]^+$ 386.1545, found 386.1550.

Preparation of product 2,6-di-*tert*-butyl-4-(2-(3-chlorophenyl)-1*H*-indol-1-yl)phenol (7e)

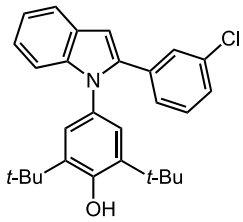

7e

Following General Procedure C, amine **1e** (114.8 mg, 0.5 mmol, 1 equiv), 2,6-di-tert-butyl-1,4-benzoquinone (110.2 mg, 0.5 mmol, 1 equiv), TFA (2 μL, 0.025 mmol, 0.05 equiv), and dioxane (2 mL) at 100 ºC for 12 h afforded, after column chromatography (20 % dichloromethane in hexanes), 203.3 mg (94 %) of indole **7e** as a white solid. m.p.: 120–123 °C. ^{1}H NMR (400 MHz, $CDCl_3$) δ 7.75 – 7.52 (m, 1H), 7.36 (d, *J* = 8.0 Hz, 1H), 7.28 – 7.09 (m, 4H), 7.00 (s, 2H), 6.82 (s, 1H), 5.29 (s, 1H), 1.37 (s, 18H). ^{13}C NMR (101 MHz, $CDCl_3$) δ 153.0, 139.4, 139.0, 137.1, 134.8, 133.9, 129.6, 129.3, 129.1, 128.1, 127.2, 127.1, 124.7, 122.7, 120.8, 120.7, 111.0, 103.3, 34.6, 30.3. FTIR 3619, 3080, 3057, 2957, 1597, 1457, 1437, 1281, 1209, 1153, 780, 747, 693 cm^{-1}. HRMS (ESI) *m/z* calcd for $[C_{28}H_{31}ClNO]^+$ 432.2084, found 432.2072.

Preparation of 2,6-di-*tert*-butyl-4-(2-(4-chlorophenyl)-1*H*-indol-1-yl)phenol (7f)

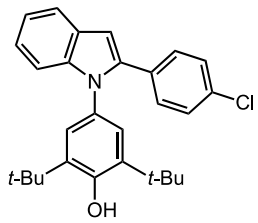

7f

Following General Procedure C, amine **1f** (68.9 mg, 0.3 mmol, 1 equiv), 2,6-di-tert-butyl-1,4-benzoquinone (66.1 mg, 0.3 mmol, 1 equiv), TFA (1.2 μL, 0.015 mmol, 0.05 equiv), and dioxane (1.2 mL) at 100 ºC for 12 h afforded, after column chromatography (10 % dichloromethane in hexanes), 122.2 mg (94 %) of indole **7f** as a white solid. m.p.: 195–196 °C. ^{1}H NMR (500 MHz, $CDCl_3$) δ 7.68 (m, 1H), 7.33 (d, *J* = 7.9 Hz, 1H), 7.24 – 7.12 (m, 6H), 6.98 (s, 2H), 6.77 (s, 1H), 5.27 (s, 1H), 1.35 (s, 18H). ^{13}C NMR (126 MHz, $CDCl_3$) δ

152.9, 139.7, 139.0, 136.9, 133.2, 131.6, 130.3, 129.7, 128.2, 128.1, 124.6, 122.5, 120.7, 120.7, 111.0, 103.1, 34.6, 30.3. FTIR 3610, 3074, 3055, 2955, 1592, 1459, 1434, 1282, 1150, 780, 743, cm^{-1}. HRMS (ESI) *m/z* calcd for $[C_{28}H_{31}ClNO]^+$ 432.2084, found 432.2075.

Preparation of product 2,6-di-*tert*-butyl-4-(2-(4-fluorophenyl)-1*H*-indol-1-yl)phenol (7g)

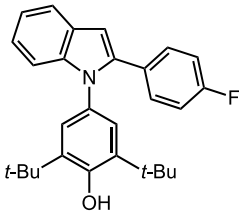

7g

Following General Procedure C, amine **1g** (106.6 mg, 0.5 mmol, 1 equiv), 2,6-di-tert-butyl-1,4-benzoquinone (110.2 mg, 0.5 mmol, 1 equiv), TFA (2 μL, 0.025 mmol, 0.05 equiv), and dioxane (2 mL) at 100 ºC for 24 h afforded, after column chromatography (10 % dichloromethane in hexanes), 186.9 mg (94 %) of indole **7g** as a white solid. m.p.: 152–153 °C. ^{1}H NMR (500 MHz, $CDCl_3$) δ 7.71 (m, 1H), 7.39 (m, 1H), 7.25 – 7.18 (m, 4H), 7.03 (s, 2H), 6.97 (m, 2H), 6.78 (s, 1H), 5.29 (s, 1H), 1.39 (s, 18H). ^{13}C NMR (126 MHz, $CDCl_3$) δ 162.2 (d, *J* = 247.9 Hz), 152.8, 140.0, 138.7, 136.9, 130.9 (d, *J* = 8.1 Hz), 129.7, 129.3 (d, *J* = 3.5 Hz), 128.1, 124.6, 122.3, 120.60, 115.0 (d, *J* = 21.8 Hz), 110.9, 102.7, 34.5, 30.3. ^{19}F NMR (471 MHz, $CDCl_3$) δ -114.8. FTIR 3631, 3060, 3037, 2955, 1495, 1454, 1434, 1281, 1229, 1194, 1140, 837, 785, 748 cm^{-1}. HRMS (ESI) *m/z* calcd for $[C_{28}H_{31}FNO]^+$ 416.2384, found 416.2387.

Preparation of 2,6-di-*tert*-butyl-4-(2-(4-(trifluoromethyl)phenyl)-1*H*-indol-1-yl)phenol (7h)

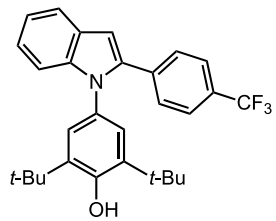

7h

Following General Procedure C, amine **1h** (131.6 mg, 0.5 mmol, 1 equiv), 2,6-di-tert-butyl-1,4-benzoquinone (110.2 mg, 0.5 mmol, 1 equiv), TFA (2 μL, 0.025 mmol, 0.05 equiv), and dioxane (2 mL) at 100 ºC for 12 h afforded, after column chromatography (5 %

dichloromethane in hexanes), 207.2 mg (89 %) of indole **7h** as a white solid. m.p.: 200–203 °C. ^{1}H NMR (500 MHz, $CDCl_3$) δ 7.60 (m, 1H), 7.39 (d, *J* = 8.2 Hz, 2H), 7.28 (s, 1H), 7.22 (d, *J* = 8.1 Hz, 2H), 7.12 (ddd, *J* = 8.3, 6.9, 1.4 Hz, 1H), 7.08 (td, *J* = 7.3, 1.2 Hz, 1H), 6.88 (s, 2H), 6.75 (s, 1H), 5.17 (s, 1H), 1.24 (s, 18H). ^{13}C NMR (126 MHz, $CDCl_3$) δ 152.9, 139.2, 139.1, 137.0, 136.8, 129.6, 129.3, 129.1 (q, *J* = 32.4 Hz), 128.0, 125.0 (q, *J* = 3.9 Hz), 124.6, 124.3 (q, *J* = 272.1 Hz), 122.9, 121.0, 120.8, 111.1, 103.9, 34.6, 30.3. ^{19}F NMR (471 MHz, $CDCl_3$) δ -62.6. FTIR 3634, 3058, 2963, 1617, 1457, 1437, 1323, 1206, 1152, 1109, 1063 cm^{-1}. HRMS (ESI) *m/z* calcd for $[C_{29}H_{30}F_3NO]^+$ 466.2362, found 466.2354.

Preparation of 2,6-di-*tert*-butyl-4-(2-(4-(*tert*-butyl)phenyl)-1*H*-indol-1-yl)phenol (7i)

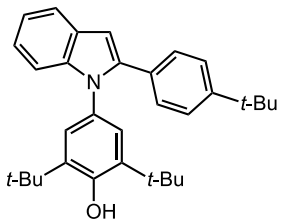

7i

Following General Procedure C, amine **1i** (200 mg, 0.80 mmol, 1 equiv), 2,6-di-tert-butyl-1,4-benzoquinone (175 mg, 0.80 mmol, 1 equiv), TFA (3.0 μL, 0.040 mmol, 0.05 equiv), and dioxane (3.2 mL) at 100 ºC for 5 h afforded, after column chromatography (15 % dichloromethane in hexanes), 337.4 mg (94 %) of indole **7i** as a white solid. m.p.: 218–219 °C. ^{1}H NMR (500 MHz, $CDCl_3$) δ 7.66 (dd, J = 7.8, 1.5 Hz, 1H), 7.44 – 7.34 (m, 1H), 7.24 (d, J = 1.8 Hz, 1H), 7.21 – 7.11 (m, 2H), 7.14 – 7.08 (m, 2H), 6.95 (s, 2H), 6.74 (s, 1H), 5.19 (s, 1H), 1.31 (s, 18H), 1.28 (s, 9H). ^{13}C NMR (126 MHz, $CDCl_3$) δ 152.3, 150.2, 141.0, 138.2, 136.4, 130.1, 129.8, 129.1, 128.2, 124.8, 124.43, 121.9, 120.4, 120.3, 110.1, 102.2, 34.6, 34.4, 31.3, 30.2. FTIR 3624, 3061, 2951, 1601, 1498, 1455, 1438, 1306, 1212, 1153 cm^{-1}. HRMS (ESI) *m/z* calcd for $[C_{32}H_{40}NO]^+$ 454.3110, found 454.3089.

Preparation of 2,6-di-*tert*-butyl-4-(2-(4-methoxyphenyl)-1*H*-indol-1-yl)phenol (7j)

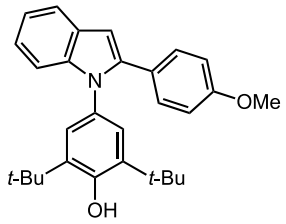

7j

Following General Procedure C, amine **1j** (112.6 mg, 0.5 mmol, 1 equiv), 2,6-di-tert-butyl-1,4-benzoquinone (110.2 mg, 0.5 mmol, 1 equiv), TFA (2.0 μL, 0.025 mmol, 0.05 equiv), and dioxane (2 mL) at 100 ºC for 5 h afforded, after column chromatography (15 % dichloromethane in hexanes), 172.3 mg (80 %) of indole **7j** as a white solid. m.p.: 171–172 °C. ^{1}H NMR (500 MHz, $CDCl_3$) δ 7.67 (dd, *J* = 7.2, 1.8 Hz, 1H), 7.37 – 7.31 (m, 1H), 7.21 – 7.07 (m, 4H), 7.00 (s, 2 H), 6.79 (d, J = 8.8 Hz, 2H), 6.71 (s, 1H), 5.23 (s, 1H), 3.79 (s, 3H), 1.35 (s, 18H). ^{13}C NMR (126 MHz, $CDCl_3$) δ 159.0, 152.6, 140.9, 138.6, 136.7, 130.5, 130.0, 128.3, 125.7, 124.7, 121.9, 120.4, 120.4, 113.6, 110.8, 101.9, 55.5, 34.5, 30.3, 29.9. FTIR 3627, 3055, 2954, 2870, 1608, 1500, 1457, 1437, 1247, 1207, 1152 cm^{-1}. HRMS (ESI) *m/z* calcd for $[C_{29}H_{34}NO_2]^+$ 428.2590, found 428.2593.

Preparation of 2,6-di-*tert*-butyl-4-(2-(3-methoxyphenyl)-1*H*-indol-1-yl)phenol (7k)

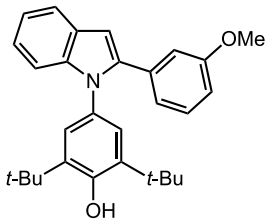

7k

Following General Procedure C, amine **1k** (112.7 mg, 0.5 mmol, 1 equiv), 2,6-di-tert-butyl-1,4-benzoquinone (110.2 mg, 0.5 mmol, 1 equiv), TFA (2 μL, 0.025 mmol, 0.05 equiv), and dioxane (2 mL) at 100 ºC for 12 h afforded, after column chromatography (30 % dichloromethane in hexanes), 191.2 mg (89 %) of indole **7k** as a white solid. m.p.: 125–127 °C. ^{1}H NMR (400 MHz, $CDCl_3$) δ 7.77 (m, 1H), 7.45 (m, 1H), 7.31 – 7.22 (m, 3H), 7.11 (s, 2H), 7.05 (dt, *J* = 7.8, 1.2 Hz, 1H), 6.89 (s, 1H), 6.85 (ddd, *J* = 8.2, 2.6, 1.0 Hz, 1H), 6.67 (dd, *J* = 2.6, 1.5 Hz, 1H), 5.33 (s, 1H), 3.60 (s, 3H), 1.43 (s, 18H). ^{13}C NMR (101 MHz, $CDCl_3$) δ 159.1, 152.7, 140.8, 138.8, 136.9, 134.2, 130.1, 129.2, 128.1, 124.8, 122.3, 121.7, 120.7, 120.5, 114.2, 113.6, 110.9, 102.7, 54.9, 34.5, 30.3. FTIR: 3625, 3059, 2956, 1602,

1457, 1436, 1225, 1160. HRMS (ESI) *m/z* calcd for $[C_{29}H_{34}NO_2]^+$ 428.2590, found 428.2590.

Preparation of 2,6-di-*tert*-butyl-4-(3-methyl-1*H*-indol-1-yl)phenol (7l)

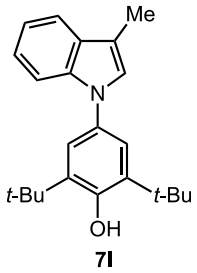

7l

Large scale reaction. To a 250-mL round bottom flask was added a magnetic stirbar, amine **1l** (3 g, 22.52 mmol, 1 equiv), 2,6-di-tert-butyl-1,4-benzoquinone (4.96 g, 22.52 mmol, 1 equiv), TFA (86 µL, 1.13 mmol, 0.05 equiv), and dioxane (60 mL). A reflux condenser was attached, and the system was flushed with Ar. An Ar balloon was placed at the top of the condenser and the reaction was heated to 100 ºC. After 21 h, the reaction was concentrated *in vacuo* and the crude product was recrystallized from hot hexanes to afford 7.0 g (92 %) of indole **7l** as a brown solid. m.p.: 146–148 ºC. ^{1}H NMR (500 MHz, $CDCl_3$) δ 7.64 (m, 1H), 7.45 (d, *J* = 8.2 Hz, 1H), 7.27 (s, 2H), 7.22 (dd, *J* = 8.2, 6.9 Hz, 1H), 7.17 (t, *J* = 7.4 Hz, 1H), 7.11 (s, 1H), 5.26 (s, 1H), 2.42 (s, 3H), 1.50 (s, 18H). ^{13}C NMR (126 MHz, $CDCl_3$) δ 152.3, 137.2, 136.6, 132.0, 129.3, 126.2, 122.1, 121.7, 119.4, 119.2, 111.8, 110.5, 34.7, 30.4, 9.8. IR 3640, 2965, 1602, 1465, 1438, 1208, 1152 cm^{-1}. HRMS (ESI) *m/z* calcd for $[C_{23}H_{30}NO]^+$ 336.2322, found 336.2338.

Preparation of 2,6-di-*tert*-butyl-4-(2-methyl-1*H*-indol-1-yl)phenol (7m)

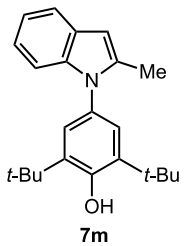

7m

Following General Procedure C, amine **1m** (133.2 mg, 1.0 mmol, 1 equiv), 2,6-di-tert-butyl-1,4-benzoquinone (220.3 mg, 1.0 mmol, 1 equiv), TFA (4 µL, 0.05 mmol, 0.05 equiv), and dioxane (4 mL) at 100 ºC for 20 h afforded, after column chromatography (20 % dichloromethane in hexanes), 316.9 mg (94 %) of indole **7m** as a white solid. m.p.: 141–142 ºC. ^{1}H NMR (400 MHz,$CDCl_3$) δ 7.57 (ddd, *J* = 6.2, 2.9, 1.3 Hz, 1H), 7.12 (s, 2H), 7.11 – 7.05 (m, 3H), 6.30 (s, 1H), 5.34 (s, 1H),

2.30 (s, 3H), 1.47 (s, 18H). ^{13}C NMR (101 MHz, $CDCl_3$) δ 153.3, 138.6, 137.6, 137.0, 129.7, 128.1, 124.6, 120.9, 119.8, 119.6, 110.3, 100.6, 34.7, 30.4, 13.6. FTIR: 3640, 3059, 2957, 1461, 1438, 1230, 1119 cm^{-1}. HRMS (ESI) *m/z* calcd for $[C_{23}H_{30}NO]^+$ 336.2322, found 336.2327.

Preparation of 2,6-di-*tert*-butyl-4-(2,3-dimethyl-1*H*-indol-1-yl)phenol (7n)

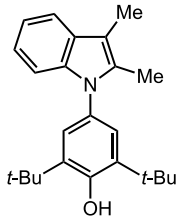

7n

Following General Procedure C, amine **1n** (147.2 mg, 1.0 mmol, 1 equiv), 2,6-di-tert-butyl-1,4-benzoquinone (220.3 mg, 1.0 mmol, 1 equiv), TFA (4.0 μL, 0.05 mmol, 0.05 equiv), and dioxane (4 mL) at 100 ºC for 18 h afforded, after column chromatography (10 % dichloromethane in hexanes), 331.1 mg (95 %) of indole **7n** as a white solid. m.p.: 138–139 ºC. ^{1}H NMR (400 MHz, $CDCl_3$) δ 7.56 (m, 1H), 7.15 – 7.08 (m, 5H), 5.33 (s, 1H), 2.35 (d, *J* = 0.8 Hz, 3H), 2.25 (d, *J* = 0.8 Hz, 3H), 1.48 (s, 18H). ^{13}C NMR (101 MHz, $CDCl_3$) δ 153.1, 137.6, 136.9, 133.4, 130.0, 128.6, 124.7, 121.0, 119.2, 117.9, 110.0, 107.2, 34.7, 30.44, 11.2, 9.0. FTIR: 3637, 3055, 2957, 1603, 1463, 1437, 1233, 1119 cm^{-1}. HRMS (ESI) *m/z* calcd for $[C_{24}H_{32}NO]^+$ 350.2478, found 350.2481.

Preparation of 2,6-di-*tert*-butyl-4-(5-methyl-1*H*-indol-1-yl)phenol (7o)

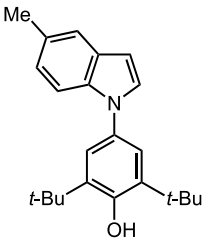

7o

Compound **7o** was prepared by a slight modification of General Procedure C. Accordingly, to a 50-mL round bottom flask were added a magnetic stir bar, amine **1o** (82 mg, 0.616 mmol, 1 equiv), and 2,6-di-tert-butyl-1,4-benzoquinone (135.6 mg, 0.616 mmol, 1 equiv). The flask was sealed with a septum and evacuated/backfilled with Ar (3 cycles). Dioxane (15 mL) and TFA (5 μL, 0.062 mmol, 0.05 equiv), were added by syringe and the reaction was heated in an oil bath to 100 ºC with stirring and monitored by TLC. After 18 h the reaction was cooled to room

temperature, opened to air, and quenched with 1–2 drops of Et_3N. The reaction mixture was concentrated *in vacuo*, and the product was purified by flash column chromatography (20 % dichloromethane in hexanes) which afforded 136.5 mg (66 %) of indole **7o** as a white solid. m.p.: 114–115 ºC. ^{1}H NMR (400 MHz, $CDCl_3$) δ 7.60 (d, *J* = 8.0 Hz, 1H), 7.31 (s, 2H), 7.28 (m, 1H), 7.26 (d, *J* = 3.2 Hz, 1H), 7.02 (ddd, *J* = 8.1, 1.5, 0.6 Hz, 1H), 6.62 (dd, *J* = 3.3, 0.9 Hz, 1H), 5.32 (s, 1H), 2.49 (s, 3H), 1.52 (s, 18H). ^{13}C NMR (101 MHz, $CDCl_3$) δ 152.6, 137.2, 137.0, 132.0, 131.9, 128.1, 126.8, 122.0, 121.8, 120.7, 110.5, 102.3, 34.7, 30.4, 22.1. FTIR: 3625, 3104, 2960, 1602, 1510, 1461,1225, 1113. HRMS (ESI) *m/z* calcd for $[C_{23}H_{30}NO]^+$ 336.2322, found 336.2329.

Preparation of 2,6-di-*tert*-butyl-4-(6-fluoro-2-phenyl-1*H*-indol-1-yl)phenol (7p)

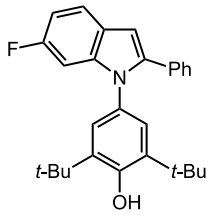

7p

Following General Procedure C, amine **1p** (213.3 mg, 1.0 mmol, 1 equiv), 2,6-di-tert-butyl-1,4-benzoquinone (220.3 mg, 1.0 mmol, 1 equiv), TFA (4 μL, 0.05 mmol, 0.05 equiv), and dioxane (4 mL) at 100 ºC for 22 h afforded, after column chromatography (5 % ethyl acetate in hexanes), 389.1 mg (94 %) of indole **7p** as a white solid. m.p.: 164–165 ºC. ^{1}H NMR (500 MHz, $CDCl_3$) δ 7.59 (ddd, *J* = 8.5, 5.4, 1.7 Hz, 1H), 7.26 – 7.17 (m, 5H), 7.04 (dt, *J* = 10.1, 2.1 Hz, 1H), 6.97 (s, 1H), 6.93 (t, *J* = 9.1 Hz, 1H), 6.75 (d, *J* = 1.7 Hz, 1H), 5.26 (s, 1H), 1.35 (s, 18H). ^{13}C NMR (126 MHz, $CDCl_3$) δ 160.1 (d, *J* = 237.8 Hz), 152.7, 141.5, 138.7 (d, *J* = 11.9 Hz), 136.8, 132.7, 129.5, 129.0, 127.9, 127.2, 124.5, 124.3, 121.2 (d, *J* = 10.0 Hz), 109.0 (d, *J* = 24.5 Hz), 102.5, 97.2 (d, *J* = 27.0 Hz), 34.4, 30.1. FTIR 3636, 2966, 1603, 1485, 1439, 1208, 1152 cm^{-1}. HRMS (ESI) *m/z* calcd for $[C_{28}H_{31}FNO]^+$ 416.2390, found 416.2399.

Preparation of 2,6-di-*tert*-butyl-4-(5-chloro-2-phenyl-1*H*-indol-1-yl)phenol (7q)

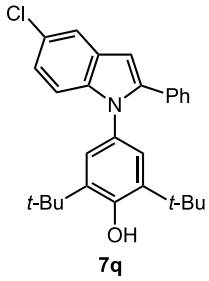

7q

Following General Procedure C, amine **1q** (114.9 mg, 0.5 mmol, 1 equiv), 2,6-di-tert-butyl-1,4-benzoquinone (110.2 mg, 0.5 mmol, 1 equiv), TFA (2 μL, 0.025 mmol, 0.05 equiv), and dioxane (2 mL) at 100 ºC for 22 h afforded, after column chromatography (10–15 % dichloromethane in hexanes), 224.7 mg (99 %) of indole **7q** as a white solid. m.p.: 192–193 ºC. ^{1}H NMR (500 MHz, $CDCl_3$) δ 7.62 (d, *J* = 2.0 Hz, 1H), 7.25 – 7.20 (m, 4H), 7.20 – 7.15 (m, 2H), 7.11 (dd, *J* = 8.8, 1.9 Hz, 1H), 6.94 (d, *J* = 2.0 Hz, 2H), 6.69 (s, 1H), 5.24 (s, 1H), 1.32 (s, 18H). ^{13}C NMR (126 MHz, $CDCl_3$) δ 152.9, 142.3, 137.1, 136.9, 132.6, 129.5, 129.3, 129.2, 128.1, 127.6, 126.0, 124.5, 122.4, 119.9, 112.0, 102.2, 34.5, 30.3. FTIR 3633, 2961,1605, 1463, 1437, 1206, 1151 cm^{-1}. HRMS (ESI) *m/z* calcd for $[C_{28}H_{31}ClNO]^+$ 432.2084, found 432.2101.

Preparation of 1-(3,5-di-*tert*-butyl-4-hydroxyphenyl)-2-phenyl-1*H*-indole-5-carbonitrile (7r)

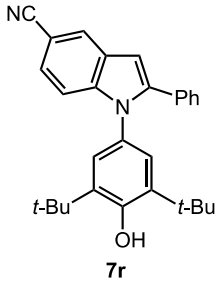

7r

Compound **7r** was prepared by a slight modification of General Procedure C. To a 25-mL thick-walled sealed tube were added amine **1r** (211 mg, 0.958 mmol, 1 equiv), 2,6-di-tert-butyl-1,4-benzoquinone (211 mg, 0.958 mmol, 1 equiv), toluene (3.8 mL), and TFA (7 μL, 0.096 mmol, 0.1 equiv). The tube was flushed with Ar, sealed, and heated to 120 ºC for 4 h. The reaction was cooled to room temperature, opened to air, and 1–2 drops of triethylamine were added. The reaction mixture was concentrated *in vacuo*, and the product was purified by flash column chromatography (40–50 % dichloromethane in hexanes) to afford 300.8 mg (74 %) of indole **7r** as a white solid. m.p.: 207–209 ºC. ^{1}H NMR (500 MHz, $CDCl_3$) δ 8.02 (d, *J* =

1.4 Hz, 1H), 7.43 – 7.35 (m, 2H), 7.28 – 7.23 (m, 3H), 7.21 – 7.16 (m, 2H), 6.95 (s, 2H), 6.82 (s, 1H), 5.31 (s, 1H), 1.33 (s, 18H). ^{13}C NMR (126 MHz, $CDCl_3$) δ 153.3, 143.5, 140.2, 137.1, 132.0, 129.3, 128.8, 128.2, 128.02, 127.96, 126.1, 125.1, 124.5, 121.0, 111.8, 103.4, 103.0, 34.6, 30.2. FTIR 3633, 2965, 2221, 1604, 1471, 1439, 1210, 1153 cm^{-1}. HRMS (ESI) *m/z* calcd for $[C_{29}H_{31}N_2O]^+$ 423.2436, found 423.2475.

Preparation of methyl 1-(3,5-di-*tert*-butyl-4-hydroxyphenyl)-2-phenyl-1*H*-indole-5-carboxylate (7s)

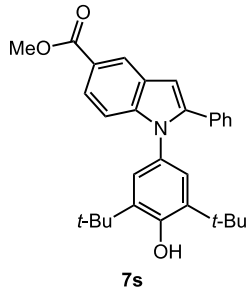

7s

Compound **7s** was prepared by a slight modification of General Procedure C. Accordingly, to a 10-mL round bottom flask were added a magnetic stir bar, amine **1s** (253.3 mg, 1.0 mmol, 1 equiv), 2,6-di-tert-butyl-1,4-benzoquinone (220.3 mg, 1.0 mmol, 1 equiv). The flask was sealed with a septum and evacuated/backfilled with Ar (3 cycles). Dioxane (4 mL) and TFA (4 μL, 0.05 mmol, 0.05 equiv) were added by syringe and the reaction was heated in an oil bath to 100 ºC with stirring and monitored by TLC. After 21 h, an additional amount of TFA was added (4 μL, 0.05 mmol, 0.05 equiv) and heating continued for 7 h. The reaction was cooled to room temperature, opened to air, and quenched with 1–2 drops of Et_3N. The reaction mixture was concentrated *in vacuo*, and the product was purified by flash column chromatography (40 % dichloromethane in hexanes) to afford 434.5 mg (95 %) of indole **7s** as a white solid. m.p.: 198–200 ºC. ^{1}H NMR (500 MHz, $CDCl_3$) δ 8.47 (d, *J* = 1.6 Hz, 1H), 7.91 (dd, *J* = 8.7, 1.6 Hz, 1H), 7.38 (d, *J* = 8.7 Hz, 1H), 7.31 – 7.24 (m, 3H), 7.22 (m, 2H), 7.00 (s, 2H), 6.87 (s, 1H), 5.30 (s, 1H), 3.97 (s, 3H), 1.36 (s, 18H). ^{13}C NMR (126 MHz, $CDCl_3$) δ 168.3, 153.0, 142.6, 141.1, 136.9, 132.5, 129.3, 128.1, 127.8, 127.6, 124.5, 123.60, 123.56, 122.4, 110.6, 103.8, 52.0, 34.6, 30.3. FTIR 3634, 2957, 2880, 1714, 1604, 1437,

1308, 1209, 1152, 913 cm^{-1}. HRMS (ESI) *m/z* calcd for $[C_{30}H_{34}NO_3]^+$ 456.2539, found 456.2546.

Preparation of 2,6-di-*tert*-butyl-4-(5-methoxy-2-phenyl-1*H*-indol-1-yl)phenol (7t)

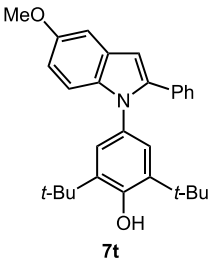

7t

Following General Procedure C, amine **1t** (260.0 mg, 1.15 mmol, 1 equiv), 2,6-di-tert-butyl-1,4-benzoquinone (254.0 mg, 1.15 mmol, 1 equiv), TFA (4.5 μL, 0.058 mmol, 0.05 equiv), and dioxane (6 mL) at 100 ºC for 6 h afforded, after column chromatography (40–50 % dichloromethane in hexanes), 463.4 mg (94 %) of indole **7t** as a tan solid. m.p.: 160–161 ºC. ^{1}H NMR (400 MHz, $CDCl_3$) δ 7.29 – 7.19 (m, 6H), 7.15 (d, *J* = 2.5 Hz, 1H), 6.98 (s, 2H), 6.86 (ddd, *J* = 8.9, 2.6, 1.0 Hz, 1H), 6.70 (s, 1H), 5.22 (s, 1H), 3.89 (s, 3H), 1.34 (s,18H). ^{13}C NMR (101 MHz, $CDCl_3$) δ 154.8, 152.6, 141.5, 136.7, 134.2, 133.2, 130.1, 129.2, 128.6, 128.0, 127.2, 124.5, 112.4, 111.7, 102.5, 102.3, 56.1, 34.5, 30.3. FTIR 3629, 3063, 2956, 1603, 1471, 1438, 1215, 1148 cm^{-1}. HRMS (ESI) *m/z* calcd for $[C_{29}H_{34}NO_2]^+$ 428.2584, found 428.2587.

Preparation of 2,6-di-*tert*-butyl-4-(2-phenyl-1*H*-pyrrolo[3,2-*b*]pyridin-1-yl)phenol (7u)

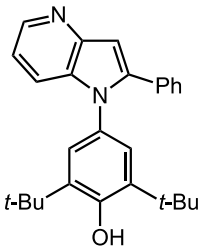

7u

Following General Procedure C, amine **1u** (64 mg, 0.326 mmol, 1 equiv), 2,6-di-tert-butyl-1,4-benzoquinone (71.8 mg, 0.326 mmol, 1 equiv), TFA (1 μL, 0.016 mmol, 0.05 equiv), and dioxane (1.3 mL) at 100 ºC for 21 h afforded, after recrystallization from dichloromethane/hexanes, 100 mg (77 %) of azaindole **7u** as a white solid. m.p.: 188–190 ºC. ^{1}H NMR (500 MHz, $CDCl_3$ + DMSO-d_6) δ 8.39 (m, 1H), 7.64 (m, 1H), 7.29 (m, 3H), 7.24 (m, 2H), 7.14 (m, 1H), 7.10 (m, 1H), 7.14 – 7.08 (m, 1H), 6.89 (m, 3H), 1.28 (s, 18H). ^{13}C NMR (126 MHz, $CDCl_3$ + DMSO) δ 152.8, 145.9, 143.4, 143.3, 140.0, 131.63, 130.96, 128.8, 128.4, 127.89, 127.69, 123.3,

117.4, 117.0, 102.9, 34.5, 29.9. IR 3539, 3060, 2959, 1603, 1470, 1438, 1220 cm^{-1}. HRMS (ESI) *m/z* calcd for $[C_{27}H_{30}N_2O]^+$ 399.2436, found 399.2430.

Preparation of 10-(5,7-dimethyl-2-phenyl-1*H*-indol-1-yl)phenanthren-9-ol (7w)

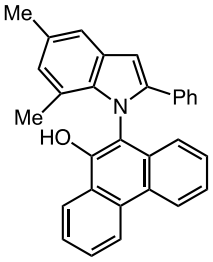

7w

Following General Procedure C, amine **1w** (111.7 mg, 0.5 mmol, 1 equiv), 9,10-phenanthrenequinone (104.1, 0.5 mmol, 1 equiv), TFA (2 μL, 0.025 mmol, 0.05 equiv), and dioxane (1.25 mL) at 100 ºC for 15 h afforded, after column chromatography (30–50 % dichloromethane in hexanes), 171.6 mg (83 %) of indole **7w** as an off-white solid. m.p.: 255–257 ºC. ^{1}H NMR (500 MHz, $CDCl_3$) δ 8.67 (d, *J* = 8.3 Hz, 1H), 8.57 (d, *J* = 8.3 Hz, 1H), 8.41 (d, *J* = 8.1 Hz, 1H), 7.75 (m, 1H), 7.69 (t, *J* = 7.6 Hz, 1H), 7.46 – 7.40 (m, 2H), 7.35 – 7.29 (m, 3H), 7.08 – 7.03 (m, 3H), 6.91 (s, 1H), 6.74 – 6.67 (m, 2H), 6.13 (s, 1H), 2.44 (s, 3H), 1.70 (s, 3H). ^{13}C NMR (126 MHz, $CDCl_3$) δ 148.5, 143.5, 136.4, 132.5, 132.2, 131.5, 130.9, 130.2, 128.31, 128.23 (2C), 128.0, 127.9, 127.5, 126.9, 125.9, 124.9, 124.4, 123.8, 122.9, 122.8, 122.4, 122.3, 118.6, 116.4, 105.2, 21.3, 17.4. FTIR 3474, 3030, 2922, 1631, 1603, 1450, 1213, 846, 755 cm^{-1}. HRMS (ESI) *m/z* calcd for $[C_{30}H_{24}NO]^+$ 414.1858, found 414.1873.

Note: enantiomers (+)-**7w** and (–)-**7w** were resolved by HPLC (CHIRALPAK IA column, gradient 0.5% to 4% *i*-PrOH/hexanes, 30 min ramp, 1 mL/min).

Characterization of N-Aryl Pyrroles (11)

Preparation of 2,6-di-*tert*-butyl-4-(2-(4-fluorophenyl)-1*H*-pyrrol-1-yl)phenol (11a)

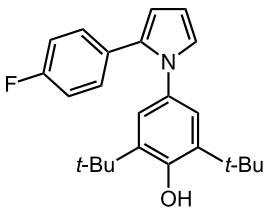

11a

Following General Procedure D, amine **10a** (22.6 mg, 0.137 mmol, 1 equiv), 2,6-di-*tert*-butyl-1,4-benzoquinone (60.3 mg, 0.274 mmol, 2 equiv), and a solution of TFA in dioxane (0.0125 M, 0.55 mL, 0.05 equiv) at 100 ºC for 19 h afforded, after column chromatography (10 % dichloromethane in hexanes), 25 mg (50 %) of **11a** as light-yellow film. ^{1}H NMR (500 MHz, $CDCl_3$) δ 7.05 (dd, *J* = 8.9, 5.4 Hz, 2H), 6.94 (dd, *J* = 2.8, 1.8 Hz, 1H), 6.93 – 6.87 (m, 4H), 6.38 (dd, *J* = 3.6, 1.8 Hz, 1H), 6.33 (dd, *J* = 3.6, 2.8 Hz, 1H), 5.19 (s, 1H), 1.32 (s, 18H). ^{13}C NMR (126 MHz, $CDCl_3$) δ 161.6 (d, *J* = 245.7 Hz), 152.5, 136.5, 132.9, 132.0, 130.3 (d, *J* = 7.8 Hz), 129.7 (d, *J* = 3.4 Hz), 124.0, 122.6, 114.8 (d, *J* = 21.5 Hz), 109.7, 108.6, 34.5, 30.2. ^{19}F NMR (376 MHz, $CDCl_3$) δ -116.5. FTIR 3620, 2978, 1593, 1468, 1210 cm^{-1}. HRMS (ESI) *m/z* calcd for $[C_{24}H_{29}FNO]^+$ 366.2228, found 366.2224.

Preparation of 2,6-di-*tert*-butyl-4-(2-phenyl-1*H*-pyrrol-1-yl)phenol (11b)

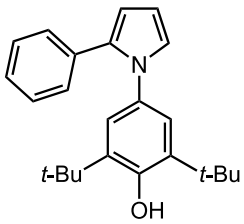

11b

Following General Procedure D, amine **10b** (167.6 mg, 1.14 mmol, 1 equiv), 2,6-di-*tert*-butyl-1,4-benzoquinone (502.3 mg, 2.28 mmol, 2 equiv), TFA (4.3 µL, 0.057 mmol, 0.05 equiv), and dioxane (4.6 mL) at 100 ºC for 5 h afforded, after column chromatography (10 % dichloromethane in hexanes), 192.6 mg (49 %) of **11b** as an off-white solid. m.p.: 92–94 °C. ^{1}H NMR (500 MHz, $CDCl_3$) δ 7.19 (dd, J = 8.1, 6.3 Hz, 2H), 7.17 – 7.12 (m, 1H), 7.12 – 7.04 (m, 2H), 6.96 (t, J = 2.2 Hz, 1H), 6.93 (s, 2H), 6.43 (dd, J = 3.6, 1.8 Hz, 1H), 6.34 (t, J = 3.2 Hz, 1H), 5.16 (s, 1H), 1.32 (s, 18H). ^{13}C NMR (126 MHz, $CDCl_3$) δ 152.4, 136.4, 134.0, 133.5, 132.3, 128.7, 127.9, 126.2, 123.9, 122.6, 109.8, 108.7, 34.5, 30.2, 29.9. FTIR

3633, 3058, 2954, 1602, 1467, 1438, 1202, 1147 cm^{-1}. HRMS (ESI) *m/z* calcd for $[C_{24}H_{30}NO]^+$ 348.2327, found 348.2316.

Preparation of 2,6-di-*tert*-butyl-4-(2-(3-methoxyphenyl)-1*H*-pyrrol-1-yl)phenol (11c)

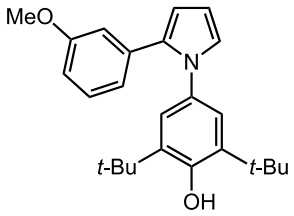

11c

Following General Procedure D, amine **10c** (35 mg, 0.197 mmol, 1 equiv), 2,6-di-*tert*-butyl-1,4-benzoquinone (87 mg, 0.395 mmol, 2 equiv) and a solution of TFA in dioxane (0.0125 M, 0.79 mL, 0.05 equiv) at 100 ºC for 22 h afforded, after column chromatography (20 % dichloromethane in hexanes), 38.6 mg (52 %) of pyrrole **11c** as a colorless film. ^{1}H NMR (500 MHz, $CDCl_3$) δ 7.14 (t, *J* = 7.9 Hz, 1H), 6.97 (s, 2H), 6.81 (m, 1H), 6.71 (dd, *J* = 8.3, 2.6 Hz, 1H), 6.51 (m, 1H), 6.46 (dd, *J* = 3.6, 1.8 Hz, 1H), 6.35 (t, *J* = 3.2 Hz, 1H), 5.20 (s, 1H), 3.55 (s, 3H), 1.34 (s, 18H). ^{13}C NMR (126 MHz, $CDCl_3$) δ 159.0, 152.5, 136.6, 134.6, 133.9, 132.4, 129.0, 124.0, 122.9, 121.1, 113.2, 112.9, 109.7, 108.6, 54.9, 34.5, 30.2. FTIR 3639, 2959, 1604, 1478, 1437, 1208 cm^{-1}. HRMS (ESI) *m/z* calcd for $[C_{25}H_{32}NO_2]^+$ 378.2433, found 378.2448.

Preparation of 2,6-di-*tert*-butyl-4-(2-(2,6-difluorophenyl)-1*H*-pyrrol-1-yl)phenol (11d)

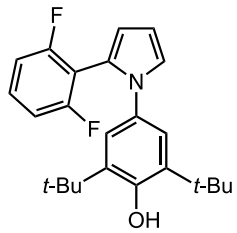

11d

Following General Procedure D, amine **10d** (60.2 mg, 0.329 mmol, 1 equiv), 2,6-di-*tert*-butyl-1,4-benzoquinone (144.8 mg, 0.657 mmol, 2 equiv) and a solution of TFA in dioxane (0.0125 M, 1.3 mL, 0.05 equiv) at 100 ºC for 22 h afforded, after column chromatography (15 % dichloromethane in hexanes), 81.4 mg (65 %) of pyrrole **11d** as a light blue solid. m.p.: 133–134 ºC. ^{1}H NMR (500 MHz, $CDCl_3$) δ 7.20 (tt, *J* = 8.4, 6.3 Hz, 1H), 7.06 (dd, *J* = 2.8, 1.8 Hz, 1H), 6.92 (s, 2H), 6.81 (dd, *J* = 8.3, 6.9 Hz, 2H), 6.45 (dd, *J* = 3.6, 1.7 Hz, 1H), 6.41 (dd, *J* = 3.6, 2.8 Hz, 1H), 5.12 (s, 1H), 1.31 (s, 18H). ^{13}C NMR (126 MHz, $CDCl_3$) δ 161.0 (dd,

J = 248.9, 6.3 Hz), 152.4, 136.3, 132.3, 129.4 (t, *J* = 10.0 Hz), 123.6, 121.4, 120.0, 112.7, 111.79 (t, *J* = 19.9 Hz), 111.4 – 111.0 (m), 108.9, 34.4, 30.2. ^{19}F NMR (471 MHz, $CDCl_3$) δ -110.28 (m). FTIR 3636, 2962, 2878, 1590, 1473, 1214 cm^{-1}. HRMS (ESI) *m/z* calcd for $[C_{24}H_{28}F_2NO]^+$ 384.2133, found 384.2142.

Preparation of 2,6-di-*tert*-butyl-4-(2-(2,3-dihydrobenzofuran-5-yl)-1*H*-pyrrol-1-yl)phenol (11e)

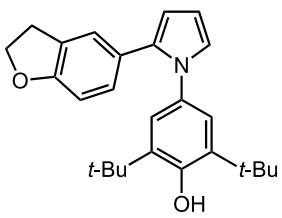

11e

Following General Procedure D, amine **10e** (84 mg, 0.444 mmol, 1 equiv), 2,6-di-*tert*-butyl-1,4-benzoquinone (195.6 mg, 0.888 mmol, 2 equiv) and a solution of TFA in dioxane (0.0125 M, 1.8 mL, 0.05 equiv) at 100 ºC for 22 h afforded, after column chromatography (30 % dichloromethane in hexanes), 61.1 mg (35 %) of pyrrole **11e** as a light orange solid. m.p.: 136–137 ºC. ^{1}H NMR (500 MHz, $CDCl_3$) δ 6.94 (s, 2H), 6.92 (m, 2H), 6.86 (dd, *J* = 8.2, 1.9 Hz, 1H), 6.64 (d, *J* = 8.2 Hz, 1H), 6.32 (m, 2H), 5.16 (s, 1H), 4.53 (t, *J* = 8.6 Hz, 2H), 3.09 (t, *J* = 8.6 Hz, 2H), 1.34 (s. 18H). ^{13}C NMR (126 MHz, $CDCl_3$) δ 158.8, 152.3, 136.4, 134.2, 132.4, 128.9, 126.5, 126.2, 125.5, 123.1, 122.7, 108.9, 108.7, 108.3, 71.4, 34.5, 30.3, 29.8. FTIR 3638, 2960, 1493, 1441, 1211, 1154 cm^{-1}. HRMS (ESI) *m/z* calcd for $[C_{26}H_{32}NO_2]^+$ 390.2433, found 390.2451.

Preparation of 2,6-di-*tert*-butyl-4-(2-(4-methylphenyl)-5-phenyl-1*H*-pyrrol-1-yl)phenol (11f)

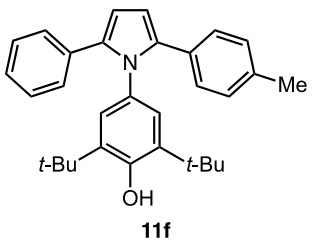

11f

Following General Procedure D, amine **10f** (76 mg, 0.32 mmol, 1 equiv), 2,6-di-*tert*-butyl-1,4-benzoquinone (141 mg, 0.64 mmol, 2 equiv) and a solution of TFA in dioxane (0.0125 M, 1.3 mL, 0.05 equiv) at 100 ºC for 22 h afforded, after column

chromatography (10–15 % dichloromethane in hexanes), 82 mg (59 %) of pyrrole **11f** as a white solid. m.p.: 147–149 ºC. ^{1}H NMR (500 MHz, $CDCl_3$) δ 7.21 – 7.12 (m, 3H), 7.08 (m, 2H), 7.00 (d, *J* = 8.0 Hz, 2H), 6.97 (d, *J* = 7.9 Hz, 2H), 6.68 (d, *J* = 1.2 Hz, 2H), 6.46 (d, *J* = 3.6 Hz, 1H), 6.44 (d, *J* = 3.6 Hz, 1H), 5.11 (s, 1H), 2.30 (s, 3H), 1.18 (s, 18H). ^{13}C NMR (126 MHz, $CDCl_3$) δ 152.4, 135.9, 135.7, 135.3, 133.9, 131.0, 130.1, 129.1, 129.1, 128.5, 127.8, 126.1, 125.5, 109.2, 108.9, 34.3, 30.1, 21.2. FTIR 3638, 2960, 2892, 1604, 1438, 1210, 1153 cm^{-1}. HRMS (ESI) *m/z* calcd for $[C_{31}H_{36}NO]^+$ 438.2797, found 438.2791.

Evidence for Carbocationic Intermediate

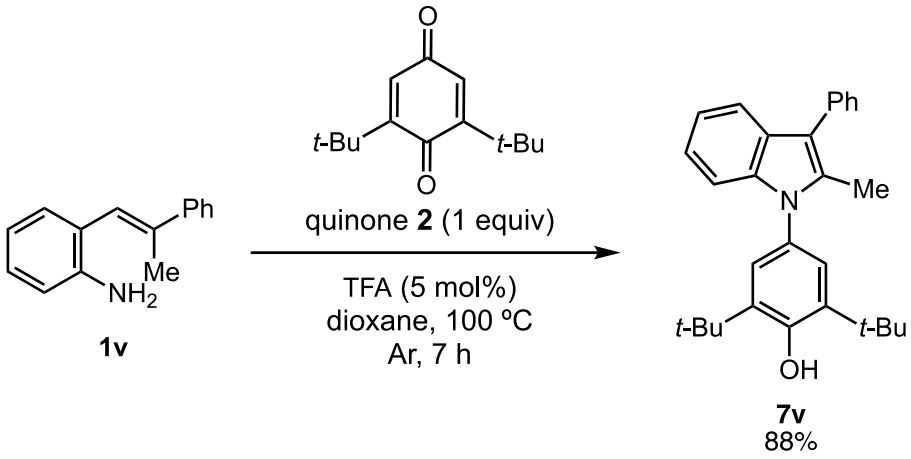

Following General Procedure C, amine **1v** (72.7 mg, 0.347 mmol, 1 equiv), 2,6-di-*tert*-butyl-1,4-benzoquinone **2** (76.5 mg, 0.347 mmol, 1 equiv), TFA (~1.3 μL, 0.017 mmol, 0.05 equiv), and dioxane (1.4 mL) at 100 ºC for 6 h afforded, after column chromatography (30 % dichloromethane in hexanes), 126 mg (88 %) of indole **7v** as a white foam. m.p.: 150–151 ºC. ^{1}H NMR (500 MHz, $CDCl_3$) δ 7.71 (m, 1H), 7.59 (d, *J* = 7.9 Hz, 2H), 7.49 (t, *J* = 7.4 Hz, 2H), 7.32 (td, *J* = 7.4, 1.3 Hz, 1H), 7.18 (s, 2H), 7.14 (m, 3H), 5.36 (s, 1H), 2.35 (d, *J* = 1.0 Hz, 3H), 1.48 (d, *J* = 1.2 Hz, 18H). ^{13}C NMR (126 MHz, $CDCl_3$) δ 153.4, 138.0, 137.0, 135.9, 134.1, 129.8, 129.5, 128.6, 127.1, 125.9, 124.8, 121.6, 120.2, 118.7, 114.7, 110.4, 34.7, 30.5, 12.3. FTIR 3660, 3089, 2973, 1614, 1467, 1440 cm^{-1}. HRMS (ESI) *m/z* calcd for $[C_{29}H_{34}NO]^+$ 412.2640, found 412.2646.

Structural assignment of **7v** was made based on ^{1}H, ^{13}C, NOESY, DEPT, HSQC and NOESY experiments. Key correlations are shown below in Figures B6 and B7.

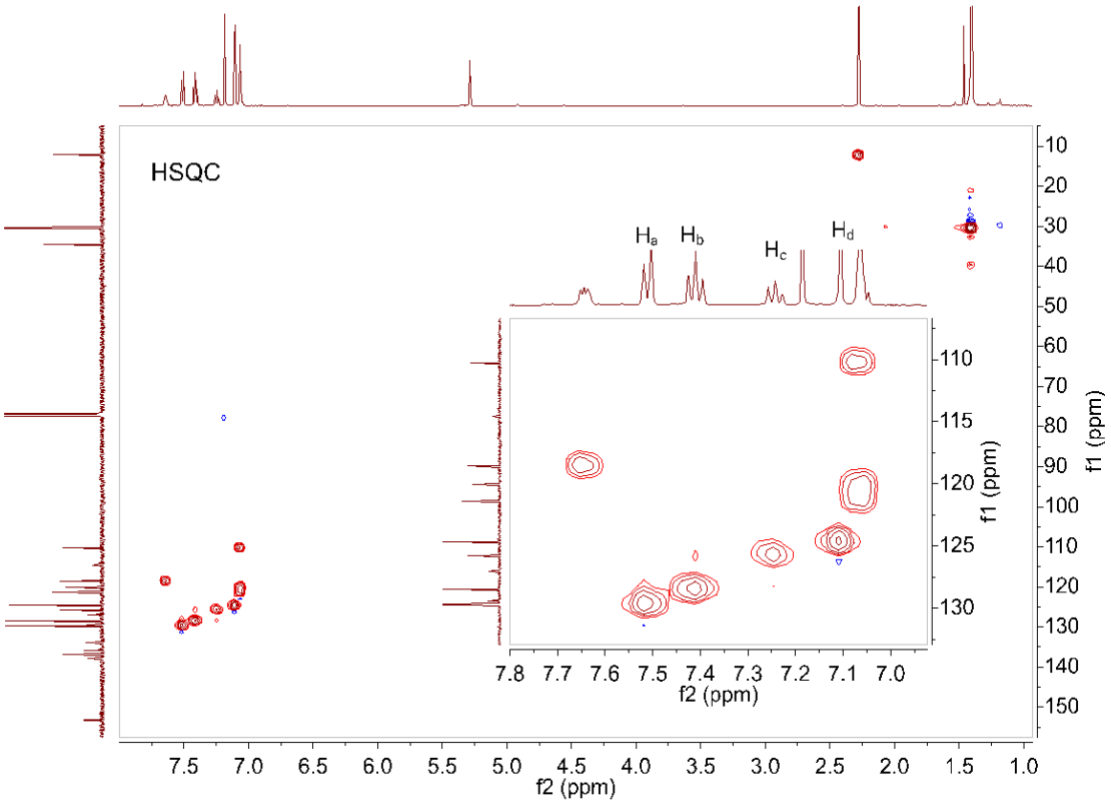

Figure B6. HSQC NMR spectra of **7v**.

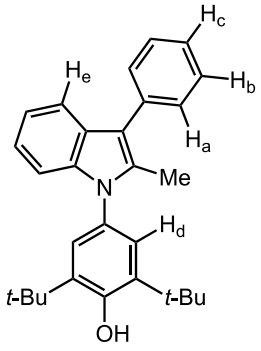

7v

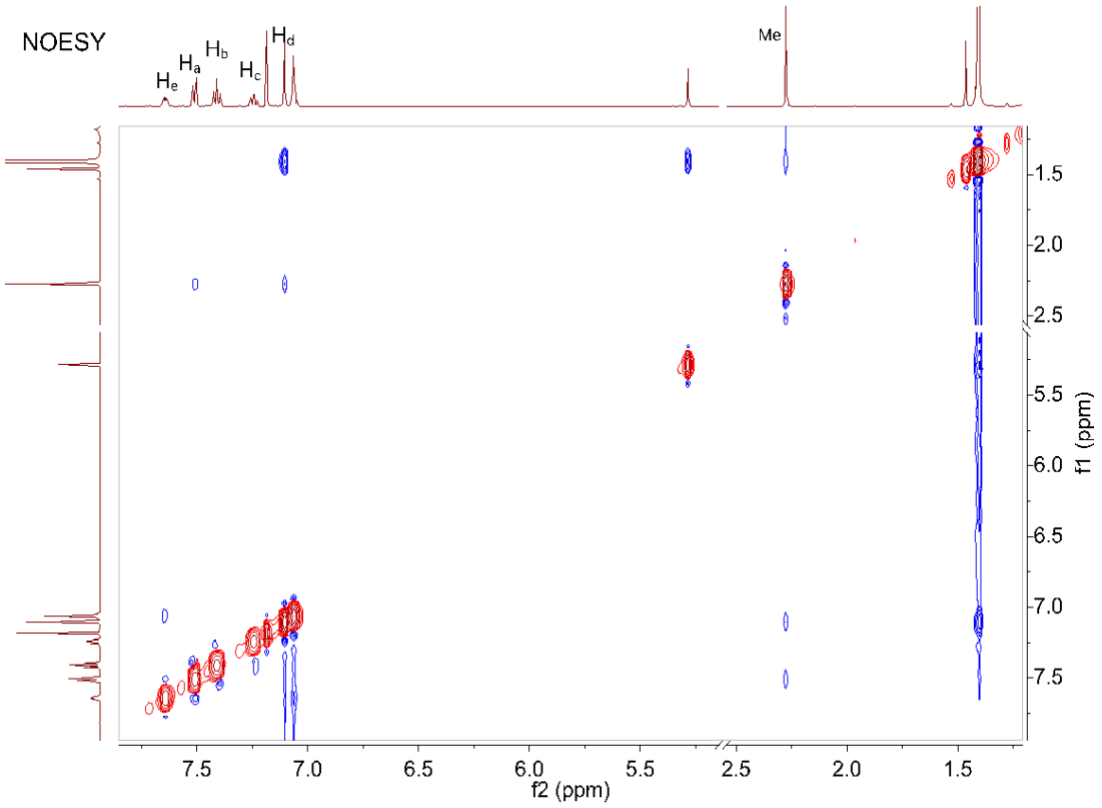

Figure B7. NOESY NMR spectra of **7v**.

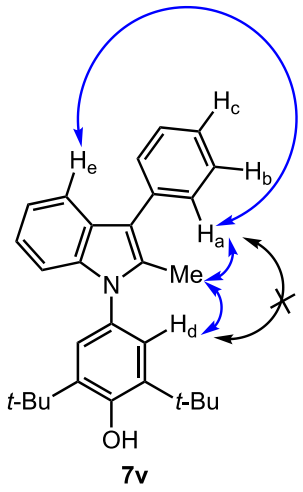

7v

Oxidative Dearylation of Indole 7a: Preliminary Experiments

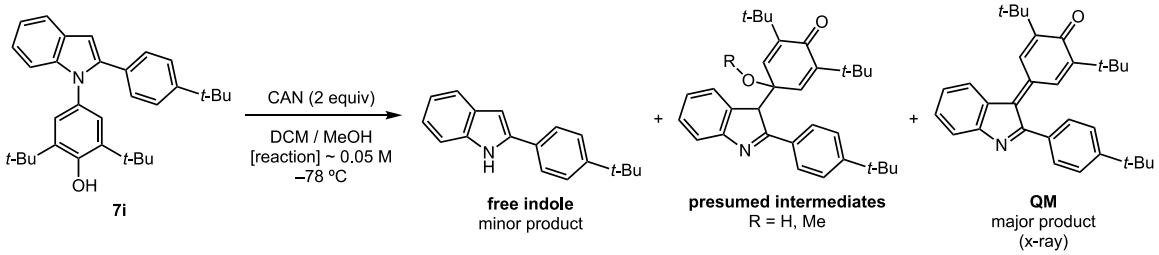

Initial oxidative dearylation experiments were performed with N-aryl indole **7i**. Experiments run at room temperature led to complex mixtures of products. At low temperature (–78 ºC) and concentration ~0.05 M, the desired free indole was formed in low yields, together with other byproducts, such as quinone methide **QM** which was isolated and characterized by NMR and x-ray crystallography. Based on the integrations in the ^{1}H NMR spectra of the crude reaction mixtures, we tentatively assigned the structures of byproducts that could not be isolated. They are thought to be the tertiary alcohol or corresponding methyl ether that likely result from nucleophilic addition of the free indole to the iminium species generated by 2e^{-} oxidation of **7i**, followed by hydrolysis/methanolysis. Acid-catalyzed hydrolysis of the crude mixture allowed for conversion of all byproducts to the desired indole.

Characterization of QM: Dark yellow solid. m.p.: 142–143 °C. Crystals suitable for X-ray diffraction analysis were grown through slow evaporation of a methanolic solution of the title compound at room temperature (*vide infra*). ^{1}H NMR (500 MHz, $CDCl_3$) δ 8.10 (d, J = 2.6 Hz, 1H), 7.83 (d, J = 7.7 Hz, 1H), 7.60 (dd, J = 7.7, 1.1 Hz, 1H), 7.50 (d, J = 8.4 Hz, 2H), 7.46 (d, J = 8.3 Hz, 2H), 7.40 (td, J = 7.6, 1.0 Hz, 1H), 7.31 – 7.19 (m, 1H), 7.15 (d, J = 2.5 Hz, 1H), 1.41 (s, 9H), 1.35 (s, 9H), 0.93 (s, 9H). ^{13}C NMR (151 MHz, $CDCl_3$) δ 186.8, 170.7, 156.0, 153.1, 152.9, 149.3, 142.1, 137.9, 134.8, 130.8, 130.5, 130.3, 130.1, 128.9, 128.8,

126.2, 125.79, 125.76, 121.9, 36.5, 35.6, 35.0, 31.4, 29.9, 29.2. FTIR 3050, 2955, 2923, 1617, 1447, 1364, 1206, 1150 cm^{-1}. HRMS (ESI) *m/z* calcd for $[C_{32}H_{38}NO]^+$ 452.2953, found 452.2962.

Hypothesis for Unproductive Dimerization

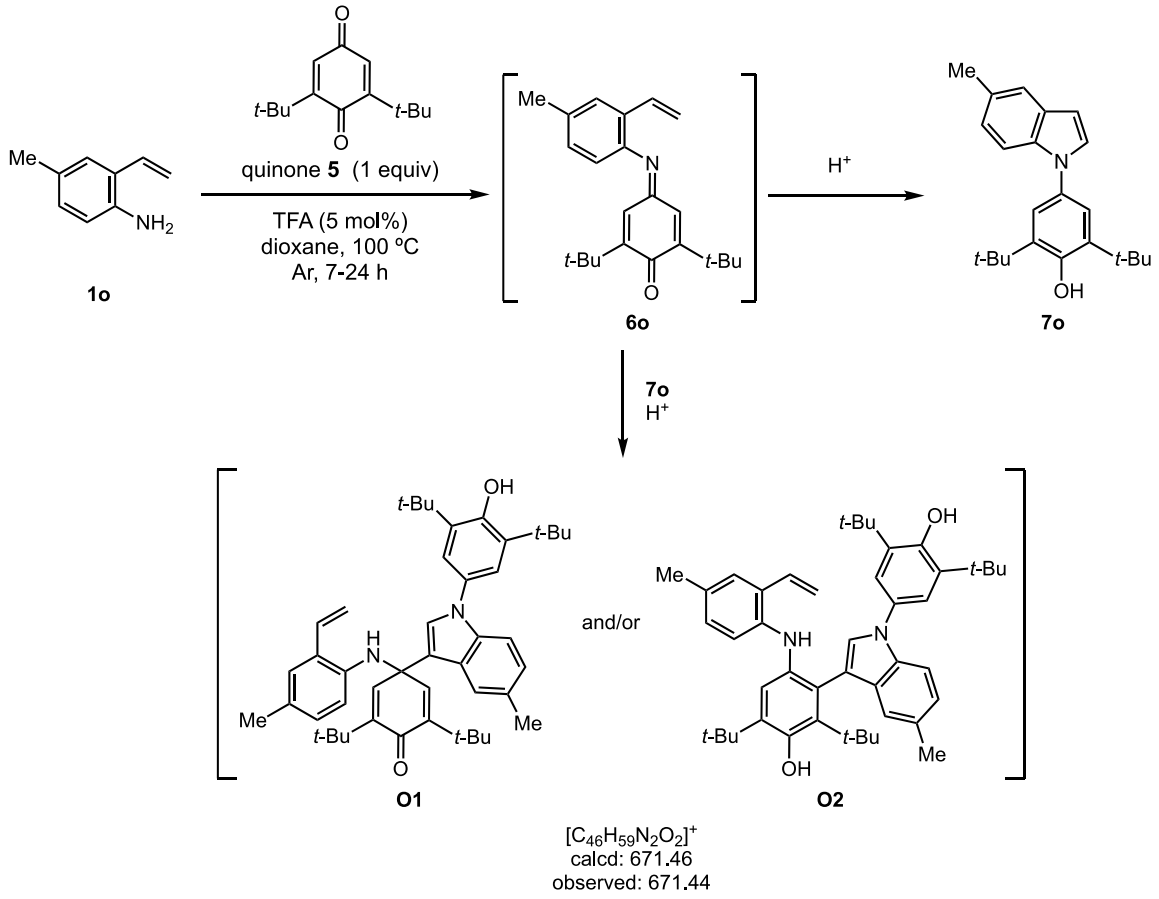

Under standard reaction conditions (0.25 M aniline in dioxane, quinone **2** (1 equiv), 5 mol % TFA, 100 ºC) aniline **1o**, afforded the expected indole product **7o** in only 15 % yield. Analysis of the reaction mixture and by low resolution mass spectrometry suggested the formation of dimerization product(s), judging from the observed mass peaks. Attempts to purify/isolate a higher molecular weight product (or products) were unsuccessful. However, based on the obtained MS data, we conjecture that the presumed products originate by either 1,2- or 1,4-addition of the nucleophilic indole product **7o** to the electrophilic iminoquinone intermediate **6o** aided by the acid catalyst to give **O1** or **O2**, respectively. Consistent with

this side reaction is the fact that dilution of the reaction to 0.04 M provided indole **7o** in higher yield (66 %).

Intermolecular Alkene Hydroamination with Iminoquinone 12: Attempted Desilylation

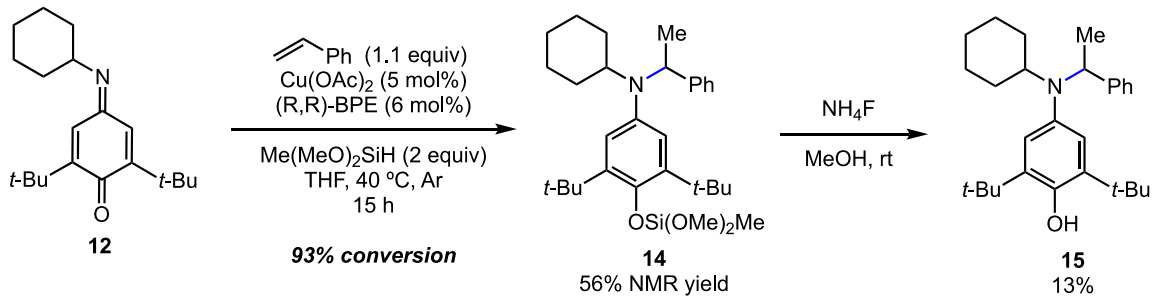

The primary product (**14**, 56 % NMR yield) was prepared according to the procedure in the main text of Chapter 5. The reaction was concentrated *in vacuo* and analyzed by ^{1}H NMR (see Figure B8). **14** was partially purified by silica gel column chromatography (first column: 3 % EtOAc in hexanes; second column: gradient 20–50 % DCM in hexanes) leading to partial desilylation of 14 to give phenol 15 (14:15 ratio = 1:1). The mixture of **14** and **15** (9.3 mg) was dissolved in THF (0.5 mL) and treated with $NH_4Cl_{(aq)}$ and solid KF (20 mg) at room temperature for 2 h. The reaction was then extracted with EtOAc, dried over Na_2SO_4, and concentrated *in vacuo* to give again a mixture of **14** and **15** (1:3 ratio). Silica gel column chromatography (gradient 20–70 % DCM in hexanes) afforded 15 (5.1 mg, 13 %) as a light-yellow film. ^{1}H NMR (400 MHz, $CDCl_3$) δ 7.40 – 7.34 (m, 2H), 7.31 – 7.26 (m, 2H), 7.22 – 7.15 (m, 1H), 6.68 (s, 2H), 4.75 (s, 1H), 4.59 (q, *J* = 6.7 Hz, 1H), 3.04 (ddd, *J* = 10.8, 7.5, 3.2 Hz, 1H), 2.01 – 1.93 (m, 1H), 1.86 (m, 1H), 1.76 – 1.68 (m, 2H), 1.54 (m, 1H), 1.35 (s, 18H), 1.30 (d, *J* = 6.6 Hz, 3H), 1.18 (dddd, *J* = 14.0, 11.8, 6.6, 2.9 Hz, 4H), 1.08 – 0.93 (m, 1H). ^{13}C NMR (126 MHz, $CDCl_3$) δ 148.7, 146.4, 138.8, 135.2, 128.1, 127.4, 126.3, 122.0,

58.4, 56.3, 34.4, 32.1, 30.64, 30.52, 26.33, 26.28, 26.25, 21.1. FTIR 3590, 2973, 1471, 1439, 1218 cm^{-1}. HRMS (ESI) *m/z* calcd for $[C_{28}H_{42}NO]^+$ 408.3261, found 408.3255.

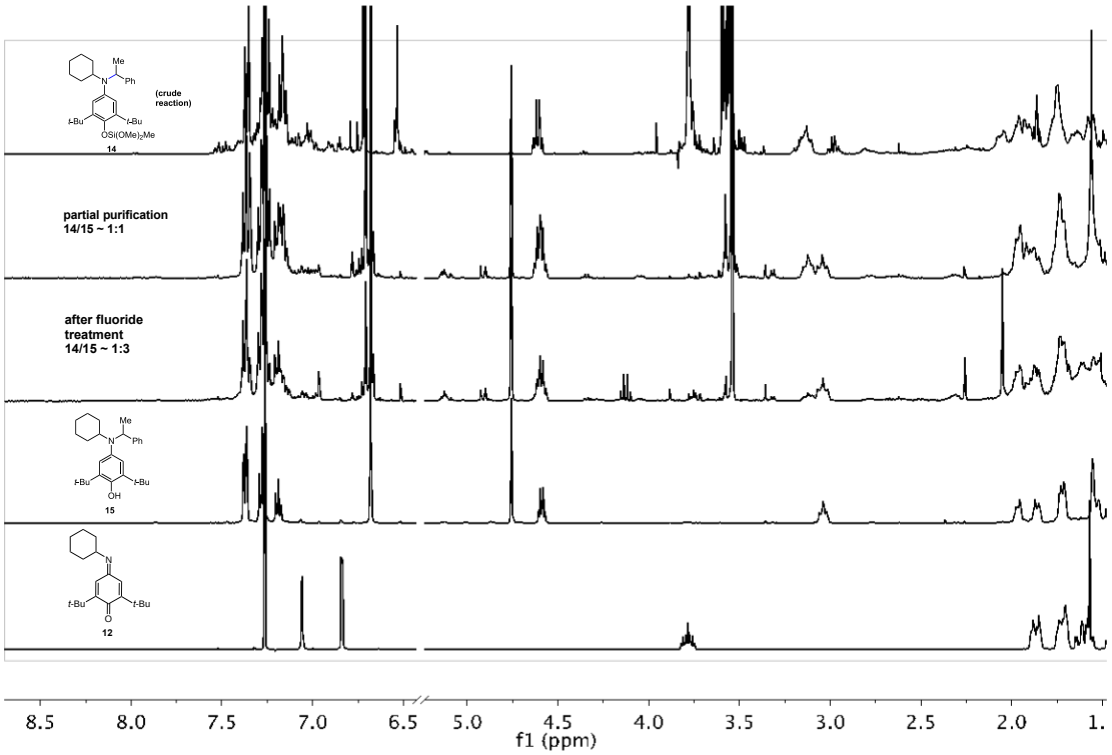

Figure B8. Stacked ^1H NMR spectra of crude intermolecular hydroamination reaction followed by partial purification of the product, treatment with KF, isolated product **15**, and starting iminoquinone **12**.

Synthesis of Representative Iminoquinones for Further Experimentation

Preparation of 4-((2-allylphenyl)imino)-2,6-di-*tert*-butylcyclohexa-2,5-dien-1-one (A1)

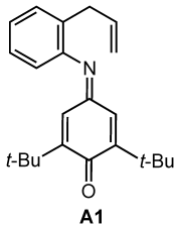

A1

To a 7-mL vial were added a magnetic stir bar, 2-allylaniline (99 mg, 0.743 mmol, 1 equiv), 2,6-di-*tert*-butyl-1,4-benzoquinone (163.8 mg, 0.743 mmol, 1 equiv), THF (3.7 mL), and BF_3•OEt_2 (18 μL, 0.149 mmol, 0.2 equiv). The vial was flushed with Ar and heated in an aluminum block at 70 ºC. After 24 h, the reaction was cooled, opened to air, and concentrated. Flash column chromatography (2.5 % diethyl ether in hexanes) afforded iminoquinone **A1** as a red oil (201 mg, 81 %). ^{1}H NMR (500 MHz, $CDCl_3$) δ 7.26 (d, *J* = 2.9 Hz, 1H), 7.21 (td, *J* = 7.5, 1.6 Hz, 1H), 7.15 (td, *J* = 7.5, 1.4 Hz, 1H), 7.05 (d, *J* = 2.6 Hz, 1H), 6.67 (d, *J* = 2.5 Hz, 1H), 6.59 (dd, *J* = 7.6, 1.4 Hz, 1H), 5.88 (ddt, *J* = 16.7, 10.0, 6.5 Hz, 1H), 5.03 – 4.88 (m, 2H), 3.31 (dt, *J* = 6.6, 1.6 Hz, 2H), 1.34 (s, 9H), 1.17 (s, 9H). ^{13}C NMR (126 MHz, $CDCl_3$) δ 187.9, 158.7, 153.7, 153.1, 148.6, 136.8, 134.6, 131.4, 130.0, 126.6, 125.7, 122.0, 119.7, 115.9, 36.0, 35.8, 35.5, 29.6, 29.5. FTIR 3029, 2960, 1653, 1629, 1478 cm^{-1}. HRMS (ESI) *m/z* calcd for $[C_{26}H_{30}NO]^+$ 336.2322, found 336.2320.

Preparation of 2,6-di-*tert*-butyl-4-((2-phenoxyphenyl)imino)cyclohexa-2,5-dien-1-one (A2)

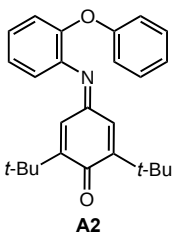

A2

To a 7-mL vial were added a magnetic stir bar, 2-phenoxyaniline (92.6 mg, 0.5 mmol, 1 equiv), 2,6-di-*tert*-butyl-1,4-benzoquinone (110.2 mg, 0.5 mmol, 1 equiv), dioxane (1.25 mL), and TFA (2 μL, 0.025 mmol, 0.05 equiv). The vial was flushed with Ar, capped and heated in an aluminum block at 100 ºC. After 5 h, the reaction was cooled, opened to air, and concentrated. Flash column chromatography (first column: 20 % DCM in hexanes; second column: 4 % acetone in

hexanes) afforded iminoquinone **A2** (139.5 mg, 72 %) as a red oil. ^{1}H NMR (500 MHz, $CDCl_3$) δ 7.26 (m, 2H), 7.20 – 7.11 (m, 2H), 7.06 – 7.00 (m, 2H), 6.94 (d, *J* = 2.6 Hz, 1H), 6.92 – 6.85 (m, 3H), 6.75 (d, *J* = 2.6 Hz, 1H), 1.28 (s, 9H), 1.21 (s, 9H). ^{13}C NMR (126 MHz, $CDCl_3$) δ 187.8, 160.0, 157.1, 153.4, 153.0, 146.4, 141.5, 134.6, 129.7, 126.5, 124.1, 123.2, 122.5, 122.4, 120.2, 118.3, 35.77, 35.46, 29.57, 29.54. FTIR 3029, 2958, 1650, 1631, 1362, 1247 cm^{-1}. HRMS (ESI) *m/z* calcd for $[C_{26}H_{30}NO_2]^+$ 388.2271, found 388.2263.

Preparation of 2,6-di-*tert*-butyl-4-(*p*-tolylimino)cyclohexa-2,5-dien-1-one (A3)

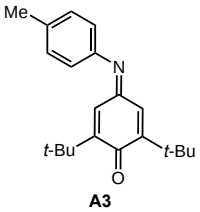

A3

To a 50-mL round bottom flask were added a magnetic stir bar, 4-methylaniline (580 mg, 5.45 mmol, 1.2 equiv), 2,6-di-*tert*-butyl-1,4-benzoquinone (1 g, 4.54 mmol, 1 equiv), THF (19 mL) and $BF_3{\cdot}OEt_2$ (110 μL, 0.91 mmol, 0.2 equiv). A reflux condenser was attached to the flask, the system was flushed with Ar and heated in an oil bath at 70 ºC. After 5.5 h the reaction cooled, opened to air and concentrated *in vacuo*. Flash column chromatography (40 % DCM in hexanes) afforded iminoquinone **A3** (777 mg, 55 %) as a red solid. m.p.: 72–73 ºC. ^{1}H NMR (500 MHz, $CDCl_3$) δ 7.20 (m, 2H), 7.04 (d, *J* = 2.6 Hz, 1H), 6.88 (d, *J* = 2.6 Hz, 1H), 6.81 (m, 2H), 2.38 (s, 3H), 1.33 (s, 9H), 1.21 (s, 9H). ^{13}C NMR (126 MHz, $CDCl_3$) δ 188.0, 158.5, 153.6, 152.9, 147.4, 135.6, 135.0, 129.7, 121.8, 121.4, 35.9, 35.5, 29.61, 29.59, 21.2. FTIR 3030, 2958, 2867, 1649, 1631, 1499, 1362 cm^{-1}. HRMS (ESI) *m/z* calcd for $[C_{21}H_{28}NO]^+$ 310.2165, found 310.2157.

Attempted Intermolecular Cyclization with Unconjugated π-Systems

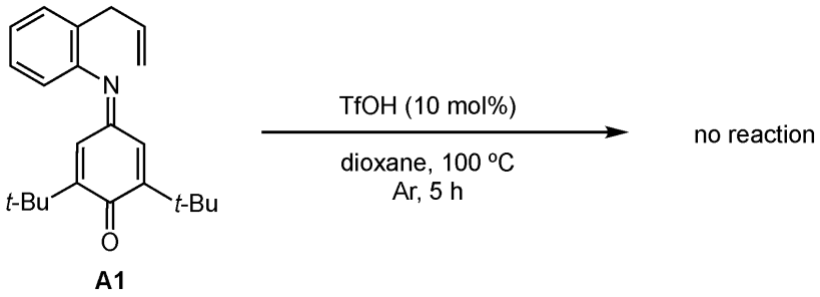

To a 7-mL vial were added a magnetic stir bar, iminoquinone **A1** (52.6 mg, 0.157 mmol, 1 equiv), and dioxane (0.6 mL). The vial was capped and flushed with Ar. Triflic acid (~ 2 μL, 0.016 mmol, ~ 0.1 equiv) was added and the vial was heated in an aluminum block at 100 °C for 5 h. The reaction was cooled at room temperature and analyzed by TLC. No conversion was observed.

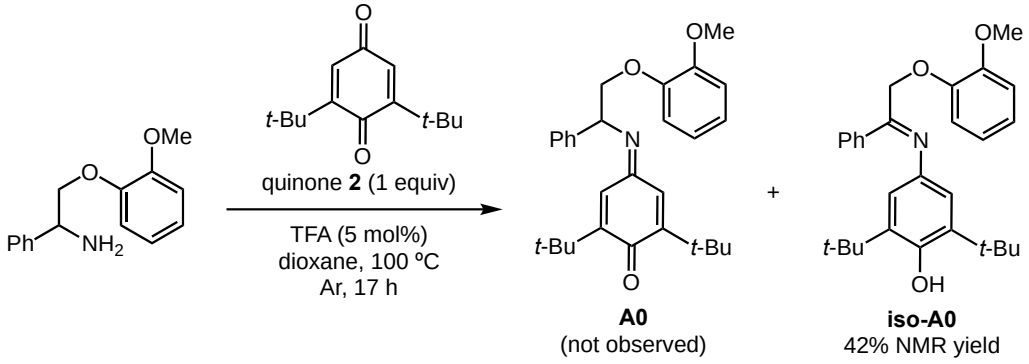

To a 7-mL vial were added a magnetic stir bar, 2-(2-methoxyphenoxy)-1-phenylethan-1-amine (101 mg, 0.415 mmol, 1 equiv), 2,6-di-*tert*-butyl-1,4-benzoquinone (91.5 mg, 0.415 mmol, 1 equiv), and dioxane (1.7 mL). The vial was capped and flushed with Ar. TFA (~ 2 μL, 0.025 mmol, ~ 0.05 equiv) was added and the vial was heated in an aluminum block at

100 ºC for 17 h. The reaction was cooled at room temperature and opened to air, and 1,3,5-trimethoxybenzene (69.8 mg, 0.415 mmol, 1 equiv) was added. The reaction mixture was concentrated and analyzed by ^{1}H NMR (75 % conversion). Remarkably, the crude ^{1}H NMR was not consistent with the expected iminoquinone **A0**, but with its tautomer **iso-A0**. The structural assignment of **iso-A0** was made based on the following resonances: 8.01 (m, 2H, *ortho* protons on phenyl group). 7.61 (m, 1H, *para* proton on phenyl group), 6.89 (s, 2H, phenolic C–H), 5.35 (s, 2H, methylene protons), 3.88 (s, 3H, OMe protons), 1.42 (s, 18H, equivalent *tert*-butyl protons).

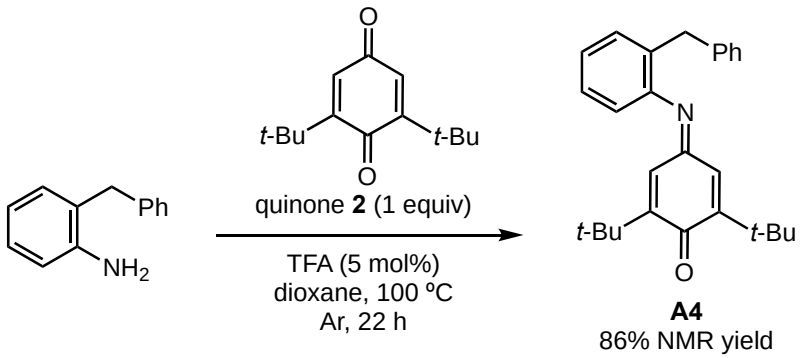

A4
86% NMR yield

To a 7-mL vial were added a magnetic stir bar, amine 2-benzylaniline (91.7 mg, 0.5 mmol, 1 equiv), 2,6-di-*tert*-butyl-1,4-benzoquinone (110.2 mg, 0.5 mmol, 1 equiv) and dioxane (2 mL). The vial was capped and flushed with Ar. TFA (~2 μL, 0.025 mmol, ~0.05 equiv) was added and the vial was heated in an aluminum block at 100 ºC for 22 h. The reaction was cooled at room temperature and opened to air, and 1,3,5-trimethoxybenzene (84.1, 0.5 mmol, 1 equiv) was added. The reaction mixture was concentrated and analyzed by ^{1}H NMR (88 % conversion).

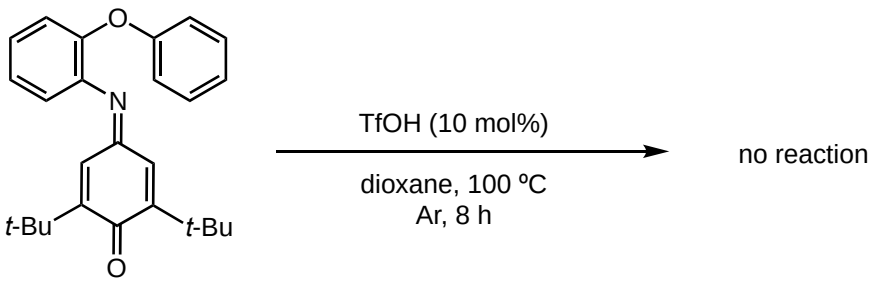

A2

To a 7-mL vial were added a magnetic stir bar, iminoquinone **A2** (92.6 mg, 0.5 mmol, 1 equiv), and dioxane (2 mL). The vial was capped and flushed with Ar. Triflic acid (~2 μL, 0.016 mmol, ~0.1 equiv) was added and the vial was heated in an aluminum block at 100 ºC for 5 h. The reaction was cooled at room temperature and analyzed by TLC. No conversion was observed.

Attempted Intermolecular Amination of π-Nucleophiles with Iminoquinone A6

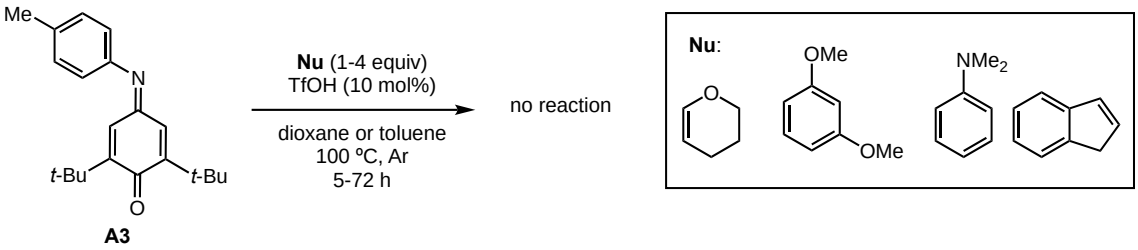

To a 7-mL vial were added a magnetic stir bar, iminoquinone **A3** (1 equiv), nucleophile (1–4 equiv), and dioxane (2 mL). The vial was capped and flushed with Ar. Triflic acid (0.1 equiv) was added and the vial was heated in an aluminum block at 100 ºC for 5–72 h. The reaction was cooled at room temperature, opened to air, quenched by adding a few drops of triethylamine, and analyzed by TLC and NMR. Little or no conversion was observed in any of these experiments.

Evaluation of Iminoquinones derived from 2-(Hetero)aryl Anilines – Phenanthridine Synthesis (Select Example)

Synthesis of 2-arylaniline S5[14]

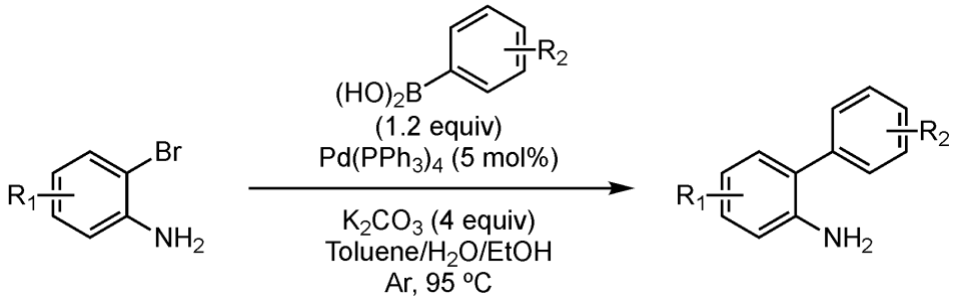

To a round bottom flask were added a magnetic stir bar, 2-bromoaniline derivative (1 equiv), arylboronic acid (1.2 equiv), potassium carbonate (4 equiv) and $Pd(PPh_3)_4$ (0.05 equiv). The flask was evacuated/backfilled with Ar (3 cycles) and toluene, water, and ethanol (5:2:1 ratio, reaction concentration with respect to aniline = 0.15 M) were added by syringe. The reaction was heated in an oil bath to 95 ºC for 14-18 h. The reaction was then cooled to room temperature, opened to air, diluted with water (5 mL), and extracted with dichloromethane (3 x 30 mL). The combined organic extracts were washed with water and brine, dried over sodium sulfate, and concentrated. The aniline derivative was purified by flash column chromatography.

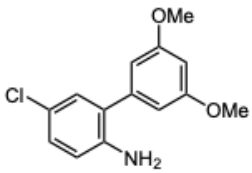

S5

Amine **S5** was obtained in 86% yield as a light-yellow oil. ^{1}H NMR (500 MHz, $CDCl_3$) δ 7.15 – 7.06 (m, 2H), 6.68 (d, *J* = 8.4 Hz, 1H), 6.55 (d, *J* = 2.0 Hz, 2H), 6.47 (d, *J* = 2.1 Hz, 1H), 3.82 (s, *J* = 1.3 Hz, 8H). ^{13}C NMR (126 MHz, $CDCl_3$) δ 161.3, 142.2, 140.3, 129.8, 128.9, 128.4, 123.1, 116.8, 107.0, 100.0, 55.6.

Preparation of 3,5-di-*tert*-butyl-2'-chloro-7',9'-dimethoxy-5'*H*-spiro[cyclohexane-1,6'-phenanthri-dine]-2,5-dien-4-one (P1)

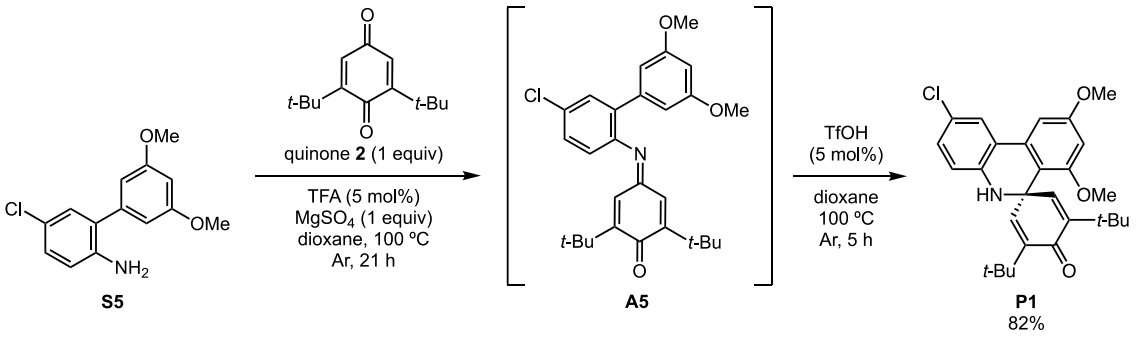

To a 10-mL round bottom flask were added a magnetic stir bar, amine **S5** (263.7 mg, 1 mmol, 1 equiv), 2,6-di-*tert*-butyl-1,4-benzoquinone (220.3 g, 1 mmol, 1 equiv), magnesium sulfate (120.4 mg, 1 mmol, 1 equiv), and dioxane (4 mL). The flask was capped with a septum and flushed with Ar, and TFA (8 μL, 0.1 mmol, 0.1 equiv) was added. The reaction was heated in an oil bath at 100 ºC for 21 h. At this point, nearly complete conversion of amine **S5** to iminoquinone **A5** was observed by TLC. Triflic acid (4 μL, 0.05 mmol, 0.05 equiv) was added and heating continued for 5 h. The reaction was then cooled and opened to air, and a few drops of triethylamine were added. The reaction was concentrated *in vacuo*. Flash column chromatography (5–10 % EtOAC in hexanes) followed by crystallization from hexanes/DCM at room temperature afforded phenanthridine **P1** (381.6, 82 %) as a yellow solid. m.p.: 243–245 ºC. ^{1}H NMR (600 MHz, $CDCl_3$) δ 7.57 (d, *J* = 2.3 Hz, 1H), 7.05 (dd, *J* = 8.4, 2.3 Hz, 1H), 6.88 (d, *J* = 2.3 Hz, 1H), 6.68 (s, 2H), 6.53 (d, *J* = 8.4 Hz, 1H), 6.35 (d, *J* = 2.3 Hz, 1H), 3.89 (s, 3H), 3.58 (s, 3H), 1.21 (s, 18H). ^{13}C NMR (151 MHz, $CDCl_3$) δ 187.0, 160.8, 158.2, 144.0, 141.4, 140.5, 132.5, 129.2, 123.9, 123.6, 120.7, 115.9, 114.2,

99.5, 99.0, 55.6, 55.1, 54.8, 3.70, 29.7. HRMS (ESI) *m/z* calcd for $[C_{28}H_{33}ClNO_3]^+$ 466.2143, found 466.2132.

Crystallographic Information

Crystals of QM suitable for single crystal x-ray diffraction were grown through slow evaporation of a concentrated methanolic solution of the material at room temperature. Crystals of P1 suitable for single x-ray diffraction were grown from a solution of DCM/hexanes at room temperature. Crystallographic data for compounds **P1** and **QM** were deposited in the CCDC database with deposition numbers 1977125 and 1977124, respectively. X-rays were provided by a Bruker MicroStar microfocus rotating anode operating at 45kV and 60 mA and equipped with dual (Platinum 135 and Apex II) CCD detectors and Helios multilayer x-ray optics.

Table B1: Crystal Refinement Data

	P1 (q99h)	**QM** (v33d)
CCDC accession code	1977125	1977124
Empirical formula	$C_{28}H_{32}ClNO_3$	$C_{32}H_{37}NO$
Formula weight	465.99	451.62
Temperature	200(2) K	200(2) K
Wavelength	1.54178 Å	1.54178 Å
Crystal system	monoclinic	monoclinic
Space group	$P2_1/c$	$P2_1/n$
a	25.3509(7) Å	5.9632(3) Å
b	11.9191(3) Å	38.327(2) Å
c	17.6258(5) Å	33.9389(19) Å
a	90°	90°
β	109.3893(10)°	94.962(2)°
γ	90°	90°
Volume	5023.8(2) $Å^3$	7727.8(7) $Å^3$
Z	8	12
Density (calculated)	1.232 Mg/m^3	1.165 Mg/m^3
Absorption coefficient	1.571 mm^{-1}	0.525 mm^{-1}
F(000)	1984	2928
Crystal size	0.180 × 0.150 × 0.140 mm^3	0.230 × 0.085 × 0.020 mm^3
Theta range	3.697 to 70.365°	1.152 to 68.304°
Index ranges	$-29 \le h \le 30$, $-14 \le k \le 14$, $-19 \le l \le 21$	$-7 \le h \le 5$, $-45 \le k \le 43$, $-40 \le l \le 38$
Reflections collected	45465	76418
Independent reflections	9296 [R_{int} = 0.0321]	13786 [R_{int} = 0.0916]
Completeness/θ_{max}	99.5%/66.000°	99.7%/66.000°
Absorption correction	Multi-scan	Multi-scan
Max. and min. transmission	1.000 and 0.814	1.000 and 0.720
Refinement method	Full-matrix least-squares on F^2	Full-matrix least-squares on F^2
Data / restraints / parameters	9296 / 0 / 620	13786 / 0 / 974
Goodness-of-fit on F^2	1.021	1.016
Final R indices [I>2σ(I)]	R_1 = 0.0524, wR_2 = 0.1399	R_1 = 0.0758, wR_2 = 0.2163
R indices (all data)	R_1 = 0.0578, wR_2 = 0.1451	R_1 = 0.1185, wR_2 = 0.2625
Largest diff. peak and hole	0.676 and -1.082 $e^-/Å^3$	0.319 and -0.252 $e^-/Å^3$

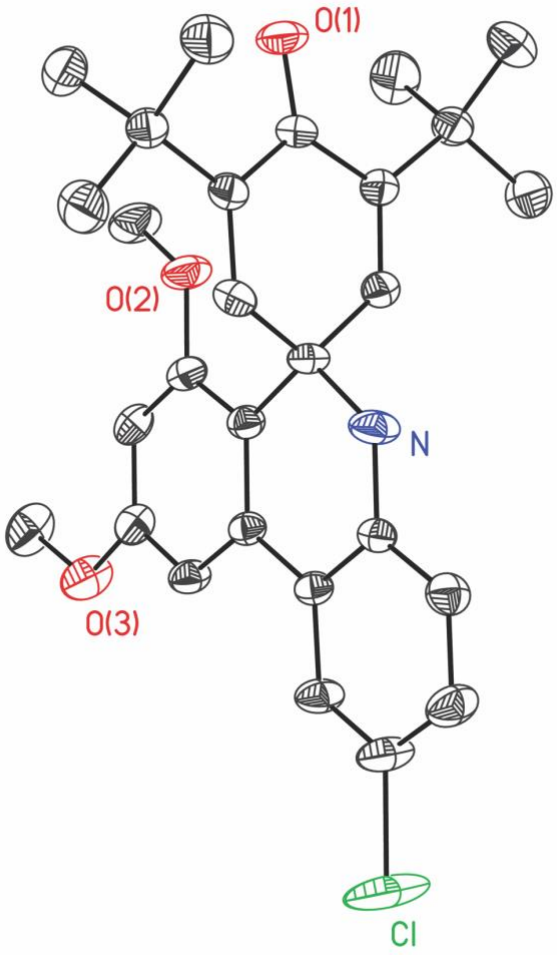

Figure B9. Solid state structure of **P1**. Displacement ellipsoids are shown at the 50 % probability level. All hydrogen atoms are omitted for clarity.

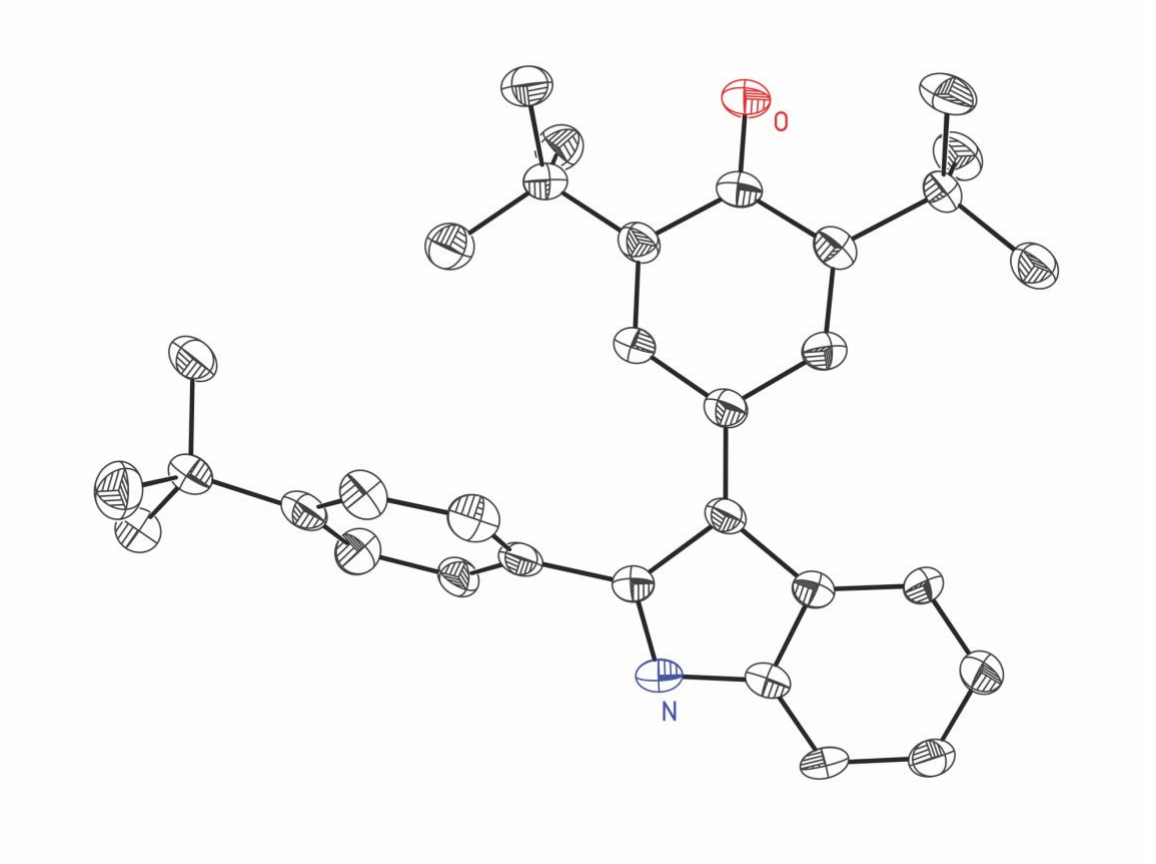

Figure B10. Solid state structure of **QM**. Displacement ellipsoids are shown at the 50 % probability level. All hydrogen atoms are omitted for clarity.

References

[1] Alt, I. T.; Plietker, B., Iron-Catalyzed Intramolecular C(sp^2)-H Amination. *Angew. Chem. Int. Ed.* **2016**, *55*, 1519-1522.

[2] Shen, M.; Leslie, B. E.; Driver, T. G., Dirhodium(II)-catalyzed intramolecular C-H amination of aryl azides. *Angew. Chem. Int. Ed.* **2008**, *47*, 5056-5059.

[3] Ortgies, S.; Breder, A., Selenium-Catalyzed Oxidative C(sp^2)–H Amination of Alkenes Exemplified in the Expedient Synthesis of (Aza-)Indoles. *Org. Lett.* **2015**, *17*, 2748-2751.

[4] Hou, Y.; Ma, J.; Yang, H.; Anderson, E. A.; Whiting, A.; Wu, N., Palladium-catalysed ligand-free reductive Heck cycloisomerisation of 1,6-en-α-chloro-enamides. *Chem. Comm.* **2019**, *55*, 3733-3736.

[5] Nguyen, Q.; Sun, K.; Driver, T. G., Rh_2(II)-Catalyzed Intramolecular Aliphatic C–H Bond Amination Reactions Using Aryl Azides as the N-Atom Source. *J. Am. Chem. Soc.* **2012**, *134*, 7262-7265.

[6] Barmettler, P.; Hansen, H.-J., Acid-Catalyzed [3,3]-Sigmatropic Rearrangements of *N*-Propargylanilines. *Helv. Chim. Acta* **1990**, *73*, 1515-1573.

[7] Youn, S. W.; Ko, T. Y.; Jang, M. J.; Jang, S. S., Silver(I)-Mediated C–H Amination of 2-Alkenylanilines: Unique Solvent-Dependent Migratory Aptitude. *Adv. Synth. Catal*. **2015**, *357*, 227-234.

[8] Lee, B. S.; Lee, J. H.; Chi, D. Y., Novel Synthesis of 2-Chloroquinolines from 2-Vinylanilines in Nitrile Solvent. *J. Org. Chem.* **2002**, *67*, 7884-7886.

[9] Denmark, S. E.; Wang, Z., Cross-coupling of vinylpolysiloxanes with aryl iodides. *J. Organomet. Chem.* **2001**, *624*, 372-375.

[10] Ascic, E.; Buchwald, S. L., Highly Diastereo- and Enantioselective CuH-Catalyzed Synthesis of 2,3-Disubstituted Indolines. *J. Am. Chem. Soc.* **2015**, *137*, 4666-4669.

[11] Harmata, M.; Kahraman, M., A General, Regioselective Synthesis of 2-Alkenylanilines. *Synthesis* **1995**, 713-716.

[12] Niu, C.; Li, J.; Doyle, T. W.; Chen, S.-H., Synthesis of 3-aminopyridine-2-carboxaldehyde thiosemicarbazone (3-AP). *Tetrahedron* **1998**, *54*, 6311-6318.

[13] Mori-Quiroz, L. M.; Londhe, S. S.; Clift, M. D., Formal α-Allylation of Primary Amines by a Dearomative, Palladium-Catalyzed Umpolung Allylation of N-(Aryloxy)imines. *J. Org. Chem.* **2020**, *85*, 14827-14846.

[14] Stokes, B. J.; Jovanović, B.; Dong, H.; Richert, K. J.; Riell, R. D.; Driver, T. G., Rh_2(II)-Catalyzed Synthesis of Carbazoles from Biaryl Azides. *J. Org. Chem.* **2009**, *74*, 3225-3228.